

Andreev tunneling and quasiparticle  
excitations in mesoscopic normal  
metal - superconductor structures



# Andreev tunneling and quasiparticle excitations in mesoscopic normal metal - superconductor structures

**Ville F. Maisi**

Doctoral dissertation for the degree of Doctor of Science in  
Technology to be presented with due permission of the  
School of Science for public examination and debate in Auditorium AS1  
at the Aalto University School of Science (Espoo, Finland) on  
the 30<sup>th</sup> of April 2014 at 12 noon.

**Aalto University**  
**School of Science**  
**Olli V. Lounasmaa Laboratory**  
**PICO group**

**Centre for Metrology and**  
**Accreditation (MIKES)**  
**Electricity group**

**Supervising professor**

Jukka Pekola

**Thesis advisor**

Antti Manninen

**Preliminary examiners**

Alexey Ustinov, Karlsruhe Institute of Technology, Germany

Alexander Melnikov, Russian Academy of Sciences, Russia

**Opponent**

Hugues Pothier, CEA Saclay, France

MIKES Publications  
DOCTORAL DISSERTATIONS 2014

© Ville Maisi

ISBN 978-952-6682-10-5

ISBN 978-952-6682-11-2 (pdf)

ISSN 1235-2704 (printed)

ISSN 1797-9730 (pdf)

Multiprint Oy  
Espoo 2014

Finland

**Author**

Ville F. Maisi

---

**Name of the doctoral dissertation**

Andreev tunneling and quasiparticle excitations in mesoscopic normal metal - superconductor structures

---

**Publisher** MIKES

---

**Unit** Olli V. Lounasmaa Laboratory, School of Science

---

**Series** MIKES Publications DOCTORAL DISSERTATIONS 2014

---

**Field of research** Low Temperature Physics

---

**Manuscript submitted** 15.1.2014**Date of the defense** 30.4.2014

---

**Permission to publish granted** 11.3.2014**Language** English

---

**Article dissertation** (summary + original articles)

---

**Abstract**

Mesoscopic physics deals with systems whose size is between everyday macroscopic scale and the microscopic scale of individual atoms. With mesoscopic structures the flow of single electrons can be controlled. This thesis focuses on the control of single electrons with normal metal - superconductor structures. The emphasis is put on understanding the limitations of the control in the so-called SINIS turnstile, which is a device transporting one electron at a time. By repeating the drive with frequency  $f$ , the resulting electrical current in ideal operation  $I = ef$  could be utilized as the new definition in the SI unit system. Here  $e$  is the elementary charge.

In the first part of the thesis, we review the physics of tunnel-coupled normal metals and superconductors and present the operation principle of the SINIS turnstile. We then show parallel operation of ten such devices. This allows one to reach larger currents required for high accuracy measurements. In addition we show that the experimental setup needs to be carefully designed in order to avoid spurious effects due to environmentally assisted tunneling.

The second part of the thesis focuses on Andreev tunneling. In this process two electrons tunnel at once in form of a Cooper pair. Andreev tunneling leads to transfer errors, when the tunneling of a single electron is preferred. We discuss the experimental detection techniques of Andreev tunneling based on direct current measurements as well as on electron counting. Furthermore, we show experimentally that by having large enough energy cost for charging the structures, achieved by decreasing the size of the system, Andreev tunneling is suppressed and the accuracy of the turnstile improves. The electron counting techniques allows us to study nontrivial statistics of Andreev tunneling.

In the last part of the thesis, excitations in a superconductor are considered. At low temperatures, the number of excitations of a superconductor should diminish exponentially. However, excess excitations in form of broken Cooper pairs are typically present limiting the performance of superconducting circuits. We discuss ways of probing the excitations in the normal metal - superconductor based structures. We investigate the diffusion of the quasiparticles and their relaxation to normal metallic traps or due to recombination into Cooper pairs via electron-phonon interaction.

**Keywords** Single-electron transport, Quantum metrology, Andreev tunneling, Quasiparticle excitations in superconductor

---

**ISBN (printed)** 978-952-6682-10-5**ISBN (pdf)** 978-952-6682-11-2

---

**ISSN (printed)** 1235-2704**ISSN (pdf)** 1797-9730

---

**Location of publisher** Espoo **Location of printing** Espoo **Year** 2014

---

**Pages** 239

---



**Tekijä**

Ville F. Maisi

**Väitöskirjan nimi**

Andreev-tunnelointi ja kvasipartikkelieksitaatiot mesoskooppisissa normaali metalli - suprajohde -rakenteissa

**Julkaisija** MIKES

**Yksikkö** Olli V. Lounasmaa -laboratorio, Perustieteiden korkeakoulu

**Sarja** MIKES Publications DOCTORAL DISSERTATIONS 2014

**Tutkimusala** Kylmäfysiikka

**Käsikirjoituksen päivämäärä** 15.1.2014

**Väitöspäivä** 30.4.2014

**Julkaisuluvan myöntämispäivä** 11.3.2014

**Kieli** Englanti

**Yhdistelmäväitöskirja** (yhteenvedo-osa + erillisartikkelit)

**Tiivistelmä**

Mesoskooppinen fysiikka käsittelee rakenteita, joiden koko on jokapäiväisen makroskooppisen mittakaavan ja mikroskooppisen atomimittakaavan välillä. Mesoskooppisissa rakenteissa pystytään siirtämään elektroneja hallitusti yksitellen. Tämä väitöskirja keskittyy yksittäisten elektronien siirtoon normaalimetalleissa ja suprajohdeissa. Eräs työn tärkeimmistä painopisteistä on ymmärtää niinkutsutun SINIS-käätöportin toiminnan rajoitukset. SINIS-käätöportti on laite, jolla pystytään siirtämään elektroneja yksitellen suprajohdeilta toiselle. Toistotaajuudella  $f$  saadaan näin aikaiseksi sähkövirta  $I = ef$ , jossa  $e$  on alkeisvaraus.

Väitöskirjan ensimmäisessä osassa käsitellään elektronien tunneloitumista normaalimetallin ja suprajohdeiden välillä ja esitetään SINIS-käätöportin toimintaperiaate. Käyttämällä kymmentä käätöporttia rinnakkain saavutetaan riittävä virtataso tarkkuusmittauksiin. Lisäksi näytämme, että näyte pitää suojata hyvin, jotta korkeammista lämpötiloista tuleva säteily ei heikennä laitteen toimintaa.

Työn toisessa osassa keskitymme niinkutsuttuun Andreev-tunnelointiin. Kyseisessä prosessissa kaksi elektronia tunneloituu samanaikaisesti muodostaen Cooperin parin suprajohdeelle. Andreev-prosessi aiheuttaa virheitä laitteisiin, joiden toiminta perustuu yhden elektronin tunnelointiin. Käsittelemme kokeellisia tekniikoita, joilla Andreev-tunnelointi havaitaan ja lisäksi osoitamme, että tämä prosessi voidaan välttää SINIS-käätöportissa. Lisäksi tutkimme elektronilaskentaa käyttäen Andreev-tunneloinnin statistisia ominaisuuksia.

Väitöskirjan viimeisessä osassa käsitellään suprajohdeiden eksitaatioita. Matalassa lämpötilassa eksitaatioiden pitäisi hävitä eksponentiaalisesti. Tyypillisesti näin ei kuitenkaan käy, vaan ylimääräisiä eksitaatioita jää suprajohdeeseen hajonneiden Cooperin parien muodossa. Nämä eksitaatiot heikentävät suprajohdeiden ominaisuuksia. Esitämme tässä osassa tapoja, joilla eksitaatioita voidaan havaita käyttäen normaalimetallin ja suprajohdeiden välisiä tunneliliitoksia. Tutkimme eksitaatioiden diffuusiota ja relaksaatiota näillä menetelmillä. Tutkituissa rakenteissa relaksaatio aiheutuu tunneloitumisesta normaalimetallisiin osiin tai rekombinoitumisesta Cooperin pareiksi.

**Avainsanat** Yhden elektronin ilmiöt, kvanttimitrologia, Andreev-tunnelointi, kvasipartikkelieksitaatiot suprajohdeissa

**ISBN (painettu)** 978-952-6682-10-5

**ISBN (pdf)** 978-952-6682-11-2

**ISSN (painettu)** 1235-2704

**ISSN (pdf)** 1797-9730

**Julkaisupaikka** Espoo

**Painopaikka** Espoo

**Vuosi** 2014

**Sivumäärä** 239



# Preface

This thesis was initiated by a common interest shared by the Low Temperature Laboratory (OVVL) at Aalto University and the Centre for Metrology and Accreditation (MIKES). Both of the institutes were curious to know about the accuracy obtainable with the so-called SINIS turnstile. At the time I began the thesis, the SINIS turnstile was a promising new device for generating a well known electrical current. MIKES was interested to know whether the SINIS turnstile could be utilized to redefine the SI unit of electrical current whereas Low Temperature Laboratory was more interested in understanding the physics of the device. For achieving both of these goals, the accuracy of the device needed to be increased by several orders of magnitude and this became the goal for my thesis. First of all, I want to express my gratitude to both of the institutes for allowing me to work jointly in them. In addition to administrative staff, I especially thank my instructor Prof. Jukka Pekola from OVVL and Dr. Antti Manninen from MIKES for taking care of the required arrangements.

The role of my thesis instructor Prof. Jukka Pekola was not at all limited to the administrative duties. In fact, he deserves the greatest acknowledgment of this thesis. Without his inspiring ideas, effective solutions to problems, professional instruction ranging from sample fabrication and English grammar to detailed theoretical calculations, and devotion and enthusiasm towards research, this thesis would not exist in the form you have it now. A good example about depth at which Jukka is involved to the everyday work in the laboratory, is the case when we repaired together one of the dilution refrigerators during the days between Christmas and new year. Having such a talented instructor on a day-to-day basis is a tremendous privilege for a young student striving to become a physicist. Thank you for that!

In addition to Jukka, Dr. Matthias Meschke has contributed remarkably

for the thesis. He is the one who does the silent but very important work for keeping all equipment running and in good condition. I also thank for his patience and helpfulness for teaching me hands-on how to build, operate and repair various gadgets and master the device fabrication. Working with the talented group members of PICO group of OVVL and electricity group of MIKES has been also a great asset. Especially working more closely with Olli-Pentti Saira, Antti Kemppinen, Sergey Kafanov, Helena Knowles, Jonne Koski, Thomas Aref, Emma Mykkänen and Elsa Mannila has been very fruitful. Jukka also initiated many valuable contacts to other research groups. Collaborating with Yuri Pashkin, Dmitri Averin, Frank Hekking, Mikko Möttönen, Andreas Heimes, Dimitri Golubev, Christian Flindt, Dania Kambly, Sergey Lotkhov, Martin Gustafsson, Per Delsing and Angelo Di Marco has been essential for the thesis and has given new ways to approach the same problems. I want to thank especially Prof. Frank Hekking for teaching the calculation techniques used in this thesis.

The experimental results of the thesis have benefited from the expertise of the OVVL mechanical workshop staff. They have been able to materialize many designs in short notice, for example the shielded sample holders used in Publication VI as well as a missing collar for helium transfer dewar which I by accident shipped away. I also acknowledge the access to clean room facilities of Micronova and financial support of The National Doctoral Programme in Nanoscience (NGS-NANO).

Last but not least, I want to thank my gorgeous family and especially my beloved wife Hanna who has taken care of many things during all these years. She has been there for me and the whole family whenever needed. She has also (nearly) always remembered to remind me about important things.

Helsinki, March 15, 2014,

Ville Maisi

# Contents

<b>Preface</b>	<b>1</b>
<b>Contents</b>	<b>3</b>
<b>List of Publications</b>	<b>5</b>
<b>Author's Contribution</b>	<b>7</b>
<b>1. Introduction</b>	<b>11</b>
<b>2. Electron tunneling between a superconductor and a normal metal</b>	<b>17</b>
2.1 Superconductivity . . . . .	17
2.2 Electron tunneling . . . . .	20
2.2.1 Hamiltonian and current operator . . . . .	20
2.2.2 Determination of tunneling rates . . . . .	22
<b>3. Charging energy - the SINIS turnstile</b>	<b>29</b>
3.1 Energy considerations . . . . .	29
3.2 Master equation . . . . .	32
3.3 Current quantization in the SINIS turnstile . . . . .	35
<b>4. Environmentally activated tunneling</b>	<b>39</b>
4.1 The $P(E)$ theory . . . . .	39
4.2 Electromagnetic environment as an origin of Dynes DoS . .	43
4.3 Subgap leakage of NIS junctions . . . . .	45
<b>5. Higher order processes - Andreev tunneling</b>	<b>47</b>
5.1 Determination of Andreev tunneling rates . . . . .	48
5.2 Measuring Andreev tunneling: subgap current . . . . .	50
5.3 Real-time detection of Andreev tunneling events . . . . .	53

5.4	Influence of Andreev tunneling on SINIS turnstile . . . . .	58
5.5	Full Counting Statistics (FCS) of Andreev Events . . . . .	60
5.5.1	Master equation approach to FCS . . . . .	60
5.5.2	FCS of Andreev tunneling . . . . .	62
<b>6.</b>	<b>Quasiparticle excitations in a superconductor</b>	<b>67</b>
6.1	Probing quasiparticles with NIS junctions . . . . .	68
6.2	Diffusion equation for quasiparticles . . . . .	73
6.3	Branch imbalance in SINIS turnstile . . . . .	76
6.4	Electron-phonon interaction in the superconducting state . .	77
6.4.1	Derivation of heat flux and related quantities . . . . .	78
6.4.2	Recombination rates on a small superconducting island	80
6.4.3	Single quasiparticle effects . . . . .	81
<b>7.</b>	<b>Summary</b>	<b>85</b>
	<b>Bibliography</b>	<b>89</b>
	<b>Publications</b>	<b>95</b>

# List of Publications

This thesis consists of an overview and of the following publications which are referred to in the text by their Roman numerals.

**I** V. F. Maisi, Yu. A. Pashkin, S. Kafanov, J. S. Tsai and J. P. Pekola. Parallel pumping of electrons. *New J. Phys.* **11**, 113057 (2009).

**II** J. P. Pekola, V. F. Maisi, S. Kafanov, N. Chekurov, A. Kemppinen, Yu. A. Pashkin, O.-P. Saira, M. Möttönen and J. S. Tsai. Environment-Assisted Tunneling as an Origin of the Dynes Density of States. *Phys. Rev. Lett.* **105**, 026803 (2010).

**III** O.-P. Saira, M. Möttönen, V. F. Maisi and J. P. Pekola. Environmentally activated tunneling events in a hybrid single-electron box. *Phys. Rev. B* **82**, 155443 (2010).

**IV** V. F. Maisi, O.-P. Saira, Yu. A. Pashkin, J. S. Tsai, D. V. Averin and J. P. Pekola. Real-Time Observation of Discrete Andreev Tunneling Events. *Phys. Rev. Lett.* **106**, 217003 (2011).

**V** T. Aref, V. F. Maisi, M. Gustafsson, P. Delsing and J. P. Pekola. Andreev tunneling in charge pumping with SINIS turnstiles. *Europhys. Lett.* **96**, 37008 (2011).

**VI** O.-P. Saira, A. Kemppinen, V. F. Maisi and J. P. Pekola. Vanishing quasiparticle density in a hybrid Al/Cu/Al single-electron transistor. *Phys. Rev. B* **85**, 012504 (2012).

- VII** H. S. Knowles, V. F. Maisi and J. P. Pekola. Probing quasiparticle excitations in a hybrid single electron transistor. *Appl. Phys. Lett.* **100**, 262601 (2012).
- VIII** J. P. Pekola, O.-P. Saira, V. F. Maisi, A. Kemppinen, M. Möttönen, Yu. A. Pashkin and D. V. Averin. Single-electron current sources: towards a refined definition of ampere. *Rev. Mod. Phys.* **85**, 1421 (2013).
- IX** V. F. Maisi, S. V. Lotkhov, A. Kemppinen, A. Heimes, J. T. Muhonen and J. P. Pekola. Excitation of Single Quasiparticles in a Small Superconducting Al Island Connected to Normal-Metal Leads by Tunnel Junctions. *Phys. Rev. Lett.* **111**, 147001 (2013).
- X** A. Di Marco, V. F. Maisi, J. P. Pekola and F. W. J. Hekking. Leakage current of a superconductor–normal metal tunnel junction connected to a high-temperature environment. *Phys. Rev. B* **88**, 174507 (2013).
- XI** V. F. Maisi, D. Kambly, C. Flindt and J. P. Pekola. Full counting statistics of Andreev tunneling. *Phys. Rev. Lett.* **112**, 036801 (2014).

# Author's Contribution

## **Publication I: "Parallel pumping of electrons"**

The author took part in designing the devices, performed the measurements and wrote the manuscript.

## **Publication II: "Environment-Assisted Tunneling as an Origin of the Dynes Density of States"**

The author fabricated the single NIS junctions, had significant role in the measurements and did most of the numerical analysis of the results and prepared part of the manuscript.

## **Publication III: "Environmentally activated tunneling events in a hybrid single-electron box"**

The author assisted in device fabrication and measurements and took part in manuscript preparation.

## **Publication IV: "Real-Time Observation of Discrete Andreev Tunneling Events"**

The author had main responsibility in sample design, measurements, and result analysis and wrote majority of the manuscript.

**Publication V: “Andreev tunneling in charge pumping with SINIS turnstiles”**

The author advised in the measurements, did the master equation based analysis and took part in manuscript preparation.

**Publication VI: “Vanishing quasiparticle density in a hybrid Al/Cu/Al single-electron transistor”**

The author fabricated the reference sample, designed and built shielded sample holders used in cryostat PT and took part in analysis and manuscript preparation.

**Publication VII: “Probing quasiparticle excitations in a hybrid single electron transistor”**

The author had main responsibility in sample design, did most of the calculations and took part in manuscript preparation.

**Publication VIII: “Single-electron current sources: towards a refined definition of ampere”**

The author wrote sections III.B.2-3 and G.6 and took part in preparation of the other sections.

**Publication IX: “Excitation of Single Quasiparticles in a Small Superconducting Al Island Connected to Normal-Metal Leads by Tunnel Junctions”**

The author fabricated some of the samples, performed most of the experiments, did major part of the calculations and wrote most of the manuscript.

**Publication X: “Leakage current of a superconductor–normal metal tunnel junction connected to a high-temperature environment”**

The author took part in calculations and manuscript preparation.

**Publication XI: “Full counting statistics of Andreev tunneling”**

The author prepared the sample, did the measurements and took part in manuscript preparation.



# 1. Introduction

Using low temperatures freezes out unwanted degrees of freedom. This allows one to study fundamental properties of matter in high detail and make predictions on what happens at higher temperatures where the excitations are present. In addition, fully new phenomena take place at low temperatures. For example the discreteness of electron charge results in single-electron effects where the electrons are transported sequentially. On the other hand, superconductivity with dissipation-free electrical current and other peculiar properties arises at low temperatures and provides opportunities for a vast range of possible applications.

This thesis deals with small metallic systems at low temperatures where single-electron effects and superconductivity play an important role. These essential concepts in view of the present thesis are reviewed in Chapter 2. We focus on structures where superconducting and normal metallic structures are coupled weakly by an insulating tunnel barrier. The electrons may pass through such a barrier by tunneling. The weak coupling favors that the electrons tunnel one by one. On the other hand, in superconductors the electrons are paired as Cooper pairs. Breaking such a pair and having a single-electron process requires minimally an energy  $\Delta$  per particle, known as the energy gap [1]. Because of the pair breaking energy cost, the single-electron tunneling process is suppressed if energies exceeding  $\Delta$  are not available. In this case the transport must involve simultaneously two electrons in form of a Cooper pair. A process where a complete Cooper pair moves from a superconductor to a normal metal or vice versa is known as Andreev reflection. It was first used to describe thermal conductance between two metals [2], one superconducting the other one normal. In the case of a tunnel barrier, the process is known as Andreev tunneling, which is the topic of Chapter 5. We will learn that at low bias, Andreev tunneling is the dominant process [3–9]. However, if

small metallic structures are considered, the charging of a metallic island by an additional electron is associated with an energy cost characterized by charging energy  $E_c = e^2/(2C_\Sigma)$ , where  $e$  is the elementary charge and  $C_\Sigma$  the sum of all capacitances contacted to the island. We observe that if  $E_c$  is made larger than the pair breaking energy  $\Delta$ , Andreev tunneling becomes suppressed. This is observed in this thesis, e.g., in direct current measurements. In addition, Andreev tunneling is studied by detecting discrete tunneling events in real-time. The observation of the individual events allows one to study the statistics of them. In Sect. 5.5 we find out that the interplay of single-electron and two-electron tunneling leads to non-trivial super-Poissonian statistics. The findings of this chapter are important for understanding the limitations of hybrid normal metal - superconductor systems, especially for single-electron applications.

The peculiar properties of the superconductors are based on the fact that a single electron excitation requires an energy exceeding  $\Delta$ . If this energy is not available, all the electrons are paired, there are no excitations, and hence dissipation is also absent. However, when the number of excitations becomes low, their relaxation also becomes weak and typically excess excitations remain. These residual quasiparticles influence adversely the performance of superconducting circuits [10–19], as discussed in Chapter 6. We first discuss how the excitations can be experimentally probed with tunnel junctions between a normal metal and a superconductor. We observe that the number of them is suppressed when the structures are well protected from the high temperature environment, and when efficient relaxation is provided.

In Sect. 6.2 we consider the electrical heat conduction and relaxation in superconducting leads. Heat transport along a superconductor is governed by diffusion of the excitations. With tunnel junction based structures we show that the injection and probing of quasiparticles can be done simultaneously. In this way, we see that the diffusion equation approach is adequate for describing the relaxation in superconducting lines with relaxation being dominated by diffusive transport of excitations to normal metallic parts and further relaxation there. In this case, the inherent quasiparticle relaxation of the superconductor by recombination is not taken into account since it is weak as compared to relaxation in normal metallic traps. In Sect. 6.4 we consider a small superconducting island where the electrons cannot diffuse to normal metallic parts. Then the electron-phonon interaction leading to energy loss and recombination

into Cooper pairs, which is the inherent relaxation mechanism, becomes important. By injecting and detecting the excitations, as in Sect. 6.2, we are now able to probe the electron-phonon interaction. The probing is done down to a level where there is only one broken Cooper pair present, hence allowing to determine its recombination rate. In the absence of injection, there are essentially no excitations present.

One of the main motivations for studying the physical phenomena of this thesis has been the possibility to obtain quantized electrical current in such structures. Here quantization does not refer to quantum mechanics. The quantization is based in this case on the fact that all electrons carry the same elementary electronic charge  $e$ , which was first observed in micrometer-sized oil droplets [20, 21]. The quantized current  $I = nef$  results when  $n$  electrons are transported in a cycle which is repeated at a frequency  $f$  [22–30]. In Fig. 1.1 the principles of the very first devices achieving the current quantization experimentally as well as the most prominent candidates for reaching high accuracy and large enough output current are shown. Figure 1.1 (a) represents a normal metallic turnstile where only one radio frequency (RF) signal is needed to obtain the quantization [31]. A voltage bias is applied to the device to set the preferred direction for tunneling. The offset charge of the central island is driven periodically to plunge an electron to the middle island and then to push it out to the other lead and hence one electron is transported per cycle through the device. The two islands next to the middle one are required to block the static current flow when degeneracy point of the middle island is passed.

In panel (b) a device similar to the one in panel (a) but one island less is shown. By using two RF drives, one for each island, the electrons can be pumped without an external bias voltage, or even against a small bias [25]. First the left gate offset charge is changed to pull an electron into the left island from the left lead. Then the gate offset is moved back and simultaneously the right gate offset charge is changed to move an electron from the left island to the right one. Finally, the offset charge of the right island is brought back to the starting value and an electron tunnels out from it to the right lead and a single electron is transported through the device. The accuracy of these two normal metallic devices is limited by co-tunneling of electrons. The co-tunneling can however be reduced by adding more islands in series [28]. The highest accuracy reached so far with single-electron sources was obtained with the approach shown

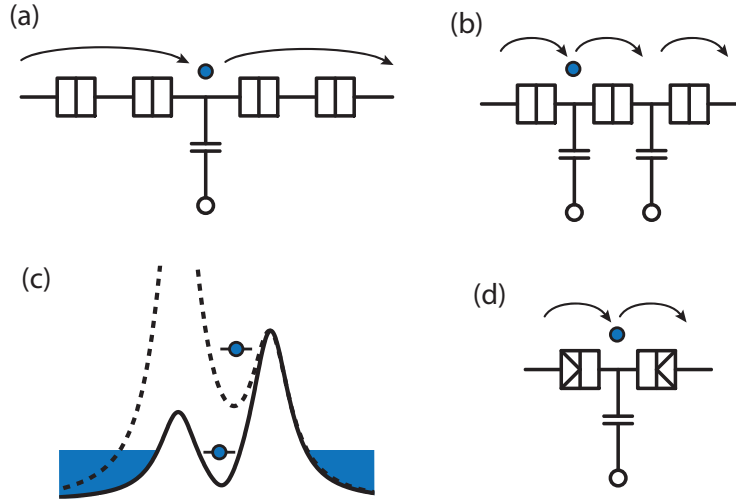


**Figure 1.1. Various single-electron sources.** (a) The normal metallic turnstile. Three normal metallic islands are connected with tunnel junctions. A gate drive is applied to the central island to obtain quantized current. (b) Normal metallic single-electron pump. The gate offset charge of two islands are driven periodically. A quantized current is obtained without applying a bias voltage since electrons are moved from one island to another by changing the electron numbers of the two island controllably. (c) Potential landscape of a semiconductor pump. The height of the left barrier is changed cyclically to form a quantum dot, trap one electron to it from the left reservoir and plunge it to the right reservoir. The solid and dashed lines show schematically the potential for two different barrier gate values. (d) The SINIS turnstile. The hysteresis needed for the turnstile operation is achieved with superconducting leads instead of the two extra islands as in panel (a). The superconducting electrodes provide in addition protection against co-tunneling.

in panel (b) with seven junctions in series with an error per pumped electron of 15 parts in  $10^9$  [32]. However, the complexity of the device operation was significantly increased and the overall magnitude of output current reduced.

Almost at the same time as the operation principle of the metallic devices was demonstrated, semiconductor electron pumps were also developed [33]. Their operation is based on not only tuning the number of electrons on a conducting island with a gate offset charge but on the possibility to open and close tunnel barriers with gate electrodes. In Fig. 1.1 (c) we show a potential energy along a device which has recently been used to obtain the highest quantization accuracy with an error smaller than 1.2 parts in  $10^6$  in a semiconductor devices [30]. It is operated by raising and lowering a tunnel barrier. Together with another static tunnel barrier, a quantum dot is formed dynamically, a single-electron captured to it and plunged over the static barrier. Hence a single-electron is transported in each cycle and quantized current results.

In this thesis, we focus on the so-called SINIS turnstile [34], which is

presented schematically in Fig.1.1 (d). It is operated like the normal metallic turnstile of panel (a). The difference is that the turnstile operation is achieved by using superconducting leads instead of the two extra islands. The superconductors suppress effectively the co-tunneling errors [34] and hence the SINIS turnstile is considered as a potential candidate to reach high accuracy. Its operation principle is simple enough to operate many of them in parallel as described in Sect. 3.3. The Andreev tunneling, the excitations in superconductors as well as photon assisted tunneling discussed in Sect. 4 all contribute to the errors of the current quantization of the SINIS turnstile. These error sources are addressed in this thesis. By optimizing the operation, the best quantization accuracy so far with such a device was obtained with a relative uncertainty as low as  $10^{-4}$ . However, we believe that after the error sources identified in this thesis have been suppressed by further optimization, the relative accuracy of the device can be improved to the level of  $10^{-7}$  or below.

In addition to the single-electron sources presented in this chapter, there is a vast range of many other approaches studied as well. A more comprehensive discussion of the alternative possibilities is presented in Publication VIII.



## 2. Electron tunneling between a superconductor and a normal metal

Electrons in a superconductor form Cooper pairs. The pairing is due to an attractive interaction which is incorporated into the microscopic description of free electrons in a metal to formulate the so-called Bardeen-Cooper-Schrieffer (BCS) theory [35]. This theory is typically the starting point for considering superconductors. Here we first outline the basic results of the BCS theory in Sect. 2.1 relevant for this thesis. Then in Sect. 2.2 we consider single-electron processes between a normal metal and a superconductor separated by a thin insulating barrier. We see that the energy exceeding  $\Delta$ , for tunneling to take place, can be provided either thermally or by a voltage bias.

### 2.1 Superconductivity

The electrons in a superconductor are described in BCS theory by a pairing Hamiltonian, see, eg., Ref. [1],

$$\hat{H}_S = \sum_{k\sigma} \varepsilon_k c_{k\sigma}^\dagger c_{k\sigma} + \sum_{kl} V_{kl} c_{k\uparrow}^\dagger c_{-k\downarrow}^\dagger c_{-l\downarrow} c_{l\uparrow}. \quad (2.1)$$

Here the first part describes electron states with energy  $\varepsilon_k$ , momentum  $k$  and spin  $\sigma$ , and  $c_{k\sigma}^\dagger$  is the corresponding creation operator. The second part is the coupling leading to superconductivity. It pairs electrons with momenta and spin being  $k \uparrow$  and  $-k \downarrow$ . Next we assume  $c_{-k\downarrow} c_{k\uparrow}$  to have an expectation value  $b_k = \langle c_{-k\downarrow} c_{k\uparrow} \rangle$ , and that the fluctuations  $(c_{-k\downarrow} c_{k\uparrow} - b_k)$  away from this value are small. By keeping only the leading order terms, we obtain from Eq. (2.1)

$$\hat{H}_S = \sum_{k\sigma} \varepsilon_k c_{k\sigma}^\dagger c_{k\sigma} - \sum_k \left( \Delta_k c_{k\uparrow}^\dagger c_{-k\downarrow}^\dagger + \Delta_k^* c_{-k\downarrow} c_{k\uparrow} - \Delta_k b_k^* \right), \quad (2.2)$$

where  $\Delta_k = -\sum_l V_{kl} b_l$ . Equation (2.2) can be diagonalized with the so-called Bogoliubov transformation [36, 37] by introducing new fermionic

creation operators  $\gamma_{k\sigma}^\dagger$  relating to the electron operators by

$$\begin{cases} c_{k\uparrow}^\dagger &= v_k^* \gamma_{-k\downarrow} + u_k \gamma_{k\uparrow}^\dagger \\ c_{-k\downarrow}^\dagger &= -v_k^* \gamma_{k\uparrow} + u_k \gamma_{-k\downarrow}^\dagger. \end{cases} \quad (2.3)$$

The commutation relations yield  $|u_k|^2 + |v_k|^2 = 1$ . By choosing  $u_k$  and  $v_k$  in such a way that  $2\varepsilon_k u_k v_k + \Delta_k^* v_k^2 - \Delta_k u_k^2 = 0$ , the off-diagonal elements of  $\hat{H}_S$  vanish when expressed in terms of  $\gamma_{k\sigma}$ . The Hamiltonian is then

$$\hat{H}_S = \sum_{k\sigma} E_k \gamma_{k\sigma}^\dagger \gamma_{k\sigma}, \quad (2.4)$$

where we have energy

$$E_k = \sqrt{\varepsilon_k^2 + |\Delta_k|^2}, \quad (2.5)$$

for the excitations with creation operator  $\gamma_{k\sigma}^\dagger$ . The constant condensation energy is neglected because it does not contribute to the calculations presented in this thesis. Only the energy differences are relevant. The coefficients of the transformation in the diagonalized form are given by

$$|v_k|^2 = 1 - |u_k|^2 = \frac{1}{2} \left( 1 - \frac{\varepsilon_k}{E_k} \right). \quad (2.6)$$

Equation (2.3) can be written as  $c_{k\sigma}^\dagger = v_{k\sigma}^* \gamma_{-(k\sigma)} + u_{k\sigma} \gamma_{k\sigma}^\dagger$ , where  $v_{k\uparrow} \equiv v_k$ ,  $v_{k\downarrow} \equiv -v_{-k}$ ,  $u_{k\uparrow} \equiv u_k$  and  $u_{k\downarrow} \equiv u_{-k}$ . This notation is convenient for the forthcoming calculations. The Hamiltonian of Eq. (2.4) allows to obtain the temperature dependence of  $\Delta_k$  as well as the critical temperature  $T_C$ , where the material becomes superconducting [1]. In the following we assume that  $\Delta_k = \Delta$ , i.e., that the energy gap is independent of the wavevector  $k$ . This assumption is well valid and justified for our considerations since only states with  $|k|$  close to the Fermi wavevector  $k_F$  are relevant and the materials we consider are isotropic, i.e. there are no strong directional dependencies. Also, we take  $\Delta$  to be temperature independent since we consider superconductor temperatures  $T_S < T_C/3$ , where the temperature dependency of  $\Delta$  is exponentially weak [1].

Having Eq. (2.5), we can readily obtain the density of states (DoS) of a superconductor which is in a very essential role for understanding the properties of a metal in superconducting state. The DoS yields the number per unit volume and energy of electronic states at a given energy  $E$ , which we measure with respect to the Fermi level. Equation (2.5) links the energy of an unpaired electron  $\varepsilon_k$  to the excitation energy  $E_k$  with the energy gap  $\Delta_k$ . Since we assume a wavevector independent energy gap  $\Delta$ , the wavevector  $k$  is irrelevant and we may drop it off and obtain  $E = \sqrt{\varepsilon^2 + |\Delta|^2}$ . Throughout this thesis, we consider small energies, up

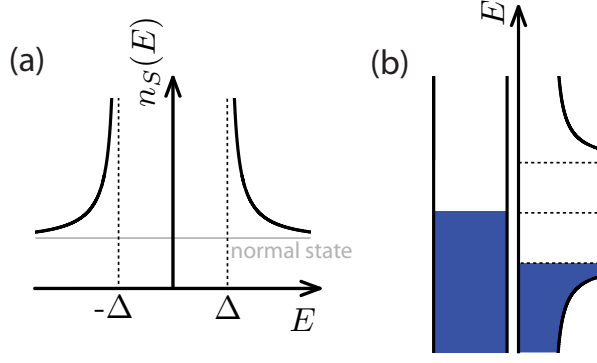


**Figure 2.1. Density of states of a superconductor.** (a), The density of states (DoS)  $n_S(E)$  for quasiparticle excitations with energy  $E$ . The curve is normalized with respect to the constant normal state DoS shown as a grey line. (b), DoS with the occupations in the low temperature limit. Left side shows the normal state case and the right hand side shows the superconducting case. For normal metal, DoS is constant and levels below Fermi level  $E < 0$  are all filled shown by the blue area and levels above,  $E > 0$  are all vacant. Similarly, for superconductor, all states at  $E < -\Delta$  are all filled and all with  $E > \Delta$  are vacant. The region  $-\Delta < E < \Delta$  is known as the energy gap as there are no electronic states at all.

to a few meV, around the Fermi energy, which, in turn, is on the eV range. Therefore we assume that the unpaired energies  $\varepsilon$  have a constant density of states around the Fermi level. We obtain the superconducting DoS, normalized with respect to the normal state value, as

$$n_S(E) = \frac{d\varepsilon}{dE} = \frac{|E|}{\sqrt{E^2 - \Delta^2}}, \quad (2.7)$$

for  $|E| > \Delta$  and  $n_S(E) = 0$  for  $|E| < \Delta$ . This result is plotted in Fig. 2.1 (a). We observe that an excitation, see Eq. (2.5), carries an energy  $|E| > \Delta$ , reflecting the fact that the minimum energy cost for an unpaired electron is  $\Delta$ . In the DoS this is seen as the energy gap: there are no states available for  $|E| < \Delta$ . Note that in Fig. 2.1 (a) we have reflected the DoS for negative energies such that it reduces correctly to the normal state result when  $\Delta \rightarrow 0$ . We find out in Sect. 2.2 that the reflection to negative energies is illustrative for considering the electron tunneling. This approach is known as the semiconductor model [1] since the energy gap of a superconductor reminds greatly the bandgap of a semiconductor and the coherent effects of a superconductor are not relevant in this picture. In Fig. 2.1 (b) we present the occupations of the energy levels for a superconductor and a normal metal in the zero temperature limit. The states with  $E < 0$  are occupied by electrons and states with  $E > 0$  are vacant.

## 2.2 Electron tunneling

A tunnel contact or a tunnel junction is a structure where two metals are not in a direct contact but they are separated by a thin insulating layer. The insulating layer can be vacuum or made of an electrically insulating material such as aluminum oxide, as in this thesis. In Fig. 2.2 (a) such a junction is presented. The junction is formed here between the overlapping region of a normal metallic (N) copper and superconducting (S) aluminum. Together with the insulating layer (I) they form an NIS junction which is the basic building block used in this thesis. In panel (b) the current  $I$  through the junction is measured against bias voltage  $V_b$ . Next we discuss the origin and characteristics of this current.

Classically, electrical current cannot flow from one of the metals to the other because electrons cannot cross the insulating barrier. However, with thin barriers, we must consider the situation quantum mechanically. Quantum mechanics predicts that the electronic states are not fully confined inside the conducting regions but they extend to the insulating material. This effect decays exponentially with respect to the distance from the conductor and hence is not relevant at large distances. At short distances, i.e. in the case of tunnel contacts, this gives rise to electron transport between neighboring metals. Next, we derive the tunneling rates for such contacts.

### 2.2.1 Hamiltonian and current operator

A normal metal and a superconductor contacted by a tunnel junction has a Hamiltonian

$$\hat{H} = \hat{H}_S + \hat{H}_N + \hat{H}_T + \hat{H}_B, \quad (2.8)$$

where  $\hat{H}_S$  is the Hamiltonian of a superconductor given by Eq. (2.4).  $\hat{H}_N$  is similarly the Hamiltonian for the normal metal with  $V_{kl} = 0$ . It reads

$$\hat{H}_N = \sum_{k\sigma} (\epsilon_k + e\delta\hat{V}(t)) a_{k\sigma}^\dagger a_{k\sigma}, \quad (2.9)$$

where  $a_{k\sigma}^\dagger$  is the creation operator of an electron with wavevector  $k$  and spin  $\sigma$ . We allow here for generality voltage fluctuations  $\delta\hat{V}(t)$  to add or remove energy from the electrons. The fluctuations are caused by photons coupling to the system and they are described by

$$\hat{H}_B = \sum_{\lambda} \hbar\omega_{\lambda} b_{\lambda}^\dagger b_{\lambda}, \quad (2.10)$$

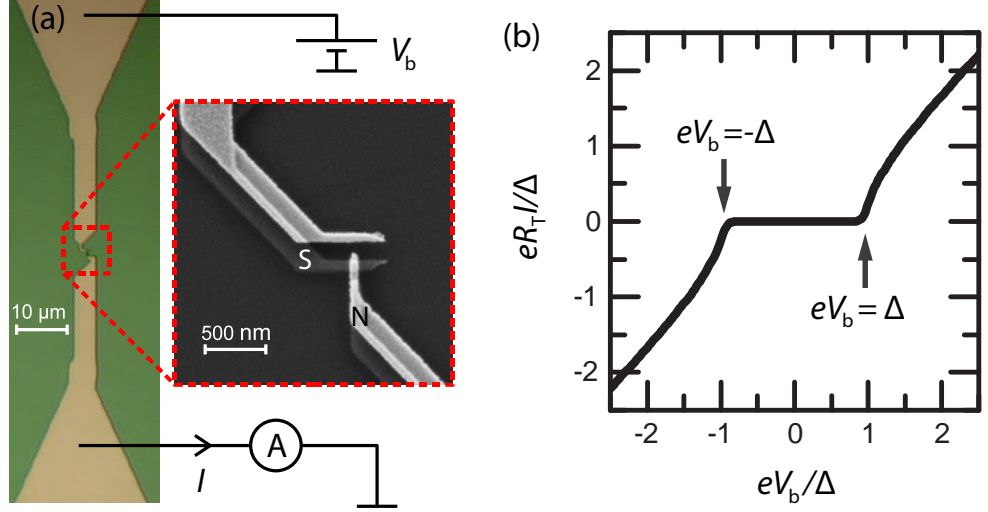


**Figure 2.2. A typical NIS junction.** (a), Optical microscope picture (left) and a scanning electron micrograph (right) of a typical NIS junction used in this thesis. In the optical microscope image, the topmost normal metallic copper film is visible. This can be seen in the scanning electron micrograph as the bright parts whereas the lower superconducting aluminum layer gives weaker contrast. The structures of this thesis are fabricated with so-called shadow evaporation technique [38] allowing single-electron device fabrication [39]. The junction is biased with a voltage bias  $V_b$  and current  $I$  through it is measured. The experimental current - voltage curve is presented in panel (b). The axes are normalized with respect to the tunnel resistance  $R_T = 600 \text{ k}\Omega$  and superconductor gap  $\Delta = 200 \text{ } \mu\text{eV}$ .

with eigenenergies  $\hbar\omega_\lambda$ . Here  $b_\lambda^\dagger$  and  $b_\lambda$  are the corresponding bosonic creation and annihilation operators. In this section we consider the case  $\delta\hat{V}(t) = 0$ , when  $\hat{H}_B$  does not play a role, but we return to the photon environment in Sect. 4. The last part of Eq. (2.8) is the tunnel coupling of the two metals

$$\hat{H}_T = \sum_{kq\sigma} t_{kq} c_{q\sigma}^\dagger a_{k\sigma} + \text{h.c.}, \quad (2.11)$$

where h.c. stands for hermitian conjugate and we assumed spin independent and spin conserving coupling  $t_{kq}$ . In order to calculate the tunnel current  $I = \langle \hat{I} \rangle$ , or the corresponding tunneling rate  $\Gamma = I/e$ , we need the current operator  $\hat{I}$ . The most straightforward way to obtain it is to consider it in Heisenberg picture:

$$\hat{I}_H = e \frac{d}{dt} \hat{N}_{N,H} = \frac{ie}{\hbar} [\hat{H}, \hat{N}_{N,H}] \Rightarrow \hat{I} = \frac{ie}{\hbar} [\hat{H}, \hat{N}_N] = \frac{ie}{\hbar} [\hat{H}_T, \hat{N}_N], \quad (2.12)$$

where subindex  $H$  denotes Heisenberg picture and  $\hat{N}_N = \sum_{k\sigma} a_{k\sigma}^\dagger a_{k\sigma}$ , is the electron number operator of the normal metal. By using Eq. (2.11) we obtain

$$\hat{I} = \frac{ie}{\hbar} \sum_{kq\sigma} (t_{kq} c_{q\sigma}^\dagger a_{k\sigma} - \text{h.c.}). \quad (2.13)$$

## 2.2.2 Determination of tunneling rates

To calculate the average current  $I$ , we use density matrix formalism in the interaction picture. The average value of the current is expressed as  $I = \langle \hat{I} \rangle = \text{Tr}(\rho \hat{I})$ , where  $\text{Tr}$  stands for a trace over the Fock space spanned by the electronic creation and annihilation operators and the density matrix  $\rho$  follows the Liouville equation of motion [40]

$$\frac{\partial}{\partial t} \rho = -\frac{i}{\hbar} [\hat{H}, \rho]. \quad (2.14)$$

Now we move to the interaction picture. We make an unitary transformation  $\hat{A}_I = S \hat{A} S^\dagger$  for operator  $A$ , where the transformation  $S$  satisfies

$$\frac{\partial}{\partial t} \hat{S} = \frac{i}{\hbar} \hat{H}_0 \hat{S}, \quad (2.15)$$

with  $\hat{H}_0 = \hat{H}_N + \hat{H}_S + \hat{H}_B$ , being the (time-dependent) reservoir part of the Hamiltonian of Eq. (2.8). By inspection we see that the transformation

$$\hat{S} = e^{\frac{i}{\hbar} (\hat{K}_0 t + \hat{\varphi}(t) \hat{N}_N)}. \quad (2.16)$$

satisfies the requirement of Eq. (2.15) with  $\hat{K}_0 = \sum_{k\sigma} \epsilon_k^N a_{k\sigma}^\dagger a_{k\sigma} + \hat{H}_S + \hat{H}_B$  being the time independent part of  $\hat{H}_0$  and  $\hat{\varphi}(t) \equiv \frac{e}{\hbar} \int_{t_0}^t dt' \delta \hat{V}(t')$ . With Equation (2.15) we obtain from Eq. (2.14)

$$\frac{\partial}{\partial t} \rho_I = -\frac{i}{\hbar} [\hat{H}_{T,I}, \rho_I]. \quad (2.17)$$

This can be solved formally by integration to yield

$$\rho(t) = \rho_0 - \frac{i}{\hbar} \int_{t_0}^t dt' [\hat{H}_T(t'), \rho(t')], \quad (2.18)$$

where  $\rho_0 = Z^{-1} e^{\beta(-\hat{K}_0 + \mu_N \hat{N}_N)}$  is the initial solution taken to be at equilibrium (grand canonical) with respect to the leads at temperature  $T$ . Here  $Z$  is the partition function and  $\beta = (k_B T)^{-1}$ . The operators in Eq. (2.18) with explicit time dependence, are taken to be in the interaction picture  $\hat{A}(t) \equiv \hat{A}_I$ . We allow for a chemical potential shift between the normal metal and the superconductor. It is caused by the voltage bias across the junction and the charging effects discussed in Sect. 3. The chemical potential of the superconductor is set to zero without losing generality and hence the shift equals the chemical potential  $\mu_N$  of the normal metal.

Now the current can be calculated as  $I = \langle \hat{I} \rangle = \text{Tr}(\rho_I \hat{I}_I)$ . Using Eq. (2.18) leads to a series expansion. The first non-zero term corresponds to single-electron tunneling and is given by

$$I = -\frac{i}{\hbar} \text{Tr} \left( \int_{-t_0}^t dt' [\hat{H}_T(t'), \rho_0] \hat{I}(t) \right) = \frac{i}{\hbar} \int_{-t_0}^t dt' \langle [\hat{H}_T(t'), \hat{I}(t)] \rangle_0, \quad (2.19)$$

where  $\langle \hat{A} \rangle_0 = \text{Tr}(\rho_0 \hat{A})$  denotes a thermal average of  $\hat{A}$ . Equation (2.19) contains both processes, from superconductor to normal metal and vice versa. Later on, we need both these processes separately. Therefore we identify terms containing  $a_{k\sigma}^\dagger a_{k\sigma}$  to correspond to tunneling from the normal metal to the superconductor since this term requires the initial state  $k\sigma$  of the normal metal to be occupied in order for  $a_{k\sigma}$  to yield a non-zero result. Collecting only such terms we obtain the tunneling rate from normal metal to the superconductor as

$$\Gamma_{N \rightarrow S} = \frac{I_{N \rightarrow S}}{e} = \frac{1}{\hbar^2} \int_{-t_0}^t dt' \sum_{kq q' \sigma} \left\{ \begin{aligned} & \left\langle t_{kq}^* a_{k\sigma}^\dagger(t) c_{q\sigma}(t) t_{kq'} c_{q'\sigma}^\dagger(t') a_{k\sigma}(t') \right\rangle_0 \\ & + \left\langle t_{kq'}^* a_{k\sigma}^\dagger(t') c_{q'\sigma}(t') t_{kq} c_{q\sigma}^\dagger(t) a_{k\sigma}(t) \right\rangle_0 \end{aligned} \right\}. \quad (2.20)$$

Next we plug in Eq. (2.3) and obtain

$$\Gamma_{N \rightarrow S} = \frac{1}{\hbar^2} \int_{-t_0}^t dt' \sum_{kq\sigma} |t_{kq}|^2 \left\{ \begin{aligned} & |v_{q\sigma}|^2 \left\langle a_{k\sigma}^\dagger(t) \gamma_{-(q\sigma)}^\dagger(t) \gamma_{-(q\sigma)}(t') a_{k\sigma}(t') \right\rangle_0 + \\ & |u_{q\sigma}|^2 \left\langle a_{k\sigma}^\dagger(t) \gamma_{q\sigma}(t) \gamma_{q\sigma}^\dagger(t') a_{k\sigma}(t') \right\rangle_0 + \\ & |v_{q\sigma}|^2 \left\langle a_{k\sigma}^\dagger(t') \gamma_{-(q\sigma)}^\dagger(t') \gamma_{-(q\sigma)}(t) a_{k\sigma}(t) \right\rangle_0 + \\ & |u_{q\sigma}|^2 \left\langle a_{k\sigma}^\dagger(t') \gamma_{q\sigma}(t') \gamma_{q\sigma}^\dagger(t) a_{k\sigma}(t) \right\rangle_0 \end{aligned} \right\}. \quad (2.21)$$

Next we assume  $\delta\hat{V} = 0$  and use  $a_{k\sigma}(t) = e^{-i\epsilon_k t/\hbar} a_{k\sigma}$  and  $\gamma_{q\sigma}(t) = e^{-iE_q t/\hbar} \gamma_{q\sigma}$ .

Also we take the initial time  $t_0 \rightarrow \infty$ . By identifying Dirac delta functions

$\delta(x) = \frac{1}{2\pi} \int_{-\infty}^{\infty} dt e^{ixt}$ , we get

$$\Gamma_{N \rightarrow S} = \frac{2\pi}{\hbar} \sum_{kq\sigma} |t_{kq}|^2 \left\{ \begin{aligned} & |v_{q\sigma}|^2 \left\langle a_{k\sigma}^\dagger a_{k\sigma} \gamma_{-(q\sigma)}^\dagger \gamma_{-(q\sigma)} \right\rangle_0 \delta(\epsilon_k + E_q) + \\ & |u_{q\sigma}|^2 \left\langle a_{k\sigma}^\dagger a_{k\sigma} \gamma_{q\sigma} \gamma_{q\sigma}^\dagger \right\rangle_0 \delta(\epsilon_k - E_q) \end{aligned} \right\}, \quad (2.22)$$

which is a Fermi golden rule result. Now we change the sums over  $k$  and  $q$  to integrals over energies  $\epsilon_k$  and  $E_k$  which we relabeled as  $\epsilon$  and  $E$  correspondingly. We also make a change of variables for the  $v_{q\sigma}$  term and assume a constant normal state density of states. We obtain

$$\Gamma_{N \rightarrow S} = \frac{1}{e^2 R_T} \int_{-\infty}^{\infty} dE n_S(E) f_N(E - \mu_N) (1 - f_S(E)), \quad (2.23)$$

where  $R_T$  is the tunnel resistance of the junction since it determines the ohmic behaviour of the junction at high bias voltage.  $n_S(E)$  is the DoS of a superconductor of Eq. (2.7) and  $f_N$  the Fermi occupation probability for the normal metal, and  $f_S$  for the superconductor. The remaining terms of Eq. (2.19) yield

$$\Gamma_{S \rightarrow N} = \frac{1}{e^2 R_T} \int_{-\infty}^{\infty} dE n_S(E) (1 - f_N(E - \mu_N)) f_S(E), \quad (2.24)$$

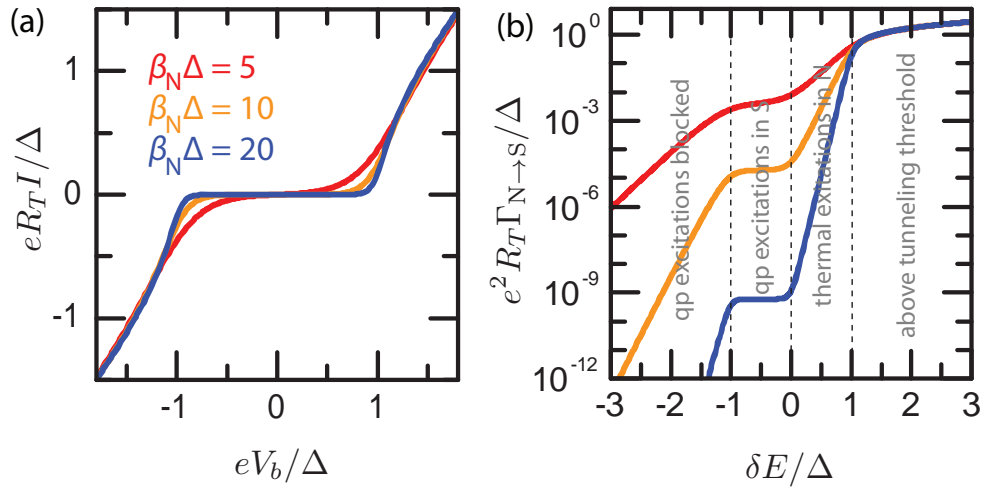


**Figure 2.3. Calculated current and tunneling rates in an NIS junction.** (a), Single-electron current  $I$  through a voltage biased NIS junction at various normal metal temperatures ( $\beta_N = 1/k_B T_N$ ). (b), The corresponding tunneling rate  $\Gamma_{N \rightarrow S}(\delta E)$  as a function of the energy gained  $\delta E$  in the tunneling process.

which is the tunneling rate from the superconductor to the normal metal. For a single NIS junction biased with voltage  $V_b$  the chemical potential shift is  $\mu_N = eV_b$  and the total tunnel current is  $I = e(\Gamma_{N \rightarrow S} - \Gamma_{S \rightarrow N})$ , which we present for three different temperatures in Fig. 2.3 (a). The lowest temperature result catches well the features of the experimental curve of Fig. 2.2 (b). This tunneling current through an NIS junction was measured already in 1960 by I. Giaever [41] and it was one of the first experimental evidences of the existence of the superconductor energy gap  $\Delta$ . The energy gap appears in the curves as suppressed current at  $|eV_b| < \Delta$ , since single-electron tunneling to a superconductor involves an unpaired electron with an energy cost of at least  $\Delta$ . This feature is smeared as temperature increases, as shown in Fig. 2.3 (a). It demonstrates that in addition to the biasing, the energy can be provided also by the thermal bath.

The chemical potential shift  $\mu_N$  appearing in Eq. (2.23) is the energy gained by the electron in the tunneling process from N to S. On the other hand, in Eq. (2.24) it is the energy cost for the opposing tunneling process. It is instructive to write both of the rates as a function of the energy gain  $\delta E$  which the electron obtains in a tunneling process. With this, we have

$$\Gamma_{N \rightarrow S}(\delta E) = \frac{1}{e^2 R_T} \int_{-\infty}^{\infty} dE n_S(E) f_N(E - \delta E) (1 - f_S(E)) \quad (2.25)$$

and

$$\Gamma_{S \rightarrow N}(\delta E) = \frac{1}{e^2 R_T} \int_{-\infty}^{\infty} dE n_S(E) (1 - f_N(E + \delta E)) f_S(E). \quad (2.26)$$

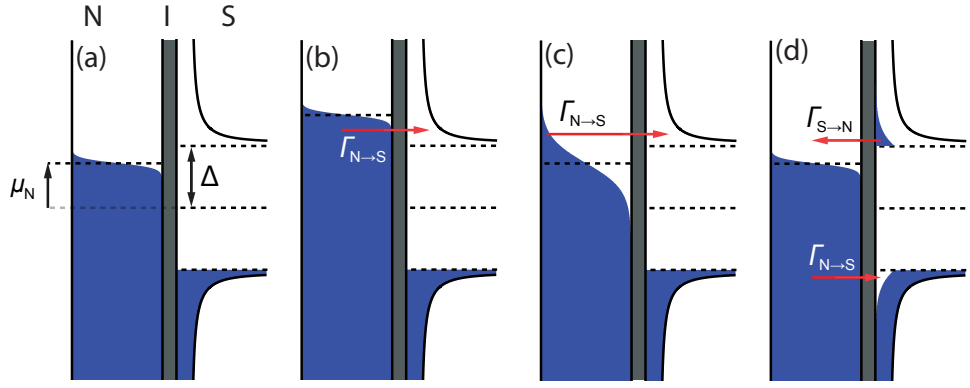


**Figure 2.4. Schematic presentation of tunneling in an NIS junction.** (a), Density of states of a normal metal (N) and a superconductor (S) which are shifted by the chemical potential  $\mu_N$ . Blue color represents occupied states and white empty states which follow Fermi distribution. In panel (a),  $\mu_N < \Delta$  and hence tunneling is suppressed. In panel (b),  $\mu_N > \Delta$ , and hence tunneling is taking place even at low temperatures with the rate  $\Gamma_{N \rightarrow S}$ . In panel (c) the temperature of the normal metal is elevated with respect to (a), which increases  $\Gamma_{N \rightarrow S}$ . Panel (d) shows tunneling rates for an elevated temperature of the superconductor.

It is now straightforward to show that  $\Gamma_{S \rightarrow N}(\delta E) = \Gamma_{N \rightarrow S}(\delta E)$ , i.e. that the tunneling rate depends on the energy gained by the electron but not whether it is coming from a normal metal or a superconductor. Hence we could drop subscripts  $N \rightarrow S$  and  $S \rightarrow N$  off. However, the discussion below is more apparent with the direction explicitly considered. We can for example distinguish the hole and particle like excitations on a superconductor explicitly. Therefore we still keep the subindices.

Now we are ready to consider the tunneling rates in an NIS junction in more detail with the density of states (DoS) diagrams shown in Fig. 2.4. See Sect. 2.1 for obtaining the diagrams. We assume the occupation of the states to follow Fermi distribution. In the diagram in panel (a) we take the temperature of the superconductor to be  $T_S = 0$ , i.e. all the states on the lower branch,  $E < -\Delta$ , are occupied and all at the higher one,  $E > \Delta$ , are vacant. The chemical potential  $\mu_N$  shifts the two densities with respect to each other and electrons tunnel then horizontally. Tunneling is possible if an occupied state is found on one side and a vacant one on the other. The probability for having an occupied state in normal metal is  $f_N$  and in superconductor  $f_S$ , while the probability to have a vacant one on the other sides are  $(1 - f_S)$  and  $(1 - f_N)$  respectively. The tunneling rates of Eqs. (2.23) and (2.24) are then obtained by integrating over the product of the two DoSes and these probabilities.

In panel (a) the condition of having occupied state on one side and vacant on the other is not met for a considerable amount of states ( $\mu_N < \Delta$ ) and

hence current is exponentially suppressed. In panel (b) we have  $\mu_N > \Delta$ . The occupied states of N are now so high that the tunneling to the upper empty branch of S becomes possible. This produces the onset of current at  $eV_b = \Delta$ , seen in Fig. 2.3 (a). In panel (c) of Fig. 2.4 we show elevated temperature of N in comparison to (a). High energy states are now thermally populated at N and hence current for  $eV_b < \Delta$  is increased, causing the smearing. In panel (d) elevated temperature of S is shown. Some of the states at the lower branch are vacant and some at the higher branch are occupied. These quasiparticle excitations give rise to tunneling. From the higher branch of the superconductor, the electrons tunnel to the normal metal. On the other hand, the vacancies on the lower branch are filled by electrons tunneling from the normal metal leading to current in the opposite direction.

As a summary, we present Fig. 2.3 (b), where  $\Gamma_{N \rightarrow S}$  is plotted as a function of the energy gain  $\delta E$ . We observe that there are four regimes of tunneling. For  $\delta E > \Delta$ , the zero temperature tunneling threshold is exceeded and the tunneling rate is insensitive to temperature. For  $0 < \delta E < \Delta$ , the current becomes exponentially suppressed at low temperatures as only electrons at high enough energy at the normal metal are able to tunnel. For  $-\Delta < eV_b < 0$ , the tunneling is dominated by quasiparticle excitations at the superconductor, see the rate  $\Gamma_{N \rightarrow S}$  in panel (d) of Fig. 2.4. The quasiparticle excitations cause a bias independent rate as all the excitations are at high energies  $|E| > \Delta$  in the BCS density of states. For  $eV_b < -\Delta$ , even the quasiparticle tunneling is suppressed as there are no occupied states available on the normal metallic leads which could tunnel and fill the vacant excitation states of the superconductor.

The rates at  $\delta E < 0$  are not seen in Fig. 2.3 (a) since they are overwhelmed by the opposing rate with  $\delta E > 0$ . Therefore, typically a single voltage biased NIS junction cannot be used to probe the excitations in a superconductor. However, if the temperature of the superconductor  $T_S$  is higher than the temperature of the normal metal  $T_N$ , the quasiparticle excitations of the superconductor dominate the current also in a region where  $\delta E > 0$ . However, as the vacancies on the lower branch of the superconductor generate current with the same magnitude but opposite direction as the particle excitations on the upper branch, the resulting net current is zero. Again the NIS junction cannot be used for probing the total number of excitations on a superconductor. However, it is possible to probe whether the two branches have non-equal number of excitations.

This situation is known as branch imbalance [42]. In order to probe the total number of such excitations, we either need to observe the tunneling events individually or rectify the current to one preferred direction. These options are discussed in Sect. 6.1.



### 3. Charging energy - the SINIS turnstile

In Sect. 2.2 we calculated the single-electron tunneling rates for a voltage biased NIS junction. Now we extend the discussion to describe a single-electron transistor (SET) [39, 43, 44]. A typical SET studied in this thesis is shown in Fig. 3.1 (a). In this device, we have a normal metallic island (N) contacted to superconducting leads (S) by NIS junctions forming a device called SINIS turnstile. The operation of the SET is controlled by applying bias voltage ( $V_1$  and  $V_2$ ) and by polarizing the island with a gate voltage  $V_g$ . Typically, current  $I$  through the device is measured. We first consider the charging energy cost of a small metallic island in Sect. 3.1. Then we discuss in Sect. 3.2 the static operation of the SINIS turnstile and finally in Sect. 3.3 we apply a radio frequency drive to the gate and obtain the quantization of electrical current.

#### 3.1 Energy considerations

In order to describe the transport in an SET, we need to consider the energy required for charging the island with  $n$  electrons and include it to the energy gain  $\delta E$  discussed in Sect. 2.2.2. Since electrons tunnel sequentially, we may consider the tunnel junctions of Fig. 3.1 as capacitive elements before and after a tunneling event. Also the gate electrodes are capacitively coupled to the island. These elements are described by capacitances  $C_i$  with voltages  $V_i$  applied to them. Now let  $Q_i$  be the charge at the capacitor  $i$  and  $V_I$  the voltage at the island. We can express  $V_I$  and the charge  $ne$  at the island as

$$\begin{cases} V_I &= V_i - \frac{Q_i}{C_i} \\ ne &= \sum_i Q_i. \end{cases} \quad (3.1)$$

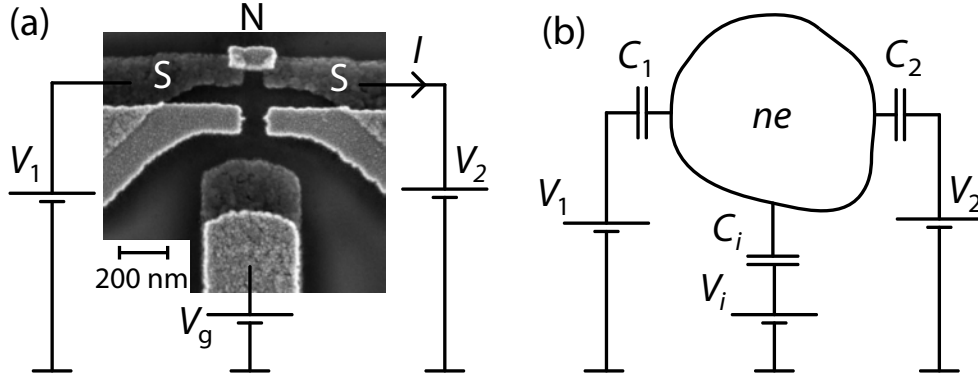


**Figure 3.1. Hybrid SET.** (a), A typical single electron transistor (SET) studied in this thesis. Superconducting leads (S) are contacted to a normal metallic island (N) by thin insulating barriers (I) to form a SINIS structure. (b), The circuit describing the SET from the point of view of electrostatics. The island has charge  $ne$  with  $n$  being the number of electrons. For energy considerations the tunnel junctions and the coupling between the gate and the island appear as capacitances  $C_i$  connected between voltage sources  $V_i$  and the island. We allow here the number of voltage sources to be arbitrary and thus we consider a more general situation than in panel (a).

Taking the upper equation for  $i$  and  $j$ , multiplying by  $C_i C_j$  and summing over  $j$  leads to

$$Q_i = C_i V_i + \frac{C_i}{C_\Sigma} e(n - n_g), \quad (3.2)$$

where  $C_\Sigma = \sum_i C_i$  is the total capacitance to the island and  $n_g = \sum_i C_i V_i / e$  the so-called gate offset. Now we are ready to determine the energy stored in the circuit. It is given by the Gibbs free energy where we take the energy stored in the capacitor and subtract the energy provided by the voltage sources. We obtain the charging energy as

$$E_{\text{ch}} = \sum_i \left( \frac{Q_i^2}{2C_i} - Q_i V_i \right). \quad (3.3)$$

Plugging Eq. (3.2) to Eq. (3.3) leads to a simple form

$$E_{\text{ch}}(n) = E_c (n - n_g)^2, \quad (3.4)$$

where  $E_c = \frac{e^2}{2C_\Sigma}$  is known as the charging energy, a characteristic energy for charging the island by one electron. To obtain Eq. (3.4), we took only the part depending on  $n$ , since only the energy differences when  $n$  changes are relevant for electron tunneling. When one electron tunnels into (+) or out from (-) the island, the energy gain of charging is

$$\delta E^\pm = -(E_{\text{ch}}(n \pm 1) - E_{\text{ch}}(n)) = \mp 2E_c (n - n_g \pm 1/2). \quad (3.5)$$

In addition we must consider the energy supplied by the voltage source. For an electron which tunnels from the voltage source  $V_i$ , the total energy gain is

$$\delta E_i^\pm = \mp 2E_c (n - n_g \pm 1/2) \mp eV_i. \quad (3.6)$$

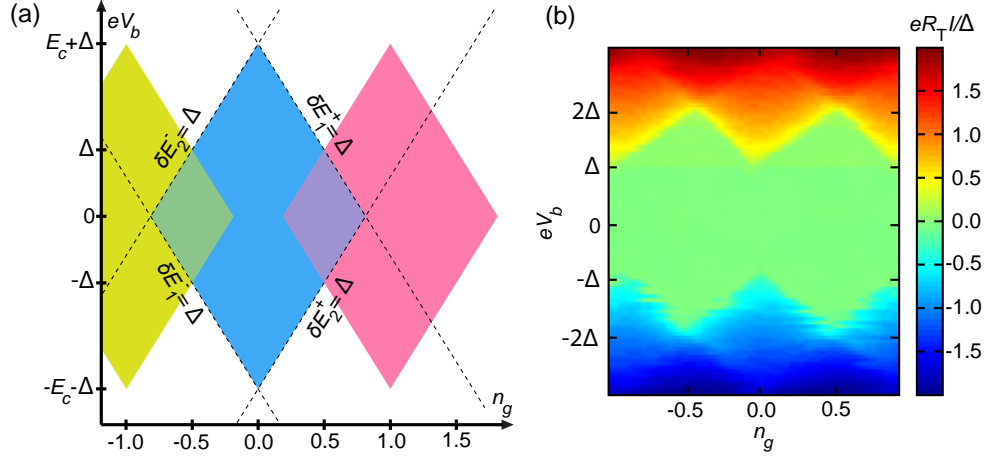


**Figure 3.2. Stability diagram of a SINIS turnstile.** (a), Tunneling thresholds  $\delta E_i^\pm = \Delta$  are shown as dotted lines for  $n = 0$ . These lines bound a Coulomb diamond, shown as a blue region, where the single-electron tunneling is suppressed due to an energy cost. Green and red areas show similar diamonds for  $n = -1$  and  $n = 1$  respectively. On the white area, none of the charge states  $n$  is stable and current runs through the SET. (b), Experimental current - voltage curve of a SINIS turnstile with  $E_c = 1.2\Delta$ . Coulomb diamonds of panel (a) are represented by the green area with suppressed current ( $I = 0$ ).

The tunneling rates for the corresponding processes are calculated with Eqs. (2.25) and (2.26) by substituting  $\delta E$  by the expression of Eq. (3.6).

Let us now consider the single-electron transistor with normal metallic island and two superconducting leads, see Fig. 3.1 (a). We take  $V_b = V_1 = -V_2$  to be the bias voltage per junction. On a qualitative level, the operation of the device can be understood by simple energy considerations. Let us consider the island to have  $n$  electrons on the island. The single-electron tunneling is suppressed if none of the tunneling processes gain energy to break a Cooper pair, i.e.  $\delta E_i^\pm < \Delta$ . These conditions bound a region colored blue in Fig. 3.2 (a) for  $n = 0$ . It is known as a Coulomb diamond. The boundaries of the diamond,  $\delta E_i^\pm = \Delta$ , are known as tunneling thresholds, since once they are crossed, tunneling becomes energetically possible and electron number  $n$  changes. At low bias,  $|eV_b| < \Delta$ , crossing a tunneling threshold leads to another Coulomb diamond, either  $n = -1$  or  $n = 1$  shown as green and red respectively, and the current is again suppressed. At higher bias,  $|eV_b| > \Delta$ , there is no stable charge state after crossing the threshold. This means that electron tunneling out of and into the island are both possible and current runs through the device. In Fig. 3.2 (b) experimental data for such a device is shown. The diamonds correspond to a region where the current is suppressed. The size and the shape of the diamonds allow us to obtain a rough estimate of  $\Delta = 220 \mu\text{eV}$  and  $E_c = 1.2\Delta$ .

It is worthwhile to note that by using a normal metallic island, the supercurrent through the device is suppressed unlike in a fully superconducting SET [1]. In order to have supercurrent in a SINIS transistor, the superconducting leads should induce superconductivity to the island with so-called proximity effect [45], which, however would call for clean metal-to-metal contacts. The tunnel barriers of the turnstile suppress the proximity effect down to a level where it does not influence the turnstile operation.

### 3.2 Master equation

So far, we have made energy considerations of the SINIS turnstile. Now we consider how the current  $I$  through the device is calculated. This is achieved with the help of a master equation. We assign a probability  $P(n)$  for having  $n$  excess electrons on the island. The time evolution of  $P(n)$  with single-electron tunneling is

$$\frac{d}{dt}P(n) = -\Gamma_{n,n}P(n) + \Gamma_{n-1,n}P(n-1) + \Gamma_{n+1,n}P(n+1), \quad (3.7)$$

where  $\Gamma_{n+1,n}$  is the sum of tunneling rates decreasing the electron number from  $n+1$  to  $n$  and  $\Gamma_{n-1,n}$  contains the rates increasing it from  $n-1$  to  $n$ .  $\Gamma_{n,n} = \Gamma_{n,n-1} + \Gamma_{n,n+1}$  is the sum of all rates away from the state with  $n$  excess electrons. Once  $P(n)$  is known, the current through junction  $i$  is obtained as

$$I_i = -e \sum_n P(n) \left[ \Gamma_{S \rightarrow N}(\delta E_i^+(n)) - \Gamma_{N \rightarrow S}(\delta E_i^-(n)) \right]. \quad (3.8)$$

In Fig. 3.3 (a) we plot  $I$  calculated with the master equation and compare the result to experimental data. We observe that there is a decent but not quantitative correspondence if we assume that the system is not overheated. Next we take into account the overheating of the normal metallic island as will be discussed below [16]. This assumption results in a better correspondence between the experimental data and calculations and allows one to extract the value of  $E_c$  reliably.

In addition to the electrical current, it is possible to consider heat flow with the master equation approach [46, 47]. Considering overheating is especially important at low temperatures. For example, in order to estimate the device parameters precisely for a SINIS turnstile, the heating of the normal metallic island needs to be considered: the electrons on a small island, operated at low temperatures, are poorly coupled thermally

to the substrate. The heat flow  $\dot{Q}$  to the normal metallic island has an expression resembling Eq. (3.8), reading

$$\dot{Q} = \sum_{n,i} P(n) \left[ \dot{Q}_{S \rightarrow N}(\delta E_i^+(n)) + \dot{Q}_{N \rightarrow S}(\delta E_i^-(n)) \right]. \quad (3.9)$$

Here  $\dot{Q}_{S \rightarrow N}(\delta E_i^+(n))$  and  $\dot{Q}_{N \rightarrow S}(\delta E_i^-(n))$  are the heat fluxes to the island for electrons tunneling in and out from the island with  $n$  electrons on the island. Note that for the heat flow into the island, we sum over the two junctions  $i$  whereas the electric current through the island is calculated for one of the junctions only. The heat fluxes are calculated with the operator for power deposited to the normal metal as

$$\dot{Q} = \frac{d}{dt} \hat{H}_N = \frac{i}{\hbar} [\hat{H}_T, \hat{H}_N]. \quad (3.10)$$

As a result of a similar analysis as in Eqs. (2.25) and (2.26), one obtains

$$\dot{Q}_{N \rightarrow S} = \frac{1}{e^2 R_T} \int_{-\infty}^{\infty} dE (-E + \delta E) n_S(E) f_N(E - \delta E) (1 - f_S(E)), \quad (3.11)$$

and

$$\dot{Q}_{S \rightarrow N} = \frac{1}{e^2 R_T} \int_{-\infty}^{\infty} dE (E + \delta E) n_S(E) (1 - f_N(E + \delta E)) f_S(E). \quad (3.12)$$

These equations are similar to Eqs. (2.25) and (2.26) but here the integrand contains the energy  $E \mp \delta E$  removed from or deposited to the normal metal. The heat flux to the superconductor can be calculated similarly. The only difference in the final result is that the energy removed or deposited is  $E$ . Summing the heat fluxes to the normal metal and the superconductor gives the total heat dissipated in the circuit as  $P = IV_{\text{tot}}$ , where  $I$  is the current through the system biased at voltage  $V_{\text{tot}}$ .

The heat injected to the normal metallic island  $\dot{Q}$  of Eq. (3.9) needs to be removed in order to avoid overheating. The bottle neck for heat removal in this case is the electron-phonon coupling [48]. The corresponding heat current is given by [48]

$$\dot{Q}_{\text{e-ph}} = \Sigma V (T_N^5 - T_0^5), \quad (3.13)$$

where  $\Sigma$  is a material constant,  $V$  the volume of the island,  $T_N$  the temperature of the normal metallic electrons and  $T_0$  the temperature of the phonons. We let  $T_N$  differ from  $T_0$ , the latter being at the base temperature of the cryostat, and find its value via the heat balance  $\dot{Q} = \dot{Q}_{\text{e-ph}}$ . This procedure is done iteratively by calculating the solution of the master equation for various values of  $T_N$ . In Fig. 3.3 (a) we show results of such calculations for one of the devices studied. We obtain parameter

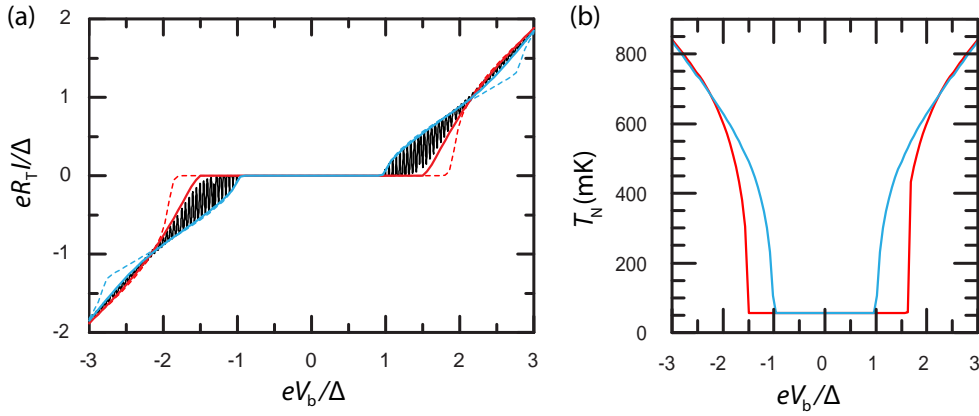


**Figure 3.3. Current - voltage curves of a SINIS transistor.** (a), Measured current of a SINIS transistor shown as a black line. Gate offset  $n_g$  is swept quickly and  $V_b$  slowly to obtain the so-called envelope curve where the current oscillates up and down to show the minimal and maximal values. Solid blue and red curves show simulations based on the master equation at  $n_g = 0.5$  and  $n_g = 0$  respectively. Here the electronic temperature of the island  $T_N$  is determined such that the energy balance  $\dot{Q} = \dot{Q}_{e-ph}$  holds. Dotted lines show similar simulations but with the island assumed to be fully thermalized to bath temperature. (b), Temperature of the island extracted from simulations of panel (a). Note that  $T_N$  increases up to 800 mK already at the bias voltage of  $\pm 3\Delta/e$ .

values  $R_T = 130 \text{ k}\Omega$  by fitting the slope at high bias,  $\Delta = 216 \text{ }\mu\text{eV}$  by fitting the size of the region with suppressed current, and  $E_c/\Delta = 0.9$  by fitting the current - voltage curves at  $n_g = 0$  and  $n_g = 0.5$ . The island volume  $V = 700 \text{ nm} \times 100 \text{ nm} \times 30 \text{ nm}$  was estimated from a scanning electron micrograph and material constant  $\Sigma = 2 \cdot 10^9 \text{ WK}^{-5}\text{m}^{-3}$ , consistent with other experiments [16], was used for the copper island. A value  $T_0 = 50 \text{ mK}$  was used based on the reading of the thermometer of the cryostat.

We observe that to obtain a good fit, the heating needs to be taken into account. If the island is assumed to be at the base temperature, shown as dotted lines in Fig. 3.3 (a), the fit is not perfect as already pointed out. However, the node points which are at  $eV_b \approx \pm 2\Delta$  for Fig. 3.3 (a), are not sensitive to heating but depend on  $E_c$ . This fact makes it possible to estimate  $E_c$  without performing a tedious overheating analysis. In Fig. 3.3 (b) the electronic temperature of the island is shown. It is extracted from the master equation calculation. We observe that the island heats up to 500 mK and above, which demonstrates the weakness of electron-phonon coupling at low temperatures. Based on Eq. (3.13), the temperature of the cryostat, assumed to be equal to the phonon temperature  $T_0$ , is fully irrelevant in this situation.

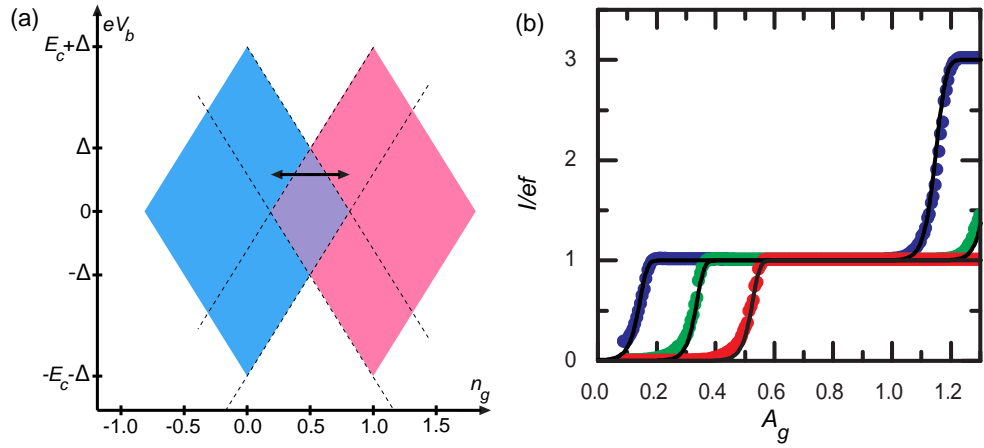


**Figure 3.4. Quantized current in a SINIS transistor.** (a), A stability diagram presenting the electron transfer. By moving between two Coulomb diamonds cyclically at  $|eV_b| < \Delta$ , one electron is taken into the island and another pushed out in each cycle. With non-zero  $V_b$ , the electrons have a preferred direction for tunneling and current  $I = ef$  results. (b), Measured current plateau of a SINIS turnstile (dots) and simulations based on Eq. (3.7) shown as black lines.

### 3.3 Current quantization in the SINIS turnstile

In Sect. 3.2 we considered the operation of a SINIS turnstile under fixed (time-independent) conditions and saw that the current is suppressed for  $|eV_b| < \Delta$ . Now we apply a periodic drive to the gate offset  $n_g$  and find out that quantized electrical current is obtained [34] in similar way as in the normal metallic turnstiles [31]. When a non-zero bias voltage with  $|eV_b| < \Delta$  is applied, the electron tunneling has a preferred direction. As  $n_g$  is changed such that we move between two stability diamonds as shown in Fig. 3.4 (a), one electron is pulled into the island from one junction and another one is pushed out from the opposite one. This leads to one electron being transported through the device in each cycle. In Fig. 3.4 (b) experimental data in such an operation is shown for three different bias voltages  $V_b = 60, 110, 160 \mu\text{V}$  as red, green and blue points. Note that here and throughout in this thesis we give the bias values per junction. For a SINIS turnstile, the total bias voltage is then twice this value. Device parameter values are  $R_T = 155 \text{ k}\Omega$ ,  $\Delta = 216 \mu\text{eV}$  and  $E_c = 0.63 \Delta$ . The drive frequency is  $f = 10 \text{ MHz}$ . We observe that the measured current  $I$  forms a plateau at the value  $ef$  which indicates that electrons are being transported one by one. The rise to the plateau and beyond it are determined by the tunneling thresholds. The higher the bias, the earlier the current increases as a function of the gate amplitude  $A_g$ .

The shape of these current-voltage curves can be calculated by solving

Eq. (3.7) numerically and calculating the average current of one cycle with Eq. (3.8). We show the resulting current curves in Fig. 3.4 (b) as solid black lines and we see that the overall features of the pumping plateau are described well by the sequential single-electron tunneling model. In the forthcoming chapters, we consider the current at the plateau and different processes which influence the value of the current at the plateau. We will see that many of the error sources can be suppressed and hence we expect the device to reach a relative accuracy on the level of  $10^{-7}$  or below [49]. This would be just barely sufficient for metrological applications [50–52].

It is advisable to operate the SINIS turnstile at the highest possible frequency since it results in maximal output current and minimizes possible frequency independent errors such as thermal errors [34]. High currents are preferred since they are easier to measure precisely. The current of the turnstile is limited by an average time  $\tau_{\text{tun}}$  needed for an electron tunneling event to occur. In order to avoid missed tunneling events, the requirement  $\tau_{\text{tun}} \ll 1/\Gamma$  must be satisfied, where  $\Gamma$  is the tunneling rate of the process. The tunneling rate  $\Gamma$  scales linearly with the tunnel junction conductance  $G_T = R_T^{-1}$ . However,  $G_T$  must be limited to avoid errors arising from higher order tunneling processes [49]. Thus the highest output current of a single turnstile is few tens of picoamperes if the relative accuracy of  $10^{-7}$  is required [49, 53].

One of the advantages of the SINIS turnstile is that the operation principle is simple. This allows to obtain higher output currents with parallelization. In Publication I, we have shown that ten such devices can be operated in parallel. A reason hindering a large scale parallelization of any single-electron device is the presence and the variation of the offset charges nearby the islands. These are random and they have to be compensated for each SET island separately by a gate voltage. This is the main drawback of the devices which provide today the best quantization accuracy. These devices are based on  $N$  normal metallic islands tunnel coupled in series and they reach a relative uncertainty of  $10^{-8}$  for the current quantization [25, 28]. However, the obtainable output current of the order of 1 pA is two to three orders of magnitude below the required level for quantum metrological applications, apart from the capacitance standard [32]. The SINIS turnstile has two benefits over the normal metallic arrays in terms of output current. First, the obtainable current is  $(N + 1)/2$  times higher since a cycle involves only two tunneling events whereas in the array  $N + 1$  events are present. On the other hand,

with the gate control of  $N$  islands in the array, we can control  $N$  turnstiles in parallel. With the same complexity in the experimental setup, we can thus obtain roughly a factor of  $N^2/2$  higher currents with a SINIS turnstile. With the ten devices of Publication I, 100 pA output current sufficient for metrological applications [50, 51] was obtained.



## 4. Environmentally activated tunneling

In the considerations of Sect. 2.2.2 we assumed ideal voltage bias for the tunnel junctions. The energy conservation required then that the electrons gain or lose always a known amount of energy set by the voltage sources and charging effects. In the energy diagrams of Fig. 2.4, this was seen as electrons tunneling always horizontally. However, the experiments are typically carried out in a non-ideal configuration. Instead of an ideal voltage bias, there are voltage fluctuations present which are modelled with a photon bath [23, 54, 55]. With this relatively simple model, several experimental observations are explained, see e.g. Refs. [56, 57]. These fluctuations may arise from a dissipative circuit near the device, from thermal radiation, from the electronics used in the measurements or they can be inherent for the device, as is the case for shot-noise in electron tunneling [58, 59]. If the photons carry sufficiently large energy,  $E \gtrsim \Delta$ , they may provide it to the electrons so that they are able to create excitations in a superconductor and therefore single-electron tunneling becomes activated even when it would otherwise be suppressed. In this chapter, we consider this effect with the so-called  $P(E)$  theory [23]. In Sect. 4.1 we first review the results of the  $P(E)$  theory. Then in Sect. 4.2 we show theoretically and experimentally that a hot resistive environment is an origin of Dynes density of states in NIS junctions. Finally in Sect. 4.3, the low bias leakage of NIS junctions is considered for other environments as well.

### 4.1 The $P(E)$ theory

In the  $P(E)$  theory the electromagnetic environment is modelled with a frequency dependent impedance  $Z(\omega)$ . We take it to have temperature  $T_{\text{env}}$  which may differ from the temperature where the tunnel junctions

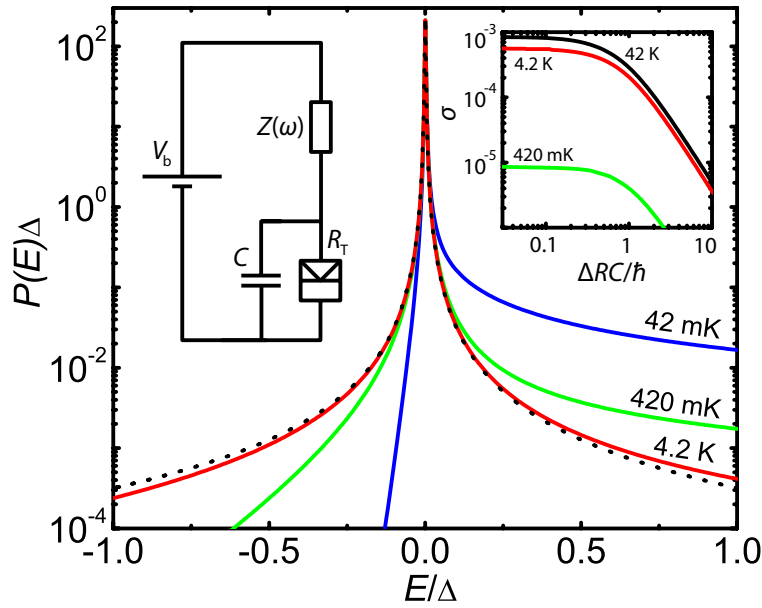


**Figure 4.1. Photon assisted tunneling.** The probability density  $P(E)$  that the environment absorbs energy  $E$  from an electron which tunnels. The different curves correspond to different temperatures of the environment. We have taken  $\sigma_0 = \frac{R}{R_Q} \frac{k_B T_{\text{env}}}{\Delta} = 10^{-3}$ , which determines the leakage at high temperature and low capacitance, for all the curves. Here the environmental impedance  $Z(\omega)$  is taken to be resistive with resistance  $R$ .  $T_{\text{env}}$  is the temperature of the environment and  $R_Q = \hbar/e^2$ . Dotted line is the analytic expression of Eq. (4.21). The schematic shows a single NIS junction biases by voltage  $V_b$ . However, the environmental impedance  $Z(\omega)$  makes this voltage fluctuate. These fluctuations are shunted by capacitance  $C$ . Panel on the right shows the effective leakage  $\sigma$  for a single junction as a function of  $C$ . Figure adapted from Publication II.

are located. In addition to  $Z(\omega)$  we include also a capacitance  $C$  to shunt the junctions for demonstrating that at large enough values of  $C$  the photons are not coupled to the junction. The circuit we consider is shown in Fig. 4.1 for a single junction. The results apply directly also to multijunction circuits such as a SET with rescaled parameter values [23]. The impedance  $Z(\omega)$  and the capacitance  $C$ , forming the total impedance  $Z_t(\omega) = (Z(\omega)^{-1} + i\omega C)^{-1}$ , are modelled by a set of harmonic oscillators, see Eqs. (2.8) and (2.10). Now we relax the assumption  $\delta\hat{V} = 0$ , which was done to obtain Eq. (2.22). If that assumption is not made, we have

$$\begin{aligned}
 \Gamma_{N \rightarrow S} = & \frac{1}{\hbar^2} \int_{-t_0}^t dt' \sum_{kq\sigma} |t_{kq}|^2 \left\{ \right. \\
 & |v_{q\sigma}|^2 e^{\frac{i}{\hbar}(\epsilon_k + E - q)(t-t')} f_k f_{-q} \langle e^{i\hat{\varphi}(t)} e^{-i\hat{\varphi}(t')} \rangle_0 \\
 & + |u_{q\sigma}|^2 e^{\frac{i}{\hbar}(\epsilon_k - E - q)(t-t')} f_k (1 - f_q) \langle e^{i\hat{\varphi}(t)} e^{-i\hat{\varphi}(t')} \rangle_0 \\
 & + |v_{q\sigma}|^2 e^{-\frac{i}{\hbar}(\epsilon_k + E - q)(t-t')} f_k f_{-q} \langle e^{i\hat{\varphi}(t')} e^{-i\hat{\varphi}(t)} \rangle_0 \\
 & \left. + |u_{q\sigma}|^2 e^{-\frac{i}{\hbar}(\epsilon_k - E - q)(t-t')} f_k (1 - f_q) \langle e^{i\hat{\varphi}(t')} e^{-i\hat{\varphi}(t)} \rangle_0 \right\}.
 \end{aligned} \tag{4.1}$$

We see that the effect of the environment is described by terms  $\langle e^{i\hat{\varphi}(t_1)} e^{-i\hat{\varphi}(t_2)} \rangle_0$ . For the coupling of the photon bath to the tunnel junction we assume it to be linear in bosonic annihilation and creation operators [60], i.e.

$$\hat{\varphi}(t) = \sum_{\lambda} c_{\lambda} b_{\lambda}^{\dagger}(t) + h.c. = \sum_{\lambda} c_{\lambda} b_{\lambda}^{\dagger} e^{i\omega_{\lambda} t} + h.c., \quad (4.2)$$

where  $c_{\lambda}$  are constants defining the environment and its coupling and *h.c.* stands for hermitian conjugate. To proceed, we used identity  $e^{\hat{A}+\hat{B}} = e^{\hat{A}} e^{\hat{B}} e^{-[\hat{A}, \hat{B}]/2}$ , which holds if  $[\hat{A}, \hat{B}]$  commutes with  $\hat{A}$  and  $\hat{B}$ . Since

$$[i\hat{\varphi}(t), i\hat{\varphi}(t')] = \sum_{\lambda} |c_{\lambda}|^2 \left( e^{i\omega_{\lambda}(t-t')} - e^{-i\omega_{\lambda}(t-t')} \right) = c(t-t') \quad (4.3)$$

is a complex number, it commutes with  $i\hat{\varphi}(t)$  and  $i\hat{\varphi}(t')$ . Therefore we obtain

$$e^{i\hat{\varphi}(t)} e^{-i\hat{\varphi}(t')} = e^{-c(t-t')/2} e^{i(\hat{\varphi}(t)-\hat{\varphi}(t'))}. \quad (4.4)$$

Next, we use the identity  $\langle e^{\hat{A}} \rangle_0 = e^{\frac{1}{2}\langle \hat{A}^2 \rangle_0}$ , which holds for thermal average where  $\hat{A}$  is a linear combination of bosonic creation and annihilation operators. Also, we are interested only on the steady-state case when the time difference  $t - t'$  matters but not the initial time. Therefore we may set  $t' = 0$  without losing generality, and remember that  $t$  is the time difference. Then we have

$$\langle e^{i\hat{\varphi}(t)} e^{-i\hat{\varphi}(0)} \rangle_0 = e^{J(t)}, \quad (4.5)$$

where

$$J(t) = -\frac{1}{2} \left( c(t) + \langle (\hat{\varphi}(t) - \hat{\varphi}(0))^2 \rangle_0 \right). \quad (4.6)$$

By using Eq. (4.2), we obtain

$$J(t) = \sum_{\lambda} |c_{\lambda}|^2 \left\{ e^{i\omega_{\lambda} t} n(\omega_{\lambda}) + e^{-i\omega_{\lambda} t} (n(\omega_{\lambda}) + 1) - (2n(\omega_{\lambda}) + 1) \right\}, \quad (4.7)$$

where  $n(\omega_{\lambda}) = \langle b_{\lambda}^{\dagger} b_{\lambda} \rangle_0 = (e^{\beta_{\text{env}} \hbar \omega_{\lambda}} - 1)^{-1}$ , is the Bose-Einstein distribution at thermal equilibrium with  $\beta_{\text{env}} = 1/(k_B T_{\text{env}})$ . Now we express  $J(t)$  in frequency basis as

$$J(t) = \int d\omega e^{-i\omega t} \sum_{\lambda} |c_{\lambda}|^2 \left\{ \delta(\omega + \omega_{\lambda}) n(\omega_{\lambda}) + \delta(\omega - \omega_{\lambda}) (n(\omega_{\lambda}) + 1) - \delta(\omega) (2n(\omega_{\lambda}) + 1) \right\}, \quad (4.8)$$

and use the fluctuation dissipation theorem [61] to link it to the environmental impedance  $Z_t(\omega)$ . For voltage fluctuations across the impedance  $Z_t(\omega)$  we have

$$\langle \delta \hat{V}^2 \rangle = \hbar \omega \text{Re}(Z_t(\omega)) \coth(\beta_{\text{env}} \hbar \omega / 2). \quad (4.9)$$

The voltage fluctuations can be related to the phase fluctuations as

$$\hat{\phi} = \frac{e}{\hbar} \int dt \delta \hat{V} \Rightarrow \langle \hat{\phi}^2 \rangle = \frac{e^2}{(\hbar\omega)^2} \langle \delta \hat{V}^2 \rangle = \frac{e^2}{\hbar\omega} \text{Re}(Z_t(\omega)) \coth(\beta_{\text{env}} \hbar\omega/2). \quad (4.10)$$

On the other hand, from Eq. (4.2) we obtain

$$\begin{aligned} \langle \hat{\phi}^2 \rangle &= \frac{1}{2} \int dt e^{i\omega t} \langle \{ \hat{\varphi}(t), \hat{\varphi}(0) \} \rangle_0 \\ &= 2\pi \sum_{\lambda} |c_{\lambda}|^2 \left( n(\omega_{\lambda}) + 1/2 \right) \left( \delta(\omega + \omega_{\lambda}) + \delta(\omega - \omega_{\lambda}) \right). \end{aligned} \quad (4.11)$$

Combining Eqs. (4.10) and (4.11) leads to

$$\begin{aligned} &\sum_{\lambda} |c_{\lambda}|^2 \left( n(\omega_{\lambda}) + 1/2 \right) \left( \delta(\omega + \omega_{\lambda}) + \delta(\omega - \omega_{\lambda}) \right) \\ &= \frac{\text{Re}(Z_t(\omega))}{\omega R_K} \coth(\beta_{\text{env}} \hbar\omega/2), \end{aligned} \quad (4.12)$$

where  $R_K = h/e^2$  is the resistance quantum, also known as the von Klitzing constant [62]. Next, we want to plug the result of Eq. (4.12) to Eq. (4.8). In addition, we need the zero temperature limit of Eq. (4.12). Since,  $\omega_{\lambda} > 0$ , by letting  $T_{\text{env}} \rightarrow 0$ , we have

$$\begin{cases} \frac{1}{2} \sum_{\lambda} |c_{\lambda}|^2 \delta(\omega + \omega_{\lambda}) = -\frac{\text{Re}(Z_t(\omega))}{\omega R_K}, & \omega > 0 \\ \frac{1}{2} \sum_{\lambda} |c_{\lambda}|^2 \delta(\omega - \omega_{\lambda}) = +\frac{\text{Re}(Z_t(\omega))}{\omega R_K}, & \omega < 0. \end{cases} \quad (4.13)$$

Plugging Eqs. (4.12) and (4.13) to Eq. (4.8) leads to

$$\begin{aligned} J(t) &= 2 \int_0^{\infty} \frac{d\omega}{\omega} \frac{\text{Re}(Z_t(\omega))}{R_K} \left\{ \coth\left(\frac{\beta_{\text{env}} \hbar\omega}{2}\right) \cos \omega t - i \sin \omega t \right\} \\ &\quad - 2 \sum_{\lambda} |c_{\lambda}|^2 \left( n(\omega_{\lambda}) + 1/2 \right) \delta(\omega) \end{aligned} \quad (4.14)$$

From Eq. (4.7) we see that  $J(0) = 0$ . Requiring this for Eq. (4.14) yields,  $\sum_{\lambda} |c_{\lambda}|^2 \left( n(\omega_{\lambda}) + 1/2 \right) \delta(\omega) = \int_0^{\infty} \frac{d\omega}{\omega} \frac{\text{Re}(Z_t(\omega))}{R_K} \coth\left(\frac{\beta_{\text{env}} \hbar\omega}{2}\right)$  and we finally obtain

$$J(t) = 2 \int_0^{\infty} \frac{d\omega}{\omega} \frac{\text{Re}(Z_t(\omega))}{R_K} \left\{ \coth\left(\frac{\beta_{\text{env}} \hbar\omega}{2}\right) (\cos \omega t - 1) - i \sin \omega t \right\}, \quad (4.15)$$

which is the result in Ref. [23]. We continue now with Eq. (4.1). Taking  $t_0 \rightarrow \infty$  we get

$$\begin{aligned} \Gamma_{N \rightarrow S} &= \frac{1}{\hbar^2} \int_{-\infty}^{\infty} dt \sum_{kq\sigma} |t_{kq}|^2 \left\{ |v_{q\sigma}|^2 e^{\frac{i\hbar}{\hbar}(\epsilon_k + E - q)} f_k f_{-q} e^{J(t)} \right. \\ &\quad \left. + |u_{q\sigma}|^2 e^{\frac{i\hbar}{\hbar}(\epsilon_k - E - q)} f_k (1 - f_q) e^{J(t)} \right\}. \end{aligned} \quad (4.16)$$

Now we define a function

$$P(E) = \frac{1}{2\pi\hbar} \int dt e^{J(t)} e^{\frac{i\hbar}{\hbar} E}, \quad (4.17)$$

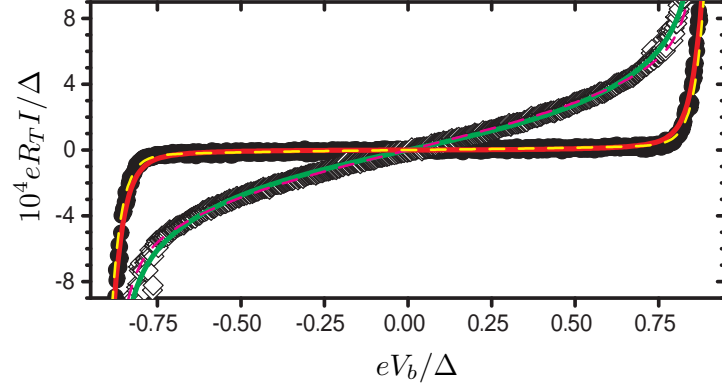


**Figure 4.2. Leakage current of an NIS junction caused by electromagnetic environment.** Measured IV curves of an NIS junction with  $R_T = 761$  k $\Omega$  on the ground plane (solid symbols) and of a similar junction with  $R_T = 627$  k $\Omega$  without the ground plane (open symbols). Solid lines present the results of the full  $P(E)$  theory for capacitance  $C = 10$  pF (red line) and  $C = 0.3$  pF or smaller (green line). The resistance and the temperature of the environment are set to  $R = 2$   $\Omega$  and  $T_{\text{env}} = 4.2$  K, respectively, and  $\Delta = 200$   $\mu\text{eV}$ . The dashed lines correspond to the Dynes model with the parameters yielding the best fit to the data. The normalized zero-bias slope is  $5.3 \times 10^{-4}$  for the green line and  $2.6 \times 10^{-5}$  for the red line.

and obtain

$$\Gamma_{N \rightarrow S} = \frac{2\pi}{\hbar} \sum_{kq\sigma} |t_{kq}|^2 \left\{ |v_{q\sigma}|^2 P(\epsilon_k + E_{-q}) f_k f_{-q} + |u_{q\sigma}|^2 P(\epsilon_k - E_{-q}) f_k (1 - f_q) \right\}. \quad (4.18)$$

Finally, we change the summing to integration and make a change of variables to the  $v_{q\sigma}$  term and obtain

$$\Gamma_{N \rightarrow S}(\delta E) = \frac{1}{e^2 R_T} \int d\epsilon dE n_S(E) f_N(\epsilon - \delta E) (1 - f_S(E)) P(\epsilon - E). \quad (4.19)$$

This reduces to Eq. (2.25) if  $Z_t(\omega) = 0$ . In that particular case  $P(E) = \delta(E)$ . From Eq. (4.19) the  $P(E)$  function can be interpreted as a probability density that the electron which tunnels, emits energy  $E$  to the impedance  $Z_t(\omega)$ . Note that  $P(-E)$  is then the probability density of the electron to absorb energy  $E$ . By calculating the remaining terms, we obtain the tunneling rate to the reverse direction as

$$\Gamma_{S \rightarrow N}(\delta E) = \frac{1}{e^2 R_T} \int d\epsilon dE n_S(E) (1 - f_N(\epsilon + \delta E)) f_S(E) P(E - \epsilon). \quad (4.20)$$

With Eqs. (4.19) and (4.20) we are now ready to consider quantitatively the effect of the environment to an NIS junction.

## 4.2 Electromagnetic environment as an origin of Dynes DoS

We consider now a hot resistive environment with resistance  $R \ll R_K$ . With this impedance, the noise spectrum is white with a thermal cutoff. In

Publication II the resistive environment was utilized to show theoretically as well as experimentally that environmentally activated tunneling gives rise to leakage at sub-gap voltages in NIS junction based devices and it accounts for the phenomenological Dynes DoS typically used for modelling the leakage [63, 64]. In Fig. 4.1 the  $P(E)$  function is presented for various temperatures  $T_{\text{env}}$  and shunting capacitances  $C$ . If the temperature of the environment satisfies  $T_{\text{env}} > E/k_B$  and the capacitance is low,  $C < \hbar/(\Delta R)$ , the  $P(E)$  function of Eq. (4.17) is approximately Lorentzian:

$$P(E) = \frac{1}{\pi\Delta} \frac{\sigma_0}{\sigma_0^2 + (E/\Delta)^2}, \quad (4.21)$$

where  $\sigma_0 = \frac{R}{R_Q} \frac{k_B T_{\text{env}}}{\Delta}$  and  $R_Q = \hbar/e^2$ . See supplemental material of Publication II for derivation. When this is plugged into Eqs. (4.19) and (4.20) and the current through a voltage biased NIS junction,  $I = e(\Gamma_{N \rightarrow S} - \Gamma_{S \rightarrow N})$ , is evaluated, we obtain the same result as if we would do the calculation in the absence of the environment (Eqs. (2.25) and (2.26)) but use for the superconductor an effective density of states

$$n_S^\sigma(E) = \left| \text{Re} \left( \frac{E/\Delta + i\sigma}{\sqrt{(E/\Delta + i\sigma)^2 - 1}} \right) \right|, \quad (4.22)$$

which is known as the Dynes density of states [63, 64]. Here  $\sigma = \sigma_0$  is taken as a lifetime broadening of a level at energy  $E$ . For the derivation, see supplemental material of Publication II. Typically  $\sigma = 10^{-3} \dots 10^{-6}$  for aluminum based devices, so that the level broadening effect is small. In addition to the small broadening around energy  $E$ , the finite lifetime in Dynes DoS results in electronic states which are distant from the non-broadened energy levels. From Eq. (4.22) we see that we obtain states into the superconductor gap  $|E| < \Delta$ . For small energies  $E$ , we have  $n_S^\sigma(E) \approx \sigma$ . These subgap states cause linear leakage at low bias  $|eV_b| < \Delta$  and thus the Dynes DoS is often used to account such features in the experiment [65–70]. In view of the electro-magnetic environment as the origin of the Dynes DoS, these are not true electronic states but a result of photons providing the required energy for the unpaired electron in the superconductor. This was proven by measuring two NIS junctions, where one was on top of a ground plane and another one did not have it. The results are shown in Fig. 4.2. The device on top of the ground plane shows the anticipated linear leakage at low bias which is suppressed by an order of magnitude as compared to the junction off the ground plane. Inserting the ground plane increases the capacitance  $C$  between the junction electrodes. The voltage fluctuations are then suppressed and hence

$\sigma$  is decreased, see Fig. 4.1. This experiment demonstrates that one needs to shield carefully the sample against the fluctuations. The same effect was shown in Publication III in an electron counting experiment. The technique is discussed in detail in Sect. 5.3.

### 4.3 Subgap leakage of NIS junctions

The discussion of the leakage current of an NIS junction studied in Publication II was extended in Publication X to the case of a general  $Z(\omega)$ . The obtained results are limited to low bias voltages  $|eV_b| < \Delta$ . In other words, the emphasis is put on describing the subgap leakage and the broadening at  $|eV_b| > \Delta$  is not considered. In addition, the temperatures  $T_N$  and  $T_S$  at the junction are assumed to satisfy  $T_N, T_S \ll \Delta/k_B$ . Under these assumptions, the subgap current arising from environmental activation reads

$$I_{\text{sg}} \approx \sigma_{\text{env}} \frac{V}{R_T}, \quad (4.23)$$

where we have the leakage parameter

$$\sigma_{\text{env}} = 2 \int_{\Delta}^{\infty} dE n_S(E) P(-E). \quad (4.24)$$

Furthermore, expanding  $P(E)$  of Eq. (4.17) up to the first order of  $J(t)$  yields

$$\begin{aligned} P(E) &\approx \frac{1}{2\pi\hbar} \int dt e^{iEt/\hbar} [1 + J(t)] \\ &\approx \delta(E) + \frac{1}{\hbar} \int_0^{\infty} \frac{d\omega}{\omega} \frac{\text{Re}(Z_t(\omega))}{R_K} \left\{ \left[ \coth(\beta_{\text{env}}\hbar\omega/2) - 1 \right] \delta(E/\hbar + \omega) \right. \\ &\quad \left. + \left[ \coth(\beta_{\text{env}}\hbar\omega/2) + 1 \right] \delta(E/\hbar - \omega) - 2\hbar \coth(\beta_{\text{env}}\hbar\omega/2) \delta(E) \right\}. \end{aligned} \quad (4.25)$$

In this form, the  $P(E)$  function consists of both elastic and inelastic contributions. The inelastic one involves an exchange of exactly one photon between the junction and environment. In such one photon regime, the environment is weakly coupled to the junction. Evaluating the integral over  $\omega$  and plugging the result into Eq. (4.24) yields

$$\sigma_{\text{env}} = 4 \int_{\Delta}^{\infty} dE n_S(E) \frac{\text{Re}(Z_t(\omega))}{R_K} \frac{n(E)}{E}, \quad (4.26)$$

where  $n(E) = (e^{\beta_{\text{env}}E} - 1)^{-1}$  is the Bose-Einstein distribution of the photons. Equation (4.26) allows one to evaluate the low bias leakage for any environment weakly coupled to the junction. For the validity of the

weak coupling, see details in Publication X. With a resistive environment, Eq. (4.26) reduces to the result obtained in Sect. 4.2. An effective approach to suppress the leakage current is to place a resistive transmission line between the hot environment and the junction. A relevant parameter for the leakage suppression is the transmission coefficient  $\mathcal{T}_C(\omega)$ , which defines the damping of voltage fluctuations at frequency  $\omega$  when passing the transmission line. In Publication X it was shown that with the transmission line  $|\mathcal{T}_C(E/\hbar)|^2$  appears in the integrand of Eq. (4.26). The transmission coefficient  $\mathcal{T}_C$  decreases exponentially as the length  $l$  or the resistivity per unit length  $R_0$  of the line increases. Thus the subgap leakage was shown to scale as  $\sigma_{\text{env}} \propto e^{-l\sqrt{2\Delta R_0 C_0/\hbar}}$ , where  $C_0$  is the capacitance per unit length of the line. Utilizing the exponential suppression, it is possible to reach  $\sigma_{\text{env}} \lesssim 10^{-7}$ , as shown experimentally in Publication VI.

Suppressing the environmentally activated tunneling and obtaining a small value for  $\sigma_{\text{env}}$  has a direct influence on the current quantization accuracy of a SINIS turnstile. The influence of environmentally activated tunneling on the turnstile was experimentally demonstrated in Publication II by comparing a turnstile with and without the ground plane. Protection against environmentally activated tunneling is of paramount importance also for the experiments on Andreev tunneling of Chapter 5 and on quasiparticle excitations of Chapter 6. In these experiments, a ground plane, a better shielded sample holder or both were utilized for the protection. As a final remark of this chapter, we note that the electromagnetic environment not only causes spurious effects. By engineering it, the tunneling rates can be influenced in a way which improves the performance of the turnstile or other SET devices [71–73].

## 5. Higher order processes - Andreev tunneling

In Chapter 2 sequential single-electron tunneling in NIS junctions was discussed. This is often the dominant mechanism of charge transport. Multi-electron processes are especially important in the subgap regime where the bias voltage per junction satisfies  $|V_b| < \Delta/e$  and single-electron processes are suppressed, see Figs. 2.2 (b) and 2.3. In this case, multi-electron processes which avoid Cooper pair breaking are energetically favorable. One such process is elastic cotunneling, where an electron first tunnels from normal metal to a superconductor and then coherently to another normal metal [49, 74]. For the NISIN transistor of Sect. 6.4 this process is possible but the rates are lower than what we can detect with direct current measurements [74, 75]. For the other structures of this thesis cotunneling without breaking Cooper pairs is not allowed ideally since the second normal metallic part is missing. Therefore we neglect it in this thesis.

The other two-electron process avoiding the pair breaking energy cost involves a Cooper pair tunneling into a normal metal as two unbound electrons or reversely two electrons from the normal metal tunnel into the superconductor and form a Cooper pair. Processes, where normal metallic electrons are converted to Cooper pairs or vice versa are known as Andreev processes [2]. In the case of tunnel junctions we use the term "Andreev tunneling" since it corresponds to a two-electron tunneling process. Being the simplest process which avoids Cooper pair breaking, Andreev tunneling is also the one which produces typically the largest current. As more and more electrons are involved in a multi-electron process, the magnitude of the resulting current decreases. This is because the probability for  $N$  electrons to tunnel in the process is proportional to  $\mathcal{T}^N$ , where  $\mathcal{T} \ll 1$  is an average transmission probability for a single-electron [76]. The process being energetically possible and involving the smallest num-

number of electrons is hence dominant. This is reflected in the resulting tunneling rate of an  $N$  electron process which scales as  $R_T^{-N}$ .

In this chapter, we consider Andreev tunneling in NIS junctions [3–6, 8, 70, 77]. We first determine the tunneling rates and then discuss how to observe them experimentally. We also demonstrate experimentally that the Andreev tunneling can be suppressed with charging energy costs. This makes three-electron processes dominant [49]. We will also see that the Andreev tunneling imposes constraints to the design of a SINIS turnstile when maximal accuracy is pursued.

## 5.1 Determination of Andreev tunneling rates

The tunneling rates for Andreev tunneling are obtained similarly as the single-electron rates. In this case, we take the second non-zero term in the series expansion of Eq. (2.18). Plugging this into  $I = \text{Tr}(\rho_I \hat{I}_I)$  yields

$$I_{\text{AR}} = -\frac{i}{\hbar^3} \int_{t_0}^t dt_1 \int_{t_0}^{t_1} dt_2 \int_{t_0}^{t_2} dt_3 \left\langle \left[ \hat{H}_T(t_3), \left[ \hat{H}_T(t_2), \left[ \hat{H}_T(t_1), \hat{I}(t) \right] \right] \right] \right\rangle_0 \quad (5.1)$$

Following the same steps as for the first order, collecting only terms not containing energy cost of  $\Delta$  and taking terms corresponding to tunneling from normal metal to superconductor, one arrives at the Andreev tunneling rate

$$\Gamma_{\text{N} \rightarrow \text{S}}^{\text{AR}}(\delta E) = \frac{\hbar \Delta^2}{16\pi e^4 R_T^2 \mathcal{N}} \int d\epsilon f_N(\epsilon - \delta E/2) f_N(-\epsilon - \delta E/2) \times \left| a(\epsilon + E_C - i\delta\epsilon/2) + a(-\epsilon + E_C - i\delta\epsilon/2) \right|^2, \quad (5.2)$$

where

$$a(\epsilon) = \frac{1}{\sqrt{\epsilon^2 - \Delta^2}} \ln \left( \frac{\Delta - \epsilon + \sqrt{\epsilon^2 - \Delta^2}}{\Delta - \epsilon - \sqrt{\epsilon^2 - \Delta^2}} \right), \quad (5.3)$$

and  $\delta E$  is the electrostatic energy gained for the two electrons which tunnel [49, 78]. By considering  $n$  changing by two in Eq. (3.4) and taking into account that two electrons are provided by the voltage supply  $V_i$ , we obtain the energy gain for adding ( $++$ ) or removing ( $--$ ) two electrons from the SET island as

$$\delta E_i^{\pm\pm} = E_c(n - n_g)^2 - E_c(n \pm 2 - n_g)^2 \mp 2eV_i = \mp 4E_c(n - n_g \pm 1) \mp 2eV_i. \quad (5.4)$$

Similarly as for the single-electron tunneling rates of Eqs. (2.25) and (2.26), for Andreev tunneling we also have  $\Gamma_{\text{N} \rightarrow \text{S}}^{\text{AR}}(\delta E) = \Gamma_{\text{S} \rightarrow \text{N}}^{\text{AR}}(\delta E)$ , i.e. the tunneling direction does not matter for a given energy gain  $\delta E$ .

For obtaining Eq. (5.2) a few remarks need to be made. First of all, it was taken into account that the junction consists of several conduction

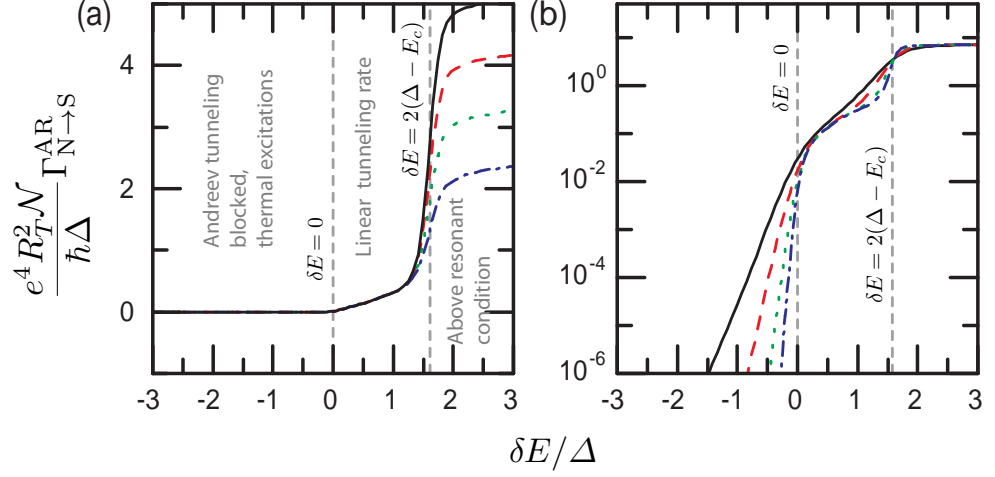


**Figure 5.1. Andreev tunneling rates.** (a), Andreev tunneling rate  $\Gamma_{N \rightarrow S}^{\text{AR}}$  as a function of the energy gain  $\delta E$ . The curves from top to bottom are calculated with  $\hbar \sum_{\pm} \Gamma_{N \rightarrow S}(\delta E^{\pm}) / \Delta = 10^{-5}, 10^{-4}, 10^{-3}$  and  $10^{-2}$  respectively. The tunneling threshold  $\delta E = 0$  and the resonant condition  $\delta E = 2(\Delta - E_c)$  are shown as dotted grey lines. Curves are calculated with  $\Delta / k_B T_N = 40$ . (b), Similar curves but for different temperatures  $\Delta / k_B T_N = 10, 15, 25$  and  $40$ . Here we use  $\hbar \sum_{\pm} \Gamma_{N \rightarrow S}(\delta E^{\pm}) / \Delta = 10^{-5}$ .

channels;  $\mathcal{N}$  is the effective number of them. This scales the tunneling rate as  $1/\mathcal{N}$  compared to the result obtained with a single channel. We can express the number of conduction channels as  $\mathcal{N} = A/A_{\text{ch}}$ , where  $A_{\text{ch}}$  is the area of one channel and  $A$  the total area of the junction. For aluminum oxide tunnel barriers, we expect  $A_{\text{ch}} = 2 \text{ nm}^2$  based on the estimate given in Publication IV. Experimental findings in Publication IV, Publication V and Refs. [5, 70] suggest, however, that the actual value for  $A_{\text{ch}}$  is roughly an order of magnitude higher resulting in an order of magnitude higher tunneling rate than expected.

Secondly, we have introduced a lifetime broadening with a term  $i\delta\epsilon = i\hbar \sum_{\pm} \Gamma_{N \rightarrow S}(\delta E^{\pm})$  to Eq. (5.2). Otherwise the Andreev tunneling rate would diverge. The broadening is determined by the first order tunneling rates  $\sum_{\pm} \Gamma_{N \rightarrow S}(\delta E^{\pm})$ , which according to the uncertainty relation make the energy states uncertain as the lifetime of the state is finite. In Fig. 5.1 (a) we have plotted  $\Gamma_{N \rightarrow S}^{\text{AR}}$  for different values of  $\delta\epsilon$ . The rate depends only logarithmically on  $\delta\epsilon$  and only if the energy gain in Andreev process satisfies  $\delta E_i^{\pm\pm} > 2(\Delta - E_c)$ , which corresponds to the competing single-electron tunneling threshold condition  $\delta E_i^{\pm} > \Delta$ . In this thesis we focus mainly on Andreev tunneling rates at  $\delta E_i^{\pm\pm} < 2(\Delta - E_c)$ , where they are not sensitive to the broadening. Because of these two reasons, the actual value for the broadening does not play a major role for the results obtained.

From the rates of Fig. 5.1 we also see that Andreev tunneling is acti-

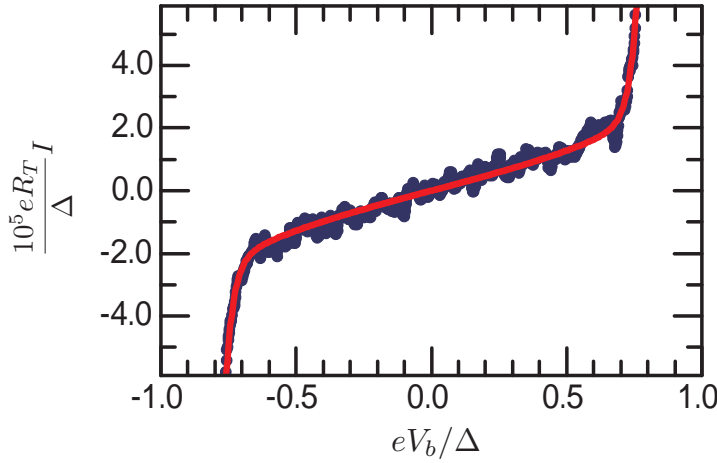


**Figure 5.2. Andreev tunneling in a NIS junction.** The black dots show measured subgap current of an NIS junction. The data is taken from Fig. 4.2. The solid red line is a calculated curve with Andreev tunneling producing the linear slope as in environmental activation.

vated as soon as  $\delta E_i^{\pm\pm} > 0$ . The superconductor gap  $\Delta$  does not appear in this condition at all reflecting the fact that no pair breaking is involved in the process. Once the threshold condition is satisfied, the tunneling rate grows linearly in  $\delta E_i^{\pm\pm}$  giving rise to linear current - voltage relation. With  $\delta E_i^{\pm\pm} < 0$ , tunneling is exponentially suppressed and the rates are set by thermal activation. All these features are similar to single-electron tunneling in a fully normal metallic tunnel junction, i.e. Eq. (2.23) with  $\Delta = 0$ . Such a linear leakage current can be present also in an NIS junction ( $\Delta \neq 0$ ) because of environmentally activated tunneling as in Sect. 4 ( $\sigma \neq 0$  in Eq. (4.22)). Therefore one needs to pay special attention to distinguish different tunneling processes producing similar features. This will be the topic of the next section. First we demonstrate that indeed, Andreev tunneling leads to similar features for voltage biased NIS junctions as the environmentally assisted tunneling. Then we show that by utilizing charging energy costs, one can clearly distinguish these two effects.

## 5.2 Measuring Andreev tunneling: subgap current

The most obvious way to probe experimentally the Andreev tunneling in NIS junctions is to investigate the tunneling current in the subgap region,  $|eV_b| < \Delta$ . The simplest experiment is to measure a single voltage biased junction [5, 70] as was described in Sections. 2.2.2 and 4. We actually take the data of Fig. 4.2 which was interpreted there as envi-

ronmentally activated single-electron tunneling and show that, with free parameters, it can be fitted as well with the expressions governing Andreev tunneling. Thus the interpretation of the subgap currents of a NIS junction is not necessarily unambiguous. In Fig. 5.2 we replicate the experimental data obtained with the junction on top of the ground plane as dark blue dots. In addition, we show simulations where Andreev and single-electron tunneling without environmental activation is considered as red line. The current is obtained as  $I = e(\Gamma_{N \rightarrow S}(eV_b) + 2\Gamma_{N \rightarrow S}^{\text{AR}}(2eV_b) - \Gamma_{S \rightarrow N}(-eV_b) - 2\Gamma_{S \rightarrow N}^{\text{AR}}(-2eV_b))$ . The linear part of the calculated current at  $-0.7 \Delta < eV_b < 0.7 \Delta$  is caused solely by Andreev tunneling. The steep increase at  $eV_b \approx \Delta$  is because of thermally activated single-electron tunneling.

One approach to resolve the origin of the observed current is to consider the magnitude of the slope and find out whether it is consistent with Andreev tunneling. At low energies  $\epsilon$ , we obtain  $a(\epsilon) = \pi/2$  from Eq. (5.3). In addition, taking  $E_c = 0$  and  $T_N = 0$ , we obtain from Eq. (5.2) for small bias voltages

$$\Gamma_{N \rightarrow S}^{\text{AR}} = \frac{1}{8\mathcal{N}} \frac{R_K}{eR_T^2} V_b, \quad (5.5)$$

which is consistent with the BTK calculations [3]. Equation (5.5) yields the ratio of the conductances in the subgap and asymptotic bias regimes as

$$\sigma^{\text{AR}} = \frac{2e\Gamma_{N \rightarrow S}^{\text{AR}}}{V_b} R_T = \frac{1}{4\mathcal{N}} \frac{R_K}{R_T}, \quad (5.6)$$

which shows that the ratio is set by  $R_K A_{\text{ch}} / (R_T A)$ . The area of the junction used in the measurement of Fig. 5.2 is  $A = 80 \text{ nm} \times 110 \text{ nm}$  based on a scanning electron micrograph, and the tunnel resistance  $R_T = 760 \text{ k}\Omega$  is obtained from the asymptotic slope of the current-voltage graph. For getting the subgap slope of Fig. 5.2 correct, we need to take  $A_{\text{ch}} = 30 \text{ nm}^2$ . This value is the same as the values obtained in the experiments below indicating that Andreev tunneling causes the leakage in this case. The junctions considered in this thesis are relatively small,  $A \lesssim (100 \text{ nm})^2$ , and opaque,  $R_T \gtrsim 100 \text{ k}\Omega$ . For such junctions the Andreev tunneling is ballistic and given by Eq. (5.2). For larger, more transparent junctions the Andreev tunneling becomes diffusive producing a zero-bias anomaly in the measurement which helps to identify Andreev tunneling [5, 6, 70]. Still the measured current typically has an extra linear subgap part.

The considerations above apply to a voltage biased NIS junction. In Publication IV the influence of the charging energy to Andreev tunneling was considered. From Eq. (5.4) we see that the Andreev threshold  $\delta E_i^{\pm\pm} = 0$

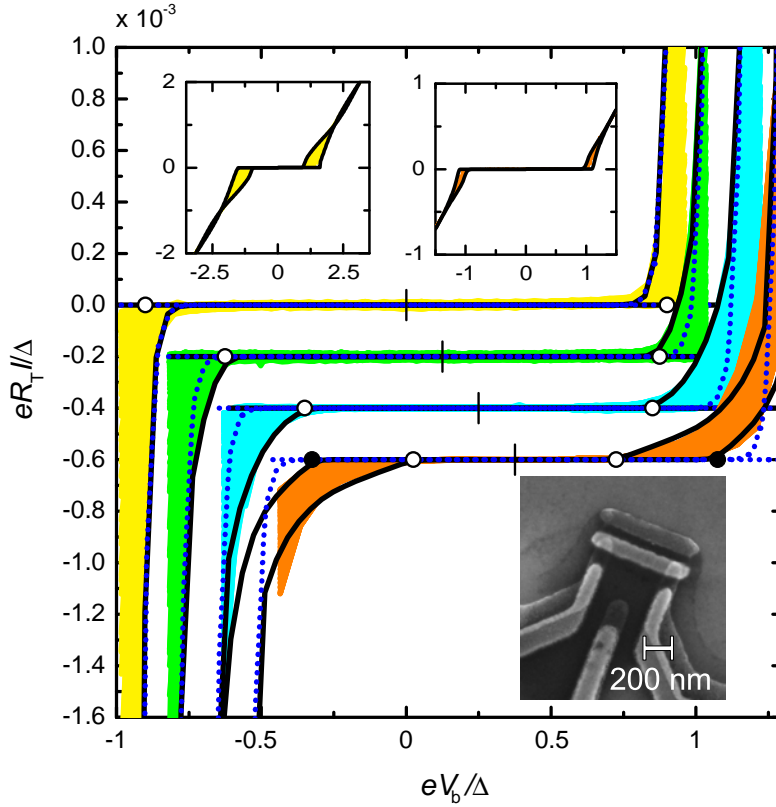


**Figure 5.3. Andreev tunneling in SINIS transistors.** Colored regions show measured subgap current for devices with charging energies  $E_c/k_B = 2.3, 1.9, 1.5,$  and  $0.86$  K from top (yellow) to bottom (orange) at all gate offset values (the "colored" areas). The insets depict the larger scale measurements for samples with the highest and lowest charging energies and a scanning electron micrograph of one of the measured SETs. Solid black lines are theoretical curves at degeneracy (maximal current) and in Coulomb blockade (minimal current) with Andreev tunneling taken into account. Dotted blue lines present fits excluding Andreev processes. Tunneling resistances of the samples were  $R_T = 129, 78, 55,$  and  $31$  k $\Omega$  in order of decreasing  $E_c$ , and superconducting gap  $\Delta = 216$   $\mu$ eV for all of them. Open (solid) circles present the expected thresholds  $|eV_b| = E_c$  and  $2E_c$  for Andreev tunneling at degeneracy and in Coulomb blockade, respectively. This figure is adapted from Publication IV.

is exceeded if the bias per junction satisfies  $|eV_b| > E_c$  for degeneracy,  $n_g = 1/2$ , and  $|eV_b| > 2E_c$  for Coulomb blockade,  $n_g = 0$ . Here we have again taken  $V_b = V_1 = -V_2$  for the SET. The degeneracy case minimizes the required bias voltage. Therefore we expect that no Andreev current will flow below this voltage and above it Andreev tunneling is activated for a certain gate offset range around  $n_g = 1/2$ . Likewise, Coulomb blockade maximizes the required bias and hence we expect Andreev current to flow at all values of  $n_g$  starting from  $|eV_b| = 2E_c$ . These voltage thresholds are indeed the features that are observed in SINIS single-electron transistors. In Fig. 5.3 we present data for four devices. The charging energy is ranging from  $E_c = 70$   $\mu$ eV to  $E_c = 200$   $\mu$ eV. There is indeed no subgap current at  $|eV_b| < E_c$ , whereas at higher voltage values the current is non-

vanishing. The maximum value of the current is obtained with  $n_g = 1/2$  and it increases linearly for higher biases  $V_b$ . The onsets at  $eV_b = \pm E_c$  are clear fingerprints of two electrons being involved in the transport. Furthermore, the linear increase after the threshold is in agreement with the Andreev tunneling rates discussed in Sect. 5.1.

The Andreev tunneling rates can be incorporated in the master equation (3.7) by adding terms  $\Gamma_{n-2,n}P(n-2)$  and  $\Gamma_{n+2,n}P(n+2)$  which correspond to tunneling of two electrons into or out from the island. The rates  $\Gamma_{n\pm 2,n}$  are set by  $\Gamma_{N\rightarrow S}^{\text{AR}}$  and  $\Gamma_{S\rightarrow N}^{\text{AR}}$ . For calculating the current with Eq. (3.8), we add these rates multiplied by a factor two since two electrons tunnel in each event. The full equations are given in Publication V. We show in Fig. 5.3 calculations including Andreev tunneling at  $n_g = 1/2$  and  $n_g = 0$  as black lines. For reference, simulations but excluding Andreev tunneling are given as dotted blue lines. For low charging energy devices, the features of the excess current are captured well by including Andreev tunneling rates. At higher  $E_c$ , the leakage in the gap vanishes gradually and only thermally activated single-electron tunneling persists. The slope at which the current rises above the threshold bias  $|eV_b| = E_c$  is set by the magnitude of Andreev tunneling. It allows us to determine the size of a single conduction channel as  $A_{\text{ch}} = 30 \text{ nm}^2$ .

### 5.3 Real-time detection of Andreev tunneling events

An alternative approach for the detection of Andreev tunneling is to utilize electron counting techniques which was done in Publication IV. In such a setup, a charge sensitive electrometer is used for monitoring the number of electrons on a metallic island. As the number changes because of tunneling, we see a jump in the detector signal thus allowing one to detect the tunneling event. A typical device used as an electrometer is a single-electron transistor, but also quantum point contacts can be utilized for charge detection [79–81]. In our case we can use a SINIS transistor since that can be fabricated in the same process as the studied systems. For a detailed discussion about the operation, sensitivity and bandwidth of such electrometers, see Publication VIII and Ref. [82].

The electron counting provides us a major advantage as compared to the direct current measurement. With it, we are able to determine directly the number of electrons passed in each tunneling event. This is based on the fact that the change in detector signal is ideally proportional to

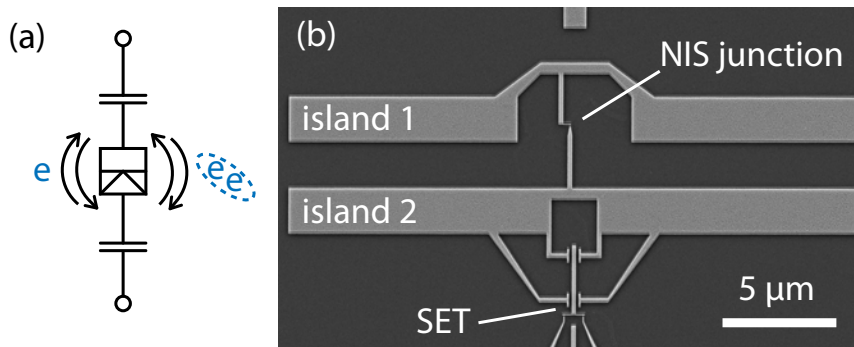


**Figure 5.4. Andreev tunneling in a single electron box.** (a), An isolated single-electron box (SEB) consists of two islands. One is superconducting and the other normal metallic. Single-electron and Andreev tunneling is possible in the NIS tunnel junction connecting the two islands. An SET electrometer and a gate offset voltage can be coupled to either of the islands capacitively. (b), Scanning electron micrograph of an isolated SEB. The two islands are  $25 \mu\text{m}$  long horizontal bars shaped in the middle to accommodate the connecting NIS junction and coupling to the electrometer shown at the bottom.

the number of electrons leaving or entering the island. This advantage is obtained by utilizing the charging effect of a small island: what we detect is a change in the electrostatic potential of the island as electrons tunnel.

In Fig. 5.4 (a) we show schematically the system we study. It is an isolated single electron box (SEB) consisting of a normal metallic and superconducting island. They are connected by an NIS junction allowing single-electron and two-electron Andreev tunneling to take place. To detect the tunneling events, the two islands are capacitively coupled to other parts. Typically one of the islands is coupled to the electrometer, allowing one to monitor the number of electrons on that island, and the other one to a gate electrode, which allows one to tune the offset charge  $n_g$  of the SEB. An actual device is shown in panel (b).

The SINIS SET which is used as the electrometer is biased slightly above the threshold condition,  $eV_b \gtrsim \Delta$ , where the current depends strongly on its offset charge  $n_{g,\text{det}}$ . It is tuned such that the current is half way between its maximum and minimum values. This way the dynamical range for the detection is optimized but typically the sensitivity set by  $dI/dn_{g,\text{det}}$  is also close to its maximum value around this point. With SET electrometers, subelectron sensitivity of the order of  $10^{-5} \text{ e/Hz}^{1/2}$  is obtainable [83–86]. Once the detector is tuned to the operation point, time traces of the detector current are recorded under different biasing conditions of the SEB. When the SEB offset charge  $n_g$  is changed, the offset charge  $n_{g,\text{det}}$  of the detector must be compensated to keep it at the operation point. This is due to unavoidable cross-couplings. The compensation

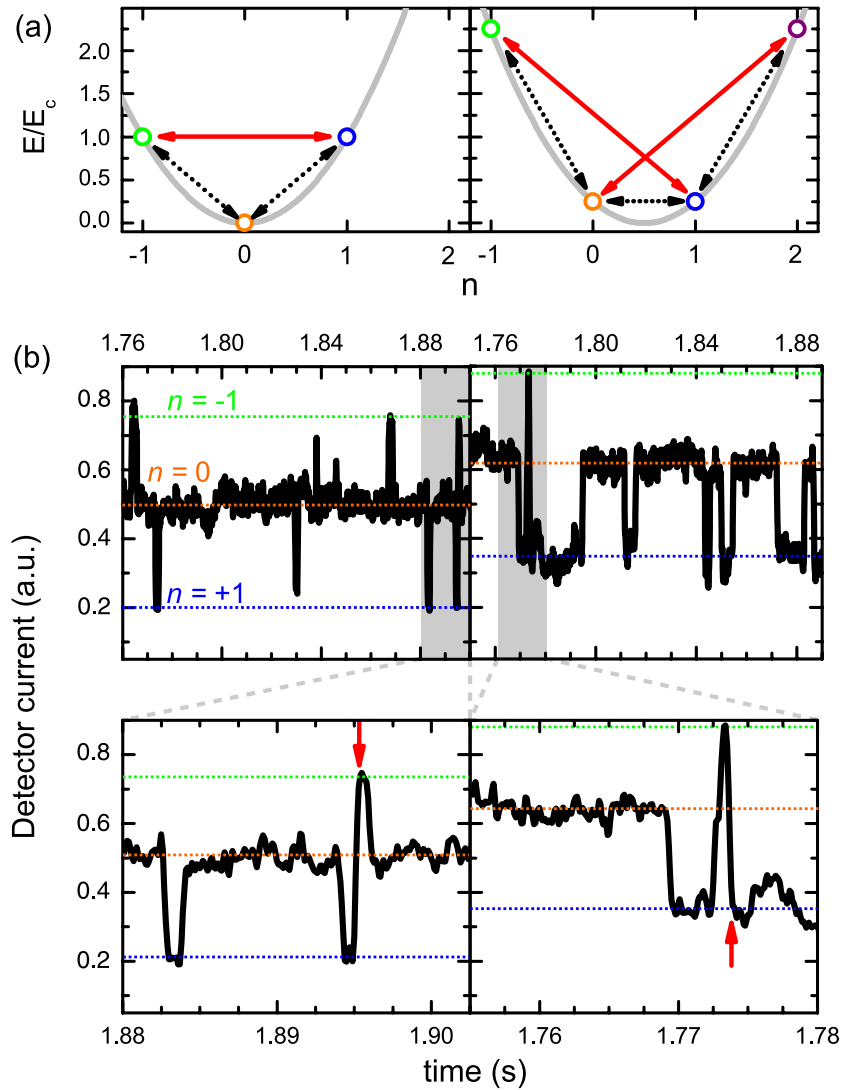


**Figure 5.5. SEB time traces.** Charging energy  $E$  for  $n$  excess electrons on the island. The left panel is for Coulomb blockade,  $n_g = 0$ , and the right one for degeneracy,  $n_g = 1/2$ . (b), Time traces at Coulomb blockade (left panels) and at degeneracy (right panel). Short time intervals are zoomed in the panels at the bottom and they show possible two-electron tunneling events. Figure adapted from Publication IV.

is however straightforward to do: Only a linear component needs to be subtracted from the detector gate offset. The compensation coefficient is found by trial and error.

When the offset of the SEB is tuned, two extreme cases are found: Coulomb blockade and degeneracy. The energy  $E$  for  $n$  excess electrons on one of the islands as well as typical timetraces recorded at these extreme cases are shown in Fig. 5.5. In Coulomb blockade, one of the charge states has the lowest energy and the states around it are equally high in energy. In the time traces, we see that the box stays most of the time at the lowest energy state  $n = 0$  and equally likely switches to either  $n = +1$  or  $n = -1$ . When the system enters one of the higher states we see that

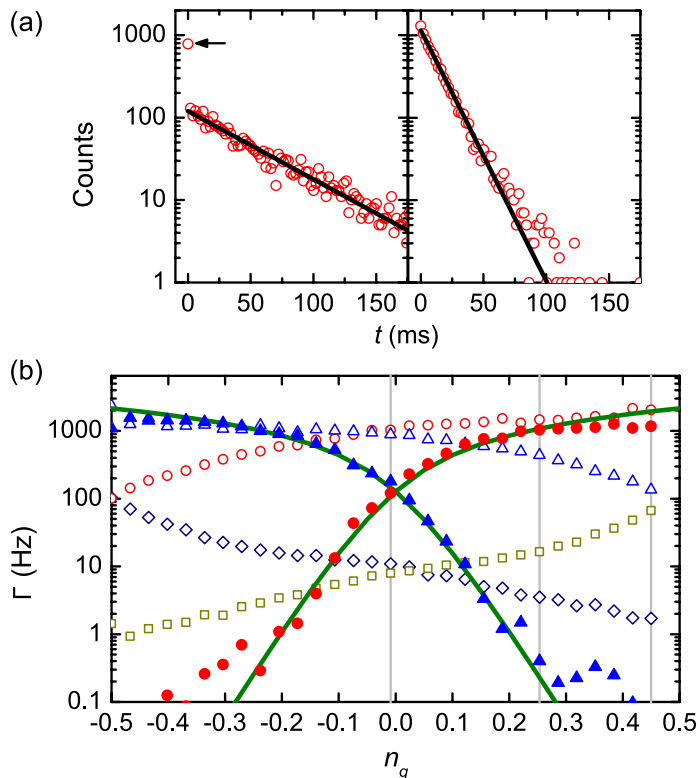


**Figure 5.6. Waiting time histograms and tunneling rates in the SEB of Fig. 5.4.**

(a), Waiting time of the charge state  $n$  with the lowest energy  $E$  in Coulomb blockade (left) and at degeneracy (right). (b), Tunneling rates for single-electron processes (open symbols) and Andreev tunneling (filled symbols) for the two directions. The two single-electron processes with lower rates are tunneling from lower energy state to higher ones and the two processes with higher rates are for the reverse processes. The results are obtained at the base temperature of 60 mK of our cryostat. Figure adapted from Publication IV

Andreev tunneling events shown as red arrows in panel (a) do not involve energy cost and become therefore probable. We indeed see on the blow up that there are fast transitions between  $n = \pm 1$  without intermediate halt at  $n = 0$ .

At degeneracy, which is the other extreme, two charge states represent the degenerate minimum energy states. The time spent in these two states is equal. Entering other states requires in this case at least twice as much energy as in Coulomb blockade and therefore it is more unlikely. Since Andreev tunneling from the lower lying states involves also a large energy cost, it is not as probable as in Coulomb blockade.

Because the SET electrometer has a finite bandwidth, there is one issue which needs to be analysed in order to confirm the detection of two-electron events. The possible two-electron tunneling events pointed by red arrows in Fig. 5.5 could in principle be just two single-electron events occurring subsequently so quickly that the detector cannot resolve them

separately. This possibility is ruled out by assuming only single-electron events to occur. By considering the waiting time spent in the state  $n = 0$  before a tunneling event occurs, we get the distributions shown in Fig. 5.6 (a). The fast transients indicated by the red arrows in Fig. 5.5 contribute to short waiting times  $t$ . If those would be originating fully from single-electron tunneling, the waiting time distribution would be exponential (Poisson process). However, we see that this is not the case in Coulomb blockade, where the data point at the smallest  $t$  is almost an order of magnitude higher than the exponential distribution at larger values. Therefore these events are dominantly of other origin suggesting that they are true two-electron events.

For consolidating that the two-electron processes are indeed Andreev tunneling, we next consider the tunneling rates for all processes. For obtaining the rates, firstly, we need to distinguish between one- and two-electron processes. We interpret transitions with charge number changing by  $\Delta n = \pm 2$  and occurring within 0.4 ms as two-electron tunneling and all other events as one-electron tunneling. The time window here was chosen to be approximately equal to the risetime of the detector so that essentially all excess events in the histograms of Fig. 5.6 (a) were captured. In order to calculate the tunneling rates, we use the following arguments: The average waiting time for a given charge number  $n$  is  $\langle t \rangle = 1/\Gamma_\Sigma$ , where  $\Gamma_\Sigma = \sum_j \Gamma_j$  is the sum of all tunneling rates  $\Gamma_j$  out from this state. The probability that the tunneling event that took place corresponds to a process with rate  $\Gamma_j$  is  $P(\Gamma_j) = \Gamma_j/\Gamma_\Sigma$ . Hence we may write the number of events corresponding to this process as  $N_j = N_\Sigma P(\Gamma_j) = N_\Sigma \langle t \rangle \Gamma_j$ , where  $N_\Sigma = \sum_j N_j$  is the sum of all events out from this particular state. We find that

$$\Gamma_j = \frac{N_j}{N_\Sigma \langle t \rangle}, \quad (5.7)$$

where the denominator,  $N_\Sigma \langle t \rangle$ , is the total time spent in the initial charge state. Therefore counting the number of occurred events for a given process and dividing by the time spent in the initial state yields the tunneling rate for that process. In Fig. 5.6 (b) the tunneling rates for all processes in our system are plotted as a function of the gate offset charge  $n_g$  of the SEB. The solid green lines are theoretical calculations of Eq. (5.2) for Andreev tunneling, where a value  $A_{\text{ch}} = 30 \text{ nm}^2$  was used. This value defining the magnitude of Andreev tunneling is in agreement with the one obtained in Sect. 5.2 from direct current measurements. Furthermore, we observe that the Andreev tunneling rates obtained experimentally have the cor-

rect functional dependency on  $n_g$  as indicated by the solid green lines.

In this section, we have seen that the Andreev tunneling is activated in Coulomb blockade and suppressed at degeneracy. In Sect. 5.2, see Fig. 5.3, we however saw that Andreev tunneling is stronger at degeneracy than in Coulomb blockade when an SET is biased. At first these observations seem contradictory. The results of the present section assumed that single-electron processes excite the system to states  $n = \pm 1$  in Coulomb blockade allowing for the Andreev process. If this is not present, the Andreev tunneling would have to start from state  $n = 0$  and the energy cost for tunneling would be higher than at degeneracy. This is the case presented in Sect. 5.2 leading to larger Andreev current at degeneracy thus resolving the contradiction. Having just two coexisting different kinds of tunneling processes leads to relatively rich characteristics and the manifestation of various features depends on the relative rates of the two tunneling processes.

#### 5.4 Influence of Andreev tunneling on SINIS turnstile

Above we discussed Andreev tunneling under static biases  $V_b$  and  $n_g$ . Now we consider the case studied in Publication V where  $n_g$  is periodically driven and quantized current plateaus form in the SINIS turnstile. Andreev tunneling leads to pumping errors [49]. Occasionally, an Andreev tunneling event happens instead of single-electron tunneling. Two electrons are transported in this case and the current is enhanced.

An illustrative way to consider the competition between single-electron and Andreev tunneling is to draw stability diagrams shown in Fig. 5.7 (a) and (b) for both of the processes. The thresholds are obtained by requiring  $\delta E^\pm = \Delta$  in Eq. (3.6) for single-electron processes and  $\delta E^{\pm\pm} = 0$  in Eq. (5.4) for Andreev processes. We observe that the thresholds run in parallel and form diamonds of similar shape. If  $E_c < \Delta$ , the diamond set by Andreev tunneling is smaller than the single-electron one and Andreev tunneling becomes activated first. For  $E_c > \Delta$ , the situation is reversed and single-electron tunneling is activated first. This is reflected in the current quantization of the devices. In panels (c) and (d) we show the first pumping plateau for the low and high charging energy device. We see that the current for the low  $E_c$  device is higher than  $ef$  whereas for the high  $E_c$  device the current at the plateau is significantly closer to  $ef$ . The measured data points and the calculated curves match well together. The

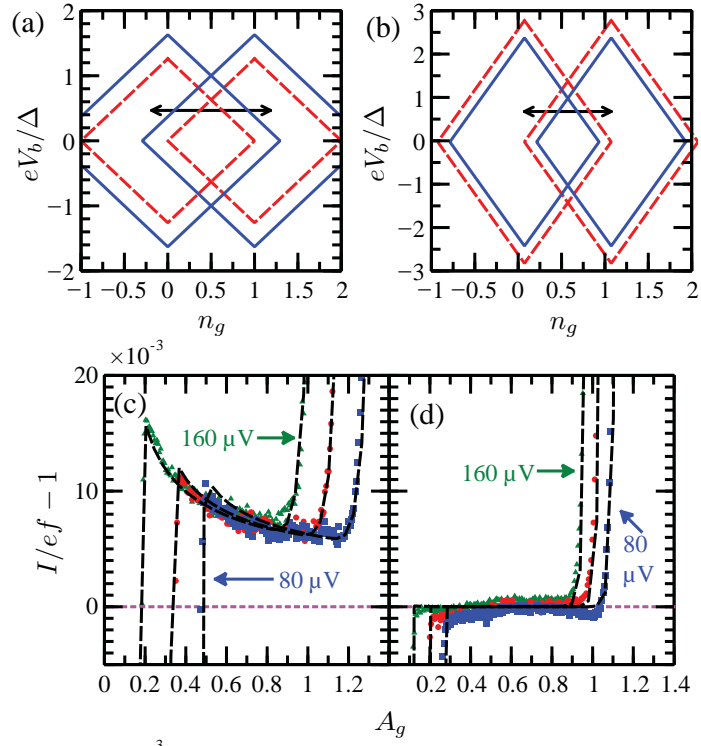


**Figure 5.7. Andreev tunneling in SINIS turnstiles.** Stability diamonds for single-electron tunneling (solid blue lines) and Andreev tunneling (dotted red lines) for  $E_c = 0.63\Delta$  in panel (a) and  $E_c = 1.4\Delta$  in panel (b). The first quantized current plateau at  $f = 10$  MHz for  $E_c = 0.63\Delta$  in panel (c) and  $E_c = 1.4\Delta$  in panel (d). The points are experimental data with the bias voltage per junction of  $V_b = 80, 120$  and  $160 \mu\text{V}$  and dashed black lines are numerically calculated curves where Andreev tunneling is taken into account.  $A_g$  is the amplitude of the gate offset drive. The error of the current measurement is smaller than 1 % and limited by the uncertainty of the gain of the current preamplifier. A  $10^{-3}$  level correction is made to the gain in order to match the absolute values of the current for the simulated and measured currents. Figure adapted from Publication V.

fast increase of current is caused by exceeding the single-electron tunneling thresholds. Ideally the current should take the value  $ef$  between the rising intervals. However, because of Andreev tunneling this does not happen for the low  $E_c$  device. The deviation of the value of the current on the plateau from  $ef$  is proportional to the magnitude of Andreev tunneling and hence to  $A_{\text{ch}}$ . For the simulations we have used  $A_{\text{ch}} = 30 \text{ nm}^2$ , again in quantitative agreement with findings in previous chapters.

For the high  $E_c$  device, the numerical calculations are insensitive to Andreev tunneling. This is because for  $E_c > \Delta$ , Andreev tunneling is energetically unfavored as compared to the single-electron process: it costs more energy to charge the island with two electrons than to break a Cooper pair. Hence, utilizing a high  $E_c$  device leads to better current quantization free of Andreev tunneling. In practice, it is considered to be sufficient to have  $E_c \gtrsim 2\Delta$ . In this case, the Andreev tunneling thresh-

olds at thermally optimal bias,  $eV_b \approx \Delta/2$ , are at larger  $n_g$  than the back-tunneling thresholds and do not anymore limit the device performance [49, 53].

## 5.5 Full Counting Statistics (FCS) of Andreev Events

In Sects. 3.2 and 5.2, a master equation was utilized to calculate single-electron and two-electron Andreev tunneling on a small metallic island. As a result, we were able to describe how average current depends on various quantities such as externally controllable bias and gate voltages. Although the average quantities reveal many features of the studied system, they typically cannot provide direct information about fluctuations and noise [87] which have non trivial features in superconducting systems. For example the shot-noise is doubled in Andreev processes compared to single-electron transport [88–90] and it results in positive cross-correlations in Cooper pair splitters [77, 91]. In this section we discuss how quantities beyond the average values can be treated for the tunnel junctions with the so-called full counting statistics (FCS) techniques and how the FCS can be straightforwardly accessed experimentally with the electron counting techniques [92–96]. We first review the essential parts of FCS based on a master equation approach [97–100] and then consider the experiment of Publication XI where Andreev tunneling occurs in avalanches and results in super-poissonian statistics.

### 5.5.1 Master equation approach to FCS

We consider probability  $p_m(n, t)$  of having  $m$  excess electrons on the island while  $n$  electrons have been transported in total at time  $t$ . Taking into account single-electron and two-electron tunneling the master equation reads

$$\begin{aligned} \frac{d}{dt} p_m(n) = & -\Gamma_{\Sigma, m} p_m(n) + \Gamma_{m-2}^{++} p_{m-2}(n-2) + \Gamma_{m-1}^+ p_{m-1}(n-1) \\ & + \Gamma_{m+1}^- p_{m+1}(n \pm 1) + \Gamma_{m+2}^{--} p_{m+2}(n \pm 2), \end{aligned} \quad (5.8)$$

where we dropped the time variable, which is the same for all terms and  $\Gamma_m^\pm$  is single-electron tunneling rate into (+) or out from (–) the island with initially  $m$  electrons and  $\Gamma_m^{\pm\pm}$  the two-electron rate into (++) or out from (--) the island with initially  $m$  electrons [97, 100].  $\Gamma_{\Sigma, m} = \Gamma_m^+ + \Gamma_m^- + \Gamma_m^{++} + \Gamma_m^{--}$ . The choice of + and – in the last two terms of the first row determines whether we consider the total number of tunnel-

ing events irrespective of the direction (–) or the net number of electrons tunneling in one direction, subtracting the tunneling to the opposing direction. Also counting the tunneling events for example on only one of the SET junctions is straightforward to do by using terms where  $n$  remains unchanged for the other junction. This is important for example when the current noise of a SET is considered.

To get the statistics of  $n$ , we are interested in the moment generating function

$$M(\chi) = \langle e^{\chi n} \rangle = \sum_n e^{\chi n} P(n, t), \quad (5.9)$$

where  $P(n, t) = \sum_m p_m(n, t)$  is the probability of having  $n$  events at time  $t$ . Once  $M(\chi)$  is known, the moments are obtained simply by differentiation with respect to  $\chi$ . Also the distribution of the events  $P(n, t)$  is obtained by a Fourier transformation as we can see from the right hand side of Eq. (5.9). Now we write  $z = e^\chi$  and

$$M(z) = \sum_m g_m(z, t), \quad (5.10)$$

where  $g_m(z, t) = \sum_n z^n p_m(n, t)$ . With Eq. (5.8) we obtain a master equation for  $g_m$ :

$$\begin{aligned} \frac{d}{dt} g_m &= -\Gamma_{\Sigma, m} g_m + \Gamma_{m-2}^{++} z^2 g_{m-2} + \Gamma_{m-1}^+ z g_{m-1} \\ &+ \Gamma_{m+1}^- z g_{m+1} + \Gamma_{m+2}^{--} z^2 g_{m+2}. \end{aligned} \quad (5.11)$$

Here we again dropped arguments  $z$  and  $t$  which are the same for all terms and we count the number of all events. We now consider vector  $\bar{g}$  whose elements are  $g_m$ . Equation (5.11) can be then written as

$$\frac{d}{dt} \bar{g}(z, t) = \bar{M}(z) \bar{g}(z, t), \quad (5.12)$$

where

$$\bar{M}(z) = \begin{bmatrix} \ddots & & & & & & \\ z^2 \Gamma_{m-2}^{++} & z \Gamma_{m-1}^+ & -\Gamma_{\Sigma, m} & z \Gamma_{m+1}^- & z^2 \Gamma_{m+2}^{--} & & \\ & z^2 \Gamma_{m-1}^{++} & z \Gamma_m^+ & -\Gamma_{\Sigma, m+1} & z \Gamma_{m+2}^- & z^2 \Gamma_{m+3}^{--} & \\ & & & & \ddots & & \end{bmatrix}. \quad (5.13)$$

Equation (5.12) can be solved formally to get  $\bar{g}(z, t) = e^{\bar{M}(z)t} \bar{g}(z, 0)$ , where  $\bar{g}(z, 0)$  is the configuration at the beginning of the counting. The quantity  $\bar{g}(z, 0)$  is taken such that only the states with  $n = 0$  have non-zero probability and their population is given by solving the steady state  $\frac{d}{dt} \bar{g}(z) = 1, t) = 0$ .<sup>1</sup> Having  $g_m(z, t)$ , we obtain the moment generating function with

<sup>1</sup>By taking  $z = 1$  in Eq. (5.12), it reduces to the standard master equation (3.7).

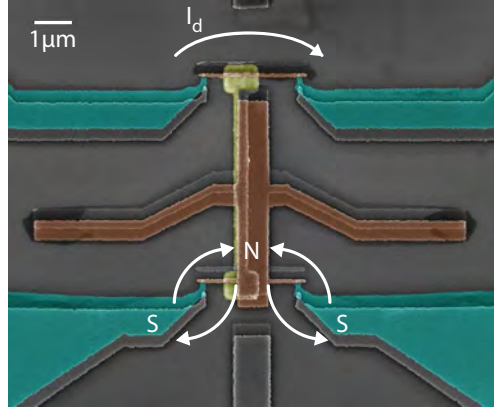


**Figure 5.8. The structure for detecting Andreev avalanches.** Two SINIS transistors with the islands coupled capacitively to each other with a metallic strip (yellow). The transistor on top with higher  $E_c$  is used as an electrometer. The number of excess electrons  $N$  on the other transistor island is read via the current  $I_d$  flowing through it. Figure adapted from Publication XI.

Eq. (5.12) and we can readily use it to obtain any statistics we are interested in.

### 5.5.2 FCS of Andreev tunneling

The electron counting techniques discussed in Sect. 5.3 allow one readily to perform FCS experiments. The structure which was used in Publication XI is shown in Fig. 5.8. Instead of measuring the number of excess electrons  $N$  in a isolated box, we measure them in an island of a SINIS turnstile. These two setups behave identically when the transistor is kept at zero bias as we did in the experiments below. However the transistor structure allows us to measure transport characteristics and extract parameter values  $R_T = 490 \text{ k}\Omega$ ,  $\Delta = 210 \text{ }\mu\text{eV}$  and  $E_c = 40 \text{ }\mu\text{eV}$ , as described in Sect. 3.2. The drawback is that the rates will be twice as high as compared to the isolated box, trivially because there are two junctions contributing to tunneling.

First we tune the offset charge to degeneracy  $n_g = 1/2$ . The charge states  $N = 0$  and  $N = 1$  are the lowest lying ones with equal energy as shown in Fig. 5.9 (a), and results in a time trace where single-electron tunneling takes place between the two states as shown in panel (b). Now we can obtain experimentally the FCS distribution. We recorded 3 s time traces and chopped them in bins of length  $t$ . By counting the number of events in each time bin, we build the probability histogram  $p(n, t)$  for observing  $n$  tunneling events in time  $t$  shown in Fig. 5.9 (c).

For predicting the experimental distribution, we take Eq. (5.12) with the

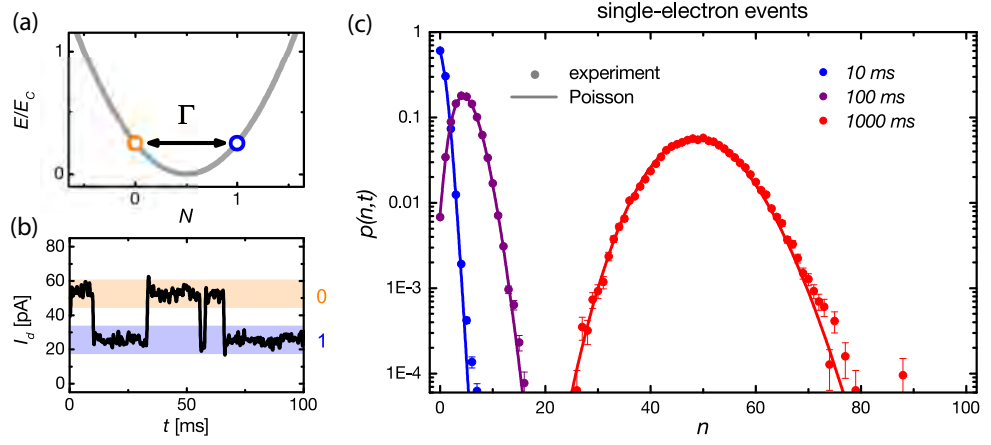


**Figure 5.9. Statistics of single-electron tunneling.** (a), Charge degeneracy ( $n_g = 0.5$ ) where only single-electron tunneling is active as shown by the time trace of the detector current in panel (b). The energy parabola is obtained from Eq. (3.4). (c), Probability  $p(n, t)$  for observing  $n$  single-electron events in time window  $t = 10, 100$  and  $1000$  ms. Solid lines are Poisson distributions. Figure adapted from Publication XI.

two states  $N = 0, 1$  as

$$\frac{d}{dt} \begin{bmatrix} g_0(z, t) \\ g_1(z, t) \end{bmatrix} = \begin{bmatrix} -\Gamma & z\Gamma \\ z\Gamma & -\Gamma \end{bmatrix} \begin{bmatrix} g_0(z, t) \\ g_1(z, t) \end{bmatrix}, \quad (5.14)$$

where  $\Gamma = 49$  Hz is the degeneracy tunneling rate, determined from the time traces by evaluating the average waiting time before a tunneling event occurs. Equation (5.14) can be straightforwardly solved to yield  $M(z) = g_0 + g_1 = e^{(z-1)\Gamma t}$ , which is the moment generating function of a Poisson distribution with mean  $\langle n \rangle = \Gamma t$ . Therefore  $p(n, t) = \frac{1}{2\pi} \int_0^{2\pi} d\chi e^{-in\chi} M(e^{i\chi}) = \frac{(\Gamma t)^n}{n!} e^{-\Gamma t}$ , which is presented as solid lines in Fig. 5.9 (c). We observe that the experimental statistics follow the Poisson distribution as expected.

In Fig. 5.10 the same experiment is repeated in Coulomb blockade,  $n_g = 0$ . In this case the energy diagram of panel (a) has  $N = 0$  as the most probable state and the tunneling to  $N = \pm 1$  involves an energy cost. A typical time trace is shown in panel (b). Most of the time the box is in the charge state  $N = 0$ . Then a single-electron event moves the system to either of the states  $N = \pm 1$ . In these states two-electron Andreev tunneling with rate  $\Gamma_A$  is energetically neutral as shown by the red horizontal line of panel (a). Because of the pair breaking energy cost  $\Delta$ , the single-electron rate  $\Gamma_d$  down to  $N = 0$  is exponentially suppressed in temperature as discussed in Sect. 2.2.2. Therefore it is possible to have  $\Gamma_A > \Gamma_d$ . In this case, multiple Andreev tunneling events take place before the system relaxes back to  $N = 0$ . Such a set of parameters results in bunching of the tunneling events with a typical avalanche shown in panel (b).

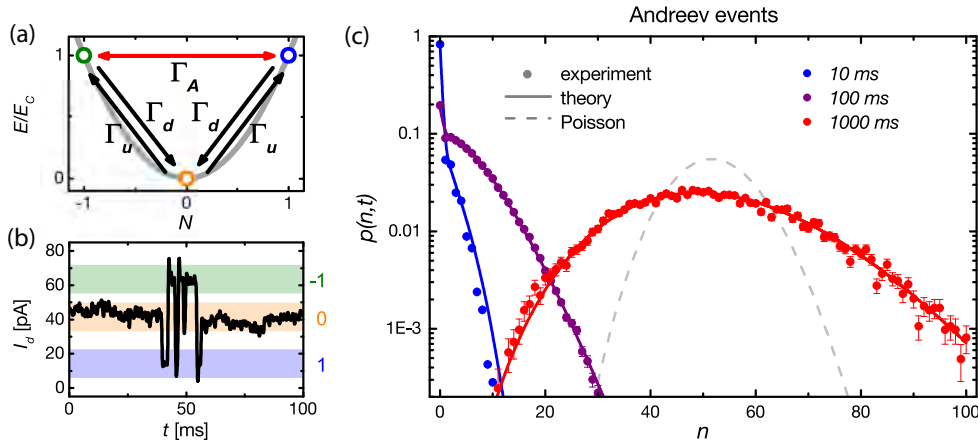


**Figure 5.10. Statistics of two-electron Andreev tunneling.** (a), A schematic on charging energy costs and tunneling processes in Coulomb blockade ( $n_g = 0$ ). Charge state  $N = 0$  is preferred as shown by the measured time trace in panel (b). (c), Probability  $p(n, t)$  for observing  $n$  single-electron events in time window  $t = 10, 100$  and  $1000$  ms. Solid lines are theoretical predictions based on Eq. (5.15). Figure adapted from Publication XI.

The statistics of Andreev tunneling shown in Fig. 5.10 (c), demonstrate that the distributions are broader than the Poisson distribution, reflecting the fact that the bunching makes the signal more noisy. To corroborate this, we again take Eq. (5.12) but now counting only the number of Andreev events. Since the states  $N = \pm 1$  are identical, we simplify the problem by summing them to  $g_A = g_1 + g_{-1}$ . We then obtain

$$\frac{d}{dt} \begin{bmatrix} g_A(z, t) \\ g_0(z, t) \end{bmatrix} = \begin{bmatrix} \Gamma_A(z-1) - \Gamma_d & 2\Gamma_u \\ \Gamma_d & -2\Gamma_u \end{bmatrix} \begin{bmatrix} g_A(z, t) \\ g_0(z, t) \end{bmatrix}. \quad (5.15)$$

Solving Eq. (5.15) and taking the Fourier transform, leads to the theoretical lines of Fig. 5.10 (c). The tunneling rates  $\Gamma_u = 12$  Hz,  $\Gamma_d = 250$  Hz and  $\Gamma_A = 610$  Hz were estimated by counting the number of occurred events and dividing by the time spent in the initial state as in Sect. 5.3. Note that the broader distribution obtained here is not because of the Andreev process carrying two electrons unlike in Ref. [90]. Since we count the number of *pairs* this effect does not show up in the statistics. The distribution is broader solely because of the bunching of the tunneling events. If one would count the number of electrons instead, it would lead to an additional factor of two in the variance as in Ref. [90].

In Publication XI it was furthermore shown by expanding the cumulant generating function in by the lowest order in  $\Gamma_u$  that the FCS in this case can be approximated as a sum of independent Poisson processes that generate avalanches of  $m$  Andreev events with a probability

$$q(m) = \frac{\Gamma_d}{\Gamma_A + \Gamma_d} \left( \frac{\Gamma_A}{\Gamma_A + \Gamma_d} \right)^m, \quad (5.16)$$

where  $\Gamma_A/(\Gamma_A + \Gamma_d)$  is the probability of having one more Andreev event in state  $N = \pm 1$  and  $\Gamma_d/(\Gamma_A + \Gamma_d)$  is the probability of having a tunneling event down to  $N = 0$  at the end. The distribution  $q(m)$  was determined experimentally and good agreement with Eq. (5.16) was found.



## 6. Quasiparticle excitations in a superconductor

As the temperature  $T_S$  of a superconductor is lowered, the thermal excitations in form of unpaired electrons diminish exponentially. This happens since according to Eq. (2.5), all excitations carry energy which is at least  $\Delta$ . Because of the exponentially small number of carriers, many quantities such as electrical heat conduction and recombination of broken Cooper pairs in a superconductor become also exponentially weak. Having such a strong dependency makes the temperature an inconvenient parameter for quantifying the excitations: a 10 % change in it may lead to an order of magnitude change in the number of excitations. Therefore one needs to know the ratio  $\Delta/k_B T$  very well in order to know even roughly the number of excitations and quantities depending on it.

A more natural parameter for describing excitations in a superconductor at low temperatures is the number of excitations in unit volume, the quasiparticle density  $n_{qp}$ . It is a convenient quantity for analysing the properties of a superconductor in the sense that the quantities depending on the excitations follow a power law. For example heat conduction is approximately linear in  $n_{qp}$  and electron-phonon recombination rate scales as  $n_{qp}^2$ . In Sect. 6.1 we will first formulate the relation between  $T_S$  and  $n_{qp}$  and consider experimental ways to probe the excitations with NIS junctions. Then we consider the heat conduction along a superconducting line and obtain a diffusion equation for  $n_{qp}$ . By injecting quasiparticles with a SINIS turnstile allows us to probe the diffusion and relaxation of the quasiparticles to a normal metallic trap. We also learn that evacuation of the quasiparticle excitations is of paramount importance in order to obtain good current quantization in the turnstile.

Then in Sect. 6.4 we consider electron-phonon interaction in superconducting state. That provides an inherent mechanism for the excitations to relax. We use a small superconducting island connected with NIS junc-

tions to normal metallic leads to probe the relaxation rates. We are able to show that the island is free of quasiparticle excitations for most of the time. Hence we can probe the recombination of quasiparticles down to a single quasiparticle pair. We also see that the island cannot be considered to have a certain temperature  $T_S$  but the dynamics of quasiparticles needs to be accounted explicitly. An extended master equation is needed which describes simultaneously the charge and energy flow on the superconducting island.

In Sect. 2.1 we presented the density of states of a superconductor with two branches, one with energy  $E < -\Delta$  and one with  $E > \Delta$ . The excitations of a superconductor consist of either occupied states at  $E > \Delta$  (particle like excitations) or vacant states at  $E < -\Delta$  (hole excitations). If the excitations are thermal, the number of excitations on the branches are equal. However, if electrons are predominantly injected to  $E > \Delta$ , the number of excitations in this branch is expected to be higher. Similarly, if electrons are removed from  $E < -\Delta$ , the hole excitations are more abundant. While the increased number of excitations leads to increased temperature  $T_S$ , the difference of excitations in the two branches induces a shift in the chemical potential [1]. In the SINIS turnstile such branch imbalance is likely to occur since electrons are removed from one superconducting lead and injected to another. The possibility for the branch imbalance is discussed in Sect. 6.3. Yet we find that the branch imbalance is negligible in the turnstile suggesting that the branch relaxation is faster than the quasiparticle injection.

## 6.1 Probing quasiparticles with NIS junctions

In Sect. 2.2.2 we saw that the temperature of the superconductor, in form of quasiparticle excitations, cannot be probed with a single NIS junction since the rates in the forward and backward direction compensate each other or the rates caused by the excitations are overwhelmed by rates from other mechanisms. In this section we discuss two ways of probing the excitations. The probing can be done either by making an electron counting experiment or by measuring the current - voltage characteristics of a SET structure. These both approaches utilize Coulomb charging energy in the same way as was done in Chap. 5 for observing Andreev tunneling. In the first one, it is used for obtaining a measurable signal and in the latter one to rectify the current caused by the quasiparticles.

In the experiments of this thesis, quasiparticle excitations are injected to energies close to the gap edges,  $E \approx \Delta$  since we consider the low bias conditions. In this case the excitations can be described in terms of chemical potential shift  $\delta\mu$  and elevated temperature  $T_S$  [1]. The chemical potential shifts if there is an imbalance in the populations of quasiparticles in the two branches,  $E \leq -\Delta$  and  $E \geq \Delta$ , respectively. Such charge imbalance was observed for the first time in the classic experiment by J. Clarke [42]. There the imbalance was obtained by connecting an NIS and an SIS junction in series. In the SIS junction the current is carried by Cooper pairs which do not influence the quasiparticle excitations whereas electron tunneling in the NIS junction creates excitations only on one of the branches.

The other parameter  $T_S$  characterizing the excitations describes the overall number of them. Let us now find the relation between  $T_S$  and the quasiparticle density. We assume vanishing charge imbalance. Then the quasiparticle density on one of the branches is

$$n_{\text{qp,b}} = D(E_F) \int_{\Delta}^{\infty} dE n_S(E) f_S(E), \quad (6.1)$$

where  $D(E_F)$  is the normal state density of states at the Fermi level. For aluminum, we have  $D(E_F) = 1.45 \times 10^{47} \text{ J}^{-1}\text{m}^3$ , see Ref. [101]. To get the total density of all quasiparticles we have to multiply  $n_{\text{qp,b}}$  by two due to the two branches:  $n_{\text{qp}} = 2n_{\text{qp,b}}$ . On the other hand, if we take Eq. (2.26) with energy gain  $-\Delta < \delta E < \Delta$ , the tunneling of quasiparticle excitations is the dominant process provided that  $T_N$  is low. We then have  $1 - f_N(E + \delta E) \approx 1$  for  $E > \Delta$ . Hence

$$\Gamma_{\text{S} \rightarrow \text{N}} = \frac{1}{e^2 R_T} \int_{\Delta}^{\infty} dE n_S(E) f_S(E) = \frac{n_{\text{qp}}}{2e^2 R_T D(E_F)}, \quad (6.2)$$

which is the value for the tunneling rate at  $-\Delta < \delta E < 0$  in Fig. 2.3 (b). Equation (6.2) yields a direct relation between the quasiparticle density and tunneling rate and it can be used to estimate the quasiparticle density as was done in Publications VI, VII and IX. A specific feature of the quasiparticle excitations is that the tunneling rate does not depend on the energy gain  $\delta E$  since the excitations are at high energies. This feature is useful for arguing that the tunneling is originating from quasiparticle excitations.

Now we assume in addition that there are not many excitations present. This low temperature limit,  $k_B T \ll \Delta$ , is relevant for results presented in this thesis. In this case we have  $f_S(E) \approx e^{-E/k_B T_S}$  for  $E \geq \Delta$  and Eq. (6.1)

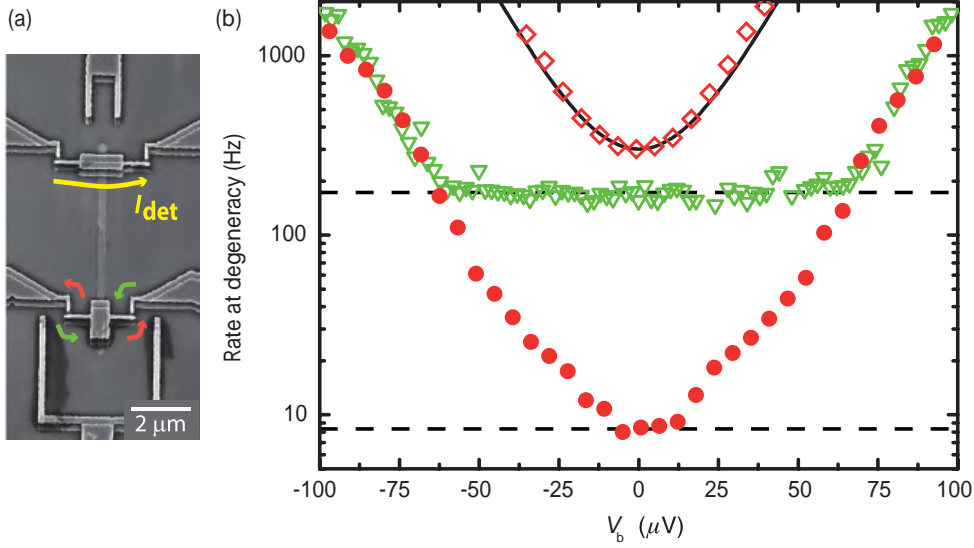


**Figure 6.1. Probing quasiparticle excitations by electron counting.** (a), Two SETs capacitively coupled as in Fig. 5.8. The upper one monitors the charge state of the lower one. (b), The tunneling rate at degeneracy as a function of bias voltage  $V_b$  per junction. Solid red dots are measured at the base temperature of 50 mK. Open diamonds have been measured at 158 mK temperature. Solid black line shows the rates calculated with Eqs. (2.25) and (2.26). Open green triangles are results at the base temperature for a reference sample without normal metallic traps. Quasiparticle relaxation is weaker compared to the case of solid red dots and the tunneling rate is higher at low  $V_b$ . For ease of comparison, the tunneling rates are scaled for the latter structure by the ratio of junction conductances  $\frac{1/R_{T1,t}+1/R_{T2,t}}{1/R_{T1}+1/R_{T2}}$ , where  $R_{T1,t} = R_{T2,t} = 1.1 \text{ M}\Omega$  are the resistances of the device with direct trap and  $R_{T1} = 2.0 \text{ M}\Omega$ ,  $R_{T2} = 25 \text{ M}\Omega$  are those for the device without the traps. Figure adapted from Publication VI.

simplifies to

$$n_{\text{qp}} \approx D(E_F) \sqrt{2\pi} \sqrt{k_B T_S \Delta} e^{-\frac{\Delta}{k_B T_S}}. \quad (6.3)$$

Equation (6.3) shows that  $n_{\text{qp}}$  and hence also the tunneling rates caused by quasiparticle excitations are exponentially dependent on temperature as we expected.

Let us now consider the counting experiment of Publication VI for determining the quasiparticle density. In Fig. 6.1 we show the experimental structure. It consists of two SINIS type SETs where the islands are capacitively coupled. One of the SETs is used as an electrometer to read the number of electrons on the other SET island similarly as in Sect. 5.3. The SET, from which the tunneling events are counted, is tuned to charge degeneracy and the tunneling rate shown in Fig. 6.1 (b) is obtained at different bias voltages  $V_b$  (per junction). The open green triangles present the tunneling rates at base temperature for a sample without a quasiparticle trap with direct N-S contact. In this case we observe a bias independent rate at small  $V_b$ , as we would expect for tunneling by quasiparticle excita-

tions. The measured values  $\Gamma_{S1 \rightarrow N} + \Gamma_{S2 \rightarrow N} = 50$  Hz,  $R_{T1} = 2.0$  M $\Omega$  and  $R_{T2} = 25$  M $\Omega$ , yield  $n_S = 0.3$   $\mu\text{m}^{-3}$  (Eq. (6.2)). In Ref. [82] it was estimated that such a density is obtained with pair breaking rate of  $2.2 \cdot 10^5$  Hz/ $\mu\text{m}^3$  for the 30 nm thick aluminum film. This value is well inline with the upper limit of  $f_{\text{cpb}} = 2$  kHz for the Cooper pair breaking in an island with volume  $V = 1.06$   $\mu\text{m} \times 145$  nm  $\times 25$  nm, discussed in Sect. 6.4.3. These numbers yield an upper limit for the pair breaking rate  $f_{\text{cpb}}/V = 5 \cdot 10^5$  Hz/ $\mu\text{m}^3$ .

The red dots of Fig. 6.1 (b) show the tunneling rate for a sample having a direct metal-to-metal quasiparticle trap at 10  $\mu\text{m}$  distance from the junction. Now the current caused by quasiparticles is absent as we observe a bias dependent rate. We can however obtain an upper limit for the quasiparticle density by taking the lowest rate  $\Gamma_{S1 \rightarrow N} + \Gamma_{S2 \rightarrow N} = 8$  Hz and use the tunneling resistances  $R_{T1} = R_{T2} = 1.1$  M $\Omega$ . With these we obtain  $n_{\text{qp}} = 0.03$   $\mu\text{m}^{-3}$ , presenting the lowest reported quasiparticle density observed so far. It is significantly lower than typical values for fully superconducting systems [10–13]. See, however, Ref. [102] where a similar value as ours was subsequently obtained. Efficient trapping of the quasiparticles with normal metallic structures as well as admitting only low frequency signals in the experiment allows us to reach the small quasiparticle densities in the NIS junction based devices.

In addition to the counting techniques, direct current measurements of a SINIS SET allow one to probe the quasiparticles as was done in Publication VII. In order to detect the quasiparticle excitations, the superconducting leads were intentionally designed so that the quasiparticles do not relax to a trap efficiently. A scanning electron micrograph of the device designed for such an experiment is shown in Fig. 6.2 (a). The superconducting leads are 120 nm wide and 20  $\mu\text{m}$  long; beyond the end of the line, a wider section with quasiparticle trapping is reached. Since quasiparticles need to diffuse through the long and narrow line before relaxation, they are easily accumulated close to the junctions. Figure 6.2 (b) presents the measured subgap current of the device. The dark blue and red parts are caused by thermal excitations on the normal island and allows us to determine the degeneracy points for the graph. When the bias is lowered, we notice that the current at degeneracy vanishes whereas in Coulomb blockade a finite current persists.

In Fig. 6.2 (c) we show a numerical calculation with the parameter values  $R_T = 90$  k $\Omega$ ,  $E_c = 0.74$   $\Delta$  and  $\Delta = 216$   $\mu\text{eV}$  of the experiment of panel (b). We have taken an elevated temperature  $T_S = 205$  mK for the super-

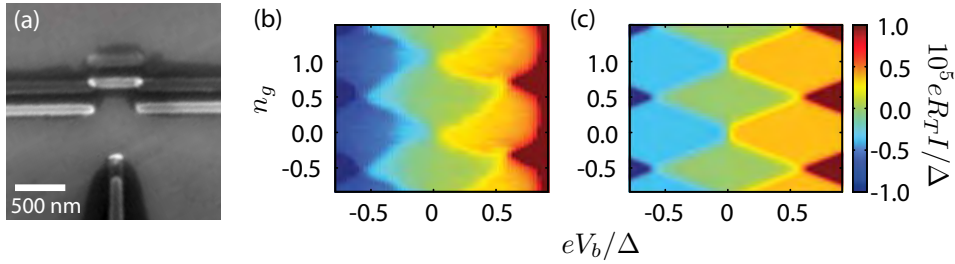


**Figure 6.2. Probing quasiparticle excitations with a SINIS SET.** (a), Scanning electron micrograph of a SINIS transistor designed for weak quasiparticle relaxation. (b), measured subgap current  $I$  as a function of the gate offset charge  $n_g$  and bias voltage  $V_b$ . (c), Simulated subgap current by elevated superconductor temperature. Figure adapted from Publication VII.

conductor, corresponding to  $n_{\text{qp}} = 20 \mu\text{m}^{-3}$ . We observe that the features of panel (b) are reproduced with good quantitative correspondence suggesting that the origin of the observed current is the presence of excess quasiparticle excitations. The current at degeneracy vanishes for small  $V_b$ . In this case, the SINIS transistor operates essentially as a single NIS junction which is insensitive to quasiparticle excitations as discussed in Sect. 2.2.2.

The current in Coulomb blockade is constant against  $V_b$  and  $n_g$  reflecting the bias independent tunneling rates of the quasiparticle excitations. The untrivial feature of the current being maximal in Coulomb blockade and not at degeneracy is understood with the following reasoning: when the excitations tunnel to the normal metallic island, the charge of the island moves away from the lowest energy state. Hence another tunneling event occurs soon after the first one to return the island charge to the preferred value. This tunneling occurs dominantly in the forward bias direction rectifying the quasiparticle excitation current and yielding a non-zero current. At degeneracy, the quasiparticle excitations cause tunneling between the two lowest charge states. The electrons tunnel equally to the forward and backward directions. Since these two charge states are equal in energy, no additional tunneling occurs for restoring the island charge back to the initial value.

The current at the light blue and orange terraces of Fig. 6.2 (b) and (c) is limited by the tunneling rate due to quasiparticle excitations of Eq. (6.2). The current through the device is given there as

$$I = \frac{n_{\text{qp}}}{eR_T D(E_F)}. \quad (6.4)$$

Since  $I$  is directly proportional to  $n_{\text{qp}}$ , measuring the current at the terrace probes directly the quasiparticle density as soon as we know  $R_T$  and

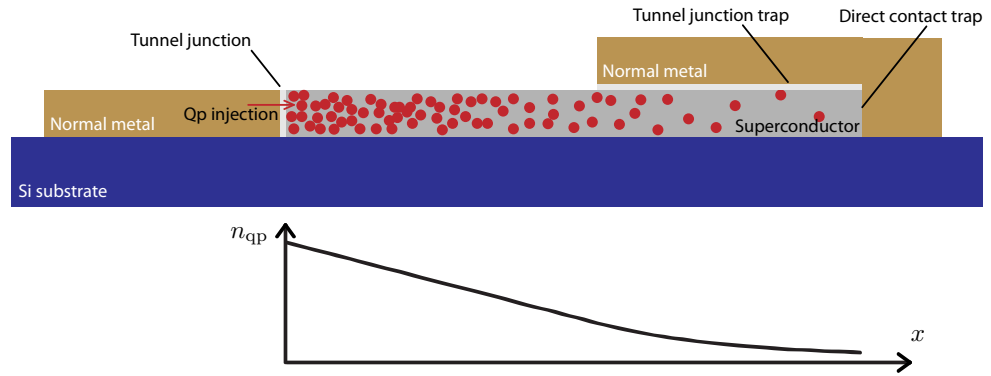


**Figure 6.3. Diffusion of quasiparticles in a superconducting lead.** Quasiparticles are injected from the normal metal to the superconductor via a tunnel junction. In order not to tunnel back to the normal metal, the quasiparticles need to diffuse through the bare superconducting section before reaching a trap which is either another (large) tunnel junction to a normal metal or a direct metal-to-metal contact on the right. Below,  $n_{\text{qp}}$  is sketched at different positions. In the bare diffusion part,  $n_{\text{qp}}$  is linear in distance and with the tunnel junction trap, it decays exponentially. For a direct contact trap we may generally assume  $n_{\text{qp}}$  to take the equilibrium value since there the quasiparticle relaxation is strong compared to the tunnel junctions.

$D(E_F)$ . Having shown the sensitivity to quasiparticle excitations, the device was placed in a sample holder which protects better against stray infra-red radiation coming from the high temperature parts of the cryostat. Unlike in the first setup, in this case the experiment of Fig. 6.2 (b) showed no current around Coulomb blockade, see Publication VII, suggesting that  $n_{\text{qp}}$  is much lower now. The quasiparticle excitations are not anymore generated by Cooper-pair breaking due to stray radiation.

## 6.2 Diffusion equation for quasiparticles

We consider diffusion and relaxation of the quasiparticles in a superconducting lead. A typical situation is sketched in Fig. 6.3. Quasiparticle excitations are generated by electrons tunneling from normal metal to a superconductor. The excitations may tunnel back to the normal metal which is usually an unwanted process. To avoid this to happen, they need to diffuse through the superconducting line and relax. The inherent relaxation mechanism in the superconducting material, the electron-phonon interaction [12, 103, 104], is so weak that the dominant relaxation is provided in the devices studied in this section by diffusion into a normal metallic trap which either has a direct metal-to-metal contact to the superconductor or is separated by a tunnel barrier [105–107]. After reaching the normal metal, the quasiparticles relax there efficiently since the electron-phonon

relaxation rate is several orders of magnitude stronger in a normal metal than in a superconductor, see e.g. Publication IX and Ref. [108].

To obtain a diffusion equation for the quasiparticles we consider electrical heat conduction in a superconductor. The heat flow of the quasiparticles  $\vec{J}$  follows the equation  $\nabla \cdot \vec{J} = -p_{\text{trap}}$ , where  $p_{\text{trap}}$  is the power removed from the quasiparticle population per unit volume. We use Fourier's law  $\vec{J} = -\kappa_S \nabla T_S$ , where

$$\kappa_S = \frac{6}{\pi^2} \frac{L_0 T_S}{\rho_n} (\beta_S \Delta)^2 e^{-\beta_S \Delta}, \quad (6.5)$$

is the heat conductivity of a superconductor at low temperatures  $k_B T_S \ll \Delta$ , see Ref. [109].  $L_0$  is the Lorenz number and  $\rho_n$  the normal state resistivity. Working out the derivatives leads to

$$D \left( \nabla^2 n_{\text{qp}} + \frac{k_B T_S}{2\Delta \cdot n_{\text{qp}}} |\nabla n_{\text{qp}}|^2 \right) = p_{\text{trap}}, \quad (6.6)$$

where  $D = \sqrt{2k_B T_S \Delta} / (\sqrt{\pi} e^2 D(E_F) \rho_n)$ . This diffusion model has been used successfully in several experiments, see Refs. [106, 107, 110–112] and Publication VII. In the absence of a quasiparticle trap, we take  $p_{\text{trap}} = 0$ . For a tunnel junction trap we consider the heat extracted from the superconductor as in Eqs. (3.11) and (3.13) for the normal metal. The results are the same in this case except that in the integrand the energy  $E \pm \delta E$  deposited to the normal metal is substituted with the energy  $E$  extracted from the superconductor. For the traps we have no bias voltage or charging effects so that  $\delta E = 0$ . We obtain then

$$p_{\text{trap}} = \frac{P_{\text{trap}}}{Ad} = \frac{\Delta}{e^2 R_T Ad D(E_F)} (n_{\text{qp}} - n_{\text{qp}0}), \quad (6.7)$$

where  $n_{\text{qp}0}$  is the quasiparticle density in the absence of injection,  $A$  is the trap area yielding resistance  $R_T$  and  $d$  is the thickness of the film. We have assumed here that there is no gradient perpendicular to the film, i. e., we consider the diffusion equation only in two dimensions. This is a good approximation for the thin films used as at least one of the dimensions parallel to the film is much larger than the film thickness  $d$ . One obtains Eq. (6.7) also by multiplying Eq. (6.2) by  $\Delta$  and 2, which are the energy carried by a single quasiparticle and the number of branches respectively, and normalizing by the junction area and film thickness. At low temperatures,  $k_B T_S / \Delta \ll 1$ , we may in addition neglect the second term in Eq. (6.6) and obtain a simple diffusion equation

$$D \nabla^2 n_{\text{qp}} = p_{\text{trap}}. \quad (6.8)$$

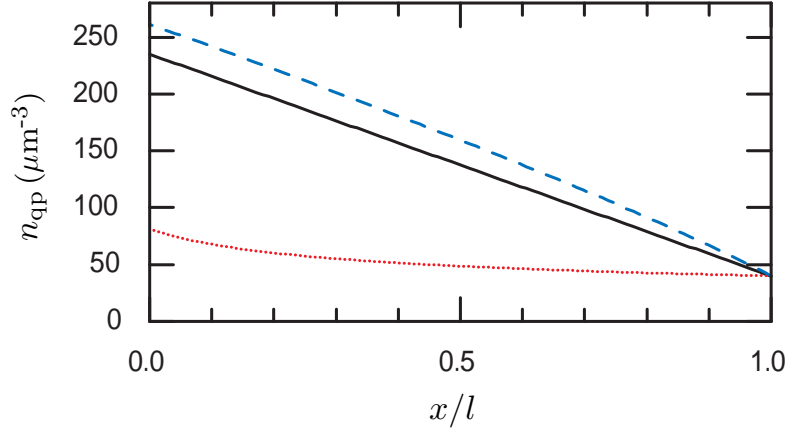


**Figure 6.4. Approximation in quasiparticle diffusion calculations.** Quasiparticle diffusion calculations for a superconducting line of  $l = 20 \mu\text{m}$  length. The cross-sectional area is  $120 \text{ nm} \times 25 \text{ nm}$  and the quasiparticle injection rate at  $x = 0$  is 50 MHz corresponding to the structure representing weakest relaxation and employing maximal quasiparticle injection in Publication VII. The solid black line is calculated with Eq. (6.8) and the dashed blue line with Eq. (6.6). For the dotted red line, a constant heat conduction is assumed.

The approximation to obtain Eq. (6.8) is essentially the following. We consider the derivatives of strong exponential dependencies only. The exponential dependence of  $\kappa_S$  on  $T_S$  in Eq. (6.5) is also included. Therefore this approximation is not as restrictive as a typical one in heat conduction calculations where the conductivity is assumed to be constant. In Publication VII the heat diffusion in superconducting leads was experimentally studied. The quasiparticles were injected by a SINIS turnstile operated at the first current plateau. The quasiparticle injection rate is then equal to the pumping frequency  $f$ . Measuring the dependence of the current on the pumping plateau against bias voltage allows one to determine  $n_{\text{qp}}$ . These measurements were repeated for several geometries and frequencies. Equation (6.8) was successfully used to predict the findings with the normal state resistivity  $\rho_n = 30 \text{ n}\Omega\text{m}$  and the residual quasiparticle density of the aluminum film being the only fitting parameters. The same value of  $\rho_n$  was used for all different geometries and injection rates. The residual quasiparticle density  $n_{\text{qp}0}$  depends, however, on the particular geometry as expected.

To elaborate on the difference between Eqs. (6.6), (6.8) and the more limiting assumption of constant heat conduction, let us consider as an example the case of the  $20 \mu\text{m}$  long aluminum line of Fig. 6.2 which had the weakest quasiparticle relaxation in Publication VII. In Fig. 6.4 we present the calculations based on Eqs. (6.6), (6.8) and the constant heat conduction. We observe that using Eq. (6.8) makes only an approximately

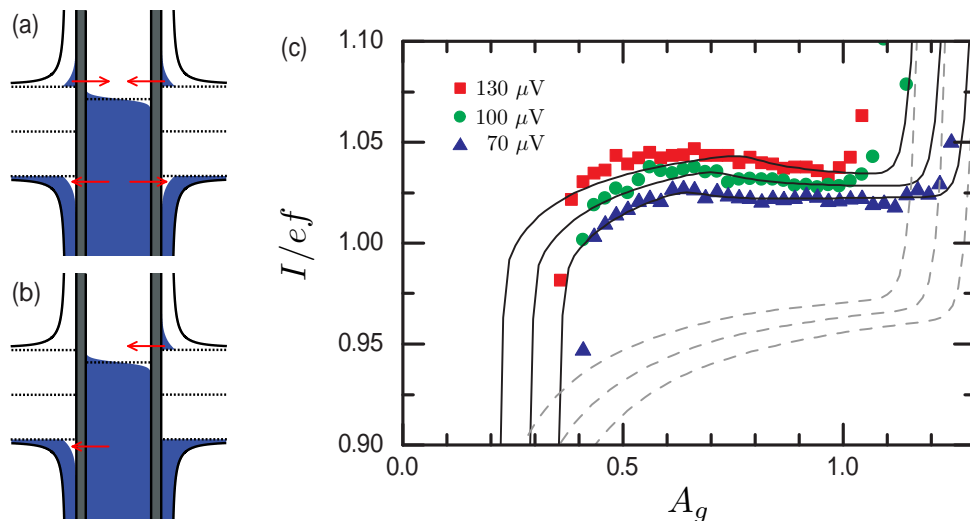


**Figure 6.5. Branch imbalance in SINIS turnstile.** (a), The DoS of a SINIS turnstile with quasiparticle excitations but no branch imbalance. The upper branch,  $E > \Delta$ , has the same number of excitations as the lower one,  $E < -\Delta$ . (b), The DoS with branch imbalance. Electrons are removed from the left superconductor resulting in hole excitations and deposited to the right superconductor resulting in particle excitations. Red arrows show the processes causing error to the operation. (c), Measured current  $I$  of the SINIS turnstile as a function of the gate amplitude  $A_g$  with  $f = 5$  MHz and bias voltages  $V_b = 70, 100$  and  $130 \mu\text{V}$ . The geometry of the device is similar to the one in Fig. 6.2 (a). Solid black lines are numerical calculations of Eq. (3.7) assuming no branch imbalance corresponding to panel (a) and dashed gray lines are with no branch-to-branch relaxation corresponding to panel (b).

10 % error compared to the accurate result of Eq. (6.6). However, if we would assume the heat conduction to be constant in the lead and taking the value at  $x = 0$ , the quasiparticle number would be underestimated by a factor of 3. This shows that Eq. (6.8) is sufficient for obtaining a quantitative understanding about quasiparticle relaxation in superconducting leads even for weak relaxation. In this example the quasiparticle density exceeds the thermal population by an order of magnitude. The more crude approximation of constant heat conduction is, however, not applicable here.

### 6.3 Branch imbalance in SINIS turnstile

For analysing the quasiparticle excitations under turnstile operation, we assumed no branch imbalance. The density of states (DoS) and the quasiparticle excitations of a SINIS turnstile without the branch imbalance are shown in Fig. 6.5 (a). Each of the superconductor branches have the same number of excitations. The excitations contribute to errors in turnstile operation with the processes indicated by the red arrows. In Fig. 6.5 (b)

we present a similar sketch but in presence of full branch imbalance. In this case, the excitations produce error processes to the backward direction only. If the relaxation between the branches is weak compared to the quasiparticle injection rate, the excitations of a SINIS turnstile would have the distribution of panel (b). The operation tends to form branch imbalance: on one of the superconducting leads quasiparticles are removed from the lower branch and they are deposited to the upper branch on the other superconductor leading to the situation of Fig. 6.5 (b).

In Fig. 6.5 (c) we present experimental data for a turnstile which has similar geometry as the one in Fig. 6.2 (a). The superconducting leads are 200 nm wide, 20  $\mu\text{m}$  long and 25 nm thick. The geometry is chosen for having weak relaxation for the quasiparticles so that they dwell nearby the device and produce an observable signal on the pumping plateau. The device parameter values are  $R_T = 700 \text{ k}\Omega$ ,  $\Delta = 236 \text{ }\mu\text{eV}$  and  $E_c/\Delta = 1.0$ . The drive frequency is  $f = 5 \text{ MHz}$ . Solid black curves show numerical calculations of Eq. (3.7) assuming no branch imbalance and taking  $n_{\text{qp}} = 1000 \text{ }\mu\text{m}^{-3}$ . Dashed gray line shows similar calculations but with the quasiparticles lying on one of the superconductor branches only, see panel (b). Based on the numerical calculations, we conclude that there is no significant charge imbalance in the SINIS turnstile: a 10 % difference in the population of the two branches would already lead to discrepancy between the experimental data and the numerical calculation. The position and the shape of the plateau fits the calculation without branch imbalance. If the branch imbalance is taken into account, the plateau shape is different and it lies below  $I = ef$ . In this case the quasiparticle excitations generate error in the backward direction only. In order to match the experimental and the modeled curves, a 7 % correction would be required for the current amplifier gain. This is not feasible since the accuracy of the gain is typically better than 1 %. For the calculation without branch imbalance such correction is not needed. A quantitative analysis of the relaxation rates of the two branches is outside of the scope of this thesis.

#### 6.4 Electron-phonon interaction in the superconducting state

In Sect. 6.2 we considered the relaxation of quasiparticles in superconducting leads. There, we neglected the relaxation mechanisms in the superconductor itself since in that case normal metallic parts of the structures were providing the dominant relaxation route. In order to observe

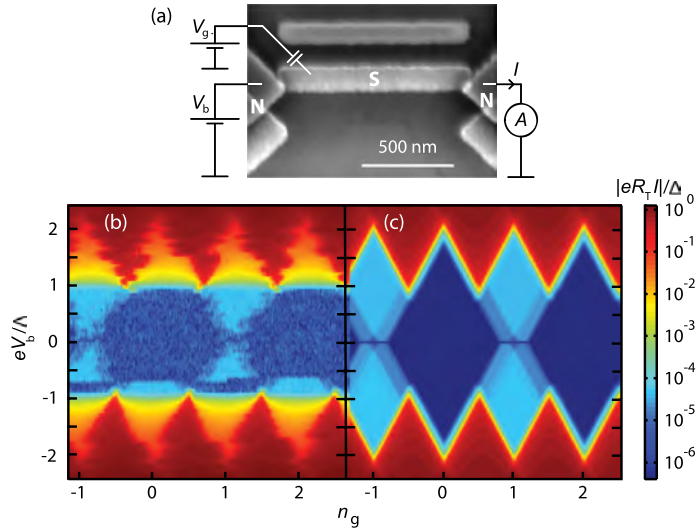


**Figure 6.6. Probing quasiparticles on a small superconducting island.** (a), A superconducting island (S) coupled to normal metallic leads (N) via two tunnel junctions. (b), The measured current  $I$  as a function of the bias voltage  $V_b$  and gate offset charge  $n_g$ . (c), Result of a numerical calculation based on Eq. (6.14) with the parameter values corresponding to the measurement in panel (b). Figure adapted from Publication IX.

the relaxation in the superconductor one can use fully superconducting systems [11, 12, 102, 108, 113, 114]. Another approach, involving normal metals, is shown in Fig. 6.6, see also Ref. [115]. It is based on having a small superconducting island weakly coupled to normal metallic leads and was utilized in Publication IX to study excitation and relaxation dynamics on the superconducting island down to a single excitation. Minimizing the relaxation to normal metallic parts allows us to probe the inherent relaxation mechanism of a superconductor, the electron-phonon interaction [103], as well as relaxation of single excitations via tunneling. First, in Sect. 6.4.1 we discuss the electron-phonon interaction and derive recombination rates essential for this system and then in Sect. 6.4.2 we present the experiments allowing one to study the relaxation dynamics quantitatively.

#### 6.4.1 Derivation of heat flux and related quantities

For studying the electron-phonon interaction in the superconducting state we utilize the same perturbative formalism as in Sect. 2.2. In this case the Hamiltonian reads

$$\hat{H} = \hat{H}_S + \hat{H}_p + \hat{H}_{e-ph}, \quad (6.9)$$

where  $\hat{H}_S$  is given by Eq. (2.4) and

$$\hat{H}_p = \sum_q \hbar\omega_q b_q^\dagger b_q, \quad (6.10)$$

is the Hamiltonian for phonons.  $b_q^\dagger$  is the creation operator of a phonon with energy  $\hbar\omega_q$  and wavevector  $q$ . The coupling of the electron and phonon systems is assumed to have the form

$$\hat{H}_{e\text{-ph}} = \nu \sum_{k,q} \omega_q^{1/2} (c_k^\dagger c_{k-q} b_q + c_k^\dagger c_{k+q} b_q^\dagger). \quad (6.11)$$

as in Ref. [116]. The operator of heat flux to the phonons is

$$\dot{\hat{H}}_p = \frac{i}{\hbar} [\hat{H}, \hat{H}_p] = \frac{i}{\hbar} [\hat{H}_{e\text{-ph}}, \hat{H}_p] = i\nu \sum_{k,q} \omega_q^{3/2} (c_k^\dagger c_{k-q} b_q - c_k^\dagger c_{k+q} b_q^\dagger). \quad (6.12)$$

By evaluating the expectation value of  $\dot{\hat{H}}_p$  with the technique of Sect. 2.2 we obtain the heat flux due to electron-phonon interaction as

$$\begin{aligned} \dot{Q}_{e\text{-ph}} &= \frac{\Sigma V}{24\zeta(5)k_B^5} \int_0^\infty d\epsilon \epsilon^3 (n(\epsilon, T_S) - n(\epsilon, T_P)) \int_{-\infty}^\infty dE \times \\ &n_S(E) n_S(E + \epsilon) \left( 1 - \frac{\Delta^2}{E(E + \epsilon)} \right) (f(E) - f(E + \epsilon)), \end{aligned} \quad (6.13)$$

where  $\Sigma$  is the electron-phonon coupling constant,  $V$  the volume of the superconductor,  $\zeta(5) = 1.037$  a value of the Riemann zeta function,  $n(\epsilon, T) = (e^{\epsilon/k_B T} - 1)^{-1}$  the Bose-Einstein distribution at temperature  $T$ ,  $T_P$  is the temperature of the phonons,  $T_S$  the electron temperature of the superconductor and  $\epsilon$  is the phonon energy. See the supplemental material of Publication IX for intermediate steps. Equation (6.13) is also found in Ref. [108], where the heat flux was measured by using superconducting tunnel junctions, and it was derived there by kinetic Boltzmann equation calculations [117].

The heat flux of Eq. (6.13) consists of scattering and recombination. In the recombination process two electrons form a Cooper pair thus changing the number of excitations. Scattering on the other hand does not change the number of quasiparticle excitations but it leads to heat flux as it changes the energy which a quasiparticle carries. Equation (6.13) can be split into recombination and scattering terms which at low temperature,  $T_P \ll T_S \ll \Delta/k_B$  read

$$\begin{aligned} \dot{Q}_{\text{rec}}(T_S) &\approx \frac{\pi V \Sigma}{3\zeta(5)k_B^5} (k_B T_S \Delta^4 + \frac{7}{4} (k_B T_S)^2 \Delta^3) e^{-2\Delta/k_B T_S}, \\ \dot{Q}_{\text{sc}}(T_S) &\approx V \Sigma T_S^5 e^{-\Delta/k_B T_S}. \end{aligned}$$

Since recombination involves two quasiparticles, each carrying an energy of at least  $\Delta$ , the exponential suppression involves energy  $2\Delta$ . Similarly,

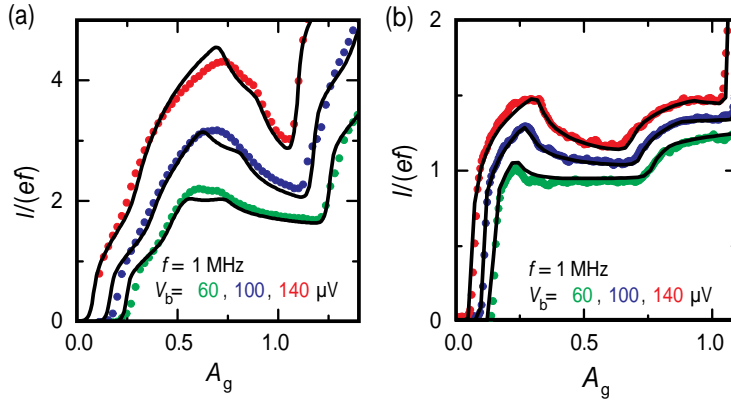


**Figure 6.7. Current of a NISIN transistor under turnstile operation.** The current  $I$  through the transistor is shown for various bias voltages  $V_b$  as a function of the gate offset amplitude  $A_g$  in the range where the first quantized plateau  $I = ef$  should form for  $E_c = 240 \mu\text{eV}$  in panel (a) and  $E_c = 620 \mu\text{eV}$  in panel (b). Dots present measured values and solid black lines numerical calculations based on Eq. (3.7). Figure adapted from Publication IX.

scattering involves energy  $\Delta$  in the exponential suppression. The scattering involves a single quasiparticle and it takes place within one of the branches only. The heat flux scales thus as  $\dot{Q}_{sc} \propto n_{qp} \propto e^{-\Delta/k_B T_S}$ .

#### 6.4.2 Recombination rates on a small superconducting island

Let us now turn back to consider the device presented in Fig. 6.6. The single-electron tunneling processes for this device are identical to the SINIS turnstile, see discussion under Eq. (2.26) and Ref. [49]. Therefore we may drive it by a gate voltage as was done for the SINIS turnstile and ideally quantized current plateaus would form. However, the single-electron tunneling creates quasiparticle excitations on the superconducting island. The excitations cannot relax to normal metallic traps as easily as in the "large" and "trapped" superconducting leads of Sect. 6.2. The weak thermal coupling provides an efficient way of probing the electron-phonon relaxation. In Fig. 6.7 we show the region where the first pumping plateau should form for the two different devices presented. We observe that the current plateaus are practically absent. The experimental curves have nontrivial features which are sensitive to the charging energy of the device and they are reproduced accurately by the numerical results based on the master equation approach of Eq. (3.7). In the simulations, the temperature of the superconductor  $T_S$  is allowed to differ from the phonon temperature  $T_0$ . For each point of Fig. 6.7,  $T_S$  is found by balancing the heat injection via tunneling with the electron-phonon heat flux of Eq. (6.13). The experiment and the heat balance calculations were repeated at vari-

ous pumping frequencies  $f$  in Publication IX and a good agreement with Eq. (6.13) was found over a wide range of heat fluxes.

### 6.4.3 Single quasiparticle effects

In the experiments of Fig. 6.7, the average number of excitations was of the order  $N_{\text{qp}} \sim 10$ . When an electron tunneling event takes place, this number is changed by one and in a recombination process it changes by two. Such processes cause fluctuations to  $N_{\text{qp}}$  within the turnstile cycle [75]. Since the average number of excitations is an order of magnitude larger than the fluctuations, it is an adequate approximation to model the system by using a time-independent temperature for the superconducting island. However, if the frequency is lowered, or ultimately in a static situation, the number of quasiparticles decreases close to  $N_{\text{qp}} = 0$  at low temperatures [4, 7, 74, 118, 119]. This is obviously a situation where such a thermal description is not valid. Looking back to Fig. 6.6 (b) we notice that for  $|eV_b| < \Delta$ , the periodicity in  $n_g$  is doubled as compared to that at  $|eV_b| > \Delta$ . For the high bias, the operation is equivalent to that of a SINIS device with 1e-periodicity and no significant sensitivity to the single-quasiparticle excitations. At low bias values the situation is opposite. If  $n_g$  is set close to an even integer, the island holds an even number of electrons which are all paired [118]. Hence the current vanishes. If  $n_g$  is close to an odd integer, there is an odd number of electrons on the island and one of them is naturally unpaired. It remains as a quasiparticle excitation carrying an energy of at least  $\Delta$ . With the given energy, it can readily escape from the island by tunneling to a normal metal lead. Due to charging energy costs, proportional to  $E_c$ , another electron tunnels, however, into the superconducting island to recover the preferred number of electrons. For  $E_c \sim \Delta$ , both of these processes are active. Such a situation was realized in the experiment. The cycle then repeats and causes an experimentally observable current "terrace" similar in shape to those in Figs. 6.2 (b) and (c).

If the superconducting island is assumed to have an average temperature  $T_S$ , we can utilize the master equation (3.7) with elevated  $T_S$  for the calculations. This would result in a graph similar to that in Fig. 6.2 (c). The result is correct apart from the current terrace around even  $n_g$  values. Therefore the change in the parity in Fig. 6.6 is a clear sign of at most a single quasiparticle present. To model this situation correctly, we

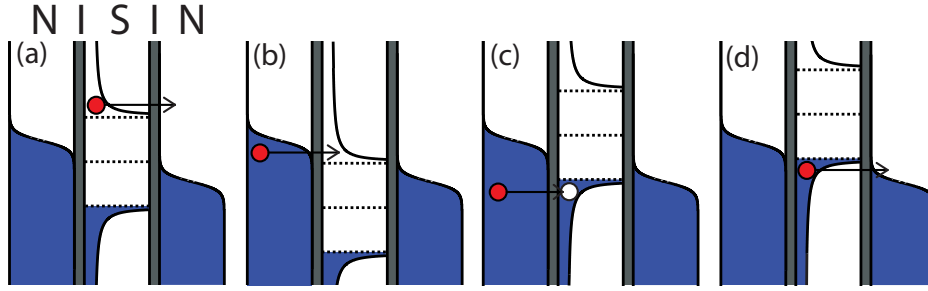


**Figure 6.8. Tunneling in a NISIN transistor.** (a), The tunneling rate  $\Gamma_{N \rightarrow N-1, N_S \rightarrow N_S-1}$  is generated by quasiparticle excitations in the superconductor with energy  $E > \Delta$  tunneling out of the island. The opposing process, tunneling into  $E > \Delta$ , contributes to  $\Gamma_{N \rightarrow N+1, N_S \rightarrow N_S+1}$  shown in panel (b). Similarly, tunneling with energies  $E < -\Delta$  contributes to  $\Gamma_{N \rightarrow N+1, N_S \rightarrow N_S-1}$ , shown in panel (c), and  $\Gamma_{N \rightarrow N-1, N_S \rightarrow N_S+1}$ , shown in panel (d). Figure adapted from Publication IX.

extend the master equation (3.7) to

$$\frac{d}{dt} P(N, N_S) = \sum_{N', N'_S} \Gamma_{N' \rightarrow N, N'_S \rightarrow N_S} P(N', N'_S), \quad (6.14)$$

where  $P(N, N_S)$  is the probability of having  $N$  excess electrons and  $N_S$  quasiparticle excitations on the island, and  $\Gamma_{N' \rightarrow N, N'_S \rightarrow N_S}$  is the transition rate from  $N', N'_S$  to  $N, N_S$ . The rates are set by electron tunneling and recombination. Tunneling is calculated using Eqs. (2.25) and (2.26) by treating separately processes where energy is removed and deposited to the superconductor as shown in Fig. 6.8. For explicit formulas of the tunneling rates, see the supplemental material of Publication IX.

At low temperatures, we may assume each quasiparticle excitation to carry energy  $E = \Delta$ . Then we obtain the recombination rate from Eq. (6.14) by dividing  $\dot{Q}_{\text{rec}}$  by  $2\Delta$ , the latter being the energy carried by the two recombining quasiparticles. Rewriting the result in terms of  $N_S$  leads to

$$\Gamma_{N \rightarrow N, N_S \rightarrow N_S-2} \approx \frac{\Sigma \Delta^2}{12\zeta(5) D(E_F)^2 k_B^5 V} N_S^2, \quad (6.15)$$

for  $N_S \geq 2$ . For  $N_S = 0, 1$  we have  $\Gamma_{N \rightarrow N, N_S \rightarrow N_S-2} = 0$  since a single excitation cannot pair.

With Eq. (6.14), the experiment of Fig. 6.6 (b) is reproduced up to a high degree as shown in Fig. 6.6 (c). The current terrace around odd values of  $n_g$  with  $|eV_b| < \Delta$  is caused by the single quasiparticle excitation. The current at the terrace is set by Eq. (6.4) with  $n_{\text{qp}} = 1/V$  which is the quasiparticle density due to a single excitation. Hence the current at the terrace allows one to determine the single quasiparticle relaxation rate via tunneling. In addition, in pumping experiments at lower frequencies than that in Fig. 6.7, recombination rates of Eq. (6.15) are probed down to

a single quasiparticle pair as reported in Publication IX. In the modeling based on Eq. (6.14), the energy relaxation of the quasiparticle due to scattering was neglected as all the quasiparticles were assumed to be injected near the gap edges. In Ref. [75] an alternative formalism is used, which allows one to consider the scattering relaxation as well. It is shown there that for the transport and quasiparticle relaxation in a NISIN transistor, it is not important to take into account the scattering explicitly. However, if the quasiparticles are injected to energies  $E \gg \Delta$ , and the device operation is sensitive to the exact distribution, this would be an issue [120].

In addition to the probing of electron-phonon interaction, the NISIN transistor can be utilized to probe the Cooper pair breaking in a superconductor. The vanishing current at even values of  $n_g$  in Fig. 6.6 (b) allows one to estimate an upper limit for the spontaneous Cooper pair breaking rate on the island which depends presumably on the microwave background in the setup. The broken Cooper pairs would result in a terrace around even values of  $n_g$ . Therefore the measurement resolution allows us to determine an upper limit for the number of broken Cooper pairs on the superconducting island. With the relaxation dynamics described above, we evaluate the pair breaking rate to be less than 2 kHz which in turn corresponds to less than 0.1 aW power on the superconducting island.



## 7. Summary

This thesis focused on studying electrical transport in nanoscaled tunnel junctions between a normal metal and a superconductor. The main emphasis was put on understanding the two-electron Andreev tunneling and quasiparticle excitations in the superconductor. We demonstrated various experimental methods for detecting these phenomena and utilized them to study what kind of influences these two phenomena impose on the devices based on tunnel junctions and superconductors in general. Further on, we analyzed which quantities influence on the two phenomena and how.

For the two-electron Andreev tunneling we showed that charging effects give rise to such features in the current-voltage curves which distinguish this process from other leakage sources. This distinction is not possible for voltage biased NIS junctions. We saw that Andreev tunneling becomes suppressed if the charging energy is made sufficiently large, an essential feature for improved accuracy of the SINIS turnstile. In addition, we utilized counting techniques for demonstrating in real time the presence of two electrons carrying the current in the Andreev process. The electron counting allowed us to consider the statistics as well.

For investigating the quasiparticle excitations we also used the electron counting techniques. We demonstrated that the excitations give rise to a tunneling rate which is independent of the energy cost and that with sufficient shielding the excitations become largely suppressed. With the help of charging effects we were able to probe the excitations by a simpler direct current measurement where the quasiparticles generate a bias independent current. By driving a SINIS turnstile, a controlled injection and detection of quasiparticles was obtained. The diffusion and relaxation of the excitations in superconducting leads was studied. The inverse NISIN structure, on the other hand, was utilized to study the recombina-

tion mechanism of the superconductors by phonon emission, down to the level of a few excitations only.

The suppressed Andreev tunneling in a SINIS turnstile, which we demonstrated experimentally, is an important step towards optimizing the accuracy of the turnstile. With the Andreev tunneling being suppressed, the fundamental multi-electron process limiting the accuracy is the co-tunneling of a Cooper pair and an electron [49]. Based on the present knowledge, a relative accuracy on the  $10^{-7}$  level is obtainable with an output current on the level of 10 pA. This would call for ten parallel devices, also demonstrated in this thesis, in order to obtain sufficiently large current for metrological applications [50, 51]. On the other hand the studies on quasiparticle excitations showed us that providing sufficient relaxation for them is a crucial issue for the accuracy of the SINIS turnstile and requires a careful optimization for reaching the highest accuracy for the current quantization. With the best devices used in this thesis, the relative accuracy of the SINIS turnstile was shown to be on the low  $10^{-4}$  level but still limited by the quasiparticle excitations. For reaching  $10^{-7}$  relative accuracy, the evacuation and relaxation of the excitations need to be increased by a factor of 1000. In order to fulfill this requirement, the most apparent approach would be to decrease the normal state resistivity  $\rho_n$ , which in principle should be feasible with ultra pure aluminum [121]. However, obtaining single crystalline structure and small number of impurities yielding low  $\rho_n$  will be troublesome for thin films. Increasing the film thickness might help for this goal as the surface scattering will be then weaker. The thicker film would also help the evacuation of the excitations since then they would spread to a larger volume. In addition, creating vortices by applying a magnetic field, the relaxation on the superconducting leads might be increased [104]. If all these approaches turn out to be futile, increasing the tunnel resistances of the device will increase the relative accuracy: the obtainable output current is proportional to the drive frequency being inversely proportional to resistance:  $f \propto 1/R_T$ . The error in the current on the other hand is proportional to  $f/R_T \propto 1/R_T^2$ , since  $f$  is the injection frequency of the quasiparticles and  $1/R_T$  their tunneling rate causing the errors. Hence the relative accuracy limited by the quasiparticles scales as  $1/R_T$ . Increasing the resistance is however not a tempting option since it would call for more devices in parallel.

Instead of improving the accuracy of a device itself, there is an alterna-

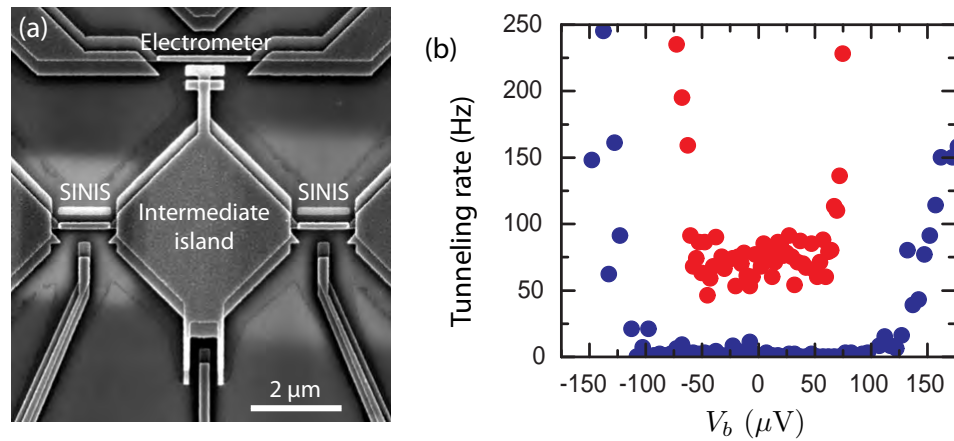


**Figure 7.1. Error counting in SINIS turnstiles.** (a), Two SINIS turnstiles connected in series with an intermediate island in between. An electrometer reads the number of excess electrons on the intermediate island. (b), Tunneling rate to the intermediate island as a function of the bias voltage  $V_b$  per junction. For red points, the SINIS turnstiles are kept at degeneracy and for the blue points they are in Coulomb blockade. The bias independent tunneling rate at degeneracy suggests that there are excess quasiparticles present.

tive approach to satisfy the stringent accuracy requirement. In this approach errors are detected by electron counting techniques and the error is taken into account when determining the obtained current [122, 123]. A possible device for error counting of a SINIS turnstile is shown in Fig. 7.1 (a). It consists of two SINIS turnstiles which have an intermediate island in between. The number of electrons on the intermediate island is monitored by an electrometer. Both of the turnstiles are operated at the same frequency. If either of the turnstiles fails to transport an electron in a cycle, it is detected by the electrometer. If the errors occur at a low frequency  $f_{\text{err}} \ll f_{\text{det}}$ , the electrometer is able to resolve them reliably and thus they can be taken into account. Here  $f_{\text{det}}$  is the bandwidth of the detector. For this setup, we need to know which direction the errors occur in order to compensate them. Since the operation of the turnstile can be described with a high precision as shown in this thesis, it provides a solid basis for arguments about the direction. Alternative approach would be to add one more turnstile in series and detect electrons on two intermediate islands allowing to resolve the direction of tunneling [81]. In Fig. 7.1 (b) we present the measured tunneling rate to the intermediate island under static conditions when the turnstiles are either at degeneracy or in Coulomb blockade. We observe that at degeneracy, we have a bias independent tunneling rate suggesting that there are excess quasiparticles present. We expect the relaxation of the quasiparticles to be weak on the superconducting intermediate island. Hence, finding excess quasiparti-

cles on it is not surprising. In order to accomplish the error counting in the turnstiles, a stronger quasiparticle relaxation is needed especially for the intermediate island. With the direct metal-to-metal traps, more efficient trapping should be feasible [112]. This, however, remains to be tested. Hopefully in the future we will also see whether either the SINIS turnstile or the competing semiconductor pumps [30, 124–126] reach the demanding accuracy requirements and fulfill all the requirements for the redefinition of the SI unit system.

# Bibliography

- [1] M. Tinkham, *Introduction to superconductivity*, 2nd ed. (McGraw-Hill, New York, 1996).
- [2] A. F. Andreev, Sov. Phys. JETP **19**, 1228 (1964).
- [3] G. E. Blonder, M. Tinkham, and T. M. Klapwijk, Phys. Rev. B **25**, 4515 (1982).
- [4] T. M. Eiles, J. M. Martinis, and M. H. Devoret, Phys. Rev. Lett. **70**, 1862 (1993).
- [5] H. Pothier, S. Guéron, D. Esteve, and M. H. Devoret, Phys. Rev. Lett. **73**, 2488 (1994).
- [6] F. W. J. Hekking and Y. V. Nazarov, Phys. Rev. B **49**, 6847 (1994).
- [7] J. M. Hergenrother, M. T. Tuominen, and M. Tinkham, Phys. Rev. Lett. **72**, 1742 (1994).
- [8] S. Rajauria, P. Gandit, T. Fournier, F. W. J. Hekking, B. Pannetier, and H. Courtois, Phys. Rev. Lett. **100**, 207002 (2008).
- [9] A. S. Vasenko, E. V. Bezuglyi, H. Courtois, and F. W. J. Hekking, Phys. Rev. B **81**, 094513 (2010).
- [10] M. D. Shaw, R. M. Lutchyn, P. Delsing, and P. M. Echternach, Phys. Rev. B **78**, 024503 (2008).
- [11] R. Barends, J. J. A. Baselmans, S. J. C. Yates, J. R. Gao, J. N. Hovenier, and T. M. Klapwijk, Phys. Rev. Lett. **100**, 257002 (2008).
- [12] J. M. Martinis, M. Ansmann, and J. Aumentado, Phys. Rev. Lett. **103**, 097002 (2009).
- [13] P. de Visser, J. Baselmans, P. Diener, S. Yates, A. Endo, and T. Klapwijk, Phys. Rev. Lett. **106**, 167004 (2011).
- [14] H. Paik, D. I. Schuster, L. S. Bishop, G. Kirchmair, G. Catelani, A. P. Sears, B. R. Johnson, M. J. Reagor, L. Frunzio, L. I. Glazman, S. M. Girvin, M. H. Devoret, and R. J. Schoelkopf, Phys. Rev. Lett. **107**, 240501 (2011).
- [15] Y. Makhlin, G. Schön, and A. Shnirman, Rev. Mod. Phys. **73**, 357 (2001).
- [16] F. Giazotto, T. T. Heikkilä, A. Luukanen, A. M. Savin, and J. P. Pekola, Rev. Mod. Phys. **78**, 217 (2006).

- [17] L. Sun, L. DiCarlo, M. D. Reed, G. Catelani, L. S. Bishop, D. I. Schuster, B. R. Johnson, G. A. Yang, L. Frunzio, L. Glazman, M. H. Devoret, and R. J. Schoelkopf, *Phys. Rev. Lett.* **108**, 230509 (2012).
- [18] M. Lenander, H. Wang, R. C. Bialczak, E. Lucero, M. Mariani, M. Neeley, A. D. O'Connell, D. Sank, M. Weides, J. Wenner, T. Yamamoto, Y. Yin, J. Zhao, A. N. Cleland, and J. M. Martinis, *Phys. Rev. B* **84**, 024501 (2011).
- [19] A. J. Ferguson, N. A. Court, F. E. Hudson, and R. G. Clark, *Phys. Rev. Lett.* **97**, 106603 (2006).
- [20] R. A. Millikan, *Phys. Rev. (Ser. I)* **32**, 349 (1911).
- [21] R. A. Millikan., *Phys. Rev.* **2**, 109 (1913).
- [22] D. V. Averin and K. K. Likharev, "Mesoscopic phenomena in solids," (Nature Publishing Group, Amsterdam, 1991) p. 173.
- [23] G. L. Ingold and Y. V. Nazarov, "Single charge tunneling, coulomb blockade phenomena in nanostructures, ch 2," (Plenum Press, New York, 1992) p. 21.
- [24] D. Esteve, "Single charge tunneling, coulomb blockade phenomena in nanostructures, ch 3," (Plenum Press, New York, 1992).
- [25] H. Pothier, P. Lafarge, C. Urbina, D. Esteve, and M. H. Devoret, *Europhys. Lett.* **17**, 249 (1992).
- [26] D. V. Averin and Y. V. Nazarov, "Single charge tunneling, coulomb blockade phenomena in nanostructures, ch 9," (Plenum Press, New York, 1992).
- [27] M. H. Devoret, D. Esteve, and C. Urbina, *Nature* **360**, 547 (1992).
- [28] M. W. Keller, J. M. Martinis, N. M. Zimmerman, and A. H. Steinbach, *Appl. Phys. Lett.* **69**, 1804 (1996).
- [29] A. Fujiwara and Y. Takahashi, *Nature* **410**, 560 (2001).
- [30] S. P. Giblin, M. Kataoka, J. D. Fletcher, P. See, T. J. B. M. Janssen, J. P. Griffiths, G. A. C. Jones, I. Farrer, and D. A. Ritchie, *Nature Comm.* **3**, 930 (2012).
- [31] L. J. Geerligs, V. F. Anderegg, P. A. M. Holweg, J. E. Mooij, H. Pothier, D. Esteve, C. Urbina, and M. H. Devoret, *Phys. Rev. Lett.* **64**, 2691 (1990).
- [32] M. W. Keller, A. L. Eichenberger, J. M. Martinis, and N. M. Zimmerman, *Science* **285**, 1706 (1999).
- [33] L. P. Kouwenhoven, A. T. Johnson, N. C. van der Vaart, C. J. P. M. Harman, and C. T. Foxon, *Phys. Rev. Lett.* **67**, 1626 (1991).
- [34] J. P. Pekola, J. J. Vartiainen, M. Möttönen, O.-P. Saira, M. Meschke, and D. V. Averin, *Nature Phys.* **4**, 120 (2008).
- [35] J. Bardeen, L. N. Cooper, and J. R. Schrieffer, *Phys. Rev.* **108**, 1175 (1957).
- [36] N. N. Bogoliubov, *Zh. Eksperim. Teor. Fiz.* **34**, 58 (1958).
- [37] J. G. Valatin, *Nuovo Cimento* **7**, 843 (1958).

- [38] G. J. Dolan, *Appl. Phys. Lett.* **31**, 337 (1977).
- [39] T. A. Fulton and G. Dolan, *Physical Review Letters* **59**, 109 (1987).
- [40] F. Schwabl, *Quantum Mechanics*, 3rd ed. (Springer, Berlin, 2002).
- [41] I. Giaever, *Phys. Rev. Lett.* **5**, 147 (1960).
- [42] J. Clarke, *Phys. Rev. Lett.* **28**, 1363 (1972).
- [43] D. V. Averin and K. K. Likharev, *J. Low Temp. Phys.* **62**, 345 (1986).
- [44] K. K. Likharev, *IEEE Trans. Magn.* **23**, 1142 (1987).
- [45] P. G. De Gennes, *Superconductivity of Metals and Alloys* (Advanced Book Program, Perseus Books, New York, 1999).
- [46] O.-P. Saira, M. Meschke, F. Giazotto, A. M. Savin, M. Möttönen, and J. P. Pekola, *Phys. Rev. Lett.* **99**, 027203 (2007).
- [47] S. Kafanov, A. Kemppinen, Y. A. Pashkin, M. Meschke, J. S. Tsai, and J. P. Pekola, *Phys. Rev. Lett.* **103**, 120801 (2009).
- [48] F. C. Wellstood, C. Urbina, and J. Clarke, *Phys. Rev. B* **49**, 5942 (1994).
- [49] D. V. Averin and J. P. Pekola, *Phys. Rev. Lett.* **101**, 066801 (2008).
- [50] K. K. Likharev and A. B. Zorin, *J. Low Temp. Phys.* **59**, 347 (1985).
- [51] F. Piquemal, *C.R. Physique* **5**, 857 (2004).
- [52] J. Flowers, *Science* **306**, 1324 (2004).
- [53] A. Kemppinen, S. Kafanov, Y. A. Pashkin, J. S. Tsai, D. V. Averin, and J. P. Pekola, *Appl. Phys. Lett.* **94**, 172108 (2009).
- [54] M. H. Devoret, D. Esteve, H. Grabert, G.-L. Ingold, H. Pothier, and C. Urbina, *Phys. Rev. Lett.* **64**, 1824 (1990).
- [55] S. M. Girvin, L. I. Glazman, M. Jonson, D. R. Penn, and M. D. Stiles, *Phys. Rev. Lett.* **64**, 3183 (1990).
- [56] J. M. Martinis and M. Nahum, *Phys. Rev. B* **48**, 18316 (1993).
- [57] J. M. Hergenrother, J. G. Lu, M. T. Tuominen, D. C. Ralph, and M. Tinkham, *Phys. Rev. B* **51**, 9407 (1995).
- [58] W. Schottky, *Ann. Phys.* **57**, 541 (1918).
- [59] A. N. Korotkov, *Phys. Rev. B* **49**, 10381 (1994).
- [60] A. O. Caldeira and A. J. Leggett, *Phys. Rev. Lett.* **46**, 211 (1981).
- [61] H. B. Callen and T. A. Welton, *Phys. Rev.* **83**, 34 (1951).
- [62] K. von Klitzing, G. Dorda, and M. Pepper, *Phys. Rev. Lett.* **45**, 494 (1980).
- [63] R. C. Dynes, V. Narayanamurti, and J. P. Garno, *Phys. Rev. Lett.* **41**, 1509 (1978).
- [64] R. C. Dynes, J. P. Garno, G. B. Hertel, and T. P. Orlando, *Phys. Rev. Lett.* **53**, 2437 (1984).

- [65] G. O’Neil, D. Schmidt, N. Miller, J. Ullom, K. Iwrin, A. Williams, G. Arnold, and S. Ruggiero, *Journal of Low Temperature Physics* **151**, 70 (2008).
- [66] H. Courtois, S. Rajauria, P. Gandit, F. Hekking, and B. Pannetier, *Journal of Low Temperature Physics* **153**, 325 (2008).
- [67] P. Koppinen, T. Kühn, and I. Maasilta, *J. Low Temp. Phys.* **154**, 179 (2009).
- [68] H. Jung, Y. Kim, K. Jung, H. Im, Y. A. Pashkin, O. Astafiev, Y. Nakamura, H. Lee, Y. Miyamoto, and J. S. Tsai, *Phys. Rev. B* **80**, 125413 (2009).
- [69] D. C. Ralph, C. T. Black, and M. Tinkham, *Phys. Rev. Lett.* **74**, 3241 (1995).
- [70] T. Greibe, M. P. V. Stenberg, C. M. Wilson, T. Bauch, V. S. Shumeiko, and P. Delsing, *Phys. Rev. Lett.* **106**, 097001 (2011).
- [71] A. B. Zorin, S. V. Lotkhov, H. Zangerle, and J. Niemeyer, *J. Appl. Phys.* **88**, 2665 (2000).
- [72] S. V. Lotkhov, S. A. Bogoslovsky, A. B. Zorin, and J. Niemeyer, *Appl. Phys. Lett.* **78**, 946 (2001).
- [73] V. Bubanja, *Phys. Rev. B* **83**, 195312 (2011).
- [74] D. V. Averin and Y. V. Nazarov, *Phys. Rev. Lett.* **69**, 1993 (1992).
- [75] A. Heimes, V. F. Maisi, D. S. Golubev, M. Marthaler, G. Shcön, and J. P. Pekola, arXiv:1310.6508 (2013).
- [76] L. Landau and E. Lifshitz, “Quantum mechanics,” (Pergamon, 1980) p. Sec. 43.
- [77] J. Wei and V. Chandrasekhar, *Nature Phys.* **6**, 494 (2010).
- [78] F. W. J. Hekking, L. I. Glazman, K. A. Matveev, and R. I. Shekhter, *Phys. Rev. Lett.* **70**, 4138 (1993).
- [79] M. Field, C. Smith, M. Pepper, D. Ritchie, J. Frost, G. Jones, and D. Hasko, *Phys. Rev. Lett.* **70**, 1311 (1993).
- [80] M. C. Cassidy, A. S. Dzurak, R. G. Clark, K. D. Petersson, I. Farrer, D. A. Ritchie, and C. G. Smith, *Appl. Phys. Lett.* **91**, 222104 (2007).
- [81] B. Küng, C. Rössler, M. Beck, M. Marthaler, D. S. Golubev, Y. Utsumi, T. Ihn, and K. Ensslin, *Phys. Rev. X* **2**, 011001 (2012).
- [82] O.-P. Saira, *Electrostatic control of quasiparticle transport in superconducting hybrid nanostructures* (PhD Thesis, O. V. Lounasmaa Laboratory, Aalto University, 2013).
- [83] G. Zimmerli, T. M. Eiles, R. L. Kautz, and J. M. Martinis, *Applied Physics Letters* **61**, 237 (1992).
- [84] V. A. Krupenin, *J. Appl. Phys.* **84**, 3212 (1998).
- [85] L. Roschier, R. Tarkiainen, M. Ahlskog, M. Paalanen, and P. Hakonen, *Appl. Phys. Lett.* **78**, 3295 (2001).
- [86] W. Lu, Z. Ji, L. Pfeiffer, K. W. West, and A. J. Rimberg, *Nature* **423**, 422 (2003).

- [87] R. Landauer, *Nature* **392**, 1998 (1998).
- [88] V. A. Khlus, *Sov. Phys. JETP* **66**, 1243 (1987).
- [89] M. J. M. de Jong and C. W. J. Beenakker, *Phys. Rev. B* **49**, 16070 (1994).
- [90] X. Jehl, M. Sanquer, R. Calemczuk, and D. Mailly, *Nature* **405**, 50 (2000).
- [91] A. Das, Y. Ronen, M. Heiblum, D. Mahalu, A. V. Kretinin, and H. Shtrikman, *Nat. Commun.* **3**, 1165 (2012).
- [92] S. Gustavsson, R. Leturcq, B. Simovič, R. Schleser, T. Ihn, P. Studerus, K. Ensslin, D. C. Driscoll, and A. C. Gossard, *Phys. Rev. Lett.* **96**, 076605 (2006).
- [93] C. Fricke, F. Hohls, W. Wegscheider, and R. J. Haug, *Phys. Rev. B* **76**, 155307 (2007).
- [94] E. Sukhorukov, A. N. Jordan, S. Gustavsson, R. Leturcq, T. Ihn, and K. Ensslin, *Nature Phys.* **3**, 243 (2007).
- [95] N. Ubbelohde, C. Fricke, C. Flindt, F. Hohls, and R. J. Haug, *Nature Comm.* **3**, 612 (2012).
- [96] T. Fujisawa, T. Hayashi, T. Ritsuya, and Y. Hirayama, *Science* **312**, 1634 (2006).
- [97] D. A. Bagrets and Y. V. Nazarov, *Phys. Rev. B* **67**, 085316 (2003).
- [98] C. Emary, D. Marcos, R. Aguado, and T. Brandes, *Phys. Rev. B* **76**, 161404 (2007).
- [99] C. Flindt, T. c. v. Novotný, A. Braggio, M. Sassetti, and A.-P. Jauho, *Phys. Rev. Lett.* **100**, 150601 (2008).
- [100] C. Flindt, T. c. v. Novotný, A. Braggio, and A.-P. Jauho, *Phys. Rev. B* **82**, 155407 (2010).
- [101] N. Ashcroft and N. Mermin, *Solid State Physics* (Saunders College, Philadelphia, 1976).
- [102] D. Riste, C. C. Bultink, M. J. Tiggelman, R. N. Schouten, K. W. Lehnert, and L. DiCarlo, *Nature Comm.* **4**, 1913 (2013).
- [103] A. Rothwarf and B. N. Taylor, *Phys. Rev. Lett.* **19**, 27 (1967).
- [104] J. T. Peltonen, J. T. Muhonen, M. Meschke, N. B. Kopnin, and J. P. Pekola, *Phys. Rev. B* **84**, 220502 (2011).
- [105] J. P. Pekola, D. V. Anghel, T. I. Suppala, J. K. Suoknuuti, A. J. Manninen, and M. Manninen, *Appl. Phys. Lett.* **76**, 2782 (2000).
- [106] S. Rajauria, H. Courtois, and B. Pannetier, *Phys. Rev. B* **80**, 214521 (2009).
- [107] G. C. O'Neil, P. J. Lowell, J. M. Underwood, and J. N. Ullom, *Phys. Rev. B* **85**, 134504 (2012).
- [108] A. V. Timofeev, C. P. Garcia, N. B. Kopnin, A. M. Savin, M. Meschke, F. Gizotto, and J. P. Pekola, *Phys. Rev. Lett.* **102**, 017003 (2009).

- [109] J. Bardeen, G. Rickayzen, and L. Tewordt, *Phys. Rev.* **113**, 982 (1959).
- [110] J. N. Ullom, P. A. Fisher, and M. Nahum, *Phys. Rev. B* **58**, 8225 (1998).
- [111] A. V. Timofeev, M. Helle, M. Meschke, M. Möttönen, and J. P. Pekola, *Phys. Rev. Lett.* **102**, 200801 (2009).
- [112] J. T. Peltonen, P. Virtanen, M. Meschke, J. V. Koski, T. T. Heikkilä, and J. P. Pekola, *Phys. Rev. Lett.* **105**, 097004 (2010).
- [113] B. I. Miller and A. H. Dayem, *Phys. Rev. Lett.* **18**, 1000 (1967).
- [114] G. Catelani, J. Koch, L. Frunzio, R. J. Schoelkopf, M. H. Devoret, and L. I. Glazman, *Phys. Rev. Lett.* **106**, 077002 (2011).
- [115] D. M. Ginsberg, *Phys. Rev. Lett.* **8**, 204 (1962).
- [116] A. L. Fetter and J. D. Walecka, *Quantum Theory of Many-Particle Systems* (McGraw-Hill).
- [117] D. V. Averin and A. N. Korotkov, *Sov. Phys. JETP* **70**, 937 (1990).
- [118] P. Lafarge, P. Joyez, D. Esteve, U. C., and D. M. H., *Nature* **365**, 422 (1993).
- [119] G. Schön and A. Zaikin, *Europhys. Lett.* **26**, 695 (1994).
- [120] J. Wenner, Y. Yin, E. Lucero, R. Barends, Y. Chen, B. Chiaro, J. Kelly, M. Lenander, M. Mariantoni, A. Megrant, C. Neill, P. J. J. O'Malley, D. Sank, A. Vainsencher, H. Wang, T. C. White, A. N. Cleland, and J. M. Martinis, *Phys. Rev. Lett.* **110**, 150502 (2013).
- [121] E. Hashimoto, Y. Ueda, and T. Kino, *J. Phys. IV France* **5**, C7 (1995).
- [122] M. Wulf, *Phys. Rev. B* **87**, 035312 (2013).
- [123] J. Bylander, T. Duty, and P. Delsing, *Nature* **434**, 361 (2005).
- [124] S. P. Giblin, S. J. Wright, J. D. Fletcher, M. Kataoka, M. Pepper, T. J. B. M. Janssen, D. A. Ritchie, C. A. Nicoll, D. Anderson, and G. A. C. Jones, *New J. Phys.* **12**, 073013 (2010).
- [125] S. J. Wright, M. D. Blumenthal, G. Gumbs, A. L. Thorn, M. Pepper, T. J. B. M. Janssen, S. N. Holmes, D. Anderson, G. A. C. Jones, C. A. Nicoll, and D. A. Ritchie, *Phys. Rev. B* **78**, 233311 (2008).
- [126] S. J. Wright, M. D. Blumenthal, M. Pepper, D. Anderson, G. A. C. Jones, C. A. Nicoll, and D. A. Ritchie, *Phys. Rev. B* **80**, 113303 (2009).

# Publication I

V. F. Maisi, Yu. A. Pashkin, S. Kafanov, J. S. Tsai and J. P. Pekola. Parallel pumping of electrons. *New J. Phys.* 11, 113057 (2009).

© (2009) IOP Publishing Ltd and Deutsche Physikalische Gesellschaft.  
Reprinted with permission.



## Parallel pumping of electrons

Ville F Maisi<sup>1,2,4</sup>, Yuri A Pashkin<sup>3,5</sup>, Sergey Kafanov<sup>2</sup>,  
Jaw-Shen Tsai<sup>3</sup> and Jukka P Pekola<sup>2</sup>

<sup>1</sup> Centre for Metrology and Accreditation (MIKES), P O Box 9, 02151 Espoo, Finland

<sup>2</sup> Low Temperature Laboratory, Helsinki University of Technology, P O Box 3500, 02015 TKK, Finland

<sup>3</sup> NEC Nano Electronics Research Laboratories and RIKEN Advanced Science Institute, 34 Miyukigaoka, Tsukuba, Ibaraki 305-8501, Japan  
E-mail: ville.maisi@mikes.fi

*New Journal of Physics* **11** (2009) 113057 (9pp)

Received 26 August 2009

Published 30 November 2009

Online at <http://www.njpp.org/>

doi:10.1088/1367-2630/11/11/113057

**Abstract.** We present the simultaneous operation of ten single-electron turnstiles leading to one order of magnitude increase in current level up to 100 pA. Our analysis of device uniformity and background charge stability implies that the parallelization can be made without compromising the strict requirements of accuracy and current level set by quantum metrology. In addition, we discuss how offset charge instability limits the integration scale of single-electron turnstiles.

Realization of a standard for electrical current based on the discreteness of the electron charge  $e$  is one of the major goals of modern metrology. The theoretical basis for obtaining current  $I = nef$  when  $n$  electrons are sequentially transferred at frequency  $f$  has been well known for more than two decades [1]–[5]. With multijunction devices it has been possible to demonstrate pumping with a relative accuracy of  $10^{-8}$  up to picoampere level [6]. Although the accuracy is more than an order of magnitude better than what can be obtained from the present definition of ampere [7], the output current level is too small for applications apart from the capacitance standard [8]. In order to create sufficient current in this fashion with the desired accuracy, parallelization of multiple pumps is inevitable. In this paper, we demonstrate parallel electron pumps with quantized current plateaux. The parallelization is effected in up to ten devices,

<sup>4</sup> Author to whom any correspondence should be addressed.

<sup>5</sup> On leave from Lebedev Physical Institute, Moscow 119991, Russia.

leading to a current level exceeding 100 pA. This is already enough for the closure of the so-called quantum metrological triangle [9, 10], which would then justify the current standard based on single electron transport.

The idea in the quantum metrological triangle is to probe the consistency of the current from an electron pump against two other quantum phenomena, namely resistance from the quantum Hall effect and voltage from the ac Josephson effect. This verification would yield a consistency check for two fundamental physical constants, the charge of electron  $e$  and Planck's constant  $\hbar$ , and enable one to define the SI units of electrical quantities directly from quantum mechanics. One option to make the verification is to use topologically defined current transformers to compare the current from the quantum Hall effect to the current from electron transport [10]. The quantum Hall effect requires a current of about  $1 \mu\text{A}$  to obtain  $10^{-8}$  relative uncertainty. The transformer can bring this current down to 100 pA, which until now has been impossible to obtain accurately using single-electron transport devices. Another method to make the comparison has been proposed [11], but currently at least a similar magnitude of current is required. To obtain higher current levels, various approaches have been studied [12]–[19], such as surface acoustic waves, superconducting devices, and semiconductor quantum dots, but the accuracy of these devices remains limited. Two separate semiconductor quantum dot devices have recently been operated in parallel [20]. The hybrid turnstile [21, 22] used in this work holds the promise of achieving extremely low pumping errors [23], similar to multijunction circuits. In addition, due to their simplicity, turnstiles can be scaled up to higher integration levels for parallel operation as they require only one tuning signal per device.

The scheme of parallel turnstiles is shown in a scanning electron micrograph in figure 1(a). In each of the repeated cells there is one individual device. It is a single-electron transistor (SET) where the tunnel junctions are formed by an overlap between superconducting leads and a normal metal island. These devices use the superconducting gap of the leads to provide the necessary hysteresis in operation instead of the series junctions used in earlier turnstiles [24]. With respect to parallelization, these devices require one independent dc gate voltage  $V_{g,i}$  per device to compensate for the inevitable offset charges. The other signals, bias voltage  $V_b$  for setting the preferred tunnelling direction, and the RF gate voltage  $V_{RF}$  used for pumping, can be common to all the devices.

The circuits were fabricated on thermally oxidized Si chips using one photolithography and three electron-beam lithography steps. The chip size was  $3.6 \text{ mm} \times 3.6 \text{ mm}$ . Firstly, Ti/Au (5/95 nm) leads and contact pads were made using a standard lift-off photolithography process. The pads were located at the edges of the chip with the leads stretching to the chip centre, leaving a square-shaped  $80 \mu\text{m} \times 80 \mu\text{m}$  area free for fine structures. Then, in this area, a  $3/20 \text{ nm}$  thick Ti/Au RF gate was deposited through a conventional soft mask formed in the bi-layer resist by electron-beam lithography. The RF gate was connected to one of the leads and covered in the next step by a patterned spin-on glass layer to isolate it from the turnstiles made above the RF gate. Finally, SINIS-type turnstiles were fabricated using two-angle deposition through a suspended mask created in a Ge layer using a tri-layer electron-beam process. The turnstile pattern was exposed in the top layer of polymethylmethacrylate and then, after development, transferred into the Ge layer by reactive ion etching in  $\text{CF}_4$  gas. The undercut under the Ge mask was formed by etching of the bottom copolymer with oxygen in the electron-cyclotron-resonance machine. Deposition of the turnstile leads (Al) and islands (Au/Pd) was performed in an e-gun evaporator with an oxidation step in between, and measurements were performed immediately after the final deposition in a  $^3\text{He}/^4\text{He}$  dilution refrigerator at temperatures below

0.1 K. Standard dc, and RF voltage sources were used with resistive dividers and attenuators to set the operation voltages. Current was measured with a room-temperature low-noise current amplifier.

The operation of a hybrid turnstile can be understood by considering the energy thresholds for single-electron tunnelling. The thresholds are determined by the externally controllable bias voltage  $V_b$  and gate offset  $n_g = (C_{g,i}V_{g,i} + C_{RF,i}V_{RF})/e$ , where  $C_{g,i}$  and  $C_{RF,i}$  are the coupling capacitances from the dc and RF gates to the island, respectively. In figure 1(b), we present the measured dc current and the thresholds of one of the devices on the  $V_b$ - $n_g$  plane. The stable regions for the charge states  $n = 0$  and 1 (red and black boxes, respectively) overlap, and ideally no dc current flows even at a finite bias voltage up to  $V_b = 2\Delta/e$ . Here  $\Delta$  is the energy gap of the superconductor and  $n$  is the excess number of electrons in the island. The broad stability regions enable one to pump electrons sequentially by moving the gate offset  $n_g$  along the horizontal pumping trajectory shown as the solid blue line. To obtain high accuracy, the turnstile should spend enough time beyond the thresholds shown as solid lines, but should not cross the thresholds of backtunnelling shown as dashed lines. All devices should cross the forward tunnelling thresholds in concert while avoiding the backward tunnelling.

To test this uniformity in a parallel setup, four turnstiles were connected to a common drain while the source sides were left separate for individual characterization. Afterwards they were connected together to a common bias voltage source to demonstrate parallel pumping. The dc current-voltage characteristics of one turnstile are shown in figure 1(c), where the gate voltage is swept back and forth so that we obtain both extreme cases of gate open ( $n_g = 0.5$ ) and gate closed ( $n_g = 0$ ). Also, the current-voltage simulations for both of these cases are shown. These curves are calculated with sequential tunnelling approximation and are used to extract the device parameters that are listed in table 1. From pumping measurements, the rising edge to the first plateau was determined as the RF gate voltage  $V_{RF}$  for which the current is half the value at the plateau. The measured variation of  $V_{RF}$  between the devices was  $\pm 7\%$ . According to numerical simulations, this narrows the metrologically flat part of the plateau by about 10%.

In addition to the crucial parameters determining the thresholds, individual tunnelling resistances  $R_T$  of the turnstiles are obtained from simulations. This parameter, together with the total capacitance  $C$  and superconducting energy gap  $\Delta$ , determine the maximum operation frequency of a turnstile [25]. However, for parallelization, there are no constraints on the similarity of the tunnelling resistances. The largest of them determines the maximum operational frequency of the system. For an aluminium-based device, the maximum current is limited to somewhat above 10 pA when a metrologically accurate operation is required [23, 25]. Parallel operation is therefore necessary to obtain higher current levels while simultaneously preserving high pumping accuracy.

After the characterization of individual turnstiles, they were connected in parallel and the pumping curves presented in figure 2 were measured. Here, we have changed the gate states of one (figure 2(a)), two (b), three (c) and four (d) devices simultaneously while keeping others at gate open. We thus obtain current plateaus where zero to eight electrons are transported within one cycle. This measurement demonstrates that we can fully control the dc gate states of each device. The gate state of each individual device  $i$  was extracted from the total current through all of the devices by sweeping gate voltage  $V_{g,i}$ . The gate open states correspond to the maximum values of current. Cross-coupling between the gates was less than 3% and hence only one iteration round after a rough setting of the gates was needed to obtain the gate states correctly to within 1%.

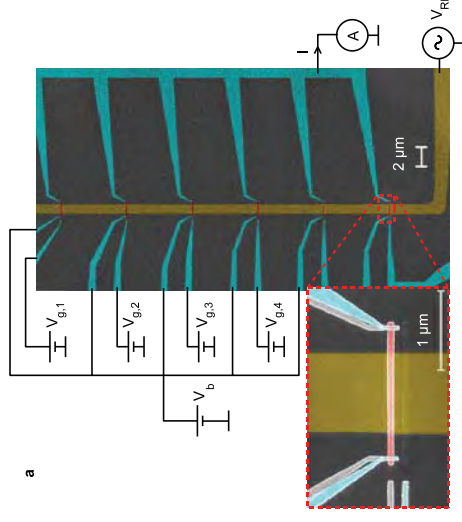


**Figure 1.** Parallelization scheme and the operation principle of a single turnstile. (a) Scanning electron micrograph of parallel turnstiles. Different metal layers are coloured for clarity. Normal metal islands (red) are placed on top of a common radio frequency (RF) gate (yellow). This gate is insulated from the islands by an  $\text{SiO}_2$  layer. Blue regions denote the superconducting aluminium wires. The tunnel junctions are formed under the islands by oxidizing aluminium. One gate line with dc voltage  $V_{g,i}$  is needed for each of the devices, while the bias voltage  $V_b$  and the RF signal  $V_{RF}$  can be common to all turnstiles. (b) Stability diagram of turnstile D (see table 1) and the tunnelling thresholds for electron pumping. For tunnelling into the island the requirement is  $-2E_c(n + 1/2 - n_g) \pm eV_b/2 \geq \Delta$  and for tunnelling out from the island it is given by  $2E_c(n - 1/2 - n_g) \pm eV_b/2 \geq \Delta$ . The upper (lower) sign corresponds to the junction that lies on the positive (negative) side of the bias.  $E_c = e^2/2C$  is the charging energy of the island with total capacitance  $C$  and  $n$  is the number of excess electrons in the island.  $n_g = (C_{g,i}V_{g,i} + C_{RF,i}V_{RF})/e$  is a normalized gate-induced offset charge used for controlling the energy thresholds. The green region inside solid black lines is stable for  $n = 0$ , while the green region inside solid red lines is stable for  $n = 1$ . Solid lines are thresholds for desired transitions during pumping while dashed lines correspond to backtunnelling in the wrong direction. The solid blue curve shows the ideal pumping curve with positive bias voltage at gate open. (c) Current-voltage characteristics of turnstile D. The gate offset charge is swept back and forth so that the envelopes correspond to the gate being open or closed. Simulations used to extract device parameters from these extremum cases are shown by black solid lines.

Next, to demonstrate reproducibility and robustness, ten turnstiles were operated similarly by a single RF drive. Two chips were used from different batches, with six turnstiles on one chip and four on the other. All ten devices were bonded to one common bias line and hence

**Table 1.** Parameters of the four turnstiles A–D.  $R_T$  and  $C_{RF}$  are estimated from the measurement data with an uncertainty of 1%.  $\Delta$  and  $E_c/\Delta$  are fitted with the help of numerical simulations to within 2% precision.

	$2R_T$ (k $\Omega$ )	$\Delta$ ( $\mu$ V)	$E_c/\Delta$	$C_{RF}$ (aF)	$V_{rm}$ (mV)
A	490	213	1.03	25.3	3.82
B	580	214	1.10	23.5	3.60
C	610	214	1.10	24.7	3.83
D	742	215	1.16	23.4	4.12

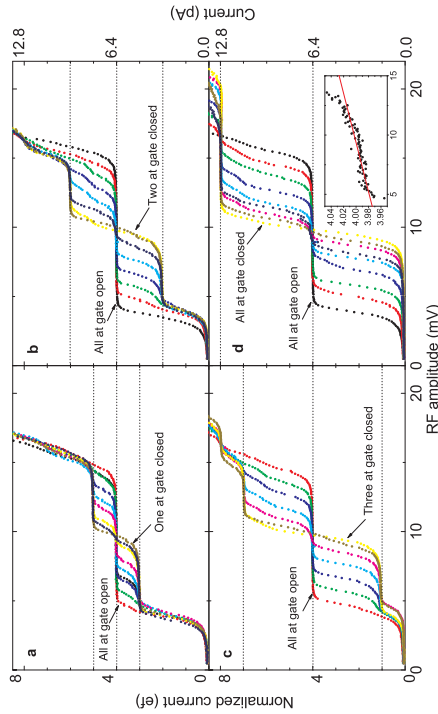


**Figure 2.** Parallel pumping of four turnstiles at  $f = 10$  MHz. From (a) to (d), one to four devices are tuned between gate open and gate closed states, respectively, while the rest of the turnstiles are kept at gate open. This yields plateaux where 4 or  $4 \pm N$  electrons are pumped in each cycle, where  $N$  is the number of tuned devices. The case  $N = 4$  shows pumping curves similar to those of a single turnstile but with four times higher current. The inset in panel (d) shows a zoom where all devices are pumping one electron in a cycle. The solid red line is a linear fit which gives a plateau resistance of 500 G $\Omega$  with respect to RF voltage. The flatness of the plateau per turnstile is similar to what was observed for individual turnstiles. The accuracy of the measurements was limited by the drift of the current amplifier to the 10 fA level. The bias voltage was set to 200  $\mu$ V during the measurements.

no preliminary characterization of individual devices was made. The results for different bias voltages are shown in figure 3. This setup yields 104.1 pA at the first plateau with a pumping frequency of 65 MHz, which demonstrates a current level large enough to close the quantum metrological triangle [10]. In the present experiment, the number of parallel devices was limited by the number of dc lines available.

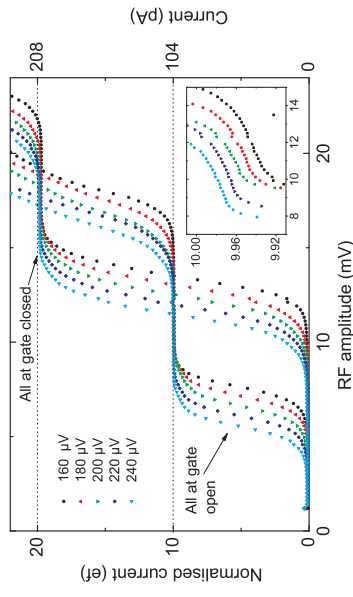


**Figure 3.** Ten turnstiles working at  $f = 65$  MHz at different bias voltages. All turnstiles are set to either gate open or gate closed state. The current at the first plateau is approximately 104.1 pA. The inset shows a close-up of the first plateau. The estimated uncertainty of the current scale, based on the calibration of the pre-amp, is of the same order as the observed deviations from  $I = 10 ef$ .

In more general terms, the number of devices that can be operated in parallel simultaneously is determined by the offset charge stability. The strategy of a pumping experiment is to first set the gate of each turnstile, then perform the pumping measurement, and afterwards check the offset charges again. If they are not within the limits, one discards the data. It is worth noting that, unlike deviations in device parameters, the positive and negative changes in offset charge yield errors in pumping current in the same direction, and these types of error do not then average out with many devices as is the case for parameter deviations. To study the stability of the ten devices, the dc gate modulation was measured as a function of time for each of the turnstiles simultaneously. The time for one cycle was chosen to be 10 min, which was equal to the time required to measure the data of one curve in figure 2. The gate stability for a typical turnstile is shown in figure 4(a). From the measured data, histograms of the offset charge changes were determined for each of the devices, as shown in figure 4(b). Moreover, in the inset a histogram for the corresponding maximum change of the ten turnstiles is presented. From this we obtain a 73% probability of obtaining valid data with this measurement setup, as described in the caption. Additionally, we can estimate the maximum number of turnstiles operable in parallel to be 17 in the present case, which would yield an efficiency of 50%. By making the measurement period smaller, one could increase the number of devices as they have less time to get offset. We estimate that the measurement period can be decreased by one or two orders of magnitude. This will allow one to increase the number of parallel devices accordingly. Also, different materials or fabrication methods can provide smaller drifts and hence allow a larger integration scale. In our devices, the typical spectral density of charge noise followed the relation  $S_q(f) = \alpha^2/f^2$  in the observed frequency range  $f = 1 \mu\text{Hz} - 1 \text{mHz}$  with  $\alpha = 10^{-6} \text{e}\sqrt{\text{Hz}}$ . The magnitude is somewhat similar to previously reported values [26, 27]. We note that even better performance with no drifts has been observed for metallic single-electron devices previously [28, 29]. If such an improvement could be reliably achieved, one

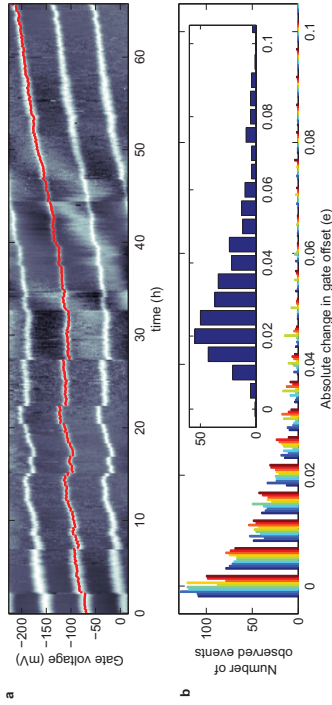


**Figure 4.** Stability of offset charges. (a) Gate modulation of one of the turnstiles as a function of time. The light/dark areas correspond to maximum/minimum current. The red dots show one of the gate open states, which is changing due to variations in the offset charges. These data are obtained as one set within sequential sweeping of the gate charges of the ten turnstiles. These ten sweeps are then repeated every 10 min. (b) A histogram of the changes in the offset charge between each sweeping set. The different colours denote different individual devices. In the inset, a histogram of the largest change in each set is shown. The total number of sweeps per turnstile is 410. Although for individual devices the changes are peaked at zero, for ten turnstiles it is more likely that at least one of the devices has changed by a few per cent. To obtain an estimate for the maximum number of devices that can operate in parallel, we assume that the offset charge changes are independent as the average correlation coefficient between the devices was 0.12. This gives a lower limit for the probability of having  $N$  turnstiles in correct gate states as  $p_N = p_1^N$ , where  $p_1$  is the probability of having one turnstile in a correct state. The flatness of the theoretical current plateaux is such that with the observed 10% variation in tunnelling thresholds we can still tolerate a 5% change in gate offsets. With the measured data, this will lead to  $p_1 = 0.96$  and  $p_{10} = 0.71$ . This is consistent with the value  $p_{10} = 0.73$  obtained from the data in the inset of (b). Therefore the requirement for efficiency of  $p_N \geq 0.5$  will limit the number of parallel turnstiles to  $N = 17$  according to the presented data.

could further increase the number of parallel devices. However, for ten turnstiles and the present measurement time, this improvement is not required.

The main result of the present work is the controlled operation of parallel electron pumps. The stability of offset charges was studied and it is shown to allow more than ten parallel devices to be operated without significantly compromising the accuracy. These devices are prominent in fulfilling the strict accuracy requirements for closure of the quantum metrological triangle, and as the outcome of this work we show that the obtained current level achieves this. The flatness of the plateaux is preserved in parallel operation. Moreover, references [22, 30] and our recent

unpublished work suggest that the sub-gap leakage, which is the remaining error source, can be significantly decreased by proper design of the electromagnetic environment.

### Acknowledgments

We acknowledge M Meschke and A Kemppinen for assistance with measurements and O Astafiev, M Mötönen, S Lotkhov, A Maminin and M Paalanen for discussions. The work was partially supported by the Technology Industries of Finland Centennial Foundation, the Academy of Finland and the Japan Science and Technology Agency through the CREST Project. The research conducted within the EURAMET joint research project REUNIAM and the EU project SCOPE received funding from the European Community's Seventh Framework Programme under Grant Agreements No. 217257 and No. 218783.

### References

- [1] Averin D V and Likharev K K 1991 *Mesoscopic Phenomena in Solids* (Amsterdam: Elsevier) pp 173–271
- [2] Ingold G-L and Nazarov Yu V 1992 *Single Charge Tunneling, Coulomb Blockade Phenomena in Nanostructures* (NATO ASI Series B vol 294) (New York: Plenum) ch 2
- [3] Esteve D 1992 *Single Charge Tunneling, Coulomb Blockade Phenomena in Nanostructures* (NATO ASI Series B vol 294) (New York: Plenum) ch 3
- [4] Averin D V and Likharev K K 1992 *Single Charge Tunneling, Coulomb Blockade Phenomena in Nanostructures* (NATO ASI Series B vol 294) (New York: Plenum) ch 9
- [5] Devoret M H, Esteve D and Urbina C 1992 Single-electron transfer in metallic nanostructures *Nature* **360** 547–53
- [6] Keller M W, Martinis J M, Zimmerman N M and Steinbach A H 1996 Accuracy of electron counting using a 7-junction electron pump *Appl. Phys. Lett.* **69** 1804–6
- [7] Taylor B N and Witt T J 1989 New international electrical reference standards based on the Josephson and quantum hall effects *Metrologia* **26** 47–62
- [8] Keller M W, Eichenberger A L, Martinis J M and Zimmerman N M 1999 A capacitance standard based on counting electrons *Science* **285** 1706–9
- [9] Likharev K K and Zorin A B 1985 Theory of the Bloch-wave oscillations in small Josephson junctions *J. Low Temp. Phys.* **59** 347–82
- [10] Piquemal F 2004 Fundamental electrical standards and the quantum metrological triangle *C. R. Phys.* **5** 857–79
- [11] Delahaye J, Hassel J, Lindell R, Sillanpää M, Paalanen M, Seppä H and Hakonen P 2003 Low-noise current amplifier based on mesoscopic Josephson junction *Science* **299** 1045–8
- [12] Fujiwara A, Zimmerman N M, Ono Y and Takahashi Y 2004 Current quantization due to single-electron transfer in si-wire charge-coupled devices *Appl. Phys. Lett.* **84** 1323–5
- [13] Mooji J E and Nazarov Yu V 2006 Superconducting nanowires as quantum phase-slip junctions *Nat. Phys.* **2** 169–72
- [14] Vartiainen J J, Mötönen M, Pekola J P and Kemppinen A 2007 Nanoampere pumping of Cooper pairs *Appl. Phys. Lett.* **90** 082102
- [15] Nguyen F, Boulant N, Ithier G, Bertet P, Pothier H, Vion D and Esteve D 2007 Current to frequency conversion in a Josephson circuit *Phys. Rev. Lett.* **99** 187005
- [16] Blumenthal M D, Kaestner B, Li L, Giblin S, Janssen T J B M, Pepper M, Anderson D, Jones G and Ritchie D A 2007 Gigahertz quantized charge pumping *Nat. Phys.* **3** 343–7
- [17] Wright S J *et al* 2008 Enhanced current quantization in high-frequency electron pumps in a perpendicular magnetic field *Phys. Rev. B* **78** 233311

- [18] Kaestner B, Leicht C, Kashcheyevs V, Pierz K, Siegner U and Schumacher H W 2009 Single-parameter quantized charge pumping in high magnetic fields *Appl. Phys. Lett.* **94** 012106
- [19] Koenig D R, Weig E M and Kothaus J P 2008 Ultrasonically driven nanomechanical single-electron shuttle *Nat. Nanotechnol.* **3** 482–5
- [20] Wright S J, Blumenthal M D, Pepper M, Anderson D, Jones G A C, Nicoll C A and Ritchie D A 2009 Parallel quantized charge pumping. arXiv:0906.5384
- [21] Pekola J P, Vartiainen J J, Mötönen M, Saira O-P, Meschke M and Averin D V 2008 Hybrid single-electron transistor as a source of quantized electric current *Nat. Phys.* **4** 120–4
- [22] Kemppinen A, Meschke M, Mötönen M, Averin D V and Pekola J P 2009 Quantized current of a hybrid single-electron transistor with superconducting leads and a normal-metal island *Eur. Phys. J.* **172** 311–21
- [23] Averin D V and Pekola J P 2008 Nonadiabatic charge pumping in a hybrid single-electron transistor *Phys. Rev. Lett.* **101** 066801
- [24] Geerligs L J, Anderregg V F, Holweg P A M, Mooij J E, Pothier H, Esteve D, Urbina C and Devoret M H 1990 Frequency-locked turnstile device for single electrons *Phys. Rev. Lett.* **64** 2691–4
- [25] Kemppinen A, Kafanov S, Pashkin Yu A, Tsai J S, Averin D V and Pekola J P 2009 Experimental investigation of hybrid single-electron turnstiles with high charging energy *Appl. Phys. Lett.* **94** 172108
- [26] Eiles T M, Martinis J M and Devoret M H 1993 Even-odd asymmetry of a superconductor revealed by the coulomb blockade of andreev reflection *Phys. Rev. Lett.* **70** 1862–5
- [27] Astafiev O, Pashkin Yu A, Nakamura Y, Yamamoto T and Tsai J S 2006 Temperature square dependence of the low frequency  $I/f$  charge noise in the josephson junction qubits *Phys. Rev. Lett.* **96** 137001
- [28] Wolf H, Ahlers F J, Niemeyer J, Scherer H, Weimann T, Zorin A B, Krupenin V A, Lotkhov S V and Preshov D E 1997 Investigation of the offset charge noise in single electron tunneling devices *IEEE Trans. Instrum. Meas.* **46** 503–6
- [29] Zimmerman N M, Huber W H, Simonds B, Hourdakakis E, Fujiwara A, Ono Y, Takahashi Y, Inokawa H, Furlan M and Keller M W 2008 Why the long-term charge offset drift in si single-electron tunneling transistors is much smaller (better) than in metal-based ones: Two-level fluctuator stability *J. Appl. Phys.* **104** 033710
- [30] Lotkhov S V, Kemppinen A, Kafanov S, Pekola J P and Zorin A B 2009 Pumping properties of the hybrid single-electron transistor in dissipative environment. arXiv:0905.3402



## Publication II

**J. P. Pekola, V. F. Maisi, S. Kafanov, N. Chekurov, A. Kemppinen, Yu. A. Pashkin, O.-P. Saira, M. Möttönen and J. S. Tsai. Environment-Assisted Tunneling as an Origin of the Dynes Density of States. *Phys. Rev. Lett.* **105**, 026803 (2010).**

© (2010) American Physical Society.

Reprinted with permission.



## Environment-Assisted Tunneling as an Origin of the Dynes Density of States

J. P. Pekola,<sup>1</sup> V. F. Maisi,<sup>2</sup> S. Kafanov,<sup>1</sup> N. Chekurov,<sup>3</sup> A. Kemppinen,<sup>2</sup> Yu. A. Pashkin,<sup>4,\*</sup> O.-P. Saira,<sup>1</sup> M. Möttönen,<sup>1,5</sup> and J. S. Tsai<sup>4</sup>

<sup>1</sup>Low Temperature Laboratory, Aalto University, P.O. Box 13500, FI-00076 Aalto, Finland

<sup>2</sup>Centre for Metrology and Accreditation (MIKES), P.O. Box 9, 02151 Espoo, Finland

<sup>3</sup>Department of Micro and Nanosciences, Aalto University, P.O. Box 13500, FI-00076 Aalto, Finland

<sup>4</sup>NEC Nano Electronics Research Laboratories and RIKEN Advanced Science Institute, 34 Miyukigaoka, Tsukuba, Ibaraki 305-8501, Japan

<sup>5</sup>Department of Applied Physics/COMP, Aalto University, P.O. Box 15100, FI-00076 Aalto, Finland

(Received 26 February 2010; published 6 July 2010)

We show that the effect of a high-temperature environment in current transport through a normal metal–insulator–superconductor tunnel junction can be described by an effective density of states in the superconductor. In the limit of a resistive low-Ohmic environment, this density of states reduces into the well-known Dynes form. Our theoretical result is supported by experiments in engineered environments. We apply our findings to improve the performance of a single-electron turnstile, a potential candidate for a metrological current source.

DOI: 10.1103/PhysRevLett.105.026803

PACS numbers: 73.40.Gk, 06.20.Jr, 72.70.+m, 73.20.At

**Introduction.**—The density of states (DOS) of the carriers governs the transport rates in a mesoscopic conductor [1], e.g., in a tunnel junction. Understanding the current transport in a junction in detail is of fundamental interest, but it plays a central role also in practical applications, for instance, in the performance of superconducting qubits [2], of electronic coolers and thermometers [3], and of a single-electron turnstile to be discussed in this Letter [4]. When one or both of the contacts of a junction are superconducting, the one-electron rates at small energy bias should vanish at low temperatures because of the gap in the Bardeen-Cooper-Schrieffer (BCS) DOS [5]. Yet, a small linear in voltage leakage current persists in the experiments [3,6–10] that can often be attributed to the Dynes DOS, a BCS-like expression with lifetime broadening [11,12]. A junction between two leads admits carriers to pass at a rate that depends on the DOS of the conductors, the occupation of the energy levels, and the number of conduction channels in the junction [13]. In general, basic one-electron tunneling coexists with many-electron tunneling, for instance, cotunneling in multijunction systems [14], or Andreev reflection in superconductors [15,16]. However, when the junction is made sufficiently opaque, a common situation in practice, only one-electron tunneling governed by the Fermi golden rule should persist. We demonstrate experimentally that the subgap current in a high-quality opaque tunnel junction between a normal metal and a superconductor can be ascribed to photon-assisted tunneling. We show theoretically that this leads exactly to the Dynes DOS with an inverse lifetime of  $e^2 k_B T_{\text{env}} R / \hbar^2$ , where  $T_{\text{env}}$  and  $R$  are the temperature and effective resistance of the environment.

We employ a tunnel junction with a normal metal–insulator–superconductor (NIS) structure; see Fig. 1(a). The essentially constant DOS in the normal metal renders

the NIS junction an ideal probe for the superconductor DOS. Because of the BCS energy gap in an NIS system, the tunneling current is expected to be exponentially suppressed with decreasing temperature. Yet in the experiments a small subgap current persists as shown in Fig. 1(b). This leakage is typically attributed to Andreev current [17–20], smeared DOS of the superconductor [21], nonvanishing DOS in the insulator within the gap [9], nonequilibrium quasiparticles [22], or physical imperfections in the junction. Our junctions, like the one in Fig. 1, are made opaque with large normal-state resistance  $R_T$  to efficiently suppress the Andreev current. A convenient way to account for the smearing of the  $IV$  characteristics is to use the so-called Dynes model [11,12] based on an expression of the BCS DOS with lifetime broadening. The Dynes DOS, normalized by the corresponding normal-state DOS, is given by

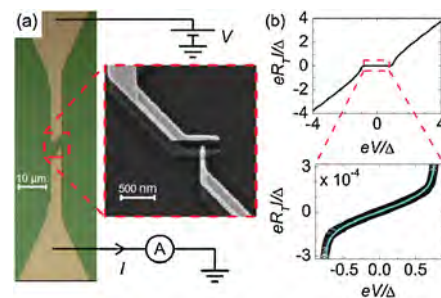


FIG. 1 (color online). (a) Geometry of the measured single NIS junctions made of aluminum (low contrast) as the superconductor and copper (high contrast) as the normal metal. The tapered ends lead to  $250 \times 250 \mu\text{m}^2$  pads. (b) Typical  $IV$  characteristics, measured at 50 mK for a sample with  $R_T = 30 \text{ k}\Omega$ . Linear leakage is observed deep in the gap region  $|eV| \ll \Delta \approx 200 \mu\text{eV}$ , consistent with the Dynes model using  $\gamma = 1.8 \times 10^{-4}$ , shown by the cyan line.

$$n_S^D(E) = \left| \Re e \left( \frac{E/\Delta + i\gamma}{\sqrt{(E/\Delta + i\gamma)^2 - 1}} \right) \right|, \quad (1)$$

where  $\Delta$  is the BCS energy gap. A nonvanishing  $\gamma$  introduces effectively states within the gap region,  $|E| < \Delta$ , as opposed to the ideal BCS DOS obtained with  $\gamma = 0$  resulting in vanishing DOS within the gap. This model reproduces the features observed in our measurements as is shown in Fig. 1(b). We show that, effectively, the Dynes DOS can be produced from the ideal BCS DOS by weak dissipative environment at temperature  $T_{\text{env}} \gtrsim \Delta/k_B$  promoting photon-assisted tunneling. A similar environment model with comparable parameter values has also been introduced by other authors to explain, e.g., observations of excess errors in normal-state electron pumps [23,24] and Andreev reflection dominated charge transport at low bias voltages in NISIN structures [25].

*Theoretical results.*—For inelastic one-electron tunneling, the rates in forward (+) and backward (−) directions through an NIS junction can be written as

$$\Gamma_{\pm} = \frac{1}{e^2 R_T} \int_{-\infty}^{\infty} dE \int_{-\infty}^{\infty} dE' n_S(E') f_N(E \mp eV) \times [1 - f_S(E')] P(E - E'), \quad (2)$$

at bias voltage  $V$ . Here,  $P(E)$  refers to the probability density for the electron to emit energy  $E$  to the environment [13]. The occupations in the normal and superconducting leads are given by the Fermi functions  $f_{N/S}(E) = [e^{E/(k_B T_{N/S})} + 1]^{-1}$ , respectively. In an ideally voltage-biased junction,  $P(E) = \delta(E)$ . The current through the junction at low temperature of the leads,  $T_N, T_S \rightarrow 0$ , is then  $I^0(V) \equiv e(\Gamma_+^0 - \Gamma_-^0) = \frac{1}{eR_T} \int_0^V dE n_S(E)$ . Thus we obtain the well-known expression for the conductance of the junction as

$$dI^0/dV = R_T^{-1} n_S(eV). \quad (3)$$

In view of Eq. (1), the nonzero linear conductance at low bias voltages, typically observed in experiments as shown in Fig. 1(b), suggests that the superconductor has nonvanishing constant density of states within the gap. Within the Dynes model of Eq. (1), the normalized DOS at low energies  $|E| \ll \Delta$  equals  $\gamma$ , the ratio of the conductance at zero bias and that at large bias voltages. Although this approach is correct mathematically, it is hard to justify the presence of subgap states physically.

Here we base our analysis on the pure BCS DOS ( $\gamma = 0$ ) and show that the Dynes model in Eq. (1) is consistent with weakly dissipative environment when Eq. (2) is used to obtain the current  $I(V) = e(\Gamma_+ - \Gamma_-)$ . The effective resistance value  $R = \alpha R_{\text{env}}$  of the environment arises generally from a possibly larger real part of the environment impedance,  $R_{\text{env}}$ , which is suppressed by a factor of  $\alpha$  due to low-temperature filtering; see Fig. 2. With this environment, one obtains the probability density  $P(E)$  in the limit

of small  $R \ll R_Q \equiv \hbar/e^2$  and for energies  $E \ll \hbar(RC)^{-1}$ ,  $k_B T_{\text{env}}$  as a Lorentzian [26]

$$P(E) \simeq \frac{1}{\pi \Delta} \frac{\sigma}{\sigma^2 + (E/\Delta)^2}, \quad (4)$$

where  $\sigma = Rk_B T_{\text{env}}/(R_Q \Delta)$ . As the current of an NIS junction is determined by the values of  $P(E)$  at  $|E| \lesssim \Delta$ , we can apply Eq. (4) when  $k_B T_{\text{env}} \gtrsim \Delta$ ; see Fig. 2 for a numerical demonstration. For a general symmetric  $P(E)$  and  $T_N, T_S \rightarrow 0$ , one obtains from Eq. (2) in analogy with Eq. (3):  $I(V) = \frac{1}{eR_T} \int_0^V dE n_S^\sigma(E)$ , and

$$dI/dV = R_T^{-1} n_S^\sigma(eV), \quad (5)$$

where the effective DOS is given by the convolution

$$n_S^\sigma(E) \equiv \int_{-\infty}^{\infty} dE' n_S(E') P(E - E'). \quad (6)$$

For the weak resistive environment described by Eq. (4), the convolution of a Lorentzian gives

$$n_S^\sigma(E) = \left| \Re e \left( \frac{E/\Delta + i\sigma}{\sqrt{(E/\Delta + i\sigma)^2 - 1}} \right) \right|. \quad (7)$$

This expression is identical to the Dynes DOS in Eq. (1) by setting  $\sigma = \gamma$ , with the equivalent inverse lifetime  $e^2 k_B T_{\text{env}} R / \hbar^2$ . The correspondence between the  $P(E)$  theory and the Dynes model, our main theoretical result, is valid for nonzero lead temperatures as well, as we show in the supplementary material [26]. Below, we present numerical and experimental studies verifying our claim.

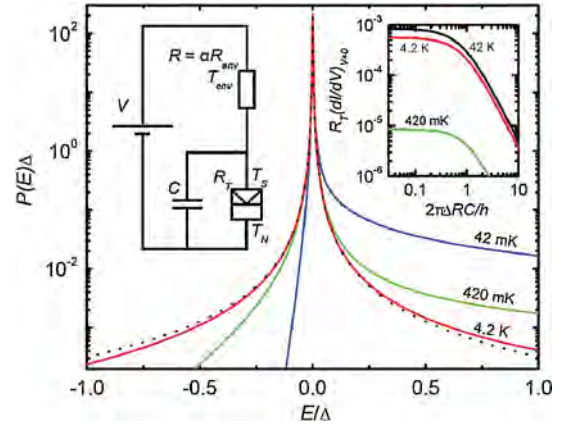


FIG. 2 (color online). The probability density  $P(E)$  calculated for  $\sigma = 10^{-3} = RT_{\text{env}} k_B / (R_Q \Delta)$  and for a few values of the environment temperature  $T_{\text{env}} = 0.042, 0.42, \text{ and } 4.2$  K. The dotted line is the corresponding Lorentzian limit of Eq. (4). The left inset shows the employed circuit model of an NIS junction (the rectangular symbol at the bottom right) in an  $RC$  environment. The right inset shows the calculated zero-bias conductance of the NIS junction as a function of the capacitance  $C$  with the environment corresponding to  $\sigma = 10^{-3}$  and  $T_{\text{env}} = 0.42, 4.2, \text{ and } 42$  K. We use  $\Delta = 200 \mu\text{eV} \simeq k_B \times 2.3$  K for aluminum.

*Experiments on single junctions.*—The leakage induced by the electromagnetic environment can be decreased by efficient rf filtering of the leads and electromagnetic shielding of the sample. One way to do this without affecting the properties of the junction itself is to increase the capacitance  $C$  across it; see Fig. 2. In this way, one approaches the case of an ideally voltage-biased junction. In Fig. 2, we present the zero-bias conductance of an NIS junction as a function of the shunting capacitance  $C$  based on the full numerical  $P(E)$  calculation. For low  $C$ , the result using Eq. (7) is valid, but for sufficiently high  $C$ , i.e., for  $\Delta RC/\hbar \gtrsim 1$ , the leakage decreases significantly, demonstrating that capacitive shunting is helpful in suppressing the photon-assisted tunneling.

To probe the effect of the capacitive shunting in our experiments, we introduced a ground plane under the junctions. The junctions were made on top of an oxidized silicon wafer, where first a conductive 100-nm-thick Al layer working as the ground plane was sputtered. On top of this, a 400-nm-thick insulating high-quality  $\text{Al}_2\text{O}_3$  film was formed by atomic layer deposition. The junctions were patterned by conventional soft-mask electron beam lithography on top of  $\text{Al}_2\text{O}_3$ . For comparison, junctions were made both with and without the ground plane.

The experiments reported here were performed in a  $^3\text{He}$ - $^4\text{He}$  dilution refrigerator with a base temperature of about 50 mK. All the leads were filtered by using 1.5 m of Thermocoax cable between the 1-K stage and the sample stage at the base temperature. The  $IV$  curves such as the one in Fig. 1(b) are thermally smeared at elevated temperatures, but below 200 mK we observe hardly any temperature dependence. Figure 3 shows the  $IV$  curves measured at the base temperature for one junction on top of a ground plane and for a similar junction without the ground plane, together with numerical results from the  $P(E)$  theory. The capacitive shunting decreases the zero-bias conductance significantly. The shunt capacitance values employed in the  $P(E)$  theory, 10 and 0.3 pF, respectively, match well with the estimates for the experimental values in each case. The sample without a ground plane with  $C = 0.3$  pF is already entering the regime, where the capacitance is too small to play a role. We used an effective environment resistance of  $R = 2 \Omega$  at  $T_{\text{env}} = 4.2$  K, close to the values inferred by Hergenrother *et al.* [25] in the case of incomplete shielding. However, the choice of  $T_{\text{env}}$  is somewhat arbitrary here:  $T_{\text{env}} > 4.2$  K with correspondingly lower  $R$  would yield a slightly improved fit to the data, but  $T_{\text{env}} = 4.2$  K, the temperature of the outer shield, was chosen as a natural surrounding in the measurement setup. Our results with capacitive shunting, on the other hand, correspond to much improved shielding in the language of Ref. [25]. Although the experiments of Ref. [25] are quite different from ours, their situation resembles ours in the sense that photons with a very high frequency of  $\Delta/\hbar \gtrsim 50$  GHz are responsible for tunneling.

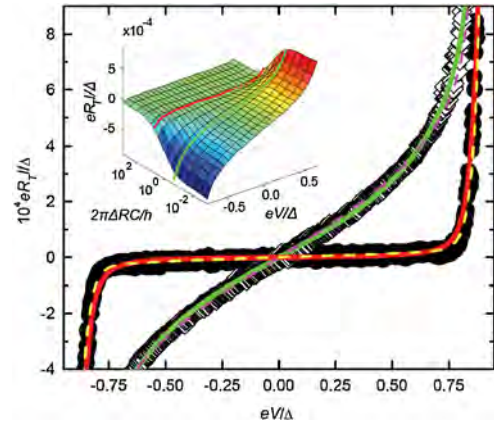


FIG. 3 (color online). Measured  $IV$  curves of an NIS junction with  $R_T = 761$  k $\Omega$  on the ground plane (solid symbols) and of a similar junction with  $R_T = 627$  k $\Omega$  without the ground plane (open symbols). Solid lines present the results of the full  $P(E)$  theory for capacitance  $C = 10$  pF (red line) and  $C = 0.3$  pF (green line). The resistance and the temperature of the environment are set to  $R = 2 \Omega$  and  $T_{\text{env}} = 4.2$  K, respectively, and  $\Delta = 200 \mu\text{eV}$ . The dashed lines correspond to the Dynes model with the parameters yielding the best fit to the data. The normalized zero-bias slope is  $5.3 \times 10^{-4}$  for the green line and  $2.6 \times 10^{-5}$  for the red line. The inset shows  $IV$  curves based on the full  $P(E)$  calculation as functions of the shunt capacitance  $C$ . The red and green lines are reproduced on this graph from the main figure.

*SINIS turnstile.*—As a practical application, we discuss the SINIS turnstile, which is a hybrid single-electron transistor (SET) and a strong candidate for realizing the unit ampere in quantum metrology [4,27–30]. In the previous experimental studies [4,27,29], its accuracy was limited by the subgap leakage. Here we test the influence of the ground plane on the flatness of the current plateaus at multiples of  $ef$ , where  $f$  is the operating frequency. The ground plane had a 20- $\mu\text{m}$ -wide gap under the SET to reduce the stray capacitance to the rf gate. The ground plane layer was covered by a 300-nm-thick insulating layer of spin-on glass, on top of which the rf gate and dc leads were evaporated. Another 300-nm spin-on glass layer was used to cover the rf gate, and the SET was fabricated on top of this layer. The device is shown in Fig. 4(a). This sample geometry is designed for parallel pumping [30], but here we concentrate on a single device.

Figure 4(b) shows that in this case, the introduction of the ground plane reduces the subgap leakage by roughly 2 orders of magnitude as opposed to a typical turnstile without the ground plane (the latter data from Ref. [29]). In the turnstile operation, the current was recorded as a function of the amplitude of the sinusoidal rf drive,  $A_g$ , at several bias voltages. In Fig. 4(c), we show the quantized current plateau at  $f = 10$  MHz, and the averaged current on this plateau is given in Fig. 4(d) as a function of the bias voltage. The differential conductance at the plateau divided

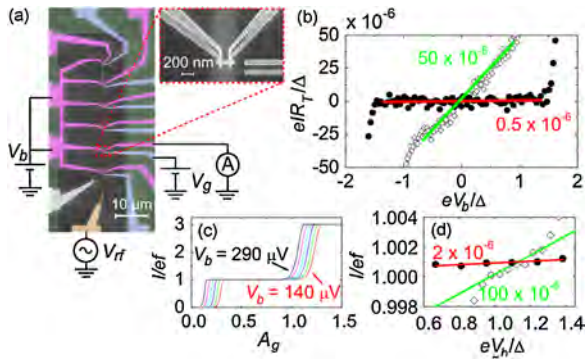


FIG. 4 (color online). (a) Scanning electron micrographs of the SINIS turnstiles. (b) Subgap  $IV$  curves of the measured transistors in the gate-open state (charge degeneracy). The slope of the linear fit corresponds to the leakage of  $0.5 \times 10^{-6}$  for the sample with the ground plane (filled circles) and  $50 \times 10^{-6}$  for the sample without the ground plane (open diamonds) in units of the asymptotic conductance of each SET. (c) Current through the turnstile on the ground plane as a function of the amplitude of the applied sinusoidal gate drive at  $f = 10$  MHz. The gate offset was set to the charge degeneracy point, and the bias voltage was varied uniformly between  $V_b = 140$  and  $290 \mu\text{V}$ . (d) Current at the first plateau as a function of  $V_b$  obtained from data similar to those in (c) (filled circles) showing leakage of  $2 \times 10^{-6}$  and for the sample without the ground plane (open diamonds) with leakage of  $100 \times 10^{-6}$  and a reduced step width.

by the asymptotic conductance of the SET is  $2 \times 10^{-6}$ . This result is much improved over those of the earlier measurements [4,27,28] and that of the reference sample without the ground plane.

In conclusion, we have shown analytically that the Dynes density of states can originate from the influence of the electromagnetic environment of a tunnel junction, and it is not necessarily a property of the superconductor itself. Our experiments support this interpretation: We were able to reduce the leakage of an NIS junction by an order of magnitude by local capacitive filtering. We stress that capacitive shunting does not necessarily suppress the subgap leakage of an NIS junction, if the leakage is caused by the poor quality of the junction or by true states within the gap due to, e.g., the inverse proximity effect [3]. Protecting the junctions against photon-assisted tunneling improves the performance of, e.g., single-electron pumps. Contrary to the resistive environment aiming at the same purpose [28], capacitive shunting does not limit the tunneling rates.

We thank D. Averin, P. Delsing, M. Gustafsson, H. Im, S. Lotkhov, A. Manninen, M. Paalanen, and V. Shumeiko for discussions and M. Meschke, J. Peltonen, and I. Iisakka for technical support. This work has been supported by Technology Industries of Finland Centennial Foundation,

the Academy of Finland, Emil Aaltonen Foundation, the Funding Program for World-Leading Innovative R&D on Science and Technology (FIRST), CREST-JST, MEXT kakenhi “Quantum Cybernetics,” and the European Community’s FP7 Programme under Grant Agreements No. 228464 (MICROKELVIN, Capacities Specific Programme), No. 217257 (EURAMET joint research project REUNIAM), and No. 218783 (SCOPE).

\*On leave from P.N. Lebedev Physical Institute, Moscow 119991, Russia.

- [1] Ya. M. Blanter and M. Büttiker, *Phys. Rep.* **336**, 1 (2000).
- [2] *Quantum Computing with Superconducting Qubits*, Quantum Inf. Process. Vol. 8 (Springer, New York, 2009), pp. 51–281.
- [3] F. Giazotto *et al.*, *Rev. Mod. Phys.* **78**, 217 (2006).
- [4] J. P. Pekola *et al.*, *Nature Phys.* **4**, 120 (2008).
- [5] J. Bardeen, L. N. Cooper, and J. R. Schrieffer, *Phys. Rev.* **108**, 1175 (1957).
- [6] G. C. O’Neill *et al.*, *J. Low Temp. Phys.* **151**, 70 (2008).
- [7] S. Rajauria *et al.*, *J. Low Temp. Phys.* **153**, 325 (2008).
- [8] P. Koppinen *et al.*, *J. Low Temp. Phys.* **154**, 179 (2009).
- [9] H. Jung *et al.*, *Phys. Rev. B* **80**, 125413 (2009).
- [10] D. C. Ralph *et al.*, *Phys. Rev. Lett.* **74**, 3241 (1995).
- [11] R. C. Dynes *et al.*, *Phys. Rev. Lett.* **41**, 1509 (1978).
- [12] R. C. Dynes *et al.*, *Phys. Rev. Lett.* **53**, 2437 (1984).
- [13] G. L. Ingold and Yu. V. Nazarov, in *Single Charge Tunneling*, edited by H. Grabert and M. H. Devoret, NATO ASI Series B, Vol. 294 (Plenum Press, New York, 1992), pp. 21–107.
- [14] D. V. Averin and Yu. V. Nazarov, *Phys. Rev. Lett.* **65**, 2446 (1990).
- [15] A. F. Andreev, *Zh. Eksp. Teor. Fiz.* **46**, 1823 (1964) [*Sov. Phys. JETP* **19**, 1228 (1964)].
- [16] G. E. Blonder *et al.*, *Phys. Rev. B* **25**, 4515 (1982).
- [17] T. M. Eiles *et al.*, *Phys. Rev. Lett.* **70**, 1862 (1993).
- [18] H. Pothier *et al.*, *Phys. Rev. Lett.* **73**, 2488 (1994).
- [19] J. M. Hergenrother *et al.*, *Phys. Rev. Lett.* **72**, 1742 (1994).
- [20] S. Rajauria *et al.*, *Phys. Rev. Lett.* **100**, 207002 (2008).
- [21] M. Nahum and J. M. Martinis, *Appl. Phys. Lett.* **63**, 3075 (1993).
- [22] J. M. Martinis *et al.*, *Phys. Rev. Lett.* **103**, 097002 (2009).
- [23] M. W. Keller *et al.*, *Phys. Rev. Lett.* **80**, 4530 (1998).
- [24] J. M. Martinis and M. Nahum, *Phys. Rev. B* **48**, 18316 (1993).
- [25] J. M. Hergenrother *et al.*, *Phys. Rev. B* **51**, 9407 (1995).
- [26] See supplementary material at <http://link.aps.org/supplemental/10.1103/PhysRevLett.105.026803> for derivation.
- [27] A. Kemppinen *et al.*, *Eur. Phys. J. Special Topics* **172**, 311 (2009).
- [28] S. V. Lotkhov *et al.*, *Appl. Phys. Lett.* **95**, 112507 (2009).
- [29] A. Kemppinen *et al.*, *Appl. Phys. Lett.* **94**, 172108 (2009).
- [30] V. F. Maisi *et al.*, *New J. Phys.* **11**, 113057 (2009).

On-line material

J. P. Pekola, V. F. Maisi, S. Kafanov, N. Chekurov, A. Kemppinen,  
 Yu. A. Pashkin, O.-P. Saira, M. Möttönen, and J. S. Tsai  
 (Dated: June 13, 2010)

TUNNELING RATES IN A RESISTIVE ENVIRONMENT

Let us consider an NIS tunnel junction with a normal-metal and a superconducting lead separated by a thin oxide layer, shown in Fig. 1 of the original article. We assume that the junction is in an ideal voltage bias  $V$  and neglect the charging energy of the single junction justified by the large capacitance provided by the leads. As in the fully normal-metal case [1], sequential tunneling rates  $\Gamma_{+/-}$  for single-electron events along/against the bias are obtained to be

$$\Gamma_{\pm} = \frac{1}{e^2 R_T} \int_{-\infty}^{\infty} \int_{-\infty}^{\infty} dE dE' n_S(E') f_N(E \mp eV) [1 - f_S(E')] P(E - E'), \quad (\text{S-1})$$

where  $R_T$  is the asymptotic resistance of the junction,  $n_S$  is the Bardeen-Cooper-Schrieffer (BCS) density of states (DOS) in the superconductor, and the Fermi functions for the superconductor  $f_S$  and the normal metal  $f_N$  are governed by the temperatures  $T_S$  and  $T_N$ , respectively. The function  $P(E)$  can be interpreted as the probability density to emit energy  $E$  to the environment. The average electric current through the junction is given by  $I = e(\Gamma_+ - \Gamma_-)$ . Thus the current-voltage ( $IV$ ) response of the system, which is typically the only experimental observable for a single junction, is given by

$$I(V) = \frac{1}{e R_T} \int_{-\infty}^{\infty} \int_{-\infty}^{\infty} dE dE' n_S(E') [1 - f_S(E')] [f_N(E - eV) - f_N(E + eV)] P(E - E'). \quad (\text{S-2})$$

We note that in an ideal case with no coupling to an external electro-magnetic environment in the tunneling process,  $P(E)$  is a delta function and Eqs. (S-1-S-2) reduce into the typical Fermi golden rule results with one-dimensional integrals. Generally,  $P(E)$  can be written as

$$P(E) = \frac{1}{2\pi\hbar} \int_{-\infty}^{\infty} \exp\left(J(t) + \frac{i}{\hbar} Et\right) dt, \quad (\text{S-3})$$

and by modeling the environment by an impedance  $Z(\omega)$  in a thermal equilibrium at temperature  $T_{\text{env}}$ , one obtains [1]

$$J(t) = 2 \int_0^{\infty} \frac{d\omega}{\omega} \frac{\text{Re}[Z(\omega)]}{2\pi R_Q} \left[ \coth\left(\frac{\hbar\omega}{2k_B T_{\text{env}}}\right) (\cos \omega t - 1) - i \sin \omega t \right], \quad (\text{S-4})$$

where  $R_Q = \hbar/e^2$  is the resistance quantum. For a purely resistive environment,  $\text{Re}[Z(\omega)] = R/[1 + (\omega RC)^2]$ , where  $R$  is the resistance of the environment and  $C$  is the total capacitance at the junction including the junction capacitance and parallel shunt capacitors. Although this rather simple model has essentially only two free parameters,  $R$  and  $T_{\text{env}}$ , for low values of capacitance  $C$ , it has been successfully applied to explain several experimental observations [2, 3].

In our case of a resistive environment, the integral in Eq. (S-4) can be evaluated to yield

$$J(t) = \frac{\rho}{2} \left[ \cot(B)(1 - e^{-|\tau|}) - \frac{|\tau|}{B} - 2 \sum_{n=1}^{\infty} \frac{1 - e^{-n\pi|\tau|/B}}{n\pi [1 - (n\pi/B)^2]} - i \text{sign}(\tau) (1 - e^{-|\tau|}) \right], \quad (\text{S-5})$$

where  $\rho = R/R_Q$ ,  $\tau = t/(RC)$  and  $B = \hbar/(2k_B T_{\text{env}} RC)$ . For  $|\tau| \gg 1, B$ , we can neglect all the terms in Eq. (S-5) containing  $|\tau|$  in the exponent. Use of this approximation for evaluating  $P(E)$  according to Eq. (S-3) is justified if the energy exchange  $E$  with the environment satisfies  $|E| \ll \hbar/(RC)$ ,  $k_B T_{\text{env}}$ . For low bias voltages in an NIS junction, an electron needs to absorb energy of  $\Delta - eV$  in order to tunnel. Therefore, the BCS gap gives the relevant scale of the energy exchange at low bias voltages. At higher voltages, the current is essentially linear in  $V$  and insensitive to

the functional form of  $P(E)$ . Hence the conditions above can be taken to  $\Delta \ll \hbar/(RC)$ ,  $k_B T_{\text{env}}$ . Thus, under these circumstances we simplify Eq. (S-5) into

$$J(t) = -\frac{\rho}{2} \left[ \alpha + \frac{|\tau|}{B} + i \text{sign}(\tau) \right], \quad (\text{S-6})$$

where  $\alpha$  is the sum of all terms in Eq. (S-3) independent of  $\tau$ . By evaluating the integral in Eq. (S-3) with  $J(t)$  from Eq. (S-6), we obtain

$$P(E) = \frac{1}{\pi} e^{-\rho\alpha/2} \frac{(\rho k_B T_{\text{env}}) \cos(\rho/2) + E \sin(\rho/2)}{(\rho k_B T_{\text{env}})^2 + E^2}. \quad (\text{S-7})$$

Here, the normalization condition  $\int_{-\infty}^{\infty} P(E) dE = 1$  yields  $e^{-\rho\alpha/2} = 1/\cos(\rho/2)$ . Furthermore, the situation  $\rho \ll 1$  is met in experiments [2, 3] unless the environment in the immediate vicinity of the junction is deliberately engineered to be high Ohmic [4]. Together with the assumption  $|E| \ll k_B T_{\text{env}}$  cast above, Eq. (S-7) assumes the form

$$P(E) = \frac{1}{\pi} \frac{(\rho k_B T_{\text{env}})}{(\rho k_B T_{\text{env}})^2 + E^2}. \quad (\text{S-8})$$

We note that since we neglected the term  $E \sin(\rho/2)$  in Eq. (S-7), the detailed balance  $P(-E) = e^{-E/(k_B T_{\text{env}})} P(E)$  is not perfectly satisfied. Due to our assumption of high temperature  $|E| \ll k_B T_{\text{env}}$ , the error due to the slight breaking of the detailed balance is, however, small. As shown below, the fact that the  $P(E)$  function is symmetric, as in Eq. (S-8), is crucial in reducing  $IV$  characteristics given by Eq. (S-2) into the typical form with a one-dimensional integral in the energy domain. In this form, the effect of the environment is only to effectively modify the BCS DOS.

### EFFECTIVE DENSITY OF STATES

Let us come back to Eq. (S-2) yielding the current–voltage characteristics of an NIS junction. Since the BCS DOS vanishes inside the energy gap  $|E| < \Delta$ , Eq. (S-2) can be expressed in the form

$$I(V) = \frac{1}{eR_T} \int_{-\infty}^{\infty} dE \int_0^{\infty} dE' n_S(E') [f_N(E - eV) - f_N(E + eV)] P(E - E'), \quad (\text{S-9})$$

if the temperature of the superconductor satisfies  $T_S \ll \Delta/k_B$ . This condition is met in the experiments reported here since  $T_S < 100$  mK  $\ll \Delta/k_B \approx 2$  K. We expand the integral in Eq. (S-9) as

$$\begin{aligned} I(V) = & \frac{1}{eR_T} \int_{-\infty}^0 dE \int_0^{\infty} dE' n_S(E') [f_N(E - eV) - f_N(E + eV)] P(E - E') + \\ & \frac{1}{eR_T} \int_0^{\infty} dE \int_0^{\infty} dE' n_S(E') [f_N(E - eV) - f_N(E + eV)] P(E - E'). \end{aligned} \quad (\text{S-10})$$

By negating the integral variables in Eq. (S-10) and employing the symmetry of the Fermi function  $f(-x) = 1 - f(x)$ , of the BCS density of states  $n_S(-x) = n_S(x)$ , and of the  $P(E)$  function  $P(-E + E') = P(E - E')$ , we obtain

$$I(V) = \frac{1}{eR_T} \int_0^{\infty} dE n_{\text{eff}}(E) [f_N(E - eV) - f_N(E + eV)], \quad (\text{S-11})$$

where we have introduced the effective DOS

$$n_{\text{eff}}(E) = \int_{-\infty}^{\infty} dE' n_S(E') P(E - E'). \quad (\text{S-12})$$

We stress that to obtain Eq. (S-11) which corresponds exactly to current through an ideal NIS junction without coupling to environment but with a modified DOS, we only assumed that the superconductor is at low temperature and the environment is at high temperature. In this case, it is not possible to distinguish only from the  $IV$  characteristics whether the observed DOS arises, e.g., from some intrinsic property of the superconductor such as lifetime broadening, or from the electromagnetic environment described by  $P(E)$ . As reported in the original manuscript, we can make this distinction by engineering the environment thus showing that it gave the dominating contribution to the effective DOS.

## EQUIVALENCE OF THE P(E) AND DYNES DENSITY OF STATES

The Dynes DOS [5, 6] is given by

$$n_S^D(E) = \left| \Re \left[ \frac{E/\Delta + i\gamma}{\sqrt{(E/\Delta + i\gamma)^2 - 1}} \right] \right|, \quad (\text{S-13})$$

from which the BCS DOS  $n_S$  is obtained in the limit  $\gamma \rightarrow 0$ . Thus  $n_S(E \pm i\gamma\Delta) = n_S^D(E)$ , where the sign can be chosen freely. To show that the effective DOS arising from the environment in Eq. (S-8) is equivalent to the Dynes model with  $\gamma = 2\pi Rk_B T_{\text{env}}/(R_K\Delta)$ , we write the inverse Fourier transform of  $n_S^D$  as

$$\mathcal{F}^{-1}(n_S^D) = \int_{-\infty}^{\infty} n_S[\omega - i \text{sign}(t)\gamma\Delta] e^{i\omega t} d\omega / \sqrt{2\pi} = e^{-\gamma\Delta|t|} \mathcal{F}^{-1}(n_S). \quad (\text{S-14})$$

On the other hand,

$$n_S^D = \mathcal{F}[\mathcal{F}^{-1}(n_S^D)] = \mathcal{F}[e^{-\gamma\Delta|t|} \mathcal{F}^{-1}(n_S)] = \mathcal{F}(e^{-\gamma\Delta|t|}) * n_S = n_{\text{eff}}, \quad (\text{S-15})$$

where  $*$  denotes a convolution integral and we have used the identity  $\mathcal{F}^{-1}(f * g) = \mathcal{F}^{-1}(f) \mathcal{F}^{-1}(g)$ . Thus the effective DOS in Eq. (S-12) with the environment given by Eq. (S-8) is equivalent to the Dynes model.

- 
- [1] G. L. Ingold and Yu. V. Nazarov, Charge Tunneling Rates in Ultrasmall Junctions, in *Single charge tunneling*, Vol. 294 of *NATO ASI Series B*, edited by Grabert, H. & Devoret, M. H. (Plenum Press, New York, 1992), pp. 21–107.
  - [2] J. M. Martinis and M. Nahum, *Phys. Rev. B* **48**, 18316 (1993).
  - [3] J. M. Hergenrother, J. G. Lu, M. T. Tuominen, D. C. Ralph, and M. Tinkham, *Phys. Rev. B* **51**, 9407 (1995).
  - [4] S. V. Lotkhov, A. Kemppinen, S. Kafanov, J. P. Pekola, and A. B. Zorin, *Appl. Phys. Lett.* **95**, 112507 (2009).
  - [5] R. C. Dynes, V. Narayanamurti, and J. P. Garno, *Phys. Rev. Lett.* **41**, 1509 (1978).
  - [6] R. C. Dynes, J. P. Garno, G. P. Hertel, and T. P. Orlando, *Phys. Rev. Lett.* **53**, 2437 (1984).



## Publication III

O.-P. Saira, M. Möttönen, V. F. Maisi and J. P. Pekola. Environmentally activated tunneling events in a hybrid single-electron box. *Phys. Rev. B* **82**, 155443 (2010).

© (2010) American Physical Society.

Reprinted with permission.



**Environmentally activated tunneling events in a hybrid single-electron box**O.-P. Saira,<sup>1,2</sup> M. Möttönen,<sup>1,2</sup> V. F. Maisi,<sup>3</sup> and J. P. Pekola<sup>1</sup><sup>1</sup>*Low Temperature Laboratory, Aalto University, P.O. Box 15100, FI-00076 AALTO, Finland*<sup>2</sup>*Department of Applied Physics/COMP, Aalto University, P.O. Box 14100, FI-00076 AALTO, Finland*<sup>3</sup>*Centre for Metrology and Accreditation (MIKES), P.O. Box 9, 02151 Espoo, Finland*

(Received 28 September 2010; published 26 October 2010)

We have measured individual tunneling events and Coulomb step shapes in single-electron boxes with opaque superconductor–normal metal tunnel junctions. We observe anomalous broadening of the Coulomb step with decreasing temperature in a manner that is consistent with activation of first-order tunneling events by an external dissipative electromagnetic environment. We demonstrate that the rates for energetically unfavorable tunneling events saturate to finite values at low temperatures, and that the saturation level can be suppressed by more than an order of magnitude by a capacitive shunt near the device. The findings are important in assessing the performance limits of any single-electronic device. In particular, master-equation-based simulations show that the electromagnetic environment realized in the capacitively shunted devices allows for a metrologically accurate charge pump based on hybrid tunnel junctions.

DOI: [10.1103/PhysRevB.82.155443](https://doi.org/10.1103/PhysRevB.82.155443)

PACS number(s): 73.23.Hk, 05.40.Ca, 74.45.+c

**I. INTRODUCTION**

Various kinds of electron pumps and turnstiles based on single electronics are under active investigation at the moment in order to redefine the unit ampere and to provide the current source for the quantum metrological triangle experiment.<sup>1</sup> The performance requirements in metrology are demanding. To improve the existing uncertainties of fundamental constants, elementary charges have to be transferred at a frequency on the order of 1 GHz with an error rate less than  $10^{-7}$ . With present-day thin-film technology, it is straightforward to realize electron pumps where the error rates due to thermally activated one-electron processes are below the metrological bound at subkelvin temperatures. Residual pumping errors in normal metal pumps are generally attributed to cotunneling<sup>2</sup> and environmental activation (EA),<sup>3</sup> although a quantitative theoretical analysis of the experimentally observed error rates is still lacking. A more recently developed candidate is the hybrid turnstile, consisting of a single-electron transistor (SET) with normal metal-insulator-superconductor (NIS) junctions.<sup>4</sup> Theoretically, the SINIS turnstile has the potential to reach metrological accuracy<sup>5</sup> but the experimental results have been limited by the leakage current present when the turnstile is biased at its operating point.<sup>6</sup> Leakage in NIS structures is often attributed to a finite density of states (DOS) within the Bardeen-Cooper-Schrieffer (BCS) energy gap, which is modeled with the phenomenological Dynes DOS.<sup>7</sup> In Ref. 8, it was shown algebraically that a high-temperature environment ( $k_B T_{\text{env}} \gtrsim \Delta$ ) can manifest itself as smearing of the DOS in the superconducting electrode of a bare NIS junction, which was experimentally verified. On the contrary, in a Coulomb-blockaded system embedded in an environment, the device response depends on one-electron tunneling rates in a way that cannot be expressed in terms of an effective DOS. A tunneling electron can overcome the Coulomb blockade by absorbing energy from the environment, which degrades the performance of the device.

In the present work, we study experimentally hybrid tunnel junctions in the EA regime. We demonstrate that EA

causes the observed low-temperature saturation of one-electron tunneling rates near the degeneracy point between two charge states, in the energy range that determines the accuracy of the SINIS turnstile when operated with a sinusoidal drive signal. Hybrid tunnel junctions are well suited for this investigation, as the EA effects are dramatic owing to sharp features in the superconductor DOS, which has been previously exploited in the study of photon-assisted tunneling by microwave irradiation in SETs.<sup>9</sup> The simplest system where a quantized island charge can be observed is the single-electron box, first studied in Ref. 10. In the present work, we probed the charge state of a galvanically isolated hybrid single-electron box by a capacitively coupled SET electrometer. Owing to the superconducting energy gap, the tunneling rates near degeneracy are sufficiently low so that individual tunneling events can be observed without additional trapping nodes that are required for normal metal devices. We emphasize that this is the same qualitative difference that allows quantized current pumping using the SINIS turnstile with only one Coulomb-blockaded island whereas the normal metal pumps always have at least two islands. For demonstrating the EA effects, we measured samples with and without a ground plane, i.e., a capacitive shunt in the electrical leads acting as a filter for high-frequency environmental noise. We present data from four samples in total. Samples G1 and G2 have a ground plane as shown in Fig. 1(a) whereas reference samples R1 and R2 do not have one. Samples G1, G2, and R1 were fabricated simultaneously on the same chip and have identical design for the metal layers. Sample R2 is otherwise similar but has a SISIS-type detector as opposed to the SINIS type found in all the other samples. Figure 1(b) illustrates the layout of the active region with the single-electron box and the electrometer.

Two gate electrodes allow for independent tuning of the detector and the box. Whenever the box gate voltage was changed, a compensation signal was subtracted from the detector gate voltage canceling the direct capacitive coupling to the detector island. For the following discussion, one can consider the compensated box gate voltage to be the only external control signal. Due to the compensation, charge

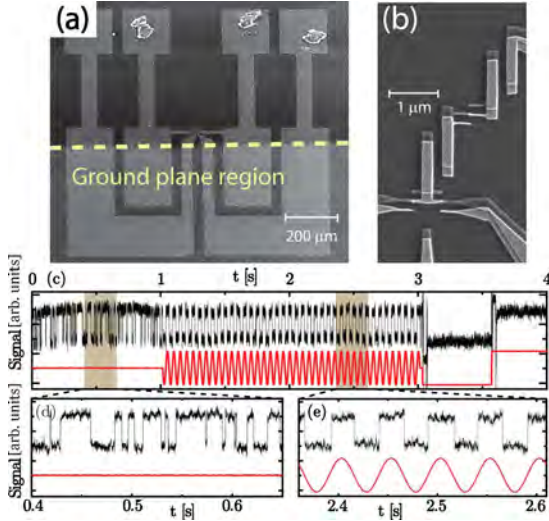


FIG. 1. (Color online) (a) Large-scale electron micrograph of a sample showing the bonding pads and the electrical leads to the active region in the middle. A copper ground plane isolated from the thin-film metal structures by 120 nm aluminum oxide layer is indicated in the bottom half of the picture. (b) Active region of a single-electron box similar to the measured samples. The hybrid single-electron box is shown in the middle, and the electrometer SET below it. The thin-film copper layer appears lighter compared to the aluminum layer. Tips of the gate electrodes can be seen at the bottom and top right. (c) Four-second real-time electrometer trace (top black) recorded from sample G2 demonstrating the ability to accurately control the charge state of the box. The control sequence (bottom red) applied to the box gate is as follows: 0–1 s degeneracy point, also detailed in panel (d), showing stochastic switching between the two charge states with nearly equal occupation. 1–3 s sinusoidal drive between the charge states at 20 Hz, also detailed in panel (e). 3–3.5 s and 3.5–4 s “hold” mode in the first and second charge state, respectively. The sample stage temperature is 60 mK.

states of the box correspond to fixed detector current levels. The response of the box state to a gate control sequence is demonstrated in Figs. 1(c)–1(e), displaying a real-time measurement of sample G2.

All the tunnel junctions were oxidized strongly, resulting in specific resistances of  $3 \text{ k}\Omega \mu\text{m}^2$ , or about  $300 \text{ k}\Omega$  for the detector junctions and up to  $3.5 \text{ M}\Omega$  for the smaller box junction. High resistance is required for the box junction to bring the tunneling rates down into the measurement bandwidth. The detector current was read out in dc-SET configuration using a room-temperature current amplifier, limiting the usable bandwidth to about 5 kHz.

## II. THEORY OF ENVIRONMENTALLY ACTIVATED TUNNELING

Due to small tunnel junctions and the lack of galvanic connection, the charging energy of the box for a single-electron tunneling was at least 4 K in all of the samples. Hence, in all of the experiments performed in dilution refrigerator temperatures, at most two charge states of the box have a non-negligible occupancy. We can safely assume that an equilibrium quasiparticle energy distribution is reached

before each tunneling event as the highest tunneling rates considered in the experiment were below 10 kHz. Thus, a complete model for the internal dynamics of the box is a two-state fluctuator, the states of which we will denote by 1 and 2. Neglecting backaction from the detector, the transition rates are symmetric and given by  $\Gamma^\pm = \Gamma(\pm E)$ , where  $E = U_2 - U_1$  is the difference in the electrostatic energy of the two charge states and  $\Gamma(E)$  is the golden rule tunneling rate<sup>11</sup>

$$\Gamma(E) = \frac{1}{e^2 R_T} \int_{-\infty}^{\infty} dE_1 \int_{-\infty}^{\infty} dE_2 n_S(E_1) f_S(E_1) [1 - f_N(E_2)] P(E_1 - E_2 + E). \quad (1)$$

Above,  $n_S$  is the DOS for the superconducting electrode,  $f_{N(S)}$  is the occupation factor for quasiparticle energy levels in the N(S) electrode, and  $P(E')$  gives the probability for emitting energy  $E'$  to the environment. In our model, we use the pure BCS density of states  $n_S(E) = |\text{Re} \frac{E}{\sqrt{E^2 - \Delta^2}}|$  with  $\Delta = 200 \mu\text{eV}$  for the superconducting gap parameter of aluminum. As we will show in Appendix B, the quasiparticles in the N electrode are thermalized by electron-phonon coupling and in the S electrode through the large overlap with the copper shadow. Hence, the occupation factors are taken to be Fermi functions at sample stage temperature  $T_0$ , i.e.,  $f_{N(S)}(E) = [1 + \exp(E/k_B T_0)]^{-1}$ . The probability for a two-electron process to change the box charge state is low, as for all those processes the energy cost due to charging energy and Cooper pair breaking is the same or greater, but the rate prefactor is much smaller than for one-electron tunneling.

## III. MODEL OF THE ELECTRICAL ENVIRONMENT

Electromagnetic environment appears in the  $P(E)$  theory through the expression  $\text{Re}[Z_t(\omega)]$ , where  $Z_t(\omega)$  is the total impedance of the environment including the parallel junction capacitance, as seen from the two electrodes of the junction. We model the external environment as a parallel  $RC$  element with the resistor  $R$  at liquid-helium temperature in the same manner as in Refs. 8 and 9. Assume that the box electrodes have a mutual capacitance of  $C_j$ , the main contribution of which is from the junction area, and that the two electrodes are coupled to the environment through capacitances  $C_1$  and  $C_2$ , respectively. Then, the impedance  $Z_t(\omega)$  can be evaluated as

$$Z_t(\omega) = \frac{1}{i\omega C_j} \parallel \left( \frac{1}{i\omega C_0} + R \parallel \frac{1}{i\omega C} \right), \quad (2)$$

where  $C_0 = (1/C_1 + 1/C_2)^{-1}$  is the series capacitance of the coupling capacitances  $C_1$  and  $C_2$  and  $A \parallel B := (1/A + 1/B)^{-1}$  is used to denote parallel impedance. Under the assumption  $C_j \ll C$ , we have the algebraic result

$$\text{Re}[Z_t(\omega)] = \text{Re} \left[ \frac{R/\kappa}{1 + i\omega(R/\kappa)(\kappa C)} \right], \quad (3)$$

where  $\kappa = 1 + C_j/C_0$ . We refer to  $\kappa$  as the decoupling factor, as  $\kappa = 1$  corresponds to the case where a bare junction is directly connected to the environment. In the hybrid single-electron box samples, a typical box junction has  $C_j = 0.2 \text{ fF}$

based on the observed charging energies of 4–5 K whereas the couplings are of the order  $C_{1,2}=0.02$  fF based on the gate modulation periods and geometric modeling. Hence, one can expect  $\kappa$  on the order of 20. It is hard to give an accurate estimate of  $\kappa$  based on the conductor geometry as the environmental noise can couple to the box from all of the gate and bias lines but on the other hand the common-mode component of the noise does not affect tunneling through the junction. We do not try to determine an explicit value for  $\kappa$  but instead use  $R_{\text{eff}}:=R/\kappa$  and  $C_{\text{eff}}:=\kappa C$  directly as fitting parameters. When computing the theoretical predictions, the  $P(E)$  function for given environmental parameters is evaluated numerically.

#### IV. MEASUREMENT RESULTS

A basic measurable quantity of the box is the charge-state occupation probability that depends on the ratio of forward and backward tunneling rates and assumes the form  $p = \Gamma^- / (\Gamma^+ + \Gamma^-)$  for state 1. For an NIN junction under negligible environmental influence, one has the analytic result  $\Gamma^\pm = \frac{1}{eR_T} \frac{\pm E}{1 - \exp(\mp E/k_B T_0)}$ , giving a Fermi form for the occupation as a function of the energy difference  $E$  of the charge states,  $p_{\text{NIN}} = [1 + \exp(E/k_B T_0)]^{-1}$ . Occupation factors can be determined from the Coulomb staircase, i.e., the detector dc current as a function of the control gate, by normalizing the current levels of consecutive plateaus to 0 and 1, respectively. Because at most two states are active, detector non-linearity with respect to box charge does not affect the results. The occupation can be determined whenever the detector has sufficient sensitivity to the box charge, even when the tunneling rates are beyond the measurement bandwidth. If the tunneling rates are low enough so that the detector can separate the charge states, we calculate the occupation from the weight of histogram peaks which gives improved immunity to low-frequency drifts in the detector signal.

We determine the width of a step shape obtained from experiment or numerical calculation by fitting a Fermi function to it. Numerical results indicate that for the environmental parameters considered in the present work, the Coulomb steps at high temperatures in both NIN and NIS states have the Fermi form given above, with the width corresponding to the common temperature of the bath and the quasiparticles in both electrodes. In NIN state, the linear relation between step width and temperature is valid down to our base temperature of 60 mK. However, in NIS state the step width behaves anomalously at temperatures below 200 mK with strong dependence on the environmental parameters. Experimentally, the hybrid box can be brought into NIN state by an external magnetic field. In Fig. 2 we show the data from all four samples measured in the temperature range 60–300 mK (60–400 mK for sample R2) in both NIS and NIN states. The NIN data in panels (c)–(f) for all samples displays linear behavior down to the base temperature, indicating that the box quasiparticle temperatures were not elevated due to external noise heating. The energy difference  $E$  depends linearly on the control gate voltage with the conversion factor determined by the coupling capacitances and the box charg-

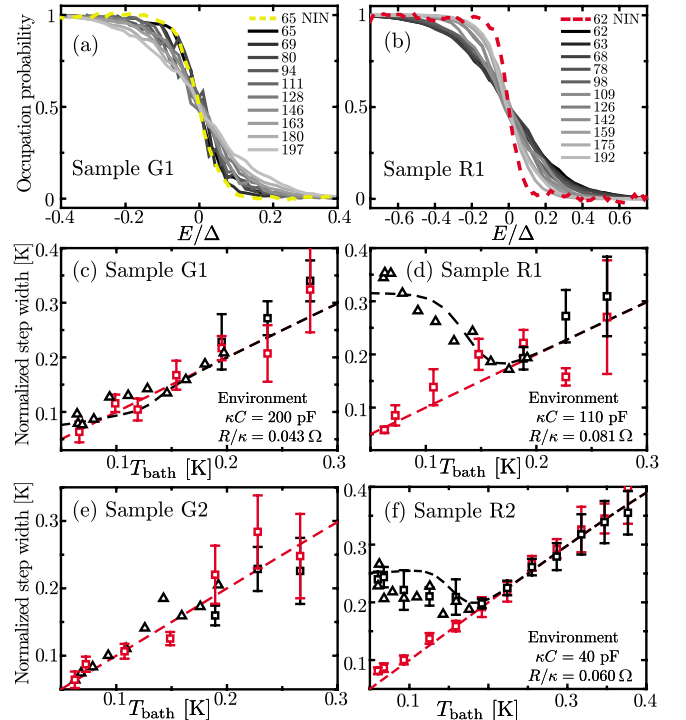


FIG. 2. (Color online) [(a) and (b)] Grayscale lines: Coulomb staircase in the NIS state, i.e., charge-state occupation probability near the degeneracy point as a function of the energy difference for samples G1 and R1 at temperature points in the range 60–200 mK corresponding to the step width data presented in panels (c) and (d). The curves shown here are obtained by analyzing real-time electrometer traces where the two states are separable. For sample G1 with the ground plane, the step sharpens with reduced temperature, whereas for the reference sample R1 the opposite is observed. Colored dashed line: staircase in the NIN state at the base temperature. [(c)–(f)] Step widths as a function of temperature in NIS state (black symbols) and NIN state (red symbols). Black triangles correspond to step widths determined using real-time traces. In NIN state (red squares) and in NIS state at elevated temperatures (black squares), the step widths have been determined from electrometer dc averaged over the charge-state fluctuations. Dashed lines show the predictions of  $P(E)$  theory for NIS state (black) and NIN state (red).

ing energy. We determined the conversion factor from gate-voltage offset into energy by requiring that the step widths in the linear regime correspond to energy  $k_B T_0$ . For samples G1 and R1, we display theoretical predictions using environmental parameters that yield best fit to the data presented in both Figs. 2 and 3. For sample R2, provisional parameters reproducing the observed step widths are used. The data for sample G2 can be reproduced by parameters that are similar to those of sample G1. We note that if at least part of the environment noise is capacitively coupled, adding shunting capacitance over the sample will also decrease the effective source resistance.

In the NIS data for the unshielded samples R1 and R2, EA effects can be observed at temperatures below 200 mK as broadening of the step with decreasing temperature. At low temperatures, the tunneling rates for small energy differences are set by EA and consequently the step width is determined

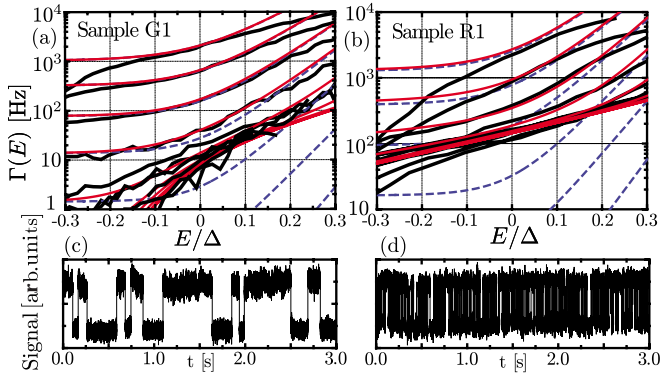


FIG. 3. (Color online) [(a) and (b)] Tunneling rates as a function of energy difference for samples G1 and R1, respectively, at temperatures in the range 60–200 mK corresponding to the NIS state data presented in Figs. 2(a) and 2(b). Black curves are experimental data whereas red curves show the theoretical predictions using the same parameter values as in Fig. 2. For reference, we plot orthodox theory rates without environment as dashed blue lines. The experimental rates are most reliable near the degeneracy point. Counting errors due to missed events increase as one of the tunneling rates grows beyond the detector bandwidth, explaining the discrepancy between experiment and theory for sample R1 at high temperatures. [(c) and (d)] Individual traces at the base temperature near the degeneracy point for samples G1 and R1, respectively, demonstrating the reduction in tunneling rates by capacitive shunting.

by the environmental parameters. When the temperature is sufficiently high, thermal activation (TA) due to broadening of the quasiparticle energy distribution begins to govern the tunneling rates, and a linear relation between step width and temperature is restored. The EA-limited step width can correspond to a higher temperature than where the transition to TA regime occurs, which results in a width minimum at finite temperature. The measured step width for ground plane samples G1 and G2 is nearly linear for the whole experimental temperature range which is reflected in smaller  $R_{\text{eff}}$  and larger  $C_{\text{eff}}$  for the environment.

We determined the tunneling rates by stepping the control gate voltage across the degeneracy point, identified as the midpoint of a Coulomb staircase step. At each gate position, a 3 s trace of the output of the detector current amplifier was recorded at 100 kHz sampling rate followed by digital low-pass filtering with a sharp cut off at 5 kHz. The whole sweep was discarded if an abrupt change in the detector or box operating point due to shifts in background charges was observed. The tunneling events were identified using threshold detection with the transition thresholds set based on the histogram computed for a trace. The tunneling rates are estimated as  $\Gamma^{\pm} = \bar{\tau}_{1(2)}^{-1}$ , where  $\bar{\tau}_{1(2)}$  is the mean observed lifetime of state 1(2). Due to the possibility of missed events, the rate estimates obtained from a trace are reliable only if both rates satisfy  $1/t_0 \ll \Gamma^{\pm} \ll B_{\text{det}}$ , where  $t_0$  is the length of the trace and  $B_{\text{det}}$  is the detector bandwidth.

In Figs. 3(a) and 3(b), we present the measured tunneling rates at different bath temperatures in the range 60–200 mK for the shielded sample G1 and the reference sample R1. We also show the  $P(E)$  theory predictions using the same environment parameters as in Fig. 2. For comparison, the tunnel-

ing rates without EA are also shown. The tunneling resistance  $R_T$  of the box junction, an otherwise inaccessible parameter, was determined from the data at 180 mK where tunneling rates depend weakly on the environmental parameters, but are still within the detector bandwidth. The values obtained this way are 3.5 M $\Omega$  for sample G1 and 2.0 M $\Omega$  for R1. In the tunneling rate data, the agreement is good for the two samples in the  $E$  range where both rates  $\Gamma^{\pm} = \Gamma(\pm E)$  are below 1 kHz. Above that, the experimentally determined rates are smaller than the real values due to missed events. For both samples, the floor where low-temperature rates saturate to is set by the environment. In sample R1, the tunneling rates recorded at 125 and 140 mK are lower than the base-temperature rates, which we interpret as an artifact due to reduced sensitivity of the detector SET at higher temperatures. As illustrated in Figs. 3(c) and 3(d), in the ground plane sample G1 the base temperature tunneling rate at the degeneracy point is an order of magnitude smaller than in the unshielded sample R1, even after accounting for the difference in tunneling resistances.

## V. DISCUSSION

To relate the observed tunneling rate data to the pumping performance of the SINIS turnstile, we performed master-equation-based simulations of electron transfer during the pumping cycle. For the simulations, we assumed a high-quality turnstile with realistic parameters  $R_T = 0.5$  M $\Omega$  per junction,  $E_c/k_B = 5$  K, and a quasiparticle temperature of 50 mK for all electrodes. Gate-dependent first-order tunneling rates were calculated according to Eq. (1) using the environment parameters that we extracted for the shielded sample G1. At 20 MHz pumping frequency, the simulations predict an EA-limited total error rate of  $1.7 \times 10^{-6}$  for a sinusoidal gate drive, and  $1.8 \times 10^{-7}$  for a square wave drive. Cancellation of pumping errors of different signs is not included in these figures and hence the relative deviation of the average pumped current from the ideal value  $I = ef$  is smaller. It remains an open technological challenge to realize a similar or better environment for an SET with galvanic connections to biasing leads.

In summary, we have measured single-electron tunneling rates in an NIS single-electron box near the degeneracy point in two qualitatively different electromagnetic environments. The agreement to a model of first-order tunneling activated by absorption of photons from a warm environment is excellent. Accounting for the enhanced decoupling in the present experiment due to lack of galvanic connections, the parameter values we obtained for the external environment are comparable with those presented in Ref. 8. The results indicate that environmental fluctuations deteriorate the performance of single-electronic devices due to enhancement of tunneling rates in the energetically unfavorable direction. The measurements on the sample with an on-chip capacitive shunt indicate that the environment-induced error rate of the SINIS turnstile can be suppressed to the metrological level with an appropriate filtering of high-frequency noise. We emphasize that the model of environmentally assisted tunneling explains the observed tunneling rates without any subgap states in the superconductor.

## ACKNOWLEDGMENTS

We thank M. Meschke and S. Kafanov for helpful discussions. The work has been supported partially by the Academy of Finland, Väisälä Foundation, Emil Aaltonen Foundation, and the Finnish National Graduate School in Nanoscience. The research conducted within the EU project SCOPE received funding from the European Community's Seventh Framework Programme under Grant Agreement No. 218783.

## APPENDIX A: DETECTOR BACKACTION

Typical value for the average detector current used in the real-time counting experiment was 0.5 nA. Low detector current has the benefit of reduced heating and backaction at the cost of signal-to-noise ratio. To assess experimentally the effect of detector backaction, we measured the tunneling rates at base temperature at different operation points of the detector. In the parameter range where tunneling events could still be reliably detected, we observed that the tunneling rate at the degeneracy point for the shielded sample G2 was modulated by factor three. For the unshielded sample R1, we found no change within experimental error. We were able to reproduce these results qualitatively using a model similar to Ref. 12, where the effective position of the box gate fluctuates due to changes in the charge state of the detector island. Detector backaction is not included in the theoretical curves of Figs. 2 and 3, which may affect the values of fitted environment parameters for the shielded sample but does not change the conclusions of the paper about the role of the external environment.

## APPENDIX B: QUASIPARTICLE THERMALIZATION IN THE BOX ELECTRODES

Here, we address the issue of quasiparticle heating and thermalization in the electrodes of the hybrid single-electron box. The heat associated with quasiparticle tunneling governed by Eq. (1) can be calculated as a function of the charging energy difference  $E$  as

$$\dot{Q}_S(E) = -\frac{1}{e^2 R_T} \int_{-\infty}^{\infty} dE_1 E_1 \int_{-\infty}^{\infty} dE_2 n_S(E_1) f_S(E_1) [1 - f_N(E_2)] P(E_1 - E_2 + E), \quad (\text{B1})$$

$$\dot{Q}_N(E) = \frac{1}{e^2 R_T} \int_{-\infty}^{\infty} dE_1 \int_{-\infty}^{\infty} dE_2 E_2 n_S(E_1) f_S(E_1) [1 - f_N(E_2)] P(E_1 - E_2 + E) \quad (\text{B2})$$

for the S and N electrodes, respectively. The average energy deposited per individual tunneling event can be evaluated as  $\dot{Q}_{N,S}(E)/\Gamma(E)$ . For the single-electron box with two active

TABLE I. Calculated heat loads to the box electrodes from quasiparticle tunneling in various configurations at 60 mK.

Sample	NIN state	NIS state, to N	NIS state, to S
R1	$4.7 \times 10^{-20}$ W	$1.2 \times 10^{-21}$ W	$5.3 \times 10^{-21}$ W
G1	$1.7 \times 10^{-20}$ W	$5.5 \times 10^{-24}$ W	$2.4 \times 10^{-22}$ W

charge states, the average heat load is given by

$$\langle \dot{Q}_{N,S} \rangle = \frac{\dot{Q}_{N,S}(E)/\Gamma(E) + \dot{Q}_{N,S}(-E)/\Gamma(-E)}{1/\Gamma(E) + 1/\Gamma(-E)}. \quad (\text{B3})$$

Numerical calculations show that the maximum heating occurs at the degeneracy point, i.e.,  $E=0$ . Using the sample and environment parameters extracted from the tunneling rate data, the heat loads in samples R1 and G1 calculated from Eqs. (B1)–(B3) are presented in Table I.

In the N electrode, hot quasiparticles can thermalize through electron-phonon coupling. The electron-phonon heat flow is given by<sup>13</sup>

$$\dot{Q}_{e\text{-ph}} = \Sigma \mathcal{V} (T_N^5 - T_{N,\text{ph}}^5), \quad (\text{B4})$$

where  $\Sigma$  is the material-dependent electron-phonon coupling constant,  $\mathcal{V}$  is the island volume, and  $T_{N,\text{ph}}$  is the temperature of the island phonons, assumed to equal the sample stage temperature  $T_0$ . We use the literature value<sup>13</sup> for copper  $\Sigma = 2 \times 10^9$  W m<sup>-3</sup> K<sup>5</sup> and  $\mathcal{V} = 0.3 \times 1.5 \times 0.04$   $\mu\text{m}^3$ . The island phonons are assumed to be well thermalized to the sample stage. Using the heat load values presented in Table I at the base temperature  $T_0 = 60$  mK, we find that the N electrode quasiparticle temperature is elevated at most 0.02 mK.

In the S electrode, the electron-phonon heat flow is exponentially suppressed below the critical temperature.<sup>14</sup> Hence, the dominant heat-conduction channel is through the  $0.3 \times 1.3$   $\mu\text{m}^2$  overlap with the copper shadow. Using the specific resistance value 3 k $\Omega$   $\mu\text{m}^2$  obtained for the SET junctions, we get  $R_T = 8$  k $\Omega$  for the overlap junction. We obtain a lower bound for the heat flow by considering only first-order quasiparticle tunneling. In order to determine the quasiparticle saturation temperature, henceforth denoted by  $T_S^0$ , we then evaluate the heat flow through the junction from Eq. (B1) as a function of  $T_S$  with  $T_N = 60$  mK. Environmental fluctuations can be neglected due to large junction capacitance, i.e., we use  $P(E) = \delta(E)$ . For the S electrode heat loads presented in Table I, we find that  $T_S^0 = 116$  mK for sample R1 and 100 mK for sample G1. However, the tunneling rates in the parameter range accessed in the experiment have a very weak dependence on  $T_S$ . The theoretical curves presented in the paper are calculated with  $T_S = T_0$ , and there is a negligible difference between them and curves calculated with  $T_S = T_S^0$ .

- <sup>1</sup>N. Feltin and F. Piquemal, *Eur. Phys. J. Spec. Top.* **172**, 267 (2009).
- <sup>2</sup>S. V. Lotkhov, S. A. Bogoslovsky, A. B. Zorin, and J. Niemeyer, *Appl. Phys. Lett.* **78**, 946 (2001); H. D. Jensen and J. M. Martinis, *Phys. Rev. B* **46**, 13407 (1992).
- <sup>3</sup>M. Covington, M. W. Keller, R. L. Kautz, and J. M. Martinis, *Phys. Rev. Lett.* **84**, 5192 (2000); M. W. Keller, J. M. Martinis, and R. L. Kautz, *ibid.* **80**, 4530 (1998).
- <sup>4</sup>J. P. Pekola, J. J. Vartiainen, M. Möttönen, O.-P. Saira, M. Meschke, and D. V. Averin, *Nat. Phys.* **4**, 120 (2008).
- <sup>5</sup>D. V. Averin and J. P. Pekola, *Phys. Rev. Lett.* **101**, 066801 (2008).
- <sup>6</sup>S. V. Lotkhov, A. Kemppinen, S. Kafanov, J. P. Pekola, and A. B. Zorin, *Appl. Phys. Lett.* **95**, 112507 (2009); A. Kemppinen, S. Kafanov, Yu. A. Pashkin, J. S. Tsai, D. V. Averin, and J. P. Pekola, *ibid.* **94**, 172108 (2009).
- <sup>7</sup>R. C. Dynes, V. Narayanamurti, and J. P. Garno, *Phys. Rev. Lett.* **41**, 1509 (1978).
- <sup>8</sup>J. Pekola, V. Maisi, S. Kafanov, N. Chekurov, A. Kemppinen, Y. Pashkin, O. Saira, M. Möttönen, and J. Tsai, *Phys. Rev. Lett.* **105**, 026803 (2010).
- <sup>9</sup>J. M. Hergenrother, J. G. Lu, M. T. Tuominen, D. C. Ralph, and M. Tinkham, *Phys. Rev. B* **51**, 9407 (1995).
- <sup>10</sup>P. Lafarge, H. Pothier, E. R. Williams, D. Esteve, C. Urbina, and M. H. Devoret, *Z. Phys. B: Condens. Matter* **85**, 327 (1991).
- <sup>11</sup>G.-L. Ingold and Y. V. Nazarov, *Single Charge Tunneling* (Plenum Press, New York, 1992), pp. 21–106.
- <sup>12</sup>B. A. Turek, K. W. Lehnert, A. Clerk, D. Gunnarsson, K. Bladh, P. Delsing, and R. J. Schoelkopf, *Phys. Rev. B* **71**, 193304 (2005).
- <sup>13</sup>F. Giazotto, T. T. Heikkilä, A. Luukanen, A. M. Savin, and J. P. Pekola, *Rev. Mod. Phys.* **78**, 217 (2006).
- <sup>14</sup>A. V. Timofeev, C. P. García, N. B. Kopnin, A. M. Savin, M. Meschke, F. Giazotto, and J. P. Pekola, *Phys. Rev. Lett.* **102**, 017003 (2009).

# Publication IV

V. F. Maisi, O.-P. Saira, Yu. A. Pashkin, J. S. Tsai, D. V. Averin and J. P. Pekola.  
Real-Time Observation of Discrete Andreev Tunneling Events. *Phys. Rev. Lett.* **106**, 217003 (2011).

© (2011) American Physical Society.

Reprinted with permission.



## Real-Time Observation of Discrete Andreev Tunneling Events

V. F. Maisi,<sup>1,2,\*</sup> O.-P. Saira,<sup>1</sup> Yu. A. Pashkin,<sup>3,†</sup> J. S. Tsai,<sup>3</sup> D. V. Averin,<sup>4</sup> and J. P. Pekola<sup>1</sup>

<sup>1</sup>*Low Temperature Laboratory, Aalto University, P.O. Box 13500, 00076 Aalto, Finland*

<sup>2</sup>*Centre for Metrology and Accreditation (MIKES), P.O. Box 9, 02151 Espoo, Finland*

<sup>3</sup>*NEC Green Innovation Research Laboratories and RIKEN Advanced Science Institute,*

*34 Miyukigaoka, Tsukuba, Ibaraki 305-8501, Japan*

<sup>4</sup>*Department of Physics and Astronomy, Stony Brook University, SUNY, Stony Brook, New York 11794-3800, USA*

(Received 28 February 2011; published 25 May 2011)

We provide a direct proof of two-electron Andreev transitions in a superconductor–normal-metal tunnel junction by detecting them in a real-time electron counting experiment. Our results are consistent with ballistic Andreev transport with an order of magnitude higher rate than expected for a uniform barrier, suggesting that only part of the interface is effectively contributing to the transport. These findings are quantitatively supported by our direct current measurements in single-electron transistors with similar tunnel barriers.

DOI: 10.1103/PhysRevLett.106.217003

PACS numbers: 74.50.+r, 73.23.-b, 73.40.Gk

Electronic transport across a boundary between conductors with dissimilar carriers is a nontrivial process. Of particular interest in this respect is the transport through a superconductor–normal-metal interface that at low energies is dominated by Andreev reflection [1–10], where a Cooper pair in a superconductor is converted into two electrons in the normal metal or vice versa. Here we employ electron counting techniques [11–17] to detect these Andreev events. Since the observed rate depends on the coherence of the two electrons involved in the transition, we obtain, as a result, a fingerprint of the junction electrodes and the tunnel barrier.

The techniques used for observing individual electrons are based on the Coulomb blockade effect where the electrostatic energy of a small metallic island changes noticeably when only one elementary charge  $e$  is placed on or removed from it. In the present experiment, we employ an isolated single-electron box where a superconducting island is connected to a normal metal one [17], but neither of these two is connected galvanically to the external circuitry. The electron tunneling rates between the islands are then sufficiently low to be monitored by low-frequency electrometry and are described in detail by relatively simple theoretical considerations [17,18]. We use a single-electron transistor (SET) [11–15,17,19–22] as an ultrasensitive electrometer. With charge sensitivity as good as  $10^{-5}e/\sqrt{\text{Hz}}$  [22–24], it is capable to detect individual electrons with high precision. In Fig. 1, we show a micrograph of our sample fabricated by standard  $e$ -beam processing.

The tunneling rates and resulting charge distribution between the two islands of the isolated box can be adjusted with an offset charge induced by a gate voltage. The electrostatic energy of a state with  $n$  excess electrons on one of the islands is given by  $E_n = E_c(n - n_g)^2$ , where  $E_c$  is the charging energy for individual electrons and  $n_g$  is the

normalized offset charge that can be viewed as the polarization charge on the gate capacitor and determines the energetically preferred way to occupy the different charge states  $n$  [20]. In Fig. 2(a), the two extreme cases are shown. In the Coulomb blockade regime for single electrons,  $n_g$  is an integer and the state  $n = n_g$  has the minimal energy  $E_n = 0$ . To enter an excited state, one electron can tunnel either into or out of the island [dotted black lines with arrows in Fig. 2(a)], but energy  $E_c$  has to be provided for the tunneling electron in addition to the Cooper pair breaking energy equal to or larger than the superconducting energy gap  $\Delta$  [25]. In the other extreme, at degeneracy with half-integer  $n_g$ , two electron states differing by charge  $e$  have equal minimal energy and hence are equally populated. The tunneling rate between them is higher than in the Coulomb blockade regime as no extra energy for charging is needed. For Andreev reflection [solid red lines with

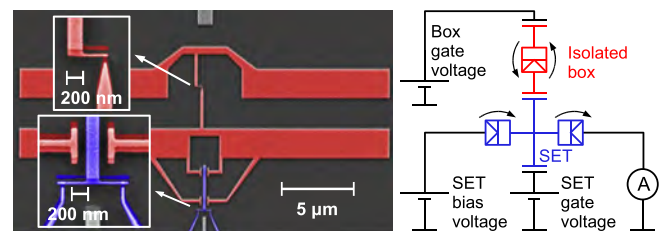


FIG. 1 (color online). Scanning electron micrograph of the measured structure and the schematic layout of the measurement setup. The isolated electron box consists of two metallic islands, seen as  $25 \mu\text{m}$  long rectangles (colored red). They are connected to each other by a normal-metal–insulator–superconductor tunnel junction. Tunneling of electrons through the junction is monitored with a dc SET electrometer (in blue) coupled capacitively to one of the box islands. The normal-metal–insulator–superconductor junction (top) and detector (bottom) are shown magnified on the left side of the main micrograph.

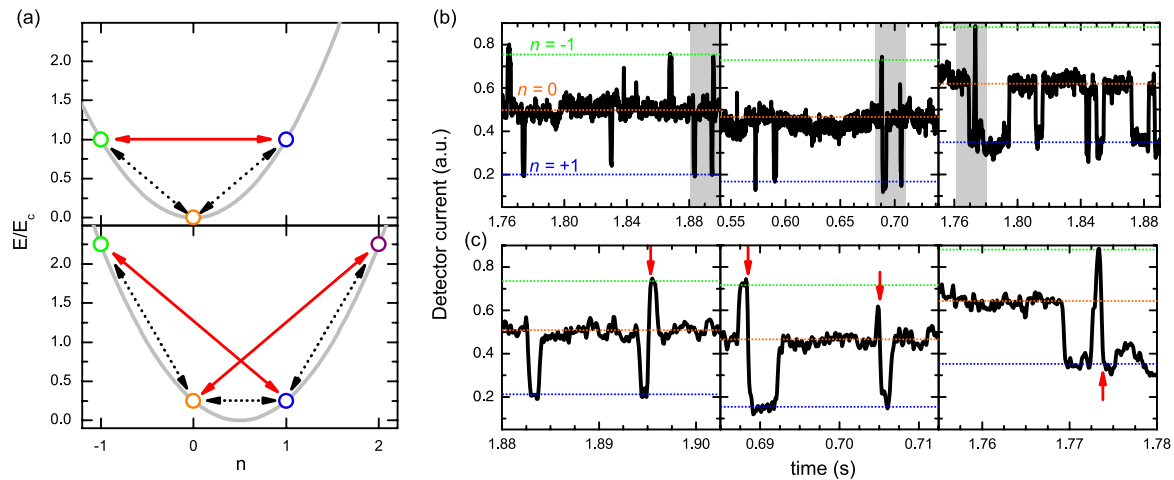


FIG. 2 (color online). Energy levels of the various charge states and typical observed time traces of the current through the detector. (a) Low lying levels of the box in the Coulomb blockade (upper panel) and at degeneracy (lower panel). Dotted (black) and solid (red) arrows indicate one- and two-electron processes, respectively. (b) Measured time traces of the detector current showing the charge state of the electron box as a function of time. The leftmost panel presents the case of Coulomb blockade. The rightmost panel depicts the opposite limit where the two charge states are equal in energy (degeneracy). The trace in the center is taken halfway between these two cases. (c) Gray sections of the traces of (b) zoomed. Vertical arrows indicate two-electron events.

arrows in Fig. 2(a)], the energy cost of charging is calculated similarly, but now the initial and final states are separated by two electrons, and the energy cost of breaking a Cooper pair is avoided since complete pairs tunnel at once.

In the experiment (see the supplemental material for additional details [26]), we measured time traces of the detector current at various biasing conditions of the box. With all the other parameters fixed, the detector gate voltage was adjusted to maximize charge sensitivity and dynamic range. The observed current jumps [Figs. 2(b) and 2(c)] are attributed to the tunneling events between the two islands. The switching rate depends on the gate voltage of the box and hence on its charge state, being lowest in the Coulomb blockade regime (leftmost panel) and highest at degeneracy (rightmost panel). The events observed in the traces [gray regions of Fig. 2(b) zoomed in 2(c)] indicate that individual electrons tunnel between the islands: In the Coulomb blockade regime they hop rarely from the lowest ( $n = 0$ ) to the higher ( $n = \pm 1$ ) energy states and back, while at degeneracy the electrons tunnel frequently between the two lowest states and only occasionally the system enters a higher lying level. More interestingly, the traces also show the coincident events, pointed out by the vertical arrows, where two electrons appear to tunnel simultaneously. In the following, we show that most of these events represent Andreev tunneling.

Because of the finite measurement bandwidth, limited to 1 kHz by the dc readout of the electrometer, events resembling two-electron Andreev tunneling could in principle arise from almost coincidental tunneling of two independent quasiparticles. To assess this option, we recorded time traces for several minutes at each gate offset value. From the traces we determined the distribution of the

time  $t$  spent in the state  $n = 0$  before a transition took place. In Fig. 3(a), we show such a distribution on the left for Coulomb blockade ( $n_g = 0$ ), in the center for  $n_g = 0.25$ , and on the right for near degeneracy ( $n_g = 0.45$ ). A direct transition (Andreev tunneling) between states  $n = \pm 1$  contributes here as essentially a  $t = 0$  event since the time separation between the two electrons tunneling in the Andreev process should be on the order of  $\hbar/\Delta$ , which is many orders of magnitude smaller than the time scales relevant in Fig. 3(a). Overall, the distribution is exponential as we have Poisson distributed one-electron tunneling processes. However, at small lifetimes in the Coulomb blockade regime, the data point indicated by the horizontal arrow does not follow the exponential dependence and corresponds to excessively many events. This clear separation of the short-lifetime events from the one-electron transitions shows that the majority of these events are not coincidental one-electron tunneling but rather two electrons tunneling concurrently. When the box offset charge is adjusted closer to degeneracy, the anomalous data point gradually merges to the rest of the data, in accordance with its interpretation in terms of Andreev transitions, since the energy cost of the two-electron tunneling increases. We emphasize that the charging energy should be small ( $E_c < \Delta$ ) for Andreev tunneling to occur, since for large  $E_c$ , it is not energetically favorable [17].

For quantitative analysis, we counted the number of events  $N_j$  for each possible forward and backward one- and two-electron tunneling process for each initial charge state  $n$ . The corresponding tunneling rate was then obtained as  $\Gamma_j = N_j / (\langle t \rangle N_\Sigma)$ , where  $\langle t \rangle$  is the average lifetime of the initial state  $n$  and  $N_\Sigma$  the total number of all transitions out of this state. The denominator  $\langle t \rangle N_\Sigma$  therefore corresponds to the total time spent in the initial state.

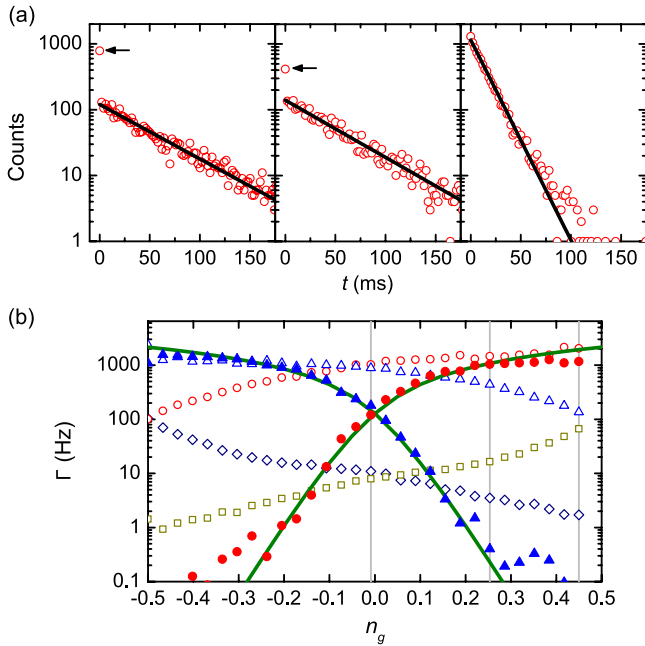


FIG. 3 (color online). Lifetime distributions and tunneling rates. (a) Lifetime distributions of the  $n = 0$  charge state in the Coulomb blockade, at an intermediate gate position, and close to degeneracy, from left to right. The corresponding gate positions are indicated by vertical lines in (b). Excessively many events at small times are pointed out by horizontal arrows. (b) One-electron (open symbols) and two-electron (solid symbols) tunneling rates estimated from the counted events at the base temperature. Red circles and blue triangles denote the tunneling rates out of states  $n = -1$  and  $1$ , respectively. Dark blue diamonds and dark yellow squares denote tunneling rates out of state  $0$  to states  $-1$  and  $1$ , respectively. Dark green solid lines present calculated Andreev rates with  $\zeta = 4 \times 10^{-5}$ .

Transitions with the charge number changing by  $\Delta n = \pm 2$  and occurring within  $0.4$  ms were interpreted as two-electron tunneling and all other events as one-electron tunneling. The time window was chosen such that it essentially captures all the excess events shown in the histograms of Fig. 3(a) but minimizes the number of coincidental one-electron events. The results for both processes at the temperature of  $60$  mK are shown in Fig. 3(b). The parameter values which determine the first-order tunneling rates in the box junction, the tunneling resistance  $R_T = 2$  M $\Omega$ , the superconducting energy gap  $\Delta = 216$   $\mu$ eV, and the charging energy  $E_c = 0.2\Delta$ , were determined from the one-electron tunneling rates measured at temperatures ranging from  $60$  to  $200$  mK as in Ref. [17].

For analyzing the Andreev tunneling rates quantitatively, we assume a ballistic model of the tunnel barrier. Then, the rate is given by Eq. (3) of Ref. [27]. Apart from the parameter values obtained from one-electron tunneling, the only parameter to be determined for the two-electron tunneling is its overall magnitude controlled by  $\zeta \equiv (\hbar/R_T e^2)/\mathcal{N}$ , where  $\mathcal{N}$  is the effective number of the conduction channels in the junction,  $\mathcal{N} = A/A_{\text{ch}}$ . Here  $A_{\text{ch}}$  is the area of one conduction channel and

$A = 40$  nm  $\times$   $35$  nm the junction area estimated from the scanning electron micrograph. Ideally, for our aluminum oxide tunnel barriers one should have  $A_{\text{ch}} \approx 2$  nm $^2$ ; see the supplemental material [26]. However, to fit the observed tunneling rates, we must adopt an order of magnitude higher value,  $A_{\text{ch}} = 30$  nm $^2$ , leading to an order of magnitude higher rates. As a result, we obtain the green lines of Fig. 3(b) for forward and backward tunneling, demonstrating a good agreement between theory and experiments at different charging energy costs tuned by  $n_g$ .

An order of magnitude larger area of a conduction channel is in line with independently performed SET measurements described in detail below and with the conclusions in, e.g., Refs. [6,10], for larger tunnel junctions that exhibit diffusive Andreev tunneling. We attribute this to the imperfections of the barrier, with only a small portion of the junction area dominating the transport. This fact can be understood by noting that the standard parameters of the aluminum oxide tunnel barriers [26,28,29] imply that, for example, variation of the barrier thickness by one atomic layer (i.e., by about  $0.3$  nm) results in the specific conductance change by about a factor of  $10$ . This means that even relatively small fluctuations of the barrier thickness of the magnitude of one to two atomic layers in comparison with the average barrier thickness of  $6$  atomic layers can reduce the effective area of the region dominating the barrier transparency to about  $10\%$  of the total junction area.

As an additional way of studying the two-electron tunneling, we measured current-voltage characteristics of basic SET structures with superconducting leads and a normal metal island. A micrograph of one of the four devices is shown in the inset in Fig. 4. All the SETs were fabricated in the same batch so that the junction area ( $E_c$ ) varies with constant  $\zeta \propto (AR_T)^{-1}$ . Here Andreev tunneling has to be extracted from the measured data containing a contribution also from one-electron processes. Each of the SETs was biased at voltage  $V$ , and the current  $I$  flowing through the device was measured. At each bias voltage, the gate offset of the island was varied so that the maximal and minimal currents, corresponding to degeneracy and Coulomb blockade, respectively, were observed. The measured current values between these extremes are shown as the colored regions in Fig. 4 for the four devices having different  $E_c$ . The parameter values for  $E_c$ ,  $R_T$ , and  $\Delta$  were determined from large scale data dominated by one-electron tunneling. Insets show the data for samples with the highest and lowest  $E_c$ . In the subgap region  $eV < 2\Delta$ , we have no current flowing through the highest charging energy sample (top) apart from the thermally activated single-electron tunneling. With smaller  $E_c$ , the onset of the Andreev current penetrates deeper into the subgap region with the threshold at  $eV = 2E_c$ , seen both in the experimental data and in the fits including Andreev processes (solid black lines), as the energy cost for two electrons tunneling into the island is lowered. With high

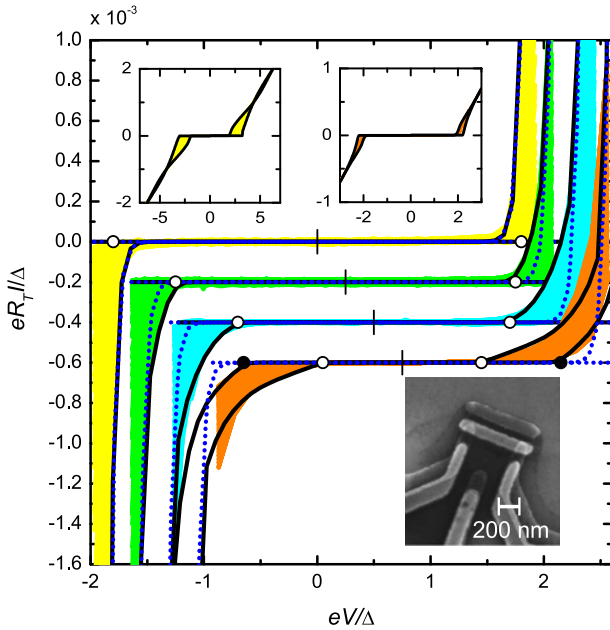


FIG. 4 (color online). Detection of Andreev current in SETs. Colored regions show measured subgap current for devices with charging energies  $E_c/k_B = 2.3, 1.9, 1.5,$  and  $0.86$  K from top (yellow) to bottom (orange) at all gate offset values. The insets depict the larger scale measurements for samples with the highest and lowest charging energies and a scanning electron micrograph of one of the measured SETs. Solid black lines are fitted theoretical curves at degeneracy (maximal current) and in Coulomb blockade (minimal current) when Andreev tunneling is taken into account. Dotted blue lines present fits excluding Andreev processes. Tunneling resistances of the samples were  $R_T = 129, 78, 55,$  and  $31$  k $\Omega$  in order of decreasing  $E_c$ , and superconducting gap  $\Delta = 216$   $\mu$ eV for all of them. Open (solid) circles present the expected thresholds  $eV = \pm 2E_c$  ( $eV = \pm 4E_c$ ) for Andreev tunneling at degeneracy (Coulomb blockade).

charging energies  $E_c \geq \Delta$ , it is sufficient to take into account only one-electron tunneling in the fits (dotted blue lines). In the numerical simulations for all the samples, we obtain as the only fit parameter for the subgap currents  $\zeta \approx 4 \times 10^{-4}$ , yielding the area of one conduction channel to be  $A_{\text{ch}} = 30$  nm<sup>2</sup>. This value was adopted to the analysis of the counting data above. Note that to increase the measured signal the SET junctions were oxidized less to have larger specific conductance ( $\zeta$ ) than the box junction.

In conclusion, we have detected tunneling in the time domain, allowing us to distinguish two-electron Andreev transitions from the usual one-electron processes unambiguously and on the level of individual events. This technique, unlike the direct current measurements, addresses the transition rates in the two directions separately, allowing for the study of the bias dependence of these rates also in the regime where currents are far too low to be detected by standard current measurements. The counting experiments disclose the detailed statistics of the two

processes, and the results are consistent with the direct current measurements performed: As a technological result, both measurements indicate that the tunnel barriers are nonuniform.

The work has been supported partially by the Academy of Finland, Technology Industries of Finland Centennial Foundation, Väisälä Foundation, the Finnish National Graduate School in Nanoscience, MEXT kakenhi “Quantum Cybernetics,” the JSPS through its FIRST Program, and the European Community’s Seventh Framework Program under Grant Agreement No. 218783 (SCOPE). D. V. A. was supported in part by IARPA.

\*ville.maisi@mikes.fi

†On leave from Lebedev Physical Institute, Moscow 119991, Russia.

- [1] A. F. Andreev, Zh. Eksp. Teor. Fiz. **46**, 1823 (1964) [Sov. Phys. JETP **19**, 1228 (1964)].
- [2] G. E. Blonder, M. Tinkham, and T. M. Klapwijk, Phys. Rev. B **25**, 4515 (1982).
- [3] T. M. Eiles, J. M. Martinis, and M. H. Devoret, Phys. Rev. Lett. **70**, 1862 (1993).
- [4] P. Lafarge *et al.*, Nature (London) **365**, 422 (1993).
- [5] F. W. J. Hekking and Y. V. Nazarov, Phys. Rev. B **49**, 6847 (1994).
- [6] H. Pothier *et al.*, Phys. Rev. Lett. **73**, 2488 (1994).
- [7] S. Rajauria *et al.*, Phys. Rev. Lett. **100**, 207002 (2008).
- [8] A. S. Vasenko *et al.*, Phys. Rev. B **81**, 094513 (2010).
- [9] J. Wei and V. Chandrasekhar, Nature Phys. **6**, 494 (2010).
- [10] T. Greibe *et al.*, Phys. Rev. Lett. **106**, 097001 (2011).
- [11] J. M. Martinis, M. Nahum, and H. D. Jensen, Phys. Rev. Lett. **72**, 904 (1994).
- [12] P. D. Dresselhaus *et al.*, Phys. Rev. Lett. **72**, 3226 (1994).
- [13] S. V. Lotkhov *et al.*, Appl. Phys. Lett. **75**, 2665 (1999).
- [14] W. Lu *et al.*, Nature (London) **423**, 422 (2003).
- [15] J. Bylander, T. Duty, and P. Delsing, Nature (London) **434**, 361 (2005).
- [16] T. Fujisawa *et al.*, Science **312**, 1634 (2006).
- [17] O.-P. Saira *et al.*, Phys. Rev. B **82**, 155443 (2010).
- [18] J. P. Pekola *et al.*, Phys. Rev. Lett. **105**, 026803 (2010).
- [19] P. Lafarge *et al.*, Z. Phys. B **85**, 327 (1991).
- [20] D. V. Averin and K. K. Likharev, J. Low Temp. Phys. **62**, 345 (1986).
- [21] T. A. Fulton and G. J. Dolan, Phys. Rev. Lett. **59**, 109 (1987).
- [22] G. Zimmerli *et al.*, Appl. Phys. Lett. **61**, 237 (1992).
- [23] V. A. Krupenin *et al.*, J. Appl. Phys. **84**, 3212 (1998).
- [24] L. Roschier *et al.*, Appl. Phys. Lett. **78**, 3295 (2001).
- [25] I. Giaever, Phys. Rev. Lett. **5**, 147 (1960).
- [26] See supplemental material at <http://link.aps.org/supplemental/10.1103/PhysRevLett.106.217003> for details about sample fabrication, measurements, data analysis, and channel size estimate.
- [27] D. V. Averin and J. P. Pekola, Phys. Rev. Lett. **101**, 066801 (2008).
- [28] Z. Tan *et al.*, Appl. Phys. Lett. **93**, 242109 (2008).
- [29] M. Prunnila *et al.*, J. Vac. Sci. Technol. B **28**, 1026 (2010).

# Publication V

T. Aref, V. F. Maisi, M. Gustafsson, P. Delsing and J. P. Pekola. Andreev tunneling in charge pumping with SINIS turnstiles. *Europhys. Lett.* **96**, 37008 (2011).

© (2011) EPLA.

Reprinted with permission.



# Andreev tunneling in charge pumping with SINIS turnstiles

T. AREF<sup>1,2(a)</sup>, V. F. MAISI<sup>2</sup>, M. V. GUSTAFSSON<sup>3</sup>, P. DELSING<sup>3</sup> and J. P. PEKOLA<sup>1</sup>

<sup>1</sup> *Low Temperature Laboratory, Aalto University - P.O. Box 13500, 00076 Aalto, Finland, EU*

<sup>2</sup> *Centre for Metrology and Accreditation (MIKES) - P.O. Box 9, 02151 Espoo, Finland, EU*

<sup>3</sup> *Department of Microtechnology and Nanoscience (MC2), Chalmers University of Technology SE-412 96 Göteborg, Sweden, EU*

received 20 June 2011; accepted in final form 9 September 2011

published online 13 October 2011

PACS 74.45.+c – Proximity effects; Andreev reflection; SN and SNS junctions

PACS 85.35.Gv – Single electron devices

PACS 06.20.F– – Units and standards

**Abstract** – We present measurements on hybrid single-electron turnstiles with superconducting leads contacting a normal island (SINIS). We observe Andreev tunneling of electrons influencing the current plateau characteristics of the turnstiles under radio-frequency pumping. The data is well accounted for by numerical simulations. We verify the dependence of the Andreev tunneling rate on the turnstile's charging energy. Increasing the charging energy effectively suppresses the Andreev current.

Copyright © EPLA, 2011

**Introduction.** – At the present time, there does not exist a quantum current standard though such standards exist for both voltage and resistance. A strong candidate for such a standard is a turnstile with a small normal metal island connected by tunnel junctions to superconducting leads (SINIS) [1]. These hybrid turnstiles pump electrons one at a time producing a well-defined current of  $I = ef$  where  $e$  is the electron charge and  $f$  is the frequency of pumping. Understanding and eliminating error processes in these turnstiles is vital for realizing a quantum metrological triangle (QMT), a key goal in metrology [2]. In closing the QMT, the three standards of voltage, resistance and current would be compared against each other via Ohm's law. Closing the QMT will allow the most accurate comparison of the Josephson constant  $K_J = 2e/h$  and the von Klitzing constant  $R_K = h/e^2$  (*i.e.* the charge of the electron and Planck's constant) to date.

There exist several potential quantum current standard candidates. The NIST seven junction pump has demonstrated a current accuracy of 1.5 parts in  $10^8$  [3,4] but is limited to maximum currents of approximately 1 pA. Other candidates with the potential for metrological accuracy at metrologically relevant currents include semiconductor tunable barrier pumps, charge-coupled device pumps [5], tunnel junction pumps [6–8], quantum dot pumps [9], surface acoustic wave pumps [10] and quantum phase slip nanowire pumps [11]. In general, the accuracy

of these quantum currents standards is not yet comparable to the accuracy of the quantum Hall and Josephson effect standards. A semiconducting quantum dot parallel pump recently demonstrated an accuracy of 1.5 in  $10^5$  at 54 pA [12]. The minimum required current magnitude for closing the metrological triangle is about 100 pA with an accuracy of about 1 part in  $10^8$ , which has not yet been achieved.

The SINIS turnstile operates by using energy barriers to control the flow of electrons. The normal metal island is capacitively coupled to a gate electrode. By applying an appropriate voltage to the gate, single electrons can be added and removed from the normal metal island. In essence, the SINIS turnstile operates as a single-electron transistor, with the superconducting gap providing extra protection against unwanted tunneling of the electrons.

There are multiple transport processes that can occur in a SINIS turnstile. The dominant one employed in charge pumping is sequential single-electron tunneling through the insulating barrier. The dominant two-electron process causing errors is Andreev tunneling. In Andreev tunneling, an electron in the normal metal is reflected as a hole (or a hole as an electron) at the interface of the NIS junction. This forms (or removes) a Cooper pair in the superconducting electrode and can be alternatively viewed as two electrons tunneling simultaneously across the insulating barrier [13]. It has been shown that errors arising from sequential  $1e$ -tunneling in turnstiles such as environmental activation can be effectively suppressed by proper

<sup>(a)</sup>E-mail: Thomas.Aref@aalto.fi

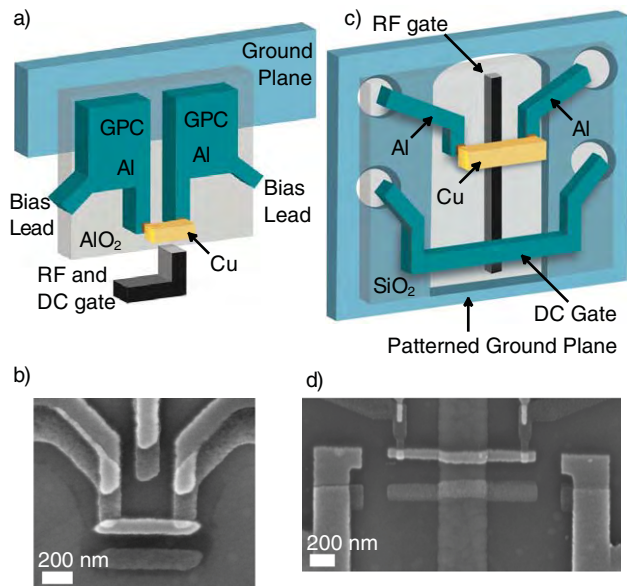


Fig. 1: (Colour on-line) Experimental set-up (a) Layout for sample of type one. The leads are coupled to the ground plane by large ground plane couplers (GPC) yet the turnstile itself is off the ground plane. (b) A SEM micrograph of the first sample type showing the turnstile and combined RF gate. The GPC and ground plane are not shown. This is sample S1 with junction area 50 nm by 125 nm. (c) The second sample set-up with the samples in the patterned part of the ground plane. The device design is modified to include a separate RF and DC gate. (d) A SEM micrograph of the second sample type showing the turnstile and the DC gate on top of the RF gate. This is sample S4 with junction area 60 nm by 70 nm.

filtering including an on-chip capacitively coupled ground plane [14]. Higher-order, multiple-electron error processes not eliminated by this filtering may then be observed. Many experimental observations of Andreev currents have been reported previously [15–17]. Andreev processes in devices with Coulomb blockade have been studied previously, both theoretically [18] and experimentally [13,19]. Only recently were individual Andreev reflection events detected in NIS junctions [20,21].

Here we demonstrate that the Andreev tunneling process is detectable in single-electron turnstile current pumping plateaus and that the resulting error effect can be minimized by increasing the charging energy of the turnstile. The data is well accounted for by numerical simulations with reasonable parameter values and the observed behavior is physically intuitive.

**Experiment.** – To form the SINIS turnstile, a normal copper island is connected to two superconducting aluminum electrodes using double angle evaporation with an intermediate oxidation step. Two types of devices were fabricated using electron beam lithography. The first type of sample used one step of lithography and aligned the device with a ground plane as shown in fig. 1(a). Large pads ensured capacitive coupling between the device and the ground plane, strongly suppressing environmental

noise [14,20]. These large pads are marked ground plane couplers (GPC) and are electrically isolated from the ground plane by atomic layer deposition (ALD) grown aluminum oxide. This device design allows simple single sample fabrication but is difficult to parallelize. A single gate line is used as both a DC gate and an RF gate. A scanning electron microscope (SEM) micrograph of the first type of sample is shown in fig. 1(b).

The second type of sample involves multiple steps of lithography as shown in fig. 1(c). In the first step, a ground plane is patterned to allow device fabrication on top of it. The turnstile sits in the patterned gap in the ground plane and only the leads are directly above it. Patterning the ground plane in this manner prevents formation of short circuits when wire bonding. After lithography, an insulating layer of silicon oxide is deposited by plasma-enhanced chemical-vapor deposition (PECVD). A second step of lithography is performed to form the turnstiles and individual DC gates for each turnstile. The lithography used a three layer mask with a hard germanium layer which allowed smaller features than the two-layer PMMA patterning used for the first type. The advantage of this fabrication method is that the separate DC gates enables parallelization. Parallelization is essential for metrological purposes as it is difficult to get large enough currents from a single device [22]. A SEM micrograph of the second type of sample is shown in fig. 1(d).

Measurements are done at a base temperature of approximately 70 mK. A typical current *vs.* voltage envelope measurement reveals the superconducting gap and single-electron transistor behavior of the turnstile as shown in fig. 2(a). To measure the pumped current of the turnstile, a fixed bias voltage is applied to one of the turnstile’s bias leads while current is measured on the other lead. A sine wave of amplitude  $V_{AC}$  (resulting in a normalized amplitude  $A_g = C_g V_{AC}/e$ ) with a frequency  $f$  is applied to the RF gate. As  $A_g$  increases past a threshold value, the likelihood of transporting one electron through the turnstile in a single cycle approaches unity, giving rise to a quantized current plateau.

We observe current quantization as shown in fig. 2(b). Zooming in on the current plateau reveals characteristic excess current above the expected  $I = ef$  behavior due to Andreev tunneling. For samples with small charging energy ( $E_C < \Delta$ ), as shown in fig. 2(c), the current plateau is enhanced above the expected value particularly for low  $A_g$  values in the plateau. These deviations are suppressed for samples with large charging energies ( $E_C > \Delta$ ), as shown in fig. 2(d). Amplifier gain is corrected on the  $10^{-3}$  level to match the simulated plateaus. This does not influence the interpretation of excess current on the  $10^{-2}$  level. Qualitatively, as  $A_g$  is increased for the situation  $E_C < \Delta$ , we encounter an energy threshold that permits Andreev tunneling before the single-electron tunneling threshold is encountered, allowing enhanced current flow for low charging energy samples. This charging energy dependence is indicative of the Andreev effect [20,23].

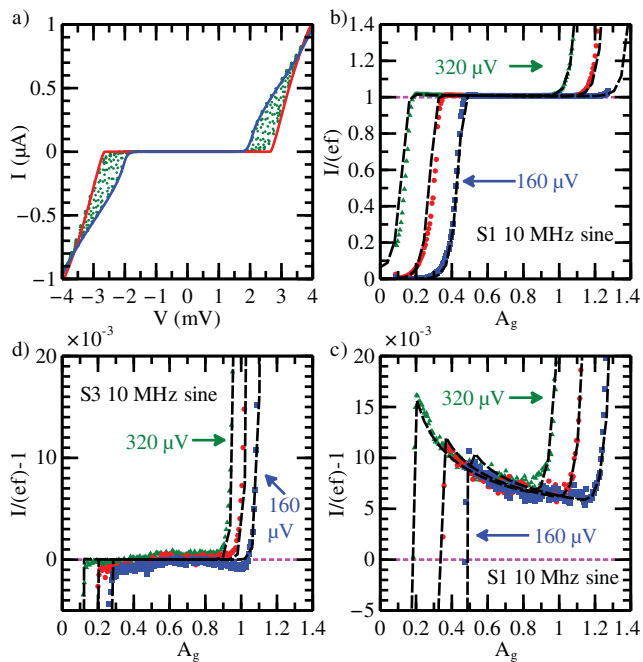


Fig. 2: (Colour on-line) 10 MHz sine wave current pumping with simulations. (a) DC current *vs.* voltage envelope measurement for sample S1 (green points). The red and blue lines are simulations of the measurement. (b) Current pumping plateaus for low-charging-energy sample S1 with a 10 MHz sine wave. (c) Close-up of (b) showing the Andreev tunneling. (d) Close-up of current pumping plateaus of sample S3 (high charging energy, low resistance) with a 10 MHz sine wave showing the absence of Andreev tunneling due to higher charging energy. Bias voltages are: 160  $\mu\text{V}$  (blue), 240  $\mu\text{V}$  (red) and 320  $\mu\text{V}$  (green) with a magenta dotted line at  $I = ef$  and simulations shown as black dashed lines in figures b-d.

Figure 3 shows close-ups of the current pumping plateaus for a different conditions. In fig. 3(a), pumping of sample S1 with a 10 MHz sine wave at a different range of biases than fig. 2 is shown. In fig. 3(b) the pumping curves for the high-charging-energy, high-resistance sample S2 show a reduction below the expected  $I = ef$  due to single-electron back tunneling. This increased back tunneling at high pumping amplitude is a first-order effect, which is due to the larger resistance of the high-charging-energy sample S2 compared to S3 [24]. Figures 3(c) and (d) show sample S1 pumped with a 10 MHz square wave and a 50 MHz sine wave.

The Andreev effect is visible in a wide range of biases as shown in figs. 2(b) and (c) and 3(a) with no visible dependence on bias voltage. Although the exact position of the plateau depends on bias, there is no separation of the plateaus due to bias dependence indicating this is not an environmental activation effect [14]. By fabricating high-charging-energy samples with low resistance, we can limit both the Andreev and back tunneling effects in the turnstiles as shown in figs. 2(d). This requires small junctions with highly transparent tunnel barriers *i.e.*

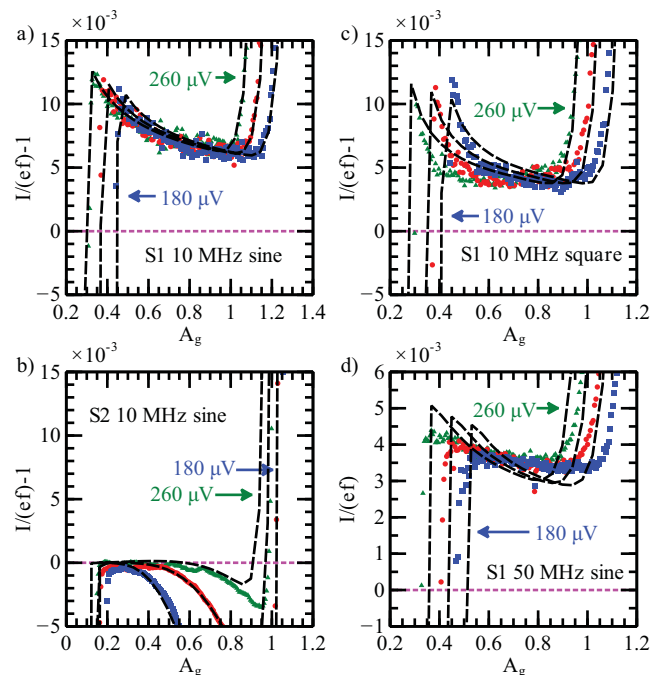


Fig. 3: (Colour on-line) Close-ups of frequency and waveform dependence of current pumping plateaus. (a) Pumping sample S1 with a 10 MHz sine wave showing the enhanced tunneling caused by the Andreev process. (b) Pumping of sample S2 (high charging energy, high resistance) with a 10 MHz sine wave showing the suppression of the enhanced Andreev tunneling. At high pumping amplitude, there is increased back tunneling compared to sample S3 due to the higher resistance of the junctions. (c) Pumping sample S1 with a 10 MHz square wave showing the different character of enhanced Andreev tunneling with a square wave drive. (d) Close-up of current pumping plateaus of sample S1 with a 50 MHz sine wave showing the smaller relative error at higher pumping frequency. The vertical scale has been changed compared to previous close-ups for clarity. The vertical scale in figures a-c are identical. The horizontal scale is not identical since the exact amplitude of RF drive applied to an individual device is not important. Bias voltages are: 180  $\mu\text{V}$  (blue), 220  $\mu\text{V}$  (red) and 260  $\mu\text{V}$  (green) with a magenta dotted line at  $I = ef$  and simulations shown as black dashed lines in all four figures.

junctions with low RC product as have been fabricated previously [24,25].

It should be noted that for device S3 with optimized tunnel barriers for suppressing Andreev and single-electron back tunneling there is still significant structure visible at the  $10^{-3}$  level. The exact origin of this structure is not yet clear. It is possibly due to quasi-particle relaxation in the aluminum leads or noise still penetrating the filtering system. Preliminary simulations indicate that this structure can be accounted for if we consider overheated superconducting leads but future research is needed in this area. The focus here was to demonstrate control over the Andreev error process. SINIS pumps are theoretically predicted to achieve an accuracy of 1 part in

$10^8$  with a current of 30 pA for a single pump [26]. The experimentally measured accuracy level to date is on the  $10^{-3}$  level *i.e.* 1 part in  $10^3$ .

**Theory.** – For the simulations shown in figs. 2 and 3, we calculate the average current flowing through the turnstile by numerically solving a master equation. The current through the left barrier (which is equal to the current through the right barrier in the steady state) is given by

$$I = e \sum_n [\Gamma_{LI}(n) - \Gamma_{IL}(n)] P(n, t), \quad (1)$$

where  $P(n, t)$  is the probability for finding  $n$  electrons on the central island at time  $t$ . The tunneling rate from the left lead to the island is  $\Gamma_{LI}(n) = \Gamma_{SN}(E_L^+(n)) + 2\Gamma_{AR}(E_L^{++}(n))$  and the tunneling rate from the island to the left lead is  $\Gamma_{IL}(n) = \Gamma_{NS}(E_L^-(n)) + 2\Gamma_{AR}(E_L^{--}(n))$ . The factor of two in front of the Andreev rate  $\Gamma_{AR}$ , compared to the single-electron rates  $\Gamma_{NS,SN}$ , is to account for the Andreev process transporting two electrons. The energy required to add or remove a single electron to/from the island (denoted by + or -) from the left or right lead (denoted by  $L$  or  $R$ ) is given by  $E_{L,R}^\pm = \pm 2E_C(n - n_g \pm 1/2) \pm eV_{L,R}$  where  $E_C = e^2/2C$  is the charging energy with  $C$  being the total capacitance of the island,  $n$  is the number of excess electrons on the island and  $n_g = C_g V_g / e$  is the normalized offset charge (the effective charge induced by applying a voltage  $V_g$  to the gate with capacitance  $C_g$ ) [27]. The energy required to add or remove two electrons to/from the island (denoted by ++ or --) in the Andreev process is given by  $E_{L,R}^{\pm\pm} = \pm 4E_C(n - n_g \pm 1) \pm 2eV_{L,R}$ .

The time dependence of the probability is given by the master equation [27,28]:

$$\begin{aligned} \frac{dP(n, t)}{dt} = & -\Gamma_{n,n} P(n, t) \\ & +\Gamma_{n-1,n} P(n-1, t) + \Gamma_{n+1,n} P(n+1, t) \\ & +\Gamma_{n-2,n} P(n-2, t) + \Gamma_{n+2,n} P(n+2, t), \end{aligned} \quad (2)$$

where

$$\begin{aligned} \Gamma_{n-1,n} &= \Gamma_{SN}(E_L^+(n-1)) + \Gamma_{SN}(E_R^+(n-1)), \\ \Gamma_{n+1,n} &= \Gamma_{NS}(E_L^-(n+1)) + \Gamma_{NS}(E_R^-(n+1)), \\ \Gamma_{n-2,n} &= \Gamma_{AR}(E_L^{++}(n-2)) + \Gamma_{AR}(E_R^{++}(n-2)), \\ \Gamma_{n+2,n} &= \Gamma_{AR}(E_L^{--}(n+2)) + \Gamma_{AR}(E_R^{--}(n+2)), \\ \Gamma_{n,n} &= \Gamma_{n,n-1} + \Gamma_{n,n+1} + \Gamma_{n,n-2} + \Gamma_{n,n+2}. \end{aligned} \quad (3)$$

Equation (2) tracks the flow of the probability. The higher-order Andreev tunneling effects are included by considering state changes from  $n$  to  $n \pm 2$  [26]. The rate at which single electrons tunnel from superconductor to normal metal  $\Gamma_{SN}$ , or the rate at which single electrons tunnel from the normal metal to the superconductor  $\Gamma_{NS}$ , are obtained using first-order perturbation theory [29,30].

Table 1: Sample parameters.

Name	$E_C/\Delta$	$R_T$ (k $\Omega$ )	$\Delta$ ( $\mu$ eV)	$A_{CH}$ (nm $^2$ )
S1	0.63	160	220	30
S2	2.2	1400	210	N/A
S3	1.4	430	210	N/A
S4	0.75	110	210	30

The Andreev tunneling rates  $\Gamma_{AR}$ , are given in eq. (3) in ref. [26] using second-order perturbative calculations. These rates depend on the charging energy  $E_C$ , the superconducting gap  $\Delta$ , and the tunneling resistance  $R_T$ . Values for these parameters are obtained from DC current *vs.* voltage envelope measurements (see inset of fig. 1) which depend only on  $\Gamma_{NS,SN}$ .  $\Gamma_{AR}$  has an additional fitting parameter since its magnitude is controlled by the quantity  $(\hbar/R_T e^2)/N$ , where  $N$  is the effective number of conduction channels,  $N = A/A_{CH}$  [26].  $A$  is the cross-sectional area of the junction estimated by scanning electron microscope (SEM) imaging (see fig. 1 for relevant images and area estimates) and  $A_{CH}$  is the effective area of a conduction channel used as a fitting parameter. Theoretically,  $A_{CH} \approx 2 \text{ nm}^2$  though fitted values are typically much larger than this value and are interpreted as resulting from inhomogeneities in the thickness of the oxide in the junctions [20]. In table 1, the fitting parameters  $E_C$  (in units of  $\Delta$ ),  $R_T$ ,  $\Delta$  and  $A_{CH}$  are listed for each of the samples simulated. Note that Andreev rate fitting parameters can not be determined for the high-charging-energy samples S2 and S3, since the Andreev effect is suppressed below the measurement noise.

The simulated probability evolution during charge pumping is shown in fig. 4(a) for various charge states. The corresponding rates of tunneling weighted by the occupation probabilities are shown in fig. 4(b). These plots are for simulations of sample S1 with  $V_L - V_R = 200 \mu\text{V}$ ,  $A_g = 0.74$  and  $f = 10 \text{ MHz}$ . Only forward tunneling is relevant here. In figs. 4(c) and (d), we show the calculated stability diamonds for samples S1 and S2, respectively. The minimal pair breaking energy for  $1e$ -tunneling is  $\Delta$  so the threshold for tunneling is  $E_{L,R}^\pm = \Delta$  which is shown as the blue line. For the Andreev tunneling, this pair breaking is avoided so the threshold for tunneling is  $E_{L,R}^{\pm\pm} = 0$  and is shown by the red dashed line.

**Results and discussion.** – In figs. 4(a) and (b), the probabilities and tunneling rates during one pumping cycle are shown for sample S1. As the transition rate from  $n=0$  to  $n=1$  grows, the probability for being in state  $n=0$  quickly drops in the beginning of the cycle and is replaced with a probability for being in state  $n=1$ . At the same time, there is a detectable Andreev tunneling rate for going from state  $n=0$  to  $n=2$  after which the  $n=2$  state quickly relaxes to  $n=1$  by single-electron tunneling. The low level occupation of the state  $n=2$  is also detectable. Likewise, the opposite process where an electron leaves the turnstile is observable in the second

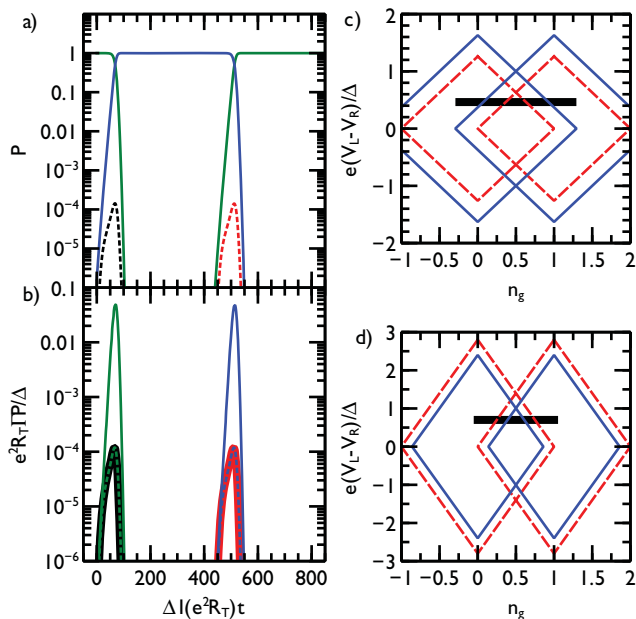


Fig. 4: (Colour on-line) (a) Probability evolution during charge pumping. The probability  $P(n, t)$  is shown for different values of  $n$ :  $n=0$  (green),  $n=1$  (blue),  $n=2$  (dotted black) and  $n=-1$  (dotted red). (b) Rates of tunneling weighted by probabilities of occupation. The single-electron tunneling rate through the left junction from  $n=0$  to  $n=1$  is shown in solid green. The Andreev tunneling rate from  $n=0$  to  $n=2$  is shown in dotted green and is on top of the relaxation rate from  $n=2$  to  $n=1$  via single-electron tunneling through the right electrode (thick black). Likewise, the single-electron tunneling rate through the right junction from  $n=1$  to  $n=0$  is shown in solid blue, the Andreev rate  $n=1$  to  $n=-1$  is shown in dotted blue and is on top of the relaxation rate from  $n=-1$  to  $n=0$  through the left junction (thick red). (c) Stability diagram of sample S1. The blue diamonds are the thresholds for single-electron tunneling, the red diamonds are the thresholds for Andreev tunneling and the thick black line is the pumping cycle used in (a) and (b). (d) Stability diagram of sample S2. The diamonds are reversed in order because of the higher charging energy of sample S2.

part of the pumping cycle. As before, when the rate from  $n=1$  to  $n=0$  grows, the most likely state becomes  $n=0$ . The transition for  $n=1$  to  $n=-1$  by Andreev tunneling is also seen whereafter the  $n=-1$  state quickly relaxes to  $n=0$  state by single-electron tunneling.

In figs. 2(b), 2(c) and 3(a), the pumping plateaus for six different biases and the corresponding fits are shown for the low-charging-energy ( $E_C < \Delta$ ) sample S1. There is excellent agreement between the fits and the data. By looking at the stability diagram shown in fig. 4(c), we can qualitatively understand the observed effect. The stability diagram shows tunneling thresholds *vs.* normalized bias voltage,  $V$ , and momentary gate charge,  $n_g$ . Starting in the diamond on the left, as the gate amplitude,  $A_g$ , is gradually increased, the Andreev threshold (shown as a red dotted line) is encountered first. Thus the Andreev process is most noticeable at low

$A_g$ . As  $A_g$  is increased further, we encounter the single-electron tunneling threshold and this process quickly dominates, obscuring the Andreev effect. This results in the enhanced current pumping plateau in figs. 2(c) and 3(a). For comparison, as can be seen in fig. 4(d), the high-charging-energy ( $E_C > \Delta$ ) sample, S2, encounters the single-electron tunneling threshold before the Andreev threshold. The Andreev effect is not observed as the electron has already tunneled before it enters the Andreev regime. Thus the plateau in figs. 3(d) and 2(d) is flat with no evidence of the enhanced tunneling effect.

The lack of dependence on bias seen in figs. 2(c) and 3(a) can similarly be explained by looking at the stability diagram. Changing the bias corresponds to changing the horizontal level of the black line in fig. 4(c). However, the Andreev tunneling thresholds run parallel to the single-electron tunneling thresholds so this has a very small effect on the observed current.

In fig. 3(c), the results from pumping with a 10 MHz square wave for sample S1 are shown. The square wave is modeled with an exponential rise to the applied voltage with risetime 2.5 ns. Compared to the sine wave pumping of the same frequency, the enhanced current for the square wave is more peaked and dies away more quickly. At an amplitude of  $A_g = 0.75$ , the square wave pumped plateau is almost flat with a current less than  $1.005ef$  (*i.e.* closer to the ideal value of  $I = ef$ ) while sine wave pumping with the same frequency and bias voltage has a plateau with significant slope at  $A_g = 0.75$  with a current greater than  $1.005ef$ . This behavior can also be qualitatively understood from the stability diagram. The square wave goes more immediately to the final  $A_g$  value thus spending less time in the vulnerable regions of the stability diagram. When we first encounter the Andreev threshold but before the single electron threshold is encountered, the Andreev process dominates and we see the sharp peak in current shown in fig. 3(c). As  $A_g$  is increased, we encounter the single-electron tunneling process threshold and the escape process is dominated by it. There is only a small possibility for the Andreev tunneling enhancement to occur since the square wave sweeps through that vulnerable region quickly. Thus the Andreev effect in the pumping plateau dies away more quickly for the square wave than for the sine wave.

In figs. 3(d), the pumping plateaus for a 50 MHz sine wave are shown with the Andreev effect visible for the low-charging-energy sample, S1. With higher frequency, more electrons are pumped per unit time producing a higher current. Thus the relative accuracy improves compared to the lower frequency 10 MHz sine wave shown in fig. 3(a) since the absolute value of the excess Andreev current remains roughly the same. The Andreev tunneling contribution to the current remains roughly unchanged because the same process as described for the lower frequency sine wave takes place. This results in the more flat slope of the 50 MHz pumping seen in fig. 3(d) but the Andreev process is still detectable. It should be noted

that the same sample parameters listed in table 1 were used for simulating 10 MHz sine wave, 10 MHz square wave and 50 MHz sine wave current pumping demonstrating the robustness of the simulation.

From the simulations, we extract an effective channel area on the order of  $30 \text{ nm}^2$  for the pumping (the effective channel area is difficult to determine precisely so the values are rounded to the nearest  $10$ 's of  $\text{nm}^2$ ). This was consistent for both samples S1 and S4 shown in fig. 1. For clarity of presentation, only the data and fits from sample S1 are shown in figs. 2 and 3. Samples S2 and S3 do not have a discernible Andreev parameter as it is suppressed by their high  $E_C$ . This is in general agreement with the effective area of  $30 \text{ nm}^2$  found in earlier work [20]. These values are approximately one order of magnitude larger than the theoretical channel area of approximately  $2 \text{ nm}^2$ , indicating that roughly only one tenth of the effective area of the junction is active in agreement with previous results [31,32].

We have shown that the enhanced current is dependent on  $E_C$ , pumping amplitude and pumping waveform shape but independent of pumping frequency and bias voltage. These are all characteristic signatures of Andreev tunneling that can be well accounted for by our theoretical model.

**Conclusion.** – We have observed the Andreev tunneling process in current pumping with a single-electron turnstile. This error process can be effectively suppressed with high charging energy leading us one step closer to a quantum current standard and completing the quantum metrological triangle. Andreev reflection as an error process can be fully eliminated with proper choice of  $E_C$  as demonstrated by these experiments.

\*\*\*

This work was funded in part by the European Community's Seventh Framework Programme under Grant Agreement No. 218783 (SCOPE), the Aalto University Postdoctoral Researcher Program and the National Doctoral Programme in Nanoscience (NGS-NANO).

## REFERENCES

- [1] PEKOLA J. P. *et al.*, *Nat. Phys.*, **4** (2008) 120.
- [2] FLOWERS J., *Science*, **306** (2004) 1324.
- [3] KELLER M. W., MARTINIS J. M., ZIMMERMAN N. M. and STEINBACH A. H., *Appl. Phys. Lett.*, **69** (1996) 1804.
- [4] KELLER M., EICHENBERGER A., MARTINIS J. and ZIMMERMAN N., *Science*, **285** (1999) 1706.
- [5] FUJIWARA A., ZIMMERMAN N. M., ONO Y. and TAKAHASHI Y., *Appl. Phys. Lett.*, **84** (2004) 1323.
- [6] GEERLIGS L. J. *et al.*, *Phys. Rev. Lett.*, **64** (1990) 2691.
- [7] POTHIER H. *et al.*, *Europhys. Lett.*, **17** (1992) 249.
- [8] LOTKHOV S. V., BOGOSLOVSKY S. A., ZORIN A. B. and NIEMEYER J., *Appl. Phys. Lett.*, **78** (2001) 946.
- [9] BLUMENTHAL M. D. *et al.*, *Nat. Phys.*, **3** (2007) 343.
- [10] SHILTON J. M. *et al.*, *J. Phys.: Condens. Matter*, **8** (1996) L531.
- [11] MOOIJ J. E. and NAZARON Y. V., *Nat. Phys.*, **2** (2006) 169.
- [12] GIBLIN S. P. *et al.*, *New J. Phys.*, **12** (2010) 073013.
- [13] HERGENROTHER J. M., TUOMINEN M. T. and TINKHAM M., *Phys. Rev. Lett.*, **72** (1994) 1742.
- [14] PEKOLA J. P. *et al.*, *Phys. Rev. Lett.*, **105** (2010) 026803.
- [15] ANDREEV A. F., *Sov. Phys. JETP*, **19** (1964) 1228.
- [16] BLONDER G. E., TINKHAM M. and KLAPWIJK T. M., *Phys. Rev. B*, **25** (1982) 4515.
- [17] TINKHAM M., *Introduction to Superconductivity* (Dover Publications) 1996.
- [18] HEKKING F. W. J., GLAZMAN L. I., MATVEEV K. A. and SHEKHTER R. I., *Phys. Rev. Lett.*, **70** (1993) 4138.
- [19] EILES T. M., MARTINIS J. M. and DEVORET M. H., *Phys. Rev. Lett.*, **70** (1993) 1862.
- [20] MAISI V. F. *et al.*, *Phys. Rev. Lett.*, **106** (2011) 217003.
- [21] SAIRA O.-P., KEMPPINEN A., MAISI V. F. and PEKOLA J. P., arXiv:1106.1326 (2011).
- [22] MAISI V. F. *et al.*, *New J. Phys.*, **11** (2009) 113057.
- [23] SAIRA O.-P., MÖTTÖNEN M., MAISI V. F. and PEKOLA J. P., *Phys. Rev. B*, **82** (2010) 155443.
- [24] KEMPPINEN A. *et al.*, *Appl. Phys. Lett.*, **94** (2009) 172108.
- [25] BRENNING H., KUBATKIN S. and DELSING P., *J. Appl. Phys.*, **96** (2004) 6822.
- [26] AVERIN D. V. and PEKOLA J. P., *Phys. Rev. Lett.*, **101** (2008) 66801.
- [27] AVERIN D. V. and LIKHAREV K. K., *J. Low Temp. Phys.*, **62** (1986) 345.
- [28] LIKHAREV K. K. and ZORIN A. B., *J. Low Temp. Phys.*, **59** (1985) 347.
- [29] INGOLD G. L. and NAZAROV Y. V., *Single Charge Tunneling, NATO ASI Ser. B*, Vol. **294** (Plenum Press, New York) 1992.
- [30] KEMPPINEN A. *et al.*, *Eur. Phys. J. ST*, **172** (2009) 311.
- [31] GREIBE T. *et al.*, *Phys. Rev. Lett.*, **106** (2011) 097001.
- [32] POTHIER H., GUERON S., ESTEVE D. and DEVORET M. H., *Phys. Rev. Lett.*, **73** (1994) 2488.

# Publication VI

O.-P. Saira, A. Kemppinen, V. F. Maisi and J. P. Pekola. Vanishing quasiparticle density in a hybrid Al/Cu/Al single-electron transistor. *Phys. Rev. B* **85**, 012504 (2012).

© (2012) American Physical Society.

Reprinted with permission.



# Vanishing quasiparticle density in a hybrid Al/Cu/Al single-electron transistor

O.-P. Saira,<sup>1</sup> A. Kemppinen,<sup>2</sup> V. F. Maisi,<sup>2</sup> and J. P. Pekola<sup>1</sup>

<sup>1</sup>*Low Temperature Laboratory, Aalto University, P.O. Box 15100, FI-00076 AALTO, Finland*

<sup>2</sup>*Centre for Metrology and Accreditation (MIKES), P.O. Box 9, FI-02151 Espoo, Finland*

(Received 2 January 2012; published 20 January 2012)

The achievable fidelity of many nanoelectronic devices based on superconducting aluminum is limited by either the density of residual nonequilibrium quasiparticles  $n_{qp}$  or the density of quasiparticle states in the gap, characterized by Dynes parameter  $\gamma$ . We infer upper bounds  $n_{qp} < 0.033 \mu\text{m}^{-3}$  and  $\gamma < 1.6 \times 10^{-7}$  from transport measurements performed on Al/Cu/Al single-electron transistors, improving previous results by an order of magnitude. Owing to efficient microwave shielding and quasiparticle relaxation, a typical number of quasiparticles in the superconducting leads is zero.

DOI: [10.1103/PhysRevB.85.012504](https://doi.org/10.1103/PhysRevB.85.012504)

PACS number(s): 74.78.Na, 74.45.+c, 74.81.Fa, 85.35.Gv

## I. INTRODUCTION

Active research and debate on the origin and density of residual quasiparticles in aluminum-based superconducting quantum circuits prevails currently.<sup>1,2</sup> Aluminum is a widely used metal in the field of low-temperature mesoscale electronics due to its superconducting properties and its tendency to form a native oxide that can be employed as a tunnel barrier. The practical performance of superconducting devices is often degraded by excess quasiparticle processes that do not follow from the assumption of full thermal equilibrium and Bardeen-Cooper-Schrieffer (BCS) form for the quasiparticle density of states of the superconducting electrodes. The figures of merit that we will address in this work are the density of nonequilibrium quasiparticles  $n_{qp}$  and the Dynes parameter  $\gamma$  for the normalized density of quasiparticle states in the gap. These parameters are presently major limiting factors for the coherence time of Josephson junction qubits,<sup>2-4</sup> relaxation time of highly sensitive radiation detectors,<sup>5</sup> the ultimate temperature reachable by normal-insulator-superconductor (NIS) junction refrigerators,<sup>6</sup> and potentially for the accuracy of the SINIS turnstile,<sup>7</sup> a contender for the realization of a metrologically accurate source of quantized electric current.

The lowest values for  $\gamma$  that have been obtained from subgap conductance measurements of NIS junctions and SINIS single-electron transistors (SETs) are  $2 \times 10^{-5}$  and  $1 \times 10^{-6}$ , respectively.<sup>7</sup> Subgap conductance of defect-free NIS junctions is dominated by two-particle Andreev tunneling.<sup>8</sup> For  $n_{qp}$ , studies on superconducting qubits<sup>2,3</sup> and resonators<sup>5</sup> have reported a low-temperature saturation to  $10\text{--}55 \mu\text{m}^{-3}$  due to an unidentified excitation mechanism. Recently, a significantly improved result  $n_{qp} < 1 \mu\text{m}^{-3}$  has been obtained by a transmon qubit realization.<sup>9</sup> A similar number can be inferred from the quasiparticle tunneling rates reported in Ref. 10 for a superconducting single-electron transistor (SET) design with normal-metal quasiparticle traps. In this work, we present quasiparticle transport measurements of Al/AIO<sub>x</sub>/Cu SETs combining carefully implemented shielding against external blackbody radiation and quasiparticle traps. The results yield unprecedented upper bounds  $n_{qp} < 0.033 \mu\text{m}^{-3}$  and  $\gamma < 1.6 \times 10^{-7}$ .

The experiment was performed on samples similar to that pictured in Fig. 1. We monitored the charge state on the central island of a hybrid, i.e., SINIS-type, SET using

another hybrid SET as an electrometer. The electrometer current  $I_{\text{det}}$  was read out using a room-temperature current amplifier in the so-called DC-SET configuration. Most of the capacitive coupling between the SETs was provided through a  $7 \mu\text{m}$  long Cr wire galvanically isolated from the SET metal layers. Following the technique introduced in Ref. 7, all electrical leads of the  $1 \times 1 \text{mm}^2$  pattern on the chip from the bonding pads to the active region were capacitively shunted by a conducting ground plane that was electrically isolated from the leads by the 25 nm AlO<sub>x</sub> layer. Pathways for quasiparticle trapping from the aluminum electrodes are provided by the overlap through the tunnel barrier oxide to the copper electrodes extending to within a few hundreds of nm of the tunnel junctions, and the ohmic contact between Al and Au films beginning  $10 \mu\text{m}$  away from the junctions. We also fabricated and measured a reference sample without the ohmic Al/Au contact, but having an otherwise equivalent design.

## II. THEORETICAL DESCRIPTION OF SINGLE-ELECTRON PROCESSES

The basis of our theoretical modeling of the charge transfer is the golden rule expression for the first-order tunneling rate,

$$\Gamma^{le}(E) = \frac{1}{e^2 R_T} \int_{-\infty}^{\infty} dE_1 \int_{-\infty}^{\infty} dE_2 n_S(E_1) f_S(E_1) \times [1 - f_N(E_2)] P(E_1 - E_2 + E), \quad (1)$$

where  $n_S(E) = |\text{Re} \frac{E}{\sqrt{E^2 - \Delta^2}}|$  is the quasiparticle density of states in the superconducting electrode,  $f_S$  ( $f_N$ ) is the occupation factor in the superconducting (normal) electrode, and  $P(E)$  is the probability to emit energy  $E$  to the electromagnetic environment during the tunneling. The occupation factors are taken to be Fermi functions at temperature  $T_N$  ( $T_S$ ), i.e.,  $f_{N,S}(E) = [1 + \exp(E/k_B T_{N,S})]^{-1}$ . The golden rule formula with  $P(E) = \delta(E)$ , equivalent to a zero-impedance environment, has been successfully used to describe a wide range of charge and energy transport phenomena in SINIS structures<sup>11</sup> in the range  $E \gtrsim \Delta$ . Next, we will consider theoretically the mechanisms that can cause excess quasiparticle processes in the subgap range  $E < \Delta$ .

(i) Even if charge transport is completely described by the above model, quasiparticle thermalization in both the N and S electrodes can be nontrivial at sub-kelvin temperatures due

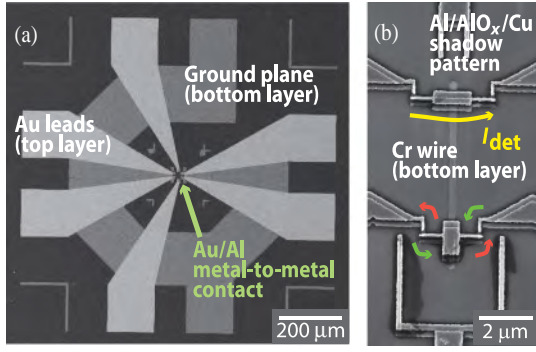


FIG. 1. (Color online) (a) Large scale electron micrograph of a sample showing the electrical connections to the active region in the middle. Portions of the ground plane, covered by an insulating  $\text{AlO}_x$  layer of 25 nm thickness, are also visible. (b) Active area of one of the measured samples, consisting of two  $\text{Al}/\text{AlO}_x/\text{Cu}/\text{AlO}_x/\text{Al}$  SETs that are coupled capacitively by a Cr wire located underneath the insulating layer. Arrows illustrate the monitored in- and out-tunneling events at the lower SET (green and red, respectively), and the macroscopic electrometer current (yellow) in a configuration where the upper SET is used as the electrometer. Shadow-evaporated leads terminate at ohmic Au/Al contacts beginning 10  $\mu\text{m}$  away from the junctions (not shown).

to strongly suppressed electron-phonon coupling. In a later section, we demonstrate that quasiparticle temperature  $T_N$  does not deviate significantly from the bath temperature  $T_0$  at temperatures above 50 mK. On the other hand, we characterize excess quasiparticle excitations in the superconductor by the density of nonequilibrium quasiparticles,

$$n_{\text{qp}} = 2D(E_F) \int_{\Delta}^{\infty} dE n_S(E) f_S(E), \quad (2)$$

where  $D(E_F)$  denotes the density of states at the Fermi energy. We use the literature value<sup>10</sup>  $D(E_F) = 1.45 \times 10^{47} \text{ m}^{-3} \text{ J}^{-1}$ . At base temperature, we have  $\Delta/(k_B T_N) \sim 50$ , and hence the induced quasiparticle tunneling in the gap assumes a bias-independent rate,

$$\Gamma_{\text{qp}}^{1e} = \frac{n_{\text{qp}}}{2e^2 R_T D(E_F)}. \quad (3)$$

(ii) Experimentally observed finite subgap conductance in NIS junctions is often modeled by introducing the lifetime broadened Dynes density of states<sup>12</sup> for the quasiparticle excitation spectrum of the S electrode,

$$n_S(E) = \left| \text{Re} \frac{E/\Delta + i\gamma}{\sqrt{(E/\Delta + i\gamma)^2 - 1}} \right|, \quad (4)$$

where parameter  $\gamma$  effectively expresses the quasiparticle density of states in the middle of the gap as a fraction of the density in the normal state. Equation (4) may not be valid far from the gap edges,<sup>13</sup> and we stress that in the present work the Dynes model is only used as a tool to assess the effect of subgap states on quasiparticle tunneling.

(iii) The  $P(E)$  function appearing in Eq. (1) can be calculated from the autocorrelation function of phase fluctuations over the junction.<sup>14</sup> In previous work,<sup>15</sup> it has been explicitly demonstrated that photon assisted tunneling (PAT) due to

microwave irradiation ( $f \gtrsim \Delta/h = 50 \text{ GHz}$ ) originating from outside the sample stage can be a dominant factor in the dynamics of metallic single-electron devices. In the present experiment, a known source of harmful phase fluctuations is the high-frequency component of detector back-action. It originates from the switching noise that results from loading and unloading the detector SET island as the probe current is transported through. In addition, blackbody radiation from higher-temperature stages of the cryostat can reach the junction due to insufficient filtering of the signal lines or leaks in the radiation shields enclosing the sample. The approximation  $P(E) = \frac{\pi S_V(lE/h)}{R_K E^2}$ , valid for  $E < 0$  and sufficiently weak  $S_V$ ,<sup>16</sup> gives a straightforward relation between the absorptive part of the  $P(E)$  and the power spectrum  $S_V(\omega)$  of the voltage noise over the junction. The above-described detector back-action is an instance of random telegraph noise (RTN), for which the relevant high-frequency part of the power spectrum can be written as  $S_V^{\text{det}}(\omega) = \left( \frac{\xi(\omega)\kappa e}{2C_{\Sigma}^{\text{det}}} \right)^2 \frac{|I_{\text{det}}|}{\pi e \omega^2}$ , where  $\kappa$  is the fraction of island charge coupled from the device under test (DUT) to the detector,  $C_{\Sigma}^{\text{det}}$  is the total capacitance of the detector SET island, and  $\xi(\omega)$  describes high-frequency attenuation of the Cr wire.<sup>17</sup>

(iv) Certain higher-order processes could appear in the experimental detector traces as single-electron processes. The processes in question are Andreev tunneling of a Cooper pair into the island followed by a rapid relaxation of a single quasiparticle through one-electron tunneling, and Cooper pair-electron cotunneling, which changes the charge on the island by one electron. Theoretical predictions for the rates can be made based on the results of Ref. 18 using the known sample parameters and a value  $g/\mathcal{N} = 10^{-5}$  for the normalized conductance per channel.<sup>19,20</sup> Predicted higher-order rates are orders of magnitude smaller than the experimental observations for bias voltages  $|V_{\text{ds}}| < 100 \mu\text{V}$ .

### III. EXPERIMENTAL METHODS

To determine experimentally the single-electron tunneling rate for a fixed bias voltage  $V_{\text{ds}}$ , the gate voltages were adjusted so that the detector was at a charge sensitive operating point, while the DUT was at charge degeneracy. At degeneracy, owing to sufficient  $E_c$  of the DUT, only the two degenerate charge states have a nonvanishing population. Hence the expected electrometer signal is RTN, and the transition rate is given by  $\Gamma = \Gamma^{1e}(eV_{\text{ds}}/2) + \Gamma^{1e}(-eV_{\text{ds}}/2)$ , where two identical junctions have been assumed. The state transitions were identified from the recorded electrometer traces by digital low-pass filtering followed by a threshold detector. We used the analytical model of Ref. 21 to compensate for missed transitions due to finite detector bandwidth.

To test the coupling of microwave radiation to the junctions, we repeated the experiments in several cryostats equipped with different wiring and shielding solutions. Two independent setups, henceforth denoted by PDR1 and PT, yield the lowest tunneling rates, suggesting that the external microwave radiation was suppressed to a negligible level. In both setups, standard solutions were used for the microwave filtering of the signal lines: 1 m of Thermocoax in PDR1 and a combination of Thermocoax and powder filters in PT. However, similar to

other recent works,<sup>22</sup> the sample chip was protected against radiation shining from the higher-temperature parts of the cryostats by two nested rf-tight shields. The microwave shields were attached to the sample stage body by either threads sealed with indium (PDR1), or by screws (PT). For illustration, we present data also from setup PDR2 that is similar to PDR1, but in which the Thermocoax lines terminate to a connector that was not sufficiently rf-tight.

#### IV. RESULTS AND CONCLUSIONS

Our main experimental data, the measured transition rates as a function of the device bias  $V_{ds}$ , are presented in Fig. 2. A saturation temperature below which the observed rates did not decrease was found around 80 mK. Using the value  $R_T = 1.1 \text{ M}\Omega$  ( $2.0 \text{ M}\Omega$  and  $25.0 \text{ M}\Omega$  for the junctions of the more asymmetric reference sample) obtained from device  $I$ - $V$  characteristic measured with an ordinary ammeter, we determined the value  $\Delta = 210 \mu\text{V}$  by fitting the 158 mK data to the thermally activated (TA) rates assuming  $T_N = T_S = T_0$ . The large scale  $I$ - $V$  characteristic is consistent with this value. Data obtained at 131 mK agrees with TA predictions for 135 mK except in the range  $|V_{ds}| < 25 \mu\text{V}$ , where the TA rates become comparable to the saturation floor. In contrast, the theoretical TA rates for 50 mK are below 0.01 Hz in the  $V_{ds}$  range that was accessible in the counting experiment.

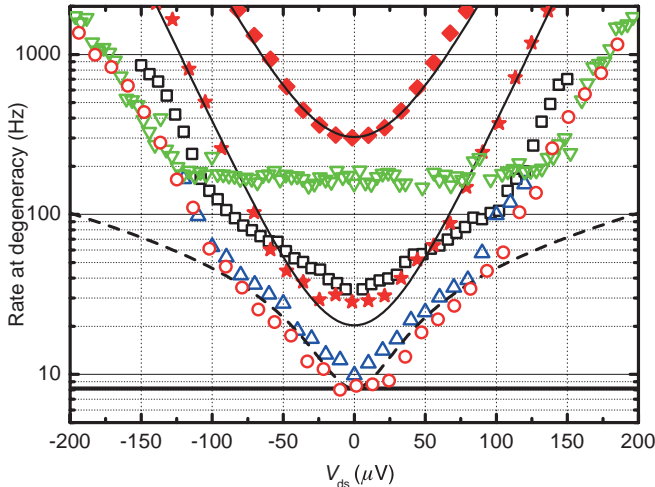


FIG. 2. (Color online) Bandwidth-corrected single-electron tunneling rates as a function of  $V_{ds}$  at charge degeneracy measured in different setups at base temperature: PT (18 mK, open upward triangles), PDR1 (50 mK, open circles), and PDR2 (50 mK, open squares). For PDR1, data from higher temperatures is also given: 131 mK (filled stars) and 158 mK (filled diamonds). All these measurements were performed with the same sample employing Au/Al contacts for quasiparticle trapping. The two thin solid lines represent thermally activated rates calculated for the known sample parameters at 158 mK and 135 mK. The dashed line is the theoretical rate for  $\gamma = 1.6 \times 10^{-7}$  at  $T_S = T_N = 50 \text{ mK}$ , and the horizontal thick line represents the rate induced by  $n_{qp} = 0.033 \mu\text{m}^{-3}$ . Open downward triangles: Base temperature data from a reference sample without Al/Au contacts measured in PDR1. For ease of comparison, tunneling rates from the reference sample have been scaled by the ratio of junction conductances  $\frac{G_L + G_R}{G_L^{ref} + G_R^{ref}}$ .

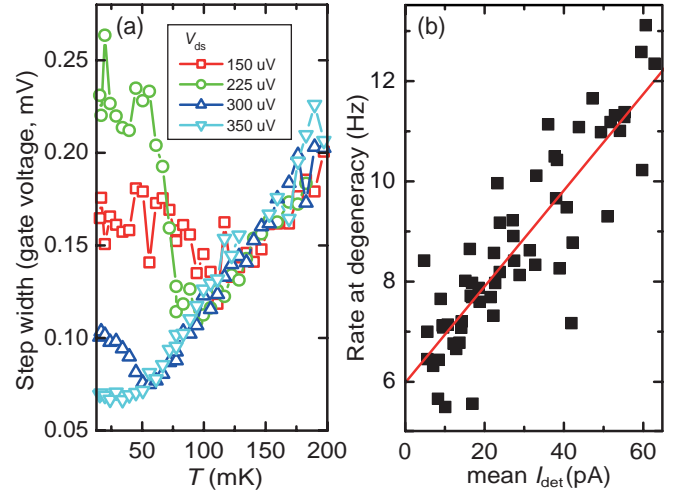


FIG. 3. (Color online) (a) Measured width of the Coulomb staircase steps as a function of bath temperature for different bias voltages of the DUT. (b) Observed zero-bias tunneling rates at base temperature for different detector currents, and a linear fit to the data. The plotted current is the mean value of the detector trace from which the transition rate was determined.

In order to aid the analysis of the base temperature results, we present two auxiliary results ruling out plausible explanations for the observed low-temperature saturation. First, to demonstrate the thermalization of the normal-metal island to 50 mK, we study the width of the transition between two charge states as the gate charge of the DUT is swept past a degeneracy point, following the procedure of Ref. 15. The obtained step widths in PT cryostat are presented in Fig. 3(a). For bias voltages far below the gap edge, anomalous broadening of the step at low temperatures is a clear indication of nonthermal processes. However, at the highest studied bias voltage  $V_{ds} = 350 \mu\text{V}$ , the linear TA regime extends down to 50 mK. Biasing of the DUT does not affect the temperature of the normal-metal island as the electronic cooling power for  $|V_{ds}| \leq 350 \mu\text{V}$  is negligible.<sup>6</sup>

Secondly, we studied experimentally the influence of detector back-action by measuring zero-bias rates at the base temperature at different operating points of the detector. A linear dependence of  $\Gamma$  on  $I_{det}$  can be observed in the data from PDR1 cryostat presented in Fig. 3(b) as predicted by the  $P(E)$  theory for the small detector currents employed here ( $I_{det} \ll e\Delta/h$ ). By extrapolating to zero detector current, we deduce that for the typical detector current of 30 pA in the time traces on which Fig. 2 is based, the contribution from detector back-action is 2-3 Hz, which is a significant but not a dominating fraction.

The tunneling rate data from the reference sample without Al/Au contacts shown in Fig. 2 displays a clear plateau consistent with a quasiparticle density of  $n_{qp} = 0.69 \mu\text{m}^{-3}$ . For this sample, the dominant quasiparticle relaxation channel at base temperature is tunneling through the oxide barrier to the normal-metal shadow. This allows us to infer a homogenous injection rate of  $r_{qp} = 3 \times 10^5 \text{ s}^{-1} \mu\text{m}^{-3}$ , presumably due to external radiation. Applying the quasiparticle diffusion model of Ref. 2 with a thermal energy distribution, the Al/Au contacts are expected to bring about a 100-fold reduction in  $n_{qp}$  at the

junctions. From the observed rates in PDR1 and PT setups, we can infer the previously stated upper bound  $n_{qp} < 0.033 \mu\text{m}^{-3}$  for the sample with Al/Au contacts as illustrated in the figure, i.e., a 20-fold reduction. Given the nominal thickness of 30 nm for the aluminum film, we find that the expected number of quasiparticles in the total volume of one of the aluminum leads is less than 0.1, i.e., the superconductors are nearly free of quasiparticles in a time-averaged sense.

However, based on the absence of a flat plateau in experimental bias dependence, nonequilibrium quasiparticles cannot account for a majority of the observed base temperature tunneling events. The curve for Dynes model with  $\gamma = 1.6 \times 10^{-7}$  is a better match to the experimental results in the range  $|V_{ds}| < 100 \mu\text{V}$ , more so for the data from PT cryostat, but the present amount of data does not allow one to make a definite statement about the presence of subgap states at the  $\gamma \sim 10^{-7}$  level.

Finally, it should be noted that the base temperature tunneling rate at zero bias is four times higher in the imperfectly shielded PDR2 setup compared to those achieved in PDR1 and PT setups. Elevated rates in PDR2 are caused by PAT due to stray blackbody radiation. The results from PDR1 and PT are very similar, and part of the discrepancy between them can be attributed to uncertainty in the detector bandwidth compensation (in the notation of Ref. 21,  $\Gamma_{det} = 2000 \text{ Hz}$  for

PDR1 and 125 Hz for PT) and different probing current. Also, for the high base temperature tunneling rates in bias range 100–200  $\mu\text{V}$ , we find PAT to be a plausible explanation. The observed rates can be reproduced by assuming a microwave noise spectrum with an exponential high-frequency cutoff corresponding to an effective temperature of 175 mK, and a spectral density of the order of 1 pV/ $\sqrt{\text{Hz}}$  at  $f = 50 \text{ GHz}$ .

In conclusion, we have demonstrated that microwave shielding and enhanced quasiparticle relaxation play a key role in achieving the highest possible performance of superconducting aluminum based devices. The possibility to employ these techniques in future realizations of quantum information processing devices presents exciting prospects.

#### ACKNOWLEDGMENTS

We acknowledge M. Möttönen, C. Flindt, P. Delsing, and T. Aref for valuable discussions during drafting of the manuscript. This work has been supported by the Academy of Finland, Väisälä Foundation, the Finnish National Graduate School in Nanoscience, Technology Industries of Finland Centennial Foundation, and the European Community's Seventh Framework Programme under Grant Agreements No. 217257 (EURAMET joint research project REUNIAM), No. 218783 (SCOPE), and No. 238345 (GEOMDISS).

<sup>1</sup>G. Catelani, J. Koch, L. Frunzio, R. J. Schoelkopf, M. H. Devoret, and L. I. Glazman, *Phys. Rev. Lett.* **106**, 077002 (2011); M. Lenander *et al.*, *Phys. Rev. B* **84**, 024501 (2011).

<sup>2</sup>J. M. Martinis, M. Ansmann, and J. Aumentado, *Phys. Rev. Lett.* **103**, 097002 (2009).

<sup>3</sup>M. D. Shaw, R. M. Lutchyn, P. Delsing, and P. M. Echternach, *Phys. Rev. B* **78**, 024503 (2008).

<sup>4</sup>Y. Makhlin, G. Schön, and A. Shnirman, *Rev. Mod. Phys.* **73**, 357 (2001).

<sup>5</sup>P. J. deVisser, J. J. A. Baselmans, P. Diener, S. J. C. Yates, A. Endo, and T. M. Klapwijk, *Phys. Rev. Lett.* **106**, 167004 (2011); R. Barends, J. J. A. Baselmans, S. J. C. Yates, J. R. Gao, J. N. Hovenier, and T. M. Klapwijk, *ibid.* **100**, 257002 (2008); R. Barends, S. vanVliet, J. J. A. Baselmans, S. J. C. Yates, J. R. Gao, and T. M. Klapwijk, *Phys. Rev. B* **79**, 020509 (2009).

<sup>6</sup>F. Giazotto *et al.*, *Rev. Mod. Phys.* **78**, 217 (2006).

<sup>7</sup>J. P. Pekola, V. F. Maisi, S. Kafanov, N. Chekurov, A. Kemppinen, Y. A. Pashkin, O. P. Saira, M. Möttönen, and J. S. Tsai, *Phys. Rev. Lett.* **105**, 026803 (2010).

<sup>8</sup>T. Greibe, M. P. V. Stenberg, C. M. Wilson, T. Bauch, V. S. Shumeiko, and P. Delsing, *Phys. Rev. Lett.* **106**, 097001 (2011).

<sup>9</sup>H. Paik *et al.*, *Phys. Rev. Lett.* **107**, 240501 (2011).

<sup>10</sup>N. A. Court, A. J. Ferguson, R. Lutchyn, and R. G. Clark, *Phys. Rev. B* **77**, 100501 (2008).

<sup>11</sup>O. P. Saira, M. Meschke, F. Giazotto, A. M. Savin, M. Möttönen, and J. P. Pekola, *Phys. Rev. Lett.* **99**, 027203 (2007).

<sup>12</sup>R. C. Dynes, V. Narayanamurti, and J. P. Garno, *Phys. Rev. Lett.* **41**, 1509 (1978); R. C. Dynes, J. P. Garno, G. B. Hertel, and T. P. Orlando, *ibid.* **53**, 2437 (1984).

<sup>13</sup>B. Mitrovic and L. A. Rozema, *J. Phys. Condens. Matter* **20**, 015215 (2008).

<sup>14</sup>G.-L. Ingold and Y. V. Nazarov, *Single Charge Tunneling* (Plenum Press, New York, 1992), pp. 21–106.

<sup>15</sup>O. P. Saira, M. Möttönen, V. F. Maisi, and J. P. Pekola, *Phys. Rev. B* **82**, 155443 (2010).

<sup>16</sup>J. M. Martinis and M. Nahum, *Phys. Rev. B* **48**, 18316 (1993).

<sup>17</sup>The expression is valid for a detector with two active charge states assuming transition rates between them are much smaller than  $\omega$ .

<sup>18</sup>D. V. Averin and J. P. Pekola, *Phys. Rev. Lett.* **101**, 066801 (2008).

<sup>19</sup>The estimate for  $g/\mathcal{N}$  is extrapolated from values of Ref. 20 by scaling with junction area and resistance.

<sup>20</sup>V. F. Maisi, O. P. Saira, Y. A. Pashkin, J. S. Tsai, D. V. Averin, and J. P. Pekola, *Phys. Rev. Lett.* **106**, 217003 (2011).

<sup>21</sup>O. Naaman and J. Aumentado, *Phys. Rev. Lett.* **96**, 100201 (2006).

<sup>22</sup>R. Barends *et al.*, *Appl. Phys. Lett.* **99**, 113507 (2011); A. Kemppinen *et al.*, *ibid.* **99**, 142106 (2011).

# Publication VII

**H. S. Knowles, V. F. Maisi and J. P. Pekola. Probing quasiparticle excitations in a hybrid single electron transistor. *Appl. Phys. Lett.* 100, 262601 (2012).**

© (2012) American Institute of Physics.

Reprinted with permission.



## Probing quasiparticle excitations in a hybrid single electron transistor

H. S. Knowles,<sup>1,2</sup> V. F. Maisi,<sup>1,3</sup> and J. P. Pekola<sup>1</sup>

<sup>1</sup>Low Temperature Laboratory (OVLL), Aalto University, P.O. Box 15100, FI-00076 AALTO, Finland

<sup>2</sup>Cavendish Laboratory, University of Cambridge, JJ Thomson Avenue, Cambridge CB3 0HE, United Kingdom

<sup>3</sup>Centre for Metrology and Accreditation (MIKES), P.O. Box 9, FI-02151 Espoo, Finland

(Received 6 April 2012; accepted 6 June 2012; published online 26 June 2012)

We investigate the behavior of quasiparticles in a hybrid electron turnstile with the aim of improving its performance as a metrological current source. The device is used to directly probe the density of quasiparticles and monitor their relaxation into normal metal traps. We compare different trap geometries and reach quasiparticle densities below  $3 \mu\text{m}^{-3}$  for pumping frequencies of 20 MHz. Our data show that quasiparticles are excited both by the device operation itself and by the electromagnetic environment of the sample. Our observations can be modelled on a quantitative level with a sequential tunneling model and a simple diffusion equation. © 2012 American Institute of Physics. [<http://dx.doi.org/10.1063/1.4730407>]

Applications of superconductors generally rely on the fact that electronic excitations can be generated only if energy higher or equal to the gap energy  $\Delta$  is available. Hence the number of the excitations is ideally exponentially small at low temperatures and the properties specific for superconductors appear. If the number of excitations, typically characterized by the density of quasiparticles, increases, the superconducting features degrade. Such an effect has been studied in several devices such as superconducting qubits,<sup>1–4</sup> superconductor-insulator-normal metal-insulator-superconductor (SINIS) microcoolers,<sup>5–8</sup> and kinetic inductance detectors.<sup>9,10</sup> In this letter, we focus on the effects of quasiparticles on a hybrid single-electron transistor. We use the Coulomb blockaded transistor for direct and simple probing of the quasiparticle excitation density. The device operates as a charge pump and is a promising candidate for the realization of a metrological current source.<sup>11</sup> We show experimentally that the quasiparticle excitations limit the current quantization. By optimizing the quasiparticle relaxation, however, we estimate that it is possible to reach metrological accuracy.

In order to observe how quasiparticles influence the performance of the turnstile, we designed samples (type A) where the quasiparticle relaxation in normal metal traps was purposefully delayed by extending the bare superconducting lines that connect the junctions to the traps. The beginning of this isolated superconducting line can be seen in the scanning electron microscope image of the turnstile in Fig. 1(a), where it connects to the normal metal island via oxide junctions that appear as lighter areas. Its extension is visible in (c) all the way through to the wide traps of overlapping superconductor and normal metal separated by an oxide layer. The sample shown in (b) (type B) has wide leads with normal metal traps close to the junctions to enable efficient quasiparticle evacuation. The samples were fabricated with the standard electron-beam lithography and shadow mask technique.<sup>12</sup> We compare the behaviour of quasiparticles in SINIS turnstile samples with different geometries. The length of the isolated superconducting line (given by the separation of the transistor junction from the trap) was varied

between  $l = 200 \text{ nm}$  and  $l = 20 \mu\text{m}$ . Measurements were performed in a dilution refrigerator at a base temperature of approximately 60 mK.

Figure 1(d) shows the current-voltage characteristics of the turnstile sample presented in (a) and (c). The black line shows the current through the turnstile when the bias voltage  $V_b$  is swept across the superconducting gap and the gate potential  $V_g$  is varied between the gate open ( $n_g = 0.5$ ) and the gate closed ( $n_g = 0$ ) states. Simulations based on sequential tunnelling are fitted to the data in order to extract the parameters of the superconducting gap  $\Delta = 216 \mu\text{eV}$ , the charging energy of the island  $E_c = 0.74\Delta$ , and the tunnelling resistance of the junction  $R_T = 91 \text{ k}\Omega$ , specific to each sample (see Table I for parameters of all samples measured). These simulations are shown in blue for the gate open and red for the gate closed state. On this coarse level, the heating

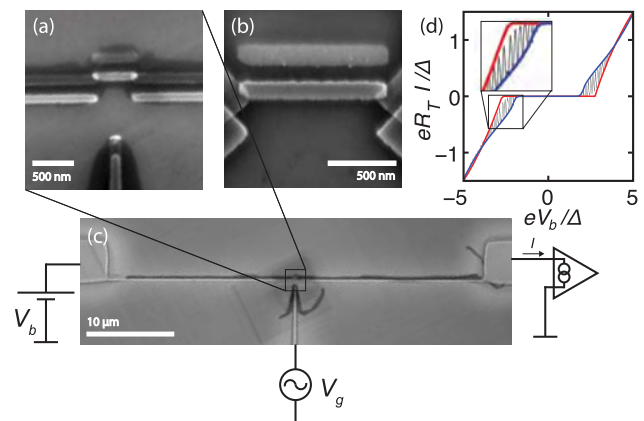


FIG. 1. (a) Scanning electron micrograph of the  $l = 20 \mu\text{m}$  type A SINIS20 turnstile showing the superconducting Al leads connected to the Cu metal island via  $\text{AlO}_2$  barrier junctions and the gate electrode used to regulate the potential of the island. (b) shows the type B SINISopen geometry sample where the normal metal traps are within 200 nm of the junctions and the leads open up straight from the junction. In (c), the full length  $l$  of the superconducting line of sample SINIS20 between the junction and the trap is visible as well as the quasiparticle traps formed by overlapping Cu and Al shadows. A sketch of the basic measurement circuitry is depicted and (d) shows the IV characteristics of the turnstile.

TABLE I. Sample parameters.

Sample	$E_c/\Delta$	$R_T$ (k $\Omega$ )	$l$ ( $\mu$ m)	$w_1$ (nm)	$w_2$ ( $\mu$ m)	$\sigma_T$ (( $\Omega$ m <sup>2</sup> ) <sup>-1</sup> )
SINIS20	0.74	91	21	120	5	$2.3 \times 10^9$
SINIS5	0.7	81	5.4	120	5	$2.7 \times 10^9$
SINIS1	0.7	85	1.1	160	5	$9.5 \times 10^8$
SINISopen	1.2	170	–	–	–	$1.0 \times 10^9$

of the superconducting leads does not make a significant contribution and can be neglected. The overheating of the normal metallic island (thickness 30 nm) is taken into account by considering the electron-phonon coupling with material parameter value of  $\Sigma = 2 \times 10^9$  WK<sup>-5</sup>m<sup>-3</sup> which is consistent with values obtained in previous experiments.<sup>13,14</sup> In the subgap and pumping experiments, we have the opposite situation: the island does not heat since the signals are much smaller but as we look at small differences, the overheating of the superconductor starts to have an effect.

We now investigate the current of the turnstile more closely for bias voltages within the superconducting gap. These measurements allow the direct probing of the quasiparticle density. This is not possible with voltage biased NIS junctions that probe the excitations more indirectly<sup>5–8,15</sup> and correspond to the gate open case in these experiments. Figure 2(a) shows the current as a function of  $V_b$  and  $V_g$ . With no quasiparticles present, we would expect zero current for low biases. However, we observe a current pattern periodic in  $V_g$  within the gap with currents rising up to 10 fA. We find that we can reproduce the measured current pattern with a simulation shown in panel (c) using a high superconductor temperature  $T_S$  that gives rise to a quasiparticle population above the gap. We compute the average current through the

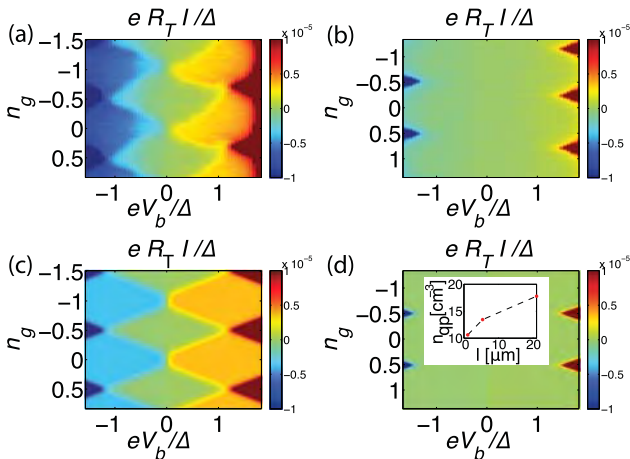


FIG. 2. (a) and (b) show the normalized current through the oxide trap turnstile of geometry  $l = 20 \mu\text{m}$  smoothed over 5 data points as a function of  $V_b$  for gate voltages varying between  $n_g = 0$  and  $n_g = 0.5$ . The charge stability measurement plotted in (a) was performed in a sample stage with a single cover; (b) shows measurements of the same sample in an indium sealed two-cover stage. In (c) and (d), we plot the normalized current computed with a simulation based on sequential tunneling for the situations of (a) and (b), respectively. The inset of (d) shows the quasiparticle density  $n_{qp}$  inferred from the temperature reproducing the measured current inside the superconducting gap as a function of the length  $l$  of the isolated superconducting line.

left junction via  $I = e \sum_n (\Gamma_{LI}(n) - \Gamma_{IL}(n)) P(n, t)$ , where  $\Gamma_{LI(IL)}$  is sequential tunnelling rate to (from) the island through the left junction and  $P(n, t)$  is the probability of the system being in the charge state  $n$  of the island. The temperatures used to fit these data are  $T_S = 205$  mK and the normal metal temperature  $T_N = 92$  mK. The current-voltage characteristics are surprising: At degeneracy (half integer  $n_g$ ) no net current flows, whereas in Coulomb blockade (integer  $n_g$ ) we obtain a finite current. The simulations give us an insight into the on-going processes: at degeneracy the hot quasiparticle excitations lying at high energies are able to tunnel in both directions equally; hence, there is no net current. In Coulomb blockade, the tunneling of a quasiparticle excitation is followed by a fast relaxation to the lowest lying charge state. The relaxation always happens in the forward direction given by  $V_b$  and leads to a net current through the device. These features are a strong indication of having quasiparticle excitations as the source of the sub-gap current in the device.

We measured the same sample in two different sample stages. Instead of having an enclosed stage with one metallic cover as in the measurement displayed in Fig. 2(a), we also used an indium sealed double hermetic metallic sample stage. In the latter case, the radio frequency (RF) line had an additional 20 cm thermocoax cable to enhance the sample shielding. This was not included in the wiring of the single cover stage. However, as the RF line is not electrically connected to the turnstile, we do not expect this to influence the direct heat conduction to the sample. The dc wiring of the two setups was similar made of approximately 2 m of thermocoax cable. The two sample stages are thermalized to the cryostat base temperature in an identical way and the sole purpose of this sealing is to create an RF shield to the sample. The result is shown in panel (b). In this case, no sub-gap current can be resolved. This behavior was fitted with temperatures of  $T_S \leq 167$  mK and  $T_N = 72$  mK, which we present in Fig. 2(d). The inset in Fig. 2(d) displays the quasiparticle density  $n_{qp}$  inferred from the relation  $n_{qp} = 2D(E_F) \int_0^\infty n_S(E) e^{-\beta E} dE = \sqrt{2\pi} D(E_F) \Delta \sqrt{k_B T} / \Delta e^{-\Delta/k_B T}$  which is valid at low temperatures  $k_B T_S \ll \Delta$  for three different samples with varying distance to the trap and measured with the poorly filtered sample stage. We use  $D(E_F) = 1.45 \times 10^{47} \text{m}^{-3} \text{J}^{-1}$  as the normal state density of states at the Fermi energy.<sup>16</sup> We observe a monotonous increase in  $n_{qp}$  with increasing distance of the trap from the junction. We deduce that the presence of environmentally excited quasiparticles is determined by both the trap relaxation rate and the diffusion rate through the superconducting line.

Next, we turn to the dynamic case of the turnstile operation. In addition to environmental excitation, quasiparticles are now injected to the superconducting leads once in every pump cycle. The pumping frequency thus allows us to control the injected power and the number of quasiparticles. Figure 3 shows current plateaus measured on type A SINIS20 sample. Three bias voltages were chosen around the optimum operation voltage of  $eV_b = \Delta$  (Ref. 17) ranging from  $0.8 \Delta/e$  to  $1.6 \Delta/e$ . Two main effects were observed: a slight overshoot for the highest bias voltage at the beginning of the plateau and a spreading of the plateau value for different  $V_b$ .

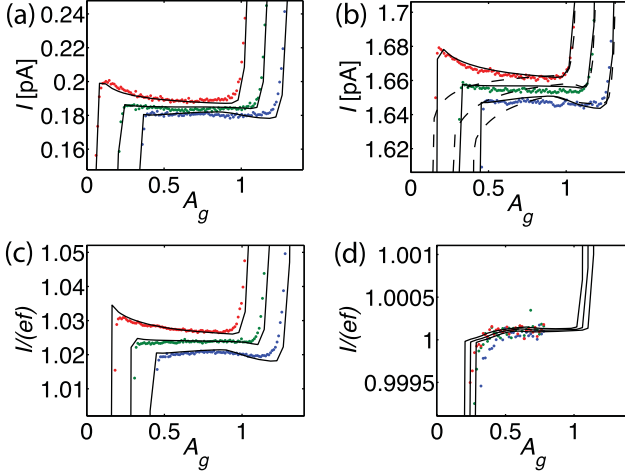


FIG. 3. Current plateaus under pumping. Current through the turnstile as a function of the gate modulation amplitude measured on the type A SINIS20 sample at (a) 1 MHz, (b) 10 MHz, and (c) 20 MHz sinusoidal  $V_g$  modulation frequency and on the type B sample SINISopen in (d) at 20 MHz. The pump was operated at bias voltage values of  $eV_b = 0.8\Delta$  (blue dots),  $eV_b = 1.2\Delta$  (green dots), and  $eV_b = 1.6\Delta$  (red dots). Fits from simulations including two-electron Andreev processes are displayed as solid black lines; dashed black lines are simulations only including single electron processes.

Simulations including single electron and two-electron Andreev processes were used to model the process. The peak at the beginning of the plateau can be reproduced by allowing for an Andreev current with a conduction channel area of  $30 \text{ nm}^2$ . This value is taken from previous experiments with similar samples.<sup>18,19</sup> The spreading of the plateaus in  $V_b$  is caused by quasiparticle excitations and follows the expected behaviour with respect to variations in geometry and pumping operation as described below.

The spread increases with the pumping frequency  $f$  from  $\Delta I = 8 \text{ fA}$  for 1 MHz (panel (a) of Fig. 3) to  $\Delta I = 15 \text{ fA}$  for 10 MHz (panel (b)). The injected power  $P_{inj}$  increases with  $f$  and we model this increase in mean number of quasiparticles in the superconductor by raising its temperature  $T_S$ . The bias-dependence of current on the plateau is not influenced by Andreev currents and we can thus fit it simply by ascribing it to the quasiparticle number. The black lines correspond to simulations with quasiparticle densities of  $n_{qp} = 41.1 \mu\text{m}^{-3}$  at 1 MHz and  $n_{qp} = 82.6 \mu\text{m}^{-3}$  at 10 MHz.

To demonstrate that the quantization can be improved by enhancing the quasiparticle relaxation, we measured the pumping plateaus of a sample with broader leads, see Fig. 1(b). Panels (c) and (d) in Fig. 3 show the comparison of poor and good quasiparticle trapping, respectively. The current quantization improves by two orders of magnitude when using leads with enhanced quasiparticle relaxation.

To model the relaxation of the quasiparticle excitations, we consider their diffusion in a thin superconducting line. The heat diffusion equation is

$$\nabla \cdot (-\kappa_S \nabla T) = -p_{\text{trap}}, \quad (1)$$

where the thermal conductivity of the superconductor is  $\kappa_S = \frac{6}{\pi^2} \left( \frac{\Delta}{k_B T} \right)^2 e^{-\Delta/k_B T} L_0 T / \rho_n$ , with the Lorentz number  $L_0$  and the normal state resistivity  $\rho_n$ .<sup>20,21</sup> The heat is removed from the superconductor by a normal metallic trap to which

it is tunnel coupled. The trap removes the heat  $p_{\text{trap}} = \frac{2\sigma_T}{e^2 d} \int_0^\infty E n_S(E) (f_N(E) - f_S(E)) dE$  per unit area, where  $\sigma_T$  is the conductance of the trap per unit area and  $d = 22 \text{ nm}$  is the thickness of the superconducting film. The power  $P_{inj}$  injected into the line during turnstile operation sets a boundary condition to the beginning of the line:  $P_{inj} = A \cdot (-\kappa_S \nabla T)$ , where  $A = wd$  is the cross-sectional area of the lead with width  $w$ . We rewrite Eq. (1) in terms of quasiparticle density  $n_{qp}$  by considering only the strong exponential dependencies on  $T$  to obtain

$$\nabla^2 n_{qp} = \lambda^{-2} (n_{qp} - n_{qp0}), \quad (2)$$

where  $\lambda^2 = \frac{\sqrt{2}d}{\sqrt{\pi\rho_n\sigma_T}} \left( \frac{k_B T}{\Delta} \right)^{1/2}$  and  $n_{qp0}$  is the quasiparticle density of the superconductor when it is fully thermalised to the normal metal. Next, we solve Eq. (2) for three different sections of the bias line for type A samples. In the first part, we treat the bare aluminium line of length  $l$  and constant width  $w_1$  with no quasiparticle trapping ( $p_{\text{trap}} = 0$ ). The next part deals with the widening of the lead from  $w_1$  to  $w_2$ , where we also neglect quasiparticle trapping since its contribution in this section of the lead is small for our samples. Then, in the last part, the lead continues with a constant cross section of  $w_2$  and is in contact with the quasiparticle trap:  $p_{\text{trap}} \neq 0$ . As a result, we obtain the quasiparticle density at the junction to be

$$n_{qp} = \frac{\sqrt{\pi} e^2 D(E_F) \rho_n P_{inj}}{\sqrt{2\Delta k_B T} wd} \left( l + w_1 \log\left(\frac{w_1}{w_2}\right) + \lambda \frac{w_1}{w_2} \right). \quad (3)$$

The first term is the diffusion in the bare aluminium wire, the second term is the spreading to the wider line, and the last term arises from the relaxation to the trap. Similarly, we can solve the diffusion for the type B sample with opening bias lines. Here, we assume that the line starts at radius  $r_0$  and the injected power is distributed evenly to all directions. We take  $r_0 = 70 \text{ nm}$  so that the area the power is injected into,  $\frac{\pi}{2} r_0 d = (50 \text{ nm})^2$ , matches the junction area of the sample. The quasiparticle density at the junction is then

$$n_{qp} = \frac{\sqrt{\pi} e^2 D(E_F) \rho_n P_{inj} K_0(r_0/\lambda)}{\sqrt{2\Delta k_B T} \theta r_0 d K_1(r_0/\lambda)}, \quad (4)$$

where  $K_n$  is the modified Bessel function of second kind and  $\theta$  the opening angle of the line.

We now compare the quasiparticle relaxation in different sample geometries. From fits to measurements similar to those shown in Fig. 3, we extract  $n_{qp}$  as a function of  $f$ . These values are displayed as dots in Fig. 4 for the SINIS20 (blue), the SINIS5 (green), and the SINISopen samples (red). Using the diffusion model described above, we calculate  $n_{qp}$  as a function of  $f$  corresponding to an injection power on the plateau given by  $P_{inj} = ef\Delta$  (solid lines). The injected heat calculated from the simulations deviated less than 10% from this power even at the highest frequencies measured. We used  $\rho_n = 31 \text{ n}\Omega\text{m}$  as the normal state resistivity for all samples. Individual sample parameters used in the simulations are listed in Table I. The measured densities clearly show a linear behavior with increasing  $f$  as predicted by the model (see Eqs. (3) and (4)). As indicated by the slopes for increasing length  $l$  of the isolated line, the further the quasiparticle

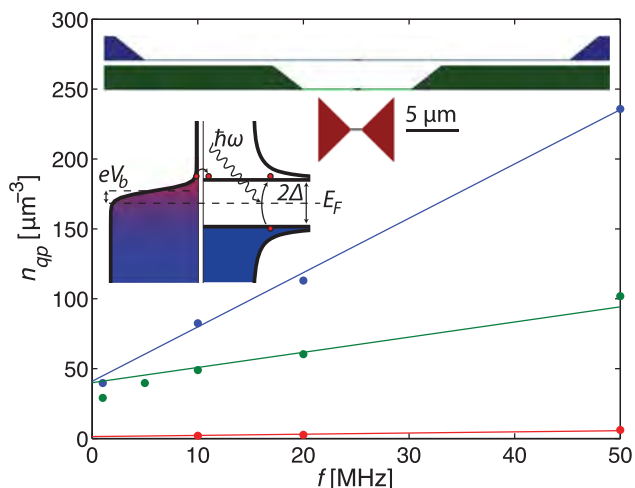


FIG. 4. Quasiparticle density as a function of the driving gate voltage  $f$ . Fits to measurements including first and second order tunnelling processes are displayed as dots and quasiparticle densities derived from the diffusion model are displayed as solid lines. We compare two type A samples with delayed relaxation, SINIS20 (blue) and SINIS5 (green) and one type B sample SINISopen (red). Diagrams of the sample geometries are displayed in the upper part of the figure, dark colours representing quasiparticle traps, lighter areas the isolated superconducting lines, and the small black bulks the normal metal islands. Below, a diagram shows the two pathways to quasiparticle excitation, during pumping via the normal metal island and through interactions with the electromagnetic environment.

trap lies from the oxide junction and the thinner the connecting line is, the slower the relaxation process is and the more the superconductor is heated. For the samples SINIS20 and SINIS5, a finite quasiparticle density is observed even in the absence of injected power. This density is of the same order of magnitude as the leakage currents shown in Fig. 2 and it points towards interactions with electromagnetic radiation from the environment. The SINISopen sample clearly shows the most efficient quasiparticle relaxation with only a few quasiparticles per  $\mu\text{m}^{-3}$  at 50 MHz driving frequency.

We have investigated the process of quasiparticle relaxation in hybrid SINIS turnstiles for various geometries. Both direct current and gate-driven pumping measurements can be well understood and simulated using models based on first and second order tunnelling processes. We were also able to model the relaxation of the excitations by a simple diffusion model. We find that the main sources for quasiparticles in the single electron transistor are those injected above the superconducting band gap during turnstile operation and those excited by radiation from a hot environment. In the best structure studied in this letter, we reached an accuracy  $\delta I/I$  of the order of  $1 \times 10^{-4}$ . We estimate that accuracy better than  $10^{-6}$  at 50 MHz would be obtained with the following improvements: The aluminum should be made an order of magnitude thicker and the trap ten times more

transparent. Alternatively, the bias leads can be extended to the third dimension. The resistance of the junctions should be increased by a factor of four and charging energy to  $E_c > 2\Delta$ . Finally, the density of environmentally activated quasiparticles needs to be reduced to a level  $n_{qp} \ll 0.1 \mu\text{m}^{-3}$  which has been demonstrated experimentally in a recent work.<sup>22</sup> With these realistic modifications, we expect to reach metrological accuracy in turnstile operation.

We thank A. Kemppinen and O.-P. Saira for useful discussions and M. Meschke for technical assistance. The work has been supported partially by the National Doctoral Programme in Nanoscience (NGS-NANO) and the European Community's FP7 Programme under Grant Agreements No. 228464 (MICROKELVIN, Capacities Specific Programme) and No. 218783 (SCOPE).

- <sup>1</sup>J. M. Martinis, M. Ansmann, and J. Aumentado, *Phys. Rev. Lett.* **103**, 097002 (2009).
- <sup>2</sup>H. Paik, D. I. Schuster, L. S. Bishop, G. Kirchmair, G. Catelani, A. P. Sears, B. R. Johnson, M. J. Reagor, L. Frunzio, L. I. Glazman, S. M. Girvin, M. H. Devoret, and R. J. Schoelkopf, *Phys. Rev. Lett.* **107**, 240501 (2011).
- <sup>3</sup>A. D. Córcoles, J. M. Chow, J. M. Gambetta, C. Rigetti, J. R. Rozen, G. A. Keefe, M. B. Rothwell, M. B. Ketchen, and M. Steffen, *Appl. Phys. Lett.* **99**, 181906 (2011).
- <sup>4</sup>P. J. de Visser, J. J. A. Baselmans, P. Diener, S. J. C. Yates, A. Endo, and T. M. Klapwijk, *Phys. Rev. Lett.* **106**, 167004 (2011).
- <sup>5</sup>J. P. Pekola, D. V. Anghel, T. I. Suppala, J. K. Suoknuuti, A. J. Manninen, and M. Manninen, *Appl. Phys. Lett.* **76**, 2782 (2000).
- <sup>6</sup>S. Rajauria, H. Courtois, and B. Pannetier, *Phys. Rev. B* **80**, 214521 (2009).
- <sup>7</sup>G. C. O'Neil, P. J. Lowell, J. M. Underwood and J. N. Ullom, e-print arXiv:1109.1273v1.
- <sup>8</sup>K. Y. Arutyunov, H.-P. Auraneva, and A. S. Vasenko, *Phys. Rev. B* **83**, 104509 (2011).
- <sup>9</sup>P. K. Day, H. G. LeDuc, B. A. Mazin, A. Vayonakis, and J. Zmuidzinas, *Nature* **425**, 817 (2003).
- <sup>10</sup>R. Barends, J. J. A. Baselmans, S. J. C. Yates, J. R. Gao, J. N. Hovenier, and T. M. Klapwijk, *Phys. Rev. Lett.* **100**, 257002 (2008).
- <sup>11</sup>J. P. Pekola, J. J. Vartiainen, M. Möttönen, O.-P. Saira, M. Meschke, and D. V. Averin, *Nat. Phys.* **4**, 120 (2008).
- <sup>12</sup>T. A. Fulton and G. J. Dolan, *Phys. Rev. Lett.* **59**, 109 (1987).
- <sup>13</sup>S. Kafanov, A. Kemppinen, Y. A. Pashkin, M. Meschke, J. S. Tsai, and J. P. Pekola, *Phys. Rev. Lett.* **103**, 120801 (2009).
- <sup>14</sup>A. V. Timofeev, M. Helle, M. Meschke, M. Möttönen, and J. P. Pekola, *Phys. Rev. Lett.* **102**, 200801 (2009).
- <sup>15</sup>J. N. Ullom, P. A. Fisher, and M. Nahum, *Phys. Rev. B* **58**, 8225 (1998).
- <sup>16</sup>C. Kittel, *Introduction to Solid State Physics* (Wiley, 2005).
- <sup>17</sup>D. V. Averin and J. P. Pekola, *Phys. Rev. Lett.* **101**, 066801 (2008).
- <sup>18</sup>T. Aref, V. F. Maisi, M. V. Gustafsson, P. Delsing, and J. P. Pekola, *EPL* **96**, 37008 (2011).
- <sup>19</sup>V. F. Maisi, O.-P. Saira, Y. A. Pashkin, J. S. Tsai, D. V. Averin, and J. P. Pekola, *Phys. Rev. Lett.* **106**, 217003 (2011).
- <sup>20</sup>J. Bardeen, G. Rickayzen, and L. Tewordt, *Phys. Rev.* **113**, 982 (1959).
- <sup>21</sup>A. A. Abrikosov, *Fundamentals of the Theory of Metals* (Elsevier Science, Amsterdam, 1988).
- <sup>22</sup>O.-P. Saira, A. Kemppinen, V. F. Maisi, and J. P. Pekola, *Phys. Rev. B* **85**, 012504 (2012).

# Publication VIII

**J. P. Pekola, O.-P. Saira, V. F. Maisi, A. Kemppinen, M. Möttönen, Yu. A. Pashkin and D. V. Averin. Single-electron current sources: towards a refined definition of ampere. *Rev. Mod. Phys.* 85, 1421 (2013).**

© (2013) American Physical Society.

Reprinted with permission.



**Single-electron current sources: Toward a refined definition of the ampere**

Jukka P. Pekola\* and Olli-Pentti Saira

*Low Temperature Laboratory (OVLL), Aalto University,  
P.O. Box 13500, FI-00076 AALTO, Finland*

Ville F. Maisi

*Low Temperature Laboratory (OVLL), Aalto University,  
P.O. Box 13500, FI-00076 AALTO, Finland  
and Centre for Metrology and Accreditation (MIKES), P.O. Box 9, 02151 Espoo, Finland*

Antti Kemppinen

*Centre for Metrology and Accreditation (MIKES), P.O. Box 9, 02151 Espoo, Finland*

Mikko Möttönen

*QCD Labs, COMP Centre of Excellence, Department of Applied Physics,  
Aalto University, P.O. Box 13500, FI-00076 AALTO, Finland  
and Low Temperature Laboratory (OVLL), Aalto University,  
P.O. Box 13500, FI-00076 AALTO, Finland*

Yuri A. Pashkin†

*NEC Smart Energy Research Laboratories and RIKEN Advanced Science Institute,  
34 Miyukigaoka, Tsukuba, Ibaraki 305-8501, Japan  
and Department of Physics, Lancaster University, Lancaster, LA1 4YB, United Kingdom*

Dmitri V. Averin

*Department of Physics and Astronomy, Stony Brook University, SUNY, Stony Brook,  
New York 11794-3800, USA*

(published 2 October 2013)

The control of electrons at the level of the elementary charge  $e$  was demonstrated experimentally already in the 1980s. Ever since, the production of an electrical current  $ef$ , or its integer multiple, at a drive frequency  $f$  has been a focus of research for metrological purposes. This review discusses the generic physical phenomena and technical constraints that influence single-electron charge transport and presents a broad variety of proposed realizations. Some of them have already proven experimentally to nearly fulfill the demanding needs, in terms of transfer errors and transfer rate, of quantum metrology of electrical quantities, whereas some others are currently “just” wild ideas, still often potentially competitive if technical constraints can be lifted. The important issues of readout of single-electron events and potential error correction schemes based on them are also discussed. Finally, an account is given of the status of single-electron current sources in the bigger framework of electric quantum standards and of the future international SI system of units, and applications and uses of single-electron devices outside the metrological context are briefly discussed.

DOI: [10.1103/RevModPhys.85.1421](https://doi.org/10.1103/RevModPhys.85.1421)

PACS numbers: 05.30.–d, 05.40.–a, 73.23.Hk

**CONTENTS**

I. Introduction	1422	E. Single-electron tunneling in semiconductor structures	1431
II. Principles of Manipulating Single Electrons	1422	F. Influence of environment on tunneling	1433
A. Charge quantization on mesoscopic conductors	1422	G. Heating of single-electron devices	1434
B. Sequential single-electron tunneling	1425	III. Realizations	1436
C. Cotunneling, Andreev reflection, and other higher-order processes	1428	A. Normal-metal devices	1436
D. Coulomb blockade of Cooper-pair tunneling	1430	B. Hybrid superconducting–normal-metal devices	1438
		1. Operating principles	1438
		2. Higher-order processes	1439
		3. Quasiparticle thermalization	1440
		C. Quantum-dot-based single-electron pumps and turnstiles	1442
		1. Introduction to quantum dots as electron pumps	1442

\*jukka.pekola@aalto.fi

†On leave from Lebedev Physical Institute, Moscow 119991, Russia.

2. Pioneering experiments	1442
3. Experiments on silicon quantum dots	1443
4. Experiments on gallium arsenide quantum dots	1445
D. Surface-acoustic-wave-based charge pumping	1446
E. Superconducting charge pumps	1447
F. Quantum phase slip pump	1448
G. Other realizations and proposals	1450
1. ac-current sources	1450
2. Self-assembled quantum dots in charge pumping	1451
3. Mechanical single-electron shuttles	1452
4. Electron pumping with graphene mechanical resonators	1453
5. Magnetic- field-driven single-electron pump	1453
6. Device parallelization	1453
H. Single-electron readout and error correction schemes	1454
1. Techniques for electrometry	1454
2. Electron-counting schemes	1457
I. Device fabrication	1458
1. Metallic devices	1458
2. Quantum dots	1459
IV. Quantum Standards of Electric Quantities and the Quantum Metrology Triangle	1459
A. The conventional system of electric units	1459
B. Universality and exactness of electric quantum standards	1460
C. The future SI	1462
D. Quantum metrology triangle	1463
1. Triangle by Ohm's law	1463
2. Electron-counting capacitance standard	1464
3. Metrological implications of single-electron transport and QMT	1464
V. Perspectives and Other Applications	1465
Acknowledgments	1466
References	1466

## I. INTRODUCTION

The future definition of the ampere is foreseen to be based on manipulating the elementary charge  $e$ . Its most direct realization would be the transport of a known number of electrons. Over the past quarter of a century, we have witnessed progress toward ever better control of individual electrons. Since single-electron tunneling is by now a well-established subject, several reviews of its different aspects exist in the literature (Averin and Likharev, 1991; Averin and Nazarov, 1992a; Sohn, Kouwenhoven, and Schön, 1997; van der Wiel *et al.*, 2002; Durrani, 2009).

Several milestones have been achieved in the progress toward a single-electron current source since the initial proposals of the single-charge oscillations (Averin, Zorin, and Likharev, 1985) and of the metrological triangle in the mid-1980s (Likharev and Zorin, 1985). The single-electron ampere is based on transporting an electron with charge  $e$ , or rather a known number  $N$  of electrons  $Ne$  in each operation of a control parameter that is cyclically repeated at frequency  $f$ , so that the output dc current is ideally equal to  $Nef$ . The needs of precision metrology generally state that this operation has to be performed at a relative error level not larger

than  $10^{-8}$  and at the same time the current level needs to be several hundreds of picoamperes (Feltin and Piquemal, 2009). Just a few years after the initial theoretical proposal of controlled single-electron tunneling (Averin and Likharev, 1986), the first metallic (Geerligs *et al.*, 1990; Pothier, 1991; Pothier *et al.*, 1992) and semiconducting (Kouwenhoven *et al.*, 1991a) single-electron turnstiles and pumps demonstrated currents  $I = Nef$  with an error of a few percent, still orders of magnitude away from what is needed. As often in precision metrology, the pursuit of higher accuracy has been a pacemaker for understanding new physics, since the errors that need to be suppressed are often a result of interesting physical phenomena. For instance, quantum multielectron processes and nonequilibrium phenomena have been intensively studied in order to improve the performance of single-electron sources. In five years, the accuracy of single-electron pumps was remarkably improved by another 5 to 6 orders of magnitude (Keller *et al.*, 1996) by effectively suppressing the so-called cotunneling current, but at the expense of significantly increased complexity of the device and reduced overall magnitude of the output current (a few picoamperes) of the pump. Alternative ideas were to be found. At the same time, single-electron conveyors in semiconducting channels using surface-acoustic wave (SAW) driving yielded promising results, in particular, in terms of significantly increased current level (Shilton, Talyanskii *et al.*, 1996). Yet likely due to overheating effects in the channel, it may turn out to be difficult to suppress thermal errors to the desired level using this technique.

Interestingly there was a decade of reduced progress in the field, until in the 2000s several new proposals and implementations were put forward. The most promising of these devices are undeniably the sources based on a quantum dot (QD) (Blumenthal *et al.*, 2007), with a single-parameter ac control (Kaestner, Kashcheyevs, Hein *et al.*, 2008), and a superconductor-insulator-normal metal-insulator-superconductor (SINIS) turnstile (Pekola *et al.*, 2008), which is a basic single-electron transistor with superconducting leads and normal-metal island. These simple devices promise high accuracy and a possibility to run many of them in parallel (Maisi *et al.*, 2009). At around the same time, other promising ideas came out, for example, a quantum-phase-slip (QPS) based superconducting current standard (Mooij and Nazarov, 2006). Quantum phase slips provide the mechanism for the existence of the Coulomb-blockade (CB) effects in superconducting wires without tunnel barriers (Astafiev *et al.*, 2012) and could potentially lead to current standards producing larger currents. Currently we are definitely witnessing a period of intense activity in the field in a well-founded atmosphere of optimism.

## II. PRINCIPLES OF MANIPULATING SINGLE ELECTRONS

### A. Charge quantization on mesoscopic conductors

We begin by summarizing the essential concepts of single-electron device physics, with the emphasis on the topics needed for the subsequent discussion of the quantized current sources. We focus mostly on metallic devices since those have

an elaborated theory based on first principles. A brief discussion of how and to what extent the main concepts can be adapted to semiconductor structures is given in Sec. II.E.

As is well known from the elementary treatments of the Bohr model in quantum mechanics, the electrostatic energy of an electron in the hydrogen atom is roughly equal to the kinetic energy of its confinement in the atomic orbitals. The fact that the characteristic energy separation of levels in the confinement energy spectrum decreases much more rapidly than the electrostatic energy with the size of the confining region ensures then that in mesoscopic conductors which are large on the atomic scale, the electrostatic energy of individual electrons can be large even in the regime where the separation of the individual energy levels associated with quantum confinement of electrons is negligible. As a characteristic estimate, the electrostatic energy of charge  $e$  of one electron on a micrometer-size conductor is on the order of a milli-electron-volt, or 10 K in temperature units, and is many orders of magnitude larger than the energy separation  $\delta E$  of electron confinement levels in the same conductor, which should be about 1 neV, well below all practical temperatures. As a result, at low but easily reachable temperatures in the kelvin and subkelvin range, the properties of mesoscopic conducting islands are dominated by the electrostatic energy of individual electrons, while small  $\delta E$  provides one of the conditions that makes it possible to use macroscopic capacitances to quantitatively describe electrostatics of these conductors even in this “single-electron” regime. The charging energy  $U$  of a system of such conductors can be expressed then as usual in terms of the numbers  $n_j$  of excess electrons charging each conductor and the capacitance matrix  $C$  [see, e.g., Landau and Lifshitz (1980a)]:

$$U(\{n_j\}) = \frac{e^2}{2} \sum_{i,j} [C^{-1}]_{i,j} n_i n_j, \quad (1)$$

where the sum runs over all conductors in the structure.

The electrostatic energy (1) creates energy gaps separating different charge configurations  $\{n_j\}$  which provide the possibility to distinguish and manipulate these charge configurations. Historically, one of the first observations of distinct individual electron charges occurred in Millikan’s experiments on motion of charged micrometer-scale droplets of oil, which produced the evidence that “all electrical charges, however produced, are exact multiples of one definite, elementary, electrical charge” (Millikan, 1911). In those experiments, the oil droplets were, however, charged randomly by an uncontrollable process of absorption of ions which exist normally in air. By contrast, in mesoscopic conductors, the charge states  $n_j$  can be changed in a controllable way. Besides the charging energy (1), such a process of controlled manipulation of individual charges in mesoscopic conductors requires two additional elements. First are the tunnel junctions formed between the nearest-neighbor electrodes of the structure which enable the electron transfer between these electrodes, and the second is the possibility to control the electrostatic energy gaps by continuous variation of charges on the junctions (Averin and Likharev, 1986). The simplest way of varying the charges on the tunnel junctions continuously is by placing the electrodes in external electrical fields (Büttiker, 1987) that create continuously varying potential differences between

the electrodes of the structure. Externally controlled gate voltages produced in this way can be used then to transfer individual electrons in the system of mesoscopic conductors.

A simple model of the sources of continuously varying external voltages is obtained by taking some of the electrodes of the structure described by the energy (1) to have very large self-capacitance and carry large charge, so that the tunneling of a few electrons does not affect the potentials created by them. For instance, the most basic single-electron structure, the single-electron box (SEB) (Lafarge *et al.*, 1991), can be simplified to two electrodes, one main island carrying the charge  $en$ , and the electrode with the charge  $e(N - n)$  creating the gate voltage  $V_g$  (see Fig. 1). Quantitatively, the structure in Fig. 1 is characterized by the capacitance matrix

$$C = \begin{pmatrix} C_0 & -C_m \\ -C_m & C_\Sigma \end{pmatrix}, \quad (2)$$

where  $C_m > 0$ . In the limit  $N, C_0 \rightarrow \infty$ , with  $eN/C_0 = V_g$ ,  $C_0$  and  $C_\Sigma$  have the meaning of the total capacitances of the gate electrode and the island, respectively, and the energy (1) of the charges shown in Fig. 1 reduces for the capacitance matrix (2) to

$$U = U_0 + E_C n^2 - e^2 n n_g / C_\Sigma. \quad (3)$$

In this equation,  $U_0$  is the  $n$ -independent energy of creating the source of the gate voltage,  $U_0 = e^2 N^2 / 2C_0$  in this case,  $E_C \equiv e^2 / 2C_\Sigma$  is the charging energy of one electron on the main electrode of the box, and  $e n_g \equiv C_g V_g$  is the charge induced on this electrode by the gate voltage  $V_g$  through the gate capacitance  $C_g = C_\Sigma - C_m$ . As one can see from Eq. (3), the gate voltage  $V_g$  indeed controls the energy gaps separating the different charge states  $n$  of the main island and therefore makes it possible to manipulate individual electron transitions changing the island charge  $en$ .

Figure 2(a) shows a scanning electron micrograph of a realistic box structure, in which, in contrast to the schematic diagram of Fig. 1, one pays attention to satisfying several quantitative requirements on the box parameters. First, the capacitance  $C_\Sigma$  needs to be sufficiently small to have significant charging energy  $E_C$ , while the gate capacitance  $C_g$

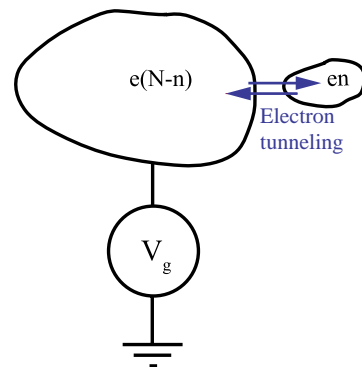


FIG. 1 (color online). Schematic diagram of the basic circuit for manipulating individual electrons, the single-electron box (SEB): a conducting island carrying electric charge  $en$ , and an electrostatically coupled external electrode with the charge  $e(N - n)$  producing the gate voltage  $V_g$ .

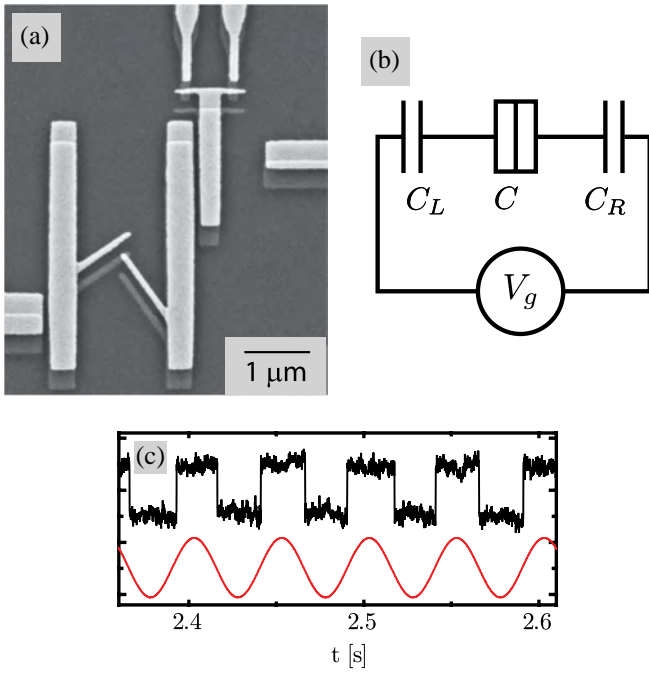


FIG. 2 (color online). Practical SEB. (a) Scanning electron micrograph of a realistic box structure, (b) its equivalent electric circuit, and (c) single-electron transitions in the box illustrating the “charge quantization”: a time-dependent gate voltage  $V_g(t)$  (sinusoidal curve) of an appropriate amplitude drives individual electron transitions changing the box state between the two discrete charge configurations, the electron on the left or on the right island. These two charge states are detected via the detector shown in the upper right corner of (a), whose two-level output current is synchronous with the oscillating  $V_g(t)$ . Adapted from Saira *et al.*, 2010 and Saira, Yoon *et al.*, 2012.

remains not very small in comparison to  $C_\Sigma$ , to be able to manipulate the charge  $en$  more easily and also to measure it. To satisfy this requirement, the box in Fig. 2(a) is composed of two relatively large similar-size islands with very small overlap between them. Its equivalent electric circuit is shown in Fig. 2(b). The charging energy of the box is described by the same expression (3), with  $en$  being the charge transferred from the left to the right island, and  $C_\Sigma$  the total mutual capacitance between the two islands,  $C_\Sigma = C + C_g$ , where  $C_g^{-1} = C_L^{-1} + C_R^{-1}$ . Connecting the box islands to the source of gate voltage  $V_g$  through the capacitances  $C_{L,R}$  on both sides serves the additional purpose of reducing coupling to parasitic voltage fluctuations in the electrodes of the structure, responsible for environment-induced tunneling discussed below. Generally, a practical geometric structure of the box islands is determined by the fact that the main contribution to the capacitance  $C_\Sigma$  comes from the tunnel junction formed in the area where the “arms” of the islands [see Fig. 2(a)] overlap. The size of this area should be minimized to increase  $E_C$ . At the same time, the islands themselves can be made much larger than the junctions, to increase the gate capacitance  $C_g$  without strongly affecting the total capacitance  $C_\Sigma$ . Besides increasing the coupling to the gate voltage created by the two outside horizontal electrodes in the box structure shown in Fig. 2(a), a larger size of the box islands also increases the coupling to the

single-electron transistor (discussed in more detail below) which measures the charge of the box and can be seen in the upper right corner of Fig. 2(a).

The main qualitative property of the SEB is that it allows one to manipulate individual electrons through variation of the gate voltage  $V_g$ . Indeed, at low temperatures  $T \ll E_C/k_B$ , the box occupies the ground state of the charging energy (3). For a given gate-voltage-induced charge  $n_g$ , the minimum is achieved when the number  $n$  of extra electrons on the island equals  $n_g$  rounded to the nearest integer. This dependence of  $n$  on  $n_g$  means that one electron is added or removed from the box island, changing  $n$  by  $\pm 1$ , whenever  $n_g$  passes through a degeneracy point, i.e.,  $n_g = 1/2$  modulo an integer, at which point the charging energies (3) of the two charge states that differ by one electron transition,  $\delta n = 1$ , are equal. If the gate voltage increases monotonically, the dependence  $n(n_g)$  has the shape of the “Coulomb staircase” (Lafarge *et al.*, 1991), with each step of the staircase corresponding to the addition of one electron with gate-voltage increase by  $\delta n_g = 1$ . If the gate voltage oscillates in time around the degeneracy point  $n_g = 1/2$ , as in Fig. 2(c), with an appropriate amplitude ( $\delta n_g \sim 1$ ), it induces back-and-forth electron transitions between the two charge states separated by one electron charge, which can be seen in Fig. 2(c) as the two-level telegraph signal of the detector measuring the box charge. Thus, Fig. 2(c) gives a practical example of manipulation of an individual electron transition in the SEB.

One of the most interesting dynamic manifestations of the manipulation of individual electrons in a system of mesoscopic conductors is the possibility to arrange the system dynamics in such a way that electrons are transferred through it one by one, in a correlated fashion. This can be achieved, for instance, if the gate voltage  $V_g$  of the SEB grows in time at a constant rate such that effectively a constant dc “displacement” current  $I = e\dot{n}_g$  is injected in the box junction. The same dynamic would be obtained if real dc current  $I$  flows into a mesoscopic tunnel junction. In this case, correlated successive transfer of electrons one by one through the junction gives rise to “single-electron tunneling” oscillations (Averin and Likharev, 1986; Bylander, Duty, and Delsing, 2005) of voltage on the junction,  $\partial U/\partial(en) = e(n - n_g)/C_\Sigma$ , with frequency  $f$  related to the current by the fundamental equation

$$I = ef. \quad (4)$$

More complex structures than a SEB or an individual tunnel junction, such as single-electron turnstile (Geerligs *et al.*, 1990) and pump (Pothier *et al.*, 1992; Keller *et al.*, 1996) discussed below, make it possible to “invert” this relation and transfer one electron per period of the applied gate-voltage oscillation with frequency  $f$ . The above discussion of the manipulation of individual electrons in the SEB shows that the charge states  $n$ , while controlled by the gate voltage  $V_g$ , remain the same in a range of variation of  $V_g$ . Physically, such “quantization of charge” results from the fact that an isolated conductor can contain only an integer total number of electrons, with the charging energy producing energy gaps separating different electron number states. Charge quantization enables one to make the accuracy of manipulation of

individual electron charges in structures such as SEBs very high, in principle approaching the metrological level. Potentially metrological accuracy also extends to the transport in turnstiles and pumps, making the current sources based on single-electron tunneling promising candidates for creation of the quantum standard of electrical current.

## B. Sequential single-electron tunneling

One of the key elements in manipulating individual electrons in systems of mesoscopic conductors is a tunnel junction, which provides the means to transfer electrons along the system, thus creating the dc current  $I$  through it. A tunnel junction (Giaever, 1960) is a system of two conductors separated by a layer of insulator that is sufficiently thin to allow electrons to tunnel between the conductors (see Fig. 3). For normal conductors, the current through the junction at small applied voltages depends linearly on the voltage and is characterized by the tunnel conductance  $G_T \equiv 1/R_T$ . In single-electron devices,  $G_T$  should satisfy two contrasting requirements. To increase the current  $I$  driven through the structure, e.g., to increase the allowed range of frequencies  $f$  for which Eq. (4) is satisfied accurately, one should maximize  $G_T$ . On the other hand, charge quantization on the electrodes of the structure requires that they are well isolated from each other, i.e.,  $G_T$  should be small. The latter condition can be formulated more quantitatively requiring that the characteristic charging energy  $E_C$  of the localized charge states is well defined despite the finite lifetime of these states  $\sim G_T/C$ , where  $C$  is the typical junction capacitance in the structure  $E_C \gg \hbar G_T/C$ . This condition can be expressed as  $G_T \ll 1/R_K$ , where  $R_K \equiv h/e^2 \simeq 25.8 \text{ k}\Omega$  is the characteristic “quantum” resistance. When this condition is satisfied, the localized charge states provide an appropriate starting point for the description of a single-electron structure, while electron tunneling can be treated as a perturbation. In what follows, we mostly concentrate on such a regime of “strong Coulomb blockade” which is necessary for implementation of precise transport of individual electrons as required for quantized current sources.

The majority of practical metallic structures employ tunnel junctions based on barriers formed by either thermal or

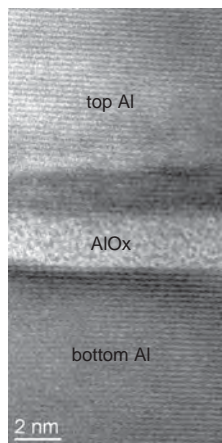


FIG. 3. High-resolution TEM image of a cross section of an aluminum oxide tunnel junction. From Prunnila *et al.*, 2010.

plasma oxidation of aluminum. The main reason for this are the superior properties of the aluminum oxide layer, in terms of its uniformity and electrical and noise properties. A typical barrier structure is shown in Fig. 3 that includes a high-resolution transmission-electron-microscopy (TEM) image of a cross section of an aluminum-based junction with amorphous  $\text{Al}_x\text{O}_y$  tunnel barrier. From the point of view of the Landauer-Büttiker formula for electric conductance of a mesoscopic conductor, the junction tunnel conductance can be expressed as  $G_T = (2/R_K)\sum_j T_j$ , where the sum is taken over spin-degenerate electron transport channels propagating across the junction, and  $T_j$  is the quantum mechanical transmission coefficient of the insulator barrier for electrons in the  $j$ th channel. The condition of the strong Coulomb blockade  $G_T \ll 1/R_K$  implies that all individual transmission coefficients are small,  $T_j \ll 1$ . Although the transmission coefficients  $T_j$  are sensitive to the atomic-scale structure of the junction, the fact that the aluminum oxide layer is relatively uniform on an intermediate space scale larger than the individual atoms (Greibe *et al.*, 2011) allows transport properties to be estimated semiquantitatively from the “bulk” properties of the barrier.

Since the tunnel current depends exponentially on the barrier parameters, the measured electron tunneling rates in high-resistance junctions and over the large voltage range allow one to estimate parameters of the aluminum oxide barrier [see, e.g., Tan *et al.* (2008)]: they yield a barrier height  $U \simeq 2 \text{ eV}$  and effective electron mass  $m_{\text{eff}} \simeq 0.5m_e$  in terms of the free electron mass  $m_e$ . While the dimensions of the typical tunnel junctions need to be small [on the order of  $\sim 100 \text{ nm}$ , also cf. Fig. 2(a)] in order to make the junction capacitance sufficiently low, they are still quite large on the atomic scale. In this regime, discreteness of the spectrum of the transverse modes  $j$  is negligible, and the tunnel conductance  $G_T$  is proportional to the junction area  $A$ . For the value of specific junction resistance  $A/G_T \sim 10 \text{ k}\Omega \mu\text{m}^2$  typical for the tunnel junctions, estimates using the barrier parameters and the simplest assumption of ballistic transport in the junction give for the barrier transparency  $T \sim 10^{-6}$  corresponding to barrier thickness close to  $2 \text{ nm}$  (cf. Fig. 3). A barrier with this thickness effectively transmits only the electrons impinging on it orthogonally. This “focusing” effect means that the tunnel conductance can be expressed in terms of one maximum value of the transmission coefficient  $G_T = \mathcal{N}T/R_K$ , where the effective number  $\mathcal{N}$  of the transport channels in the junction is not determined directly by the density of states (DOS) in the electrodes, but depends also on the characteristic “traversal energy”  $\epsilon_0$  of the barrier, which gives the energy scale on which the barrier transparency changes with energy:  $\mathcal{N} \simeq Am\epsilon_0/2\pi\hbar^2$ . For the parameters of the aluminum oxide barrier mentioned, this gives for the area per transport channel  $A/\mathcal{N} \simeq 1 \text{ nm}^2$ . As will be discussed in Sec. II.C, some of the higher-order transitions in the single-electron structures, e.g., Andreev reflection (AR), depend separately on the barrier transmission coefficients  $T_j$  and on the number  $\mathcal{N}$  of the transport modes. In contrast to this, the lowest-order electron tunneling depends only on the total junction conductance  $G_T$ .

The most straightforward approach to the description of tunneling in the single-electron structures in the

strong Coulomb-blockade regime is based on the tunnel Hamiltonian method (Cohen, Falicov, and Phillips, 1962), in which the junction is modeled with the following Hamiltonian:

$$H = H_1 + H_2 + H_T, \quad H_T = \sum_{k,p} [T_{kp} c_k^\dagger c_p + \text{H.c.}] \quad (5)$$

Here  $H_{1,2}$  are the Hamiltonians of the junction electrodes,  $H_T$  is responsible for tunneling, with  $c_k$  and  $c_p$  denoting the electron destruction operators in the two electrodes, respectively, and  $T_{kp}$  are the tunneling amplitudes. In a typical metallic mesoscopic conductor, when discreteness  $\delta E$  of the single-particle electron states is negligible, these states form a continuum with some density of states which in a normal metal, is constant on a small energy scale of interest for single-electron transport. In this case, one can treat  $H_T$  using Fermi's golden rule to obtain the rate  $\Gamma(E)$  of a tunneling process that changes the charge configuration  $\{n_j\}$  on the system of mesoscopic conductors by transferring one electron through a tunnel junction between the two conductors. For the process that changes the electrostatic energy (1) by an amount  $E = U(\{n_{j,\text{in}}\}) - U(\{n_{j,\text{fin}}\})$ , where  $\{n_{j,\text{in}}\}$  is the initial and  $\{n_{j,\text{fin}}\}$  is the final charge configuration, we obtain

$$\Gamma(E) = \frac{G_T}{e^2} \int d\epsilon f(\epsilon) [1 - f(\epsilon + E)] \nu_1(\epsilon) \nu_2(\epsilon + E). \quad (6)$$

In this expression,  $f(\epsilon)$  is the equilibrium Fermi distribution function, and  $\nu_j(\epsilon)$  is the density of the single-particle states in the  $j$ th electrode of the junction,  $j = 1, 2$ , in units of the normal density of states  $\rho_j$ , which together with the average of the squares of the tunneling amplitudes determine the tunnel conductance  $G_T = 4\pi e^2 \langle |T_{kp}|^2 \rangle \rho_1 \rho_2 / \hbar$ . Equation (6) assumes that the energy  $E \sim E_C$  is much smaller than all internal energies of the junction in the normal state, in particular, the traversal energy  $\epsilon_0$ , a condition very well satisfied for practical metallic structures in which  $E_C \sim 1$  meV, while  $\epsilon_0 \sim 1$  eV. Using the standard properties of the Fermi distribution functions, one can see directly that the rate (6) of tunneling between the two equilibrium electrodes satisfies the necessary detailed balance condition  $\Gamma_{1 \rightarrow 2}(-E) = e^{-E/k_B T} \Gamma_{2 \rightarrow 1}(E)$ . If, in addition, the densities of states are symmetric with respect to the chemical potentials of the electrodes, the tunneling rate is also symmetric,  $\Gamma_{1 \rightarrow 2}(E) = \Gamma_{2 \rightarrow 1}(E)$ , and the detailed balance condition simplifies to  $\Gamma(-E) = e^{-E/k_B T} \Gamma(E)$ . The detailed balance condition makes it possible to express the tunneling rate (6) in terms of the current-voltage characteristic  $I(V)$  of the junction at fixed bias voltage  $V$ :

$$\Gamma(E) = I(E/e) / e(1 - e^{-E/k_B T}). \quad (7)$$

For normal metal–insulator–normal metal (NIN) junctions, when both electrodes are in the normal (N) states,  $\nu_j(\epsilon) \equiv 1$ , Eq. (6) gives, in agreement with Eq. (7), for the tunneling rate

$$\Gamma(E) = \frac{G_T}{e^2} \frac{E}{1 - e^{-E/k_B T}}. \quad (8)$$

Tunneling of individual electrons with the rate (8) is an irreversible dissipative process which converts the electrostatic

energy change  $E$  into internal energy of the electron gas inside the junction electrodes. In accordance with this understanding, at small temperatures  $T$ , the rate (8) vanishes as  $e^{E/k_B T}$  for energetically unfavorable transitions with  $E < 0$ , when the energy for the transition is taken from the thermal fluctuations of the electron reservoirs. In the regime of allowed transitions  $E \sim E_C > 0$ , the magnitude of the typical transition rate  $\Gamma \sim G_T/C$  for the realistic values of the parameters  $G_T \sim 1$  M $\Omega$ ,  $C \sim 10^{-16}$ – $10^{-15}$  F is quite high, in the gigahertz range.

In superconductor–insulator–normal metal (SIN) junctions, when one of the junction electrodes is a superconductor (S), the BCS density of states  $\nu_1(\epsilon) = |\epsilon|/(\epsilon^2 - \Delta^2)^{1/2}$  for  $|\epsilon| > \Delta$ , and vanishing otherwise, implies that at temperatures well below the superconducting energy gap  $\Delta$ , the tunneling rate (6) is strongly suppressed and can be reduced into the kilohertz and even hertz range. Indeed, evaluating the integral in Eq. (6) for the SIN junction assuming  $k_B T$ ,  $E \ll \Delta$ , one gets

$$\Gamma(E) = \frac{G_T}{e^2} \sqrt{2\pi\Delta k_B T} e^{-\Delta/k_B T} \frac{\sinh(E/k_B T)}{1 - e^{-E/k_B T}}. \quad (9)$$

Figure 4 shows the tunneling rate (9) measured in an SIN junction in the configuration of a “hybrid” SEB [see Fig. 2(a)], in which one of the islands of the box is a superconductor (aluminum), the other one being normal metal (copper). The electrostatic energy change  $E$  in the case of the box follows from Eq. (3) as  $E = U(n=0) - U(n=1) = 2E_C(n_g - 1/2)$ , i.e., is proportional to the deviation of the gate voltage of the box from the degeneracy point  $n_g = 1/2$ . The measurements can be described well by Eq. (9) with reasonable values of parameters including the superconducting energy gap  $\Delta$  of aluminum.

Since the tunneling transitions described quantitatively by the rates (6)–(9) are inherently random stochastic processes,

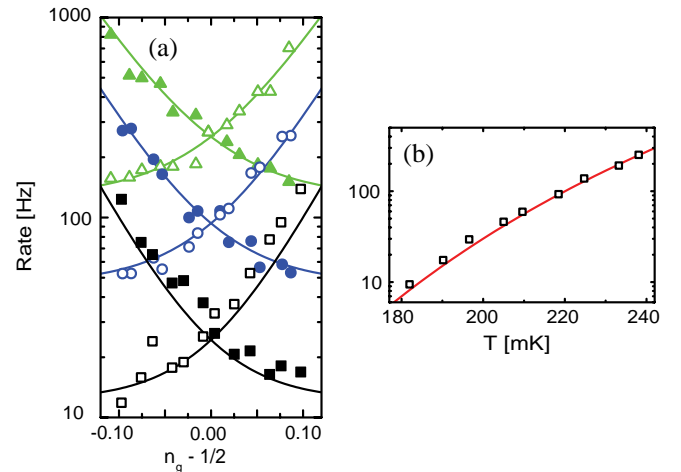


FIG. 4 (color online). (a) Measured thermally activated rates of forward  $\Gamma(E)$  and backward  $\Gamma(-E)$  tunneling in a “hybrid” SIN single-electron box at different temperatures as a function of the gate-voltage offset from the degeneracy point related to the energy change  $E$  in tunneling as  $E = 2E_C(n_g - 1/2)$ . Solid lines are the theory prediction according to Eq. (9) with fitted parameters  $E_C = 157$   $\mu\text{eV}$ ,  $\Delta = 218$   $\mu\text{eV}$ , and  $1/G_T = 100$  M $\Omega$ . (b) The tunneling rate at degeneracy  $E = 0$  as a function of temperature (squares), and best fit (solid line) to Eq. (9). Adapted from Saira, Yoon *et al.*, 2012.

dynamics of the structures in the strong Coulomb-blockade regime and electron transport properties including the dc current  $I$ , current noise, or even full statistical distribution of the transferred charge, can be obtained from the time evolution of the probabilities  $p(\{n_j\})$  of various charge configurations  $\{n_j\}$  governed by the standard rate equation for the balance of the probability fluxes. The most basic single-electron system that allows for the flow of dc current through it and gives an example of such an equation is the single-electron transistor (SET) (Averin and Likharev, 1986; Fulton and Dolan, 1987; Likharev, 1987). The transistor can be viewed as a generalization of the SEB and consists of a mesoscopic conducting island connected by two tunnel junctions to the bulk electrodes that provide the transport voltage  $V$  across it. The island is also coupled capacitively to the source of the gate voltage  $V_g$  which controls the flow of current  $I$  through the transistor between the two electrodes. An equivalent circuit of the transistor is shown in Fig. 5, and an example of its geometric structure can be seen in the upper right corner of Fig. 2(a), where it is used to measure the charge state of the SEB. The charge configuration of the transistor is characterized simply by the number  $n$  of extra electrons on its central island, and accordingly, the rate equation describing its dynamics is

$$\dot{p}(n) = \sum_{j,\pm} [p(n \pm 1)\Gamma_j^{(\mp)}(n \pm 1) - p(n)\Gamma_j^{(\pm)}(n)], \quad (10)$$

where  $p(n)$  is the probability distribution of the charge  $en$  on the central island of the transistor, and the rates  $\Gamma_j^{(\pm)}(n)$  describe the tunneling processes in junction  $j$  with the tunnel conductance  $G_j$  out of the state  $n$  in the direction that increases (+) or decreases (-)  $n$  by 1. The rates are given by Eq. (8) or (9), or their generalizations, depending on the nature of the transistor electrodes. They depend on the indices of  $\Gamma$ 's in Eq. (10) through the change  $E$  of the charging energy  $U$  of the transistor, which is a function of all these indices. The transistor energy  $U$  consists of two parts, one that coincides with the charging energy (3) of the SEB in which  $C_\Sigma = C_1 + C_2 + C_g$ , and the other  $U_V$  that is created by the transport voltage  $V$ :

$$U_V = -eNV - enV(C_2 + C_g/2)/C_\Sigma. \quad (11)$$

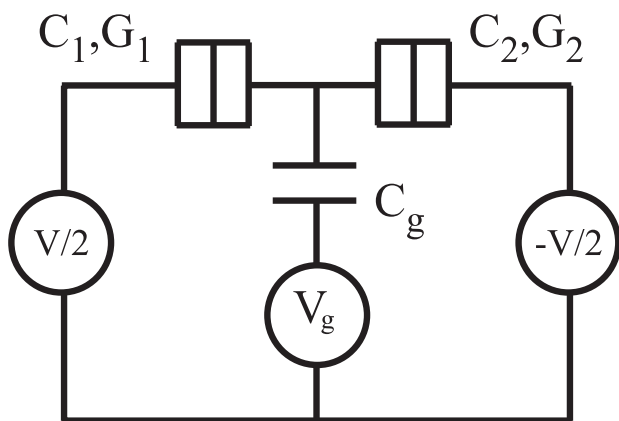


FIG. 5. Equivalent electric circuit of an SET.

Here  $N$  is the number of electrons that have been transferred through the transistor. Both the dc current  $I$  through the transistor (Averin and Likharev, 1991) and the current noise (Korotkov, 1994) can be calculated starting from Eq. (10). The main physical property of the transistor transport characteristics is that they depend periodically on the gate voltage, in particular,  $I(n_g + 1) = I(n_g)$ . This dependence of the transistor current on the charge  $en_g$  induced on its central island makes the SET a charge detector, with subelectron sensitivity approaching  $(10^{-5}-10^{-6}) e/\text{Hz}^{1/2}$  (Zimmerli *et al.*, 1992; Krupenin, 1998; Roschier *et al.*, 2001). As a result, the SET is the most standard charge detector for measurements of, e.g., individual electron dynamics in other single-electron structures [cf. Fig. 2(a)].

The hybrid SINIS or normal metal–insulator–superconductor–insulator–normal metal (NISIN) transistors have an additional important feature that distinguishes them from the SETs with normal electrodes. They provide the possibility to realize the regime of the quantized current  $I$  [Eq. (4)], when driven by an ac gate voltage  $V_g(t)$  of frequency  $f$  (Pekola *et al.*, 2008). This property of the hybrid SETs is one of the main topics of this review and is discussed in detail below.

The basic expression (6) for the tunneling rates assumes that the electrodes of the tunnel junction are in equilibrium at temperature  $T$ , with the implied assumption that this temperature coincides with fixed temperature of the whole sample. Since each electron tunneling event deposits an amount of heat  $\Delta U$  into the electron system of the electrodes, this condition requires that the relaxation processes in the electrodes are sufficiently effective to maintain the equilibrium. The relaxation rates decrease rapidly with decreasing temperature, e.g., proportional to  $T^5$  for electron-phonon relaxation in an ordinary metal; see, e.g., Giazotto *et al.* (2006). This makes the relaxation insufficient and causes the overheating effects to appear at some low temperature, in practice around 0.1 K. Therefore, the overheating sets a lower limit to the effective temperature of the transitions, in this way limiting the accuracy of control over the individual electron transport.

One more assumption underlying Eq. (9) for the tunneling rate in SIN junctions is that the electron distribution function is given by the Fermi function  $f(\epsilon)$ . As known from statistical mechanics, even in equilibrium, this requires that the total effective number of particles that participate in forming this distribution is large. In normal-metal islands, this requirement is satisfied at temperatures much larger than the single-particle level spacing,  $T \gg \delta E/k_B$ , as is the case for practically all metallic tunnel junctions. In contrast to this, in superconducting islands, this condition can be violated at temperatures below the superconducting energy gap,  $T \ll \Delta/k_B$ , when the total number of the quasiparticle excitations in the electrode is no longer large. The temperature scale of the onset of this “individual quasiparticle” regime can be estimated from  $\int_{\Delta}^{\infty} d\epsilon f(\epsilon) \nu(\epsilon) / \delta E \sim 1$ . The main qualitative feature of this regime is the sensitivity of the electron transport properties of a superconducting island to the parity of the total number of electrons on it (Averin and Nazarov, 1992b; Tuominen *et al.*, 1992). In particular, the charge tunneling rate (9) in the SIN junction should be modified in this case into the rates of tunneling of individual quasiparticles. For  $T \gg \delta E/k_B$ , these rates are still determined by the same

average  $\langle |T_{kp}|^2 \rangle$  over many single-particle states of the squares of the tunneling amplitudes (5) which gives the tunnel conductance  $G_T$ , and therefore can be expressed through  $G_T$ . In the regime of “strong” parity effects, when  $T \ll T^* \equiv \Delta/k_B \ln N_{\text{eff}}$ , where  $N_{\text{eff}} = (2\pi k_B T \Delta)^{1/2} / \delta E$  is the effective number of states for the quasiparticle excitations (Tuominen *et al.*, 1992), an ideal BCS superconductor should reach the state with no quasiparticles, if the total number  $N_0$  of electrons in the superconductor is even, and precisely one unpaired quasiparticle if  $N_0$  is odd. Although many nonequilibrium processes in realistic superconductors lead to the creation of a finite density of quasiparticle excitations which do not “freeze out” at low temperatures [see, e.g., de Visser *et al.* (2011)], one can realize the situation with the number of quasiparticles controlled as in an ideal BCS superconductor, as, e.g., in Tuominen *et al.* (1992), Lafarge *et al.* (1993), and Saira, Kemppinen *et al.* (2012). In this regime, the rates of sequential charge tunneling between the normal-metal electrode and a superconducting island depend on the parity of the total number  $N_0$  of electrons in the island (Schön and Zaikin, 1994; Maisi *et al.*, 2012). For  $T \ll T^*$ , the tunneling rates both to and from the island are dominated by the one quasiparticle that exists on the island for odd  $N_0$ . When this quasiparticle is equilibrated to the edge of the quasiparticle spectrum at energy  $\Delta$ , the rates of tunneling to and from the island (i.e., increasing and decreasing the charge  $en$  of the island) coincide, and for  $|E| \ll \Delta$  are independent of the electrostatic energy change  $E$ :

$$\Gamma^{\text{odd}} = \frac{G_T \delta E}{4e^2}. \quad (12)$$

For even  $N_0$ , when there are no quasiparticles on the island, tunneling necessarily involves the process of creation of a quasiparticle, making the tunneling rates dependent on the energy change  $E$ :

$$\Gamma^{\text{even}}(E) = \Gamma^{\text{odd}} N_{\text{eff}} e^{-(\Delta-E)/k_B T}. \quad (13)$$

In the hybrid superconductor and normal-metal structures, these tunneling rates determine the electron transport properties through a rate equation similar to Eq. (10).

### C. Cotunneling, Andreev reflection, and other higher-order processes

The sequential tunneling discussed previously represents only the first nonvanishing order of the perturbation theory in the tunnel Hamiltonian  $H_T$  (5). In the strong Coulomb-blockade regime  $G_T \ll 1/R_K$ , this approximation provides an excellent starting point for the description of electron transport, accounting quantitatively for the main observed properties of these structures. However, a more detailed picture of the transport should also include the tunneling processes of higher order in  $H_T$ , which involve transfers of more than one electron in one or several tunnel junctions. Although for  $G_T \ll 1/R_K$  the rates of these more complex multistep electron “cotunneling” processes are small in comparison with the rates of the single-step sequential electron tunneling, they are frequently important either because they provide the only energetically allowed transport mechanism or because they limit the accuracy of control of the basic

sequential single-electron transitions. The simplest example of the cotunneling is the current leakage in the SET in the CB regime (Averin and Odintsov, 1989; Geerligs, Averin, and Mooij, 1990), when the bias voltage  $V$  is smaller than the CB threshold and any single-step electron transfer that changes the charge  $en$  on the transistor island by  $\pm e$  (see Fig. 5) would increase the charging energy (3) and is suppressed. In this regime, only the two-step cotunneling process that consists of electron transfers in both junctions of the transistor in the same direction gains the bias energy (11). It achieves this by changing the number  $N$  of electrons transported through the transistor by 1 without changing the charge  $en$  on the island. Qualitatively, this process represents a quantum tunneling through the energy barrier created by the charging energy. Because of the discrete nature of charge transfer in each step of the cotunneling, its rate is not suppressed exponentially as for the usual quantum tunneling, and is smaller only by a factor  $G_T R_K \ll 1$  than the rate of sequential tunneling processes.

In a hybrid SIN junction, in addition to the charging energy, the superconducting energy gap  $\Delta$  provides an extra energy barrier to tunneling of individual electrons, suppressing the sequential tunneling rate (9) at low temperatures  $T \ll \Delta/k_B$ . The gap  $\Delta$  exists only for individual electrons, while pairs of electrons with zero total energy and momentum can enter a superconductor as a Cooper pair, in the process called Andreev reflection (Andreev, 1964). In tunnel junctions, AR can be described similarly to the cotunneling, as a perturbative two-step tunneling process, in which the transfer of the first electron is virtual and only the second electron transfer makes the process energetically favorable and real. Quantitatively, the rates of such multistep transitions can be determined through their higher-order transition amplitudes constructed according to the standard rules of perturbation theory [see, e.g., Landau and Lifshitz (1980b)]. For instance, in the simplest example of a two-step AR process in a hybrid single-electron box, the elementary amplitude  $A(\epsilon_k, \epsilon_l)$  of the process that takes two electrons in the normal electrode with energies  $\epsilon_k$  and  $\epsilon_l$  and transfers them into the superconductor as a Cooper pair can be written as

$$A(\epsilon_k, \epsilon_l) = \sum_p u_p v_p T_{kp} T_{lp} \left( \frac{1}{\Omega_p + E_i - \epsilon_k} + \frac{1}{\Omega_p + E_i - \epsilon_l} \right). \quad (14)$$

The two-step process goes through an intermediate state obtained as a result of the first step of the process. The intermediate states differ by the order of transfer of the two electrons and by the single-particle state of energy  $\epsilon_p$  in the superconductor in which the virtual quasiparticle with excitation energy  $\Omega_p = (\Delta^2 + \epsilon_p^2)^{1/2}$  is created. In addition to  $\Omega_p$ , the energy of the intermediate state includes the charging energy barrier  $E_i$  to the transfer of one electron from the normal electrode to the superconductor. The standard BCS factors  $v_p = [(1 - \epsilon_p/\Omega_p)/2]^{1/2}$  and  $u_p = [(1 + \epsilon_p/\Omega_p)/2]^{1/2}$  enter Eq. (14) because  $v_p$  is the amplitude of state  $p$  being empty in the BCS ground state, thus allowing the first electron transfer, while  $u_p$  is the overlap of the doubly occupied orbital state  $p$  with the BCS ground state, which gives the amplitude of return to the ground state after the second electron transfer. Since no

trace of the intermediate states is left in the final state obtained after the whole AR process is complete, they should be summed over coherently, at the level of the amplitude  $A(\epsilon_k, \epsilon_l)$ . By contrast, the initial states  $\epsilon_k$  and  $\epsilon_l$  of the electrons in the transition are left empty in the final state and can be used to distinguish between different transition processes. This means that they should be summed over incoherently, in the expression for the tunneling rate  $\Gamma_{\text{AR}}$ . At small temperatures  $k_B T \ll \Delta$ , one can neglect thermal excitations in the superconductor, obtaining the total AR tunneling rate as

$$\Gamma_{\text{AR}} = \frac{2\pi}{\hbar} \sum_{k,l} |A(\epsilon_k, \epsilon_l)|^2 f(\epsilon_k) f(\epsilon_l) \delta(\epsilon_k + \epsilon_l + E), \quad (15)$$

where  $E$  is the electrostatic energy change due to the complete AR tunneling process. The sum over all states  $p$  in the superconductor in Eq. (14) implies that the contribution of the individual quasiparticles [which is important in the parity-dependent transition rates (12) and (13)] is negligible in the amplitude  $A$ , and individual quasiparticles affect  $\Gamma_{\text{AR}}$  only through the change of the charging conditions for tunneling.

The result of the summation over different single-particle states in Eqs. (14) and (15) depends on the detailed structure of the SIN junction. For instance, the quadratic dependence of the AR amplitude  $A$  [Eq. (14)] on the tunneling amplitudes makes the magnitude of the Andreev reflection sensitive not only to the total tunnel conductance  $G_T$  but also to the distribution of the barrier transmission probabilities. Two main qualitative features of the aluminum oxide tunnel junctions (see Fig. 3), which are the focus of the main part of this review, are the relatively thick insulator barrier characterized by the focusing effect on the tunneling electrons and low resistance of the junction electrodes. The simplest junction model that takes into account both features assumes ballistic electron motion that can be separated into different transport channels throughout the junction. In this case, the states  $k$  and  $l$  in Eq. (15) belong to the same transport channel, and summation over different channels can be done directly and gives the effective number  $\mathcal{N}$  of the channels which, as discussed in Sec. II.B, is limited by the angular dependence of the barrier transmission probabilities [see, e.g., Averin and Bardas (1995)]. In the ballistic approximation, Eqs. (14) and (15) give for the AR tunneling rate (Hekking *et al.*, 1993; Averin and Pekola, 2008)

$$\Gamma_{\text{AR}} = \frac{\hbar G_T^2 \Delta^2}{16\pi e^4 \mathcal{N}} \int d\epsilon f(\epsilon - E/2) f(-\epsilon - E/2) \times \left| \sum_{\pm} a(\pm\epsilon - E_i - E/2) \right|^2, \quad (16)$$

where

$$a(\epsilon) \equiv (\epsilon^2 - \Delta^2)^{-1/2} \ln \left[ \frac{\Delta - \epsilon + (\epsilon^2 - \Delta^2)^{1/2}}{\Delta - \epsilon - (\epsilon^2 - \Delta^2)^{1/2}} \right].$$

Equation (16) is well defined if the relevant energies in the amplitude  $a(\epsilon)$  do not approach the edge of the superconducting energy gap  $\epsilon \simeq \Delta$ , which gives a logarithmically divergent contribution to  $\Gamma_{\text{AR}}$ . This singularity can be smeared by many mechanisms, e.g., the nonuniformity of the gap  $\Delta$  or finite transmission probability of the barrier. In the single-electron tunneling regime, one of the main broadening

mechanisms should be the lifetime of the intermediate charge state in the AR process and can be accounted for by replacing in Eq. (14) the energy  $E_i$  with  $E_i - i\gamma/2$ , where  $\gamma$  is the rate of sequential lowest-order tunneling out of the intermediate charge configuration.

Experimentally, individual AR processes can be observed directly in the time domain in the hybrid SEB (Maisi *et al.*, 2011). This observation allows one to extract the rates of AR tunneling shown in Fig. 6 as a function of the normalized gate voltage  $n_g$  which determines the energies  $E_i$  and  $E$  of the transition. Figure 6 also shows the theoretical fit based on Eq. (16). One can see that Eq. (16) describes very well the shape of the curves. The fit requires, however, a considerably smaller (roughly by a factor 15) effective number  $\mathcal{N}$  of the transport channels to describe stronger AR tunneling processes. In practice, the fact that the magnitude of AR tunneling rates is larger by roughly a factor of 10 than the theoretical expectation for a given tunnel conductance  $G_T$  is a usual feature of the tunnel junctions [see also, e.g., Pothier *et al.* (1994) and Greibe *et al.* (2011)], and in principle can be qualitatively accounted for by the variation of the barrier thickness over the junction area. Unfortunately, there is so far no quantitative experimental or theoretical evidence that the barrier nonuniformity is indeed the reason for the discrepancy between the magnitude of the lowest-order and AR tunneling.

In the structures without superconducting electrodes, multistep electron transitions, in contrast to the AR processes, involve electron transfers in different directions and/or across different tunnel junctions, since a transfer of the two electrons in the same junction and the same direction cannot make the process energetically favorable in the absence of the pairing gap  $\Delta$ . In the simplest example of the normal metal–insulator–normal metal–insulator–normal metal (NININ) SET, the two-step cotunneling process in the CB regime

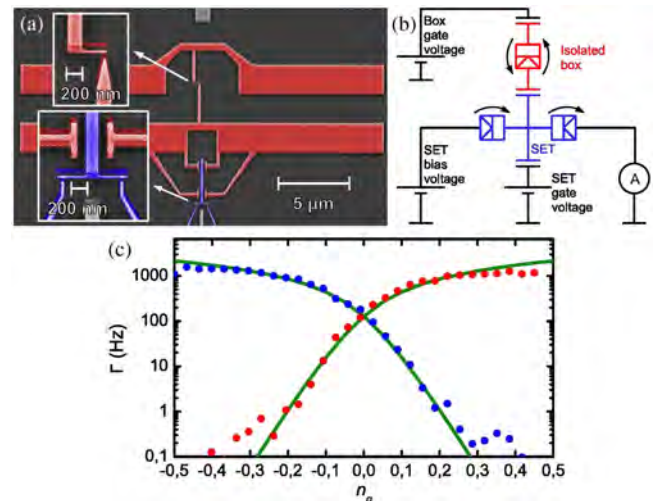


FIG. 6 (color online). Real-time detection of Andreev tunneling in an isolated SEB shown in the scanning electron micrograph of (a) and its schematic in (b). The electrometer is used for counting the single-electron and Andreev tunneling rates. (c) The tunneling rate for AR shown as dots for forward and backward directions. The lines are theoretical calculations where the nonuniformity of the tunnel barrier is taken into account. Adapted from Maisi *et al.*, 2011.

discussed qualitatively at the beginning of this section consists of two-electron transfers across the two junctions of the transistor. Quantitatively, the rate of this process is dominated by the *inelastic* contribution  $\Gamma_{\text{in}}$ , in which the single-particle states  $\epsilon_p$  and  $\epsilon_q$  of electrons in the central island of the transistor involved in the transfers are different (Averin and Odintsov, 1989). As a result, the occupation factors of these states are changed, i.e., electron-hole excitations are created after the process is completed, a fact that implies that contributions to the tunneling rates from different  $\epsilon_p$  and  $\epsilon_q$  should be summed over incoherently. The elementary amplitude  $A$  of this process consists then only of a sum over the two possibilities, one in which an electron is first transferred onto the island increasing the charging energy of the intermediate state by  $E^{(+)}$ , and the other, in which an electron tunnels first from the island still increasing the charging energy but by a different amount  $E^{(-)}$ :

$$A = T_{kp} T_{ql} \left( \frac{1}{\epsilon_p + E^{(+)} - \epsilon_k} + \frac{1}{\epsilon_l + E^{(-)} - \epsilon_q} \right). \quad (17)$$

The total rate  $\Gamma_{\text{in}}$  is given then by the sum of  $|A|^2$  over all single-particle states involved with the appropriate equilibrium occupation factors and can be expressed directly through the junction conductances as

$$\begin{aligned} \Gamma_{\text{in}}(E) = & \frac{\hbar G_1 G_2}{2\pi e^4} \int d\epsilon_k d\epsilon_p d\epsilon_q d\epsilon_l f(\epsilon_k) f(\epsilon_q) [1 - f(\epsilon_p)] \\ & \times [1 - f(\epsilon_l)] \delta(E - \epsilon_p + \epsilon_k - \epsilon_l + \epsilon_q) \\ & \times \left| \frac{1}{\epsilon_p + E^{(+)} - \epsilon_k} + \frac{1}{\epsilon_l + E^{(-)} - \epsilon_q} \right|^2, \quad (18) \end{aligned}$$

where  $E = eV$  is the energy gain due to the transfer of electron charge  $e$  through both junctions of the transistor (see Fig. 5). Equation (18) shows explicitly that the second-order electron cotunneling that involves one virtual intermediate stage is indeed smaller than the rate (6) of sequential single-electron tunneling roughly by a factor  $R_K G_T \ll 1$ . The derivation above also makes it clear that the rate of the multistep electron transitions that go through  $n$  virtual intermediate stages with larger  $n$  would be suppressed much more strongly by a factor  $(R_K G_T)^n$ .

If the energy gain  $E$  and thermal energy  $k_B T$  are smaller than the charging energy barriers  $E^{(\pm)}$ , Eq. (18) for the inelastic cotunneling rate can be simplified to

$$\Gamma_{\text{in}}(E) = \frac{\hbar G_1 G_2}{12\pi e^4} \left( \frac{1}{E^{(+)}} + \frac{1}{E^{(-)}} \right)^2 \frac{E[E^2 + (2\pi k_B T)^2]}{1 - e^{-E/k_B T}}. \quad (19)$$

This equation shows that, as a result of creation of excitations in the process of inelastic cotunneling, its rate decreases rapidly with decreasing  $E$  and  $T$ . At very low energies, the process of cotunneling in the NININ transistor will be dominated by the *elastic* contribution, in which an electron is added to and removed from the same single-particle state of the transistor island, without creating excitations on the island. Because of the restriction on the involved single-particle states, the rate of such elastic contribution contains an additional factor on the order of  $\delta E/E_C$  (Averin and Nazarov, 1990) and can win over  $\Gamma_{\text{in}}$  only at very low

temperatures, practically negligible for the structures based on the micrometer-scale metallic islands considered in this review.

The approach to multistep electron transitions in the single-electron structures illustrated in this section with the examples of Andreev reflection and electron cotunneling can be directly extended to other higher-order tunneling processes, e.g., cotunneling of a Cooper pair and an electron (Averin and Pekola, 2008), which together with Andreev reflection and electron cotunneling limit in general the accuracy of control over sequential single-electron transitions.

#### D. Coulomb blockade of Cooper-pair tunneling

In contrast to the tunneling processes considered previously, which involve electrons in the normal-metal electrodes, tunneling of Cooper pairs in a junction between two superconductors is intrinsically a dissipationless process (Josephson, 1962). As such, it should not be characterized by a tunneling rate but a tunneling amplitude. A quantitative form of the corresponding term in the junction Hamiltonian can be written most directly at low energies  $k_B T, E_C \ll \Delta$ , when the quasiparticles cannot be excited in the superconducting electrodes of the junction, and the tunneling of the Cooper pair is well separated from the tunneling of individual electrons. In this regime, a superconductor can be thought of as a Bose-Einstein condensate of a ‘‘mesoscopically’’ large number of Cooper pairs which all occupy one quantum state. Transfer of one pair between two such condensates in the electrodes of a tunnel junction does not have any non-negligible effects on the condensates apart from changing the charge  $Q = 2en$  on the junction capacitance by  $\pm 2e$ . Therefore, the part of the Hamiltonian describing the tunneling of Cooper pairs should contain the terms accounting for the changes of the charge  $Q$ . Using the standard notation  $-E_J/2$  for the amplitude of Cooper-pair tunneling and including the charging energy (3), one obtains the Hamiltonian of a superconductor-insulator-superconductor (SIS) tunnel junction or, equivalently, Cooper-pair box in the following form (Averin, Zorin, and Likharev, 1985; Büttiker, 1987):

$$H = 4E_C(n - n_g)^2 - \frac{E_J}{2} \sum_{\pm} |n\rangle \langle n \pm 1|. \quad (20)$$

Here  $n$  is the number of Cooper pairs charging the total junction capacitance, and  $n_g$  is the continuous (e.g., gate-voltage-induced) charge on this capacitance normalized now to the Cooper-pair charge  $2e$ . Similarly to the sequential tunneling rates, the Cooper-pair tunneling amplitude in the Hamiltonian (20) is a macroscopic parameter which receives contributions from all Cooper pairs in the condensate and can be expressed directly through the tunnel conductance  $G_T$  of the junction  $E_J = \pi G_T \Delta / 2e$  (Ambegaokar and Baratoff, 1963), in agreement with the simple fact that the amplitude of the two-electron tunneling should have the same dependence on the barrier transparency as the rate of tunneling of one electron. In the situation of the junction (20) realized with the actual Bose-Einstein condensates of atoms, such a ‘‘Bose-Josephson junction’’ can contain a relatively small total number of particles, and the tunnel amplitude varies then with the difference  $n$  of the number of particles in the two

condensates; see, e.g., Fölling *et al.* (2007), Averin *et al.* (2008), and Cheinet *et al.* (2008).

The dependence on the ground state of the Hamiltonian (20) on the induced charge  $n_g$  allows for qualitatively similar control of the individual Cooper pairs as for individual electrons in the normal-state SEB discussed in Sec. II.B. If  $E_J \ll E_C$ , precisely one Cooper pair is transferred through the junction, changing  $n$  by  $\pm 1$ , whenever  $n_g$  passes adiabatically through a degeneracy point  $n_g = 1/2$  modulo an integer. This leads to the same staircase-like dependence  $n(n_g)$  as in the normal case, but with each step corresponding to the transfer of one more Cooper pair with the increase of  $n_g$  by 1. The main new element of the superconducting situation is that the SIS junction is intrinsically a coherent quantum system without dissipation, and if extrinsic sources of decoherence can be made sufficiently weak, should exhibit reversible dynamics of a simple quantum system. For instance, close to the degeneracy point  $n_g = n + 1/2$  the two charge states with the same electrostatic energy,  $n$  and  $n + 1$ , are coupled by coherent quantum mechanical tunneling of a Cooper pair, and the junction behaves as a very basic quantum two-state system (Bouchiat *et al.*, 1998; Nakamura, Pashkin, and Tsai, 1999). Such two-state dynamics and general coherent quantum dynamics of the Hamiltonian (20) serve as the basis for the development of superconducting quantum information devices; for reviews, see, e.g., Averin (2000) and Makhlin, Schön, and Shnirman (2001).

Superconducting junctions also exhibit the dynamics similar to the single-electron tunneling oscillations. If the induced charge  $n_g$  grows in time at a constant rate, so that effectively a dc displacement current  $I = 2en_g$  is injected into the junction, Cooper pairs are transferred through it in a correlated manner, one by one, giving rise to the “Bloch” oscillations (Averin, Zorin, and Likharev, 1985) of voltage across the junction, with frequency  $f$  related to the current  $I$ :

$$I = 2ef. \quad (21)$$

The Hamiltonian (20) and its extensions to multijunction systems can be used to design time-dependent periodic dynamics with frequency  $f$  which transfer precisely one Cooper pair per period and therefore produce a dc current quantized according to Eq. (21). Although the system dynamics employed for such Cooper-pair pumping can be of different kinds [see, e.g., Hoehne *et al.* (2012)], the most typical is the adiabatic dynamics (Geerligs *et al.*, 1991), in which the pumped charge is related (Pekola *et al.*, 1999; Aunola and Toppari, 2003; Möttönen, Vartiainen, and Pekola, 2008) to Berry’s phase or (Faoro, Siewert, and Fazio, 2003) its non-Abelian extensions.

### E. Single-electron tunneling in semiconductor structures

One of the main features of metallic conductors used in the discussion of single-electron tunneling is the large density of free electrons in them, characterized quantitatively by the average electron-electron distance  $r$  that is not much larger than the Bohr’s radius  $a_0$ . In this regime, the electrostatic screening length  $\lambda \approx (ra_0)^{1/2}$  at low energies is also small, i.e., comparable to  $r$ . This fact has several simplifying consequences for the discussion of single-electron tunneling.

Most importantly, because of the strong screening, electrons are effectively noninteracting inside conductors at low energies relevant to the Coulomb-blockade transport. For normal metals, this makes it possible to describe the tunnel junction electrodes as reservoirs of noninteracting electrons—the model adopted above for the discussion of tunneling. (For superconducting electrodes, only superconducting pairing correlations are important.) Another consequence of a short, on the order of interatomic distance, screening length is that for all practical electrodes large on this scale the electron-electron interaction energy due to charging of the conductor as a whole is independent of the electron state inside the conductor and can be accurately described by macroscopic capacitances as was done in Eq. (1).

In the case of semiconductor single-electron structures based on quantum dots formed in two-dimensional conducting layers (see Sec. III.C for a brief discussion of the typical structures), the dot parameters, including carrier (usually, electron) concentration in the dot, can be controlled through external bias. Despite this control, and variability of the carrier concentration with the fabrication parameters, one can take  $n \sim 10^{12} \text{ cm}^{-2}$  as a typical value of concentration, which corresponds to  $r \sim 10 \text{ nm}$ . Although this electron-electron distance is considerably larger than in a good metal, the Bohr radius  $a_0 = 4\pi\epsilon_0\hbar^2/e^2m$  is also much larger in the semiconductors, e.g., gallium arsenide or silicon, used to fabricate quantum dots, because of the dielectric constant  $\epsilon \sim 10$  and effective mass  $m$  smaller than the free electron mass. This keeps the parameter  $r_s \approx r/a_0$  which determines the strength of interaction effects in an electron gas [see, e.g., Mahan (1990)] in the same weak-interaction range  $r_s \sim 1$  and makes it reasonable to describe a quantum dot in the same approximation as used previously for metallic islands: noninteracting electron gas inside the dot with the electron-electron interaction giving rise to the charging energy  $U(n)$  that depends only on the total number  $n$  of electrons in the dot and can be expressed through the constant dot capacitance  $C_\Sigma$  as in Eq. (3). Since quantum confinement of effectively noninteracting electrons inside the dot potential produces in addition an energy spectrum  $\epsilon_k$  of the single-particle states, the total dot Hamiltonian is then

$$H = U(n) + \sum_k \epsilon_k c_k^\dagger c_k, \quad n = \sum_k c_k^\dagger c_k. \quad (22)$$

Although this model of a quantum dot is the same as for the normal-metal islands, an important difference between the two situations is created by the difference in the absolute values of characteristic length scales  $r$  and  $a_0$  which are much larger for quantum dots. Because of this, already relatively “large” dots with characteristic dimensions  $d \sim 100 \text{ nm}$  can contain a small total number of electrons, starting with  $n = 1$ , and have the single-particle level spacing  $\delta E$  comparable to the charging energy  $E_c$ . This difference has two important consequences which make a quantitative description of single-electron transport in quantum dots in general more involved than in metallic structures. The larger level spacing  $\delta E$  reduces the number of the single-particle energy levels participating in the single-electron tunneling transitions through the dot making the nonequilibrium effects in energy distribution of electrons in the dot more prominent in the

regime of nonlinear transport. The small number of levels involved in transport also creates statistical correlations between occupation factors of different levels even for electrons that are effectively noninteracting inside the dot, as in the Hamiltonian (22). Combined, all this means that in contrast to metallic islands, the dynamics of the total charge  $en$  on the dot is not decoupled from the electron dynamics in the dot and depends more strongly on the relaxation processes and the structure of the energy spectrum  $\epsilon_k$ , both of which are sensitive to the effect of disorder on the dot confining potential.

For weak tunneling, a quantitative description of single-electron transport through a quantum dot, in a structure similar to a single-electron transistor (see Fig. 3), is based on a kinetic equation similar to Eq. (10) in the metallic regime (Averin, Korotkov, and Likharev, 1991; Beenakker, 1991). As qualitatively discussed previously, in the case of a dot, this equation cannot be formulated directly in terms of the probability distribution  $p(n)$  of the charge on the dot, but requires the probability  $p(n; k_1, \dots, k_n)$  that a given set of  $n$  single-particle states of the dot  $k_1, \dots, k_n$  is occupied by electrons. [Since we will not be dealing explicitly with spin-related phenomena, it is assumed for notational simplicity that  $k$  includes the spin index of the single-particle states. Also note that the order of indices of the occupied states in the argument of  $p(n; k_1, \dots, k_n)$  is irrelevant.] Expressed through this probability, the kinetic equation reads

$$\dot{p}(n; k_1, \dots, k_n) = S_{\text{tun}} + S_{\text{rel}}, \quad (23)$$

where  $S_{\text{tun}}$  and  $S_{\text{rel}}$  are, respectively, the probability flows due to electron tunneling between the dot and external electrodes which changes the charge  $en$  of the dot by  $\pm e$ , and electron transitions inside the dot (without changing  $n$ ) due to electron-phonon or residual electron-electron interactions which lead to thermalization and energy relaxation of electrons in the dot. The terms  $S_{\text{tun}}$  are expressed through the rates of tunneling between state  $k$  in the dot and reservoir  $j$ , which similarly to metallic tunnel junctions (5) can be written as  $\Gamma_{k,j} = 2\pi \langle |T_{kp}|^2 \rangle \rho_j / \hbar$ , where  $\langle \dots \rangle$  denotes averaging over the states  $p$  in reservoir  $j$  which have density  $\rho_j$ . In terms of these rates,

$$\begin{aligned} S_{\text{tun}} = & \sum_j \left\{ \sum_{k \neq \{k_i\}} \Gamma_{k,j} [p(n+1; k_1, \dots, k_n, k) \right. \\ & \times (1 - f(\epsilon_k + E_{j,n+1})) - p(n; k_1, \dots, k_n) \\ & \times f(\epsilon_k + E_{j,n+1})] + \sum_{k \in \{k_i\}} \Gamma_{k,j} [p(n-1; \{k_i\} - k) \\ & \times f(\epsilon_k + E_{j,n}) - p(n; k_1, \dots, k_n) \\ & \left. \times (1 - f(\epsilon_k + E_{j,n}))] \right\}, \quad (24) \end{aligned}$$

where  $E_{j,n}$  is the change of the energy  $U_{\text{tot}} = U(n) + U_V$  which consists of the charging energy  $U(n)$  [Eq. (3)] and the bias energy  $U_V$  [Eq. (11)], due to transfer of one electron into the  $j$ th electrode from the dot carrying charge  $en$ .

The relaxation term  $S_{\text{rel}}$  in the kinetic equation can be written similarly. For instance, in the case of electron-phonon relaxation

$$\begin{aligned} S_{\text{rel}} = & \sum_{l \neq \{k_i\}} \sum_{k \in \{k_i\}} [\gamma(\epsilon_l - \epsilon_k) p(n; \{k_i\} - k, l) \\ & - \gamma(\epsilon_k - \epsilon_l) p(n; k_1, \dots, k_n)], \quad (25) \end{aligned}$$

where  $\gamma(\epsilon)$ 's are the rates of the phonon-induced transitions between the electron states in the dot. These equations show that the general nonlinear single-electron transport through the dot depends quantitatively on its microscopic structure, in particular, energy relaxation rates. In general, sensitivity of the single-particle level structure of the dot to its geometric shape and the details of the confining potential [for a review, see, e.g., Reiman and Manninen (2002)] turns precise quantitative characteristics of the dot transport almost into the fingerprints of an individual quantum dot, even in the simplest situation of effectively noninteracting electrons in the dot. In addition, at low electron densities, electron-electron correlations inside the dot can become important, leading to formation of a finite Wigner crystal in effectively both one-dimensional and two-dimensional dots; see, e.g., Häusler and Kramer (1993) and Filinov, Bonitz, and Lozovik (2001) and references therein. From the point of view of electron transport, the main characteristic feature of such a correlated electron state is additional energy dependence of the electron tunneling rates into the dot, with tunneling suppressed by correlations at low energies (Kane and Fisher, 1992; Averin and Nazarov, 1993; Matveev and Glazman, 1993).

Despite stronger influence of internal microscopic physics on the quantum-dot transport, the charging energy  $E_C$  associated with individual electrons still remains typically the dominant energy in comparison, e.g., to the level spacing  $\delta E$ , in the case of quantum dots as well. Because of this, semiconductor quantum dots allow for qualitatively similar manipulation of individual electrons as do metallic structures. Moreover, semiconductor structures provide an additional flexibility in this respect, in that the islands and barriers defining the quantum dots can be tuned or even formed by applying external voltages to gate electrodes; see Sec. III.C for details. This is in contrast to metallic systems which are usually defined solely by the conducting and insulating regions of the fabricated structure. An example of the single-electron control in a GaAs/AlGaAs semiconductor structure, two quantum dots monitored with a quantum-point contact (QPC) operated as a charge detector (Küng *et al.*, 2012), is shown in Fig. 7. In this system, the QPC detector distinguishes different charge states of the two dots and allows one to detect transitions of individual electrons between the dots and to or from the source and drain electrodes. The observed charge dynamics as seen, e.g., in Fig. 7(c), resembles that in the metallic SEB shown in Fig. 2. Such correlated single-electron transitions in semiconductor dots, combined with the possibility of the gate-voltage control of tunnel barriers, make it possible to pump electrons by direct periodic modulation of the two barriers of a dot (Kouwenhoven *et al.*, 1991a).

Attempts to increase the magnitude of pumped current lead naturally to the situation when the barriers become nearly completely suppressed, and electrons can cross them not only by quantum tunneling through the barrier but also by classical motion over the barrier. Coulomb-blockade correlations among different charge states survive in this regime (Zimmerman *et al.*, 2004) which should be, in particular,

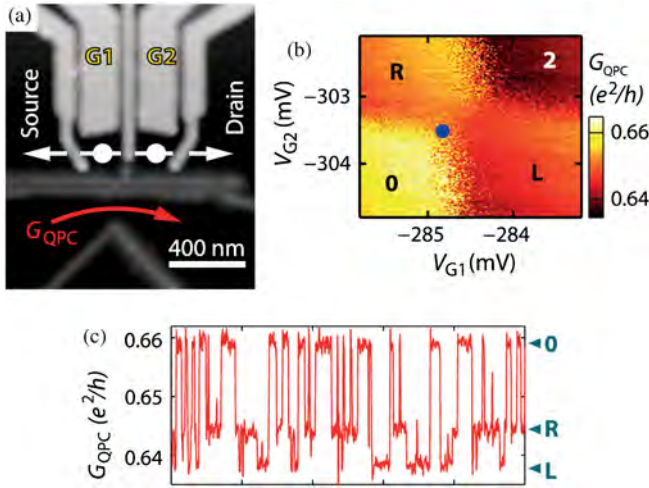


FIG. 7 (color online). Single-electron control in a semiconductor structure consisting of two lateral quantum dots measured with a quantum-point-contact (QPC) charge detector. (a) Atomic force microscope image of the structure. (b) The diagram of the equilibrium charge states of the two dots, controlled by voltages on the gates  $G1$  and  $G2$ : empty dots (0); left ( $L$ ), right ( $R$ ), or both dots (2), occupied with one electron. (c) Trace of the output signal of the QPC detector (conductance  $G_{\text{QPC}}$ ) showing random single-electron transitions between these states driven by thermal fluctuations close to the degeneracy point, when the charging energies of the states (0), ( $L$ ), and ( $R$ ) coincide. From [Küing \*et al.\*, 2012](#).

relevant for the “dynamic” quantum dots formed and destroyed by rapidly changing gate voltages; see [Blumenthal \*et al.\* \(2007\)](#) and [Fricke \*et al.\* \(2013\)](#) and references therein. The process of electron transfer through the rapidly created or destroyed barriers can lead to a stochastic uncertainty in created charge state of the quantum dot, which is described with a “decay-cascade” model ([Kashcheyevs and Kaestner, 2010](#)). Because of the uncertainty in microscopic dynamics underlying the electron transfer in quantum dots discussed above, the precise limits which the varying barriers impose on the accuracy of electron manipulation in dynamic quantum dots are still not fully understood ([Zimmerman \*et al.\*, 2004](#); [Blumenthal \*et al.\*, 2007](#); [Fujiwara, Nishiguchi, and Ono, 2008](#); [Kashcheyevs and Timoshenko, 2012](#); [Lin and Zhang, 2012](#)).

## F. Influence of environment on tunneling

Tunneling in small junctions is influenced by the electromagnetic environment. The tunneling rates are modified by photon absorption or emission; Fig. 8 schematically depicts a process where the tunneling rate in a generic junction is enhanced by absorption of a photon from the environment.

The general theoretical framework of how this happens was put forward in seminal works by [Devoret \*et al.\* \(1990\)](#) and [Girvin \*et al.\* \(1990\)](#), and later expanded by [Ingold and Nazarov \(1992\)](#). The golden-rule-type tunneling rates discussed in the earlier sections get modified as

$$\Gamma = \frac{1}{e^2 R_T} \int_{-\infty}^{\infty} \int_{-\infty}^{\infty} dE dE' \nu_1(E - \delta E) \nu_2(E') f_1(E - \delta E) \times [1 - f_2(E')] P(E - E'), \quad (26)$$

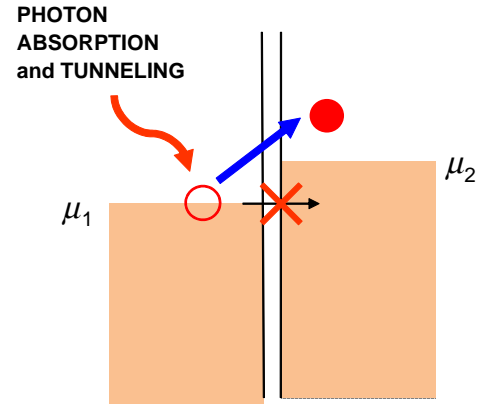


FIG. 8 (color online). A simple schematic showing photon absorption by a generic tunnel junction, and the inelastic electron tunneling from the left side of the barrier to the right.

where  $\nu_i(E)$ ,  $i = 1, 2$  are the normalized DOSs in the two electrodes,  $f_i(E)$  are the corresponding energy distributions in the electrodes, and  $\delta E$  is the energy cost in the tunneling event. The function  $P(E)$  can be interpreted as the probability density to emit energy  $E$  to the environment, which becomes a delta function in the special case of a junction with perfect voltage bias. The  $P(E)$  can be calculated as the following transformation using the phase-phase correlation function  $J(t)$ :

$$P(E) = \frac{1}{2\pi\hbar} \int_{-\infty}^{\infty} \exp\left(J(t) + \frac{i}{\hbar} Et\right) dt. \quad (27)$$

By modeling the environment by a frequency  $\omega/2\pi$  dependent impedance  $Z(\omega)$  in thermal equilibrium at temperature  $T_{\text{env}}$ , one obtains

$$J(t) = 2 \int_0^{\infty} \frac{d\omega}{\omega} \frac{\text{Re}[Z(\omega)]}{R_K} \left[ \coth\left(\frac{\hbar\omega}{2k_B T_{\text{env}}}\right) (\cos\omega t - 1) - i \sin\omega t \right], \quad (28)$$

where  $R_K = h/e^2$  is the resistance quantum.

Often one can assume that the unintentional environment can be modeled as a wideband dissipative source in the form of an  $RC$  circuit. For a purely resistive and capacitive environment

$$\text{Re}[Z(\omega)] = R/[1 + (\omega RC)^2], \quad (29)$$

where  $R$  is the resistance of the environment and  $C$  is the total capacitance including the junction capacitance and parallel shunt capacitors. This rather simple model has been successfully applied to explain several experimental observations; see, e.g., [Martinis and Nahum \(1993\)](#) and [Hergenrother \*et al.\* \(1995\)](#). For a system with intentionally enhanced capacitance, it could be used to account for experimental improvement of the characteristics of a normal metal–insulator–superconductor (NIS) junction and of a single-electron turnstile ([Pekola \*et al.\*, 2010](#)). Further improvements were obtained by [Saira \*et al.\* \(2010\)](#) and [Saira, Kempainen \*et al.\* \(2012\)](#); see Sec. III.B. We show in Fig. 9 an NIS junction and its current-voltage characteristics under different experimental conditions.

Focusing on the single-electron sources, the environment has at least two effects to be considered. (i) The coupling of

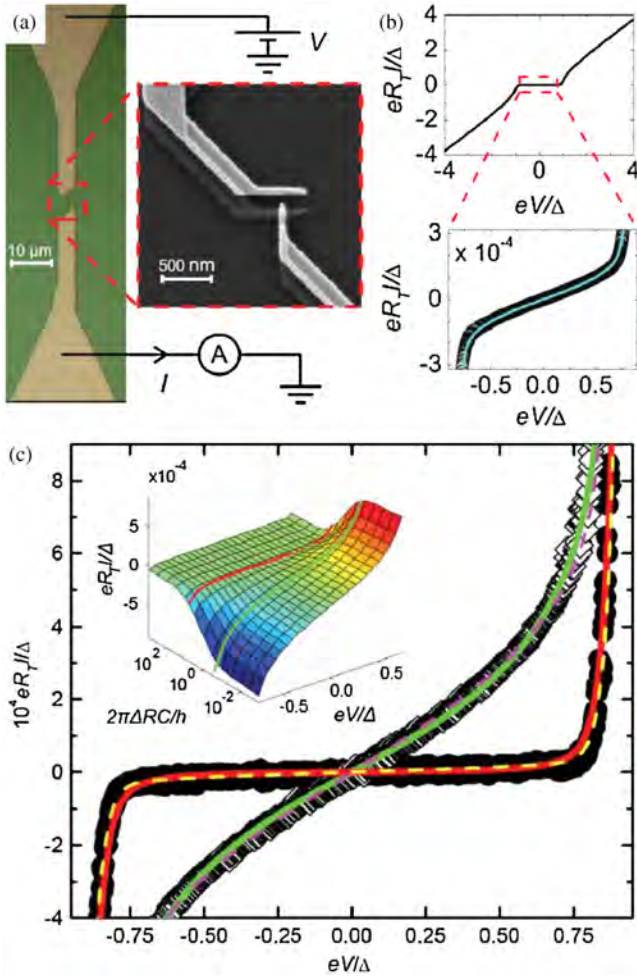


FIG. 9 (color online). NIS junctions influenced by a hot environment. (a) Geometry of a NIS junction made of aluminum (low contrast) as the superconductor and copper (high contrast) as the normal metal. The tapered ends lead to large pads. (b) Typical  $I$ - $V$  characteristics, measured at 50 mK for a junction with  $R_T = 30$  k $\Omega$ . Linear leakage, i.e., nonvanishing subgap current due to coupling to the environment, can be observed. The dotted line is the corresponding theoretical line from the  $P(E)$  theory and  $RC$  environment with dissipation  $R$  at  $T_{\text{env}} = 4.2$  K. (c) Measured  $I$ - $V$  curves of an NIS junction with  $R_T = 761$  k $\Omega$  on a ground plane providing a large protecting capacitance against thermal fluctuations (solid symbols) and of a similar junction with  $R_T = 627$  k $\Omega$  without the ground plane (open symbols). Solid lines present the theoretical results for capacitance  $C = 10$  and 0.3 pF. The resistance and the temperature of the environment are set to  $R = 2$   $\Omega$  and  $T_{\text{env}} = 4.2$  K, respectively. The inset shows  $I$ - $V$  curves based on the full  $P(E)$  calculation as functions of the shunt capacitance  $C$ . The colored lines are reproduced on this graph from the main figure. Adapted from [Pekola \*et al.\*, 2010](#).

the blackbody radiation of the hot surrounding environment can induce photon-assisted tunneling. (ii) The intentionally fabricated on-chip environment in the immediate vicinity of the single-electron circuit serves as a filter against external noise. Moreover, it can influence the tunneling rates in a way that improves the performance ([Zorin \*et al.\*, 2000](#); [Lotkhov \*et al.\*, 2001](#); [Bubanja, 2011](#)). Detailed discussion of the error processes in pumps, including those due to coupling to the environment, is given further in this review.

## G. Heating of single-electron devices

Single-electron circuits operate optimally at low temperatures. The standard condition is that  $k_B T \ll E_C$ , where  $E_C$  is the characteristic charging energy scale. Another condition in superconductor-based devices is that  $k_B T \ll \Delta$ , where  $\Delta$  is the energy gap of the superconductor. Since thermal errors in synchronized transfer of electrons are typically proportional to  $e^{-E_{CR}/k_B T}$ , where  $E_{CR}$  is the characteristic energy (in the previous examples  $E_C$  or  $\Delta$ ), it is obvious that the temperature needs to be more than an order of magnitude below  $E_{CR}/k_B$ . At low temperatures the overheating becomes a critical issue ([Giazotto \*et al.\*, 2006](#)). The energy relaxation between the electron system and the bath, typically formed by the phonons, becomes increasingly slow toward low temperatures. Moreover, the various heating rates are typically not scaling down similarly with decreasing temperature.

Heat is injected to the electron system, first and foremost, as Joule heating due to the current in a biased circuit. Other sources of heat include the application of dissipative gate voltages or magnetic flux injection, thermal radiation discussed in Sec. II.F, and shot-noise-induced dissipation by backaction from a charge or current detector. The steady-state temperature of the electron system is determined by the balance between the input powers and the heat currents via different relaxation channels. The injected energy relaxes to phonons via electron-phonon relaxation, to the leads by heat transport through the tunnel junctions, and by radiation to other dissipative elements in the cold circuit. We discuss these processes in more detail.

*Joule heating and cooling:* In a biased circuit, the total Joule power is  $P = IV$ , where  $V$  is the overall voltage and  $I$  is the current. This power can, however, be distributed very unevenly in the different parts of the circuit: in an extreme example, some parts may cool down whereas the others are heavily overheated. We now focus on dissipation in biased tunnel junctions. The basic example is a tunneling process in a junction between two conductors with essentially constant density of states, which is the case presented by normal metals. At the finite bias voltage  $V$  the tunneling electron leaves behind a holelike excitation and it creates an excited electron in the other electrode, i.e., both electrodes tend to heat up. Quantitatively we can write the expression of the power deposited in the, say, right electrode as

$$P_R = \frac{1}{e^2 R_T} \int dE E [f_L(E - eV) - f_R(E)]. \quad (30)$$

Here  $f_{L,R}$  refer to the energy distributions on the left ( $L$ ) and right ( $R$ ) sides of the junction, respectively.  $P_R = V^2/2R_T$  when  $f_L = f_R$ , i.e., when the temperatures of the two sides are equal. By symmetry, or by direct calculation, we can verify that the same amount of power is deposited into the left electrode in this situation. Thus the total power dissipation equals  $P = P_L + P_R = V^2/R_T = IV$ , as it should.

If one of the conductors is superconducting, the current-voltage characteristics are nonlinear and the power deposited into each electrode is given by

$$P_{N,S} = \frac{1}{e^2 R_T} \int dE \tilde{E}_{N/S} \nu_S(E) [f_N(E - eV) - f_S(E)]. \quad (31)$$

Here  $\tilde{E}_N = -(E - eV)$  and  $\tilde{E}_S = E$ , where  $N$  and  $S$  now refer to the normal and superconducting leads, respectively. The overall heating is again given by  $IV$ , but in this case, under bias conditions  $eV \approx \Delta$ ,  $P_N$  on the normal side can become negative [NIS cooling (Giazotto *et al.*, 2006)] and  $P_S$  on the superconductor side is always positive, i.e., it is heated up.

Finally, if both sides are superconducting, the current-voltage characteristics are highly nonlinear, but due to symmetry  $P_L = P_R = IV/2 = P/2$ .

*Other heating sources:* Overheating of a single-electron circuit can be caused by various other sources. ac gate voltages or ac magnetic fluxes can induce dissipative currents and heating due to dielectric losses, and single-electron electrometry or electrometry by a quantum-point-contact detector can cause effective heating due to the shot-noise backaction coupling to the single-electron circuit, just to mention a few possibilities.

*Energy relaxation by conduction to leads:* If a difference between the electronic temperatures  $T_L$  and  $T_R$  of the left and right leads exists,  $\Delta T \equiv T_L - T_R$ , heat  $P_{L \rightarrow R}$  can flow electronically through the tunnel barrier. In the case of a normal-normal junction, we have

$$P_{L \rightarrow R} = \frac{1}{e^2 R_T} \int dE E [f_L(E) - f_R(E)] = \frac{\pi^2 k_B^2}{6e^2 R_T} (T_L^2 - T_R^2), \quad (32)$$

where in the last step we assume that the junction is not biased. For a small temperature difference  $\Delta T$  about the mean  $T = (T_L + T_R)/2$  of the two temperatures, we can then write the thermal conductance  $G_{\text{th}} \equiv P_{L \rightarrow R}/\Delta T$  of a NIN tunnel junction as

$$G_{\text{th}} = \frac{\pi^2 k_B^2 T}{3e^2 R_T}, \quad (33)$$

which is the Wiedemann-Franz law for a conductor with resistance  $R_T$ . For either an NIS or SIS junction, heat conductance is exponentially small at low temperatures due to  $\Delta$ . Another mechanism for the heat flow is the diffusion in the leads. It is discussed, in particular, in superconducting leads in Sec. III.B.3.

*Electron-phonon relaxation:* Electron-phonon relaxation is one of the dominant and in many systems one of the best understood relaxation mechanisms. For a normal-metal conductor with a uniform temperature  $T$  that differs from the bath phonon temperature  $T_0$ , one can write quite generally (Wellstood, Urbina, and Clarke, 1994)

$$P_{\text{e-p}} = \Sigma \mathcal{V} (T^5 - T_0^5), \quad (34)$$

where  $\Sigma$  is a material constant of the order of  $10^9 \text{ W K}^{-5} \text{ m}^{-3}$  (Giazotto *et al.*, 2006), and  $\mathcal{V}$  is the volume of the conductor. This equation holds amazingly well at subkelvin temperatures for various metals, irrespective of their dimensions. In single-electron devices, we typically consider dissipation in a small Coulomb-blockaded region, whose volume is small, and thus, according to Eq. (34), the coupling to the phonon bath is weak. Because of the small dimensions, one typically assumes a spatially uniform energy distribution on the conductor; moreover, the assumption of overheating with a well-defined electron temperature is also justified quite generally.

In some cases these assumptions are not necessarily valid. An important exception is given by superconductors where energy relaxation via phonon emission becomes extremely weak due to the energy gap. At low temperatures the relaxation is limited by the emission of  $2\Delta$  phonons corresponding to the recombination of quasiparticles into Cooper pairs (Rothwarf and Taylor, 1967). In the past few years, several experiments have measured the relaxation rate in this context [see, e.g., Barends *et al.* (2008)], and the corresponding energy release rate was measured recently by Timofeev, Garcia *et al.* (2009). According to the latter measurement the recombination-related heat flux is strongly suppressed from that given in Eq. (34), being about 2 orders of magnitude weaker than in the normal state at the temperature  $T = 0.3T_C$ , where  $T_C$  is the critical temperature of aluminum. At even lower temperatures the heat current is further suppressed, eventually exponentially as proportional to  $e^{-\Delta/k_B T}$ . Besides recombination, the diffusive heat conduction is also strongly suppressed in a superconductor at  $T \ll T_C$ . This means that a superconductor is a poor material as a lead of a single-electron source, where nonequilibrium quasiparticles are injected at the rate  $f$ . The situation can be improved by inserting so-called quasiparticle traps into the circuit, discussed in Sec. III.B.3. Yet a fully superconducting Cooper-pair pump can be dissipationless ideally.

*Heating and cooling by radiation:* Coupling of a junction to the electromagnetic environment is associated with heat exchange. A hot environment can induce photon-assisted tunneling as discussed in Sec. II.F. The basic concept of radiative heat transport in an electric circuit has been known since the experiments of Johnson (1928) and Nyquist (1928) more than 80 years ago. Electromagnetic radiation on a chip has recently turned out to be an important channel of heat transport at low temperatures (Schmidt, Schoelkopf, and Cleland, 2004; Meschke, Guichard, and Pekola, 2006; Timofeev, Helle *et al.*, 2009). If two resistors  $R_1$  and  $R_2$  at temperatures  $T_1$  and  $T_2$  are connected directly to each other in a loop, the heat exchange between them can be modeled by a Langevin-type circuit analysis as indicated in Fig. 10 by the voltage sources producing thermal noise. Assuming an idealized quantum limit, where the circuit transmits all frequencies

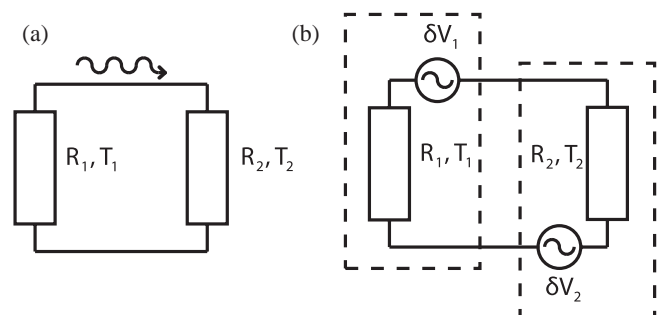


FIG. 10. (a) Radiative heat flow is caused by the photons which carry energy between resistors  $R_1$  and  $R_2$  at temperatures  $T_1$  and  $T_2$ , respectively. The heat transport can be modeled by having voltage fluctuations  $\delta V_i$  as shown in (b). Here we have assumed total transmission. The assumption can be relaxed by adding a nonzero impedance to the loop.

up to the thermal cutoff at  $\omega_{\text{th}} = k_B T_i / \hbar$ , the net heat current between the two resistors is given by

$$P_\gamma = \frac{R_1 R_2}{(R_1 + R_2)^2} \frac{\pi k_B^2}{12 \hbar} (T_1^2 - T_2^2). \quad (35)$$

This is an interesting limit which applies for circuits on a chip where the stray capacitances and inductances are small enough such that the circuit low-pass cutoff frequency exceeds  $\omega_{\text{th}}$ . Equation (35) has an important limit for the maximum coupling with  $R_1 = R_2$  and for small temperature differences  $|T_1 - T_2|$ , namely,  $G_{\text{th}} = P_\gamma / (T_1 - T_2) = \pi k_B^2 T / 6 \hbar \equiv G_Q$ , the so-called quantum of thermal conductance (Pendry, 1983). Equation (35) can also be applied in the case where one of the resistors is replaced by an NIN tunnel junction with the corresponding resistance. Another important case is that of a hot resistor  $R$  at temperature  $T_{\text{env}}$ , discussed in Sec. II.F. In this limit, with  $RC$  cut off as discussed in Sec. II.F, one finds that the heat absorption rate by a resistor or a normal tunnel junction (at  $T \ll T_{\text{env}}$ ) is given by (Pekola and Hekking, 2007)

$$P_\gamma = \frac{k_B T_{\text{env}}}{R_T C}. \quad (36)$$

### III. REALIZATIONS

#### A. Normal-metal devices

Single-electron tunneling effects provide a means to transport electrons controllably one by one. In this respect the obvious choices are metallic single-electron circuits and semiconducting quantum dots. The metallic ones can be either in their normal or superconducting state or as hybrids of the two. The quantum dots, metallic hybrids, and superconducting circuits will be discussed in later sections. The first single-electron source was a metallic (nonsuperconducting) turnstile with four tunnel junctions and one active gate (Geerligs *et al.*, 1990). The word “turnstile” refers to a device that is voltage biased at  $V_b$  between the external leads, but where the transport of electrons is impeded under idle conditions because of an energy gap. Under the active gate operation, electrons are transported synchronously one at a time. The finite voltage determines the direction of charge transport at the expense that the device is also dissipative. We discuss a more recent version of a turnstile in Sec. III.B.

The most impressive results of the early days of single-electron sources were obtained by metallic multijunction pumps, operating in a nonsuperconducting state. A prototype of them, featuring the main principle, is the three-junction pump, with two islands and a gate to each of them; see Fig. 11(a). This kind of pump was successfully operated in 1991 by Pothier *et al.* (Pothier, 1991; Pothier *et al.*, 1991, 1992). Figure 11(b) demonstrates the stability diagram of a three-junction pump, which is essentially the same as that of the more common double-island quantum-dot circuit. The two axes here are the two gate voltages  $n_{g1}$ ,  $n_{g2}$  normalized by the voltage corresponding to charge displacement of one electron, i.e.,  $n_{gi} = C_{gi} V_{g,i} / e$ , where  $C_{gi}$  is the gate capacitance of island  $i$ . The stability diagram consists of lines separating different stable charge states on the islands, indicated by indices  $(n_1, n_2)$  in the figure. The important property of this stability diagram is the existence of the nodes

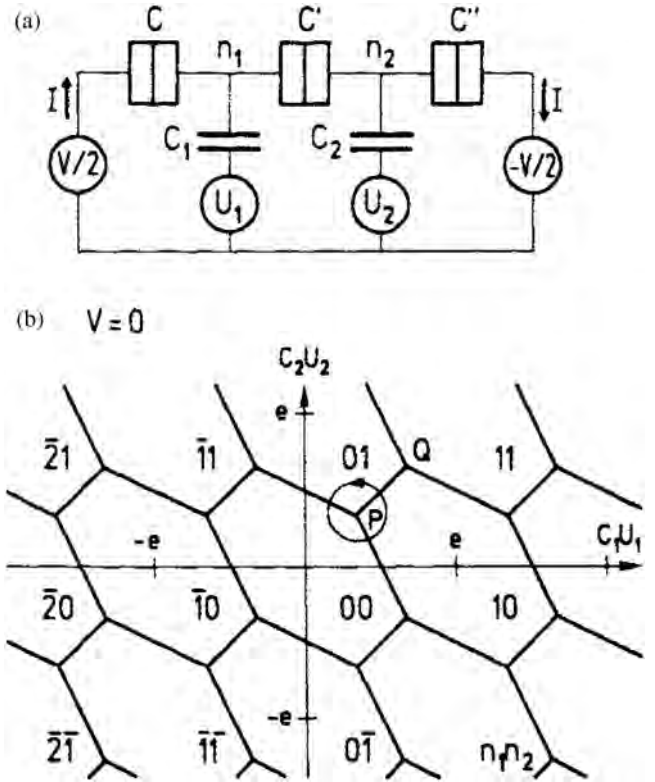


FIG. 11. A three-junction pump. Schematics shown in (a), where the pump is biased by voltage  $V$  and with gate voltages  $U_1$  and  $U_2$ . (b) The stability diagram of the three-junction pump on the plane of the gate voltages at zero bias voltage. For operation of the pump, see text. From Pothier, 1991.

where three different charge states become degenerate; these are the three states with the lowest energy. The pump is operated around such a node, setting the working point at this node by applying dc voltages to the two gates. We focus here on one such node that at  $n_{g1} = n_{g2} = 1/3$ . Now if the temporally varying gate voltages with frequency  $f$  added to these dc gate biases are such that the cyclic trajectory encircles the node at  $n_{g1} = n_{g2} = 1/3$  counterclockwise, one electron is transported through the pump from left to right. The simplest implementation of such a cyclic trajectory is a circle around the node, which is represented by two equal-amplitude (in  $n_{gi}$ ) sinusoidal voltages applied to the two gates, phase shifted by  $90^\circ$ . We take point A as the starting point of the cycle. There the system is in the charge state  $(0, 0)$ . Upon crossing the first degeneracy line, the new stable charge state is  $(1, 0)$ , meaning that an electron has to tunnel from the left lead to island 1, while moving in this part of the stability diagram. Reversible pumping is achieved when  $f$  is so slow that the transition occurs right at the degeneracy line. If, however, the pumping frequency is too fast, the tunneling does not occur before meeting the next degeneracy line, and the pumping fails. Roughly speaking, the tunneling process is stochastic, where the decay time of the Poisson process is determined by the junction resistance (see Sec. II.B), and if the pumping frequency becomes comparable to the inverse decay time for tunneling, the desired event can be missed. In the successful cycle, on the contrary, the system next crosses the degeneracy line between charge states  $(1, 0)$  and  $(0, 1)$ , and

under the same conditions, the system transits to the new stable charge state by an electron tunneling from the left island to the right one. In the remaining part of the cycle, on crossing the last degeneracy line, an electron tunnels from the right island to the right lead, completing the cycle where charge  $e$  (one electron) has been transported from the left lead to the right one. By cyclically repeating this path at frequency  $f$ , an average current  $I = ef$  runs from right to left, and this current can be read, for instance, by a regular transimpedance amplifier.

One of the advantages of the three-junction pump over the early turnstiles is that the device can be operated, in principle, reversibly, since no external bias voltage is needed. It can pump even against moderate bias. Another difference between the pump and the turnstile above is that in the pump there are no unattended islands on which the charge would be poorly controlled. Yet early realizations using fully normal-metal conductors in both the turnstiles and pumps suffered from other error sources which made these devices relatively inaccurate, on the level of 1%, even at low operation frequencies. A fundamental error source in this case is cotunneling, discussed in Sec. II.C. To circumvent this problem, a pump with a longer array of junctions is desirable: the error rate due to cotunneling is effectively suppressed by increasing the number of junctions in the array.

Theoretical analysis of cotunneling in multijunction pumps in the form of  $N$  junctions in series with nonsuperconducting electrodes was performed by Jensen and Martinis (1992) and Averin, Odintsov, and Vyshenskii (1993). Thermal cotunneling errors were analyzed with a focus on the cases  $N = 4$  and 5. The conclusion of the analysis was that under realistic experimental conditions, the  $N = 4$  pump fails to produce an accuracy better than about  $10^{-5}$ , insufficient for metrology, whereas  $N = 5$  should be sufficiently good at low operation frequencies, as far as cotunneling is concerned. This is illustrated in Fig. 12, where a relative error of  $10^{-8}$  was predicted for an  $N = 5$  pump at the operation frequency of  $f = 1.3$  MHz, assuming that the pump junctions have

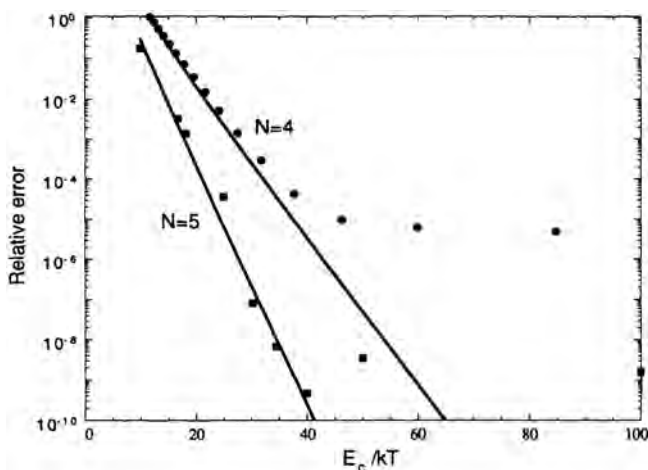


FIG. 12. Predicted relative cotunneling-induced error vs inverse temperature for multijunction pumps, with  $N = 4$  (circles) and  $N = 5$  (squares). The computer simulations (points) and the predictions of analytic results (lines) are shown. Parameters are  $R_T = 20R_K$ ,  $f = 4 \times 10^{-4}/R_T C$ , and  $CV/e = -0.15$ . Adapted from Jensen and Martinis, 1992.

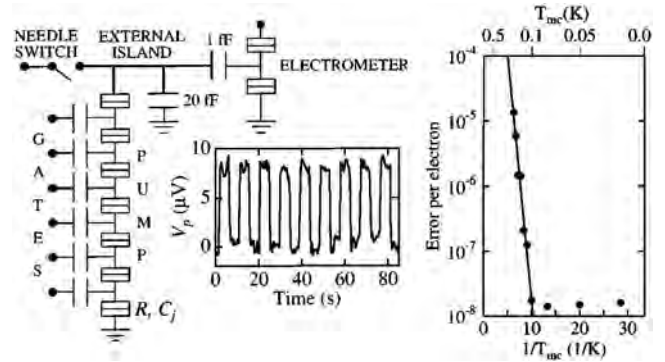


FIG. 13. The seven-junction pump. (Left) The schematic of the pump, with six islands, each with a gate. The electrons are pumped to and from the external island on the top, and the charge on the island is detected by a single-electron electrometer. (Middle) The voltage  $V_p$  on the external island vs time when pumping  $\pm e$  with a wait time of 4.5 s in between. (Right) The pumping error vs temperature of the measurement, demonstrating the 15 ppb accuracy at temperatures below 100 mK. Adapted from Keller *et al.*, 1996.

$R_T = 500\text{k}\Omega$  and  $C = 0.6\text{fF}$ , and that the working temperature is  $T = 50$  mK. All these parameters are quite realistic. In subsequent experiments (Martinis, Nahum, and Jensen, 1994), an error rate of about 0.5 ppm was achieved, which is still orders of magnitude above the prediction based on cotunneling for their circuit parameters and experimental conditions. Next, focus was turned to an  $N = 7$  pump where further improved results, 15 ppb, were obtained at pumping frequencies of about 10 MHz (Keller *et al.*, 1996). This impressive result, depicted in Fig. 13, was proposed to present a capacitance standard based on electron counting (Keller *et al.*, 1999) and it still today stands as the best achievement in this respect. However, one notes that the frequency at which such a multijunction pump can be operated is very low, resulting in currents that are too small for a metrological redefinition of the ampere.

An analysis of the pump accuracy in the framework of the orthodox theory including cotunneling was presented by Martinis, Nahum, and Jensen (1994) for the  $N = 5$  pump, and by Kautz, Keller, and Martinis (1999) for the  $N = 7$  pump. In both cases, the experimental error rates could be quantitatively explained by a theory in an intermediate temperature range, where the majority of the errors was due to thermally activated single-junction tunneling processes. The observed low-temperature saturation of the error rates was conjectured to arise from photon-assisted tunneling and cotunneling, considered in this context theoretically, e.g., by Martinis and Nahum (1993) and White and Wagner (1993). Kautz, Keller, and Martinis (2000) explained quantitatively the error rates observed in the earlier experiments performed on pumps with  $N = 4-7$  junctions by including photon-assisted processes in the model. The dominating error mechanism in the experiments was found to be photon-assisted single-electron tunneling, with negligible contribution from cotunneling. Jehl *et al.* (2003) explained error processes in a voltage-biased  $N = 7$  pump with the same model.

The rate at which photon-assisted events occur is determined by the spectral density of voltage fluctuations across the junction at frequencies  $f_{\text{ph}} \sim \Delta E/h$ , where  $\Delta E$  is the

increase in electrostatic energy for a particular tunneling process. To explain the observed leakage rates, the authors in the above studies used  $S_V(f) = \alpha/|f|$ , with the fitting parameter  $\alpha$  assuming values from  $(5 \text{ nV})^2$  to  $(50 \text{ nV})^2$ . Kautz, Keller, and Martinis (2000) motivated the  $f^{-1}$  frequency dependence of the power spectrum by the ubiquitous charge noise present in SET electrometers, typically observed at frequencies below 1 kHz. (Covington *et al.* (2000) applied a calibrated amplitude of microwave radiation to one terminal of the pump, and the resulting tunneling rates were shown to be described by the theory of photon-assisted tunneling. They suggested that the origin of the high-frequency photons responsible for error events in the pumping experiments is the presence of fluctuating nonequilibrium charges near the devices. In addition, we note that recent electron-trapping results reported by Kempinen *et al.* (2011) for a two-junction SNS-type trap with a series resistor measured in an rf-tight sample stage seem to indicate a much smaller flux of harmful photons to the junctions than was observed by, e.g., Covington *et al.* (2000).

Another successful line of metallic single-electron pumps relies on a smaller number of junctions ( $N = 3$  or  $5$ ) while employing a resistive on-chip environment to suppress harmful cotunneling and photon-assisted tunneling (Lotkhov *et al.*, 2001; Camarota *et al.*, 2012). Suppression of cotunneling by a high-impedance environment was first demonstrated by Zorin *et al.* (2000) through SET  $I$ - $V$  measurements, motivated by the earlier theoretical predictions (Golubev and Zaikin, 1992; Odintsov, Bujanja, and Schön, 1992).

## B. Hybrid superconducting–normal-metal devices

### 1. Operating principles

The hybrid turnstile, originally proposed and demonstrated by Pekola *et al.* (2008), is based on a single-electron transistor where the tunnel junctions are formed between a superconductor and a normal metal; see Fig. 14, top left. In principle, it can be realized in either a SINIS or NISIN configuration (Averin and Pekola, 2008; Kempinen, Kafanov *et al.*, 2009). However, it has turned out for several reasons that the former one is the only potential choice of the two for accurate synchronized electron transport purposes (Averin and Pekola, 2008). One reason is that in the NISIN structure tunneling strongly heats the island due to Joule power and weak energy relaxation in the small superconducting island, whereas in the SINIS case the island is of normal metal, better thermalized to the bath, and under proper operation, it can be cooled, too (Kafanov *et al.*, 2009). The NISIN turnstile may also suffer from unpredictable  $1e$ - $2e$  periodicity issues. Furthermore, a detailed analysis of the higher-order tunneling processes shows that cotunneling limits the fundamental accuracy of the NISIN turnstile, whereas uncertainties below  $10^{-8}$  are predicted for the SINIS version (Averin and Pekola, 2008). Hence we focus on the SINIS turnstile here.

The stability diagram of a conventional single-electron transistor is composed of Coulomb diamonds on the gate voltage  $V_g$ –drain-source voltage  $V_b$  plane; see Fig. 15. Gate voltages  $V_g$  are again written in dimensionless form, normalized by the voltage corresponding to charge displacement of one electron  $n_g$ . In this case the adjacent diamonds touch each

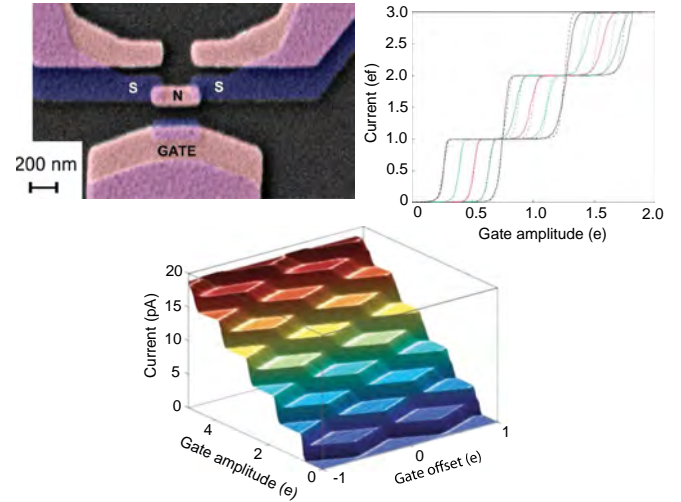


FIG. 14 (color online). The hybrid NIS turnstile. Top left: A scanning electron micrograph of a SINIS turnstile, which is a hybrid single-electron transistor with superconducting leads and a normal-metal island. Top right and bottom: Current of a turnstile under rf drive on the gate at different operation points with respect to the dc gate position and the rf amplitude of the gate. Adapted from Pekola *et al.*, 2008 and Kempinen, 2009.

other at a single point at  $V_b = 0$ , implying that the charge state is not locked for all gate-voltage values. The operation of the SINIS turnstile, on the contrary, is based on the combined effect of the two gaps: the superconducting BCS gap expands the stability regions of the charge states and the neighboring regions overlap. The principle of operation of the turnstile is illustrated in Fig. 15. When the gate charge  $n_g(t)$  alternates between two neighboring charge states, electrons are transported through the turnstile one by one. A nonzero voltage, which yields a preferred direction of tunneling, can be applied since the idle current is ideally zero in the range  $|eV_b| < 2\Delta$  at any constant gate charge value. If the gate signal is extended to span  $k + 1$  charge states, one obtains current plateaus with  $k$  electrons pumped per cycle. However,

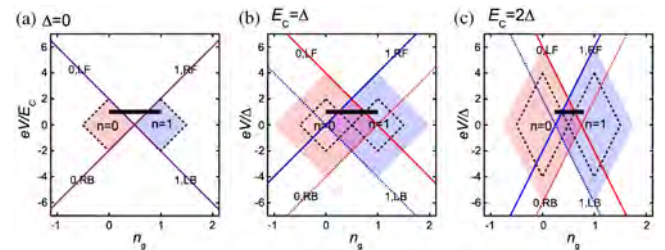


FIG. 15 (color online). Schematic picture of pumping (a) with a normal SET, (b) with a hybrid SET with  $E_C = \Delta$ , and (c) with a hybrid SET with  $E_C = 2\Delta$ . The shaded areas are the stability regions of the charge states  $n = 0$  and  $1$ . The edges of the normal SET stability regions are drawn in all figures with dashed black lines. The long shaded lines represent the transition thresholds from states  $n = 0$  and  $1$  by tunneling through the left ( $L$ ) or the right ( $R$ ) junction in the wanted forward ( $F$ , solid line) or unwanted backward ( $B$ , dashed line) direction. The thick black line corresponds to pumping with constant bias voltage  $eV_b/\Delta = 1$  and a varying gate voltage. From Kempinen, 2009.

the first plateau around the symmetric (degeneracy of two neighboring charge states) dc position of the gate is optimal for metrology. Note that if a nonzero bias voltage is applied across a normal-state SET, a gate span between different charge states always passes a region where none of the states is stable and where the current can freely flow through the device [white region in Fig. 15(a)]. Hence the normal-state SET cannot act as a turnstile even in principle, except for an experimentally infeasible gate sequence where  $n_g$  jumps abruptly between its extreme values in the Coulomb-blockaded parts of the stability diagram.

Figure 14 presents data obtained from a basic turnstile operated under various conditions (Pekola *et al.*, 2008). Several wide current plateaus with increasing gate amplitude  $A_g$  can be seen. The gate drive is expressed here as  $n_g(t) = n_{g0} + A_g w(t)$ , where  $n_{g0}$  and  $A_g$  are the gate offset and drive amplitude, respectively. The gate wave form of unit amplitude is denoted by  $w(t)$ . The optimal gate drive is symmetric with respect to the two charge states: therefore in later sections we assume that  $n_{g0} = 1/2$ . In these first experiments, the accuracy of a synchronized charge transport as  $I = Nef$ , with  $N$  the integer index of a plateau, could be verified within about 1%.

A rough estimate for the optimal bias voltage  $V_b$  is obtained by considering the dominant thermal errors (Pekola *et al.*, 2008). The probability of an electron tunneling against bias, i.e., “in the wrong direction” is given by  $\sim \exp(-eV_b/k_B T)$ . This error would lead to no net charge transferred during a pumping cycle, but it can be suppressed by increasing  $V_b$ . On the other hand, increasing  $V_b$  increases the probability of transporting an extra electron in the forward direction. The magnitude of this kind of an error can be estimated as  $\sim \exp[-(2\Delta - eV_b)/k_B T]$ , since there is an energy cost given by the voltage distance from the conduction threshold at  $2\Delta/e$ . Combining these conditions, we obtain a trade-off  $eV_b \approx \Delta$  as the optimum bias voltage, where the thermal error probability is  $\sim \exp(-\Delta/k_B T)$ . The combined thermal error probability is  $\sim 10^{-9}$  at realistic temperatures of about 100 mK and with the BCS gap of aluminum  $\Delta/k_B \approx 2.5$  K. The exact optimum of the bias close to the value given here depends on many other processes to be discussed. Experimentally, however, the choice  $eV_b = \Delta$  is a good starting point.

The optimal gate drive amplitude  $A_g$  lies somewhere between the threshold amplitudes for forward and backward tunneling which are, for the optimum bias voltage,  $A_{g,ft} = \Delta/4E_c$  and  $A_{g,bt} = 3\Delta/4E_c$ , respectively. The subgap leakage is maximized at the degeneracy point  $n_{g0} = 1/2$ . In this respect, a square-wave signal is optimal. On the other hand, passing the threshold for forward tunneling too quickly tends to heat the island, whereas a sine signal can also cool it. Hence the optimal wave form is of some intermediate form.

The SINIS turnstile presents the choice of a single-electron source which is easy to manufacture and operate, and whose characteristics can be analyzed theoretically into great detail. It promises high accuracy as discussed in Sec. III.B.2. Its operation in a parallel configuration is straightforward thanks to the simple element of a single turnstile, and therefore it can yield higher currents than the other fixed-barrier single-electron sources presented in Sec. III.A. Thus it can be considered as a promising candidate in providing a realization of the ampere.

## 2. Higher-order processes

As for the fully normal-metal pumps, the idealized picture of electron transport based on single-electron tunneling is disturbed by simultaneous tunneling of several electrons. Owing to the gap in the quasiparticle excitation spectrum of a BCS superconductor, elastic cotunneling takes place only when the bias voltage over the device exceeds  $2\Delta/e$ . The turnstile operation is achieved with voltages well below this threshold and hence cotunneling is suppressed, in contrast to purely normal-metal devices. As a general rule, any process that leaves behind an unpaired electron on a superconducting electrode incurs an energy penalty equal to  $\Delta$ .

For hybrid structures, the lowest-order tunneling process where the energy cost of breaking a Cooper pair can be avoided is Andreev tunneling (Andreev, 1964), i.e., a complete Cooper-pair tunneling through a junction. Andreev tunneling has been studied thoroughly with single NIS junctions (Blonder, Tinkham, and Klapwijk, 1982; Eiles, Martinis, and Devoret, 1993; Lafarge *et al.*, 1993; Hekking and Nazarov, 1994; Pothier *et al.*, 1994; Rajauria *et al.*, 2008; Greibe *et al.*, 2011; Maisi *et al.*, 2011) as well as in so-called Cooper-pair splitters where the electrons of a Cooper pair tunnel to different normal-metal regions (Hofstetter, Csonka, and Nygrd, 2009; Herrmann *et al.*, 2010; Wei and Chandrasekhar, 2010). In the case of a SINIS turnstile, Andreev tunneling manifests itself as two electrons being added to or removed from the island. Consecutively, increasing the charging energy of a device makes Andreev tunneling energetically unfavorable, suppressing it (Averin and Pekola, 2008; Maisi *et al.*, 2011). The impact of Andreev tunneling on the accuracy of a turnstile has been directly observed on the pumped current (Aref *et al.*, 2011). In Figs. 16(a) and 16(b), stability diamonds for single-electron and Andreev tunneling are shown for high- $E_C$  and low- $E_C$  devices, respectively. The pumping plateau of the high- $E_C$  device, shown in Fig. 16(c), is free of Andreev tunneling whereas the low- $E_C$  sample exhibits it as seen in Fig. 16(d).

For high-charging energy devices where Andreev tunneling is suppressed, the process limiting the accuracy of the SINIS turnstile is cotunneling of a Cooper pair and a single electron (Averin and Pekola, 2008). In this process, the island will be charged or discharged by a single electron while another electron effectively passes through the device. The net energy change is that of the corresponding single-electron process, plus the energy gained in transporting the Cooper pair from one electrode to another, which equals  $2eV_b$  in the forward direction. Hence, the process cannot be made energetically unfavorable in a working turnstile. However, it can be suppressed relative to the first-order processes by making the junctions opaque enough. Ideally, to obtain an accuracy of  $10^{-7}$ , one needs to limit the speed of an aluminum-based turnstile to a few tens of pA (Averin and Pekola, 2008). This theoretically predicted maximum operation speed is expected to slow down by an additional factor of 3 due to nonuniformity of the tunnel barriers (Aref *et al.*, 2011; Maisi *et al.*, 2011). Thus 10 pA is expected to be the optimum yield per aluminum-based turnstile. In addition to the Cooper-pair electron cotunneling, the cotunneling of two Cooper pairs through the device increases the leakage current (Zaikin, 1994). In optimized devices discussed above, the Cooper-pair electron cotunneling is

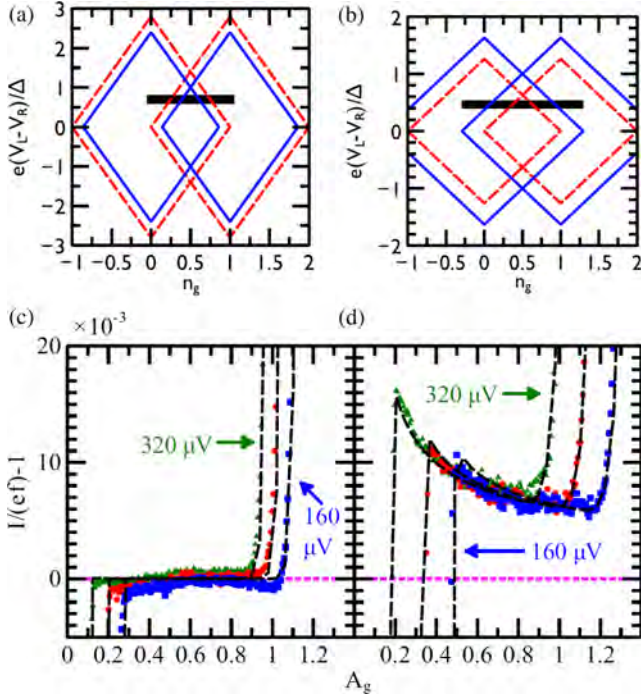


FIG. 16 (color online). (a) Stability diamonds for single-electron tunneling (solid lines) and Andreev tunneling (dotted lines) for a sample with  $E_C > \Delta$ . (b) Stability diamonds for  $E_C < \Delta$ . (c) The first pumping plateau of the high- $E_C$  device as a function of the gate-voltage amplitude  $A_g$ . The solid symbols show pumped current with  $f = 10$  MHz and three different bias voltages. Dotted lines are the simulated traces with the corresponding biasing. (d) The same data as in (c) but now for the low- $E_C$  device showing excess current due to Andreev tunneling. Adapted from [Aref \*et al.\*, 2011](#).

nevertheless the dominant process limiting the accuracy since its threshold is exceeded in the turnstile operation and it is of lower order than the Cooper-pair cotunneling.

### 3. Quasiparticle thermalization

Single-electron tunneling to or from a superconductor will generate quasiparticle excitations. Once created, the excitations carry an energy of  $\Delta$ , which enables them to cross the tunnel barrier to the normal metal if the electrostatic energy cost is lower than  $\Delta$ . Hence, they constitute a potential source of pumping errors for the hybrid turnstile. Typically the excitations are injected close to the gap edge. Also, the quasiparticles relax quickly internally compared to the weak recombination rate, so that at low temperatures we can assume them to lie close to the gap edges and have a temperature  $T_{\text{qp}}$  which is higher than the phonon bath temperature of the system. With this assumption, we calculate the density of the quasiparticle excitations to be

$$n_{\text{qp}} = 2D(E_F) \int_{\Delta}^{\infty} dE \nu_S(E) e^{-\beta E} = \sqrt{2\pi} D(E_F) \Delta \frac{e^{-\beta\Delta}}{\sqrt{\beta\Delta}}, \quad (37)$$

where  $\beta = 1/k_B T_{\text{qp}}$ , and we assumed  $e^{-\beta\Delta} \ll 1$  and a negligible branch imbalance ([Clarke, 1972](#)). The tunneling rate caused by the excitations can be calculated from the orthodox theory expressions (see Sec. II.B). It depends linearly on the

density and is independent of the biasing at low energies  $\Gamma_{\text{qp}} = n_{\text{qp}}/[2e^2 R_T D(E_F)]$ . It should be compared to the rate at which we pump electrons. As discussed, we obtain roughly 10 pA from a turnstile free of higher-order tunneling errors at an accuracy of  $10^{-7}$ . The tunneling resistance of such a device is approximately  $R_T = 1$  M $\Omega$ . To ensure that the quasiparticle excitations do not cause errors on this level, we require the tunneling rate to satisfy  $\Gamma_{\text{qp}} < 10^{-7} \times 10$  pA/e. With parameter values  $D(E_F) = 1.45 \times 10^{47}$  J $^{-1}$  m $^{-3}$  and  $\Delta = 200$   $\mu$ eV, we need  $n_{\text{qp}} < 0.04$   $\mu$ m $^{-3}$ . Such a level is demonstrated in an experiment without active driving of the system ([Saira, Kempainen \*et al.\*, 2012](#)) and is sensitive to the filtering and shielding of the sample. Also, the trapping of quasiparticles was shown to be important in this experiment.

Next we consider the relaxation of the quasiparticles. In turnstile operation, injection of hot quasiparticles through the tunnel junction drives the quasiparticle system of the superconductor actively out of equilibrium. We model the quasiparticle relaxation in the superconductor in terms of heat flow and obtain a diffusion equation for  $n_{\text{qp}}$ . Such an approach has been used to model several experiments ([Ullom, Fisher, and Nahum, 1998](#); [Rajauria, Courtois, and Pannetier, 2009](#); [O'Neil \*et al.\*, 2011](#); [Peltonen \*et al.\*, 2011](#); [Knowles, Maisi, and Pekola, 2012](#)). The heat flow of quasiparticles  $\mathbf{J}$  follows the equation  $\nabla \cdot \mathbf{J} = -p$ , where  $p$  is the power per unit volume removed from the quasiparticles. We use Fourier's law of heat conduction  $\mathbf{J} = -\kappa_S \nabla T_{\text{qp}}$ , where

$$\kappa_S = \frac{6}{\pi^2} \frac{L_0 T_{\text{qp}}}{\rho_n} (\beta\Delta)^2 e^{-\beta\Delta}$$

is the heat conductivity of a superconductor ([Bardeen, Rickayzen, and Tewordt, 1959](#)). Here  $L_0$  is the Lorenz number and  $\rho_n$  is the resistivity in the normal state. By taking the derivatives only over strong exponential dependences and using Eq. (37), we obtain a diffusion equation

$$D \nabla^2 n_{\text{qp}} = p, \quad (38)$$

where the coefficient

$$D = \frac{\sqrt{2}(k_B T_{\text{qp}} \Delta)^{1/2}}{\sqrt{\pi} e^2 \rho_n D(E_F)}$$

is assumed to be constant. To write down the source term on the right side of Eq. (38), we consider the available mechanisms of heat conduction. Electron-phonon coupling is an inherent relaxation mechanism for quasiparticles inside a superconductor. However, it is so weak that the resulting decay length of  $n_{\text{qp}}$  is usually on the millimeter scale ([Martinis, Ansmann, and Aumentado, 2009](#); [Peltonen \*et al.\*, 2011](#)). Typically, to enhance the relaxation, one uses so-called quasiparticle traps ([Pekola \*et al.\*, 2000](#); [Rajauria, Courtois, and Pannetier, 2009](#); [O'Neil \*et al.\*, 2011](#)), which are normal-metallic regions connected to the superconductor either directly or via an oxide layer. Once the hot quasiparticles enter the trap, the stronger electron-phonon relaxation in a normal metal removes their excess energy. A perfect quasiparticle trap forces the quasiparticle temperature at the interface to equal the electronic temperature of the normal metal. In the context of Eq. (38), this can be implemented as a boundary condition for  $n_{\text{qp}}$ . The boundary condition at the

junction is obtained by setting the heat flow equal to the power injected by the quasiparticle current.

When the trap is connected via an oxide barrier, the heat is carried by quasiparticle tunneling. The orthodox theory result for the source term in such a configuration is

$$\begin{aligned} p &= \frac{2\sigma_T}{e^2 d} \int_{\Delta}^{\infty} dE E n_S(E) (e^{-\beta E} - e^{-\beta_0 E}) \\ &= \frac{\sigma_T}{e^2 D(E_F) d} (n_{\text{qp}} - n_{\text{qp}0}), \end{aligned} \quad (39)$$

which is obtained by setting the chemical potential difference of the trap and the superconductor to zero and assuming the diffusion to take place in two dimensions which is well justified for the thin films typically used in the samples. We also assumed  $k_B T_{\text{qp}} \ll \Delta$ . Here  $\sigma_T$  is the electrical conductance per unit area of the trap,  $d$  is the thickness of the superconducting film,  $\beta = 1/k_B T_{\text{qp}}$ , and  $\beta_0 = 1/k_B T_0$ , where  $T_0$  is the temperature of the normal-metal electrons. We denote by  $n_{\text{qp}0}$  the quasiparticle density of a fully thermalized superconductor, i.e., one where  $T_{\text{qp}} = T_0$ .

We consider some typical geometries of superconducting leads used in devices. First take a lead with a constant cross section as shown in Fig. 17(a). We assume that a heat flow  $P_{\text{inj}}$  is injected at one end of the line, and that the other end is thermally anchored by a direct trap. For the lead itself, we assume a trap connected via an oxide barrier to be located on top. We can solve Eqs. (38) and (39) analytically in one dimension to obtain

$$n_{\text{qp}}(x) = \frac{1}{D\sqrt{k}} (e^{\sqrt{k}(2l-x)} - e^{\sqrt{k}x}) (e^{2\sqrt{k}l} + 1)^{-1} \frac{P_{\text{inj}}}{wd} + n_{\text{qp}0}.$$

Here

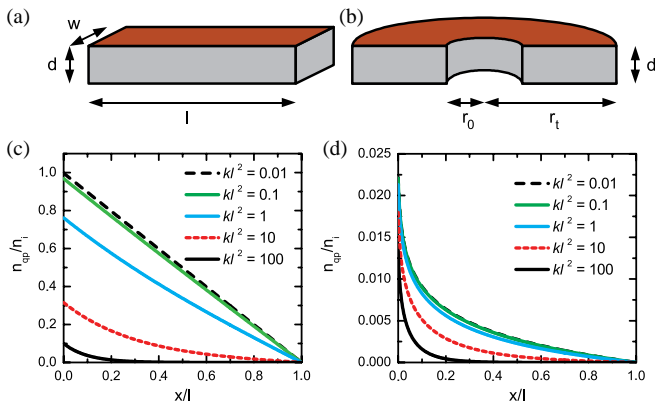


FIG. 17 (color online). Two typical geometries for a superconducting bias lead: (a) A lead having a constant cross section determined by the thickness  $d$  and width  $w$ . The length of the line is  $l$ . (b) A sector-shaped lead characterized by an opening angle  $\theta$ , initial radius  $r_0$ , and final radius  $r_t$ . For the picture  $\theta$  is set to  $180^\circ$ . The colored parts on top denote a quasiparticle trap connected via an oxide barrier. (c) Quasiparticle density  $n_{\text{qp}}$  along a constant-cross-section line with various oxide trap transparencies  $k$ , and (d) along an opening line. In the plots,  $n_{\text{qp}}$  is scaled by  $n_i = D P_{\text{inj}} / A_i$ , where the injection area  $A_i$  equals  $wd$  for (c) and  $\theta r_0 d$  for (d). For the leads in (b) and (d), we also use the notation  $x = (r - r_0)/l$  with  $l = r_t - r_0$  and have used values  $r_0 = 20$  nm and  $r_t = 5$   $\mu\text{m}$ .

$$k = \frac{\sqrt{\pi} \rho_n \sigma_T \Delta}{\sqrt{2} (k_B T_{\text{qp}} \Delta)^{1/2} d},$$

and  $x$  is the coordinate along the wire starting at the injection side ( $x = 0$ ) and ending at the direct trap ( $x = l$ ). In Fig. 17(c), we show the quasiparticle density for various values of  $\sigma_T$ . The lowest  $\sigma_T$  corresponds to the case where the quasiparticles diffuse only through the wire and then relax at the direct contact. At higher transparencies, the oxide trap starts to help for the relaxation as well. If we use parameter values  $d = 50$  nm,  $w = 100$  nm,  $l = 1$   $\mu\text{m}$ , and  $T_{\text{qp}} = 130$  mK, which are typical for fabricated samples, we see that a typical injection power of  $P_{\text{inj}} = 2$  fW yields  $n_{\text{qp}} - n_{\text{qp}0} = 10$   $\mu\text{m}^{-3}$  without the oxide trap and even with the highest transparency  $\sigma_T = (100 \text{ } \Omega \mu\text{m}^2)^{-1}$  that is possible to fabricate without pinholes (Brenning, Kubatkin, and Delsing, 2004), we get only an order of magnitude improvement.

To decrease the quasiparticle density to the acceptable level discussed, one needs to optimize the lead geometry as well. Therefore, we consider a lead that widens as shown in Fig. 17(b). In this case, we can solve a one-dimensional diffusion equation in polar coordinates. The junction is assumed to be located at radius  $r = r_0$ , and the direct contact trap to begin at radius  $r = r_t$ . Thickness of the lead and the overlaid trap are as in the previous example. The solution of Eqs. (38) and (39) can be expressed with modified Bessel functions  $I_\alpha$  and  $K_\alpha$  as

$$\begin{aligned} n_{\text{qp}}(r) &= n_{\text{qp}0} + \frac{1}{D\sqrt{k}} \frac{P_{\text{inj}}}{\theta r_0 d} \left\{ \left( K_1(\sqrt{k} r_0) \right. \right. \\ &\quad \left. \left. + \frac{K_0(\sqrt{k} r_t)}{I_0(\sqrt{k} r_t)} I_1(\sqrt{k} r_0) \right)^{-1} K_0(\sqrt{k} r) \right. \\ &\quad \left. + \left( I_1(\sqrt{k} r_0) + \frac{I_0(\sqrt{k} r_t)}{K_0(\sqrt{k} r_t)} K_1(\sqrt{k} r_0) \right)^{-1} I_0(\sqrt{k} r) \right\}. \end{aligned}$$

In Fig. 17(d), we show  $n_{\text{qp}}(r)$  for various transparencies of the oxide trap. The lowest transparencies, again, correspond to a pure diffusion limit. Note that the quasiparticle density at the junction depends only weakly on the transparency of the trap: Because of the logarithmic dependence, changing the transparency by several orders of magnitude makes less than an order of magnitude difference to  $n_{\text{qp}}(r_0)$ . In a widening lead, heat sinking is made efficient by spreading the heat to a larger volume, and the area of the trap contact is also increased. By using realistic parameter values  $d = 50$  nm,  $\theta = \pi/2$ ,  $r_0 = 50$  nm,  $r_t = 5$   $\mu\text{m}$ ,  $T_{\text{qp}} = 130$  mK,  $\rho_n = 10$  n $\Omega$  m, and  $P_{\text{inj}} = 2$  fW, we see that it is possible to reach  $n_{\text{qp}} < 1$   $\mu\text{m}^{-3}$  at the junction even without an oxide trap. Increasing the thickness of the electrode by a factor of 10 would then start to be sufficient for the metrological accuracy requirements.

Several experiments (Ullom, Fisher, and Nahum, 1998; Rajauria, Courtois, and Pannetier, 2009; O'Neil *et al.*, 2011; Knowles, Maisi, and Pekola, 2012) show that the above diffusion model is valid for quasiparticle densities of the order of  $n_{\text{qp}} \sim 10$   $\mu\text{m}^{-3}$ . A smaller quasiparticle density required for metrological applications implies that the absolute number of quasiparticles in the conductors becomes very small. With a typical volume of a lead  $100$  nm  $\times$   $100$   $\mu\text{m}^2$ ,

the quasiparticle number is  $N < 1$  with  $n_{\text{qp}} < 0.1 \mu\text{m}^{-3}$ . It is not currently obvious if such a situation can be treated with the diffusion model or whether a more elaborated theory is required. Pumping experiments on metrological accuracy can provide a way to shed light on such a situation.

### C. Quantum-dot-based single-electron pumps and turnstiles

In this section, we introduce semiconducting quantum dots and review their applications as single-electron current sources, concentrating on the experimental developments. For an overview of the related theory, we refer to Sec. II.E.

#### 1. Introduction to quantum dots as electron pumps

In contrast to conventional three-dimensional bulk conductors or more exotic two-dimensional conductors such as quantum Hall systems or graphene, semiconducting quantum dots can be regarded as zero-dimensional conductors, for which the electrons are tightly confined in all three spatial dimensions. Thus quantum dots show truly discrete excitation spectra that are reminiscent of those of natural atoms. One of the early key experiments on these *artificial atoms* (Kastner, 1993) was the observation of discrete quantum levels (Reed *et al.*, 1988; Johnson *et al.*, 1992; Su, Goldman, and Cunningham, 1992) and the shell structure in the filling of the electron states (Tarucha *et al.*, 1996).

As discussed in Sec. II.E, the conceptual difference between small metallic islands studied in the previous sections and quantum dots is that the Fermi level and hence the conduction electron density in the metallic islands is high, making the energy spacing between the spatially excited electron states extremely small. The metallic system can be typically described by a constant density of states as opposed to the strongly peaked density of states in quantum dots. Furthermore, quantum dots can contain a low number of electrons in the conduction band ranging from zero (Ashoori *et al.*, 1993; Elzerman *et al.*, 2003; Lim *et al.*, 2009) to more than hundreds, similar to natural atoms, whereas the corresponding number is orders of magnitude higher for metallic systems. In fact, the sharp potential created by a single donor atom in silicon can also be considered to be an ultrasmall quantum dot. By connecting such natural atoms to electron reservoirs, for example, SETs (Lansbergen *et al.*, 2008; Tan *et al.*, 2010; Fuechle *et al.*, 2012) and electron pumps (Lansbergen, Ono, and Fujiwara, 2012; Roche *et al.*, 2012) have been fabricated.

Figure 18 shows different types of quantum-dot architectures. The most conventional quantum dots are based on a two-dimensional degenerate electron gas (2DEG) that either forms naturally, for example, at the interface between AlGaAs and GaAs (Chang, Esaki, and Tsu, 1974) or is induced at the interface between silicon and silicon oxide by an external gate (Ando, Fowler, and Stern, 1982). Alternatively, quantum dots can be fabricated from epitaxially grown nanowires (Ohlsson *et al.*, 2002; Fasth *et al.*, 2007; Nadj-Perge *et al.*, 2010) or from lithographically defined graphene islands (Connolly *et al.*, 2012). In the conventional dots, the confinement is very strong in the direction perpendicular to the interface. Etching techniques, local anodic oxidation (Held *et al.*, 1997), pattern-sensitive

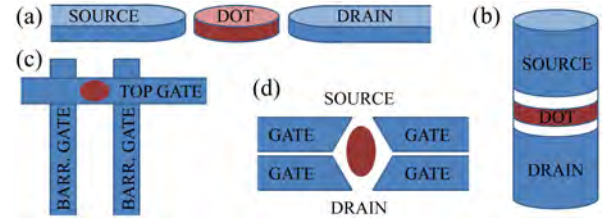


FIG. 18 (color online). (a) Lateral and (b) vertical quantum-dot arrangements. All quantum-dot pumps and turnstiles discussed are in the lateral arrangement. The electrons tunnel between the dot and the source and drain reservoirs. The tunnel barriers between the dot and the reservoirs are created either by the electrostatic potentials of nearby gate electrodes or by different materials such as AlGaAs. The gate arrangement for (c) the accumulation and (d) depletion mode quantum dots in the lateral arrangement.

oxidation (Takahashi *et al.*, 1995), or metallic electrodes [see Figs. 18(c) and 18(d)] can be employed to provide the electrostatic potential defining the well for the electrons in the plane of the interface. The in-plane diameter of this type of dot can vary from tens of nanometers to several micrometers. Thus there are plenty of atoms and electrons in the region of the dot but most of them lie in the valence band and require an energy of the order of 1 eV to be excited. Since the relevant energy scales for the spatial excitations and the single-electron charging effects are orders of magnitude lower, the occupation of the valence states can be taken fixed.

In the effective mass approximation (Ando, Fowler, and Stern, 1982), the details of the electrostatic potential and the effects of the valence electrons in the solid are coarse grained such that only the electrons in the conduction band are taken into account, and these electrons are treated as particles in the smooth potential defining the dot. This description has proved to reproduce several important experimental findings both qualitatively and quantitatively (Ando, Fowler, and Stern, 1982), and it provides insight into the single-electron phenomena in quantum dots. In particular, the potential barriers arising from the gates defining the dot can be visualized just for the small number of electrons in the conduction band.

#### 2. Pioneering experiments

Although quantum dots hold a much smaller number of electrons than metallic islands, probably their greatest benefit is that the tunnel barriers can be formed by electrostatic potentials and controlled externally by gate voltages. Thus the height of the potential barrier, through which the electrons tunnel to the source and drain reservoirs, can be controlled *in situ*. This property provides fruitful grounds for electron pumping since the dependence of the tunneling rate on the barrier height and hence on the voltage of the gate electrode is typically exponential.

The first experiments employing quantum dots for frequency-locked single-electron transport were reported by Kouwenhoven *et al.* (1991a, 1991b) [see also Kouwenhoven (1992)]. Here they used surface-gated GaAs dots as shown in Fig. 19(a). The negative voltages on gates  $C$ ,  $F$ , 1, and 2 deplete the 2DEG that is located 100 nm below the surface, thus defining the quantum dot in the center with a radius of about 300 nm and charging energy  $2E_C = e^2/C_\Sigma = 0.67$  meV. (Gates 3 and 4 are grounded and do not deplete the 2DEG.)

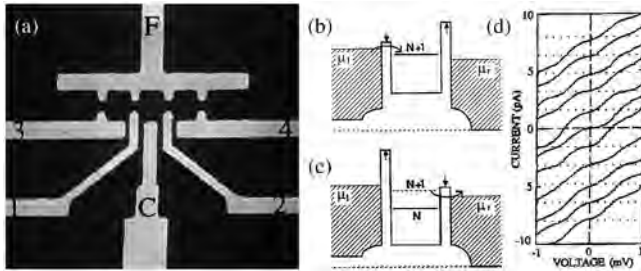


FIG. 19. The first single-electron current source based on quantum dots by Kouwenhoven *et al.* (1991b), 1991a). (a) SEM image of the device from the top; (b), (c) operation principle; and (d) measured  $I$ - $V$  curves reported. The gate configuration corresponds to the case in Fig. 18(d). The different  $I$ - $V$  curves are measured while driving the turnstile with different center-gate [gate C in (a)] voltages, rf amplitudes, and phase differences. The curves are not offset and the dashed lines show the current levels  $nef$  with  $n = -5, \dots, 5$ . Adapted from Kouwenhoven *et al.*, 1991b, 1991).

In addition to dc voltages defining the dot,  $180^\circ$ -phase-shifted sinusoidal rf drive is superimposed on gates 1 and 2, lowering one barrier at a time. This rf drive induces a turnstile operation as shown in Figs. 19(b) and 19(c) for negative bias voltage on the left side of the dot: when the voltage at gate 1 is high (low tunnel barrier) and low at gate 2 (high tunnel barrier), an excess electron enters the dot through the left barrier [see Fig. 19(b)], and when the voltage at gate 1 is low and high at gate 2, the electron escapes through the right barrier [see Fig. 19(c)]. Thus the average dc current through the device in the ideal case is given by  $I_p = ef$ , where  $f$  is the operation frequency. For bias voltages greater than the charging energy  $|eV| \geq E_C$ , more than a single electron can be transported in a cycle yielding ideally  $I_p = nef$ , where  $n$  is an integer. Signatures of this type of current quantization were observed in the experiments (Kouwenhoven *et al.*, 1991a, 1991b; Kouwenhoven, 1992) and are illustrated in Fig. 19(d). The current through the device as a function of the bias voltage tends clearly to form a staircaselike pattern with the step height  $ef$ . This was the first experimental demonstration of current quantization in quantum-dot structures. Note that in addition to the turnstile operation, Fig. 19(d) also shows the pumping of electrons against the bias voltage for certain phase differences of the driving signals. The error in the pumped current is a few percent, falling somewhat behind the first experiments on metallic structures reported by Geerligs *et al.* (1990).

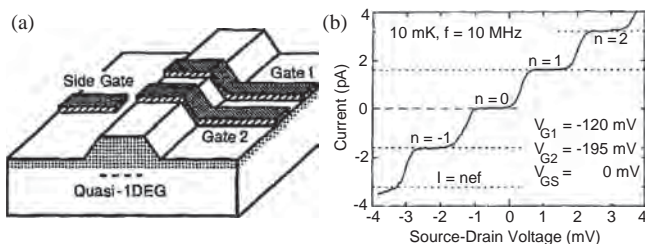


FIG. 20. (a) Schematic illustration of the device and (b) observed current plateaus during the turnstile operation. From Nagamune *et al.*, 1994.

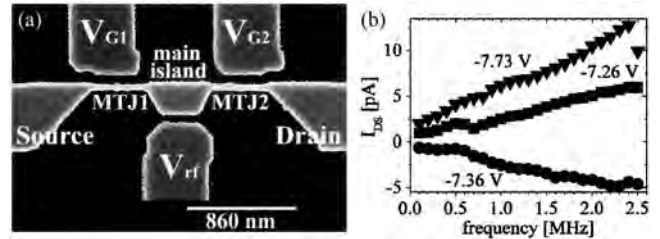


FIG. 21. (a) SEM image of the device and (b) pumped current through it in the experiments by Altebaeumer and Ahmed (2001). Different values of the current correspond to different dc voltages  $V_{G1}$  [see (a)]. Adapted from Altebaeumer and Ahmed, 2001.

The second set of experiments on single-electron turnstiles based on quantum dots was published by Nagamune *et al.* (1994). Here the quantum dot forms a gallium arsenide 2DEG that is wet etched into the shape of a 460-nm-wide wire as illustrated in Fig. 20(a). Two 230-nm-wide metallic gates are deposited perpendicular to the wire at a distance of 330 nm. This different barrier gate configuration and the higher charging energy of  $2E_C = 1.7$  meV resulted in a clear improvement of the staircase structure as shown in Fig. 20(b). However, they reported that a parallel channel forms due to the rf operation and the effect of this channel is subtracted from Fig. 20(b). They estimated the accuracy of their device to be about 0.4% if the correction from the parallel channel is taken into account.

In 1997–2001, a series of experiments was carried out on so-called multiple-tunnel junction devices as electron pumps (Tsukagoshi *et al.*, 1997; Tsukagoshi, Alphenaar, and Nakazato, 1998; Altebaeumer and Ahmed, 2001; Altebaeumer, Amakawa, and Ahmed, 2001). Here the most common device was based on either  $\delta$ -doped GaAs or phosphorus-doped silicon that was etched such that a central region is connected to source and drain reservoirs by narrow strips as shown in Fig. 21(a). The side gates near the strips are set to a constant potential and an rf drive on the central side gate induces a current that depends linearly on frequency as shown in Fig. 21(b). The explanation of this type of operation is that the dopants and disorder in the strips function as Coulomb-blockade devices themselves rather than as single tunnel junctions, which gives rise to the term multiple-tunnel junction. Since these experiments were more motivated by applications in information processing (Ono *et al.*, 2005) with only a few electrons rather than finding a metrological current source, the accuracy of the device was not studied in detail.

### 3. Experiments on silicon quantum dots

The first step toward single-electron pumping in silicon was taken by Fujiwara and Takahashi (2001) as they presented an ultrasmall charge-coupled device and demonstrated that it could be used to trap and move individual holes controllably at the temperature of 25 K. This device was fabricated with silicon-on-insulator techniques (Takahashi *et al.*, 1995) and had two adjacent polysilicon gates acting as metal-oxide-semiconductor field-effect transistors (MOSFETs). Subsequently, a rather similar device with charging energy  $2E_C = 30$  meV shown in Fig. 22(a) was utilized for electron pumping by Ono and Takahashi (2003)

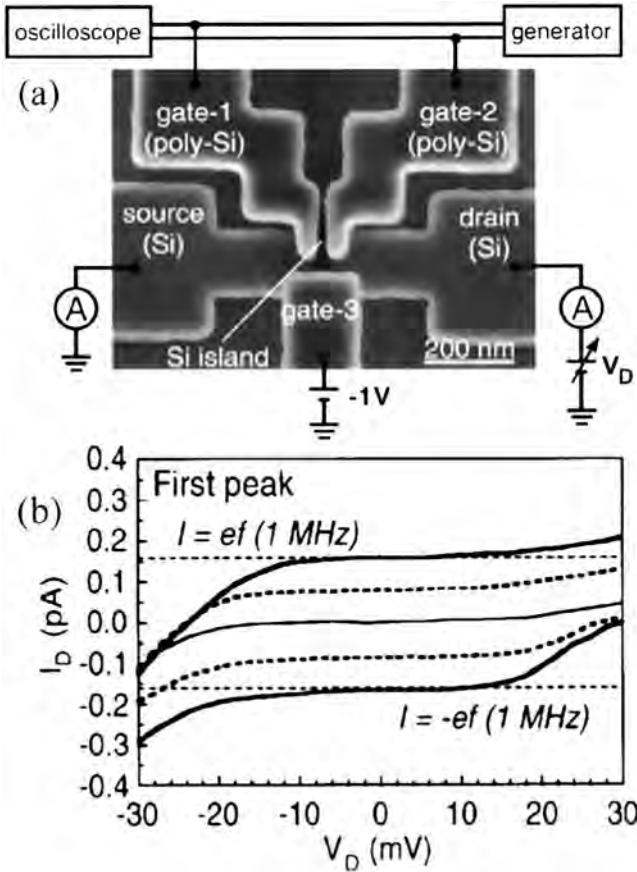


FIG. 22. (a) SEM image of the device and (b) observed current plateaus up to 1 MHz pumping frequency on a silicon quantum dot. From [Ono and Takahashi, 2003](#).

at the temperature of 25 K. They obtained an accuracy of the order of  $10^{-2}$  up to 1 MHz pumping that was also the limitation set by the calibration of their measurement equipment. Here the electron pumping was based on two sinusoidal driving signals that are offset by less than  $180^\circ$ , which causes the chemical potential of the dot to move during the cycle.

In addition to pumping, [Ono \*et al.\* \(2003\)](#) utilized the device shown in Fig. 22(a) as a single-electron turnstile. The operational principle is the same as in the pioneering experiments with GaAs quantum dots described in Figs. 19(b) and 19(c). [Ono \*et al.\* \(2003\)](#) observed current steps of  $ef$  up to  $f = 1$  MHz operation frequencies [see Fig. 23(a)]. The flatness of the plateaus was of the order of  $10^{-2}$  measured at 25 K. In these experiments, the tunnel barrier was formed by the combination of the gate voltages and the oxidation process developed by [Takahashi \*et al.\* \(1995\)](#) limiting the pumping frequencies. The first fully gate-tunable turnstile in silicon was demonstrated by [Fujiwara \*et al.\* \(2004\)](#) at 20 K with  $2E_C = 16$  meV and the relative uncertainty in the pumped current of the order  $10^{-2}$  at the maximum applied pumping frequency 100 MHz. This was a clear improvement in the speed of quantum-dot electron pumps.

[Chan \*et al.\* \(2011\)](#) used metallic aluminum gates to define a silicon quantum dot in the electron accumulation layer of the device as shown in Fig. 23(b). Although the relative variation of the current at the plateau they measured was below  $10^{-3}$  for a broad range of source-drain voltages [see Fig. 23(c)],

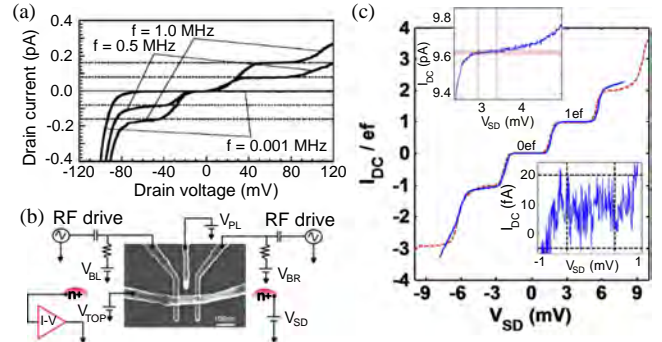


FIG. 23 (color online). (a) Measured current plateaus for different frequencies of the turnstile operation with the device shown in Fig. 22(a). From [Ono \*et al.\*, 2003](#). (b) SEM image of the silicon quantum-dot device and a schematic measurement setup employed in the experiments by [Chan \*et al.\* \(2011\)](#). (c) Measured current plateaus (solid line) and the corresponding theoretical curve (dashed line) by [Chan \*et al.\* \(2011\)](#). The insets show zooms at the  $n = 0$  (bottom) and  $n = 1$  (top) plateaus. The dashed lines show  $\pm 10^{-3}$  relative deviation from the ideal  $ef$  level. From [Chan \*et al.\*, 2011](#).

they could not strictly claim lower than 2% relative uncertainty in the current at 60 MHz pumping frequency due to the inaccurate calibration of the gain of the transimpedance amplifier employed. These experiments were carried out with  $2E_C = 2.8$  meV at 300 mK phonon temperature but the sequential tunneling model used to fit the data by [Chan \*et al.\* \(2011\)](#) suggested that the electron temperature of the dot rose up to 1.5 K. It is to be studied whether 1.5 K was due to power dissipated at the surface mount resistors in the vicinity of the sample or due to the direct heating of the 2DEG from the electrostatic coupling to the driven gate potentials.

[Fujiwara, Nishiguchi, and Ono \(2008\)](#) introduced a single-electron ratchet based on a silicon nanowire quantum dot with two polysilicon gates working as MOSFETs [[Fujiwara \*et al.\* \(2004\)](#) also employed this type of device]. In general, ratchets generate directional flow from a non-directional drive due to the asymmetry of the device. Here an oscillating voltage is applied to one of the gates such that an electron is captured through it near the maximum voltage, i.e., minimum barrier height, and ejected through the other barrier near the minimum voltage. In fact, the number of electrons pumped per cycle depends on the applied dc voltages and current plateaus up to  $5ef$  were reported. Furthermore, a nanoampere pumped current was observed at the  $3ef$  plateau with the pumping frequency  $f = 2.3$  GHz. The error in the current was estimated to be of the order of  $10^{-2}$  for the experiment carried out at 20 K temperature. Whereas in the conventional multiparameter pumps, the pumping errors arise mostly due to missed or excess tunneling events in a quasistatic Coulomb-blockade regime, the errors in the single-parameter pumps are taken to be dominated by a dynamic process, in which electrons tunnel out of the dot to the source lead.

Recently, [Jehl \*et al.\* \(2012\)](#) reported on frequency-locked single-electron pumping with a small quantum dot formed in metallic NiSi nanowire interrupted by two MOSFETs controlled by barrier gates. With rf drives on the barrier

gates, they were able to pump currents beyond 1 nA but the accuracy of the pump was not studied in detail. The MOSFET channels in this device had very sharp turn-on characteristics requiring only about 4.2 mV of gate voltage to change the conductivity of the channel by a decade, which can be important in reducing unwanted effects from the gate-voltage drive such as heating.

The first error-counting experiments in silicon were carried out by [Yamahata, Nishiguchi, and Fujiwara \(2011\)](#) [see also [Nishiguchi \*et al.\* \(2006\)](#)]. In contrast to the pioneering error-counting experiments by [Keller \*et al.\* \(1996\)](#), only a single silicon nanowire quantum dot was used as the current source and the electrons were steered into and out of a quantum dot coupled to a charge sensor. By opening the MOSFET separating the node from the drain reservoir, it was possible to use the same device as a dc current source. The observed pumping error was of the order of  $10^{-2}$  and was reported to be dominated by thermal errors at the 17 K temperature of the experiments. Furthermore, electron-counting experiments were recently carried out by [Fricke \*et al.\* \(2013\)](#) in a quantum-dot array. Further details of error-counting schemes are discussed in Sec. III.H.2.

#### 4. Experiments on gallium arsenide quantum dots

After the pioneering experiments discussed in Sec. III.C.2, the focus on single-electron sources based on gallium arsenide moved toward the idea of using SAWs to drive the single electrons in a one-dimensional channel—a topic to be discussed in Sec. III.D. In this section, we focus on gate-controlled GaAs pumps for dc current. A similar device to the ones discussed here has also been applied in the search for an ac-current standard which is the topic of Sec. III.G.1.

The seminal work by [Blumenthal \*et al.\* \(2007\)](#) took gate-controlled GaAs quantum dots a leap closer to a metrological current source, namely, they reported 547 MHz (87.64 pA) single-electron pumping with one-standard-deviation ( $1\sigma$ ) relative uncertainty of  $10^{-4}$  (see Fig. 24). However, they did not report the full dependence of the pumping errors as functions of all control parameters. As the device, they employed a chemically etched AlGaAs-GaAs wire with overlapping metallic gates as shown in Fig. 24. Only the three leftmost gates *L*, *M*, and *R* were used such that  $180^\circ$ -phase-shifted sinusoidal driving signals were applied to gates *L* and *R* in addition to dc voltages applied to all three gates. The amplitudes of the rf signals were chosen asymmetric such that the device can work as a pump rather than a turnstile. The charging energy of the device was estimated to be  $2E_C = 1$  meV, and the experiments were carried out at the bath temperature of 300 mK.

With a similar device architecture as shown in Fig. 24 but using only two gates instead of three, [Kaestner, Kashcheyevs, Amakawa \*et al.\* \(2008\)](#) demonstrated that frequency-locked single-electron pumping can be carried out with a single sinusoidal driving voltage, thus decreasing the complexity of the scheme. This type of *single-parameter pumping* with two gates is employed in the remainder of the works discussed in this section. [Maire \*et al.\* \(2008\)](#) studied the current noise of a similar single-parameter pump at  $f = 400$  MHz and estimated based on the noise level that the relative pumping error was below 4%. [Kaestner, Kashcheyevs,](#)

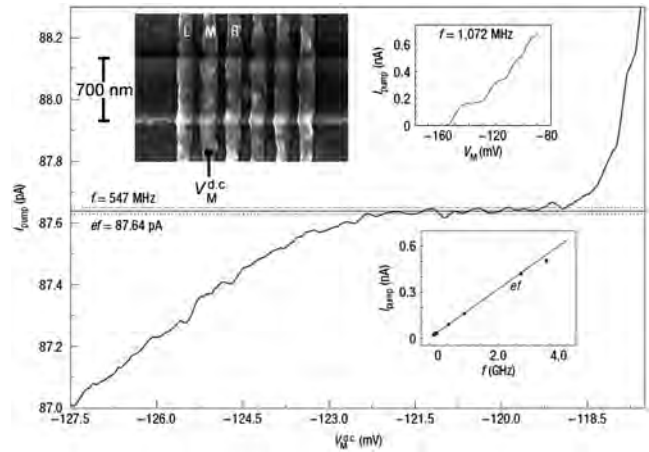


FIG. 24. Current plateau in the electron pumping experiments as a function of the middle-gate voltage at 547 MHz operation frequency. The dashed lines show  $\sigma = \pm 10$  fA uncertainty in the electrometer calibration. The top left inset shows the device used as the electron pump. The top right inset shows current plateaus at 1 GHz pumping frequency and the bottom inset shows the pumped current as a function of the operation frequency. From [Blumenthal \*et al.\*, 2007](#).

[Hein \*et al.\*, 2008](#) studied the robustness of the current plateaus as functions of all control parameters of the pump except the source-drain bias. They showed that single-parameter pumping is robust in the sense that wide current plateaus appear in the parameter space but their measurement uncertainty was limited to about  $10^{-2}$ , and hence a detailed study of the behavior of the accuracy as a function of these parameters was not available.

[Wright \*et al.\* \(2008\)](#) made an important empirical observation that the accuracy of the single-parameter pump can be improved by an application of perpendicular-to-plane magnetic field [see also [Wright \*et al.\* \(2009\)](#) and Fig. 25(b)]. They applied fields up to 2.5 T and demonstrated that the  $n = 1$  plateau as a function of the dc voltage on the nondriven gate widens noticeably with increasing magnetic field. In further studies by [Kaestner \*et al.\* \(2009\)](#) and [Leicht \*et al.\* \(2011\)](#) up to magnetic fields of 30 T, a great widening on the plateau was observed, but it essentially stopped at 5 T. On the contrary, high-resolution measurements on the pumped current up to 14 T by [Fletcher \*et al.\* \(2011\)](#) showed a continuous improvement on the pumping accuracy with increasing field [see also Fig. 25(b)]. This discrepancy is possibly explained by the different samples used in the different sets of experiments.

[Giblin \*et al.\* \(2010\)](#) employed a magnetic field of 5 T and reported 54 pA of pumped current with  $1\sigma = 15$  ppm relative uncertainty with a single-parameter sinusoidal drive. They were able to measure at such a low uncertainty with a room-temperature current amplifier since they subtracted a reference current from the pumped current and passed less than 100 fA through the amplifier. Thus the uncertainty in the gain of the amplifier did not play a role. The reference current was created by charging a low-loss capacitor and was traceable to primary standards of capacitance.

To date, the most impressive results on single-electron pumping with quantum dots have been reported by

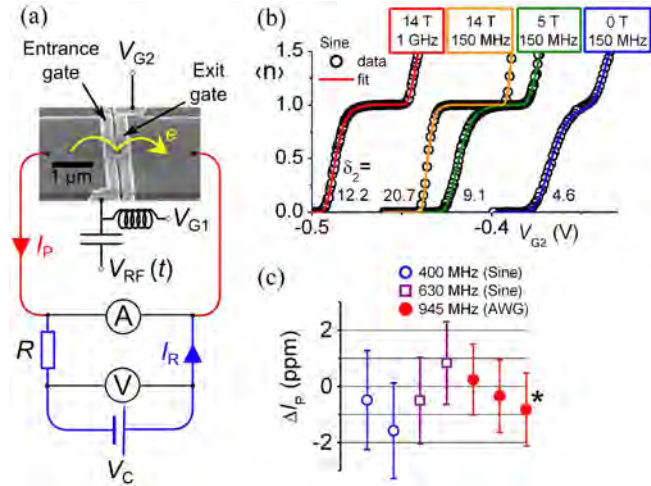


FIG. 25 (color online). (a) SEM image of the device with a schematic measurement setup. (b) Current plateaus obtained by using a sine wave drive at different frequencies and magnetic fields. (c) Relative difference of the pumped current from  $ef$  using a sine wave form and a tailored arbitrary wave form at different frequencies. The rightmost data point denoted by an asterisk shows the result with the potential of the entrance gate shifted by 10 meV from the optimal operation point. From Giblin *et al.*, 2012.

Giblin *et al.* (2012). Compared with the previous results of Giblin *et al.* (2010), they made several changes to improve the results. They used a higher magnetic field of 14 T and an advanced generation of samples with a lithographically defined place for the quantum dot in both directions in the plane [see Fig. 25(a)]. Instead of using sinusoidal wave forms, they also tailored the drive voltage so that the cycle time was distributed more evenly for the different parts of the cycle. To make traceable measurements, a reference current was created by an accurate temperature-controlled 1 G $\Omega$  resistor, a voltage source, and a high-precision voltmeter. The voltmeter and the resistor were calibrated through intermediate steps against the Josephson voltage standard and the quantum Hall resistance (QHR) standard, respectively. In this work, Giblin *et al.* (2012) reported 150 pA pumped current with relative  $1\sigma$  uncertainty of 1.2 ppm [see Fig. 25(c)]. Most of the uncertainty, 0.8 ppm, arose from the calibration of the 1 G $\Omega$  resistor. Thus it is possible that the electron pumping was actually even more accurate, as suggested by fitting the results to a so-called decay-cascade model (Kashcheyevs and Kaestner, 2010). However, there can be processes that are neglected by the model and since there is no experimental evidence on lower than 1.2 ppm uncertainty, it remains the lowest demonstrated upper bound for relative pumping errors for quantum-dot single-electron pumps. Error counting, as demonstrated in silicon by Yamahata, Nishiguchi, and Fujiwara (2011) and in aluminum by Keller *et al.* (1996), is a way to measure the pumping errors to a very high precision independent of the other electrical standards and remains to be carried out in the future for the GaAs quantum-dot pumps.

#### D. Surface-acoustic-wave-based charge pumping

After the pioneering experiments on single-electron sources based on GaAs discussed in Sec. III.C.2, the focus

in this field moved toward the idea of using SAWs to drive single electrons in a one-dimensional channel (Shilton, Mace *et al.*, 1996). Here the sinusoidal potential created for the electrons in the piezoelectric GaAs by a SAW forms a moving well that can trap an integer number of electrons and transport them in a one-dimensional channel.

The first experiments of this kind of SAW electron pumps were carried out by Shilton, Talyanskii *et al.*, (1996). They employed a SAW frequency of 2.7 GHz and observed a corresponding  $n = 1$  current plateau at 433 pA with the uncertainty of the order of  $10^{-2}$  at 1 K temperature. Talyanskii *et al.* (1997) carried out more detailed experiments on similar samples at two different SAW frequencies and the results were in agreement with the  $ef$  scaling law. Furthermore, several current plateaus were observed as a function of the gate voltage corresponding to different integer values of pumped electrons per cycle. However, the experimental uncertainty at the plateau was again of the order of  $10^{-2}$  and sharp current peaks were observed at various gate-voltage values.

After these first experiments, Janssen and Hartland (2000a, 2000b) studied the accuracy of the SAW pump and reported a 431 pA current at the center of the plateau with 200 ppm relative deviation from the ideal value. Ebbecke *et al.* (2000) demonstrated SAW pumping up to 4.7 GHz frequencies and with two parallel channels to increase the current, but the measurement accuracy was rather limited here. To improve the quality of the plateau Janssen and Hartland (2001) decreased the width of the one-dimensional channel, which helps in general. However, they observed that the required rf power to drive the electrons increases with decreasing channel width, causing severe rf heating of the sample. This heating caused the quality of the plateau to drop and the conclusion was that materials with lower losses due to rf are needed [see also Utko, Lidelof, and Gloos (2006)]. In fact, Flensburg, Niu, and Pustilnik (1999) and Ebbecke *et al.* (2003) reported that the accuracy of the SAW current is fundamentally limited in one-dimensional channels because of tunneling of electrons out from a moving dot.

To overcome the limitation pointed out by Ebbecke *et al.* (2003), the charging energy was increased in the system by defining a quantum dot with surface gates rather than utilizing an open one-dimensional channel (Ebbecke *et al.*, 2004). Thus the applied SAWs modulate both the tunnel barriers between the dot and the reservoirs and the electrochemical potential at the dot. With this technique, current plateaus were observed at a SAW frequency of 3 GHz and the reported relative deviation from the ideal value was of the order of  $10^{-3}$ . Although the results by Janssen and Hartland (2000a, 2000b) remain the most accurate ones reported to date with SAW electron pumps, and hence are not valuable for a metrological current source, single-electron transfer with SAWs can be useful in other applications. For example, McNeil *et al.* (2011) showed that an electron taken by SAWs from a quantum dot can be captured by another dot at a distance. This kind of electron transport can potentially be used to transport single spins working as quantum bits in a spin-based quantum computer (Hanson *et al.*, 2007; Morello *et al.*, 2010).

### E. Superconducting charge pumps

The envisioned advantage in pumping Cooper pairs instead of electrons is that the supercurrent produced by the Cooper-pair pumps is inherently dissipationless and the BCS gap protects the system from microscopic excitations. Thus the operation frequency of the pump can possibly be high with the system still remaining at very low temperature. Another advantage of the supercurrent is that it can sustain its coherence, and hence be virtually noiseless, in contrast to the single-electron current that is based on probabilistic tunneling. Furthermore, since the charge of a single Cooper pair is  $2e$ , single-Cooper-pair pumps yield twice the current compared with single-electron pumps operated at the same frequency. Despite these advantages, the lowest uncertainties in the achieved Cooper-pair current is at the percent level (Vartiainen *et al.*, 2007; Gasparinetti *et al.*, 2012). One reason for this is the low impedance of the device, rendering it susceptible to current noise.

Two types of Cooper-pair pumps exist in the literature: arrays of superconducting islands (Geerligs *et al.*, 1991) with source and drain leads, all separated by single Josephson junctions with fixed tunnel couplings, and a so-called sluice (Niskanen, Pekola, and Seppä, 2003; Niskanen *et al.*, 2005) that is composed of a single island connected to the leads by two SQUIDs that function as tunable Josephson junctions; see Fig. 26. As in the case of single-electron pumps, the device operation is based on Coulomb-blockade effects allowing the controlled transfer of individual Cooper pairs, which means in the case of array pumps that the fixed Josephson energies of the junctions must be much lower than the Cooper-pair charging energy of the corresponding islands. In the sluice, it is sufficient that the minimum obtainable Josephson energy is much lower than the charging energy. For the arrays, the thermal energy  $k_B T$  must be much lower than the Josephson energy that defines the energy gap between the ground state and the excited state of the quantum system at charge degeneracy. For the sluice, the maximum Josephson energy of the SQUIDs yields the minimum energy gap of the system, thus relaxing the constraint on temperature.

The first experiment demonstrating Cooper-pair pumping was performed by Geerligs *et al.* (1991). The device is a linear array of three Josephson tunnel junctions. The two superconducting islands separated by the junctions are capacitively coupled to individual gate electrodes. Except in the vicinity of the charge degeneracy points in the gate-voltage space, the number of Cooper pairs on these islands is rather well defined by the gate voltages because the Coulomb-blockade regime is employed. By biasing the device and applying sinusoidal ac voltages with appropriate amplitudes to the gates, one obtains a continuously repeated cycle, during which a Cooper pair is transferred through the device, i.e., Cooper pairs are pumped one by one. Ideally, this yields a dc current  $I = 2ef$  that is proportional to the pumping frequency  $f$ . The driving voltage at each gate should have the same frequency and a phase difference of  $\pi/2$ . The pumping direction can be reversed if the difference is changed by  $\pi$ . Thus the pumping principle is the same as for a normal pump discussed in Sec. III.A. The height of the measured current plateau follows rather well the predicted relation  $I = 2ef$  at low pumping frequencies, but deviates strongly at higher

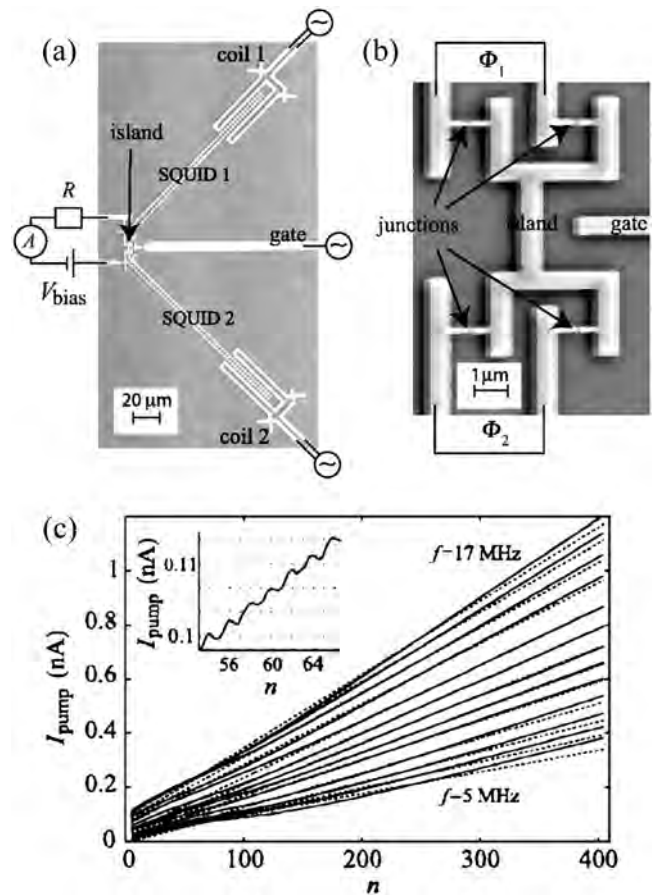


FIG. 26. (a) Scanning electron micrograph of the sluice used in the experiments by Vartiainen *et al.* (2007) with a simplified measurement setup. (b) Magnified view of the island of the device shown in (a) with four Josephson junctions. (c) Measured pumped current with the sluice (solid lines) as a function of the magnitude of the gate-voltage ramp such that  $n$  corresponds to the ideal number of elementary charges  $e$  pumped per cycle. The inset shows the steplike behavior observed in the pumped current. From Vartiainen *et al.*, 2007.

frequencies. This is explained by several mechanisms. The pumping uncertainty of the device was not assessed in detail but it seems to lie at least on the percent level with picoampere currents. One of the error mechanisms is the Landau-Zener tunneling when the system is excited to the higher-energy state without transferring a Cooper pair. This was the dominant mechanism at the high end of the studied pumping frequencies in the experiment by Geerligs *et al.* (1991) thus imposing an upper limit on the operation frequency of the device. Other error sources in the device are the tunneling of nonequilibrium quasiparticles, photon-excited tunneling, and relaxation of the excited states produced by Landau-Zener tunneling. In addition, cotunneling of Cooper pairs through the two junctions produces a steplike feature in the current plateaus, thus reducing the pumping accuracy. Later, a similar three-junction Cooper-pair pump was studied by Toppari *et al.* (2004) and essentially the same conclusions on the pumping accuracy were made. In both experiments, no  $2e$  periodicity was observed in the dc measurements, which suggests a substantial presence of nonequilibrium quasiparticles in the system.

The effect of quasiparticles on Cooper-pair pumping was also observed in the seven-junction Cooper-pair pump (Aumentado, Keller, and Martinis, 2003). The device is basically the same as the one used for pumping single electrons in the earlier experiments in the normal state (Keller *et al.*, 1996). The pump consists of 6  $\mu\text{m}$ -scale aluminum islands linked by aluminum-oxide tunnel barriers. Investigation of this circuit in the hold and pumping modes revealed that besides  $2e$  tunneling events, there is a significant number of  $1e$  events associated with the quasiparticle tunneling. All these experiments show that in order to obtain accurate Cooper-pair pumping, one must suppress unwanted quasiparticle tunneling. Leone and Lévy (2008) and Leone, Lévy, and Lafarge (2008) proposed topological protection in pumping Cooper pairs. The charge is expected to be strictly quantized determined by a Chern index. To our knowledge, this idea has not been tested experimentally.

In order to increase the output dc current and accuracy of a single pump, the sluice pump was introduced by Niskanen, Pekola, and Seppä (2003) and Niskanen *et al.* (2005). In the pumping cycle, the two SQUIDs separating the single island work in analogy with valves of a classical pump and the gate voltage controlling the island potential is analogous to a piston. At each moment of time, at least one SQUID is closed, i.e., set to minimum critical current. The gate voltage is used to move Cooper pairs through open SQUIDs with maximum critical current. If the pairs are taken into the island through the left SQUID and out of the island through the right SQUID, the resulting dc current is ideally  $I = N2ef$ , where the number of pairs transported per cycle  $N$  is determined by the span of the gate-voltage ramp. In practice, the critical current of the SQUIDs is controlled by flux pulses generated by superconducting on-chip coils. Since each operation cycle can transfer up to several hundreds of Cooper pairs, Vartiainen *et al.* (2007) managed to pump roughly 1 nA current with uncertainty less than 2% and pumping frequency of 10 MHz; see Fig. 26. The investigated high-current Cooper-pair pump demonstrated steplike behavior of the pumped current on the gate voltage; however, its accuracy was affected by the residual leakage in the tunnel junctions and the fact that the SQUIDs did not close completely due to unequal Josephson junctions in the structure.

The leakage current in the sluice can be suppressed by working with a phase bias instead of a voltage bias, as was applied by Niskanen *et al.* (2005) and Vartiainen *et al.* (2007). The only experiment reported for a phase-biased pump was carried out by Möttönen, Vartiainen, and Pekola (2008). They connected a sluice in a superconducting loop with another Josephson junction. By measuring the switching behavior of this junction from the superconducting state to the normal branch with forward and backward pumping, they were able to extract the pumped current of the sluice. However, this type of current detection did not turn out to be as sensitive as the direct measurement with a transimpedance amplifier used in the case of voltage bias. A potential way to improve the sensitivity is, instead of the switching junction, to use a cryogenic current comparator (CCC) coupled inductively to the superconducting loop. This type of an experiment has not been carried out to date. Instead, Gasparinetti *et al.* (2012) measured a sluice in the vicinity of vanishing voltage bias,

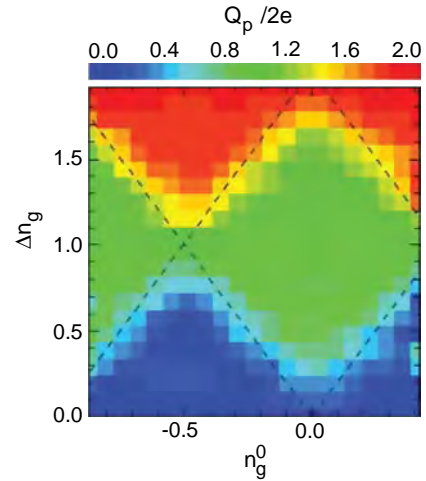


FIG. 27 (color online). Pumped average charge by Gasparinetti *et al.* (2012) for a single pumping cycle of a sluice pump near vanishing voltage bias as a function of the gate charge offset  $n_g$  and span during the pumping cycle  $\Delta n_g$ . From Gasparinetti *et al.*, 2012.

where they demonstrated single-Cooper-pair pumping plateaus in both the bias voltage and dc level of the gate voltage; see Fig. 27. The quasiparticle poisoning was reported to be suppressed compared with the previous experiments, and hence they observed clear  $2ef$  spacing of the current plateaus.

In addition to the above-mentioned pumping schemes, Nguyen *et al.* (2007) studied how a superconducting quantum bit referred to as a quantronium can be used to detect the gate charge ramp arising from a current bias on the gate electrode of the island of the device. The accuracy of this technique in converting the bias current into frequency remains to be studied in detail. Hoehne *et al.* (2012) studied another type of quantum bit, a charge qubit, for pumping Cooper pairs nonadiabatically. The aim here was to increase the pumping speed compared to adiabatic schemes but due to the accumulation of the errors from one pumping cycle to another, a waiting period between the cycles needed to be added. Furthermore, Giazotto *et al.* (2011) showed experimentally how phase oscillations can drive Cooper pairs in a system with no tunnel junctions. However, this kind of pumping was found to be very inaccurate in this proof-of-the-concept experiment.

## F. Quantum phase slip pump

There is a proposal to build a source of quantized current based on the effect of QPSs in nanowires made of disordered superconductors (Mooij and Nazarov, 2006). Phase slip events occur in thin superconducting wires where thermodynamic fluctuations of the order parameter become significant (Arutyunov, Golubev, and Zaikin, 2008). During the phase slip, the superconducting order parameter vanishes at a certain instance and position in the wire, and the phase difference between the wire ends changes by  $2\pi$ . This gives rise to a voltage pulse in accordance with the Josephson relation. If the phase slips happen frequently, they produce a finite dc voltage or a finite resistance.

Phase slips caused by thermal activation broaden the temperature range of superconducting phase transitions and

produce a resistive tail below the critical temperature of a superconductor (Tinkham, 1996). At sufficiently low temperatures quantum fluctuations take over, and the residual temperature-independent resistivity of a nanowire can be attributed to the quantum phase slips [see Arutyunov, Golubev, and Zaikin (2008) and references therein]. Thermally activated phase slips are inherently incoherent. Quantum phase slips may be coherent provided dissipation associated with every switching event is suppressed. This can be achieved in superconductors with strong disorder in which Cooper pairs localize before the superconducting transition takes place (Feigel'man *et al.*, 2007). Such a localization behavior has been observed by scanning tunneling microscopy in amorphous TiN and InO<sub>x</sub> films (Sac  p   *et al.*, 2010, 2011), which are believed to be the most promising materials for the observation of QPSs.

The key parameter describing a nanowire in the quantum phase slip regime is the QPS energy  $E_{\text{QPS}} = \hbar\Gamma_{\text{QPS}}$ , where  $\Gamma_{\text{QPS}}$  is the QPS rate. Consider a superconducting nanowire of length  $L$  and sheet resistance  $R_{\square}$ , and made of a superconductor with the superconducting transition temperature  $T_c$ , and coherence length  $\xi = (\xi_0\ell)^{1/2}$ , where  $\xi_0$  is the BCS coherence length and  $\ell$  is the electron mean free path ( $\ell \ll \xi_0$ ). Although there is no commonly accepted expression for  $\Gamma_{\text{QPS}}$ , it is agreed (Mooij and Harmans, 2005; Arutyunov, Golubev, and Zaikin, 2008) that

$$\Gamma_{\text{QPS}} \propto \exp\left(-0.15A \frac{R_K}{2R_{\square}\xi}\right),$$

where  $A$  is a constant of order unity and  $R_K = h/e^2$ . Clearly the exponential dependence of  $\Gamma_{\text{QPS}}$  on the wire resistance on the scale of  $\xi$ ,  $R_{\xi} = R_{\square}\xi$ , requires extremely good control of the film resistivity as well as the wire cross-sectional dimensions. For the nanowires to be in the quantum phase slip regime rather than in the thermally activated regime,  $E_{\text{QPS}}$  should exceed the energy of thermal fluctuations  $k_B T$ . For a typical measurement temperature of 50 mK,  $\Gamma_{\text{QPS}}/2\pi$  should be higher than 1 GHz. Although the exact estimation of  $R_{\xi}$  is rather difficult, especially in the case of strongly disordered films, the experimental data presented by Astafiev *et al.* (2012) for InO<sub>x</sub> films agrees with the following values:  $\Gamma_{\text{QPS}}/2\pi \approx 5$  GHz,  $R_{\xi} = 1$  k $\Omega$ , and  $\xi = 10$  nm.

The first experiment reporting the indirect observation of coherent QPS in nanowires was performed by Hongisto and Zorin (2012). They studied a transistorlike circuit consisting of two superconducting nanowires connected in series and separated by a wider gated segment. The circuit was made of amorphous NbSi and embedded in a network of on-chip 30-nm-thick Cr microresistors ensuring a high external electromagnetic impedance. The NbSi film had a superconducting transition temperature of  $\approx 1$  K and normal-state sheet resistance of about 550  $\Omega$  per square. Provided the nanowires are in the regime of QPSs, the circuit is dual to the dc SQUID. The samples demonstrated appreciable Coulomb-blockade voltage (the analog of the critical current of the dc SQUID) and periodic modulation of the blockade by the gate voltage. Such behavior was attributed to the quantum interference of voltages in two nanowires that were in the QPS regime. This is completely analogous to the quantum interference of currents in a dc SQUID.

An unambiguous experimental evidence of a coherent QPS was provided in the work by Astafiev *et al.* (2012). Coherent properties of quantum phase slips were proven by a spectroscopy measurement of a QPS qubit, which was proposed earlier by Mooij and Harmans (2005). The qubit was a loop that had a 40-nm-wide and about 1- $\mu$ m-long constriction. The loop was made of a 35-nm-thick superconducting disordered InO<sub>x</sub> film with  $T_c = 2.7$  K and a sheet resistance of 1.7 k $\Omega$  per square slightly above  $T_c$ . The qubit was coupled inductively to a step-impedance coplanar waveguide resonator, which was formed due to the impedance mismatch between an indium oxide strip and Au leads to which it was galvanically connected. The ground planes on both sides of the strip were made of Au. At the qubit degeneracy point at a flux bias  $(m + 1/2)\Phi_0$ , where  $m$  is an integer, there is an anticrossing in the qubit energy spectrum with a gap  $E_{\text{QPS}} = \hbar\Gamma_{\text{QPS}}$ . At this flux bias, the two quantum states  $|m\rangle$  and  $|m + 1\rangle$  corresponding to the loop persistent currents circulating in the opposite directions are coupled coherently, which gives a gap  $E_{\text{QPS}}$  between the lowest-energy bands of the qubit. With the flux offset  $\delta\Phi$  from degeneracy, the gap evolves as  $\Delta E = [(2I_p\delta\Phi)^2 + E_{\text{QPS}}^2]^{1/2}$ , where  $I_p$  is the persistent current in the loop. This gap was revealed in the spectroscopy measurements by monitoring the resonator transmission as a function of the external magnetic field and microwave frequency. When the microwave frequency matched the qubit energy gap, a dip in the transmission was observed. The width of the dip  $\sim 260$  MHz close to the degeneracy point indicated rather strong decoherence whose origin is still to be understood.

Based on the exact duality of the QPS and the Josephson effects, it is argued that it should be possible to build a QPS electric current standard, which is dual to the existing Josephson voltage standard (Mooij and Nazarov, 2006). When biased resistively and irradiated by a high-frequency signal, QPS junctions exhibit current plateaus, which could provide the basis for the fundamental standard of the electric current. When an ac signal of frequency  $f$  is applied to a Josephson junction, Shapiro voltage steps  $V_n = n(hf/2e)$ , where  $n$  is an integer, are observed. Similarly, when an ac signal is applied to a QPS junction, an equivalent of Shapiro steps will occur in the form of plateaus at constant current levels  $I_n = n2ef$ . One should note, however, that error mechanisms have not yet been analyzed for this type of quantized current source: thus it is not clear at the moment how accurate this source will be.

From a practical point of view, the realization of a QPS current source looks rather challenging because it requires fabrication of nanowires with an effective diameter  $\sim 10$  nm as well as precise control of the sheet resistance  $R_{\square}$  of the nanowire, which is in the exponent of the expression for  $E_{\text{QPS}}$ . Various approaches to the nanowire fabrication including the step decoration technique, sputtering of a superconductor on a suspended carbon nanotube, trimming of a nanowire by argon milling, etc. are described by Arutyunov, Golubev, and Zaikin (2008). Another issue is the overheating of the nanowire electron system. Assuming that the phase slip region becomes normal (which is true, for example, for Ti nanowires), for the estimation of the electron temperature, one can use Eq. (34) for the power transfer from electrons

to phonons. A nanowire with the cross-sectional dimensions  $20 \times 20 \text{ nm}^2$ , sheet resistance  $1 \text{ k}\Omega$  per square, and carrying a dc current of  $100 \text{ pA}$  will have the effective electron temperature of the order of  $250 \text{ mK}$ , which is high enough to smear the current plateaus.

One of the first attempts to observe current plateaus on the current-voltage characteristics of superconducting nanowires under rf radiation was reported by [Lehtinen, Zakharov, and Arutyunov \(2012\)](#). The nanowires were made of Ti and had length up to  $20 \mu\text{m}$  and effective diameter from  $40 \text{ nm}$  down to about  $15 \text{ nm}$ . The nanowire sheet resistance varied from about  $20 \Omega$  up to  $1.9 \text{ k}\Omega$  per square. They were biased through high-Ohmic Ti or Bi leads having total resistance of  $15 \text{ k}\Omega$  and  $20 \text{ M}\Omega$ , respectively. The low-Ohmic samples biased through  $15 \text{ k}\Omega$  exhibited a weak Coulomb blockade. The estimated  $E_{\text{QPS}}$  was  $\approx 0.1 \mu\text{eV}$  only. More resistive nanowires ( $R_{\square} = 180 \Omega$ , effective diameter  $\approx 24 \text{ nm}$ ) biased through  $20 \text{ M}\Omega$  leads had a pronounced Coulomb blockade with a critical voltage of up to  $0.4 \text{ mV}$ . The thinnest nanowires ( $R_{\square} = 1.9 \text{ k}\Omega$ , effective diameter  $\leq 18 \text{ nm}$ ) exhibited a Coulomb gap of a few hundred millivolts with the largest gap exceeding  $600 \text{ mV}$ . These gaps did not vanish above  $T_c$  of Ti, from which the authors concluded that some weak links were unintentionally formed in the thinnest nanowires. Despite the fact that the nanowires had large variations of parameters, all their current-voltage or  $dV/dI$  characteristics exhibited some quasiregular features under the external rf radiation. Those features were interpreted as being current steps formed due to the phase locking of intrinsic oscillations by the external signal.

It is interesting to note that the physics of QPSs in superconducting nanowires resembles the physics of QPSs in Josephson junction arrays ([Fisher, 1986](#)). A nanowire can be modeled as a 1D array of small superconducting islands connected by Josephson junctions. The formation of isolated superconducting regions within a nominally uniform disordered film was confirmed experimentally ([Sacépé \*et al.\*, 2010, 2011](#)). Such a weakly connected array of superconducting islands is characterized by the junction Josephson energy  $E_J$  and the island charging energy  $E_c$ . The phase and charge dynamics of the 1D array depends on the ratio  $E_J/E_c$ . In the experiment by [Pop \*et al.\* \(2010\)](#)  $E_J/E_c$  in a SQUID array was tuned *in situ* by applying a uniform magnetic flux through all SQUIDs. The state of the array was detected by an extra shunt Josephson junction. They deduced the effect of the quantum phase slips on the ground state of the array by measuring the switching current distribution of the entire Josephson circuit as a function of the external magnetic flux for different values of  $E_J/E_c$ .

## G. Other realizations and proposals

In this section we cover various ideas that have been brought up for experimental demonstration. Although their metrological relevance is still to be proven, we present them for their complementarity, potential, and for completeness.

### 1. ac-current sources

The current pumps described in Secs. III.A–III.C can be considered as single-electron injectors generating dc current.

Coulomb blockade ensures a good control of the electron number on an island during the charge transfer.

A time-controlled single-electron source generating ac current was reported by [Fève \*et al.\* \(2007\)](#). The source was made of a GaAlAs/GaAs quantum dot tunnel coupled to a large conductor through a quantum point contact (see Fig. 28). A magnetic field  $B \approx 1.3 \text{ T}$  was applied to the sample so as to work in the quantum Hall regime with no spin degeneracy. The discrete energy levels of the quantum dot were controlled by the pulse voltage  $V_{\text{exc}}$  applied to the top gate and by the QPC dc gate voltage  $V_g$ , which also controlled the transmission  $D$  of a single edge state. The dot addition energy  $\Delta + e^2/C \approx 2.5 \text{ K}$  was determined by the energy-level spacing  $\Delta$  as the Coulomb energy  $e^2/2C$  was negligibly small. As proposed by [Gabelli \*et al.\* \(2006\)](#), this circuit constitutes an effective quantum-coherent RC circuit with the effective quantum resistance  $R$  and capacitance  $C$  defined as  $R = h/2e^2$  and  $C = e^2(dN/d\varepsilon)$ , where  $dN/d\varepsilon$  is the local density of states of the mode propagating in the dot, taken at the Fermi energy ([Prêtre, Thomas, and Büttiker, 1996](#)).

The single-charge injection was achieved by the application of a high-amplitude excitation voltage  $V_{\text{exc}} \sim \Delta/e$  to the top gate, which leads to the electron escape from the dot at a typical tunnel rate  $\tau^{-1} = D\Delta/h$ , where  $\Delta/h$  is the attempt frequency. Typically, the tunnel rates are in the nanosecond time scales, and this makes single-shot charge detection a challenging task. To increase the signal-to-noise ratio, a statistical average over many individual events was used by repeating cycles of single-electron emission with period  $T$  followed by single-electron absorption (or hole emission) as shown in Fig. 28. This was done by applying a periodic square-wave voltage of amplitude  $\approx \Delta/e$  to the top gate.

When the charge on the dot is well defined, repeatable single-electron injection leads to quantization of the ac

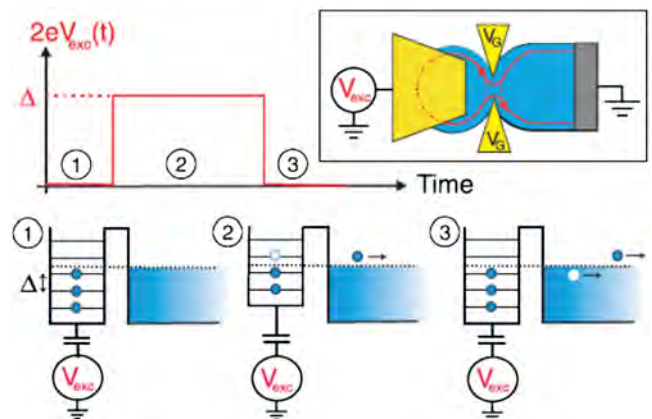


FIG. 28 (color online). Schematic of the single-charge injector and its operation principle. Starting from step 1 where the Fermi energy level of the conductor lies in between two energy levels of the dot, its potential is increased by  $\Delta$  by moving one occupied dot level above the Fermi energy (step 2). One electron then escapes from the dot. After that the potential is brought back to the initial value (step 3), where one electron can enter the dot, leaving a hole in the conductor. One edge channel of the quantum RC circuit is transmitted into the dot, with transmission  $D$  tuned by the QPC gate voltage  $V_g$ . From [Fève \*et al.\*, 2007](#).

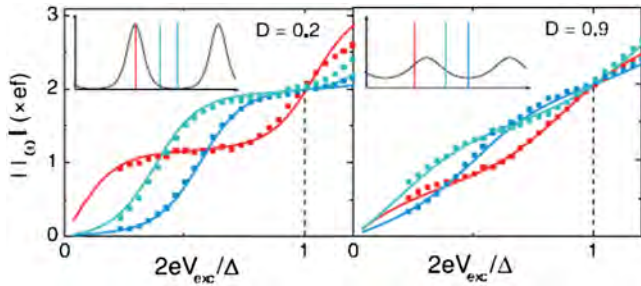


FIG. 29 (color online). ac quantization.  $|I_\omega|$  as a function of  $2eV_{\text{exc}}/\Delta$  for different dot potentials at  $D \approx 0.2$  (left) and  $D \approx 0.9$  (right). Dots are measured values and lines are theoretical predictions. Insets schematically show the dot density of states  $N(\epsilon)$ . The vertical lines indicate the dot potential for the corresponding experimental data. From [Fève \*et al.\*, 2007](#).

current.  $|I_\omega|$  as a function of  $V_{\text{exc}}$  for two values of the dc dot potential at  $D \approx 0.2$  and  $D \approx 0.9$  is shown in Fig. 29. The transmission  $D \approx 0.2$  is low enough and the electronic states in the dot are well resolved, as shown in the inset of Fig. 29 (left). On the other hand, the transmission is large enough for the escape time to be shorter than  $T/2$ . When the Fermi energy lies exactly in the middle of the density-of-states valley (rightmost vertical line in the left inset), a well-pronounced  $|I_\omega| = 2ef$  current plateau is observed centered at  $2eV_{\text{exc}}/\Delta = 1$ . It is claimed that the current uncertainty at the plateau is 5% due to the systematic calibration error. In contrast, if, with the same transmission, the Fermi energy lies on the peak (middle vertical line in the left inset), there is still a current plateau, but it is not as flat and it is sensitive to parameter variations. When transmission is increased, the charge fluctuations become stronger and the plateau gets narrow and finally nearly vanishes at  $D \approx 0.9$  even for the optimal working point, as seen from Fig. 29 (right). The experimental results (dots) are compared with the theoretical model, the solid lines [1D modeling of the circuit described by [Gabelli \*et al.\* \(2006\)](#) was used], showing excellent agreement between the two.

The device above has been described as an electron analog of the single-photon gun. It is not a source of quantized dc current as the dot emitting the electron can be recharged only through the reverse process of electron absorption. Using a similar technique of electron emission with fast pulses, but adding one more lead, one can produce a highly accurate dc current ([Giblin \*et al.\*, 2012](#)) as described in Sec. III.C.4. Recent correlation experiments on electron guns have been reported in [Bocquillon \*et al.\* \(2012\)](#).

## 2. Self-assembled quantum dots in charge pumping

The idea of using self-assembled quantum dots for charge pumping is based on conversion of optical excitation into deterministic electric current; see [Nevou \*et al.\* \(2011\)](#). In the experiment of [Nevou \*et al.\* \(2011\)](#) a plane of self-assembled InAs quantum dots is coupled to an InGaAs quantum-well reservoir through an  $\text{Al}_{0.33}\text{Ga}_{0.67}\text{As}$  barrier [see Figs. 30(a)–30(c)]. The structure is sandwiched between two  $n$ -doped GaAs regions. The device basically works as a strongly asymmetric quantum-dot infrared photodetector ([Nevou \*et al.\*, 2010](#)). In the absence of any optical excitation,

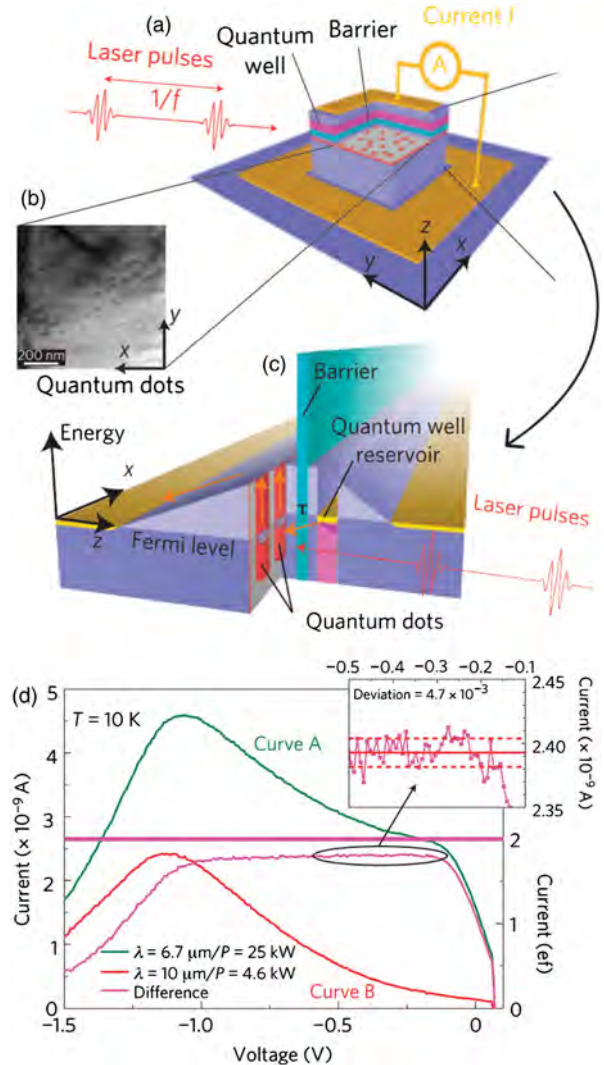


FIG. 30 (color online). (a) Schematic layout of the self-assembled quantum-dot electron pump, (b) transmission electron microscopy image of the quantum dots, (c) 3D sketch of the conduction band profile of the structure under zero bias, and (d) saturation current for two different pump wavelengths ( $\lambda = 6.7 \mu\text{m}$ : curve A and  $\lambda = 10 \mu\text{m}$ : curve B). The difference provides a current plateau that should be  $2ef$  (thick horizontal line). Inset: Variations of the measured current with respect to the average value. From [Nevou \*et al.\*, 2011](#).

electrical conduction is inhibited by the AlGaAs barrier. When a laser pulse ionizes the quantum dots, a fixed number of electrons are excited out of the dot and then swept away by the applied bias voltage, giving rise to a photocurrent. After that, the dots will be refilled from the electron reservoir by tunneling through the AlGaAs barrier. If the process is repeated at a frequency  $f$ , the current will be given by  $I = nef$ , where  $n$  is determined by the number of dots and the number of electrons per dot. To obtain the desired pumping accuracy, the laser pulse duration time must be much shorter than the refilling time, and  $f$  should not exceed the kilohertz range. Even with such a low repetition frequency, currents in the nanoampere range can be generated as the number of dots running in parallel in a typical device is tens of millions. There are error sources arising from the uncertainty in the number of quantum dots contained in one device, as well as

the variability in the quantum-dot transition energy. These errors were of the order of 10% of the pumped current in the experiment of [Nevou \*et al.\* \(2011\)](#).

### 3. Mechanical single-electron shuttles

Besides charge pumps with entirely electronic control, there is a group of devices in which a mechanical degree of freedom is involved. They are called mechanical charge shuttles, because they transfer either single charges (electrons or Cooper pairs) or portions of charges between the two electrodes due to the mechanical back-and-forth motion of a small island between the electrodes. This results in current flow, either incoherent or coherent. The concept of the mechanical electron shuttle was introduced by [Gorelik \*et al.\* \(1998\)](#) and [Isacsson \*et al.\* \(1998\)](#).

The proposed device has a small conducting island, which is mechanically attached to electrical leads with the help of an elastic insulator. The dc voltage applied between the leads and elastic properties of the insulator together with charging and discharging of the island creates instability and makes the island oscillate; see [Fig. 31\(a\)](#). For the proper operation of the shuttle, two assumptions were made: the amplitude of the mechanical oscillations is much larger than the electron tunneling distance, and the number of electrons on the island is limited. With these assumptions the island motion and charge fluctuations become strongly coupled. Depending on the shuttle details, two regimes can be distinguished: classical ([Gorelik \*et al.\*, 1998](#); [Isacsson \*et al.\*, 1998](#); [Weiss and Zwerger, 1999](#)) and quantum mechanical ([Armour and MacKinnon, 2002](#); [Fedorets \*et al.\*, 2004](#); [Johansson \*et al.\*, 2008](#); [Cohen, Fleurov, and Kikoin, 2009](#)). The shuttle, when made superconducting, can transfer not only electrons but also Cooper pairs ([Gorelik \*et al.\*, 2001](#); [Shekhter \*et al.\*, 2003](#)).

The first experimental realization of a mechanical charge shuttle that operated due to a shuttle instability was reported by [Tuominen, Krotkov, and Breuer \(1999\)](#). This was a rather bulky device even though it was scaled down considerably in size and operating voltage in comparison to the earlier electrostatic bell versions. The observed jumps of the current as a function of the bias voltage as well as hysteresis in the transport characteristics were the main indications of the shuttling regime of the device. A nanoscale version of the instability-based electron shuttle was implemented by [Kim, Qin, and Blick \(2010\)](#); see [Fig. 31\(b\)](#). The device was a Si pillar covered on top with a thick gold layer and placed in the gap between two electrodes, the source and the drain, of the central line of a coplanar waveguide. For reference, they also fabricated and measured a similar device without a pillar in the gap. The samples were measured at room temperature in vacuum. The pillar was actuated by applying a small rf signal together with a dc bias voltage across the source and drain electrodes. A clear frequency dependence was observed for the sample with a pillar in the gap, with the resonance frequency of 10.5 MHz and quality factor of about 2.5. It was estimated that the device shuttles on average 100 electrons per cycle.

Another realization of the nanoelectronic shuttling device was reported by [Moskalenko \*et al.\* \(2009a, 2009b\)](#). It had the configuration of a single-electron transistor, whose island was a gold nanoparticle placed in between the Au source and

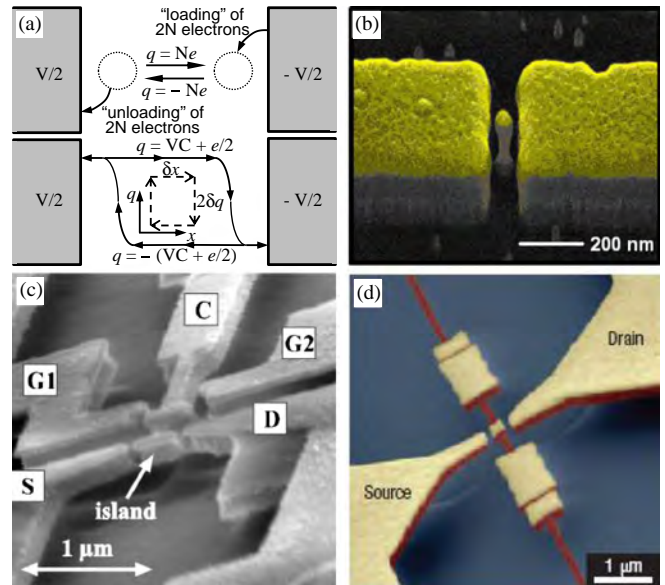


FIG. 31 (color online). (a) Model of the shuttle device proposed by [Gorelik \*et al.\* \(1998\)](#). (Top) Dynamic instabilities occur since in the presence of a sufficiently large bias voltage  $V$  the grain is accelerated by the electrostatic force toward the first electrode, then toward the other one. A cyclic change in direction is caused by the repeated loading of electrons near the negatively biased electrode and the subsequent unloading of the same charge at the positively biased electrode. As a result, the sign of the net grain charge alternates, leading to an oscillatory grain motion and charge transport. (Bottom) Charge variations on a cyclically moving metallic island. The dashed lines in the middle describe a simplified trajectory in the charge-position plane, when the island motion by  $\delta x$  and discharge by  $2\delta q$  occur instantaneously. The solid trajectory describes the island motion at large oscillation amplitudes. Periodic exchange of the charge  $2q = 2CV + 1$  between the island and the leads results in the net shuttle current  $I = 2\delta q f$ , where  $f$  is the shuttle frequency. Adapted from [Gorelik \*et al.\*, 1998](#). (b) Scanning electron micrograph of a nanopillar between two electrodes. From [Kim, Qin, and Blick, 2010](#). (c) Electron micrograph of the quantum bell: The Si beam (clapper) is clamped on the upper side of the structure. ac gates  $G1$  and  $G2$  are used for the actuation of the clapper  $C$ . Electron transport is measured from source  $S$  to drain  $D$  through the island on top of the clapper. From [Erbe \*et al.\*, 2001](#). (d) A false-color SEM image of the nanomechanical SET. A gold island is located at the center of a doubly clamped freely suspended silicon nitride string. The gold island can shuttle electrons between the source and drain electrodes when excited by ultrasonic waves. From [Koenig, Weig, and Kotthaus, 2008](#).

drain electrodes by means of an atomic force microscope. Current-voltage characteristics of the devices were measured at room temperature, and characteristic current jumps in the current-voltage curves were observed, which were attributed to the shuttling effect. They also compared characteristics of the working shuttle device from which the nanoparticle was removed. After this procedure, the current through the device dropped below the noise level.

The effect of the mechanical vibrational modes on charge transport in a nanoelectronic device was observed in a  $C_{60}$  single-electron transistor ([Park \*et al.\*, 2000](#)). In this device, a single  $C_{60}$  molecule was placed in the narrow gap between the two gold electrodes. It was found that the current flowing

through the device increases sharply whenever the applied voltage was sufficient to excite vibrations of the molecule. Although mechanical vibrations were observed in this structure, they are not related to the shuttling of electrons.

Externally driven resonant shuttles may be easier to implement in comparison to the instability-based shuttles, because a much larger displacement amplitude can be achieved. However, the drawback of using a mechanical resonator is the discrete set of eigenfrequencies, which are determined by geometry and materials. Therefore, only a limited number of frequencies are available for electron transfer. In the experiment performed by [Erbe \*et al.\* \(1998\)](#) a Si nanomechanical resonator was placed in between two contacts. The whole device, being a scaled-down version of the classical bell, was functioning as a mechanically flexible tunneling contact operating at radio frequencies. The contact was driven by  $\pi$ -shifted oscillating voltages applied on two gates. The current-frequency dependence of the device contained strong peaks, which were interpreted as being due to the mechanical resonances of the beam, indicating that shuttling was occurring. The peaks had low quality factors, ranging from 100 to 15 only. The number of electrons  $N$  shuttled per cycle was estimated from the current peak height  $I$  using the  $N = I/ef$ . Below 20 MHz,  $10^3$ – $10^4$  electrons were shuttled in each cycle. On the 73 MHz peak the number was decreased to about 130 electrons per cycle.

The same group ([Erbe \*et al.\*, 2001](#)) fabricated a singly clamped beam with a metal island on its end [see Fig. 31(c)]. It was found at 300 K that there was no detectable current through the device unless a driving ac voltage ( $\pm 3$  V) was applied to the driving gates. Under the external drive, the current exhibited several peaks, similar to those in the earlier device ([Erbe \*et al.\*, 1998](#)), which was attributed to the beam motion. The background current was explained by the thermal motion of the beam. At 4.2 K all the current peaks were suppressed except one at about 120 MHz with much smaller height (only 2.3 pA). This corresponded to shuttling on average of 0.11 electron per cycle.

[Koenig, Weig, and Kotthaus \(2008\)](#) implemented electro-mechanical single-electron transistors with a metallic island placed on a doubly clamped SiN beam [see Fig. 31(d)], which was measured at a temperature of 20 K. The observed resonance features in the SET dc current were attributed to the mechanical resonances. It was argued that the mechanical motion of the resonator was strongly nonlinear. This was imposed by the side electrodes constituting the impacting boundary conditions. The nonlinear nature of the system resulted in a shape of the resonance curves different from Lorentzian. Although the expected steplike dependence of the SET current on the source-drain voltage was not observed (because of the high measurement temperature as compared to the charging energy), they made an optimistic conclusion that the device may be useful for quantum metrology.

#### 4. Electron pumping with graphene mechanical resonators

An electron pump based on a graphene mechanical resonator in the fundamental flexural mode was introduced by [Low \*et al.\* \(2012\)](#). The resonator is actuated electrostatically by a gate electrode. Time-varying deformation of graphene

modifies its electronic energy spectrum and in-plane strain. Cyclic variation of these two properties constitutes the scheme for quantum pumping. To have a nonzero pumping current, spatial asymmetry must be introduced. It is assumed that the contacts between the graphene layer and the left and right electrodes are not equivalent, which is modeled by different densities of states. This can be achieved in the experiment by using different materials for the two electrodes. It is emphasized that Coulomb-blockade effects will favor the transfer of an integer number of electrons per cycle, so that the relation between current and frequency will be quantized. This is just a proposal and the applicability of this approach for quantum metrology is still to be verified.

#### 5. Magnetic- field-driven single-electron pump

Another proposal, not implemented though, is based on using a ferromagnetic three-tunnel-junction device for electron pumping ([Shimada and Ootuka, 2001](#)). Its islands and leads are made of ferromagnetic metals with different coercive forces. Such a device can be operated as a single-electron pump if controlled by ac magnetic fields, and not by the gate voltages. In addition to the charging effects, it makes use of the magnetic-field-induced shift of the chemical potential and magnetization reversal in the ferromagnetic electrode.

The proposed device has intrinsic limitations of the pumping speed, which are determined by the physical time constraints of the ferromagnet. The pump operation frequency must be much lower than the characteristic relaxation times. The prospects of this type of an electron pump for quantum metrology are still to be understood.

#### 6. Device parallelization

As discussed in Sec. III.A, it is possible to reach precise electron pumping with a normal-metal single-electron pump consisting of a sufficiently long array of islands. With six islands and seven junctions, the accuracy of the pumped current is at the  $10^{-7}$  level. However, the maximum current is limited to a few picoamperes. To get the current scaled up to the 100 pA level, a requirement for practical metrological applications (see Sec. IV.D.1), approximately 100 pumps should be operated in parallel. The main reason why parallelization is impractical for normal-metal devices is the tuning of the offset charges ([Keller \*et al.\*, 1996](#); [Camarota \*et al.\*, 2012](#)). Each island has an individual offset charge that has to be compensated separately. Therefore, a metrological current source implemented as parallelized normal-metal pumps would require of the order of 1000 dc lines.

Compared to normal-metal pumps, quantum-dot-based pumps allow for higher pumping speeds using fewer control lines thanks to their tunability; see Sec. III.C. Accuracy of 1.2 ppm at an output current of 150 pA has already been demonstrated with a single quantum dot ([Giblin \*et al.\*, 2012](#)). Therefore, parallelization of such pumps may not even be required if the accuracy can be improved without a loss in speed. Nevertheless, parallelization of semiconducting pumps has been considered in the literature. With two pumps, invariance with respect to gate variations has been shown to be below the 20 ppm level ([Wright \*et al.\*, 2009](#)) with output current exceeding 100 pA. In this case, all signals were

individually tuned for each device requiring two dc and one rf signals per device. However, it is possible to use common signals for rf drive and for the barrier voltages (Mirovsky *et al.*, 2010). In this case, only one dc voltage per device is required for tuning the other barrier and possible offset charges. The obtainable accuracy, depending on device uniformity, is still an open question for this approach.

For the hybrid NIS turnstiles, the maximum current per device is limited to a few tens of picoamperes, as discussed in Sec. III.B.2. Hence, at least ten devices are to be run in parallel, which has been shown to be experimentally feasible (Maisi *et al.*, 2009). In Fig. 32 we show a scanning electron micrograph of a sample used in that work and the main experimental findings. The turnstiles in these experiments suffered from photon-assisted tunneling due to insufficient electromagnetic protection (see Sec. II.F), and hence the quantization accuracy was only on the  $10^{-3}$  level. Improved accuracy is expected for a new generation of turnstile devices (Pekola *et al.*, 2010). For parallel turnstiles, a common bias voltage can be used as it is determined by the superconducting gap  $\Delta$ , which is a material constant and

varies only very little across a deposited film. Also, the rf drive can be common if the devices have roughly equal  $R_T$ ,  $E_C$ , and coupling from the rf line to the island. As the error processes that set the ultimate limit on a single turnstile accuracy are not yet determined, the exact requirements on device uniformity cannot be fully resolved.

## H. Single-electron readout and error correction schemes

### 1. Techniques for electrometry

The electrometer used to detect the presence or absence of individual charge quanta is a central component in schemes for assessing pumping errors and error correction. Figure 33(a) introduces the essential components of an electron-counting setup. In order to observe proper charge quantization, the counting island is connected to other conductors only via low-transparency tunnel contacts. The electrometer is capacitively coupled to the counting island and biased in such a manner that the small voltage drop of the counting island due to change of its charge state by one

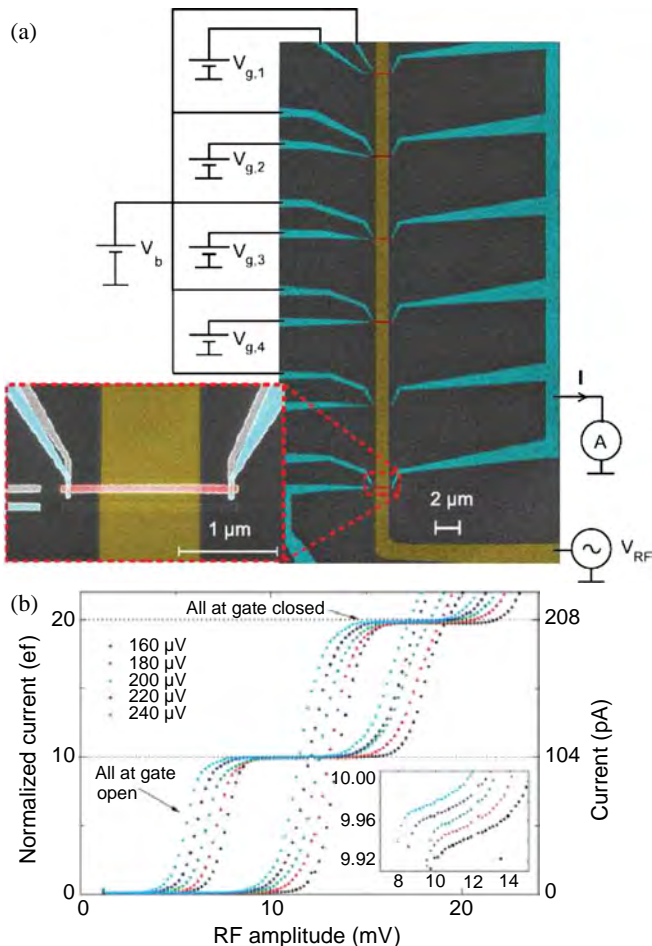


FIG. 32 (color online). (a) Scanning electron micrograph of parallel turnstiles. The turnstiles are biased with a common bias  $V_b$  and driven with a common rf gate voltage  $V_{rf}$ . Gate offset charges are compensated by individual gate voltages  $V_{g,i}$ . (b) Output current  $I$  for ten parallel devices tuned to the same operating point producing current plateaus at  $I = 10Ne_f$ . The curves are taken at different  $V_b$  shown in the top left part of the panel. From Maisi *et al.*, 2009.

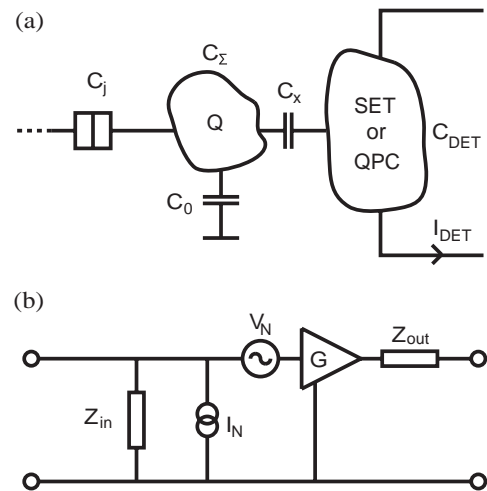


FIG. 33. (a) Circuit diagram of a charge-counting device. Electric charge  $Q$  on the island on the left is monitored. The island is coupled to an electrometer island via capacitor  $C_x$  and also tunnel coupled to an external conductor. The single-electron box configuration illustrated here requires only one tunnel junction with capacitance  $C_j$ . In addition, there is capacitance  $C_0$  to ground, which accounts also for gate electrodes and any parasitic capacitances. The probing current  $I_{det}$  through the detector is sensitive to the charge on the coupling capacitor, which is a fraction  $C_x/C_\Sigma$  of the total charge  $Q$ , where  $C_\Sigma = C_x + C_0$ . The detector is a single-electron tunneling transistor based on Coulomb blockade, and hence the total capacitance of the detector island  $C_{det}$  is of the order of 1 fF or less. (b) Circuit diagram of a general noisy electrical amplifier that can also be adapted to describe the electrometers of single-electron experiments. From Devoret and Schoelkopf, 2000. For the configuration shown in (a), one has for input impedance  $Z_{in}(\omega) = 1/j\omega C_{in}$ , where  $C_{in}^{-1} = C_x^{-1} + C_{det}^{-1}$ . The input voltage is related to the island charge  $Q$  through  $V_{in} = Q/C_\Sigma$ . The noise source  $I_N$  represents backaction and  $V_N$  the noise added by the electrometer at the output referred to the input. The gain of the amplifier is given by  $G$ . The output impedance  $Z_{out}$  equals the differential resistance at the amplifier operation point.

electron induces a measurable change in the electrical transport through the detector. The readout performance can be characterized in terms of response time (bandwidth), charge sensitivity, and backaction to the system under measurement. In the present context of electron counting, we define backaction to include all mechanisms by which the presence of the detector changes the charge transport in the measured system.

The two basic electrometer realizations providing sufficient charge sensitivity for electron-counting applications are the SET (Fulton and Dolan, 1987; Kuzmin *et al.*, 1989) and the QPC (Berggren *et al.*, 1986; Thornton *et al.*, 1986; Field *et al.*, 1993). From a sample fabrication point of view, it is convenient when the electrometer and the charge pump can be defined in the same process; hence, the QPC is the natural charge detector for quantum dots in semiconductor 2DEGs, whereas metallic single-electron devices are typically probed with SETs. Studies also exist where a metallic superconducting SET has been used as the electrometer for a semiconductor QD (Lu *et al.*, 2003; Fujisawa *et al.*, 2004; Yuan *et al.*, 2011; Fricke *et al.*, 2013), and the SET can be realized in the 2DEG as well (Morello *et al.*, 2010).

The charge sensitivity  $\delta q$  is determined by the noise of the system as a whole (Korotkov, 1994) and is conveniently expressed in units of  $e/\sqrt{\text{Hz}}$  for electrometry applications. For metallic SETs, output voltage fluctuations  $\delta V_{\text{out}}$  can be related to the charge coupled to the electrometer according to  $\delta q = C_g \delta V_{\text{out}} / (\partial V_{\text{out}} / \partial V_g)$ , where  $V_g$  is the voltage of the SET gate electrode and  $C_g$  is its capacitance to the SET island (Kuzmin *et al.*, 1989). Here  $C_g$  can be determined reliably in the experiment from the period of Coulomb oscillations. Similar calibration cannot be performed for a QPC and hence the charge sensitivity is expressed in relation to the charge of the neighboring QD (Cassidy *et al.*, 2007), corresponding to  $Q$  in Fig. 33(a). Variations of  $Q$  and  $q$  are related as  $\delta q = \kappa \delta Q$ , where  $\kappa = C_x / C_\Sigma$  is the fraction of the island charge that is coupled to the electrometer. For charge-counting applications, the relevant parameter is  $\delta Q$ . The rms charge noise for a given detection band is given by  $\Delta q = \sqrt{\int d\omega S_{Q_{\text{out}}}(\omega)}$ , which reduces to  $\delta q \sqrt{B}$  in the white noise limit, where  $B$  is the readout bandwidth. It is possible to pose the charge detection problem in the language of quantum linear amplifiers as shown in Fig. 33(b) (Devoret and Schoelkopf, 2000; Averin, 2003; Clerk *et al.*, 2010). When such a detector is modeled as a linear voltage amplifier,  $I_N$  and  $V_N$  characterize the input and output noise, respectively, and the quantum theory limit for the spectral density of fluctuations at signal frequency  $\omega$  reads  $\sqrt{S_V(\omega)S_I(\omega)} \geq \hbar\omega/2$ . Information about the electronic backaction is contained in the correlator  $\langle \delta V_{\text{in}}(t) \delta V_{\text{in}}(t') \rangle$  of the induced voltage fluctuations on the counting island. Denoting the total capacitance of the counting island by  $C_\Sigma$ , the fluctuations in the output charge signal are given by  $\delta Q_{\text{out}}(\omega) = C_\Sigma V_N(\omega)$ , and the voltage fluctuations on the counting island by  $\delta V_{\text{in}}(\omega) = I_N(\omega) / j\omega C_\Sigma$ . One thus finds  $\sqrt{S_{Q_{\text{out}}}(\omega)S_{V_{\text{in}}}(\omega)} \geq \hbar/2$  as the quantum limit.

In theory, a quantum-limited operation can be achieved with normal-state SETs operated in the cotunneling regime (Averin, 2001), superconducting SETs (Zorin, 1996, 2001),

and QPCs (Korotkov, 1999; Clerk, Girvin, and Stone, 2003; Averin and Sukhorukov, 2005). In practical devices, however, the noise spectrum up to 1–100 kHz depending on the setup is dominated by  $1/f$ -like charge noise that is intrinsic to the sample but whose microscopic physical origin is still debated (Starmark *et al.*, 1999; Vandersypen *et al.*, 2004; Buehler *et al.*, 2005). Above 1 kHz, the charge noise level is usually set by the preamplifier noise, but studies exist where the intrinsic shot noise of the electrometer was comparable to the noise of the readout electronics (Brenning *et al.*, 2006; Kafanov and Delsing, 2009). For the normal-state SET, sensitivities of the order of  $10^{-7} e/\sqrt{\text{Hz}}$  are attainable in theory with present-day fabrication technology, where the intrinsic noise is due to stochastic character of the tunneling processes and includes both shot and thermal noise (Korotkov, 1994; Korotkov and Paalanen, 1999). The best charge sensitivities reported to date for a single-electron transistor by Brenning *et al.* (2006) were almost identical in normal and superconducting states, namely, 1.0 and  $0.9 \times 10^{-6} e/\sqrt{\text{Hz}}$ , respectively, at a signal frequency of 1.5 MHz. Xue *et al.* (2009) also measured the backaction of a superconducting SET and the product of noise and backaction was found to be 3.6 times the quantum limit. For QD charge detection with QPCs, charge sensitivity of  $2 \times 10^{-4} e/\sqrt{\text{Hz}}$  referred to the QD charge has been demonstrated (Cassidy *et al.*, 2007). It appears to be easier to realize large charge coupling fraction  $\kappa$  with metallic SETs than with QPCs (Yuan *et al.*, 2011).

We now discuss the backaction mechanisms in more detail; see a schematic illustration in Fig. 34. Despite the above quantum theory result connecting backaction and noise, the electronic backaction of the electron counter can be addressed in principle independently of its charge noise, as the readout bandwidth (at most 100 MHz, see below) is much below the microwave frequencies that can promote charge transfer errors: Overcoming even a modest 100  $\mu\text{V}$  energy barrier requires photon frequencies above 24 GHz if multiphoton processes are neglected. Nevertheless, voltage fluctuations induced by the shot noise of the detector usually have a non-negligible spectral density at microwave frequencies. A fraction  $\kappa$  of the voltage fluctuations of the SET island are coupled back to the counting node. This mechanism can dominate the equilibrium thermal

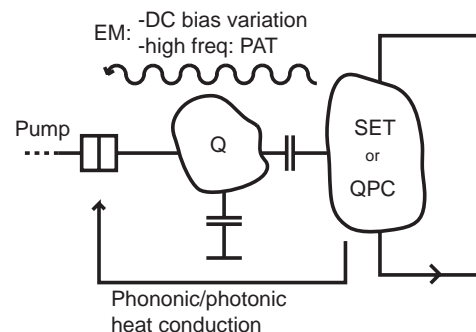


FIG. 34. Detector backaction mechanisms. The backaction can originate by direct electromagnetic (EM) coupling either by variations in pump biasing or by high-frequency photon-assisted tunneling (PAT). Another source of backaction is via heat conduction. The detector located in proximity of the device typically heats up. The heat can then be conducted to the device by either phononic or photonic coupling.

noise from resistive components at the sample stage; cf. [Martinis and Nahum \(1993\)](#). A full quantum calculation of the backaction of an SET electrometer on a Cooper-pair box has been presented by [Johansson, Käck, and Wendin \(2002\)](#). [Lotkhov and Zorin \(2012\)](#) measured the effect of photon irradiation by a nearby SET on the hold time of an electron trap. They found that the rate of electron escape events was proportional to the theoretically calculated emission rate of photons having an energy larger than the energy barrier of the trap. [Saira, Kemppinen \*et al.\* \(2012\)](#) suggest attenuating the high-frequency backaction by replacing the capacitive coupling by a lossy wire that acts as a low-pass filter for microwaves but does not affect the charge signal. For QPCs, Coulombic backaction can be divided into shot noise, which can be in principle eliminated by circuit design and fundamental charge noise ([Aguado and Kouwenhoven, 2000](#); [Young and Clerk, 2010](#)).

The low-frequency part of detector backaction manifests itself as variation of the dc bias of the pump or turnstile device. The case of an SET electrometer coupled to a single-electron box was studied by [Turek \*et al.\* \(2005\)](#). In the limit of small coupling capacitance  $C_x$ , the voltage swing on the counting island due to loading and unloading the detector island is given by  $\Delta V_{\text{in}} = \kappa e / C_{\text{det}}$ . We note that this is just a fraction  $C_x / C_{\text{det}} < 1$  of the voltage swing from loading or unloading the actual counting island with an electron. Hence, dc backaction of the detector does not necessarily place an additional constraint on the design of the electron-counting circuit.

In addition to the electronic backaction described above, one needs to consider the phononic heat conduction from the detector to the charge pump. For reaching the ultimate accuracy, the charge pumps typically require temperatures of the order of 100 mK or lower, where small on-chip dissipation can raise the local temperature significantly due to vanishing heat conductivity in the low-temperature limit ([Kautz, Zimmerli, and Martinis, 1993](#); [Giazotto \*et al.\*, 2006](#)); see also Sec. II.G. The average power dissipated by the detector is given by  $P = \langle I_{\text{det}} V_{\text{det}} \rangle$ , and it needs to be transported away by the substrate phonons or electronically via the leads. Requirement for a sufficiently large charge coupling coefficient  $\kappa$  limits the distance by which the detector and charge pump can be separated. The temperature increase by dissipated power has been studied on a silicon substrate by [Savin \*et al.\* \(2006\)](#) and they give

$$T = \left( T_0^4 + \frac{2fP}{\pi r^2 \nu \nu} \right)^{1/4}, \quad (40)$$

where  $T$  is the substrate temperature at distance  $r$  from a point source of heating power  $P$ ,  $T_0$  is the bath temperature,  $\nu \nu = 3600 \text{ W m}^{-2} \text{ K}^{-4}$  is the material parameter, and  $f = 0.72$  is a fitting parameter for their experimental observations. For an illustrative example, we estimate that the dissipated power at the electrometer in the original rf-SET paper ([Schoelkopf \*et al.\*, 1998](#)) was 120 fW based on the published numbers. According to Eq. (40), this will heat the substrate underneath nearby junctions ( $r = 200 \text{ nm}$ ) to 140 mK, which is high enough to deteriorate the performance of many single-electron devices below the metrological requirements. [Sillanpää, Roschier, and Hakonen \(2004\)](#) coupled the readout

to the Josephson inductance of a superconducting SET instead of conductance, reducing the dissipation by 2 orders of magnitude. Usually it is possible to assess the severity of detector backaction effects in the experiment by measuring the tunneling rates using different values of  $I_{\text{det}}$  [see, e.g., [Kemppinen \*et al.\* \(2011\)](#), [Lotkhov \*et al.\* \(2011\)](#), and [Saira, Kemppinen \*et al.\* \(2012\)](#)], so that any variation of the observed rates can be attributed to backaction. The picture is somewhat different in 2DEG systems due to significantly weakened electron-phonon coupling. Experimental study of phononic backaction in 2DEGs is presented by [Schinner \*et al.\* \(2009\)](#) and [Harbusch \*et al.\* \(2010\)](#).

The bandwidth of the readout,  $B$ , is commonly defined as the corner frequency of the gain from gate charge to output voltage ([Visscher \*et al.\*, 1996](#)). The performance requirements for the charge readout depend on the particular charge-counting scheme, but in general the bandwidth  $B$  places a limit on the fastest processes that can be detected and hence constrains the magnitude of the electric current that can be reliably monitored. In practice,  $B$  is limited by the inverse  $RC$  constant of the electrometer's differential resistance and the capacitive loading on its outputs. Both the QPC and SET electrometers have an impedance of the order of  $R_K = h/e^2 \approx 25.8 \text{ k}\Omega$ . For the SET,  $R \geq R_K$  is required to realize strong Coulomb blockade according to the orthodox theory of single-electron tunneling ([Averin and Likharev, 1991](#); [Ingold and Nazarov, 1992](#)). For a QPC, the most charge-sensitive operation point is around a bias point where  $\partial V / \partial I = R_K$ , midway between the first conductance plateau and pinch-off ([Cassidy \*et al.\*, 2007](#)). As the barrier capacitance is of the order of 1 fF or less for the devices, the intrinsic bandwidth is in the gigahertz range. In practice, the capacitance of the biasing leads and the input capacitance of the preamplifier dominate. When the preamplifier is located at room temperature as in the pioneering experiments ([Fulton and Dolan, 1987](#); [Kuzmin \*et al.\*, 1989](#)), the wiring necessarily contributes a capacitance of the order of 0.1–1 nF and henceforth limits the readout bandwidth to the kilohertz range ([Pettersson \*et al.\*, 1996](#); [Visscher \*et al.\*, 1996](#)). Readout by a current amplifier from a voltage-biased SET avoids the  $RC$  cutoff on the gain, but the usable bandwidth is not substantially altered as current noise increases at high frequencies where the cabling capacitance shorts the current amplifier input ([Starmark \*et al.\*, 1999](#)).

In order to increase the effective readout bandwidth, the SET impedance has to be transformed down toward the cable impedance, which is of the order of 50  $\Omega$ . Bandwidths up to 700 kHz have been achieved by utilizing a high-electron-mobility transistor (HEMT) amplifier with a low impedance output at the sample stage ([Pettersson \*et al.\*, 1996](#); [Visscher \*et al.\*, 1996](#)). The dissipated power at the HEMT in these studies was 1–10  $\mu\text{W}$  depending on the biasing, which can easily result in overheating of the electrometer and/or the coupled single-electron device. The best readout configuration to date is the rf reflectometry technique, applicable to both SETs ([Schoelkopf \*et al.\*, 1998](#)) and QPCs ([Qin and Williams, 2006](#)), where the electrometer is embedded in a radio frequency resonant circuit and the readout is achieved by measuring the damping of the resonator. A readout bandwidth of 100 MHz was achieved in the original demonstration

(Schoelkopf *et al.*, 1998). They also note that their charge sensitivity of  $1 \times 10^{-5} e/\sqrt{\text{Hz}}$  yields  $\Delta q = 0.1e$  for the full detection bandwidth, i.e., electron counting at 100 MHz would have been possible in a scenario where the charge coupling fraction  $\kappa$  was close to unity.

## 2. Electron-counting schemes

Realization of a current standard based on electron counting has been one of the key motivators for development of ultrasensitive electrometry (Schoelkopf *et al.*, 1998; Gustavsson *et al.*, 2008; Keller, 2009). First we see why direct current measurement of uncorrelated tunneling events, like those produced by a voltage-biased tunnel junction, cannot be used for a high-precision current standard: Assume a noise-free charge detector that yields the charge state of the counting island with time resolution  $\tau = 1/B$ , and that Markovian (uncorrelated) tunneling events occur at the rate  $\Gamma \ll B$ . With probability  $\Gamma\tau$ , a single tunneling event occurs during the time  $\tau$  and is correctly counted by the detector. With probability  $(\Gamma\tau)^2/2$ , two tunneling events occur within  $\tau$  and constitute a counting error. Hence, to achieve a relative error rate  $p$ , one needs  $\Gamma < 2pB$ . Even with a noiseless 100 MHz rf SET, one could not measure a direct current greater than  $2e/s$  at metrological accuracy  $p = 10^{-8}$  in this manner. Would it be practical to account statistically for the missed events in a manner similar to Naaman and Aumentado (2006) assuming truly Poissonian tunneling statistics and a well-characterized detector? The answer is unfortunately negative: If  $N$  tunneling events are observed, the number of missed events  $M$  is a Poissonian variable with a mean of  $N\Gamma\tau/2$  and standard deviation  $\delta M = \sqrt{N\Gamma\tau/2}$ . Requiring  $\delta M < pN$  gives  $N > \Gamma\tau/(2p^2)$ . For  $\Gamma = 1$  MHz and  $\tau$  and  $p$  as above, one has to average over  $N > 5 \times 10^{13}$  events, which is impractical. A more detailed calculation based on Bayesian inference presented by Gustavsson *et al.* (2009) results in the same  $N$  dependence.

Charge transport through a 1D array of tunnel junctions can take place in the form of solitons depending on device parameters (Likharev, 1988; Likharev *et al.*, 1989). Propagation of the solitons promotes time correlation in the electron tunneling events, allowing the accuracy limitations of counting uncorrelated electrons presented above to be lifted. A proof-of-concept experimental realization has been presented by Bylander, Duty, and Delsing (2005). The array is terminated at the middle island of an SET, allowing for unity charge coupling, and a signal centered around frequency  $f_c = I/e$  is expected. They claim a possible accuracy of  $10^{-6}$  based on the charge sensitivity of their electrometer only. However, the spectral peaks in the experimental data appear too wide for an accurate determination of the center frequency. Factors not included in the accuracy estimate are the instability of the bias current and SET background charge fluctuations.

Single-electron electrometry can be used to count the much rarer pumping errors instead of the total pumping current. Such an approach has been used to study the accuracy of metallic multijunction pumps that are used in the electron-counting capacitance standard (ECCS) (Keller *et al.*, 1999; Keller, Zimmerman, and Eichenberger, 2007). A circuit diagram of an ECCS experiment is shown in Fig. 35. Two cryogenic needle switches are required to operate the device

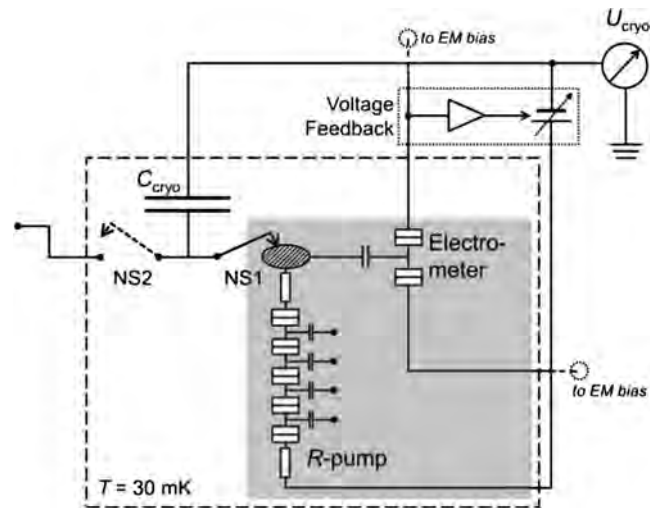


FIG. 35. Circuit diagram of a practical implementation of the electron-counting capacitance standard. Switches NS1 and NS2 are cryogenic needle switches. From Camarota *et al.*, 2012.

in different modes: determining coupling capacitances and tuning the pump drive signal (NS1 and NS2 closed), operating the pump to charge  $C_{\text{cryo}}$  (NS1 closed, NS2 open), and comparing  $C_{\text{cryo}}$  with an external traceable capacitor (NS1 open, NS2 closed). The SET electrometer is used as part of a feedback loop that maintains the voltage of the node at the end of the pump constant. With NS1 open, the pump can be operated in a shuttle mode: a charge of  $e$  is repeatedly pumped back and forth across the pump at the optimal operation frequency (which is above the detector bandwidth), and pumping errors appear as discrete jumps in the electrometer output.

An error rate of  $1.5 \times 10^{-8}$  relative to the used shuttling frequency of 5.05 MHz was demonstrated in the NIST ECCS setup (Keller *et al.*, 1996). In this experiment, the seven-junction pump illustrated in Fig. 13 was used. At Physikalisch-Technische Bundesanstalt (PTB), a relative error rate of the order of  $10^{-7}$  was reported (Camarota *et al.*, 2012) for a five-junction  $R$  pump operated at a shuttling frequency of 0.5 MHz. Recently, the PTB group improved their relative error rate to  $4.4 \times 10^{-8}$  (Scherer *et al.*, 2012). They also argued that in order to account for the possibility of pumping errors in opposite directions to cancel out each other, the proper measure of the pump accuracy in an ECCS experiment is  $\sqrt{\Gamma_{\text{err}}/\Delta t}/f$ , where  $\Gamma_{\text{err}}$  is the absolute rate at which pumping errors occur,  $\Delta t$  is the time spent at charging the capacitor, and  $f$  is the pumping frequency. Using this methodology, they inferred a relative accuracy of  $1.5 \times 10^{-8}$  for their pump. A complete ECCS experiment has not been performed with a semiconducting pump to date. Yamahata, Nishiguchi, and Fujiwara (2011) described a single-electron shuttling experiment performed on a Si nanowire, but the reported error rates are rather high, at the  $10^{-2}$  level. In semiconductor realizations, the memory node can be isolated from the rest of the lead by a FET switch that is defined with the same lithography process as the pump, eliminating the need for the needle switch.

Wulf (2012) proposed an error-accounting architecture, where a few modestly accurate charge pumps are connected

in series, and electrometers are used to observe the charge on memory nodes situated in between the pumps. Assuming that the error rate of the pumps is small in comparison to the readout bandwidth, the sign of individual pumping errors can be reliably inferred from the electrometer response. Hence, the accuracy of the pumped current can then be improved beyond the accuracy of the constituent pumps.

To date, an error-counting or -accounting algorithm integrated with continuously operating series-connected pumps has not been demonstrated experimentally. Measurements of two series-connected semiconductor QD pumps with a QPC electrometer coupled to a node in the middle were presented by Fricke *et al.* (2011), although quantized pumping errors were not observed. Recently, an initial report of on-demand single-electron transfer in a device consisting of three QD pumps and two metallic SET electrometers was presented (Fricke *et al.*, 2012, 2013). Although no detectable current was produced in this experiment due to a low repetition rate of 5 Hz, they were able to distinguish between different types of pumping errors from the electrometer signature.

## I. Device fabrication

Fabrication of charge pumps, regardless of their operational principle, requires advanced nanofabrication methods. These include, for example, electron-beam lithography, various dry etching techniques, and molecular-beam epitaxy growth of semiconductor heterostructures. In general, pumping devices can have small feature sizes in multiple layers that must be accurately aligned with each other. We begin with the description of the fabrication procedure for the metallic single-electron and Cooper-pair pumps and turnstiles described in Secs. III.A, III.B, and III.E. Subsequently, we present the fabrication methods for quantum-dot pumps and turnstiles, the operation of which is discussed in Sec. III.C.

### 1. Metallic devices

Metallic single-electron and Cooper-pair pumps and turnstiles are typically made by the angle deposition technique, which was first introduced by Dolan (1977) for the photolithography process and then later adapted by Dolan and Dunsmuir (1988) for the electron-beam lithography process. We note that there is a myriad of different ways of fabricating these devices. Below we describe only a certain fabrication process for these devices in great detail instead of giving a thorough study of all possible variations.

The process starts with the deposition of an Au layer on an Si wafer covered by a native silicon oxide. The Au pattern is formed by a standard photolithography and lift-off process using photoresist S1813 and contains contact pads and on-chip wiring as well as alignment markers for the deposition of the subsequent layers. Next, a trilayer resist structure is built (from bottom to top): copolymer/Ge/poly-methyl-methacrylate (PMMA) with the thicknesses 200, 20, and 50 nm, respectively [see Fig. 36(a)]. The polymer layers are spin coated on the wafer and baked in a nitrogen oven, and the Ge layer is deposited in an electron gun evaporator. The wafer is then cleaved into smaller pieces which are exposed and processed separately. After the exposure of the top PMMA layer on one of the pieces in the electron-beam writer,

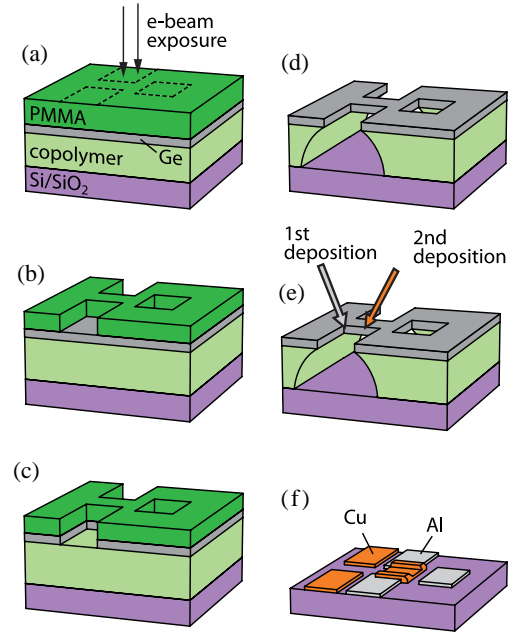


FIG. 36 (color online). Fabrication of metallic devices. (a) Buildup of a trilayer resist structure and exposure in the electron-beam writer; (b) development of the top PMMA layer; (c) transfer of the pattern formed in the resist into the Ge layer by reactive ion etching; (d) creation of the undercut in the bottom resist and removal of the top resist by oxygen plasma; (e) angle deposition of metals with an oxidation in between; (f) the resulting structure after the lift-off process.

e.g., JEOL JBX-5FE, the piece is developed at room temperature in isopropyl alcohol mixed with methyl isobutyl ketone at a ratio of 3:1. Thus, a desired pattern is formed in the PMMA layer [see Fig. 36(b)]. The pattern is transferred into the Ge layer by reactive ion etching in  $\text{CF}_4$  [see Fig. 36(c)]. The sample is then placed in an electron cyclotron resonance (ECR) etcher, in which an undercut is formed by oxygen plasma. The undercut depth is controlled by the tilt of the sample stage in the ECR machine. At the same time, the top PMMA layer is etched away. At this stage, each chip has a Ge mask supported by the copolymer layer [see Fig. 36(d)]. Some parts of the mask are suspended, forming the Dolan bridges. Although we described above a method with three layers, in many cases a bilayer mask composed of copolymer and PMMA resists is sufficient.

The chips with masks are placed in an electron gun evaporator equipped with a tilting stage. Two consecutive depositions of metal through the same mask are carried out at different angles to create a partial overlap between the metal layers [see Fig. 36(e)]. If the surface of the bottom layer (typically Al) is oxidized by introducing oxygen into the evaporation chamber, after the deposition of the top electrode, the sandwich structure composed of the overlapping metal layers with a thin oxide in between forms small tunnel junctions [see Fig. 36(f)].

The normal-metal or superconducting charge pumps are made entirely of Al, which can be turned normal at low temperatures by an external magnetic field [see Geerligs *et al.* (1990, 1991), Pothier *et al.* (1992), Keller *et al.* (1996), and Vartiainen *et al.* (2007)]. In the case of the hybrid

structures described in [Pekola \*et al.\* \(2008\)](#), [Kempainen, Kafanov \*et al.\* \(2009\)](#), [Kempainen, Meschke \*et al.\* \(2009\)](#), and [Maisi \*et al.\* \(2009\)](#), the bottom electrode was Al and the top one was either Cu or AuPd.

## 2. Quantum dots

The gate structure of the charge pumps based on quantum dots is also fabricated using electron-beam lithography. The main differences in the fabrication compared with metallic devices are the following: Ohmic contacts have to be made between metallic bonding pads on the surface of the chip and the 2DEG located typically  $\sim 100$  nm below the surface. Furthermore, the 2DEG has to be either depleted with negative gate voltage from the unwanted positions in the case of GaAs devices [see Fig. 18(d)] or accumulated with positive gate voltage in the case of MOS silicon devices [see Fig. 18(c)]. For GaAs, also etching techniques have been employed to dispose of some parts of the 2DEG leading to a smaller number of required gates [see Fig. 20(a)]. In GaAs devices, typically a single deposition of metal through a monolayer PMMA resist is sufficient to create the gate structure. For MOS silicon dots, several aligned layers of gate material are often used. However, only a single layer is typically deposited with each mask in contrast to metallic devices employing angle evaporation.

We now describe in detail a fabrication process for MOS silicon quantum dots. We begin with a high-resistivity ( $\rho > 10$  k $\Omega$  cm at 300 K) near-intrinsic silicon wafer. Phosphorus atoms are deposited on the silicon surface using standard photolithography and they diffuse to a depth of roughly  $1.5$   $\mu\text{m}$  during the growth of a 200-nm-field silicon oxide on top. All the following process steps involving etching or deposition have to be aligned with the previous ones with the help of alignment markers, a routine we do not discuss separately. Then a window with size  $30 \times 30$   $\mu\text{m}^2$  is opened to the field oxide and replaced by an 8-nm-thick high-quality SiO<sub>2</sub> gate oxide that is grown in an ultradry oxidation furnace at 800 °C in O<sub>2</sub> and dichloroethylene. This thin oxide window overlaps by a few micrometers with the ends of the metallic phosphorous-rich  $n^+$  regions. The field oxide is etched selectively above the other ends of the  $n^+$  regions formed in the previous process. The Ohmic contacts and the bonding pads are made by depositing metal on these etched regions, forming a connection to the  $n^+$  silicon. Subsequent annealing is employed to avoid the formation of Schottky barriers.

At this stage, we have bonding pads connected to the metallic  $n^+$  regions that extend some 100  $\mu\text{m}$  away from the pads to the thin oxide window with the linewidth of 4  $\mu\text{m}$ . Electron-beam lithography with a 200 nm PMMA resist and metal evaporation with an electron gun evaporator is employed to deposit the first layer of aluminum gates inside the window and their bonding pads outside the window. After the lift-off, the gates are passivated by an Al<sub>x</sub>O<sub>y</sub> layer formed by oxidizing the aluminum gates by either oxygen plasma or thermally on a hot plate (150 °C, 5 min). The oxide layer electrically completely insulates the following overlapping layers of aluminum gates that are deposited in the same way with alignment accuracy of  $\sim 20$  nm.

At least one gate has to overlap with areas where  $n^+$  regions extend to the thin oxide window. By applying positive voltage on these reservoir gates, the electrons from the  $n^+$  are attracted to the Si/SiO<sub>2</sub> interface below the reservoir gates, forming the source and drain reservoirs of the device. For example, the device shown in Fig. 23(b) is composed of one or two layers of gates: one top gate that induces the source and drain reservoir, two barrier gates below the top gate defining the quantum dot, and a plunger gate in the same layer with the barrier gates. Finally, a forming gas (95%N<sub>2</sub>, 5%H<sub>2</sub>) anneal is carried out for the sample at 400 °C for 15 min to reduce the Si/SiO<sub>2</sub> interface trap density to a level of  $\sim 5 \times 10^{10}$  cm<sup>-2</sup> eV<sup>-1</sup> near the conduction band edge. Silicon quantum dots can also be fabricated with an all-silicon process, in which the aluminum gates are replaced by conducting polysilicon gates shown in Fig. 23(a).

## IV. QUANTUM STANDARDS OF ELECTRIC QUANTITIES AND THE QUANTUM METROLOGY TRIANGLE

The ampere is one of the seven base units of the International System of Units (SI) ([Bureau International des Poids et Mesures, 2006](#)) and is defined as follows: “The ampere is that constant current which, if maintained in two straight parallel conductors of infinite length, of negligible circular cross section, and placed 1 m apart in vacuum, would produce between these conductors a force equal to  $2 \times 10^{-7}$  newton per meter of length.” The present definition is problematic for several reasons: (i) The experiments required for its realization are beyond the resources of most of the National Metrology Institutes. (ii) The lowest demonstrated uncertainties are not better than about  $3 \times 10^{-7}$  ([Clothier \*et al.\*, 1989](#); [Funck and Sienknecht, 1991](#)). (iii) The definition involves the unit of newton, kg  $\times$  m/s<sup>2</sup>, and thus the prototype of the kilogram, which is shown to drift in time ([Quinn, 1991](#)). In practice, electric metrologists are working outside the SI and employing quantum standards of voltage and resistance, based on the Josephson and quantum Hall effects, respectively.

### A. The conventional system of electric units

According to the ac Josephson effect,  $V = (h/2e)\partial\phi/\partial t$ , the voltage  $V$  applied over the Josephson junction induces oscillations of the phase difference  $\phi$  over the junction ([Josephson, 1962](#)). Phase locking  $\phi$  by a high-frequency ( $f_J$ ) signal results in quantized voltage plateaus

$$V_J \equiv \frac{n_J f_J}{K_J} \simeq n_J \frac{h}{2e} f_J, \quad (41)$$

which are often called Shapiro steps ([Shapiro, 1963](#)). Here  $n_J$  is the integer number of cycles of  $2\pi$  in which  $\phi$  evolves during one period of the high-frequency signal. The proportionality between  $V_J$  and  $f_J$  is denoted by the Josephson constant  $K_J$ . According to theory,  $K_J = 2e/h$ , but as discussed, this assumption is sometimes relaxed in metrology.

The Josephson voltage standards (JVS) have been used in electric metrology since the 1970s; see, e.g., [Kohlmann, Behr, and Funck \(2003\)](#) and [Jeanneret and Benz \(2009\)](#) for reviews. The first standards consisted of a single junction

and generated voltages only up to about 10 mV. Arrays of more than 10 000 junctions with the maximum output of 10 V were developed in the 1980s. They were based on hysteretic junctions where Shapiro steps with different  $n_J$  can exist at the same bias current. Since the 1990s, the research has focused on arrays of nonhysteretic junctions where  $n_J$  can be chosen by the applied current bias. Arrays divided in sections of  $2^m$  junctions ( $m = 0, 1, 2, \dots$ ) are called *programmable* since one can digitally select any multiple of  $f_J/K_J$  up to the number of junctions as the output voltage (Hamilton, Burroughs, and Kautz, 1995; Kohlmann *et al.*, 2007). They are practical for dc voltage metrology, but are especially developed for generating digitized ac voltage wave forms up to about 1 kHz, which is an active research topic (Behr *et al.*, 2005). Voltage wave forms at higher frequencies can be generated by pulse-driven Josephson junction arrays where the desired ac wave form is synthesized by the delta-sigma modulation of fast voltage pulses, each having the time integral of one flux quantum  $h/(2e)$  (Benz and Hamilton, 1996).

The QHR standard consists of a two-dimensional electron gas, which, when placed in a high perpendicular magnetic field, exhibits plateaus in the Hall voltage  $V_H = R_H I$  over the sample in the direction perpendicular to both the field and the bias current  $I$ . Here

$$R_H \equiv \frac{R_K}{i_K} \simeq \frac{1}{i_K} \frac{h}{e^2} \quad (42)$$

is the quantized resistance, which is proportional to the von Klitzing constant  $R_K$  and inversely proportional to the integer  $i_K$  (von Klitzing, Dorda, and Pepper, 1980). As in the case of the JVS, the theoretical equality  $R_K = h/e^2$  is sometimes relaxed in metrology. The plateau index  $i_K$  can be chosen by tuning the magnetic field. Usually the best results are obtained at  $i_K = 2$ .

Quantum Hall standards based on Si MOSFETs or GaAs/AlGaAs heterostructures were harnessed in routine metrology quickly during the 1980s; see, e.g., Jeckelmann and Jeanneret (2001), Poirier and Schopfer (2009), and Weis and von Klitzing (2011) and issue 4 of *C. R. Physique*, Vol. 369 (2011) for reviews. Different resistances can be calibrated against the QHR by using the CCC. It is essentially a transformer with an exact transform ratio due to the Meissner effect of the superconducting loop around the windings (Harvey, 1972; Gallop and Piquemal, 2006). Another way to divide or multiply  $R_H$  are parallel or series quantum Hall arrays, respectively, which are permitted by the technique of multiple connections that suppresses the contact resistances (Delahaye, 1993). One rapidly developing research topic is ac quantum Hall techniques, which can be used in impedance standards to expand the traceability to capacitance and inductance (Schurr *et al.*, 2011). An important recent discovery is that graphene can be used to realize an accurate and very robust QHR standard (Zhang *et al.*, 2005; Novoselov *et al.*, 2007; Tzalenchuk *et al.*, 2010; Janssen *et al.*, 2011).

The most precise measurement of  $K_J$  within the SI was performed by a device called a liquid-mercury electrometer with the uncertainty  $2.7 \times 10^{-7}$  (Clothier *et al.*, 1989). The SI value of  $R_K$  can be obtained by comparing the impedance of the QHR and that of the Thompson-Lampard calculable

capacitor (Thompson and Lampard, 1956; Bachmair, 2009). The lowest reported uncertainty of such comparison is  $2.4 \times 10^{-8}$  (Jeffery *et al.*, 1997). However, both the JVS and QHR are much more reproducible than their uncertainties in the SI; see Sec. IV.B. Therefore, the consistency of electric measurements could be improved by defining conventional values for  $R_K$  and  $K_J$ . Based on the best available data by June 1988, the member states of the Metre Convention made an agreement of the values that came into effect in 1990:

$$\begin{aligned} K_{J-90} &= 483\,597.9 \text{ GHz/V}, \\ R_{K-90} &= 25\,812.807 \, \Omega. \end{aligned} \quad (43)$$

Since then, electric measurements have in practice been performed using this conventional system which is sometimes emphasized by denoting the units by  $V_{90}$ ,  $\Omega_{90}$ ,  $A_{90}$ , etc., and where the JVS and QHR are called *representations* of the units.

## B. Universality and exactness of electric quantum standards

A theory can never be proven by theory, but, as argued by Gallop (2005), theories based on very general principles such as thermodynamics and gauge invariance are more convincing than microscopic theories such as the original derivation of the Josephson effect (Josephson, 1962). There are rather strong theoretical arguments for the exactness of the JVS: Bloch has shown that if a Josephson junction is placed in a superconducting ring, the exactness of  $K_J$  can be derived from gauge invariance (Bloch, 1968, 1970). Furthermore, Fulton showed that a dependence of  $K_J$  on materials would violate Faraday's law (Fulton, 1973). For quantum Hall devices, early theoretical works argued that the exactness of  $R_K$  is a consequence of gauge invariance (Laughlin, 1981; Thouless *et al.*, 1982). However, it is very complicated to model real quantum Hall bars, including dissipation, interactions, etc., and thus the universality and exactness of the QHR has sometimes been described as a “continuing surprise” (Mohr and Taylor, 2005; Keller, 2008). Extensive theoretical work, e.g., on topological Chern numbers, has strengthened the confidence in the exactness of  $R_K$ ; see Avron, Osadchy, and Seiler (2003), Bieri and Fröhlich (2011), and Doucot (2011) for introductory reviews. Recent theoretical work based on quantum electrodynamics (QED) predicts that the vacuum polarization can lead to a magnetic field dependence of both  $R_K$  (Penin, 2009, 2010a) and  $K_J$  (Penin, 2010b), but only at the level of  $10^{-20}$ . The case of single-electron transport has been studied much less and there are no such strong theoretical arguments for the lack of any corrections for the transported charge (Gallop, 2005; Stock and Witt, 2006; Keller, 2008).<sup>1</sup>

On the experimental side, comparisons between Si and GaAs quantum Hall bars show no deviations at the experimental uncertainty of  $\sim 3 \times 10^{-10}$  (Hartland *et al.*, 1991). Recently, an agreement at the uncertainty of  $8.6 \times 10^{-11}$  was found between graphene and GaAs devices (Janssen *et al.*,

<sup>1</sup>A condensed-matter correction of  $\sim 10^{-10}e$  for the charge of the electron was suggested by theory based on QED (Nordtvedt, 1970), but it was refuted by Hartle, Scalapino, and Sugar (1971) and Langenberg and Schrieffer (1971).

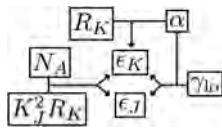


FIG. 37. Simplified sketch of the most accurate routes to information on  $\epsilon_{J,K}$ . Direct measurement of  $R_K$  together with an independent measurement of the fine structure constant ( $\alpha$ ) yields a value for  $\epsilon_K$ . Values for the sum of  $\epsilon_J$  and  $\epsilon_K$  can be obtained from the combination of the so-called watt balance experiment ( $K_J^2 R_K$ ) and a measurement of the Avogadro constant ( $N_A$ ), or from the combination of  $\alpha$  and measurements of low-field gyromagnetic ratios ( $\gamma_{10}$ ). Less accurate information is provided by measurements of high-field gyromagnetic ratios  $K_J$  and the Faraday constant  $F = eN_A$ , and by the QMT.

2011). This is an extremely important demonstration of the universality of  $R_K$  because the physics of the charge carriers is notably different in graphene and semiconductors (Goerbig, 2011). Comparisons between the JVSs have been summarized recently by Wood and Solve (2009). The lowest uncertainties obtained in comparisons between two JVSs are in the range of  $10^{-11}$ . Even much smaller uncertainties have been obtained in universality tests of the frequency-to-voltage conversion by applying the same frequency to two different junctions or junction arrays and detecting the voltage difference by a SQUID-based null detector. Several accurate experiments have indicated that the conversion is independent of, e.g., the superconducting material and the junction geometry. The lowest demonstrated uncertainty is astonishing:  $3 \times 10^{-19}$  (Clarke, 1968; Tsai, Jain, and Lukens, 1983; Jain, Lukens, and Tsai, 1987; Kautz and Lloyd, 1987).

The reproducibility and universality of the quantum standards are an indication that Eqs. (41) and (42) are exact, but a proof can be obtained only by comparison to other standards. Any one of the electric quantities  $V$ ,  $I$ , or  $R$  can be compared to the other two in a quantum metrology triangle (QMT) experiment (Likharev and Zorin, 1985); see Sec. IV.D. It is a major goal in metrology, but the insufficient performance of single-electron devices has to date prevented the reaching of low uncertainties. However, the exactness of Eqs. (41) and (42) can also be studied in the framework of the adjustment of fundamental constants. The most thorough treatment has been performed by the Committee on Data for Science and Technology (CODATA). Updated papers are nowadays published every four years; see Mohr and Taylor (2000, 2005), and Mohr, Taylor, and Newell (2008, 2012).<sup>2</sup> Karshenboim (2009) provided a useful overview. We review here the most accurate ( $< 10^{-7}$ ) routes to information on the electric quantum standards. They are also illustrated in Fig. 37. Most of the equations in this section assume that Eqs. (41) and (42) are exact, but when referring to possible deviations, we describe them by symbols  $\epsilon_{J,K,S}$ :

$$K_J = (1 + \epsilon_J) \frac{2e}{h}, \quad R_K = (1 + \epsilon_K) \frac{h}{e^2}, \quad (44)$$

$$Q_S = (1 + \epsilon_S)e.$$

In this context, the current generated by the single-electron current source is  $I_S = \langle k_S \rangle Q_S f$ , where  $\langle k_S \rangle$  is the average number of electrons transported per cycle.

There are a number of fundamental constants that are known with much smaller uncertainties than those related to electric metrology. Some constants, e.g., permeability, permittivity, and the speed of light in vacuum, and the molar mass constant,  $\mu_0$ ,  $\epsilon_0$ ,  $c$ , and  $M_u = 1 \text{ g/mol}$ , respectively, are fixed by the present SI. Examples of constants known with an uncertainty  $\leq 10^{-10}$  are the Rydberg constant  $R_\infty$  and several relative atomic masses, e.g., that of the electron  $A_r(e)$ . In the past few years, there has been tremendous progress in the determination of the fine structure constant  $\alpha$ . First the electron magnetic moment anomaly  $a_e$  was measured with high accuracy. A separate calculation based on QED gives the function  $\alpha(a_e)$ . Together these results yield a value for  $\alpha$  with an uncertainty  $0.37 \times 10^{-9}$  (Hanneke, Fogwell, and Gabrielse, 2008). Soon after, a measurement of the recoil velocity of the rubidium atom, when it absorbs a photon, yielded a value for  $\alpha$  with an uncertainty of  $0.66 \times 10^{-9}$  (Bouchendira *et al.*, 2011). These two results are in good agreement. Together they give a validity check for QED since the first result is completely dependent and the latter practically independent of that theory.

The fine structure constant is related to  $R_K$  by the exact constants  $\mu_0$  and  $c$ :

$$\alpha = \frac{\mu_0 c e^2}{2h} = \frac{\mu_0 c}{2R_K}. \quad (45)$$

This relationship means that when  $R_K$  is measured with a calculable capacitor, it also yields an estimate for  $\alpha$ . Thus, a measurement of  $R_K$  could also test QED, but in practice, the atomic recoil measurement is more accurate by about a factor of 30. A metrologically more important interpretation of this relation is that a comparison between  $\alpha$  and the weighted mean of the measurements of  $R_K$  yields an estimate of  $\epsilon_K = (29 \pm 18) \times 10^{-9}$  (Mohr, Taylor, and Newell, 2012). There is thus no proof of a nonzero  $\epsilon_K$ , but several groups are developing calculable capacitors in order to determine  $R_K$  with uncertainty below  $10^{-8}$  (Poirier and Schopfer, 2009; Poirier *et al.*, 2011).

The existing data that yield information on  $\epsilon_J$  are more discrepant. As described,  $\epsilon_J$  is related to measurements of gyromagnetic ratios [see Mohr and Taylor (2000) for a detailed description] and to the efforts for the redefinition of the kilogram (Mohr, Taylor, and Newell, 2008, 2012). The gyromagnetic ratio  $\gamma$  determines the spin-flip frequency  $f$  of a free particle when it is placed in a magnetic field  $B$ :  $\gamma = 2\pi f/B$ . The gyromagnetic ratios of a helium nucleus and a proton are accessible in nuclear and atomic magnetic resonance experiments. These ratios can be related to the gyromagnetic ratio of an electron that is linked to  $\alpha$  and  $h$ . There are two methods to produce the magnetic field: In the low-field method, it is generated by an electric current in a coil and determined from the current and the geometry. In the high-field method, the field is generated by a permanent

<sup>2</sup>The adjustments are named after the deadline for the included data, e.g., CODATA-10 is based on experimental and theoretical results that were available by 31 December 2010. The values of the constants and much more information are available at the Web site [physics.nist.gov/constants/](http://physics.nist.gov/constants/).

magnet and measured from a current induced in a coil. When the electric current is determined in terms of the JVS and QHR, the product  $K_J R_K = \sqrt{2\mu_0 c/h\alpha}$  appears in either the numerator or the denominator of  $\gamma$ , depending on which method is used. In the low-field method,  $h$  cancels out from the equations of the gyromagnetic ratios, and the experiment yields a value for  $\alpha$ . The high-field results also depend on  $\alpha$ , but since it is known much more precisely than  $h$ , they essentially yield a value for  $h$ . The high-field results on  $h$  are in good agreement with other experiments, albeit their uncertainty is not better than about  $10^{-6}$ . However, the low-field results are discrepant from the CODATA value of  $\alpha$ . By substituting Eqs. (44) into the observational equations of the low-field data, one obtains the estimate  $\epsilon_J + \epsilon_K = (-254 \pm 93) \times 10^{-9}$  (Cadoret *et al.*, 2011; Mohr, Taylor, and Newell, 2012). Since the measurements of  $R_K$  yield a much smaller value for  $\epsilon_K$ , the gyromagnetic data seem to imply a significant *negative*  $\epsilon_J$ . However, as explained below, a *positive*  $\epsilon_J$  can be found from measurements aiming at the redefinition of the kilogram.

There are essentially two candidate methods for the future realization of the kilogram: the watt balance and silicon sphere methods. The first, suggested by Kibble (1975), relates electric power to the time derivative of the gravitational potential energy:

$$mgv = \frac{V^2}{R} \propto \frac{1}{K_J^2 R_K} = h/4. \quad (46)$$

When the mass  $m$ , its velocity  $v$ , and the gravitational acceleration  $g$  are traceable to the SI, the watt balance yields a value for  $h$ . Watt balance results have already been published by four national metrology institutes, and several devices are under development; see, e.g., Li *et al.* (2012), Steiner (2013), and Stock (2013) for reviews. The silicon sphere approach is so demanding that it is employed only by the International Avogadro Coordination (IAC). The results were published in 2011; see Andreas *et al.* (2011a, 2011b) and the entire issue No. 2 of *Metrologia*, Vol. 48 (2011). This project determines the Avogadro constant  $N_A$  by fabricating spheres of enriched  $^{28}\text{Si}$  whose mass is compared to the prototype of the kilogram and whose volume is measured by laser interferometry. The lattice parameter and the relative atomic mass of  $^{28}\text{Si}$  are measured in different experiments, and the ratio of the relative and absolute mass densities yields  $N_A$ .

Results for  $h$  and  $N_A$  can be compared precisely with the help of the molar Planck constant

$$N_A h = \alpha^2 \frac{A_r(e) M_u c}{2R_\infty}. \quad (47)$$

Its uncertainty is only  $0.7 \times 10^{-9}$  (Mohr, Taylor, and Newell, 2012) and depends mainly on those of  $A_r(e)$  and  $\alpha$ . Equation (47) can be derived from the definition of the Rydberg constant by writing the inaccurate absolute mass of the electron in terms of its relative mass and  $N_A$  which links microscopic and macroscopic masses. The IAC 2011 result resolved the discrepancy of  $1.2 \times 10^{-6}$  between watt balances and the Avogadro constant determined from a sphere of natural Si that had puzzled metrologists since 1998 (Mohr and Taylor, 2000). Especially after the newest

results by Steele *et al.* (2012) there is no longer any clear discrepancy between the two methods, but the two most accurate watt balances deviate by a factor of  $260 \times 10^{-9}$  which is 3.5 times the uncertainty of their difference (Steiner *et al.*, 2007; Steele *et al.*, 2012). Also the measurements of the isotope ratio of the silicon sphere spread more than expected (Yang *et al.*, 2012). Nevertheless, by combining the Planck constants obtained from the watt balance ( $h_w$ ) and silicon sphere experiments ( $h_{\text{AvO}}$ ), we obtain an estimate of  $\epsilon_J + \epsilon_K/2 \approx (h_{\text{AvO}}/h_w - 1)/2 = (77 \pm 18) \times 10^{-9}$ . Here we neglected correlations between experiments. A more detailed analysis on the existence of  $\epsilon_{J,K}$  can be found from the CODATA papers of Mohr, Taylor, and Newell (2008, 2012); see also Keller (2008). They executed the least-squares analysis of fundamental constants several times, allowing either nonzero  $\epsilon_K$  or  $\epsilon_J$ , and including only part of the data. When they excluded the lowest-uncertainty but discrepant data, the remaining higher-uncertainty but consistent data yielded the conservative estimates  $\epsilon_K = (28 \pm 18) \times 10^{-9}$  and  $\epsilon_J = (150 \pm 490) \times 10^{-9}$ . Thus the exactness of the quantum Hall effect is confirmed much better than that of the Josephson effect.

### C. The future SI

Modernizing the SI toward a system based on fundamental constants or other true invariants of nature has long been a major goal, tracing back to a proposal by Maxwell in the 19th century; see, e.g., Flowers (2004) and references therein. Atomic clocks and laser interferometry permitted such a revision of the second and the meter. The development of quantum electric standards, watt balance experiments, the Avogadro project, and measurements of the Boltzmann constant have made the reform of the ampere, kilogram, mole, and kelvin realistic in the near future. In particular, suggestions by Mills *et al.* (2005) launched an active debate among metrologists (Mills *et al.*, 2006; Becker *et al.*, 2007; Milton, Williams, and Bennett, 2007). Soon it was agreed that the SI should not be altered before there are at least three independent experiments (from both watt balance and Avogadro constant calculations) with uncertainties  $\leq 50 \times 10^{-9}$  that are consistent within the 95% confidence intervals, and at least one of them has the uncertainty  $\leq 20 \times 10^{-9}$  (Gläser *et al.*, 2010). There have also been requests to await better results from single-electron and QMT experiments (Bordé, 2005; Milton, Williams, and Bennett, 2007), and to solve the discrepancy of low-field gyromagnetic experiments (Cadoret *et al.*, 2011).

There is already a draft chapter for the SI brochure that would adopt the new definitions: BIPM (2010); see also the whole issue 1953 in *Phil. Trans. Royal Soc., A* Vol. 369 (2011), especially Mills *et al.* (2011). In this draft, the whole system of units is scaled by a single sentence that fixes seven constants. The most substantial changes are that the base units ampere, kilogram, mole, and kelvin are defined by fixed values of  $e$ ,  $h$ ,  $N_A$ , and  $k_B$ , respectively. The new definition for the ampere reads “The ampere, A, is the unit of electric current; its magnitude is set by fixing the numerical value of the elementary charge to be equal to exactly  $1.602\,17X \times 10^{-19}$  when it is expressed in the units of second and ampere,

which is equal to coulomb.” The new definitions do not imply any particular methods for the realizations of the units. They are guided by *mises en pratique*, e.g., the ampere could be realized with the help of the JVS and QHR (CCEM Collaboration, 2012).

The new SI would significantly lower the uncertainties of many fundamental constants; see, e.g., Mills *et al.* (2011) for evaluations. One should note, however, that choosing the optimal set of fixed constants is always a trade-off. For example, since  $\alpha$  is a dimensionless number and thus independent of the choice of units, one can see from Eq. (45) that fixing  $e$  and  $h$  would make  $\mu_0$  (and  $\epsilon_0$ ) a quantity that is determined by a measurement of  $\alpha$ . Presently,  $\mu_0$  and  $\epsilon_0$  are fixed by the definition of an ampere. However, their uncertainty would be very low, the same as that of  $\alpha$ , which is  $0.32 \times 10^{-9}$  (Mohr, Taylor, and Newell, 2012). One alternative suggestion is to fix  $h$  and the Planck charge  $q_p = \sqrt{2\epsilon_0 hc}$ , which would keep  $\mu_0$  and  $\epsilon_0$  exact (Stock and Witt, 2006). It is also worth noting that out of  $h$ ,  $N_A$ , and the molar mass of carbon-12,  $M(^{12}\text{C}) = A_r(^{12}\text{C})M_u$ , only two can be fixed. The suggested SI would release the equality  $M(^{12}\text{C}) = 0.012 \text{ kg/mol}$ , which has raised criticism. In particular, there have been claims that the definition of the kilogram based on  $h$  would not be understandable for the wider audience, and a definition based on the mass of a number of elementary particles would be better in this respect (Becker *et al.*, 2007; Milton, Williams, and Bennett, 2007; Leonard, 2010; Hill, Miller, and Censullo, 2011). Milton, Williams, and Forbes (2010) studied two alternatives, fixing either  $N_A$  and  $h$  or  $N_A$  and the atomic mass constant  $m_u = M_u/N_A$ , and showed that this choice has little effect on the uncertainties of fundamental constants, mainly because the ratio  $h/m_u$  is well known from atomic recoil experiments.

#### D. Quantum metrology triangle

Phase-locked Bloch (Averin, Zorin, and Likharev, 1985) and SET (Averin and Likharev, 1986) oscillations in superconducting and normal-state tunnel junctions, respectively, were proposed as a source of quantized electric current in the mid-1980s, soon after the discovery of the QHR. Already Likharev and Zorin (1985) suggested that the quantum current standard could provide a consistency check for the existing two electric quantum standards in an experiment they named the “quantum metrology triangle.” However, the quantized current turned out to be a much greater challenge than the JVS and QHR. Still, after a quarter of a century, quantum current standards are yet to take their place in metrology. On the other hand, the progress in knowledge of  $K_J$  and  $R_K$  has also been rather slow: in CODATA-86 the uncertainties were  $300 \times 10^{-9}$  and  $45 \times 10^{-9}$ , respectively (Cohen and Taylor, 1987). These uncertainties are essentially on the same level as in CODATA-10 if the discrepancy of the data is taken into account.

The QMT experiment and its impact has been discussed, e.g., by Piquemal and Geneves (2000), Zimmerman and Keller (2003), Piquemal (2004), Gallop (2005), Keller (2008), Keller *et al.* (2008), Feltin and Piquemal (2009), and Scherer and Camarota (2012). In this review, we use the terms *QMT setup*, *experiment*, or *measurement* for any experimental setups that pursue a metrological comparison

between JVS, QHR, and a quantum current source. Development of such setups is a challenge in itself and not necessarily related to any specific single-electron source. However, as a closure of the QMT, we consider only experiments which include error counting of the single-electron device. The reason is that they are far more sensitive to errors than the JVS and QHR. Error counting allows one to separate the contribution of the average number of transported charge quanta  $\langle k_S \rangle$  from the current of the single-electron source  $I_S = \langle k_S \rangle Q_S$ . Only then can the QMT measurement yield information on fundamental constants.

The QMT setups can be divided into two categories: those that apply Ohm’s law  $V = RI$  or so-called ECCSs which utilize the definition of capacitance  $C = Q/V$ . They are sometimes called direct and indirect QMTs, respectively.

#### 1. Triangle by Ohm’s law

Applying Ohm’s law is the most obvious way to compare the three quantum electric standards. It can be realized either as a voltage balance  $V_J - R_H I_S$  or as a current balance  $V_J/R_H - I_S$ . In both cases, substituting Eqs. (44) into  $V_J = R_H I_S$  yields

$$\frac{n_J i_K}{2\langle k_S \rangle} \frac{f_J}{f_S} \approx 1 + \epsilon_J + \epsilon_K + \epsilon_S. \quad (48)$$

The major difficulty in QMT experiments is outlined as follows. Consider the ideal case where the noise of the experiment is dominated by the Johnson noise of the resistor. The relative standard deviation of the measurement result is

$$\frac{\delta I_S}{I_S} = \sqrt{\frac{4k_B T}{t R I_S^2}}. \quad (49)$$

By substituting realistic estimates  $t = 24 \text{ h}$  and  $T = 100 \text{ mK}$  for the averaging time and the temperature of the resistor, respectively, and by assuming that  $R = R_K/2$  and  $I_S = 100 \text{ pA}$ , one obtains the uncertainty  $\delta I_S/I_S \approx 7 \times 10^{-7}$ . In practical experiments, the  $1/f$  noise and the noise of the null detection circuit make the measurement even more demanding, but this simple model demonstrates that the magnitude of the current should be at least  $100 \text{ pA}$ .

Another problem is that the product  $R_H I_S$  yields a very small voltage, e.g.,  $12.9 \text{ k}\Omega \times 100 \text{ pA} = 1.29 \text{ }\mu\text{V}$ .<sup>3</sup> Even the voltage of a JVS with only one junction is typically of the order of  $70 \text{ GHz}/K_J \approx 140 \text{ }\mu\text{V}$ . Such low voltages are also vulnerable to thermoelectric effects. One way to overcome this problem is to multiply the current of the SET by a CCC with a very high winding ratio  $\sim 10\,000$  as suggested by Hartland *et al.* (1991), Sese *et al.* (1999), and Piquemal and Geneves (2000); see Fig. 38(a). It allows room-temperature detection, and that JVS, SET, and QHR can be operated in different refrigerators. This type of effort has been described by Piquemal (2004), Feltin and Piquemal (2009), Feltin *et al.* (2011), and Devoille *et al.* (2012). Another approach is to use a high-value cryogenic resistor that is calibrated against the QHR with the help of a CCC (Elmqvist, Zimmerman, and Huber, 2003; Manninen *et al.*, 2008). All parts of Ohm’s law

<sup>3</sup>A quantum voltage standard based on integrating a semiconductor pump with the QHR was pioneered by Hohls *et al.* (2011).

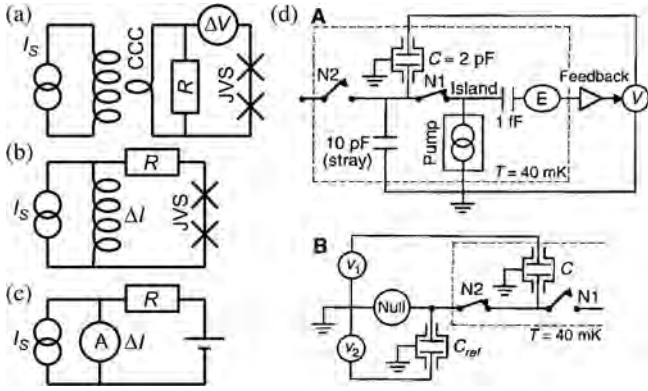


FIG. 38. (a)–(c) Variants of Ohm’s law triangles where the quantized current ( $I_S$ ) is compared to resistance ( $R$ ) calibrated against QHR and to JVS. (a) The quantized current is magnified by a CCC, which allows room-temperature null detection of the voltage difference ( $\Delta V$ ). (b) Triangle with a high-value cryogenic resistor. The current balance  $\Delta I$  can be determined, e.g., with the help of a CCC. (c) QMT experiment where the null detection is performed by a room-temperature transimpedance amplifier. (d) ECCS experiment. In the first phase (A), the electron pump charges the cryocapacitor  $C \approx 2$  pF. An SET electrometer ( $E$ ) is used to generate a feedback voltage ( $V$ ) that maintains the potential of the island at zero. Hence all the charge is accumulated to the cryocapacitor and not to the stray capacitance. The feedback voltage constitutes the third part of the  $Q = CV$  type triangle. In the second phase (B), the cryocapacitor is calibrated against the reference  $C_{ref}$  which is traceable to a calculable capacitor. From Keller *et al.*, 1999.

are in the same cryostat which can reduce thermoelectric effects; see Fig. 38(b). Only the difference current  $V_J/R_{cryo} - I_S$  needs to be amplified. Despite persistent efforts, the experimental realizations of these approaches have so far produced only preliminary results. Recently, a promising outcome was obtained by Giblin *et al.* (2012) who used a CCC with high winding ratio to calibrate a precision 1 G $\Omega$  room-temperature resistor which was used in a QMT setup; see Fig. 38(c). This experiment benefited from the relatively large current of 150 pA that was generated by a semiconducting quantum-dot pump. The uncertainty of the QMT experiment was  $1.2 \times 10^{-6}$ , but since there was no error counting, it should be interpreted as a characterization of the electron pump, not as a closure of the QMT.

## 2. Electron-counting capacitance standard

The ECCS experiment was first suggested by Williams, Ghosh, and Martinis (1992). A single-electron current source is used to charge a cryogenic capacitor  $C_{cryo}$  by a known number  $N_S$  of electrons. The generated voltage is compared to the JVS. The result

$$C_{cryo} = \frac{N_S Q_S}{V} \quad (50)$$

thus yields a quantum capacitance standard. The ECCS experiment was pioneered by Keller *et al.* (1999) [see Fig. 38(d)], where an uncertainty of  $0.3 \times 10^{-6}$  was obtained for the ECCS capacitance. In this approach, the ECCS was compared to a calculable capacitor. Then the observational equation corresponding to Eq. (48),

$$\frac{\mu_0 c n_J f_J C}{4\alpha N_S} = 1 + \epsilon_J + \epsilon_S, \quad (51)$$

does not include  $\epsilon_K$ . However, calculable capacitors have been compared to QHR with very low uncertainty, and ac QHR techniques (Schurr *et al.*, 2011; Camarota *et al.*, 2012) allow  $C_{cryo}$  to be compared directly against  $R_K$ . One should thus obtain an uncertainty of  $\sim 10^{-8}$  before there is any significant difference between the implications of the two QMT versions. An important strength of this QMT version is that the feedback electrometer also allows error counting through shuttle pumping; see Sec. III.H.2.

A major weakness of the ECCS is that it calibrates  $C_{cryo}$  at  $\sim 0.01$  Hz, but commercial capacitance bridges that are used to compare  $C_{cryo}$  to the calculable capacitor (and also ac QHR) operate at  $\sim 1000$  Hz. Zimmerman, Simonds, and Wang (2006) presented a model for the dielectric dispersion of insulating films at the surface of the electrodes of the capacitor. They fit this model to measurements of the frequency dependence and its temperature dependence in the ranges 100–3000 Hz and 4–300 K. The frequency dependence decreases at low temperatures. They evaluate that it yields an uncertainty component of  $0.2 \times 10^{-6}$  for the QMT. Keller, Zimmerman, and Eichenberger (2007) used this estimate to finish the uncertainty budget of the NIST ECCS experiment that closes the QMT at the uncertainty of  $0.9 \times 10^{-6}$ .

Recently, PTB reached the uncertainty of  $1.7 \times 10^{-6}$  in an ECCS experiment (Camarota *et al.*, 2012); see Sec. III.H.2. PTB presented their result as “preliminary” and planned both a more detailed uncertainty budget and several improvements to the experiment. Besides NIST and PTB, the ECCS has been pursued at METAS (Rüfenacht, Jeanneret, and Lotkhov, 2010).

## 3. Metrological implications of single-electron transport and QMT

So far, QMT has been closed with a reasonable uncertainty ( $\sim 10^{-6}$ ) only in the ECCS experiments of NIST (Keller, Zimmerman, and Eichenberger, 2007) and PTB (Camarota *et al.*, 2012). As shown in Sec. IV.B, an uncertainty of  $\leq 0.02 \times 10^{-6}$  is required to yield information on  $\epsilon_K$ , and an uncertainty of  $\sim 0.1 \times 10^{-6}$  would strengthen the knowledge of  $\epsilon_J$ . Thus, the NIST and PTB results can be expressed in terms of  $\epsilon_S$  only:  $\epsilon_S = (-0.10 \pm 0.92) \times 10^{-6}$  and  $\epsilon_S = (-0.3 \pm 1.7) \times 10^{-6}$ , respectively (Keller, 2008).

Milton, Williams, and Forbes (2010) analyzed a scenario where  $\epsilon_J$  is an adjusted parameter and  $\epsilon_S = \epsilon_K = 0$ . They studied the effect of QMT on the uncertainties of fundamental constants and showed that when the QMT is inaccurate, the uncertainties of  $h$ ,  $e$ , and  $m_u$  are mainly determined by the Avogadro experiment. When the QMT is improved, their uncertainties will be dominated by those of the watt balance and the direct measurement of  $R_K$ .

One problem of the QMT is that it gives only a value for the sum of the errors of the quantum standards, and, in principle, they could cancel each other. It is thus useful to have independent tests for each standard, and those for the JVS and QHR are discussed in Sec. IV.B. A test for the current standard only, i.e., an SI value for  $Q_S$ , can be obtained by combining results from three experiments: QMT, a

measurement of  $R_K$  by a calculable capacitor, and watt balance (Keller *et al.*, 2008). Applying Eqs. (46) and (50), and substituting  $R$  by  $1/\omega C$ , one obtains

$$Q_S = \frac{1}{N_S} \sqrt{\frac{mgvC}{\omega}}. \tag{52}$$

Also the Ohm’s law triangle can be used to yield a similar result, but in a less direct way. One should note that JVS and QHR are used here only as transfer standards. Keller *et al.* (2008) derived a result based on the NIST ECCS:  $Q_S = 1.602\,1763 \times 10^{-19} \pm 1.5 \times 10^{-25}$  C. This could be compared to the CODATA value for  $e$ , which, however, depends strongly on  $h$  and the exactness of  $K_J$  and  $R_K$ . Instead, it is better to compare  $Q_S$  to another value of  $e$  that is independent of JVS and QHR:  $e = \sqrt{\alpha^3 A_r(e) M_u / \mu_0 R_\infty N_A}$  (Feltn and Piquemal, 2009). Its uncertainty  $\sim 0.015 \times 10^{-6}$  is dominated by that of  $N_A$ . Using the NIST ECCS result and the NRC or IAC values for  $N_A$ , one obtains  $\epsilon_S = (-0.2 \pm 0.9) \times 10^{-6}$ .

We note that according to Eq. (51), the QMT also yields a value for  $\alpha$  independently of the QHR, which was one of the early motivations for the ECCS (Williams, Ghosh, and Martinis, 1992). This fact, however, has little importance until the uncertainty is competitive with the atomic recoil experiments ( $< 10^{-9}$ ). Then the QMT would strengthen the verification of QED.

Although single-electron transport would be conceptually the most straightforward realization of the ampere in the future SI, it is not likely that it would replace the JVS and QHR as the typical realization in the near future. The exception is naturally the growing field of metrology for small electric currents, where single electronics is expected to yield major improvements of uncertainty. On the other hand, when the accuracy of single-electron transport improves, it can yield vital information on other standards and fundamental constants.

## V. PERSPECTIVES AND OTHER APPLICATIONS

The quantum-dot pump (Kaestner, Kashcheyevs, Hein *et al.*, 2008; Giblin *et al.*, 2012) discussed in Sec. III.C has definitely proven its potential to be the basis of the future quantum standard of the ampere. The verified uncertainty of the 150 pA output current on the level of 1 ppm and the theoretically predicted 0.01 ppm uncertainty of the present device are truly remarkable figures of merit. On the other hand, a few important questions remain to be answered before one can realize the ampere with the quantum-dot pump: Superior device performance depends critically on applying a strong  $\geq 10$  T magnetic field on it. This dependence is not fully understood, and the exact magnetic field characteristics seem sample dependent. The reproducibility of the highly accurate

pumping results with samples from different fabrication runs remains to be shown. Importantly, error-counting experiments on the dot samples have not been carried out, which also prevents one from studying possible errors of other quantum standards in the QMT [see, however, recent results in Fricke *et al.* (2013)]. Future experiments will likely show whether all the relevant error processes have been accounted for in predicting the obtainable accuracy to be on the level of  $10^{-8}$ . However, even if not in the case of a bare device, the quantum-dot pump may perhaps be applicable to the realization of the ampere, if the error correction techniques that were described in Sec. III.H become feasible experimentally.

Another important development and potential future realization of the ampere is the SINIS turnstile introduced in Sec. III.B. Although presently inferior to the quantum-dot pump in the level of current output, and consequently with less definite assessment of proven accuracy (present verified uncertainty below  $10^{-4}$ ), this device does not suffer from known obstacles in the way of achieving the required accuracy. Currently, the main error mechanisms have been assessed theoretically and experimentally, including photon-assisted tunneling, Andreev current, cotunneling, residual and generated quasiparticles, and possible residual density of states in a superconductor. Positive conclusions can be drawn from individual experiments with respect to suppressing them in an optimized device. Sample fabrication and reproducibility is currently on a high level, and it has been demonstrated that the requested magnitude of current can be achieved by running many turnstiles in parallel. For the SINIS turnstile, as for the quantum-dot pump, the ultimate test would be an error-counting experiment and the quantum metrological triangle. Currently, such experiments have not been performed. As a summary of the high-accuracy pumps, we present Table I where the obtainable output current, the accuracy, and the possibility for parallelization are compared.

Presently several other new proposals are being pushed toward critical tests to study their applicability in current metrology: these include superconducting phase-slip wires, Josephson junction arrays, and mechanical shuttles, just to mention a few less conventional ideas. Although it is not on the horizon at present, it is possible that eventually one of these devices will beat the present Coulomb-blockade-based realizations both in current yield and in their robustness against transfer errors.

Developing ever more accurate current sources has constantly been a driving force for understanding the underlying physical phenomena. On the other hand, the studies for the precise control of single electrons and Cooper pairs have created special expertise that is also applicable in a variety of other research topics.

In addition to the charge degrees of freedom, the electrons hold information in their spin states which have been

TABLE I. Summary of high-accuracy single-electron sources.  $I_{\text{expt}}$  is the experimentally achieved current with uncertainty  $\delta I_{\text{expt}}$ .  $\delta I_{\text{theory}}$  is a theoretical prediction for the uncertainty.

Name	$I_{\text{expt}}$ (pA)	$\delta I_{\text{expt}}/I$	$\delta I_{\text{theory}}/I$	Parallelization
Chain of normal metallic islands	1.5	$1.5 \times 10^{-8}$	$\ll 10^{-8}$	Not feasible
Quantum-dot pump	150	$< 2 \times 10^{-6}$	$\dots$	Not needed
SINIS turnstile	3	$< 1 \times 10^{-4}$	$10^{-8}$	Possible

envisioned (Kane, 1998; Hollenberg *et al.*, 2006) to be utilized (Morello *et al.*, 2010) for quantum information processing. Although the electron transport is typically incoherent in the electron pumps, the spin-encoded information can potentially remain coherent, and hence this information can possibly be transported from the memory cell of the computer to the qubit-qubit interaction cell and back. The transport cycle has to be carried out with high accuracy for fault-tolerant computing to be possible, which creates a close connection to the metrological electron pumps.

Geometric phases (Shapere and Wilczek, 1989) in quantum mechanics have been studied extensively due to both fundamental scientific curiosity and their applications in geometric quantum computing (Zanardi and Rasetti, 1999). The simplest geometric quantum phase, the Berry phase, has already been measured in the superconducting sluice pump (Möttönen *et al.*, 2006; Möttönen, Vartiainen, and Pekola, 2008) thanks to the development of the sluice for metrology. Some theoretical work on the more complex phases referred to as holonomies has been put forward in the framework of Cooper-pair pumps (Pirkkalainen *et al.*, 2010; Solinas, Pirkkalainen, and Möttönen, 2010) but it remains to be seen if these ideas will be implemented experimentally. The main obstacle in practice is perhaps the high level of precision required for the control signals of the pumps, a problem that can possibly be solved with the help of the work on the metrological current source.

Detecting single electrons and Cooper pairs by single-electron transistors and quantum point contacts has been largely motivated by the need for tests of the charge-transport errors in metrology. During the past decade, these techniques have also been successfully implemented, e.g., in experiments on full counting statistics and noise of charge transport. The experiments on the full counting statistics of current fluctuations in a semiconductor quantum dot by real-time detection of single-electron tunneling with a quantum point contact have been successfully performed for instance by Gustavsson *et al.* (2006, 2007). In these experiments, moments of current up to the fifth and beyond could be reliably measured. Recently, single-charge-counting experiments have been applied to study energy fluctuation relations (Evans, Cohen, and Morriss, 1993; Jarzynski, 1997; Crooks, 1999; Averin and Pekola, 2011) in statistical mechanics. Experiments in steady-state nonequilibrium were performed by Küng *et al.* (2012), and the Jarzynski and Crooks relations were recently tested by Saira, Yoon *et al.* (2012). Single-charge-counting experiments allow one to test fundamental statistical mechanics and thermodynamics of classical and quantum systems.

The variety of spin-offs from the development of single-charge current sources for metrology is certainly expanding. In this way the benefits of this research will be obvious not only for the community interested in the system of units and in traceable measurements, but also for other researchers working in basic and applied sciences looking for new tools for measurements that need precise control.

## ACKNOWLEDGMENTS

We thank Simone Gasparinetti, Stephen Giblin, Juha Hassel, Panu Helistö, Antti Manninen, Matthias Meschke, Mika Prunnila, Alexander Savin, Heikki Seppä, and Jaw Shen

Tsai for useful discussions. We also thank the Academy of Finland through its Centre of Excellence Programs (Projects No. 250280 and No. 251748), MEXT Grant-in-Aid “Quantum Cybernetics,” the FIRST Project from JSPS, and the Finnish National Graduate School in Nanoscience for financial support during the preparation of this manuscript. Y.P. acknowledges partial support from EPSRC, the Royal Society, and Wolfson Foundation. A.K. and M.M. thank the Academy of Finland for financial support (Grants No. 259030, No. 135794, and No. 272806).

## REFERENCES

- Aguado, R., and L. Kouwenhoven, 2000, *Phys. Rev. Lett.* **84**, 1986.  
 Altebaeumer, T., and H. Ahmed, 2001, *Jpn. J. Appl. Phys.* **40**, 80.  
 Altebaeumer, T., S. Amakawa, and H. Ahmed, 2001, *Appl. Phys. Lett.* **79**, 533.  
 Ambegaokar, V., and A. Baratoff, 1963, *Phys. Rev. Lett.* **10**, 486.  
 Ando, T., A. B. Fowler, and F. Stern, 1982, *Rev. Mod. Phys.* **54**, 437.  
 Andreas, B., *et al.*, 2011a, *Metrologia* **48**, S1.  
 Andreas, B., *et al.*, 2011b, *Phys. Rev. Lett.* **106**, 030801.  
 Andreev, A. F., 1964, *Sov. Phys. JETP* **19**, 1228.  
 Aref, T., V. F. Maisi, M. V. Gustafsson, P. Delsing, and J. P. Pekola, 2011, *Europhys. Lett.* **96**, 37008.  
 Armour, A. D., and A. MacKinnon, 2002, *Phys. Rev. B* **66**, 035333.  
 Arutyunov, K. Y., D. S. Golubev, and A. D. Zaikin, 2008, *Phys. Rep.* **464**, 1.  
 Ashoori, R. C., H. L. Stormer, J. S. Weiner, L. N. Pfeiffer, K. W. Baldwin, and K. W. West, 1993, *Phys. Rev. Lett.* **71**, 613.  
 Astafiev, O. V., L. B. Ioffe, S. Kafanov, Y. A. Pashkin, K. Y. Arutyunov, D. Shahar, O. Cohen, and J. S. Tsai, 2012, *Nature (London)* **484**, 355.  
 Aumentado, J., M. W. Keller, and J. M. Martinis, 2003, *Physica (Amsterdam)* **18E**, 37.  
 Aunola, M., and J. J. Toppari, 2003, *Phys. Rev. B* **68**, 020502.  
 Averin, D., and A. Bardas, 1995, *Phys. Rev. B* **52**, 12873.  
 Averin, D. V., 2000, *Fortschr. Phys.* **48**, 1055.  
 Averin, D. V., 2001, *Macroscopic Quantum Coherence and Quantum Computing* (Kluwer, Dordrecht), p. 399.  
 Averin, D. V., 2003, *Quantum Noise in Mesoscopic Physics* (Kluwer, Dordrecht), p. 229.  
 Averin, D. V., T. Bergeman, P. R. Hosur, and C. Bruder, 2008, *Phys. Rev. A* **78**, 031601.  
 Averin, D. V., A. Korotkov, and K. Likharev, 1991, *Phys. Rev. B* **44**, 6199.  
 Averin, D. V., and K. K. Likharev, 1986, *J. Low Temp. Phys.* **62**, 345.  
 Averin, D. V., and K. K. Likharev, 1991, *Mesoscopic Phenomena in Solids* (Nature Publishing Group, Amsterdam), p. 173.  
 Averin, D. V., and Y. V. Nazarov, 1990, *Phys. Rev. Lett.* **65**, 2446.  
 Averin, D. V., and Y. V. Nazarov, 1992a, *Single Charge Tunneling* (Plenum Press, New York), Vol. 294.  
 Averin, D. V., and Y. V. Nazarov, 1992b, *Phys. Rev. Lett.* **69**, 1993.  
 Averin, D. V., and Y. V. Nazarov, 1993, *Phys. Rev. B* **47**, 9944.  
 Averin, D. V., and A. A. Odintsov, 1989, *Phys. Lett. A* **140**, 251.  
 Averin, D. V., A. A. Odintsov, and S. V. Vyshenskii, 1993, *J. Appl. Phys.* **73**, 1297.  
 Averin, D. V., and J. P. Pekola, 2008, *Phys. Rev. Lett.* **101**, 066801.  
 Averin, D. V., and J. P. Pekola, 2011, *Europhys. Lett.* **96**, 67004.  
 Averin, D. V., and E. V. Sukhorukov, 2005, *Phys. Rev. Lett.* **95**, 126803.  
 Averin, D. V., A. B. Zorin, and K. K. Likharev, 1985, *Sov. Phys. JETP* **61**, 407.

- Avron, J. E., D. Osadchy, and R. Seiler, 2003, *Phys. Today* **56**, No. 8, 38.
- Bachmair, H., 2009, *Eur. Phys. J. Special Topics* **172**, 257.
- Bardeen, J., G. Rickayzen, and L. Tewordt, 1959, *Phys. Rev.* **113**, 982.
- Barends, R., J. J. A. Baselmans, S. J. C. Yates, J. R. Gao, J. N. Hovenier, and T. M. Klapwijk, 2008, *Phys. Rev. Lett.* **100**, 257002.
- Becker, P., P. D. Bievre, K. Fujii, M. Glaeser, B. Inglis, H. Luebbig, and G. Mana, 2007, *Metrologia* **44**, 1.
- Beenakker, C. W. J., 1991, *Phys. Rev. B* **44**, 1646.
- Behr, R., J. M. Williams, P. Patel, T. J. B. M. Janssen, T. Funck, and M. Klönz, 2005, *IEEE Trans. Instrum. Meas.* **54**, 612.
- Benz, S. P., and C. A. Hamilton, 1996, *Appl. Phys. Lett.* **68**, 3171.
- Berggren, K., T. Thornton, D. Newson, and M. Pepper, 1986, *Phys. Rev. Lett.* **57**, 1769.
- Bieri, S., and J. Fröhlich, 2011, *C.R. Phys.* **12**, 332.
- BIPM (Bureau International des Poids et Mesures), 2010 [[http://www.bipm.org/utills/common/pdf/si\\_brochure\\_draft\\_ch2.pdf](http://www.bipm.org/utills/common/pdf/si_brochure_draft_ch2.pdf)].
- Bloch, F., 1968, *Phys. Rev. Lett.* **21**, 1241.
- Bloch, F., 1970, *Phys. Rev. B* **2**, 109.
- Blonder, G. E., M. Tinkham, and T. M. Klapwijk, 1982, *Phys. Rev. B* **25**, 4515.
- Blumenthal, M. D., B. Kaestner, L. Li, S. Giblin, T. J. B. M. Janssen, M. Pepper, D. Anderson, G. Jones, and D. A. Ritchie, 2007, *Nat. Phys.* **3**, 343.
- Bocquillon, E., F. D. Parmentier, C. Grenier, J.-M. Berroir, P. Degiovanni, D. C. Glattli, B. Plaçais, A. Cavanna, Y. Jin, and G. Fève, 2012, *Phys. Rev. Lett.* **108**, 196803.
- Bordé, C. J., 2005, *Phil. Trans. R. Soc. A* **363**, 2177.
- Bouchendira, R., P. Cladé, S. Guellati-Khélifa, F. Nez, and F. Biraben, 2011, *Phys. Rev. Lett.* **106**, 080801.
- Bouchiat, V., D. Vion, P. Joyez, D. Esteve, and M. H. Devoret, 1998, *Phys. Scr. T* **76**, 786.
- Brenning, H., S. Kafanov, T. Duty, S. Kubatkin, and P. Delsing, 2006, *J. Appl. Phys.* **100**, 114321.
- Brenning, H., S. Kubatkin, and P. Delsing, 2004, *J. Appl. Phys.* **96**, 6822.
- Bubanja, V., 2011, *Phys. Rev. B* **83**, 195312.
- Buehler, T. M., D. J. Reilly, R. P. Starrett, A. D. Greentree, A. R. Hamilton, A. S. Dzurak, and R. G. Clark, 2005, *Appl. Phys. Lett.* **86**, 143117.
- Bureau International des Poids et Mesures, 2006, *The International System of Units (SI)* (STEDI Media, Paris), 8th ed.
- Büttiker, M., 1987, *Phys. Rev. B* **36**, 3548.
- Bylander, J., T. Duty, and P. Delsing, 2005, *Nature (London)* **434**, 361.
- Cadoret, M., E. de Mirandés, P. Cladé, S. Guellati-Khélifa, F. Nez, and F. Biraben, 2011, *C.R. Phys.* **12**, 379.
- Camarota, B., H. Scherer, M. V. Keller, S. V. Lotkhov, G.-D. Willenberg, and F. J. Ahlers, 2012, *Metrologia* **49**, 8.
- Cassidy, M. C., A. S. Dzurak, R. G. Clark, K. D. Petersson, I. Farrer, D. A. Ritchie, and C. G. Smith, 2007, *Appl. Phys. Lett.* **91**, 222104.
- CCEM Collaboration, 2012, unpublished.
- Chan, K. W., M. Möttönen, A. Kemppinen, N. S. Lai, K. Y. Tan, W. H. Lim, and A. S. Dzurak, 2011, *Appl. Phys. Lett.* **98**, 212103.
- Chang, L. L., L. Esaki, and R. Tsu, 1974, *Appl. Phys. Lett.* **24**, 593.
- Cheinet, P., S. Trotzky, M. Feld, U. Schnorrberger, M. Moreno-Cardoner, S. Fölling, and I. Bloch, 2008, *Phys. Rev. Lett.* **101**, 090404.
- Clarke, J., 1968, *Phys. Rev. Lett.* **21**, 1566.
- Clarke, J., 1972, *Phys. Rev. Lett.* **28**, 1363.
- Clerk, A., S. M. Girvin, and A. Stone, 2003, *Phys. Rev. B* **67**, 165324.
- Clerk, A. A., S. M. Girvin, F. Marquardt, and R. J. Schoelkopf, 2010, *Rev. Mod. Phys.* **82**, 1155.
- Clothier, W. K., G. J. Sloggett, H. Bairnsfather, M. F. Currey, and D. J. Benjamin, 1989, *Metrologia* **26**, 9.
- Cohen, E. R., and B. N. Taylor, 1987, *Rev. Mod. Phys.* **59**, 1121.
- Cohen, G., V. Fleurov, and K. Kikoin, 2009, *Phys. Rev. B* **79**, 245307.
- Cohen, M. H., L. M. Falicov, and T. C. Phillips, 1962, *Phys. Rev. Lett.* **8**, 316.
- Connolly, M. R., *et al.*, 2012, [arXiv:1207.6597](https://arxiv.org/abs/1207.6597).
- Covington, M., M. W. Keller, R. L. Kautz, and J. M. Martinis, 2000, *Phys. Rev. Lett.* **84**, 5192.
- Crooks, G. E., 1999, *Phys. Rev. E* **60**, 2721.
- Delahaye, F., 1993, *J. Appl. Phys.* **73**, 7914.
- de Visser, P., J. Baselmans, P. Diener, S. Yates, A. Endo, and T. Klapwijk, 2011, *Phys. Rev. Lett.* **106**, 167004.
- Devoille, L., N. Feltin, B. Steck, B. Chenaud, S. Sassine, S. Djordjevic, O. Sron, and F. Piquemal, 2012, *Meas. Sci. Technol.* **23**, 124011.
- Devoret, M. H., D. Esteve, H. Grabert, G.-L. Ingold, H. Pothier, and C. Urbina, 1990, *Phys. Rev. Lett.* **64**, 1824.
- Devoret, M. H., and R. J. Schoelkopf, 2000, *Nature (London)* **406**, 1039.
- Dolan, G. J., 1977, *Appl. Phys. Lett.* **31**, 337.
- Dolan, G. J., and J. H. Dunsmuir, 1988, *Physica (Amsterdam)* **152B**, 7.
- Doucot, B., 2011, *C.R. Phys.* **12**, 323.
- Durrani, Z. A. K., 2009, *Single-electron Devices and Circuits in Silicon* (Imperial College Press, London).
- Ebbecke, J., G. Bastian, M. Blöcker, K. Pierz, and F. J. Ahlers, 2000, *Appl. Phys. Lett.* **77**, 2601.
- Ebbecke, J., N. E. Fletcher, F.-J. Ahlers, A. Hartland, and T. J. B. M. Janssen, 2003, *IEEE Trans. Instrum. Meas.* **52**, 594.
- Ebbecke, J., N. E. Fletcher, T. J. B. M. Janssen, F.-J. Ahlers, M. Pepper, H. E. Beere, and D. A. Ritchie, 2004, *Appl. Phys. Lett.* **84**, 4319.
- Eiles, T. M., J. M. Martinis, and M. H. Devoret, 1993, *Phys. Rev. Lett.* **70**, 1862.
- Elmquist, R. E., N. M. Zimmerman, and W. H. Huber, 2003, *IEEE Trans. Instrum. Meas.* **52**, 590.
- Elzerman, J. M., R. Hanson, J. S. Greidanus, L. H. Willems van Beveren, S. De Franceschi, L. M. K. Vandersypen, S. Tarucha, and L. P. Kouwenhoven, 2003, *Phys. Rev. B* **67**, 161308.
- Erbe, A., R. H. Blick, A. Tilke, A. Kriele, and J. P. Kotthaus, 1998, *Appl. Phys. Lett.* **73**, 3751.
- Erbe, A., C. Weiss, W. Zwerger, and R. H. Blick, 2001, *Phys. Rev. Lett.* **87**, 096106.
- Evans, D. J., E. G. D. Cohen, and G. P. Morriss, 1993, *Phys. Rev. Lett.* **71**, 2401.
- Faoro, L., J. Siewert, and R. Fazio, 2003, *Phys. Rev. Lett.* **90**, 028301.
- Fasth, C., A. Fuhrer, L. Samuelson, V. N. Golovach, and D. Loss, 2007, *Phys. Rev. Lett.* **98**, 266801.
- Fedorets, D., L. Y. Gorelik, R. I. Shekhter, and M. Jonson, 2004, *Phys. Rev. Lett.* **92**, 166801.
- Feigel'man, M. V., L. B. Ioffe, V. E. Kravtsov, and E. A. Yuzbashyan, 2007, *Phys. Rev. Lett.* **98**, 027001.
- Feltin, N., and F. Piquemal, 2009, *Eur. Phys. J. Special Topics* **172**, 267.
- Feltin, N., B. Steck, L. Devoille, S. Sassine, B. Chenaud, W. Poirier, F. Schopfer, G. Sprengler, S. Djordjevic, O. Sron, and F. Piquemal, 2011, *Revue Française de Métrologie* **2011-1**, 3.
- Fève, G., A. Mahé, J.-M. Berroir, T. Kontos, B. Plaçais, D. C. Glattli, A. Cavanna, B. Etienne, and Y. Jin, 2007, *Science* **316**, 1169.

- Field, M., C. Smith, M. Pepper, D. Ritchie, J. Frost, G. Jones, and D. Hasko, 1993, *Phys. Rev. Lett.* **70**, 1311.
- Filinov, A. V., M. Bonitz, and Y. E. Lozovik, 2001, *Phys. Rev. Lett.* **86**, 3851.
- Fisher, M. P. A., 1986, *Phys. Rev. Lett.* **57**, 885.
- Flensberg, K., Q. Niu, and M. Pustilnik, 1999, *Phys. Rev. B* **60**, R16291.
- Fletcher, J. D., *et al.*, 2011, [arXiv:1107.4560](https://arxiv.org/abs/1107.4560).
- Flowers, J., 2004, *Science* **306**, 1324.
- Fölling, S., S. Trotzky, P. Cheinet, M. Feld, R. Saers, A. Widera, T. Müller, and I. Bloch, 2007, *Nature (London)* **448**, 1029.
- Fricke, L., F. Hohls, N. Ubbelohde, B. Kaestner, V. Kashcheyevs, C. Leicht, P. Mirovsky, K. Pierz, H. W. Schumacher, and R. J. Haug, 2011, *Phys. Rev. B* **83**, 193306.
- Fricke, L., M. Wulf, F. Hohls, B. Kaestner, R. Dolata, P. Mirovsky, K. Pierz, T. Weimann, and H. W. Schumacher, 2012, unpublished.
- Fricke, L., *et al.*, 2013, *Phys. Rev. Lett.* **110**, 126803.
- Fuechsle, M., J. A. Miwa, S. Mahapatra, H. Ryu, S. Lee, O. Warschkow, L. C. L. Hollenberg, G. Klimeck, and M. Y. Simmons, 2012, *Nat. Nanotechnol.* **7**, 242.
- Fujisawa, T., T. Hayashi, Y. Hirayama, H. D. Cheong, and Y. H. Jeong, 2004, *Appl. Phys. Lett.* **84**, 2343.
- Fujiwara, A., K. Nishiguchi, and Y. Ono, 2008, *Appl. Phys. Lett.* **92**, 042102.
- Fujiwara, A., and Y. Takahashi, 2001, *Nature (London)* **410**, 560.
- Fujiwara, A., N. M. Zimmerman, Y. Ono, and Y. Takahashi, 2004, *Appl. Phys. Lett.* **84**, 1323.
- Fulton, T. A., 1973, *Phys. Rev. B* **7**, 981.
- Fulton, T. A., and G. Dolan, 1987, *Phys. Rev. Lett.* **59**, 109.
- Funck, T., and V. Siemknecht, 1991, *IEEE Trans. Instrum. Meas.* **40**, 158.
- Gabelli, J., G. Fève, J.-M. Berroir, B. Plaçaïs, A. Cavanna, B. Etienne, Y. Jin, and D. C. Glattli, 2006, *Science* **313**, 499.
- Gallop, J. C., 2005, *Phil. Trans. R. Soc. A* **363**, 2221.
- Gallop, J. C., and F. Piquemal, 2006, *SQUIDS for Standards and Metrology* (Wiley-VCH Verlag GmbH & Co. KGaA, Weinheim), Chap. 4, p. 95.
- Gasparinetti, S., P. Solinas, Y. Yoon, and J. P. Pekola, 2012, *Phys. Rev. B* **86**, 060502.
- Geerligs, L., D. Averin, and J. Mooij, 1990, *Phys. Rev. Lett.* **65**, 3037.
- Geerligs, L. J., V. F. Anderegg, P. A. M. Holweg, J. E. Mooij, H. Pothier, D. Esteve, C. Urbina, and M. H. Devoret, 1990, *Phys. Rev. Lett.* **64**, 2691.
- Geerligs, L. J., S. M. Verbrugh, P. Hadley, J. E. Mooij, H. Pothier, P. Lafarge, C. Urbina, D. Esteve, and M. H. Devoret, 1991, *Z. Phys. B* **85**, 349.
- Giaever, I., 1960, *Phys. Rev. Lett.* **5**, 147.
- Giazotto, F., T. T. Heikkilä, A. Luukanen, A. M. Savin, and J. P. Pekola, 2006, *Rev. Mod. Phys.* **78**, 217.
- Giazotto, F., P. Spathis, S. Roddaro, S. Biswas, F. Taddei, M. Governale, and L. Sorba, 2011, *Nat. Phys.* **7**, 857.
- Giblin, S. P., M. Kataoka, J. D. Fletcher, P. See, T. J. B. M. Janssen, J. P. Griffiths, G. A. C. Jones, I. Farrer, and D. A. Ritchie, 2012, *Nat. Commun.* **3**, 930.
- Giblin, S. P., S. J. Wright, J. D. Fletcher, M. Kataoka, M. Pepper, T. J. B. M. Janssen, D. A. Ritchie, C. A. Nicoll, D. Anderson, and G. A. C. Jones, 2010, *New J. Phys.* **12**, 073013.
- Girvin, S. M., L. I. Glazman, M. Jonson, D. R. Penn, and M. D. Stiles, 1990, *Phys. Rev. Lett.* **64**, 3183.
- Gläser, M., M. Borys, D. Ratschko, and R. Schwartz, 2010, *Metrologia* **47**, 419.
- Goerbig, M. O., 2011, *C.R. Phys.* **12**, 369.
- Golubev, D. S., and A. D. Zaikin, 1992, *Phys. Lett. A* **169**, 475.
- Gorelik, L. Y., A. Isacsson, Y. M. Galperin, R. I. Shekhter, and M. Jonson, 2001, *Nature (London)* **411**, 454.
- Gorelik, L. Y., A. Isacsson, M. V. Voinova, B. Kasemo, R. I. Shekhter, and M. Jonson, 1998, *Phys. Rev. Lett.* **80**, 4526.
- Greibe, T., M. P. V. Stenberg, C. M. Wilson, T. Bauch, V. S. Shumeiko, and P. Delsing, 2011, *Phys. Rev. Lett.* **106**, 097001.
- Gustavsson, S., R. Leturcq, T. Ihn, K. Ensslin, M. Reinwald, and W. Wegscheider, 2007, *Phys. Rev. B* **75**, 075314.
- Gustavsson, S., R. Leturcq, B. Simovič, R. Schleser, T. Ihn, P. Studerus, K. Ensslin, D. C. Driscoll, and A. C. Gossard, 2006, *Phys. Rev. Lett.* **96**, 076605.
- Gustavsson, S., R. Leturcq, M. Studer, I. Shorubalko, T. Ihn, K. Ensslin, D. C. Driscoll, and A. C. Gossard, 2009, *Surf. Sci. Rep.* **64**, 191.
- Gustavsson, S., I. Shorubalko, R. Leturcq, S. Schon, and K. Ensslin, 2008, *Appl. Phys. Lett.* **92**, 152101.
- Hamilton, C., C. Burroughs, and R. Kautz, 1995, *IEEE Trans. Instrum. Meas.* **44**, 223.
- Hanneke, D., S. Fogwell, and G. Gabrielse, 2008, *Phys. Rev. Lett.* **100**, 120801.
- Hanson, R., L. P. Kouwenhoven, J. R. Petta, S. Tarucha, and L. M. K. Vandersypen, 2007, *Rev. Mod. Phys.* **79**, 1217.
- Harbusch, D., D. Taubert, H. P. Tranitz, W. Wegscheider, and S. Ludwig, 2010, *Phys. Rev. Lett.* **104**, 196801.
- Hartland, A., K. Jones, J. M. Williams, B. L. Gallagher, and T. Galloway, 1991, *Phys. Rev. Lett.* **66**, 969.
- Hartle, J. B., D. J. Scalapino, and R. L. Sugar, 1971, *Phys. Rev. B* **3**, 1778.
- Harvey, I. K., 1972, *Rev. Sci. Instrum.* **43**, 1626.
- Häusler, W., and B. Kramer, 1993, *Phys. Rev. B* **47**, 16353.
- Hekking, F. W. J., L. I. Glazman, K. A. Matveev, and R. I. Shekhter, 1993, *Phys. Rev. Lett.* **70**, 4138.
- Hekking, F. W. J., and Y. V. Nazarov, 1994, *Phys. Rev. B* **49**, 6847.
- Held, R., T. Heinzel, P. Studerus, K. Ensslin, and M. Holland, 1997, *Appl. Phys. Lett.* **71**, 2689.
- Hergenrother, J. M., J. G. Lu, M. T. Tuominen, D. C. Ralph, and M. Tinkham, 1995, *Phys. Rev. B* **51**, 9407.
- Herrmann, L. G., F. Portier, P. Roche, A. L. Yeyati, T. Kontos, and C. Strunk, 2010, *Phys. Rev. Lett.* **104**, 026801.
- Hill, T. P., J. Miller, and A. C. Censullo, 2011, *Metrologia* **48**, 83.
- Hoehne, F., Y. A. Pashkin, O. V. Astafiev, M. Möttönen, J. P. Pekola, and J. S. Tsai, 2012, *Phys. Rev. B* **85**, 140504.
- Hofstetter, L., S. Csonka, and J. a. S. C. Nygrd, 2009, *Nature (London)* **461**, 960.
- Hohls, F., A. C. Welker, C. Leicht, L. Fricke, B. Kaestner, P. Mirovsky, A. Müller, K. Pierz, U. Siegner, and H. W. Schumacher, 2011, [arXiv:1103.1746](https://arxiv.org/abs/1103.1746).
- Hollenberg, L. C. L., A. D. Greentree, A. G. Fowler, and C. J. Wellard, 2006, *Phys. Rev. B* **74**, 045311.
- Hongisto, T. T., and A. B. Zorin, 2012, *Phys. Rev. Lett.* **108**, 097001.
- Ingold, G. L., and Y. V. Nazarov, 1992, *Single Charge Tunneling*, NATO ASI Series B, Vol. 294 (Plenum Press, New York), p. 21.
- Isacsson, A., L. Y. Gorelik, M. V. Voinova, B. Kasemo, R. I. Shekhter, and M. Jonson, 1998, *Physica (Amsterdam)* **255B**, 150.
- Jain, A. K., J. E. Lukens, and J. S. Tsai, 1987, *Phys. Rev. Lett.* **58**, 1165.
- Janssen, T. J. B. M., N. E. Fletcher, R. Goebel, J. M. Williams, A. Tzalenchuk, R. Yakimova, S. Kubatkin, S. Lara-Avila, and V. I. Fal'ko, 2011, *New J. Phys.* **13**, 093026.
- Janssen, T. J. B. M., and A. Hartland, 2000a, *Physica (Amsterdam)* **284B–288B**, 1790.
- Janssen, T. J. B. M., and A. Hartland, 2000b, *IEE Proceedings—Science, Measurement and Technology* **147**, 174.

- Janssen, T. J. B. M., and A. Hartland, 2001, *IEEE Trans. Instrum. Meas.* **50**, 227.
- Jarzynski, C., 1997, *Phys. Rev. Lett.* **78**, 2690.
- Jeanneret, B., and S. P. Benz, 2009, *Eur. Phys. J. Special Topics* **172**, 181.
- Jeckelmann, B., and B. Jeanneret, 2001, *Rep. Prog. Phys.* **64**, 1603.
- Jeffery, A.-M., R. Elmquist, L. Lee, J. Shields, and R. Dziuba, 1997, *IEEE Trans. Instrum. Meas.* **46**, 264.
- Jehl, X., M. W. Keller, R. L. Kautz, J. Aumentado, and J. M. Martinis, 2003, *Phys. Rev. B* **67**, 165331.
- Jehl, X., B. Voisin, M. Sanquer, R. Wacquez, and M. Vinet, 2012, unpublished.
- Jensen, H. D., and J. M. Martinis, 1992, *Phys. Rev. B* **46**, 13407.
- Johansson, G., A. Käck, and G. Wendin, 2002, *Phys. Rev. Lett.* **88**, 046802.
- Johansson, J. R., L. G. Mourokh, A. Y. Smirnov, and F. Nori, 2008, *Phys. Rev. B* **77**, 035428.
- Johnson, A. T., L. P. Kouwenhoven, W. de Jong, N. C. van der Vaart, C. J. P. M. Harmans, and C. T. Foxon, 1992, *Phys. Rev. Lett.* **69**, 1592.
- Johnson, J. B., 1928, *Phys. Rev.* **32**, 97.
- Josephson, B. D., 1962, *Phys. Lett.* **1**, 251.
- Kaestner, B., V. Kashcheyevs, S. Amakawa, M. D. Blumenthal, L. Li, T. Janssen, G. Hein, K. Pierz, T. Weimann, U. Siegner, and H. W. Schumacher, 2008, *Phys. Rev. B* **77**, 153301.
- Kaestner, B., V. Kashcheyevs, G. Hein, K. Pierz, U. Siegner, and H. W. Schumacher, 2008, *Appl. Phys. Lett.* **92**, 192106.
- Kaestner, B., C. Leicht, V. Kashcheyevs, K. Pierz, U. Siegner, and H. W. Schumacher, 2009, *Appl. Phys. Lett.* **94**, 012106.
- Kafanov, S., and P. Delsing, 2009, *Phys. Rev. B* **80**, 155320.
- Kafanov, S., A. Kemppinen, Y. A. Pashkin, M. Meschke, J. S. Tsai, and J. P. Pekola, 2009, *Phys. Rev. Lett.* **103**, 120801.
- Kane, B. E., 1998, *Nature (London)* **393**, 133.
- Kane, C. L., and M. P. A. Fisher, 1992, *Phys. Rev. Lett.* **68**, 1220.
- Karshenboim, S. G., 2009, *Eur. Phys. J. Special Topics* **172**, 385.
- Kashcheyevs, V., and B. Kaestner, 2010, *Phys. Rev. Lett.* **104**, 186805.
- Kashcheyevs, V., and J. Timoshenko, 2012, *Phys. Rev. Lett.* **109**, 216801.
- Kastner, M. A., 1993, *Phys. Today* **46**, No. 1, 24.
- Kautz, R. L., M. W. Keller, and J. M. Martinis, 1999, *Phys. Rev. B* **60**, 8199.
- Kautz, R. L., M. W. Keller, and J. M. Martinis, 2000, *Phys. Rev. B* **62**, 15888.
- Kautz, R. L., and F. L. Lloyd, 1987, *Appl. Phys. Lett.* **51**, 2043.
- Kautz, R. L., G. Zimmerli, and J. M. Martinis, 1993, *J. Appl. Phys.* **73**, 2386.
- Keller, M. W., 2008, *Metrologia* **45**, 102.
- Keller, M. W., 2009, *Eur. Phys. J. Special Topics* **172**, 297.
- Keller, M. W., A. L. Eichenberger, J. M. Martinis, and N. M. Zimmerman, 1999, *Science* **285**, 1706.
- Keller, M. W., J. M. Martinis, N. M. Zimmerman, and A. H. Steinbach, 1996, *Appl. Phys. Lett.* **69**, 1804.
- Keller, M. W., F. Piquemal, N. Feltin, B. Steck, and L. Devoille, 2008, *Metrologia* **45**, 330.
- Keller, M. W., N. M. Zimmerman, and A. L. Eichenberger, 2007, *Metrologia* **44**, 505.
- Kemppinen, A., 2009, Ph.D. thesis (Helsinki University of Technology), unpublished.
- Kemppinen, A., S. Kafanov, Y. A. Pashkin, J. S. Tsai, D. V. Averin, and J. P. Pekola, 2009, *Appl. Phys. Lett.* **94**, 172108.
- Kemppinen, A., S. V. Lotkhov, O.-P. Saira, A. B. Zorin, J. P. Pekola, and A. J. Manninen, 2011, *Appl. Phys. Lett.* **99**, 142106.
- Kemppinen, A., M. Meschke, M. Möttönen, D. V. Averin, and J. P. Pekola, 2009, *Eur. Phys. J. Special Topics* **172**, 311.
- Kibble, B. P., 1975, *Atomic Masses and Fundamental Constants* (Plenum, New York), Vol. 5.
- Kim, H. S., H. Qin, and R. H. Blick, 2010, *New J. Phys.* **12**, 033008.
- Knowles, H. S., V. F. Maisi, and J. P. Pekola, 2012, *Appl. Phys. Lett.* **100**, 262601.
- Koenig, D. R., E. M. Weig, and J. P. Kotthaus, 2008, *Nat. Nanotechnol.* **3**, 482.
- Kohlmann, J., R. Behr, and T. Funck, 2003, *Meas. Sci. Technol.* **14**, 1216.
- Kohlmann, J., F. Muller, O. Kieler, R. Behr, L. Palafox, M. Kahmann, and J. Niemeyer, 2007, *IEEE Trans. Instrum. Meas.* **56**, 472.
- Korotkov, A., 1999, *Phys. Rev. B* **60**, 5737.
- Korotkov, A. N., 1994, *Phys. Rev. B* **49**, 10381.
- Korotkov, A. N., and M. A. Paalanen, 1999, *Appl. Phys. Lett.* **74**, 4052.
- Kouwenhoven, L. P., 1992, *Phys. Scr.* **T42**, 133.
- Kouwenhoven, L. P., A. T. Johnson, N. C. van der Vaart, C. J. P. M. Harmans, and C. T. Foxon, 1991a, *Phys. Rev. Lett.* **67**, 1626.
- Kouwenhoven, L. P., A. T. Johnson, N. C. van der Vaart, A. van der Enden, C. J. P. M. Harmans, and C. T. Foxon, 1991b, *Z. Phys. B* **85**, 381.
- Krupenin, V. A., 1998, *J. Appl. Phys.* **84**, 3212.
- Küng, B., C. Rössler, M. Beck, M. Marthaler, D. S. Golubev, Y. Utsumi, T. Ihn, and K. Ensslin, 2012, *Phys. Rev. X* **2**, 011001.
- Kuzmin, L., P. Delsing, T. Claeson, and K. Likharev, 1989, *Phys. Rev. Lett.* **62**, 2539.
- Lafarge, P., P. Joyez, D. Esteve, C. Urbina, and M. H. Devoret, 1993, *Nature (London)* **365**, 422.
- Lafarge, P., H. Pothier, E. Williams, D. Esteve, C. Urbina, and M. Devoret, 1991, *Z. Phys. B* **85**, 327.
- Landau, L., and E. Lifshitz, 1980a, *Electrodynamics of Continuous Media* (Pergamon, New York), Sec. 2.
- Landau, L., and E. Lifshitz, 1980b, *Quantum Mechanics* (Pergamon, New York), Sec. 43.
- Langenberg, D. N., and J. R. Schrieffer, 1971, *Phys. Rev. B* **3**, 1776.
- Lansbergen, G. P., Y. Ono, and A. Fujiwara, 2012, *Nano Lett.* **12**, 763.
- Lansbergen, G. P., R. Rahman, C. J. Wellard, I. Woo, J. Caro, N. Collaert, S. Biesemans, G. Klimeck, L. C. L. Hollenberg, and S. Rogge, 2008, *Nat. Phys.* **4**, 656.
- Laughlin, R. B., 1981, *Phys. Rev. B* **23**, 5632.
- Lehtinen, J. S., K. Zakharov, and K. Yu. Arutyunov, 2012, *Phys. Rev. Lett.* **109**, 187001.
- Leicht, C., P. Mirovsky, B. Kaestner, F. Hols, V. Kashcheyevs, E. V. Kurganova, U. Zeitler, T. Weinmann, K. Pierz, and H. W. Schumacher, 2011, *Semicond. Sci. Technol.* **26**, 055010.
- Leonard, B. P., 2010, *Metrologia* **47**, L5.
- Leone, R., and L. Lévy, 2008, *Phys. Rev. B* **77**, 064524.
- Leone, R., L. P. Lévy, and P. Lafarge, 2008, *Phys. Rev. Lett.* **100**, 117001.
- Li, S., B. Han, Z. Li, and J. Lan, 2012, *Measurement* **45**, 1.
- Likharev, K., 1988, *IBM J. Res. Dev.* **32**, 144.
- Likharev, K., N. Bakhvalov, G. Kazacha, and S. Serdyokova, 1989, *IEEE Trans. Magn.* **25**, 1436.
- Likharev, K. K., 1987, *IEEE Trans. Magn.* **23**, 1142.
- Likharev, K. K., and A. B. Zorin, 1985, *J. Low Temp. Phys.* **59**, 347.
- Lim, W. H., F. A. Zwanenburg, H. Huebl, M. Möttönen, K. W. Chan, A. Morello, and A. S. Dzurak, 2009, *Appl. Phys. Lett.* **95**, 242102.
- Lin, C., and W. Zhang, 2012, *arXiv:1207.0284*.
- Lotkhov, S. V., S. A. Bogoslovsky, A. B. Zorin, and J. Niemeyer, 2001, *Appl. Phys. Lett.* **78**, 946.

- Lotkhov, S. V., O.-P. Saira, J. P. Pekola, and A. B. Zorin, 2011, *New J. Phys.* **13**, 013040.
- Lotkhov, S. V., and A. B. Zorin, 2012, *Appl. Phys. Lett.* **100**, 242601.
- Low, T., Y. Jiang, M. Katsnelson, and F. Guinea, 2012, *Nano Lett.* **12**, 850.
- Lu, W., Z. Ji, L. Pfeiffer, K. W. West, and A. J. Rimberg, 2003, *Nature (London)* **423**, 422.
- Mahan, G., 1990, *Many-particle Physics* (Plenum, New York), Chap. 5.
- Maire, N., F. Hols, B. Kaestner, K. Pierz, H. W. Schumacher, and R. J. Haug, 2008, *Appl. Phys. Lett.* **92**, 082112.
- Maisi, V. F., S. V. Lotkhov, A. Kemppinen, A. Heimes, J. T. Muhonen, and J. P. Pekola, 2012, [arXiv:1212.2755](https://arxiv.org/abs/1212.2755).
- Maisi, V. F., Y. A. Pashkin, S. Kafanov, J. S. Tsai, and J. P. Pekola, 2009, *New J. Phys.* **11**, 113057.
- Maisi, V. F., O.-P. Saira, Y. A. Pashkin, J. S. Tsai, D. V. Averin, and J. P. Pekola, 2011, *Phys. Rev. Lett.* **106**, 217003.
- Makhlín, Y., G. Schön, and A. Shnirman, 2001, *Rev. Mod. Phys.* **73**, 357.
- Manninen, A., *et al.*, 2008, in *CPEM 2008 Digest* (Johnson Printing), p. 630.
- Martiniš, J. M., M. Ansmann, and J. Aumentado, 2009, *Phys. Rev. Lett.* **103**, 097002.
- Martiniš, J. M., and M. Nahum, 1993, *Phys. Rev. B* **48**, 18316.
- Martiniš, J. M., M. Nahum, and H. D. Jensen, 1994, *Phys. Rev. Lett.* **72**, 904.
- Matveev, K. A., and L. I. Glazman, 1993, *Phys. Rev. Lett.* **70**, 990.
- McNeil, R. P. G., M. Kataoka, C. J. B. Ford, C. H. W. Barnes, D. Anderson, G. A. C. Jones, I. Farrer, and D. A. Ritchie, 2011, *Nature (London)* **477**, 439.
- Meschke, M., W. Guichard, and J. P. Pekola, 2006, *Nature (London)* **444**, 187.
- Millikan, R., 1911, *Phys. Rev. (Ser. I)* **32**, 349.
- Mills, I. M., P. J. Mohr, T. J. Quinn, B. N. Taylor, and E. R. Williams, 2005, *Metrologia* **42**, 71.
- Mills, I. M., P. J. Mohr, T. J. Quinn, B. N. Taylor, and E. R. Williams, 2006, *Metrologia* **43**, 227.
- Mills, I. M., P. J. Mohr, T. J. Quinn, B. N. Taylor, and E. R. Williams, 2011, *Phil. Trans. R. Soc. A* **369**, 3907.
- Milton, M. J. T., J. M. Williams, and S. J. Bennett, 2007, *Metrologia* **44**, 356.
- Milton, M. J. T., J. M. Williams, and A. B. Forbes, 2010, *Metrologia* **47**, 279.
- Mirovsky, P., B. Kaestner, C. Leicht, A. C. Welker, T. Weimann, K. Pierz, and H. W. Schumacher, 2010, *Appl. Phys. Lett.* **97**, 252104.
- Mohr, P. J., and B. N. Taylor, 2000, *Rev. Mod. Phys.* **72**, 351.
- Mohr, P. J., and B. N. Taylor, 2005, *Rev. Mod. Phys.* **77**, 1.
- Mohr, P. J., B. N. Taylor, and D. B. Newell, 2008, *Rev. Mod. Phys.* **80**, 633.
- Mohr, P. J., B. N. Taylor, and D. B. Newell, 2012, *Rev. Mod. Phys.* **84**, 1527.
- Mooij, J. E., and C. J. P. M. Harmans, 2005, *New J. Phys.* **7**, 219.
- Mooij, J. E., and Y. V. Nazarov, 2006, *Nat. Phys.* **2**, 169.
- Morello, A., *et al.*, 2010, *Nature (London)* **467**, 687.
- Moskalenko, A. V., S. N. Gordeev, O. F. Koentjoro, P. R. Raithby, F. French, R. W. Marken, and S. E. Savel'ev, 2009a, *Nanotechnology* **20**, 485202.
- Moskalenko, A. V., S. N. Gordeev, O. F. Koentjoro, P. R. Raithby, F. French, R. W. Marken, and S. E. Savel'ev, 2009b, *Phys. Rev. B* **79**, 241403.
- Möttönen, M., J. P. Pekola, J. J. Vartiainen, V. Brosco, and F. W. J. Hekking, 2006, *Phys. Rev. B* **73**, 214523.
- Möttönen, M., J. J. Vartiainen, and J. P. Pekola, 2008, *Phys. Rev. Lett.* **100**, 177201.
- Naaman, O., and J. Aumentado, 2006, *Phys. Rev. Lett.* **96**, 172504.
- Nadj-Perge, S., S. M. Frolov, E. P. A. M. Bakkers, and L. P. Kouwenhoven, 2010, *Nature (London)* **468**, 1084.
- Nagamune, Y., H. Sakaki, L. P. Kouwenhoven, L. C. Mur, C. J. P. M. Harmans, J. Motohisa, and H. Noge, 1994, *Appl. Phys. Lett.* **64**, 2379.
- Nakamura, Y., Y. A. Pashkin, and J. S. Tsai, 1999, *Nature (London)* **398**, 786.
- Nevou, L., V. Liverini, F. Castellano, A. Bismuto, and J. Faist, 2010, *Appl. Phys. Lett.* **97**, 023505.
- Nevou, L., V. Liverini, P. Friedli, F. Castellano, A. Bismuto, H. Sigg, F. Gramm, E. Müller, and J. Faist, 2011, *Nat. Phys.* **7**, 423.
- Nguyen, F., N. Boulant, G. Ithier, P. Bertet, H. Pothier, D. Vion, and D. Esteve, 2007, *Phys. Rev. Lett.* **99**, 187005.
- Nishiguchi, K., A. Fujiwara, Y. Ono, H. Inokawa, and Y. Takahashi, 2006, *Appl. Phys. Lett.* **88**, 183101.
- Niskanen, A. O., J. M. Kivioja, H. Seppä, and J. P. Pekola, 2005, *Phys. Rev. B* **71**, 012513.
- Niskanen, A. O., J. P. Pekola, and H. Seppä, 2003, *Phys. Rev. Lett.* **91**, 177003.
- Nordtvedt, K., 1970, *Phys. Rev. B* **1**, 81.
- Novoselov, K. S., Z. Jiang, Y. Zhang, S. V. Morozov, H. L. Stormer, U. Zeitler, J. C. Maan, G. S. Boebinger, P. Kim, and A. K. Geim, 2007, *Science* **315**, 1379.
- Nyquist, H., 1928, *Phys. Rev.* **32**, 110.
- Odintsov, A. A., V. Bujanja, and G. Schön, 1992, *Phys. Rev. B* **46**, 6875.
- Ohlsson, B. J., M. T. Björk, A. I. Persson, C. Thelander, L. R. Wallenberg, M. H. Magnusson, K. Deppert, and L. Samuelson, 2002, *Physica (Amsterdam)* **13E**, 1126.
- O'Neil, G. C., P. J. Lowell, J. M. Underwood, and J. N. Ullom, 2011, [arXiv:1109.1273v1](https://arxiv.org/abs/1109.1273v1).
- Ono, Y., A. Fujiwara, K. Nishiguchi, H. Inokawa, and Y. Takahashi, 2005, *J. Appl. Phys.* **97**, 031101.
- Ono, Y., and Y. Takahashi, 2003, *Appl. Phys. Lett.* **82**, 1221.
- Ono, Y., N. M. Zimmerman, K. Yamazaki, and Y. Takahashi, 2003, *Jpn. J. Appl. Phys.* **42**, L1109.
- Park, H., J. Park, A. K. L. Lim, E. H. Anderson, A. P. Alivisatos, and P. L. McEuen, 2000, *Nature (London)* **407**, 57.
- Pekola, J. P., D. V. Anghel, T. I. Suppala, J. K. Suoknuuti, A. J. Manninen, and M. Manninen, 2000, *Appl. Phys. Lett.* **76**, 2782.
- Pekola, J. P., and F. W. J. Hekking, 2007, *Phys. Rev. Lett.* **98**, 210604.
- Pekola, J. P., V. F. Maisi, S. Kafanov, N. Chekurov, A. Kemppinen, Y. A. Pashkin, O.-P. Saira, M. Möttönen, and J. S. Tsai, 2010, *Phys. Rev. Lett.* **105**, 026803.
- Pekola, J. P., J. J. Toppari, M. Aunola, M. T. Savolainen, and D. V. Averin, 1999, *Phys. Rev. B* **60**, R9931.
- Pekola, J. P., J. J. Vartiainen, M. Möttönen, O.-P. Saira, M. Meschke, and D. V. Averin, 2008, *Nat. Phys.* **4**, 120.
- Peltonen, J. T., J. T. Muhonen, M. Meschke, N. B. Kopnin, and J. P. Pekola, 2011, *Phys. Rev. B* **84**, 220502.
- Pendry, J. B., 1983, *J. Phys. A* **16**, 2161.
- Penin, A. A., 2009, *Phys. Rev. B* **79**, 113303.
- Penin, A. A., 2010a, *Phys. Rev. B* **81**, 089902.
- Penin, A. A., 2010b, *Phys. Rev. Lett.* **104**, 097003.
- Pettersson, J., P. Wahlgren, P. Delsing, D. Haviland, T. Claeson, N. Rorsman, and H. Zirath, 1996, *Phys. Rev. B* **53**, R13272.
- Piquemal, F., 2004, *C.R. Phys.* **5**, 857.
- Piquemal, F., and G. Geneves, 2000, *Metrologia* **37**, 207.
- Pirkkalainen, J.-M., P. Solinas, J. P. Pekola, and M. Möttönen, 2010, *Phys. Rev. B* **81**, 174506.

- Poirier, W., and F. Schopfer, 2009, *Eur. Phys. J. Special Topics* **172**, 207.
- Poirier, W., F. Schopfer, J. Guignard, O. Thévenot, and P. Gournay, 2011, *C.R. Phys.* **12**, 347.
- Pop, I. M., I. Protopopov, F. Lecocq, Z. Peng, B. Pannetier, O. Buisson, and W. Guichard, 2010, *Nat. Phys.* **6**, 589.
- Pothier, H., 1991, Ph.D. thesis (University of Paris 6), unpublished.
- Pothier, H., S. Guéron, D. Esteve, and M. H. Devoret, 1994, *Phys. Rev. Lett.* **73**, 2488.
- Pothier, H., P. Lafarge, P. F. Orfila, C. Urbina, D. Esteve, and M. H. Devoret, 1991, *Physica (Amsterdam)* **169B**, 573.
- Pothier, H., P. Lafarge, C. Urbina, D. Esteve, and M. H. Devoret, 1992, *Europhys. Lett.* **17**, 249.
- Prêtre, A., H. Thomas, and M. Büttiker, 1996, *Phys. Rev. B* **54**, 8130.
- Prunnila, M., M. Meschke, D. Gunnarsson, S. Enouz-Vedrenne, J. M. Kivioja, and J. P. Pekola, 2010, *J. Vac. Sci. Technol. B* **28**, 1026.
- Qin, H., and D. A. Williams, 2006, *Appl. Phys. Lett.* **88**, 203506.
- Quinn, T. J., 1991, *IEEE Trans. Instrum. Meas.* **40**, 81.
- Rajauria, S., H. Courtois, and B. Pannetier, 2009, *Phys. Rev. B* **80**, 214521.
- Rajauria, S., P. Gandit, T. Fournier, F. W. J. Hekking, B. Pannetier, and H. Courtois, 2008, *Phys. Rev. Lett.* **100**, 207002.
- Reed, M. A., J. N. Randall, R. J. Aggarwal, R. J. Matyi, T. M. Moore, and A. E. Wetsel, 1988, *Phys. Rev. Lett.* **60**, 535.
- Reiman, S. M., and M. Manninen, 2002, *Rev. Mod. Phys.* **74**, 1283.
- Roche, B., R.-P. Riwar, B. Voisin, E. Dupont-Ferrier, R. Wacquez, M. Vinet, M. Sanquer, J. Splettstoesser, and X. Jehl, 2012, [arXiv:1212.1142](https://arxiv.org/abs/1212.1142).
- Roschier, L., R. Tarkiainen, M. Ahlskog, M. Paalanen, and P. Hakonen, 2001, *Appl. Phys. Lett.* **78**, 3295.
- Rothwarf, A., and B. N. Taylor, 1967, *Phys. Rev. Lett.* **19**, 27.
- Rüfenacht, A., B. Jeanneret, and S. V. Lotkhov, 2010, in *CPEM 2010 Digest* (CPEM, Korea), p. 498.
- Sacépé, B., C. Chapelier, T. I. Baturina, V. M. Vinokur, M. R. Baklanov, and M. Sanquer, 2010, *Nat. Commun.* **1**, 140.
- Sacépé, B., T. Dubouchet, C. Chapelier, M. Sanquer, M. Ovidia, D. Shahar, M. Feigel'man, and L. Ioffe, 2011, *Nat. Phys.* **7**, 239.
- Saira, O.-P., A. Kemppinen, V. F. Maisi, and J. P. Pekola, 2012, *Phys. Rev. B* **85**, 012504.
- Saira, O.-P., M. Möttönen, V. F. Maisi, and J. P. Pekola, 2010, *Phys. Rev. B* **82**, 155443.
- Saira, O.-P., Y. Yoon, T. Tanttu, M. Möttönen, D. V. Averin, and J. P. Pekola, 2012, *Phys. Rev. Lett.* **109**, 180601.
- Savin, A. M., J. P. Pekola, D. V. Averin, and V. K. Semenov, 2006, *J. Appl. Phys.* **99**, 084501.
- Scherer, H., and B. Camarota, 2012, *Meas. Sci. Technol.* **23**, 124010.
- Scherer, H., B. Camarota, M. W. Keller, and S. V. Lotkhov, 2012, unpublished.
- Schinner, G. J., H. P. Tranitz, W. Wegscheider, J. P. Kotthaus, and S. Ludwig, 2009, *Phys. Rev. Lett.* **102**, 186801.
- Schmidt, D. R., R. J. Schoelkopf, and A. N. Cleland, 2004, *Phys. Rev. Lett.* **93**, 045901.
- Schoelkopf, R. J., P. Wahlgren, A. A. Kozhevnikov, P. Delsing, and D. E. Prober, 1998, *Science* **280**, 1238.
- Schön, G., and A. Zaikin, 1994, *Europhys. Lett.* **26**, 695.
- Schurr, J., J. Kučera, K. Pierz, and B. P. Kibble, 2011, *Metrologia* **48**, 47.
- Sese, J., *et al.*, 1999, *IEEE Trans. Instrum. Meas.* **48**, 370.
- Shapere, A., and F. Wilczek, 1989, *Geometric Phases in Physics* (World Scientific, Singapore).
- Shapiro, S., 1963, *Phys. Rev. Lett.* **11**, 80.
- Shekhter, R. I., Y. Galperin, L. Y. Gorelik, A. Isacsson, and M. Jonson, 2003, *J. Phys. Condens. Matter* **15**, R441.
- Shilton, J. M., D. R. Mace, V. I. Talyanskii, Y. Galperin, M. Y. Simmons, M. Pepper, and D. A. Ritchie, 1996, *J. Phys. Condens. Matter* **8**, L337.
- Shilton, J. M., V. I. Talyanskii, M. Pepper, D. A. Ritchie, J. E. F. Frost, C. J. B. Ford, C. G. Smith, and G. A. C. Jones, 1996, *J. Phys. Condens. Matter* **8**, L531.
- Shimada, H., and Y. Ootuka, 2001, *Phys. Rev. B* **64**, 235418.
- Sillanpää, M. A., L. Roschier, and P. J. Hakonen, 2004, *Phys. Rev. Lett.* **93**, 066805.
- Sohn, L. L., L. P. Kouwenhoven, and G. Schön, 1997, Eds., *Mesoscopic Electron Transport* (Kluwer, Dordrecht).
- Solinas, P., J.-M. Pirkkalainen, and M. Möttönen, 2010, *Phys. Rev. A* **82**, 052304.
- Starmark, B., T. Henning, T. Claeson, P. Delsing, and A. N. Korotkov, 1999, *J. Appl. Phys.* **86**, 2132.
- Steele, A. G., J. Meija, C. A. Sanchez, L. Yang, B. M. Wood, R. E. Sturgeon, Z. Mester, and A. D. Inglis, 2012, *Metrologia* **49**, L8.
- Steiner, R., 2013, *Rep. Prog. Phys.* **76**, 016101.
- Steiner, R., E. R. Williams, D. B. Newell, and R. Lui, 2007, *IEEE Trans. Instrum. Meas.* **56**, 592.
- Stock, M., 2013, *Metrologia* **50**, R1.
- Stock, M., and T. J. Witt, 2006, *Metrologia* **43**, 583.
- Su, B., V. J. Goldman, and J. E. Cunningham, 1992, *Science* **255**, 313.
- Takahashi, Y., M. Nagase, H. Namatsu, K. Kurihara, K. Iwadate, Y. Nakajima, S. Horiguchi, K. Murase, and M. Tabe, 1995, *Electron. Lett.* **31**, 136.
- Talyanskii, V. I., J. M. Shilton, M. Pepper, C. G. Smith, C. J. B. Ford, E. H. Linfield, D. A. Ritchie, and G. A. C. Jones, 1997, *Phys. Rev. B* **56**, 15 180.
- Tan, K. Y., K. W. Chan, M. Möttönen, A. Morello, C. Yang, J. van Donkelaar, A. Alves, J.-M. Pirkkalainen, D. N. Jamieson, R. G. Clark, and A. S. Dzurak, 2010, *Nano Lett.* **10**, 11.
- Tan, Z., V. Patel, X. Liu, J. Lukens, K. Likharev, and Y. Zhu, 2008, *Appl. Phys. Lett.* **93**, 242109.
- Tarucha, S., D. G. Austing, T. Honda, R. J. van der Hage, and L. P. Kouwenhoven, 1996, *Phys. Rev. Lett.* **77**, 3613.
- Thompson, A. M., and D. G. Lampard, 1956, *Nature (London)* **177**, 888.
- Thornton, T., M. Pepper, H. Ahmed, D. Andrews, and G. Davies, 1986, *Phys. Rev. Lett.* **56**, 1198.
- Thouless, D. J., M. Kohmoto, M. P. Nightingale, and M. den Nijs, 1982, *Phys. Rev. Lett.* **49**, 405.
- Timofeev, A. V., C. P. Garcia, N. B. Kopnin, A. M. Savin, M. Meschke, F. Giazotto, and J. P. Pekola, 2009, *Phys. Rev. Lett.* **102**, 017003.
- Timofeev, A. V., M. Helle, M. Meschke, M. Möttönen, and J. P. Pekola, 2009, *Phys. Rev. Lett.* **102**, 200801.
- Tinkham, M., 1996, *Introduction to Superconductivity* (McGraw-Hill, New York), 2nd ed.
- Toppari, J. J., J. M. Kivioja, J. P. Pekola, and M. T. Savolainen, 2004, *J. Low Temp. Phys.* **136**, 57.
- Tsai, J.-S., A. K. Jain, and J. E. Lukens, 1983, *Phys. Rev. Lett.* **51**, 1109.
- Tsukagoshi, K., B. W. Alphenaar, and K. Nakazato, 1998, *Appl. Phys. Lett.* **73**, 2515.
- Tsukagoshi, K., K. Nakazato, H. Ahmed, and K. Gamo, 1997, *Phys. Rev. B* **56**, 3972.
- Tuominen, M. T., J. M. Hergenrother, T. S. Tighe, and M. Tinkham, 1992, *Phys. Rev. Lett.* **69**, 1997.
- Tuominen, M. T., R. V. Krotkov, and M. I. Breuer, 1999, *Phys. Rev. Lett.* **83**, 3025.

- Turek, B. A., K. W. Lehnert, A. Clerk, D. Gunnarsson, K. Bladh, P. Delsing, and R. J. Schoelkopf, 2005, *Phys. Rev. B* **71**, 193304.
- Tzalenchuk, A., S. Lara-Avila, A. Kalaboukhov, S. Paolillo, M. Syvajarvi, R. Yakimova, O. Kazakova, T. J. B. M. Janssen, V. Fal'ko, and S. Kubatkin, 2010, *Nat. Nanotechnol.* **5**, 186.
- Ullom, J. N., P. A. Fisher, and M. Nahum, 1998, *Phys. Rev. B* **58**, 8225.
- Utko, P., P. E. Lindelof, and K. Gloos, 2006, *Appl. Phys. Lett.* **88**, 202113.
- Vandersypen, L. M. K., J. M. Elzerman, R. N. Schouten, L. H. Willems van Beveren, R. Hanson, and L. P. Kouwenhoven, 2004, *Appl. Phys. Lett.* **85**, 4394.
- van der Wiel, W. G., S. D. Franceschi, J. M. Elzerman, T. Fujisawa, S. Tarucha, and L. Kouwenhoven, 2002, *Rev. Mod. Phys.* **75**, 1.
- Vartiainen, J. J., M. Möttönen, J. P. Pekola, and A. Kemppinen, 2007, *Appl. Phys. Lett.* **90**, 082102.
- Visscher, E. H., J. Lindeman, S. M. Verbrugh, P. Hadley, J. E. Mooij, and W. van der Vleuten, 1996, *Appl. Phys. Lett.* **68**, 2014.
- von Klitzing, K., G. Dorda, and M. Pepper, 1980, *Phys. Rev. Lett.* **45**, 494.
- Wei, J., and V. Chandrasekhar, 2010, *Nat. Phys.* **6**, 494.
- Weis, J., and K. von Klitzing, 2011, *Phil. Trans. R. Soc. A* **369**, 3954.
- Weiss, C., and W. Zwerger, 1999, *Europhys. Lett.* **47**, 97.
- Wellstood, F. C., C. Urbina, and J. Clarke, 1994, *Phys. Rev. B* **49**, 5942.
- White, J. D., and M. Wagner, 1993, *Phys. Rev. B* **48**, 2799.
- Williams, E. R., R. N. Ghosh, and J. M. Martinis, 1992, *J. Res. Natl. Inst. Stand. Technol.* **97**, 299.
- Wood, B. M., and S. Solve, 2009, *Metrologia* **46**, R13.
- Wright, S. J., M. D. Blumenthal, G. Gumbs, A. L. Thorn, M. Pepper, T. Janssen, S. N. Holmes, D. Anderson, G. Jones, C. A. Nicoll, and D. A. Ritchie, 2008, *Phys. Rev. B* **78**, 233311.
- Wright, S. J., M. D. Blumenthal, M. Pepper, D. Anderson, G. A. C. Jones, C. A. Nicoll, and D. A. Ritchie, 2009, *Phys. Rev. B* **80**, 113303.
- Wulf, M., 2012, [arXiv:1209.1020](https://arxiv.org/abs/1209.1020).
- Xue, W. W., Z. Ji, F. Pan, J. Stettenheim, M. P. Blencowe, and A. J. Rimberg, 2009, *Nat. Phys.* **5**, 660.
- Yamahata, G., K. Nishiguchi, and A. Fujiwara, 2011, *Appl. Phys. Lett.* **98**, 222104.
- Yang, L., Z. Mester, R. E. Sturgeon, and J. Meija, 2012, *Anal. Chem.* **84**, 2321.
- Young, C. E., and A. A. Clerk, 2010, *Phys. Rev. Lett.* **104**, 186803.
- Yuan, M., F. Pan, Z. Yang, T. J. Gilheart, F. Chen, D. E. Savage, M. G. Lagally, M. A. Eriksson, and A. J. Rimberg, 2011, *Appl. Phys. Lett.* **98**, 142104.
- Zaikin, A. D., 1994, *Physica (Amsterdam)* **203B**, 255.
- Zanardi, P., and M. Rasetti, 1999, *Phys. Lett. A* **264**, 94.
- Zhang, Y., Y.-W. Tan, H. L. Stormer, and P. Kim, 2005, *Nature (London)* **438**, 201.
- Zimmerli, G., T. M. Eiles, R. L. Kautz, and J. M. Martinis, 1992, *Appl. Phys. Lett.* **61**, 237.
- Zimmerman, N. M., E. Hourdakis, Y. Ono, A. Fujiwara, and Y. Takahashi, 2004, *J. Appl. Phys.* **96**, 5254.
- Zimmerman, N. M., and M. W. Keller, 2003, *Meas. Sci. Technol.* **14**, 1237.
- Zimmerman, N. M., B. J. Simonds, and Y. Wang, 2006, *Metrologia* **43**, 383.
- Zorin, A. B., 1996, *Phys. Rev. Lett.* **76**, 4408.
- Zorin, A. B., 2001, *Phys. Rev. Lett.* **86**, 3388.
- Zorin, A. B., S. V. Lotkhov, H. Zangerle, and J. Niemeyer, 2000, *J. Appl. Phys.* **88**, 2665.

# Publication IX

V. F. Maisi, S. V. Lotkhov, A. Kemppinen, A. Heimes, J. T. Muhonen and J. P. Pekola. Excitation of Single Quasiparticles in a Small Superconducting Al Island Connected to Normal-Metal Leads by Tunnel Junctions. *Phys. Rev. Lett.* **111**, 147001 (2013).

© (2013) American Physical Society.

Reprinted with permission.



## Excitation of Single Quasiparticles in a Small Superconducting Al Island Connected to Normal-Metal Leads by Tunnel Junctions

V. F. Maisi,<sup>1,2,\*</sup> S. V. Lotkhov,<sup>3</sup> A. Kemppinen,<sup>2</sup> A. Heimes,<sup>4</sup> J. T. Muhonen,<sup>1,5</sup> and J. P. Pekola<sup>1</sup>

<sup>1</sup>Low Temperature Laboratory (OVLL), Aalto University School of Science, P.O. Box 13500, 00076 Aalto, Finland

<sup>2</sup>Centre for Metrology and Accreditation (MIKES), P.O. Box 9, 02151 Espoo, Finland

<sup>3</sup>Physikalisch-Technische Bundesanstalt, Bundesallee 100, 38116 Braunschweig, Germany

<sup>4</sup>Institut für Theoretische Festkörperphysik, Karlsruher Institut für Technologie, Wolfgang-Gaede-Strasse 1, D-76128 Karlsruhe, Germany

<sup>5</sup>Centre for Quantum Computation and Communication Technology, School of Electrical Engineering and Telecommunications, University of New South Wales, Sydney, New South Wales 2052, Australia

(Received 22 January 2013; published 3 October 2013)

We investigate the dynamics of individual quasiparticle excitations on a small superconducting aluminum island connected to normal metallic leads by tunnel junctions. We find the island to be free of excitations within the measurement resolution. This allows us to show that the residual heating, which typically limits experiments on superconductors, has an ultralow value of less than 0.1 aW. By injecting electrons with a periodic gate voltage, we probe electron-phonon interaction and relaxation down to a single quasiparticle excitation pair, with a measured recombination rate of 16 kHz. Our experiment yields a strong test of BCS theory in aluminum as the results are consistent with it without free parameters.

DOI: [10.1103/PhysRevLett.111.147001](https://doi.org/10.1103/PhysRevLett.111.147001)

PACS numbers: 74.78.Na, 74.20.Rp, 74.25.Kc, 74.40.Gh

The quasiparticle excitations describing the microscopic degrees of freedom in superconductors freeze out at low temperatures, provided no energy exceeding the superconductor gap  $\Delta$  is available. Early experiments on these excitations were performed typically close to the critical temperature with large structures so that  $N_S$ , the number of quasiparticle excitations, was high [1–9]. Later on, as the fabrication techniques progressed, it became possible to bring  $N_S$  close to unity to reveal the parity effect of electrons on a superconducting island [10–14]. In recent years, the tunneling and relaxation dynamics of quasiparticles, which we address in this Letter, have become a topical subject because of their influence on practically all superconducting circuits in the low temperature limit [15–22].

We study the quasiparticle excitations on a small aluminum island shown in Fig. 1(a). The island is connected via a thin insulating aluminum oxide layer to two normal metallic copper leads to form a single-electron transistor (SET) allowing quasiparticle tunneling. By measuring the tunnel current against source-drain bias voltage  $V_b$  and offset charge  $n_g$  of the island, we first show that the island can be cooled down to have essentially no quasiparticle excitations. Then we intentionally inject excitations to the superconductor and probe electron-phonon interaction, the inherent relaxation mechanism of a superconductor, down to a single quasiparticle pair.

The current  $I$  through the SET is governed by sequential tunneling of single quasiparticles and it exhibits Coulomb diamonds which overlap each other because of the superconductor energy gap [23,24], observed for our structure as a region bounded by the red sawtooths in Fig. 1(b). In the subgap regime,  $|eV_b| < 2\Delta$ , the current should be

suppressed if there are no quasiparticle excitations present. Nonetheless, we observe a finite current which has a period twice as long in  $n_g$  as compared to the high bias region, a unique feature of a superconducting island due to Cooper

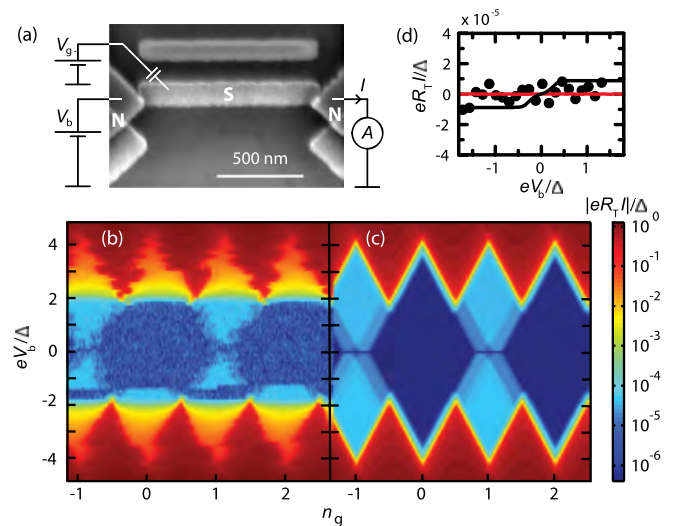


FIG. 1 (color online). (a) Scanning electron micrograph of the sample studied. It is biased with voltage  $V_b$  and a gate offset voltage  $V_g$  is applied to a gate electrode (not shown) to obtain a gate offset charge  $n_g = C_g V_g / e$ , where  $C_g$  is the gate-island capacitance. (b) Measured source-drain current  $I$  as a function of bias and gate voltages. (c) Calculated current based on sequential single-electron tunneling model. (d) Measured current at  $n_g = 0$  is shown as black dots. Black line is calculated assuming a quasiparticle generation rate of 2 kHz, and the red line is calculated assuming a vanishing generation rate.

pairing of electrons. The current is caused by a single electron unable to pair in the condensate and hence remaining as an excitation. This parity effect has been observed in the past in similar structures [11–13] but typically with two-electron Andreev tunneling being the main transport process. We focus on devices where Andreev current is suppressed by large charging energy,  $E_c > \Delta$ , which makes two-electron tunneling energetically unfavorable compared to that of a single quasiparticle [24–26]. In this case, the transport is dominated by single-electron processes allowing simple and direct probing of the quasiparticle excitations without the interfering multielectron tunneling.

For a quantitative description of the transport characteristics, we performed a numerical simulation of the device operation shown in Fig. 1(c). To describe simultaneously the charging of the island with electrons and the excitations involved in the superconducting state, we assign the probability  $P(N, N_S)$  for having  $N$  excess electrons and  $N_S$  quasiparticle excitations on the island. The time evolution of  $P(N, N_S)$  is described by a master equation

$$\frac{d}{dt}P(N, N_S) = \sum_{N', N'_S} \Gamma_{N' \rightarrow N, N'_S \rightarrow N_S} P(N', N'_S), \quad (1)$$

where  $\Gamma_{N' \rightarrow N, N'_S \rightarrow N_S}$  is the transition rate from  $N', N'_S$  to  $N, N_S$ . For  $N' = N, N'_S = N_S$  we insert a rate  $\Gamma_{N \rightarrow N, N_S \rightarrow N_S} = -\sum_{N', N'_S} \Gamma_{N \rightarrow N', N_S \rightarrow N'_S}$ , which is a sum of all rates out from the state  $(N, N_S)$ . These rates are set by electron tunneling between the island and the leads, Cooper pair breaking, and recombination of quasiparticles.

Tunneling rates are calculated by the standard first order perturbation theory [23–26]. Electrons tunneling into the superconducting island to states with energy  $E > \Delta$  in the semiconductor model [27] increase the quasiparticle number  $N_S$  and electron number  $N$  by one. Electrons tunneling to states  $E < -\Delta$  increase  $N$  and decrease  $N_S$  by one by filling a hole. Similarly, electrons tunneling out from  $E > \Delta$  decrease both  $N$  and  $N_S$  while electrons from states  $E < -\Delta$  increase  $N_S$  and decrease  $N$ . For a detailed description of these rates, see the Supplemental Material [28].

The tunneling rates depend on  $N_S$ , which is the number of excited quasiparticle states on the superconducting island. The nonequilibrium quasiparticle distribution function  $f_S(E)$  gives the probability that such a quasiparticle state with energy  $E$  is occupied. In general,  $f_S$  has a complicated form as a function of energy. However, due to the fact that quasiparticles are injected close to the gap, the resulting tunneling and recombination are not sensitive to the functional form of  $f_S$ . Because of symmetry, branch imbalance [3,27] is not created in our system and therefore we parametrize the quasiparticle number by an effectively increased temperature  $T_S$  and a Fermi distribution in the case of  $f_S$ . This gives the relation

$$N_S = \sqrt{2\pi} D(E_F) V \sqrt{\Delta k_B T_S} e^{-\Delta/k_B T_S}, \quad (2)$$

where  $D(E_F) = 1.45 \times 10^{47} \text{ J}^{-1} \text{ m}^{-3}$  is the density of states in the normal state [29] and  $V$  the volume of the island. For the normal metallic leads we use Fermi distribution with  $T_N = 60 \text{ mK}$ , equal to the base temperature of the cryostat.

For the steady-state represented by Fig. 1(c), we solve Eq. (1) with  $(d/dt)P(N, N_S) = 0$  and calculate the current as an average of the tunneling rates weighted by the probabilities  $P(N, N_S)$ . The parameter values of sample A,  $E_c = 240 \text{ } \mu\text{eV}$ ,  $\Delta = 210 \text{ } \mu\text{eV}$ , and tunneling resistances  $R_{T1} = 220 \text{ k}\Omega$  and  $R_{T2} = 150 \text{ k}\Omega$  for the two junctions were used in the simulations. They were determined from measurements in the high bias regime ( $|eV_b| > 2\Delta$ ) and hence their values are independent of the subgap features.

The simulation of Fig. 1(c) reproduces the behavior observed in the experiments. The relaxation rate of a single quasiparticle excitation in or out from the island via tunneling is expected to be  $\Gamma_{\text{qp}} \equiv \Gamma_{N+1 \rightarrow N, 1 \rightarrow 0} = [2e^2 R_T D(E_F) V]^{-1} = 190 \text{ kHz}$ , where we have used the measured dimensions for  $V = 1.06 \text{ } \mu\text{m} \times 145 \text{ nm} \times 25 \text{ nm}$ .  $R_T^{-1}$  is the average of the two conductances  $R_{T1}^{-1}$  and  $R_{T2}^{-1}$ . This rate reflects the injection,  $\propto R_T^{-1}$ , in a system with the number of states per energy being  $D(E_F)V$ . From the fit in the subgap regime, we obtain  $\Gamma_{\text{qp}} = 150 \text{ kHz}$ , consistent with the prediction. The value of  $\Gamma_{\text{qp}}$  affects only the value of current on the light blue plateau of Fig. 1(c), not the actual form or size of the terrace. As our simulation based on sequential tunneling reproduces all the features in the subgap regime, we confirm that the two-electron periodicity originates from single-electron tunneling and the operation is essentially free of multielectron tunneling processes. At odd integer values of  $n_g$ , the characteristic feature of Andreev tunneling would be a linear-in- $V_b$  current at low bias voltages and a subsequent drop [12,30], which is absent in our data. The leakage current in the subgap region does not vanish even in the zero temperature limit but remains essentially the same as presented in Fig. 1. Therefore, all quasiparticle excitations cannot be suppressed at finite bias voltages by lowering the temperature, if  $n_g$  is close to an odd integer. At  $|eV_b| > 2\Delta$ , incoherent cotunneling is activated, which we do not consider here. Also in Fig. 1(b), there is a change of parity,  $\Delta n_g = 1$ , once during the measurement due to an unknown reason [12].

At even integer values of  $n_g$ , we have ideally no current flow as all electrons are paired. If Cooper pair breaking would take place on the island with rate  $\Gamma_e \equiv \Gamma_{N \rightarrow N, 0 \rightarrow 2}$ , we would obtain two quasiparticle excitations in the superconductor. One of these excitations can then relax by tunneling to the leads followed by tunneling of a new excitation to neutralize the offset charge, similarly to the odd  $n_g$  case described above. This cycle would continue until the two quasiparticles recombine to a Cooper pair. As the recombination rate  $\Gamma_{\text{rec}} = \Gamma_{N \rightarrow N, 2 \rightarrow 0} = 16 \text{ kHz}$ , discussed below, is slower than the rates in the cycle, we have

several electrons tunneling through the device for each broken pair, hence amplifying the signal. The resulting current through the SET is then  $I/e = 4\Gamma_{qp}\Gamma_e/(\Gamma_{rec} + \Gamma_e)$ , where  $4\Gamma_{qp}$  is the tunneling rate of the two quasiparticles to the forward direction for the two junctions and  $\Gamma_e/(\Gamma_{rec} + \Gamma_e)$  the probability to be in the state with  $N_S = 2$ . Therefore, at low excitation rates,  $\Gamma_e \ll \Gamma_{rec}$ , on average  $4\Gamma_{qp}/\Gamma_{rec} = 40$  electrons tunnel through the device for each broken pair. With this model, we obtain an upper bound  $\Gamma_e = 2$  kHz for the pair breaking rate under our experimental conditions based on simulations shown in Fig. 1(d). This rate corresponds to energy absorption at less than  $2\Gamma_e\Delta = 0.1$  aW power on the superconducting island. It is in agreement with expectations: The SET is protected against high frequency photons causing pair breaking with an indium sealed Faraday cage. Also, the pair breaking caused by phonons is expected to be orders of magnitude smaller than the determined upper bound.

Under constant biasing conditions, there is at most one quasiparticle present in the subgap regime at low temperatures. The nontunneling relaxation on the island is then not possible, since recombination would call for two excitations. Therefore, the static case can be described by pure tunneling without other relaxation processes. To study recombination of two quasiparticles into a Cooper pair, we injected intentionally more quasiparticles to the island. The injection was done by a periodic drive of the gate voltage. By changing  $n_g$ , we change the potential of the superconducting island and either pull quasiparticle excitations into the island when the potential is lowered or create hole-type excitations as potential is raised and quasiparticles tunnel out. The number of injected quasiparticles and the number of quasiparticles on the island can then be determined from the resulting current curves with the help of simulations. In the experiment we approach two different limits which we will discuss in the following: When the pumping frequency is high,  $N_S$  is large. Such a situation can be described by a *thermal model*, i.e., by an increased time-independent effective temperature of the superconducting island. In the opposite limit of low frequency,  $N_S$  is small. Then the thermal model fails and we have to account for the exact time-dependent number of quasiparticles.

In Fig. 2(a) we show the measured current for three different values of bias voltage  $V_b$ . The gate drive is sinusoidal around  $n_g = 1/2$  with amplitude  $A_g$  expressed in units of  $e/C_g$  and frequency  $f = 1$  MHz corresponding to fast pumping. Without accumulation of quasiparticles to the island, the current would show quantized plateaus with spacing  $ef$ , similar to the hybrid turnstile [23]. In the curves of Fig. 2 we show the amplitude region where the first plateau with  $I = ef$  should form. The plateaulike regime within  $0 < A_g < 1$  corresponds approximately to the amplitude range of a Coulomb diamond in the stability diagram of the SET. As the island has a surplus of

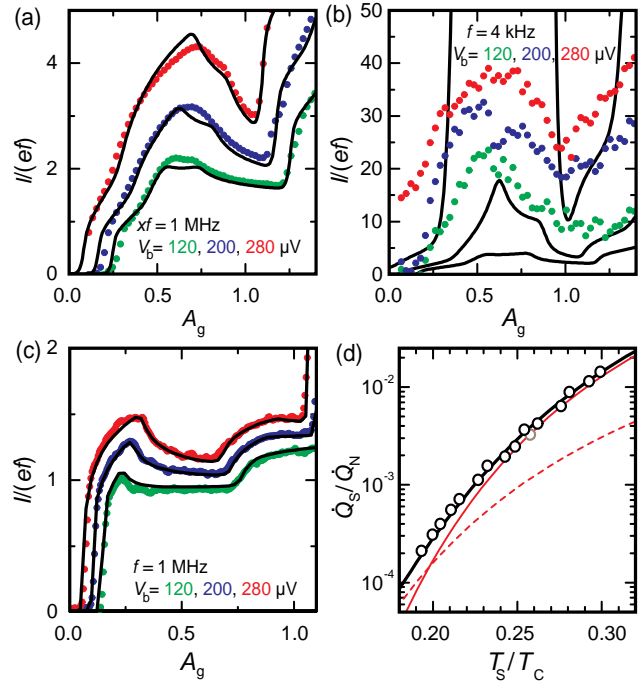


FIG. 2 (color online). (a),(b) Measured current of sample A against gate voltage amplitude  $A_g$  at  $f = 4$  and  $1000$  kHz at bias voltage values  $V_b = 120, 200, 280 \mu\text{V}$  shown as blue, red, and green dots, respectively. Black lines show simulations assuming an elevated temperature on the superconducting island. (c) Similar measurement for sample B at  $f = 1$  MHz. (d) The electron-phonon heat flux in the superconducting state normalized by that in the normal state extracted from the measurements (black circles). Temperature is expressed with respect to the critical temperature  $T_C = \Delta/1.76k_B$ . The theoretical result of Eq. (3) is shown by the black line. Solid and dotted red lines show the recombination and scattering part of Eq. (3) correspondingly. The open gray symbol is from sample B.

quasiparticles, i.e., it is heated up, the current at the plateau area is substantially higher than  $ef$  and even nonmonotonic. The nonmonotonic behavior arises as the system stays part of the cycle, towards large values of  $A_g$ , in the state ( $N = 2, N_S = 0$ ), where no current flows (for the case  $E_c \sim \Delta$ ), or Coulomb blockade forbids quasiparticle relaxation by tunneling at certain gate values (for  $E_c \sim 2\Delta$ ). We now use the thermal model where the heat injection to the island by electron tunneling is balanced by electron-phonon interaction. The heat flux into the phonon bath is given by

$$\begin{aligned} \dot{Q}_{e\text{-ph}} = & \frac{\Sigma V}{24\zeta(5)k_B^5} \int_0^\infty d\epsilon \epsilon^3 [n(\epsilon, T_S) - n(\epsilon, T_P)] \\ & \times \int_{-\infty}^\infty dE n_S(E) n_S(E + \epsilon) \left(1 - \frac{\Delta^2}{E(E + \epsilon)}\right) \\ & \times [f_S(E) - f_S(E + \epsilon)], \end{aligned} \quad (3)$$

where  $\Sigma$  is the material constant for electron-phonon coupling,  $\zeta(z)$  the Riemann zeta function,  $n_S(E)$  the BCS

density of states, and  $n(\epsilon, T) = \{\exp[\epsilon/(k_B T)] - 1\}^{-1}$  the Bose-Einstein distribution of the phonons at temperature  $T_p$ . Equation (3) is obtained by kinetic Boltzmann equation calculations [31,32]. For an alternative derivation, see Supplemental Material [28]. The simulations based on the thermal model are shown as black lines in Fig. 2(a). The electron-phonon coupling constant  $\Sigma = 1.8 \times 10^9 \text{ W K}^{-5} \text{ m}^{-3}$ , used in simulations, was measured in the normal state, where  $\dot{Q}_{e\text{-ph}} = \Sigma V(T_N^5 - T_p^5)$  and  $T_N$  is the electron temperature [33].

We expect the thermal model to be a good approach if  $N_S \gg 1$ . With the high frequency and large amplitude drive in Fig. 2(a), we have  $N_S \sim 10$  quasiparticles present for  $A_g \sim 1$ , suggesting that the thermal model is adequate for these data. If the frequency is lowered to  $f = 4$  kHz, shown in Fig. 2(b), the thermal model fails as  $N_S$  approaches unity. As a further proof of the overheating, we repeated the high frequency measurement using sample B with measured parameter values  $E_c = 620 \mu\text{eV}$ ,  $\Delta = 270 \mu\text{eV}$ ,  $R_{T1} = 1800 \text{ k}\Omega$ ,  $R_{T2} = 960 \text{ k}\Omega$ , and  $V = 800 \times 60 \times 15 \text{ nm}^3$ . The result is shown in Fig 2(c). Again, the simulations (black lines) are able to reproduce all nontrivial features of the measured curves. As a summary of the thermal model fits, we repeated the measurement of Fig. 2(a) at different frequencies and determined by numerical simulations the temperature of the superconducting island and the heat injected into it based on the measured current. The results are shown in Fig. 2(d) as black circles. The results match well with the expected electron-phonon coupling of the superconductor, Eq. (3), presented as the solid black line.

Next, we show that a rigorous way to describe a low number of excitations is to consider them explicitly with Eq. (1). We measured the characteristics at four frequencies  $f = 4, 10, 100,$  and  $1000$  kHz at  $V_b = 280 \mu\text{V}$  and again at the first plateau region, shown in Fig. 3. The thermal model is presented now as solid gray lines. In numerical calculations based on Eq. (1), we keep track of the number of excitations during the cycle and take into account the recombination rates. For low temperatures,  $T_p \ll T_S \ll \Delta/k_B$ , the heat flux of Eq. (3) decomposes to recombination terms, proportional to  $e^{-2\Delta/k_B T_S}$ , and scattering terms, proportional to  $e^{-\Delta/k_B T_S}$ , yielding

$$\begin{aligned} \dot{Q}_{\text{rec}} &= \frac{\pi V \Sigma}{3 \zeta(5) k_B^5} \left[ k_B T_S \Delta^4 + \frac{7}{4} (k_B T_S)^2 \Delta^3 \right] e^{-2\Delta/k_B T_S} \\ \dot{Q}_{\text{sc}} &= V \Sigma T_S^5 e^{-\Delta/k_B T_S}. \end{aligned} \quad (4)$$

Their contributions are presented in Fig. 2(d), and the leading order terms are consistent with the lifetimes given in Ref. [5]. Whereas the scattering does not change the number of quasiparticles  $N_S$ , recombination leads to transitions  $N_S \rightarrow N_S - 2$ . We account for this process by including the recombination rate  $\Gamma_{N \rightarrow N, N_S \rightarrow N_S - 2} = \dot{Q}_{\text{rec}}(N_S)/2\Delta \approx \Sigma \Delta^2 N_S^2 / [12 \zeta(5) D(E_F)^2 k_B^5 V]$ ,  $N_S \geq 2$ ,

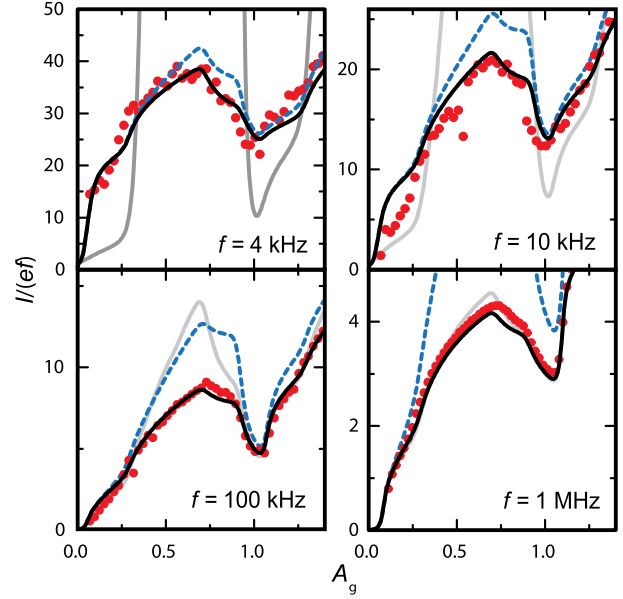


FIG. 3 (color online). Red circles show the measured current for  $f = 4$ – $1000$  kHz at  $V_b = 280 \mu\text{V}$ . Black lines are simulations based on Eq. (1). Recombination rates are taken to match the heat flux in the regime where the thermal model applies [Eq. (3)]. Dotted blue lines are calculated with vanishing electron-phonon relaxation rate and solid gray lines with the thermal model.

where the relation between the effective temperature  $T_S$  in Eq. (4) and the exact quasiparticle number  $N_S$  is given by Eq. (2). The solid black lines of Fig. 3 are calculated with the same value of  $\Sigma$  as obtained in the normal state. Blue dotted lines show similar simulations where electron-phonon relaxation is disregarded.

With the simulations based on instantaneous quasiparticle number we can reproduce the experimental features precisely with no free parameters in the calculation. At the lowest frequency,  $f = 4$  kHz, we have only one quasiparticle present for most of the time. Hence, the curves are not sensitive to the recombination. As frequency is increased, the simulations without electron-phonon relaxation deviate from the experimental data. For  $f = 10$  kHz we probe the recombination rate of a single qp pair only,  $\Gamma_{\text{rec}} = \Gamma_{N \rightarrow N, 2 \rightarrow 0} = 16$  kHz. We checked this by artificially changing the recombination rates for  $N_S > 2$ , without any significant difference in the curves. At higher frequencies, the recombination for  $N_S > 2$  becomes significant as well. The results of the two models approach each other and the thermal model becomes valid.

In summary, a small superconducting island at low temperatures has allowed us to study the dynamics of single electronic excitations and their relaxation. Under quiescent conditions we found a vanishing Cooper pair breaking rate within the measurement resolution: based on the measurement noise, we obtained an upper limit of 2 kHz for this rate. On the other hand, by periodically

pumping electrons, we controllably increased the number of quasiparticles and were able to measure the recombination rates both in the large quasiparticle number limit and for a single quasiparticle pair:  $\Gamma_{N \rightarrow N, 2 \rightarrow 0} = 16$  kHz. The recombination rates are in quantitative agreement with the relaxation measured at higher temperatures and in the normal state.

We thank D. V. Averin, G. Schön, F. W. J. Hekking, D. Golubev, O.-P. Saira, T. Heikkilä, and A. Zorin for discussions. The work has been supported partially by LTQ (Project No. 250280) CoE grant, the European Community's Seventh Framework Programme under Grant Agreement No. 238345 (GEOMDISS), and the National Doctoral Programme in Nanoscience (NGS-NANO). We acknowledge the provision of facilities and technical support by Aalto University at Micronova Nanofabrication Centre. A.K. thanks the Academy of Finland for financial support (Grant No. 259030).

\*ville.maisi@mikes.fi

- [1] A. F. G. Wyatt, V. M. Dmitriev, W. S. Moore, and F. W. Sheard, *Phys. Rev. Lett.* **16**, 1166 (1966).
- [2] A. H. Dayem and J. J. Wiegand, *Phys. Rev.* **155**, 419 (1967).
- [3] J. Clarke, *Phys. Rev. Lett.* **28**, 1363 (1972).
- [4] W. H. Parker and W. D. Williams, *Phys. Rev. Lett.* **29**, 924 (1972).
- [5] S. B. Kaplan, C. C. Chi, D. N. Langenberg, J. J. Chang, S. Jafarey, and D. J. Scalapino, *Phys. Rev. B* **14**, 4854 (1976).
- [6] T. M. Klapwijk and J. E. Mooij, *Physica (Amsterdam)* **81B +C**, 132 (1976).
- [7] C. C. Chi and J. Clarke, *Phys. Rev.* **20**, 4465 (1979).
- [8] K. E. Gray, *J. Phys. F* **1**, 290 (1971).
- [9] C. M. Wilson, L. Frunzio, and D. E. Prober, *Phys. Rev. Lett.* **87**, 067004 (2001).
- [10] D. V. Averin and Yu. V. Nazarov, *Phys. Rev. Lett.* **69**, 1993 (1992).
- [11] P. Lafarge, P. Joyez, D. Esteve, C. Urbina, and M. H. Devoret, *Phys. Rev. Lett.* **70**, 994 (1993).
- [12] T. M. Eiles, J. M. Martinis, and M. H. Devoret, *Phys. Rev. Lett.* **70**, 1862 (1993).
- [13] J. M. Hergenrother, M. T. Tuominen, and M. Tinkham, *Phys. Rev. Lett.* **72**, 1742 (1994).
- [14] G. Schön and A. D. Zaikin, *Eur. Phys. Lett.* **26**, 695 (1994).
- [15] L. Sun, L. DiCarlo, M. D. Reed, G. Catelani, L. S. Bishop, D. I. Schuster, B. R. Johnson, G. A. Yang, L. Frunzio, L. Glazman, M. H. Devoret, and R. J. Schoelkopf, *Phys. Rev. Lett.* **108**, 230509 (2012).
- [16] H. S. Knowles, V. F. Maisi, and J. P. Pekola, *Appl. Phys. Lett.* **100**, 262601 (2012).
- [17] P. J. de Visser, J. J. A. Baselmans, P. Diener, S. J. C. Yates, A. Endo, and T. M. Klapwijk, *Phys. Rev. Lett.* **106**, 167004 (2011).
- [18] M. Lenander *et al.*, *Phys. Rev. B* **84**, 024501 (2011).
- [19] J. Aumentado, M. W. Keller, J. M. Martinis, and M. H. Devoret, *Phys. Rev. Lett.* **92**, 066802 (2004).
- [20] A. J. Ferguson, N. A. Court, F. E. Hudson, and R. G. Clark, *Phys. Rev. Lett.* **97**, 106603 (2006).
- [21] J. Leppäkangas and M. Marthaler, *Phys. Rev. B* **85**, 144503 (2012).
- [22] D. Ristè, C. C. Bultink, M. J. Tiggelman, R. N. Schouten, K. W. Lehnert, and L. DiCarlo, *Nat. Commun.* **4**, 1913 (2013).
- [23] J. P. Pekola, J. J. Vartiainen, M. Möttönen, O.-P. Saira, M. Meschke, and D. V. Averin, *Nat. Phys.* **4**, 120 (2008).
- [24] D. V. Averin and J. P. Pekola, *Phys. Rev. Lett.* **101**, 066801 (2008).
- [25] V. F. Maisi, O.-P. Saira, Yu. A. Pashkin, J. S. Tsai, D. V. Averin, and J. P. Pekola, *Phys. Rev. Lett.* **106**, 217003 (2011).
- [26] T. Aref, V. F. Maisi, M. V. Gustafsson, P. Delsing, and J. P. Pekola, *Eur. Phys. Lett.* **96**, 37008 (2011).
- [27] M. Tinkham, *Introduction to Superconductivity* (McGraw-Hill, New York, 1996), 2nd ed.
- [28] See Supplemental Material at <http://link.aps.org/supplemental/10.1103/PhysRevLett.111.147001> for details.
- [29] O.-P. Saira, A. Kemppinen, V. F. Maisi, and J. P. Pekola, *Phys. Rev. B* **85**, 012504 (2012).
- [30] F. W. J. Hekking and Yu. V. Nazarov, *Phys. Rev. Lett.* **71**, 1625 (1993).
- [31] D. V. Averin and A. N. Korotkov, *Zh. Eksp. Teor. Fiz.* **97**, 1661 (1990) [*Sov. Phys. JETP* **70**, 937 (1990)].
- [32] A. V. Timofeev, C. P. Garcia, N. B. Kopnin, A. M. Savin, M. Meschke, F. Giazotto, and J. P. Pekola, *Phys. Rev. Lett.* **102**, 017003 (2009).
- [33] F. C. Wellstood, C. Urbina, and J. Clarke, *Phys. Rev. B* **49**, 5942 (1994).

# Single quasiparticle excitation dynamics on a superconducting island

## Supplemental Material

V. F. Maisi,<sup>1,2,\*</sup> S. V. Lotkhov,<sup>3</sup> A. Kemppinen,<sup>2</sup> A. Heimes,<sup>4</sup> J. T. Muhonen,<sup>1,5</sup> and J. P. Pekola<sup>1</sup>

<sup>1</sup>*Low Temperature Laboratory (OVLL), Aalto University School of Science, P.O. Box 13500, 00076 Aalto, Finland*

<sup>2</sup>*Centre for Metrology and Accreditation (MIKES), P.O. Box 9, 02151 Espoo, Finland*

<sup>3</sup>*Physikalisch-Technische Bundesanstalt, Bundesallee 100, 38116 Braunschweig, Germany*

<sup>4</sup>*Institut für Theoretische Festkörperphysik, Karlsruher Institut für Technologie, Wolfgang-Gaede-Str. 1, D-76128 Karlsruhe, Germany*

<sup>5</sup>*Centre for Quantum Computation and Communication Technology, School of Electrical Engineering and Telecommunications, University of New South Wales, Sydney NSW 2052, Australia*

### ELECTRON TUNNELING

Within first order, the tunneling rates are given by Fermi golden rule similarly as in Ref. [1]. Now as we consider also explicitly  $N_S$ , we need to split the rates so that an electron tunneling into the superconducting island to a state with energy  $E > \Delta$  in the semiconductor model [2], increases the excitation number  $N_S$  by one and an electron tunneling into a state  $E < -\Delta$ , decreases it by one as shown in Fig. 1. Likewise, an electron tunneling out from  $E > \Delta$  decreases  $N_S$  and an electron tunneling out from  $E < -\Delta$  increases it by one. Hence we obtain rates

$$\left\{ \begin{array}{l} \Gamma_{N-1 \rightarrow N, N_S-1 \rightarrow N_S} = \sum_{j=1,2} \frac{1}{e^2 R_{T,j}} \int_{\Delta}^{\infty} dE n_S(E) (1 - f_S(E, N_S)) f_N(E + \delta E_j(N)) \\ \Gamma_{N-1 \rightarrow N, N_S+1 \rightarrow N_S} = \sum_{j=1,2} \frac{1}{e^2 R_{T,j}} \int_{-\infty}^{-\Delta} dE n_S(E) (1 - f_S(E, N_S)) f_N(E + \delta E_j(N)) \\ \Gamma_{N+1 \rightarrow N, N_S-1 \rightarrow N_S} = \sum_{j=1,2} \frac{1}{e^2 R_{T,j}} \int_{-\infty}^{-\Delta} dE n_S(E) f_S(E, N_S) (1 - f_N(E + \delta E_j(N))) \\ \Gamma_{N+1 \rightarrow N, N_S+1 \rightarrow N_S} = \sum_{j=1,2} \frac{1}{e^2 R_{T,j}} \int_{\Delta}^{\infty} dE n_S(E) f_S(E, N_S) (1 - f_N(E + \delta E_j(N))), \end{array} \right. \quad (1)$$

where  $R_{T,j}$  is the tunneling resistance of junction  $j$ ,  $n_S(E)$ , the BCS density of states,  $f_S(E, N_S)$ , occupation probability for state  $E$  on the island if we have  $N_S$  quasiparticles, and  $f_N(E)$  occupation probability in the normal metallic lead at energy  $E$ .  $\delta E_j(N)$  the energy cost from biasing and charging energy [1]. We assume  $f_N$  to be a Fermi distribution with temperature equal to the bath temperature  $T_N = 60$  mK. Summing the rates which increase and decrease  $N_S$  will lead to the known tunneling rates of a normal metal superconductor tunnel junction where the integration is performed over all energies [2, 3].

For the superconductor we need to have  $f_S$  such that the number of excitations equals  $N_S$ . For the tunneling rates, as well as for the electron-phonon interaction discussed below, the functional form of the distribution is irrelevant as long as the excitations are close to the gap edges  $E \approx \pm\Delta$ , where we inject them. We also neglect the branch imbalance, i.e. assume no chemical potential shift,  $\delta\mu = 0$ , because our system is symmetrical with respect electron injection. Hence we use a Fermi distribution with temperature  $T_S$ . The relation between  $N_S$  and  $T_S$  is then

$$N_S = 2D(E_F)V \int_{\Delta}^{\infty} dE \frac{E}{\sqrt{E^2 - \Delta^2}} f_E \approx \sqrt{2\pi} D(E_F)V \sqrt{\Delta k_B T_S} e^{-\Delta/k_B T_S}, \quad (2)$$

where  $D(E_F)$  is the normal state density of states at Fermi level and  $V$  the volume of the island. The tunneling current is obtained then as

$$I = e \sum_{N, N_S, \pm} \left( \Gamma_{N \rightarrow N+1, N_S \rightarrow N_S \pm 1} - \Gamma_{N \rightarrow N-1, N_S \rightarrow N_S \pm 1} \right) P(N, N_S). \quad (3)$$

---

\*Electronic address: ville.maisi@mikes.fi

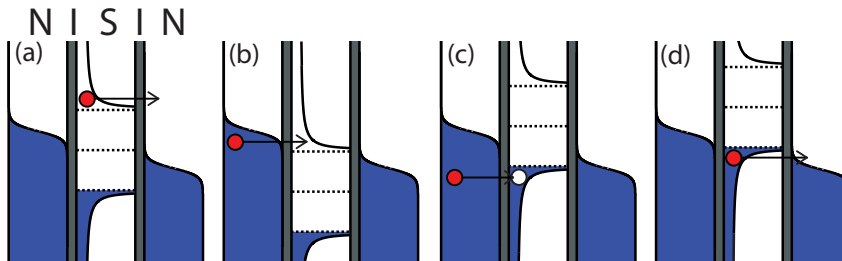


Figure 1: (color online). The four different tunneling processes changing  $N$  and  $N_S$ . (a) Electron tunneling out of the island and removing an excitation. (b) Electron tunneling into the island creating an excitation. (c) Electron tunneling into the island and removing a hole excitation. (d) Electron tunneling out and creating a hole excitation.

Including higher order tunneling to Eq. (1) of the main article and Eq. (3) is straightforward. For example Andreev current gives rise to terms  $\Gamma_{N\pm 2 \rightarrow N, N_S \rightarrow N_S}$ . These rates are calculated similarly as in Refs. [3–5] since quasiparticle number  $N_S$  is not changing. Including Andreev tunneling terms into the calculations in main text, does not change the results as  $E_c > \Delta$ . For  $E_c < \Delta$ , those terms contribute because Andreev tunneling thresholds are exceeded before the single-electron tunneling thresholds [3–5].

### ELECTRON-PHONON INTERACTION

To obtain the recombination rates for Eq. (1) and Eq. (4) of the main article we use Hamiltonian

$$H = H_s + H_p + H_{e-ph}. \quad (4)$$

Here  $H_s + H_p$  is the non-perturbed part and  $H_{e-ph}$  the perturbation from electron-phonon interaction. The BCS Hamiltonian of the superconductor is

$$H_s = \sum_{k\sigma} E_k \gamma_{k\sigma}^\dagger \gamma_{k\sigma}, \quad (5)$$

with  $E_k = \sqrt{\epsilon_k^2 + |\Delta_k|^2}$ . The diagonalizing fermionic operators  $\gamma_{k\sigma}$  are connected to the electron operators  $c_{k'\sigma'}$  by  $c_{k\sigma}^\dagger = v_{k\sigma}^* \gamma_{-(k\sigma)} + u_{k\sigma} \gamma_{k\sigma}^\dagger$ , where we use notation

$$v_{k\sigma} = \begin{cases} v_k & \text{if } \sigma = \uparrow \\ -v_{-k} & \text{if } \sigma = \downarrow \end{cases} \quad u_{k\sigma} = \begin{cases} u_k & \text{if } \sigma = \uparrow \\ u_{-k} & \text{if } \sigma = \downarrow \end{cases}. \quad (6)$$

The coefficients satisfy  $|u_k|^2 + |v_k|^2 = 1$  and  $\Delta_k^* v_k / u_k = E_k - \epsilon_k$  leading to

$$|v_k|^2 = 1 - |u_k|^2 = \frac{1}{2} \left( 1 - \frac{\epsilon_k}{E_k} \right). \quad (7)$$

Similarly, we have for the phonons

$$H_p = \sum_q \hbar \omega_q b_q^\dagger b_q. \quad (8)$$

The coupling of these two systems has the form

$$H_{e-ph} = \nu \sum_{k,q} \omega_q^{1/2} (c_k^\dagger c_{k-q} b_q + c_k^\dagger c_{k+q} b_q^\dagger). \quad (9)$$

as in Ref. [6]. The operator of heat flux to the phonons is

$$\dot{H}_p = \frac{i}{\hbar} [H, H_p] = \frac{i}{\hbar} [H_{e-ph}, H_p] = i\nu \sum_{k,q} \omega_q^{3/2} (c_k^\dagger c_{k-q} b_q - c_k^\dagger c_{k+q} b_q^\dagger). \quad (10)$$

By using the Kubo formula in the interaction picture we obtain

$$\begin{aligned}
\langle \dot{H}_p \rangle &= \langle \dot{H}_p \rangle_0 - \frac{i}{\hbar} \int_{-\infty}^t dt' \langle [\dot{H}_p(t), H_{e\text{-ph}}(t')] \rangle_0 \\
&= \frac{1}{\hbar} \sum_{\substack{k\sigma q \\ k'\sigma'}} \omega_q^2 \int_{-\infty}^t dt' \left\{ \right. \\
&\quad \left. \left\langle \left[ c_{k\sigma}^\dagger(t) c_{k-q\sigma}(t) b_q(t), c_{k'\sigma'}^\dagger(t') c_{k'+q\sigma'}(t') b_q^\dagger(t') \right] \right\rangle_0 - \right. \\
&\quad \left. \left\langle \left[ c_{k\sigma}^\dagger(t) c_{k+q\sigma}(t) b_q^\dagger(t), c_{k'\sigma'}^\dagger(t') c_{k'-q\sigma'}(t') b_q(t') \right] \right\rangle_0 \right\}.
\end{aligned} \tag{11}$$

Next we use  $b_q(t) = e^{-i\omega_q t} b_q$  and  $c_{k\sigma}^\dagger(t) = v_{k\sigma}^* \gamma_{-(k\sigma)}(t) + u_{k\sigma} \gamma_{k\sigma}^\dagger(t)$  with  $\gamma_{k\sigma}(t) = \gamma_{k\sigma} e^{-iE_k t/\hbar}$ . As an example, let us consider the first non-zero term in Eq. (11). We obtain

$$\begin{aligned}
& e^{i\omega_q(t'-t)} e^{i(-E_k t + E_{k-q} t - E_{k'} t' + E_{k'+q} t')/\hbar} v_{k\sigma}^* v_{k-q\sigma} v_{k'\sigma'}^* v_{k'+q\sigma'} \left\langle \left[ \gamma_{-(k\sigma)} \gamma_{-(k-q\sigma)}^\dagger b_q, \gamma_{-(k'\sigma')} \gamma_{-(k'+q\sigma')}^\dagger b_q^\dagger \right] \right\rangle_0 \\
= & e^{i\omega_q(t'-t)} e^{i(E_{k-q} - E_k)(t-t')/\hbar} |v_{k\sigma}|^2 |v_{k-q\sigma}|^2 \left\langle \left[ \gamma_{-(k\sigma)} \gamma_{-(k-q\sigma)}^\dagger b_q, \gamma_{-(k-q\sigma)} \gamma_{-(k\sigma)}^\dagger b_q^\dagger \right] \right\rangle_0 \\
= & e^{i\omega_q(t'-t)} e^{i(E_{k-q} - E_k)(t-t')/\hbar} |v_{k\sigma}|^2 |v_{k-q\sigma}|^2 \left\{ (1-f_k) f_{k-q} (n_q + 1) - f_k (1-f_{k-q}) n_q \right\},
\end{aligned} \tag{12}$$

where we have paired the operators as  $k = k' + q$ . For some of the terms, there exists two different pairing possibilities. From the second commutator of Eq. (11) we find similarly a term

$$e^{-i\omega_q(t'-t)} e^{-i(E_{k-q} - E_k)(t-t')/\hbar} |v_{k\sigma}|^2 |v_{k-q\sigma}|^2 \left\{ (1-f_k) f_{k-q} (n_q + 1) - f_k (1-f_{k-q}) n_q \right\}, \tag{13}$$

where the dummy summation index has been changed from  $k'$  to  $k$ . Now we can combine these two terms and do the time integration to obtain energy conservation rules as delta functions. By combining all terms similarly, assuming  $\Delta_k = \Delta e^{i\phi}$ , where  $\Delta$  is real, and changing the summing to integration we obtain from Eq. (11)

$$\begin{aligned}
\dot{Q}_{e\text{-ph}} &= \pi \nu^2 N(E_F) D(q) \int_{-\infty}^{\infty} d\epsilon_k \int d^3 q \omega_q^2 \left\{ \right. \\
&\quad \left( 1 - \frac{\Delta^2}{E_k E_{k-q}} \right) \left( (1-f_k) f_{k-q} (n_q + 1) - f_k (1-f_{k-q}) n_q \right) \delta(E_k - E_{k-q} + \hbar\omega_q) + \\
&\quad \left( 1 + \frac{\Delta^2}{E_k E_{k-q}} \right) \left( (1-f_k) (1-f_{k-q}) (n_q + 1) - f_k f_{k-q} n_q \right) \delta(E_k + E_{k-q} + \hbar\omega_q) + \\
&\quad \left( 1 + \frac{\Delta^2}{E_k E_{k-q}} \right) \left( f_k f_{k-q} (n_q + 1) - (1-f_k) (1-f_{k-q}) n_q \right) \delta(-E_k - E_{k-q} + \hbar\omega_q) + \\
&\quad \left. \left( 1 - \frac{\Delta^2}{E_k E_{k-q}} \right) \left( f_k (1-f_{k-q}) (n_q + 1) - (1-f_k) f_{k-q} n_q \right) \delta(-E_k + E_{k-q} + \hbar\omega_q) \right\},
\end{aligned} \tag{14}$$

where  $N(E_F)$  is the density of states of the normal state and  $D(q) = \frac{V}{(2\pi)^3}$  the density of states of the phonons.  $V$  is the volume of the system. Now,  $\int d^3 q = 2\pi \int_0^\infty dq q^2 \int_{-1}^1 d(\cos(\theta))$  where  $\theta$  is the angle between  $k$  and  $q$ . Furthermore  $\epsilon_k = \frac{\hbar^2 k^2}{2m}$ ,  $\epsilon_{k-q} = \frac{\hbar^2 (k-q)^2}{2m} = \epsilon_k \frac{\hbar^2 k_F}{m} q \cos(\theta)$  and  $\omega_q = c_l q$ , where  $c_l$  is the speed of sound. For integrating the delta functions over  $\cos(\theta)$ , we need

$$\left| \frac{dE_{k-q}}{d(\cos(\theta))} \right|^{-1} = \frac{E_{k-q}}{\epsilon_{k-q}} \frac{m}{\hbar^2 k_F q} = n_S(E_{k-q}) \frac{m}{\hbar^2 k_F q}, \tag{15}$$

where we have identified the density of states of the superconductor  $n_S(E) = \frac{E}{\epsilon} = \frac{E}{\sqrt{E^2 - \Delta^2}}$ . Therefore we obtain

$$\begin{aligned}
\dot{Q}_{e\text{-ph}} &= \frac{\nu^2 V}{2\pi} N(E_F) c_l^2 \int_{-\infty}^{\infty} d\epsilon_k \int_0^\infty dq q^3 \frac{m}{\hbar^2 k_F} n_S(E_{k-q}) \left\{ \right. \\
&\quad \left( 1 - \frac{\Delta^2}{E_k E_{k-q}} \right) \left( (1-f_k) f_{k-q} (n_q + 1) - f_k (1-f_{k-q}) n_q \right) \Big|_{E_{k-q}=E_k+\hbar\omega_q>0} \\
&\quad + \left( 1 + \frac{\Delta^2}{E_k E_{k-q}} \right) \left( (1-f_k) (1-f_{k-q}) (n_q + 1) - f_k f_{k-q} n_q \right) \Big|_{E_{k-q}=-E_k-\hbar\omega_q>0} \\
&\quad + \left( 1 + \frac{\Delta^2}{E_k E_{k-q}} \right) \left( f_k f_{k-q} (n_q + 1) - (1-f_k) (1-f_{k-q}) n_q \right) \Big|_{E_{k-q}=-E_k+\hbar\omega_q>0} \\
&\quad + \left. \left( 1 - \frac{\Delta^2}{E_k E_{k-q}} \right) \left( f_k (1-f_{k-q}) (n_q + 1) - (1-f_k) f_{k-q} n_q \right) \Big|_{E_{k-q}=E_k-\hbar\omega_q>0} \right\}.
\end{aligned} \tag{16}$$

Now, we change the integration variables to  $E_k = \sqrt{\epsilon_k^2 + \Delta^2}$  and  $\epsilon = \hbar\omega_q = \hbar c_l q$ . Hence, we have  $d\epsilon_k = n_S(E_k)dE_k$  and  $dq = (\hbar c_l)^{-1}d\epsilon$ . We can also use notation  $E = E_k$  and  $E' = E_{k-q}$ . Then, equation (16) yields

$$\begin{aligned} \dot{Q}_{e-\text{ph}} = & \frac{m\nu^2 V N(E_F)}{\pi \hbar^6 k_F c_l^2} \int_0^\infty dE \int_0^\infty d\epsilon \epsilon^3 n_S(E) n_S(E') \left\{ \right. \\ & \left. \left(1 - \frac{\Delta^2}{EE'}\right) \left( (1 - f(E)) f(E') (n(\epsilon) + 1) - f(E) (1 - f(E')) n(\epsilon) \right) \right|_{E'=E+\epsilon>0} \\ & + \left(1 + \frac{\Delta^2}{EE'}\right) \left( (1 - f(E)) (1 - f(E')) (n(\epsilon) + 1) - f(E) f(E') n(\epsilon) \right) \right|_{E'=-E-\epsilon>0} \\ & + \left(1 + \frac{\Delta^2}{EE'}\right) \left( f(E) f(E') (n(\epsilon) + 1) - (1 - f(E)) (1 - f(E')) n(\epsilon) \right) \right|_{E'=-E+\epsilon>0} \\ & \left. + \left(1 - \frac{\Delta^2}{EE'}\right) \left( f(E) (1 - f(E')) (n(\epsilon) + 1) - (1 - f(E)) f(E') n(\epsilon) \right) \right|_{E'=E-\epsilon>0} \right\}. \end{aligned} \quad (17)$$

Finally we can change integration variable  $E$  and the dummy variable  $E'$  as follows: for first term: no changes, for second term: change of sign for  $E'$ , for third term: change of sign for  $E$  and for the fourth term: change of sign for  $E$  and  $E'$ . Then, we see that both  $E$  and  $E'$  cover both positive and negative values and we obtain

$$\begin{aligned} \dot{Q}_{e-\text{ph}} = & \frac{m\nu^2 V N(E_F)}{\pi \hbar^6 k_F c_l^2} \int_{-\infty}^\infty dE \int_0^\infty d\epsilon \epsilon^3 n_S(E) n_S(E + \epsilon) \times \\ & \left(1 - \frac{\Delta^2}{E(E+\epsilon)}\right) \left( (1 - f(E)) f(E + \epsilon) (n(\epsilon) + 1) - f(E) (1 - f(E + \epsilon)) n(\epsilon) \right). \end{aligned} \quad (18)$$

With some algebra, we can simplify Eq. (16) to

$$\dot{Q}_{e-\text{ph}} = \frac{\Sigma V}{24\zeta(5)k_B^5} \int_0^\infty d\epsilon \epsilon^3 (n(\epsilon, T_S) - n(\epsilon, T_P)) \int_{-\infty}^\infty dE n_S(E) n_S(E + \epsilon) \left(1 - \frac{\Delta^2}{E(E + \epsilon)}\right) (f(E) - f(E + \epsilon)). \quad (19)$$

Here we have identified the electron-phonon coupling constant  $\Sigma = \frac{24\zeta(5)k_B^5 m\nu^2 N(E_F)}{\pi \hbar^6 k_F c_l^2}$  by taking the limit  $\Delta \rightarrow 0$ , which yields the normal-state result  $\dot{Q}_{e-\text{ph}} = \Sigma V (T_S^5 - T_P^5)$ . One arrives to Eq. (19) also by using kinetic equations for the electronic excitations under electron-phonon interaction [7] or by taking the result in normal state [8] and considering that in superconducting state, BCS density of states and the coherence factor needs to be taken into account [2]. Equation (19) is also found for example in Ref. [9].

For obtaining the recombination and scattering rates, we identify in Eq. (17) the first and last term to correspond to scattering and the two middle ones to recombination and pair breaking. Since the heat rate is set dominantly by the quasiparticle occupation near the gap, we can again parametrize the number of quasiparticles by an effective temperature  $T_S$  and the Fermi distribution  $f_E = (\exp(E/k_B T_S) + 1)^{-1}$  without any loss of generality. For  $T_P \ll T_S \ll \Delta/k_B$ , satisfied in the experiments, we obtain the recombination and scattering heat fluxes as

$$\begin{aligned} \dot{Q}_{\text{rec}}(T_S) & \approx \frac{\Sigma V}{12\zeta(5)k_B^5} \int_{-\infty}^\infty d\xi \int_{-\infty}^\infty d\xi' (E + E')^3 \left[1 + \frac{\Delta^2}{EE'}\right] f_E f_{E'} \\ & \approx \frac{\pi V \Sigma}{3\zeta(5)k_B^5} (k_B T_S \Delta^4 + \frac{7}{4} (k_B T_S)^2 \Delta^3) e^{-2\Delta/k_B T_S}, \\ \dot{Q}_{\text{sc}}(T_S) & \approx \frac{\Sigma V}{6\zeta(5)k_B^5} \int_{-\infty}^\infty d\xi \int_{-\infty}^\infty d\xi' \theta(E - E') (E - E')^3 \left[1 - \frac{\Delta^2}{EE'}\right] f_E \\ & \approx V \Sigma T_S^5 e^{-\Delta/k_B T_S}. \end{aligned}$$

Instead of parametrization with respect to  $T_S$ , we could also parametrize the effective temperature  $T_S$  by the quasiparticle number  $N_S$  with Eq. (2) and ask for the rate  $\Gamma_{N \rightarrow N, N_S + 2 \rightarrow N_S}$  entering the master equation for  $P(N, N_S)$ . This accounts for the transition of  $N_S + 2$  to  $N_S$  quasiparticles, whereas the number of excess electrons  $N$  is unchanged. As the quasiparticles lie close to the gap the energy loss during this process is  $2\Delta$  and therefore the rate is given by

$$\Gamma_{N \rightarrow N, N_S + 2 \rightarrow N_S} = \frac{\dot{Q}_{\text{rec}}(N_S + 2)}{2\Delta}. \quad (20)$$

In these terms the heat balance then is fully described by the master equation for  $P(N, N_S)$ .

---

[1] D. V. Averin and K. K. Likharev, "Single-electronics" in B. Altshuler et al. (eds.), *Mesoscopic Phenomena in Solids* (Elsevier, 1991), pp. 173-271.

- [2] M. Tinkham, *Introduction to superconductivity*, 2 ed. (McGraw-Hill, New York, 1996).
- [3] T. Aref, V. F. Maisi, M. V. Gustafsson, P. Delsing and J. P. Pekola, *Eur. Phys. Lett.* **96**, 37008 (2011).
- [4] D. V. Averin and J. P. Pekola, *Phys. Rev. Lett.* **101**, 066801 (2008).
- [5] V. F. Maisi, O.-P. Saira, Yu. A. Pashkin, J. S. Tsai, D. V. Averin and J. P. Pekola, *Phys. Rev. Lett.* **106**, 217003 (2011).
- [6] A. L. Fetter and J. D. Walecka, *Quantum Theory of Many-Particle Systems*, (McGraw-Hill, San Francisco, 1971).
- [7] V.G. Bar'yakther, N.N. Bychkova and V.P. Seminozhenko, *Theoretical and Mathematical Physics*, Vol. 38, No. 2 , pp. 251-262 (1979).
- [8] F.C. Wellstood, C. Urbina and J. Clarke, *Phys. Rev. B* **49**, 5942 (1994).
- [9] A. V. Timofeev, C. P. Garcia, N. B. Kopnin, A. M. Savin, M. Meschke, F. Giazotto and J. P. Pekola, *Phys. Rev. Lett.* **102**, 017003 (2009).

# Publication X

**A. Di Marco, V. F. Maisi, J. P. Pekola and F. W. J. Hekking. Leakage current of a superconductor–normal metal tunnel junction connected to a high-temperature environment. *Phys. Rev. B* 88, 174507 (2013).**

© (2013) American Physical Society.

Reprinted with permission.



# Leakage current of a superconductor–normal metal tunnel junction connected to a high-temperature environment

A. Di Marco,<sup>1</sup> V. F. Maisi,<sup>2,3</sup> J. P. Pekola,<sup>3</sup> and F. W. J. Hekking<sup>1</sup>

<sup>1</sup>*LPMMC-CNRS, Université Joseph Fourier, 25 Avenue des Martyrs BP166 38042 Grenoble Cedex, France*

<sup>2</sup>*Centre for Metrology and Accreditation (MIKES), P.O. Box 9, 02151 Espoo, Finland*

<sup>3</sup>*Low Temperature Laboratory, Aalto University, P.O. Box 13500, FI-00076 Aalto, Finland*

(Received 20 July 2013; published 11 November 2013)

We consider a voltage-biased normal metal-insulator-superconductor (NIS) tunnel junction, connected to a high-temperature external electromagnetic environment. This model system features the commonly observed subgap leakage current in NIS junctions through photon-assisted tunneling which is detrimental for applications. We first consider a NIS junction directly coupled to the environment and analyze the subgap leakage current both analytically and numerically; we discuss the link with the phenomenological Dynes parameter. Then, we focus on a circuit where a low-temperature lossy transmission line is inserted between the NIS junction and the environment. We show that the amplitude of the transmitted frequencies relevant for the photon-assisted tunneling is exponentially suppressed as the length  $\ell$  and the resistance per unit length  $R_0$  of the line are increased. Consequently, the subgap current is reduced exponentially as well. This property can not be obtained by means of lumped circuit elements. We finally discuss our results in view of the performance of NIS junctions in applications.

DOI: [10.1103/PhysRevB.88.174507](https://doi.org/10.1103/PhysRevB.88.174507)

PACS number(s): 74.55.+v, 74.25.F-, 85.25.Am, 72.70.+m

## I. INTRODUCTION

The peculiar nature of single-particle electronic transport through a normal metal-insulator-superconductor (NIS) junction is at the origin of several interesting applications. Such junctions are widely used in experiments of mesoscopic physics as a spectroscopic tool,<sup>1,2</sup> as a very sensitive thermometer,<sup>3–5</sup> and as a key element in nanorefrigeration.<sup>3,6,7</sup> Furthermore, NIS junctions are currently investigated in view of achieving a high accuracy when controlling the current through a single-electron SINIS turnstile. Such a device is one of the interesting candidates for the completion of the so-called quantum metrological triangle, i.e., it can be used to obtain a precise realization of current.<sup>8,9</sup> These applications are all based on the existence of the Bardeen-Cooper-Schrieffer (BCS) energy gap  $\Delta$  in the density of states (DOS) of the superconductor.<sup>10</sup> Ideally, one would expect no single-electron current to flow through a NIS junction at low temperature as long as the bias voltage  $V$  satisfies the inequality  $-\Delta < eV < \Delta$ .

In practice, the subgap current is different from zero. This is a central problem which limits the performance of applications based on energy-selective single-particle transport in NIS junctions. The presence of unwanted accessible states in the subgap region manifests itself as a smearing of the junction's current-voltage ( $I$ - $V$ ) characteristic as well as of its differential conductance. Giaever was the first to experimentally study the NIS junction. He noticed that this deviation from the ideal behavior was present even if the junction was kept at a temperature much lower than the critical one  $T_c$  of the superconductor.<sup>11</sup> A possible source of subgap leakage currents is the occurrence of many-electron tunneling processes, such as Andreev reflection.<sup>12–14</sup> However, these many-electron processes are strongly suppressed if the tunnel resistance  $R_T$  of the junction is chosen high enough and do not account for the observed residual subgap transport either.

Dynes modified the BCS superconducting DOS introducing a single phenomenological dimensionless parameter  $\gamma_{\text{Dynes}}$  in order to fit the behavior of the subgap quasiparticle tunneling current through a Josephson junction.<sup>15</sup> The modified DOS, normalized to the corresponding normal-state DOS at the Fermi energy, is given by

$$N_S^{\text{Dynes}}(E) = \left| \text{Re} \left[ \frac{E/\Delta + i\gamma_{\text{Dynes}}}{\sqrt{(E/\Delta + i\gamma_{\text{Dynes}})^2 - 1}} \right] \right|. \quad (1)$$

It can be seen that  $\gamma_{\text{Dynes}}$  indeed accounts for the broadening of the DOS around  $\Delta$  and the occurrence of states within the gap. This expression is frequently used in both numerical and analytical calculations,<sup>16</sup> but concerning the microscopic origin of the Dynes parameter  $\gamma_{\text{Dynes}}$ , for temperatures far below  $T_c$ , relatively little is known. In general, the smearing of the DOS can be energy dependent.

Recently, it was realized that the exchange of energy between the NIS junction and its surrounding electromagnetic environment may be one of the causes of the smearing of the BCS DOS.<sup>17,18</sup> Indeed, under certain conditions, energy absorption from such an environment enables the crossing of the tunnel barrier by single electrons even for  $|V|$  much less than  $\Delta/e$ . Within this framework, an analytical expression for  $\gamma_{\text{Dynes}}$  has been obtained in terms of the parameters characterizing the NIS junction's environment.<sup>17</sup> In this particular case, the Dynes parameter found describes the smearing at all energies. Following the idea of photon-assisted tunneling demonstrated in Ref. 17, we generalize the approach here for an external circuit characterized by an arbitrary impedance  $Z(\omega)$ , kept at a temperature  $T_{\text{env}}$  that is not necessarily the temperature  $T_{\text{jun}}$  of the NIS junction [see Fig. 1(a)]. We obtain expressions for the subgap leakage current and the subgap Dynes parameter  $\gamma_{\text{Dynes}}^{\text{sub}}$ , valid for energies smaller than the gap  $\Delta$ . Then, we turn our attention to the circuit depicted in Fig. 1(b), where we study the effects of the insertion of a

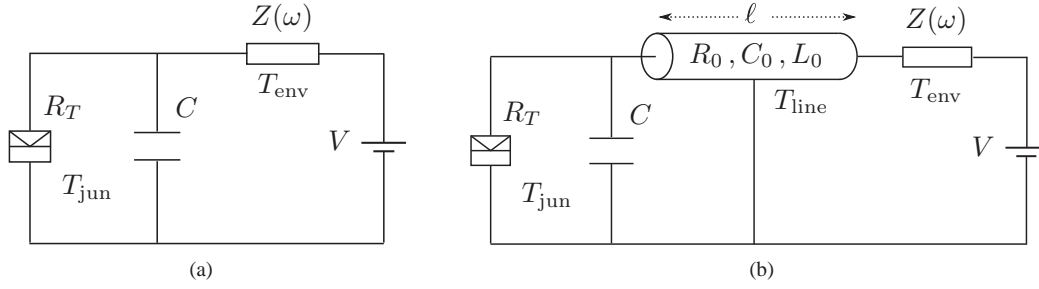


FIG. 1. Circuit representation of the two configurations studied in this paper. (a) A NIS junction at temperature  $T_{\text{jun}}$  is connected in parallel to its capacitance  $C$  and to an impedance  $Z(\omega)$  which represents the high-temperature environment at temperature  $T_{\text{env}} \gg T_{\text{jun}}$ . The whole circuit is biased by the constant voltage  $V$ . (b) A transmission line of length  $\ell$  is inserted between the junction and the impedance  $Z(\omega)$  of circuit (a). It is described by the parameters  $R_0$ ,  $C_0$ , and  $L_0$ , the resistance, the capacitance, and the inductance per unit length, respectively, as well as by its temperature  $T_{\text{line}}$  which is assumed equal to  $T_{\text{jun}}$ .

lossy transmission line, meant to act as a frequency-dependent filter, between the cold junction and the high-temperature external impedance  $Z(\omega)$ . In particular, we use our results to understand under which conditions the transmission line will behave as a filter capable of reducing the photon-assisted tunneling induced by the high-temperature external impedance and thus reducing  $\gamma_{\text{Dynes}}^{\text{sub}}$  to values that are compatible with the accuracy requirements for applications such as the SINIS turnstile.

## II. NIS JUNCTION COUPLED TO A HIGH-TEMPERATURE ENVIRONMENT

### A. Single-particle current

We start by considering the basic circuit illustrated in Fig. 1(a) where a NIS junction is connected in series to an effective high-temperature impedance  $Z(\omega)$ . The junction itself is characterized by a tunnel resistance  $R_T$  in parallel with a capacitance  $C$ . The entire circuit is voltage biased. This constitutes a minimal model for a junction embedded in an external electromagnetic environment at temperature  $T_{\text{env}}$ , which can be much higher than the temperature  $T_{\text{jun}}$  of the junction.

According to the so-called  $P(E)$  theory,<sup>19</sup> the single-particle tunneling current through a NIS junction coupled to an external environment is given by

$$I_{\text{NS}}(V) = \frac{1}{eR_T} \int dE \int dE' N_S(E') [1 - f(E')] \times \{f(E - eV) - f(E + eV)\} P(E - E'). \quad (2)$$

Here, the energy  $E$  refers to the electrons of the normal metal,  $E'$  is the energy of the superconductor quasiparticles,  $N_S(E')$  is the BCS density of states of the superconducting wire divided by the normal-metal DOS at the Fermi level, and  $f(E) = [e^{\beta_{\text{jun}} E} + 1]^{-1}$  is the Fermi-Dirac distribution with  $\beta_{\text{jun}} = 1/k_B T_{\text{jun}}$  the inverse temperature of the junction. Expression (2) does not take into account the higher-order processes in tunneling which will be ignored throughout this paper. The validity of this assumption will be discussed in Sec. IV.

The function  $P(E)$  in Eq. (2) is the probability density that the tunneling electron exchanges an amount of energy  $E$  with the environment. This process takes place through the emission

or absorption of photons. It is defined as

$$P(E) = \frac{1}{2\pi\hbar} \int_{-\infty}^{+\infty} dt e^{iEt/\hbar} e^{J(t)}, \quad (3)$$

i.e., it is the Fourier transform of the exponential of the correlation function

$$J(t) = 2 \int_0^{+\infty} \frac{d\omega}{\omega} \frac{\text{Re}[Z_{\text{tot}}(\omega)]}{R_K} \times \left\{ \coth\left(\frac{1}{2}\beta_{\text{env}}\hbar\omega\right) [\cos(\omega t) - 1] - i \sin(\omega t) \right\}. \quad (4)$$

Here,  $Z_{\text{tot}}(\omega)$  is the total impedance seen by the junction, resulting from the connection in parallel of  $C$  and  $Z(\omega)$ ,  $R_K = h/e^2$  is the quantum resistance, and  $\beta_{\text{env}} = 1/k_B T_{\text{env}}$ .

The function  $J(t)$  determines the strength of the coupling between the NIS junction and the environment. Indeed, if  $J(t) = 0$ , the probability density  $P(E)$  is equal to a Dirac delta  $\delta(E)$  and the single-particle tunneling current is elastic. Expression (2) then reduces to the standard expression for single-particle tunneling in NIS junctions valid in the absence of environment. The environment-induced inelastic tunneling processes occur only when  $J(t) \neq 0$ . In general, the time intervals where the inelastic effects are important are related to the energy ranges where  $P(E) \neq 0$ . The order of magnitude of  $J(t)$  sets the number of photons responsible for the single-particle tunneling. Depending on this number, the coupling between the NIS junction and the multimode environment can be considered weak or strong. Throughout this paper we will treat both regimes of weak and strong coupling in more detail.

In order to analyze the smearing of the NIS junction's  $I$ - $V$  characteristic due to the presence of the high-temperature environment, we will ignore the thermal smearing induced by finite temperature of the N and S electrodes. This is an adequate approximation under standard experimental conditions where  $T_{\text{jun}} \ll \Delta/k_B$ . Hereafter, we will set the temperature of the junction  $T_{\text{jun}}$  to zero. Under this assumption, the single-particle current (2) becomes

$$I_{\text{NS}}(V) \simeq \frac{1}{eR_T} \int_{-eV}^{+eV} dE \int_{\Delta}^{+\infty} dE' N_S(E') P(E - E'). \quad (5)$$

We furthermore will focus on the subgap region of the  $I$ - $V$  curve considering  $|eV| \ll \Delta$ . As a result, the integration variables  $|E| \ll E'$  in Eq. (5), and we can approximate

$P(E - E') \approx P(-E')$ . The resulting integral over  $E$  can be performed immediately to yield

$$I_{\text{NS}}^{\text{sub}}(V) \simeq \gamma_{\text{env}} \frac{V}{R_T}, \quad (6)$$

where the factor  $\gamma_{\text{env}}$  is given by the integral

$$\gamma_{\text{env}} = 2 \int_{\Delta}^{+\infty} dE' N_S(E') P(-E'). \quad (7)$$

We see that for the parameter  $\gamma_{\text{env}}$  [Eq. (7)] and hence the subgap current given by Eq. (6) to be nonzero, the function  $P(E)$  should be nonzero for energies  $E \leq -\Delta$ . This reflects the fact that under subgap conditions  $eV, k_B T_{\text{jun}} \ll \Delta$ , a nonzero single-particle current occurs only if the tunneling electrons absorb an energy  $\gtrsim \Delta$  from the environment. For instance,  $\gamma_{\text{env}} = 0$  for elastic tunneling in the absence of an environment, when  $P(E) = \delta(E)$ . We also expect  $\gamma_{\text{env}}$  to vanish when the temperature of the environment  $k_B T_{\text{env}}$  is much less than the energy gap  $\Delta$ . Indeed, due to detailed balance,<sup>19</sup>  $P(-E) = e^{-E/k_B T_{\text{env}}} P(E)$ , the function  $P(E)$  is strongly suppressed for negative energies  $E < -k_B T_{\text{env}}$ . This means that the integral in Eq. (7) will vanish unless the environment is sufficiently hot,  $k_B T_{\text{env}} \gtrsim \Delta$ .

In order to make a connection with the aforementioned approach due to Dynes, we linearize the usual expression for elastic single-particle tunneling in a NIS junction, using the Dynes DOS (1) to characterize the superconducting electrode. One obtains the linear subgap current-voltage relationship

$$I_{\text{NS}}^{\text{sub}}(V) \simeq \sqrt{\frac{\gamma_{\text{Dynes}}^2}{\gamma_{\text{Dynes}}^2 + 1}} \frac{V}{R_T}.$$

Comparing this result with Eq. (6) above, we conclude that, in the linear regime,  $\gamma_{\text{env}}$  can be related to the Dynes parameter in the subgap region  $\gamma_{\text{Dynes}}^{\text{sub}}$  according to  $\gamma_{\text{env}} = \sqrt{\gamma_{\text{Dynes}}^{\text{sub}2} / (\gamma_{\text{Dynes}}^{\text{sub}2} + 1)}$ . We see in particular that the two parameters coincide  $\gamma_{\text{Dynes}}^{\text{sub}} = \gamma_{\text{env}}$  whenever  $\gamma_{\text{env}}, \gamma_{\text{Dynes}}^{\text{sub}} \ll 1$ . This shows that fluctuations of a high-temperature electromagnetic environment constitute a possible microscopic source of the phenomenological Dynes parameter, at least under subgap conditions  $eV, k_B T_{\text{jun}} \ll \Delta$ .

### B. Weak and strong coupling

As we have seen above, the strength of the coupling between the NIS junction and the environment is determined by the function  $J(t)$ . Let us assume that this function is small, in a sense to be detailed in the following. Expanding the exponential function  $\exp[J(t)]$  up to the first order in  $J(t)$ , Eq. (3) becomes

$$P(E) \simeq \frac{1}{2\pi\hbar} \int_{-\infty}^{+\infty} dt e^{iEt/\hbar} [1 + J(t)]. \quad (8)$$

The evaluation of the integral over time in Eq. (8) gives

$$P(E) \simeq \delta(E) + \frac{1}{\hbar} \int_0^{+\infty} \frac{d\omega}{\omega} \frac{\text{Re}[Z_{\text{tot}}(\omega)]}{R_K} \times \left\{ \left[ \coth\left(\frac{1}{2}\beta_{\text{env}}\hbar\omega\right) - 1 \right] \delta\left(\frac{E}{\hbar} + \omega\right) \right.$$

$$\left. + \left[ \coth\left(\frac{1}{2}\beta_{\text{env}}\hbar\omega\right) + 1 \right] \delta\left(\frac{E}{\hbar} - \omega\right) - 2\hbar \coth\left(\frac{1}{2}\beta_{\text{env}}\hbar\omega\right) \delta(E) \right\}. \quad (9)$$

We see that the function  $P(E)$  has an elastic contribution and an inelastic one involving the exchange of exactly one photon between the junction and the environment. In fact, the first and the fourth terms represent the elastic tunneling involving zero and one virtual photon, respectively. The second and third terms are related to the process of absorption and emission of one real photon, respectively. We define this one-photon regime as weak coupling. On the other hand, the coupling becomes strong whenever the single-photon exchange between the junction and the environment is no longer the dominant effect. In this case, the higher-order terms can not be neglected in the series expansion of  $\exp[J(t)]$ , indicating that multiphoton processes have to be taken into account.

We proceed by determining the time interval where the expansion (8) holds. Given the fact that  $J(t=0) = 0$ , we expect this to be the short-time interval.<sup>19</sup> We set  $Z(\omega) = R$  for simplicity and introduce the dimensionless time  $\tau = t/R_K C$  as well as the ratio  $\rho = R/R_K$ . The quantity  $\exp\{\text{Re}[J(\tau, \rho)]\}$  decays monotonically with increasing time  $\tau$ , starting from unity at  $\tau = 0$ . The rate at which it decays depends on  $\rho$ : the larger  $\rho$ , the faster it decays, in agreement with Ref. 19. We determine the relevant short-time interval by determining the characteristic time  $\tau_{10\%}$ , at which the quantity  $\exp\{\text{Re}[J(\tau, \rho)]\}$  dropped by 10%. Figure 2(a) shows  $\tau_{10\%}$  as a function of the parameter  $\rho$ , keeping  $T_{\text{env}}$  and  $C$  fixed. The line  $\tau_{10\%}(\rho)$  separates the weak coupling regime found at short times from the strong coupling regimes reached for longer times. As expected,<sup>19</sup> with increasing  $\rho$ , the separatrix  $\tau_{10\%}(\rho)$  decreases as  $1/\rho$ , and then saturates at a value  $\tau_S \sim \sqrt{\hbar/k_B T_{\text{env}} R_K C}$  for  $\rho > \rho_{\text{th}} \sim \tau_S$ . As shown in Fig. 2(b), the curve  $\tau_{10\%}(\rho)$  shifts up when decreasing the temperature of the environment  $T_{\text{env}}$ , thereby increasing the time interval where the expansion (8) holds.

We now return to the inelastic tunneling of single electrons through the NIS junction. Under subgap conditions  $k_B T_{\text{jun}}, eV \ll \Delta$ , the energy  $E$  relevant for the photon-assisted tunneling processes is in the interval  $\Delta \lesssim E \lesssim k_B T_{\text{env}}$ . The upper bound corresponds to the largest energy the junction can absorb from the environment. In time domain, we thus have to consider the interval  $\tau_e < \tau < \tau_\Delta$  where  $\tau_\Delta = \hbar/\Delta R_K C$  and  $\tau_e = \hbar/k_B T_{\text{env}} R_K C$ . This interval is represented by the colored strip in Fig. 2(a). Note that on the logarithmic scale used here, the lower bound  $\tau_e$  almost coincides with the value  $\tau_S$  at which the separatrix saturates for large values of  $\rho$ . The intersection between  $\tau_\Delta$  and the 10% curve  $\tau_{10\%}(\rho)$  defines the characteristic resistance  $\rho_\Delta$  separating the weak and strong coupling regimes. When  $\rho < \rho_\Delta$ , coupling is weak and only single-photon absorption processes occur (green area); if  $\rho \sim \rho_\Delta$ , both single-photon and multiphoton processes occur during single-electron tunneling (yellow-orange area); as soon as  $\rho \gg \rho_\Delta$ , multiphoton processes become dominant (red area). In particular, the two limiting cases  $\rho \ll \rho_\Delta$ ,  $\rho_{\text{th}}$  and  $\rho \gg \rho_\Delta$ ,  $\rho_{\text{th}}$  are equivalent to the conditions  $R/R_K \ll \Delta/k_B T_{\text{env}}$  and  $R/R_K \gg \Delta/k_B T_{\text{env}}$ , respectively.

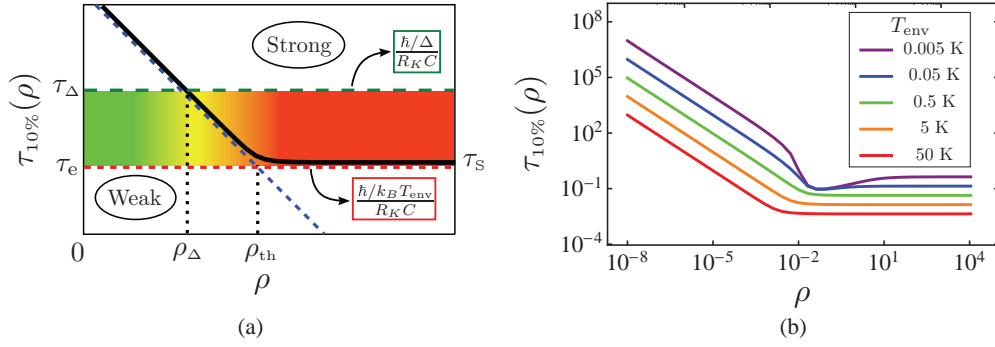


FIG. 2. (Color online) Plot of the separatrix  $\tau_{10\%}(\rho)$  as a function of the dimensionless resistance  $\rho = R/R_K$ , defined as the solution of the equation  $\exp\{\text{Re}[J(\tau_{10\%}, \rho)]\} = 0.9$  with  $C$  fixed. Both plots are in double-logarithmic scale. (a) For a fixed value of  $T_{\text{env}}$ ,  $\tau_{10\%}(\rho)$  separates the weak and strong coupling regions (black thick line). The colored strip indicates the time interval bound by  $\tau_{\Delta} = \hbar/\Delta R_K C$  (dark green dashed line) and  $\tau_e = \hbar/k_B T_{\text{env}} R_K C$  (red dashed line). The intersection between  $\tau_{\Delta}$  and the separatrix  $\tau_{10\%}(\rho)$  defines the resistance  $\rho_{\Delta}$ . The asymptotic expression for  $\tau_{10\%}(\rho)$  valid for  $\rho \rightarrow 0$  and proportional to  $1/\rho$  is also shown (blue dashed line). Its intersection with the line corresponding to  $\tau_S \sim \sqrt{\hbar/k_B T_{\text{env}} R_K C}$  defines the threshold resistance  $\rho_{\text{th}}$ . On the logarithmic scale used here,  $\tau_S$  almost coincides with  $\tau_e$ . (b) As the temperature of the environment  $T_{\text{env}}$  is decreased, the curve  $\tau_{10\%}(\rho)$  moves up, thereby increasing the weak coupling region.

### C. Subgap leakage current: Weak coupling

We start by dealing with the weak coupling case. Since we are interested in the subgap region of the  $I$ - $V$  characteristic  $k_B T_{\text{jun}}, eV \ll \Delta$ , the behavior of the function  $P(E)$  at energies  $E > -\Delta$  is irrelevant. Therefore, we can ignore the elastic contributions in Eq. (9). Evaluating the integral over frequencies in Eq. (9), the relevant contribution to the function  $P(E)$  for energies  $E \neq 0$  reads as

$$P(E) \simeq 2 \frac{\text{Re}[Z_{\text{tot}}(E/\hbar)]}{R_K} \left( \frac{1 + n(E)}{E} \right). \quad (10)$$

Here,  $n(E) = [e^{\beta_{\text{env}} E} - 1]^{-1}$  is the Bose-Einstein distribution of the photons of the environment.

The probability density (10) can be used to get a limiting expression for  $\gamma_{\text{env}}$ :

$$\gamma_{\text{env}} = 4 \int_{\Delta}^{+\infty} dE N_S(E) \frac{\text{Re}[Z_{\text{tot}}(E/\hbar)]}{R_K} \frac{n(E)}{E}. \quad (11)$$

Let us apply this result to the example of a purely resistive external environment. This model has been used before to study devices based on tunnel junctions in connection with experiments.<sup>17,20,21</sup> Replacing the external impedance  $Z(\omega)$  of the circuit of Fig. 1(a) by a pure resistance  $R$ , the real part of the total impedance is

$$\text{Re}[Z_{\text{tot}}(\omega)] = \frac{R}{1 + (\omega RC)^2}. \quad (12)$$

Numerical integration of Eq. (11) using Eq. (12) is straightforward. Results for  $R_K \gamma_{\text{env}}/R$  as a function of  $k_B T_{\text{env}}/\Delta$  are shown in Fig. 3 for various values of the parameter  $\Delta RC/\hbar$ . We see that  $\gamma_{\text{env}}$  increases monotonically with temperature. Also shown is the asymptotic linear temperature dependence of  $\gamma_{\text{env}}$  reached for temperatures  $k_B T_{\text{env}} \gg \Delta$ :

$$\gamma_{\text{env}} \simeq 2\pi \frac{R}{R_K} \frac{k_B T_{\text{env}}}{\Delta} \left[ 1 - \frac{\Delta RC/\hbar}{\sqrt{1 + (\Delta RC/\hbar)^2}} \right]. \quad (13)$$

This high-temperature expression is correct up to a constant shift  $\approx \Delta/k_B$  along the temperature axis [see Fig. 3].

From Fig. 3 we see that as the parameter  $\Delta RC/\hbar$  is increased, the slope characterizing the limiting dependence decreases: photon-assisted inelastic tunneling is effectively reduced by increasing the junction capacitance. Note that in the limit  $\Delta RC/\hbar \ll 1$ , the result (13) tends to  $\gamma_{\text{env}}^{\text{D}} = 2\pi(R/R_K)(k_B T_{\text{env}}/\Delta)$ . This formula has been already obtained in Ref. 17 using  $P(E)$  theory under similar conditions, but for any bias voltage, using a high-temperature expansion for the environment [see also Ref. 22].

Consequently, the subgap parameter  $\gamma_{\text{env}}^{\text{D}}$  coincides with the Dynes parameter  $\gamma_{\text{Dynes}}$ . In other words, within this limiting case, the thermal energy  $k_B T_{\text{env}}$  determines the NIS junction's  $I$ - $V$  characteristic even around the superconducting gap  $e|V| \sim \Delta$ .

### D. Subgap leakage current: Strong coupling

We do not aim to present a general analysis in the strong coupling limit. In the particular case where  $\text{Re}[Z_{\text{tot}}(\omega)]$  is strongly peaked around  $\omega = 0$ , the probability density  $P(E)$  can be calculated explicitly<sup>19</sup> and results for the parameter  $\gamma_{\text{env}}$  obtained. Let us illustrate this by considering a purely resistive environment. When the resistance is big,  $R \gg R_K \Delta/k_B T_{\text{env}}$

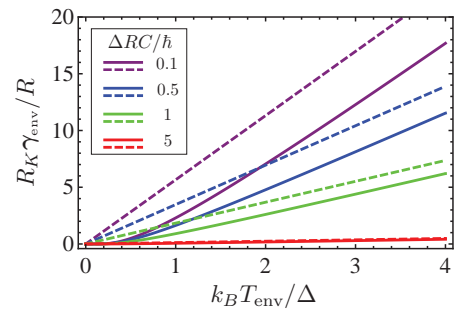


FIG. 3. (Color online) Plot of the rescaled parameter  $R_K \gamma_{\text{env}}/R$  as a function of  $k_B T_{\text{env}}/\Delta$  for different values of the ratio  $\Delta RC/\hbar$ . Solid lines are obtained by a numerical integration of Eq. (11) using Eq. (12). Dashed lines refer to the asymptotic  $\gamma_{\text{env}}$  given by Eq. (13).

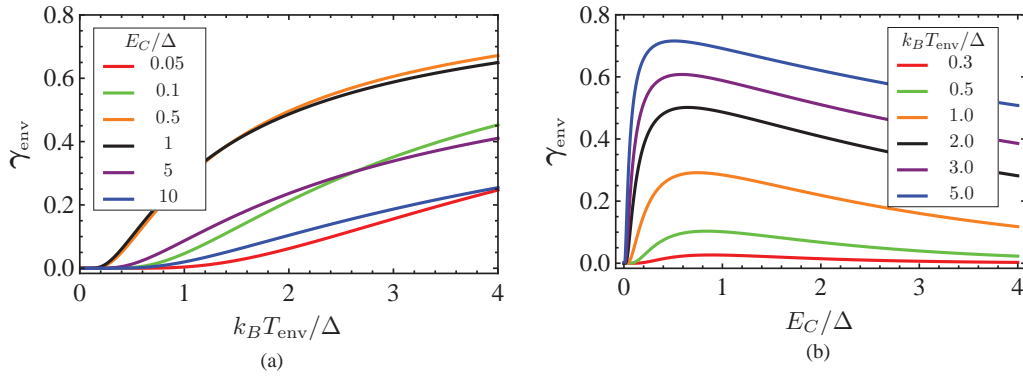


FIG. 4. (Color online) (a) Plot of the parameter  $\gamma_{\text{env}}$  as a function of  $k_B T_{\text{env}}/\Delta$  obtained considering the numerical integration of Eq. (16). Each curve refers to a certain fixed value of the ratio  $E_C/\Delta$  (see legend). (b) Numerical plot of the same quantity [Eq. (16)] as a function of  $E_C/\Delta$  for different values of the ratio  $k_B T_{\text{env}}/\Delta$ , as indicated.

(see Sec. II B), the impedance (12) becomes

$$\text{Re}[Z_{\text{tot}}(\omega)] \simeq \left(\frac{\pi}{C}\right) \delta(\omega). \quad (14)$$

As a result, the function  $P(E)$  is given by

$$P(E) \simeq \frac{1}{\sqrt{4\pi k_B T_{\text{env}} E_C}} \exp\left[-\frac{(E - E_C)^2}{4k_B T_{\text{env}} E_C}\right]. \quad (15)$$

Here, we defined the charging energy  $E_C = e^2/2C$ . Inserting the function (15) in Eq. (7), we find

$$\gamma_{\text{env}} = \frac{1}{\sqrt{\pi E_C k_B T_{\text{env}}}} \int_{-\Delta}^{+\infty} dE N_S(E) \exp\left[-\frac{(E + E_C)^2}{4E_C k_B T_{\text{env}}}\right]. \quad (16)$$

Note that this result depends on  $R$  implicitly only, through the requirement  $R \gg R_K \Delta / k_B T_{\text{env}}$ . Direct numerical integration of (16) yields  $\gamma_{\text{env}}$  as a function of  $k_B T_{\text{env}}/\Delta$  and  $E_C/\Delta$ , as shown in Figs. 4(a) and 4(b). Some remarks are in order at this point. First of all, for  $E_C \ll \Delta$ , the integral in Eq. (16) can be evaluated approximately,  $\gamma_{\text{env}} \simeq e^{-\Delta^2/k_B T_{\text{env}} E_C}$ . As in the weak coupling regime, large values of the capacitance lead to a reduction of the parameter  $\gamma_{\text{env}}$ . Upon increasing the ratio  $E_C/\Delta$ ,  $\gamma_{\text{env}}$  will first increase, then it decreases again when  $E_C/\Delta > 1$ , which is a manifestation of the Coulomb blockade. As a function of temperature,  $\gamma_{\text{env}}$  increases monotonically, similarly to the weak coupling limit. However, rather than reaching an asymptotic linear dependence,  $\gamma_{\text{env}}$  saturates at  $\gamma_{\text{env}} = 1$  for temperatures  $k_B T_{\text{env}} E_C \gg \Delta^2$ : the noise is so strong that features of the order of the gap  $\Delta$  are washed out.

### III. NIS JUNCTION COUPLED TO A HIGH-TEMPERATURE ENVIRONMENT BY MEANS OF A TRANSMISSION LINE

In the previous section, we have studied the subgap leakage current in a NIS junction which is directly coupled to the external environment  $Z(\omega)$ . We have seen that a reduction of the subgap leakage current is possible when the capacitance of the junction  $C$  is increased and/or the resistance of the environment  $R$  is decreased. Unfortunately, in real experiments  $R$ , and in particular  $C$ , can not be chosen arbitrarily and one needs other means to achieve the

accuracy requirements for the aforementioned NIS junction's applications. We therefore consider the circuit of Fig. 1(b) where the junction is indirectly coupled to the external environment via a cold, lossy transmission line acting as a frequency-dependent filter.

#### A. Voltage fluctuations in the presence of a transmission line

In order to find the correlation function  $J(t)$  in the presence of the transmission line, we follow the method developed in Ref. 23 to solve the intermediate problem of the propagation of the noise generated by the high-temperature environment with impedance  $Z(\omega)$  through the line towards the junction, as shown in Fig. 5. The line has a length  $\ell$  and is described by the parameters  $R_0$ ,  $C_0$ , and  $L_0$ , the resistance, the capacitance, and the inductance per unit length, respectively. We ignore the thermal noise produced by the impedance  $Z_J(\omega)$  and by the line, assuming both components at zero temperature. The high-temperature element produces current noise  $\delta I$  which in turn induces voltage noise  $\delta V$ .

To understand how the potential drop  $\delta V_J$  across  $Z_J(\omega)$  is connected to  $\delta V = Z(\omega) \delta I$ , we start considering the potential  $V(x)$  and the current  $I(x)$  at a given point  $x$  along the transmission line. They satisfy the two partial differential equations

$$\frac{\partial V(x)}{\partial x} = -I(x)[R_0 - i\omega L_0], \quad \frac{\partial I(x)}{\partial x} = i\omega C_0 V(x).$$

Combining them, one obtains the wave equation

$$\frac{\partial^2 V(x)}{\partial x^2} = -K^2(\omega) V(x), \quad (17)$$

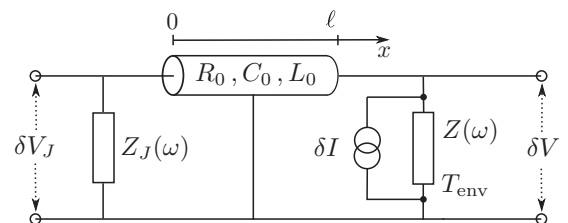


FIG. 5. Sketch of the circuit discussed in Sec. III A.

where  $K^2(\omega) = \omega^2 L_0 C_0 + i\omega R_0 C_0$  is the wave vector squared of the signal which propagates along the line. A general solution of Eq. (17) is given by

$$V(x) = A e^{iK(\omega)x} + B e^{-iK(\omega)x}. \quad (18)$$

Consequently, the current along the line is

$$I(x) = \frac{1}{Z_\infty(\omega)} [A e^{iK(\omega)x} - B e^{-iK(\omega)x}], \quad (19)$$

with  $Z_\infty(\omega) = i(R_0 - i\omega L_0)/K(\omega)$ . The parameters  $A$  and  $B$  can be determined by means of the boundary conditions

$$\begin{aligned} V(\ell) &= Z(\omega)[I(\ell) + \delta I] = Z(\omega) I(\ell) + \delta V, \\ V(0) &= -Z_J(\omega) I(0). \end{aligned}$$

As a result, the potential drop  $\delta V_J = V(0) = A + B$  across the impedance  $Z_J(\omega)$  depends on the noise  $\delta V$  according to the relation

$$\delta V_J = T(\omega) \delta V. \quad (20)$$

In this last equation, we introduced  $T(\omega)$ , the transmission function

$$\begin{aligned} T(\omega) &= \frac{2 Z_\infty(\omega) Z_J(\omega)}{[Z_\infty(\omega) + Z(\omega)][Z_\infty(\omega) + Z_J(\omega)]} \\ &\times \frac{1}{e^{-iK(\omega)\ell} - \lambda_1(\omega) \lambda_2(\omega) e^{iK(\omega)\ell}}, \end{aligned} \quad (21)$$

where

$$\lambda_1(\omega) = \frac{Z_\infty(\omega) - Z(\omega)}{Z_\infty(\omega) + Z(\omega)}, \quad \lambda_2(\omega) = \frac{Z_\infty(\omega) - Z_J(\omega)}{Z_\infty(\omega) + Z_J(\omega)}$$

are the reflection coefficients. Assuming that the potential  $\delta V$  satisfies the quantum fluctuation-dissipation theorem

$$\langle \delta V(t) \delta V(0) \rangle_\omega = 2\hbar\omega \frac{\text{Re}[Z(\omega)]}{1 - e^{-\beta_{\text{env}}\hbar\omega}},$$

the spectral density function of the potential (20) is

$$\langle \delta V_J(t) \delta V_J(0) \rangle_\omega = |T(\omega)|^2 2\hbar\omega \frac{\text{Re}[Z(\omega)]}{1 - e^{-\beta_{\text{env}}\hbar\omega}}. \quad (22)$$

This expression describes the propagation of the noise from  $Z(\omega)$  to the noiseless impedance  $Z_J(\omega)$  through the noiseless transmission line. The voltage-voltage correlation function (22) is in agreement with the general formula given in Ref. 23.

### B. Correlation function for the transmission line circuit

We use Eq. (22) to calculate the modified correlation function  $J_T(t)$  which appears in Eq. (3). According to Ref. 19,  $J(t)$  is defined as the correlation function

$$J(t) \equiv \langle \varphi_J(t) \varphi_J(0) - \varphi_J(0) \varphi_J(t) \rangle, \quad (23)$$

where the phase  $\varphi_J(t)$  is the time integral of the potential  $\delta V_J(t)$  across the NIS junction

$$\varphi_J(t) \equiv \frac{e}{\hbar} \int_{-\infty}^t \delta V_J(\tau) d\tau.$$

In other words,

$$\langle \varphi_J(t) \varphi_J(0) \rangle_\omega = \left(\frac{e}{\hbar}\right)^2 \frac{1}{\omega^2} \langle \delta V_J(t) \delta V_J(0) \rangle_\omega. \quad (24)$$

Using the fluctuation-dissipation relation (22) in Eq. (24), we rewrite Eq. (23) as a function of  $T(\omega)$ ,  $Z(\omega)$ , and  $T_{\text{env}}$ . Taking the impedance  $Z_J(\omega)$  to be the one of a capacitance  $C$ , the modified function  $J_T(t)$  reads as

$$\begin{aligned} J_T(t) &= 2 \int_0^{+\infty} \frac{d\omega}{\omega} |T_C(\omega)|^2 \frac{\text{Re}[Z(\omega)]}{R_K} \\ &\times \left\{ \coth\left(\frac{1}{2}\beta_{\text{env}}\hbar\omega\right) [\cos(\omega t) - 1] - i \sin(\omega t) \right\}. \end{aligned} \quad (25)$$

Here,  $T_C(\omega)$  is the function  $T(\omega)$  [Eq. (21)] with  $Z_J(\omega) = Z_C(\omega) = -1/i\omega C$ . Since the transmission line is considered noiseless, its temperature  $T_{\text{line}}$  should be low,  $T_{\text{line}} \ll \Delta/k_B$ . In what follows, we set  $T_{\text{line}} = T_{\text{jun}} = 0$ .

### C. Transmission function

In order to understand the effect of the insertion of the transmission line in the circuit of Fig. 1(a), a discussion about the general behavior of  $T_C(\omega)$  is necessary. In general, the modulus squared of the transmission function (21) is characterized by a series of resonance peaks, whose properties depend on  $\ell$ ,  $R_0$ ,  $C_0$ , and  $L_0$  as well as on the external impedance  $Z(\omega)$ . To have an idea of the behavior of  $|T_C(\omega)|^2$ , let us consider the case of a purely resistive environment  $Z(\omega) = R$ .

Figure 6 illustrates the behavior of  $|T_C(\omega)|^2$  as a function of  $\omega RC$  for different values of the dimensionless parameters  $z_0 = \sqrt{L_0/C_0}/R$ ,  $c_0 = \ell C_0/C$ , and  $r_0 = \ell R_0/R$ . Also shown is the Lorentzian result

$$|T_C(\omega)|^2 = 1/[1 + (\omega RC)^2] \quad (26)$$

found for  $\ell = 0$ , i.e., in the absence of the transmission line. In other words, Eq. (26) describes the spectrum of the transmitted signal through a lumped  $RC$  low-pass filter. In order for the line to be an efficient filter, we require  $|T_C(\omega)|^2$  to be below this Lorentzian curve in the relevant frequency ranges. We see that both the position and the width of the resonance peaks are proportional to  $\pi/2c_0z_0$ : the longer the transmission line, the denser around zero and the sharper are the peaks. Their height decreases rapidly as the dimensionless frequency  $\omega RC$  is increased. This can be seen in particular when the line has no losses,  $r_0 = 0$  [see Figs. 6(a)–6(d)]. Although the Lorentzian curve is approached for lossless lines when  $c_0$  or  $z_0$  is reduced, we observe no real reduction below it.

A significant reduction of the height of the peaks is possible if the line which connects the NIS junction and the environment is lossy,  $r_0 > 0$ . Indeed, we see from Figs. 6(e) and 6(f) that the bigger is  $r_0$  the smaller are the local maxima of  $|T_C(\omega)|^2$ . Moreover, the transmission function is even much smaller than  $1/[1 + (\omega RC)^2]$  when the condition  $r_0 \gg z_0$  is satisfied, as is seen in Figs. 6(f) and 7. Therefore, within this particular limit, the insertion of a resistive transmission line may be convenient.

### D. Subgap leakage current: Weak coupling

We expect that the single-photon and multiphoton regimes, weak and strong coupling, respectively, are strongly related to the resistance per unit length  $R_0$ . Let us analyze the situation proceeding as in Sec. II B. We consider the function  $\tau_{10\%}(\rho)$  for

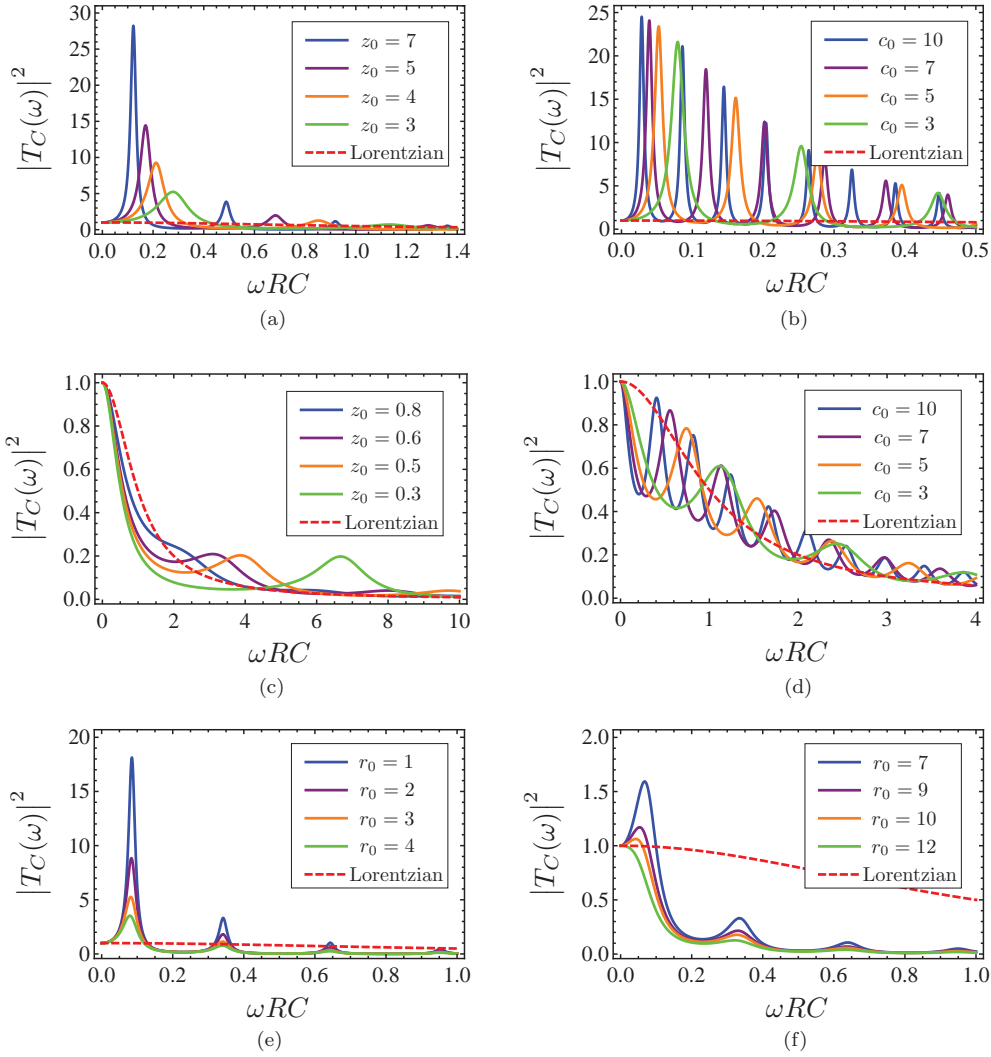


FIG. 6. (Color online) Plots of the transmission function  $|T_C(\omega)|^2$  as a function of the dimensionless variable  $\omega RC$ . Each panel corresponds to a different set of the parameters  $z_0$ ,  $c_0$ , and  $r_0$ : (a)  $r_0 = 0$ ,  $c_0 = 1$ ,  $z_0 = (7, 5, 4, 3)$ ; (b)  $r_0 = 0$ ,  $z_0 = 5$ ,  $c_0 = (10, 7, 5, 3)$ ; (c)  $r_0 = 0$ ,  $c_0 = 1$ ,  $z_0 = (0.8, 0.6, 0.5, 0.3)$ ; (d)  $r_0 = 0$ ,  $z_0 = 0.7$ ,  $c_0 = (10, 7, 5, 3)$ ; (e)  $z_0 = 10$ ,  $c_0 = 1$ ,  $r_0 = (1, 2, 3, 4)$ ; (f)  $z_0 = 10$ ,  $c_0 = 1$ ,  $r_0 = (7, 9, 10, 12)$ .

a purely resistive environment. In Fig. 8, we plot  $\tau_{10\%}(\rho)$  as a function of the dimensionless resistance  $\rho$  for different values of  $R_0$ . We see that the lossier the transmission line is, the more

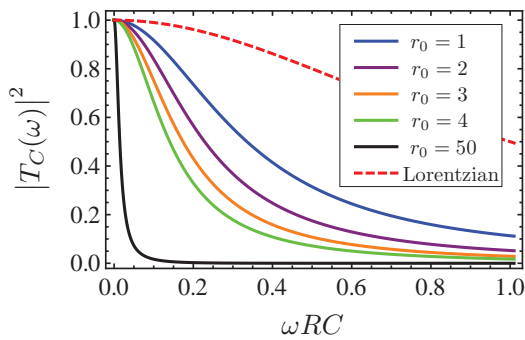


FIG. 7. (Color online) Plot of the transmission function  $|T_C(\omega)|^2$  as a function of the dimensionless variable  $\omega RC$  for different values of the parameter  $r_0$ . The other parameters are  $c_0 = 1$ ,  $z_0 = 0.7$ . Also shown is the Lorentzian corresponding to the function  $|T_C(\omega)|^2$  in the limit  $\ell \rightarrow 0$ , given by Eq. (26).

the weak coupling region spreads out. The resistance  $\rho_\Delta$ , given by the intersection between  $\tau_{10\%}(\rho)$  and the line corresponding to the dimensionless time  $\tau_\Delta = \hbar/\Delta R_K C$ , significantly shifts towards higher values of  $\rho$  as  $R_0$  is increased; the lossy line indeed protects the junction from the high-temperature external environment. Hereafter, we will therefore focus on a highly resistive transmission line and only the weak coupling regime will be treated.

With the help of Eq. (25), the function  $P(E)$  for the circuit of Fig. 1(b) can be obtained in the weak coupling regime. Proceeding as in Sec. II C, we find

$$P(E) \simeq 2 |T_C(E/\hbar)|^2 \frac{\text{Re}[Z(E/\hbar)]}{R_K} \left( \frac{1+n(E)}{E} \right). \quad (27)$$

Evaluating the relation (27) for negative energies and inserting the result into Eq. (7), the parameter  $\gamma_{\text{env}}$  can be written as

$$\gamma_{\text{env}} = 4 \int_{\Delta}^{+\infty} dE N_S(E) |T_C(E/\hbar)|^2 \frac{\text{Re}[Z(E/\hbar)]}{R_K} \frac{n(E)}{E}. \quad (28)$$

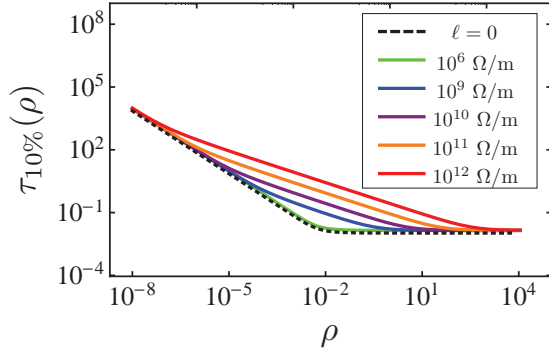


FIG. 8. (Color online) Plot of the dimensionless time  $\tau_{10\%}(\rho)$  as a function of the dimensionless resistance  $\rho = R/R_K$  for different values of the resistance per unit length  $R_0$  of the transmission line (see legend). Also shown is the curve  $\tau_{10\%}(\rho)$ , valid for the circuit of Fig. 1(a) (black dashed line). The values of the other parameters are  $\Delta \simeq 200 \mu\text{eV}$  (energy gap of aluminum),  $T_{\text{env}} = 5 \text{ K}$ ,  $C = 10 \text{ fF}$ ,  $C_0 = 6 \epsilon_0$ ,  $L_0 = \mu_0$ ,  $\ell = 10 \mu\text{m}$ .

We next specialize to the case of large resistance per unit length  $R_0$ . In order to obtain a limiting expression for  $|T_C(\omega)|^2$  for  $R_0 \rightarrow \infty$ , let us assume that the inductive properties of the line are negligible compared to  $R_0$ . Since the relevant frequency scale is given by  $\Delta/\hbar$ , this means that the condition  $R_0 \gg L_0 \Delta/\hbar$  should hold. Within this  $RC$  limit, we find that the wave vector  $K(\omega)$  of the signal propagating through the transmission line has an imaginary part equal to  $\sqrt{\omega R_0 C_0}/2$ . As a result, the amplitude of the noise is exponentially attenuated along the line [see Eqs. (18) and (19)] being proportional to  $\exp[-\ell\sqrt{2\omega R_0 C_0}]$ . We see that the bigger  $\ell$  and  $R_0$  are, the smaller is the voltage noise which reaches the junction. In particular, an exponential suppression of the propagating signal is achieved when the inequality  $\ell\sqrt{2\Delta R_0 C_0}/\hbar \gg 1$  is valid as well. This additional condition allows us to write the equation

$$|e^{-iK(\omega)\ell} - \lambda_1(\omega)\lambda_2(\omega)e^{iK(\omega)\ell}|^2 \simeq 4e^{\ell\sqrt{2\omega R_0 C_0}}.$$

Then, the modulus squared of the transmission function  $T_C(\omega)$  becomes

$$|T_C(\omega)|^2 \simeq \left| \frac{Z_\infty(\omega) Z_C(\omega) e^{-\ell\sqrt{2\omega R_0 C_0}/2}}{[Z_\infty(\omega) + Z(\omega)][Z_\infty(\omega) + Z_C(\omega)]} \right|^2, \quad (29)$$

where  $Z_\infty(\omega) \simeq (1+i)\sqrt{R_0/2\omega C_0}$  for a line in the  $RC$  limit. Combining the two conditions used so far, we find that the approximated function (29) holds when the resistance of the transmission line  $\ell R_0$  is much bigger than its characteristic impedance  $Z_\infty = \sqrt{L_0/C_0}$ .

Increasing the resistance per unit length  $R_0$ , one also expects that interference effects become negligible. Indeed, when  $R_0$  is very big, the amplitude of the signal across the junction is much smaller than its starting value and its reflected counterpart vanishes rapidly before reaching the noise source again. In terms of our description of the transmission line given in Sec. III A, this happens when the reflection coefficients  $\lambda_1(\omega)$  and  $\lambda_2(\omega)$  tend to 1. In fact, in this limit, the potential drop (18) tends to 0 across the junction and to  $\delta V$  across the impedance  $Z(\omega)$ . For a purely resistive environment, this regime is reached when  $R_0$  is such that the two inequalities

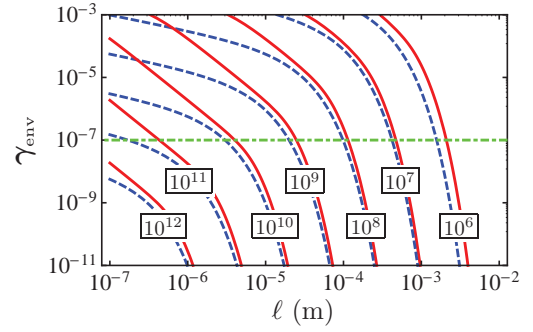


FIG. 9. (Color online) Plot of the parameter  $\gamma_{\text{env}}$  [Eq. (28)] as a function of the length of the transmission line  $\ell$ . The red solid line is obtained by means of the numerical integration of Eq. (28) for a purely resistive environment. The blue dashed line is the plot of the asymptotic parameter given by Eq. (31). These two curves are plotted for different values of the resistance per unit length  $R_0$  ( $\Omega/\text{m}$ ) (as indicated in the graph). All the plots are obtained considering the gap parameter of the aluminum,  $\Delta \simeq 200 \mu\text{eV}$ . The other parameters are  $T_{\text{env}} = 5 \text{ K}$ ,  $C = 10 \text{ fF}$ ,  $R = 10 \Omega$ ,  $C_0 = 6 \epsilon_0$ ,  $L_0 = \mu_0$ .

$R^2 \ll \hbar R_0/2C_0\Delta$  and  $\Delta R_0 C^2/\hbar C_0 \gg 2$  hold, in other words, when the resistance of the environment  $R$  is much smaller than  $R_0 C/2C_0$ . Equation (29) then reduces to the asymptotic expression

$$|T_C(\omega)|^2 \simeq \frac{e^{-\ell\sqrt{2\omega R_0 C_0}}}{1 + \omega R_0 C^2/C_0}. \quad (30)$$

Unlike the lumped  $RC$  low-pass filter described by the  $1/\omega$ -decaying Eq. (26), in this case we see that the amplitude of the transmitted frequencies relevant for the photon-assisted tunneling is exponentially suppressed as the length  $\ell$  and the resistance per unit length  $R_0$  of the line are increased. By means of Eq. (30), the integral in Eq. (28) can be evaluated approximately with the result

$$\gamma_{\text{env}} \simeq 4 \frac{R}{R_K} \frac{1}{e^{\Delta/k_B T_{\text{env}}} - 1} \times \sqrt{\frac{\pi}{\ell\sqrt{2\Delta R_0 C_0}/\hbar}} \frac{e^{-\ell\sqrt{2\Delta R_0 C_0}/\hbar}}{1 + \Delta R_0 C^2/\hbar C_0}. \quad (31)$$

We notice that also the asymptotic parameter  $\gamma_{\text{env}}$  decreases exponentially in terms of  $\ell$  and  $R_0$ ; the dependence on the junction capacitance  $C$  is rather weak. The insertion of a highly resistive and noiseless transmission line between the NIS junction and the high-temperature environment indeed helps to suppress the subgap leakage current. The plot of Fig. 9 shows the exponential decay for a set of values of  $R_0$  and  $\ell$  that can be used in real experiments. Particularly interesting is the region where  $10^8 \Omega/\text{m} \lesssim R_0 \lesssim 10^{10} \Omega/\text{m}$  and  $10 \mu\text{m} \lesssim \ell \lesssim 10^2 \mu\text{m}$ . A transmission line with these values of  $R_0$  and  $\ell$  allows one to go far below  $\gamma_{\text{env}} \simeq \gamma_{\text{Dynes}}^{\text{sub}} \sim 10^{-7}$ , i.e., a value of  $\gamma_{\text{env}}$  which guarantees the achievement of the accuracy requirements for the superconducting gap-based technological applications of the NIS junction.<sup>9</sup>

#### IV. MULTIPARTICLE TUNNELING

Our analysis focuses on the single-particle subgap current through the NIS junction. We ignore the contribution due

to higher-order processes in tunneling, such as Andreev reflection.<sup>12–14</sup> Hence, in order to establish the validity of our single-particle tunneling assumption, one has to compare the parameter  $\gamma_{\text{env}}$  characterizing the leakage current with the dimensionless Andreev subgap conductance  $g_A = G_A R_T$ . In ballistic junctions, second-order perturbation theory yields the standard two-particle subgap conductance

$$G_A \simeq R_K / [R_T^2 (k_F^2 S)], \quad (32)$$

where  $k_F^2 S$  is the number of conduction channels in the tunnel barrier. Two-electron tunneling can be ignored as long as  $\gamma_{\text{env}} > R_K / R_T k_F^2 S$ . Typical estimates<sup>14</sup> yield  $R_K / R_T k_F^2 S \sim 10^{-7}$ .

On the other hand, in the diffusive case, the electrons reflected by the barrier are backscattered by the impurities randomly situated close to the barrier in the normal metal. Interference between the electrons in a region characterized by the coherence length  $\xi_N = \sqrt{\hbar D / \max\{eV, k_B T_{\text{jun}}\}}$ , where  $D$  is the diffusion coefficient, affects the two-particle tunneling probability.<sup>24</sup> As a result,  $G_A$  is given by

$$G_A \simeq R_N / R_T^2, \quad (33)$$

where  $R_N$  is the resistance of the diffusive normal metal over a length  $\xi_N$ . General estimates are hard to give in this situation since the result is strongly geometry dependent; the condition  $\gamma_{\text{env}} > R_N / R_T$  will be more stringent than the one for the ballistic case, especially under subgap conditions where  $\xi_N$  and hence  $R_N$  can be large.

Should Andreev reflection become dominant, one can always suppress it efficiently using the Coulomb blockade feature<sup>14</sup> that suppresses two-particle tunneling more strongly than single-particle tunneling.

## V. CONCLUSIONS

In conclusion, we studied the single-particle tunneling current through a voltage-biased NIS junction. Due to the presence of the superconducting energy gap  $\Delta$  in the BCS density of states, when the junction is kept at the temperature  $T_{\text{jun}} \ll \Delta / k_B$ , no current is expected to flow within the subgap region  $-\Delta < eV < \Delta$ . Actually, even if the higher-order tunneling processes are suppressed, a small subgap current is still measured experimentally. This leakage current limits the accuracy in applications involving NIS junctions. The origin of the leakage current is the exchange of energy exceeding the gap  $\Delta$  between the junction and the external high-temperature environment in which it is embedded. We studied this mechanism analytically and numerically. In particular, we found that a cold and lossy transmission line inserted between the junction and the environment reduces exponentially the subgap leakage current acting as a frequency-dependent filter. This indirect configuration helps to achieve the required suppression of noise.

## ACKNOWLEDGMENTS

The authors thank W. Belzig and G. Rastelli for useful discussions. Financial support from the Marie Curie Initial Training Network (ITN) Q-NET (Project No. 264034), from Institut Universitaire de France, and from Aalto University's ASCI visiting professor programme is gratefully acknowledged. The work was partially supported by the Academy of Finland through its LTQ (Project No. 250280) COE grant (V.F.M. and J.P.P.), and the National Doctoral Programme in Nanoscience, NGS-NANO (V.F.M.).

- <sup>1</sup>H. Pothier, S. Guéron, Norman O. Birge, D. Esteve, and M. H. Devoret, *Phys. Rev. Lett.* **79**, 3490 (1997).  
<sup>2</sup>H. Courtois, M. Meschke, J. T. Peltonen, and J. P. Pekola, *Phys. Rev. Lett.* **101**, 067002 (2008).  
<sup>3</sup>F. Giazotto, T. T. Heikkilä, A. Luukanen, A. M. Savin, and J. P. Pekola, *Rev. Mod. Phys.* **78**, 217 (2006).  
<sup>4</sup>J. M. Rowell and D. C. Tsui, *Phys. Rev. B* **14**, 2456 (1976).  
<sup>5</sup>D. R. Schmidt, C. S. Yung, and A. N. Cleland, *Appl. Phys. Lett.* **83**, 1002 (2003).  
<sup>6</sup>N. Nahum, T. M. Eiles, and John M. Martinis, *Appl. Phys. Lett.* **65**, 3123 (1994).  
<sup>7</sup>M. M. Leivo, J. P. Pekola, and D. V. Averin, *Appl. Phys. Lett.* **68**, 1996 (1996).  
<sup>8</sup>A. Kemppinen, M. Meschke, M. Möttönen, D. V. Averin, and J. P. Pekola, *Eur. Phys. J. Special Topics* **172**, 311 (2009).  
<sup>9</sup>J. P. Pekola, O.-P. Saira, V. F. Maisi, A. Kemppinen, M. Möttönen, Yu. A. Pashkin, D. V. Averin, [Rev. Mod. Phys. (to be published)].  
<sup>10</sup>J. Bardeen, L. N. Cooper, and J. R. Schrieffer, *Phys. Rev.* **108**, 1175 (1957).  
<sup>11</sup>I. Giaever, H. R. Hart Jr., and K. Megerle, *Phys. Rev.* **126**, 941 (1962).  
<sup>12</sup>A. F. Andreev, Zh. Eksp. Teor. Fiz. **46**, 1823 (1964) [Sov. Phys.–JETP **19**, 1228 (1964)].  
<sup>13</sup>G. E. Blonder, M. Tinkham, and T. M. Klapwijk, *Phys. Rev. B* **25**, 4515 (1982).

- <sup>14</sup>V. F. Maisi, O.-P. Saira, Yu. A. Pashkin, J. S. Tsai, D. V. Averin, and J. P. Pekola, *Phys. Rev. Lett.* **106**, 217003 (2011).  
<sup>15</sup>R. C. Dynes, V. Narayanamurti, and J. P. Garno, *Phys. Rev. Lett.* **41**, 1509 (1978).  
<sup>16</sup>For a recent reference, see T. Greibe, M. P. V. Stenberg, C. M. Wilson, T. Bauch, V. S. Shumeiko, and P. Delsing, *Phys. Rev. Lett.* **106**, 097001 (2011).  
<sup>17</sup>J. P. Pekola, V. F. Maisi, S. Kafanov, N. Chekurov, A. Kemppinen, Yu. A. Pashkin, O.-P. Saira, M. Möttönen, and J. S. Tsai, *Phys. Rev. Lett.* **105**, 026803 (2010).  
<sup>18</sup>O.-P. Saira, M. Möttönen, V. F. Maisi, and J. P. Pekola, *Phys. Rev. B* **82**, 155443 (2010).  
<sup>19</sup>G. L. Ingold and Yu. V. Nazarov, in *Single Charge Tunneling*, edited by H. Grabert and M. H. Devoret NATO ASI Series B (Plenum, New York, 1992), Vol. 294, pp. 21–107.  
<sup>20</sup>J. M. Martinis and M. Nahum, *Phys. Rev. B* **48**, 18316 (1993).  
<sup>21</sup>J. M. Hergenrother, J. G. Lu, M. T. Tuominen, D. C. Ralph, and M. Tinkham, *Phys. Rev. B* **51**, 9407 (1995).  
<sup>22</sup>H. Grabert, G.-L. Ingold, and B. Paul, *Europhys. Lett.* **44**, 360 (1998).  
<sup>23</sup>J. Siewert, Y. V. Nazarov, and G. Falci, *Europhys. Lett.* **38**, 365 (1997).  
<sup>24</sup>F. W. J. Hekking and Yu. V. Nazarov, *Phys. Rev. Lett.* **71**, 1625 (1993); *Phys. Rev. B* **49**, 6847 (1994).



# Publication XI

V. F. Maisi, D. Kambly, C. Flindt and J. P. Pekola. Full counting statistics of Andreev tunneling. *Phys. Rev. Lett.* 112, 036801 (2014).

© (2014) American Physical Society.

Reprinted with permission.



## Full Counting Statistics of Andreev Tunneling

Ville F. Maisi,<sup>1,2</sup> Dania Kambly,<sup>3</sup> Christian Flindt,<sup>3</sup> and Jukka P. Pekola<sup>1</sup>

<sup>1</sup>*Low Temperature Laboratory (OVLL), Aalto University School of Science, P.O. Box 13500, 00076 Aalto, Finland*

<sup>2</sup>*Centre for Metrology and Accreditation (MIKES), P.O. Box 9, 02151 Espoo, Finland*

<sup>3</sup>*Département de Physique Théorique, Université de Genève, 1211 Genève, Switzerland*

(Received 25 September 2013; published 23 January 2014)

We employ a single-charge counting technique to measure the full counting statistics of Andreev events in which Cooper pairs are either produced from electrons that are reflected as holes at a superconductor–normal-metal interface or annihilated in the reverse process. The full counting statistics consists of quiet periods with no Andreev processes, interrupted by the tunneling of a single electron that triggers an avalanche of Andreev events giving rise to strongly super-Poissonian distributions.

DOI: 10.1103/PhysRevLett.112.036801

PACS numbers: 73.23.Hk, 72.70.+m, 74.50.+r

Superconductors are materials that below a critical temperature lose their electrical resistance and thereby allow a supercurrent to flow [1]. Inside the superconducting gap electrons combine into Cooper pairs that carry electrical charge through the superconductor without dissipation. The conversion of a Cooper pair into normal-state electrons (or vice versa) is known as an Andreev process [2]. In a direct Andreev process, an electron in a normal-state material is reflected as a hole at the interface with a superconductor where a Cooper pair is formed. Moreover, with several normal-state electrodes coupled to the same superconductor, crossed Andreev reflections may occur where electrons coming from different electrodes combine into a Cooper pair.

Cooper pairs consist of highly quantum-correlated electrons and may thus serve as a source of entanglement when split into different normal-state electrodes [3–5]. The entanglement of the spatially separated electrons can be detected through current noise measurements [5]. Experiments on superconductor–normal-metal junctions have also revealed a doubling of the shot noise due to the conversion of Cooper pairs into normal-state electrons [6]. However, a complete understanding of the fundamental tunneling processes at a superconductor–normal-metal interface requires measurements beyond the average current and the noise only. Higher-order correlation functions are encoded in the full counting statistics (FCS), which quantifies the probability  $p(n, t)$  of observing  $n$  charge transfer events during the time span  $[0, t]$ . The FCS of normal-state electrons has been addressed both theoretically [7–9] and experimentally [10–21]. In contrast, measurements of the FCS of charge transfer into superconductors have so far been lacking despite great theoretical interest [22–31].

In this Letter we report measurements of the FCS of Andreev events occurring between a normal-metal island and two superconducting leads. Our measurements of the FCS allow us to develop a detailed understanding of the elementary tunneling processes at the superconductor–normal-metal interfaces. Figure 1(a) shows our SINIS

structure consisting of a normal-state copper island (N) connected by insulating (I) aluminum-oxide tunnel barriers (of a few nanometers thickness [32]) to a pair of superconducting (S) aluminum leads. The structure was

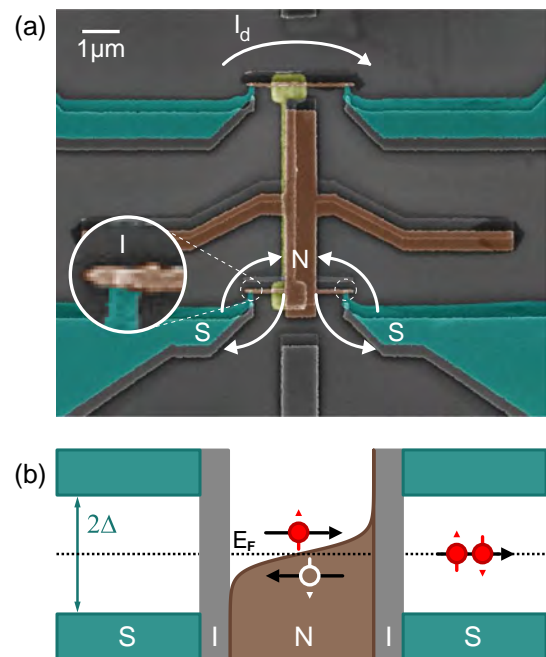


FIG. 1 (color online). SINIS structure and Andreev processes. (a) A metallic normal-state (N) island (brown) is connected by insulating (I) tunneling barriers to superconducting (S) leads (green). The current  $I_d$  through a separate single-electron transistor (SET) is sensitive to the charge occupation of the island and is used to read out the number  $N$  of excess charges on the island. A copper electrode (yellow) increases the capacitive coupling of the normal-state island to the SET and improves the detector signal-to-noise ratio. (b) An electron above the Fermi level of the normal-state island is reflected as a hole and a Cooper pair is formed in one of the superconductors. Without a voltage across the SINIS, the Fermi energy  $E_F$  of the normal-state material lies in the middle of the superconducting gap  $2\Delta$ .

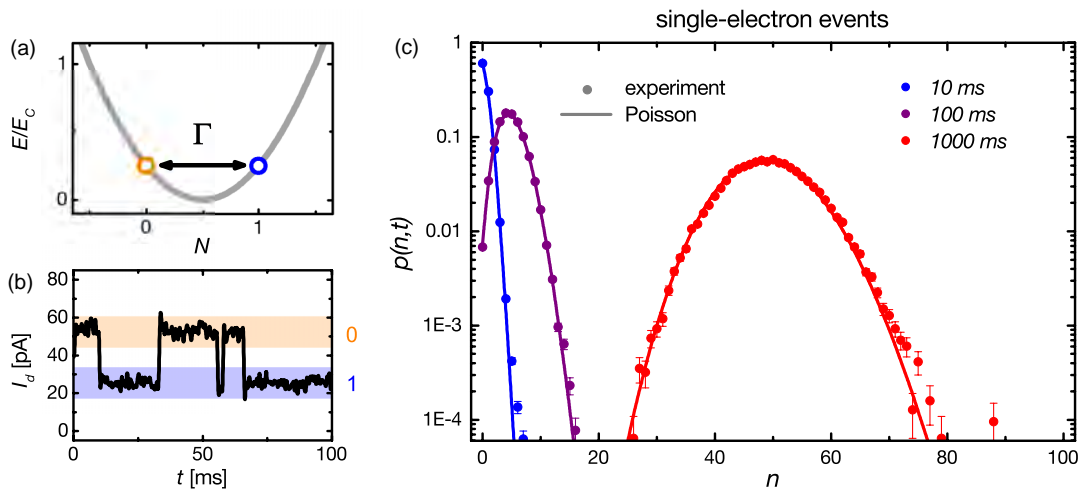


FIG. 2 (color online). FCS of single-electron events. (a) Charging diagram showing Eq. (1) with  $N_g = 0.5$ . The charge states with  $N = 0$  or  $N = 1$  excess charges on the island are degenerate. The transitions  $0 \rightleftharpoons 1$  occur with rate  $\Gamma = 49$  Hz. Other charge states are energetically unfavorable. (b) Time trace of the current  $I_d$  in the SET detector, which switches between two levels corresponding to  $N = 0$  and  $N = 1$ , respectively. (c) Measured FCS of single-electron events for different observation times  $t = 10, 100,$  and  $1000$  ms. Poisson distributions given by Eq. (2) are shown with full lines.

patterned on an oxidized silicon chip using standard  $e$ -beam lithography techniques. A copper coupling strip was first formed and covered with a 50 nm thick aluminum-oxide layer grown by atomic layer deposition. Gold leads (not shown) were then patterned, making a direct metallic contact to the superconducting leads. Finally, the SINIS structure and the gate leads were formed by  $e$ -beam evaporation at different angles. Tunnel barriers were created by thermal oxidation in between.

The number of excess electrons  $N$  on the island is discrete and can be controlled by applying a voltage  $V_g$  to a gate electrode below it. We parametrize the offset voltage by the variable  $N_g = C_g V_g / e$ , where  $C_g$  is the gate capacitance and  $e$  the electronic charge. The energy required for charging the island with  $N$  electrons is [33]

$$E = E_c (N - N_g)^2, \quad (1)$$

where the charging energy  $E_c = e^2 / 2C_\Sigma$  contains the total island capacitance  $C_\Sigma$ . The structure was designed to have a large capacitance, such that the charging energy is smaller than the superconducting gap  $\Delta$  of aluminum, thereby allowing for Andreev processes to occur between the island and the superconducting leads, see Fig. 1(b). The charging energy  $E_c = 40 \mu\text{eV}$ , the superconducting gap  $\Delta = 210 \mu\text{eV}$ , and the tunnel resistance  $R_T = 490 \text{ k}\Omega$  were determined by measuring the current-voltage characteristics of the SINIS structure. Measurements were performed in a dilution refrigerator at 50 mK bath temperature. The charge state of the island was monitored using a nearby single-electron transistor (SET), whose conductance depends

strongly on the number of excess charges on the island [12,13,15,17,19,21,34,35].

To illustrate the basic operating principle of our device we first tuned the offset voltage to  $N_g = 0.5$ . Figure 2(a) shows the energy for different numbers of excess charges. The states  $N = 0$  and  $N = 1$  are degenerate, while all other charge states are energetically unfavorable. In this case, single electrons may tunnel on and off the island from the aluminum leads with rate  $\Gamma$ . The origin of the single-electron tunneling is addressed in Ref. [36]. Figure 2(b) shows a measured time trace of the current  $I_d$  in the SET detector, which switches between two values corresponding to  $N = 0$  and  $N = 1$ . We count the number of single-electron tunneling events on and off the island. No voltage bias is applied. Figure 2(c) displays the measured distribution  $p(n, t)$  of the number  $n$  of single-electron events that have occurred during the time span  $[0, t]$ . The mean number of events increases with the observation time  $t$  and the distribution grows wider. The single-electron events are uncorrelated and should be distributed according to a Poisson distribution

$$p(n, t) = \frac{(\Gamma t)^n}{n!} e^{-\Gamma t} \quad (2)$$

with mean  $\langle n \rangle = \Gamma t$ . From this mean value we can extract the tunneling rate  $\Gamma$ . Figure 2(c) then shows that the FCS of single-electron events indeed is well captured by the Poisson distribution above.

We are now ready to measure the FCS of Andreev events. To this end, we tuned the offset voltage to  $N_g = 0$ . In this case, the charging diagram in Fig. 3(a) is slightly more involved: The lowest-energy state of the system is the configuration with  $N = 0$  excess charges. However, a

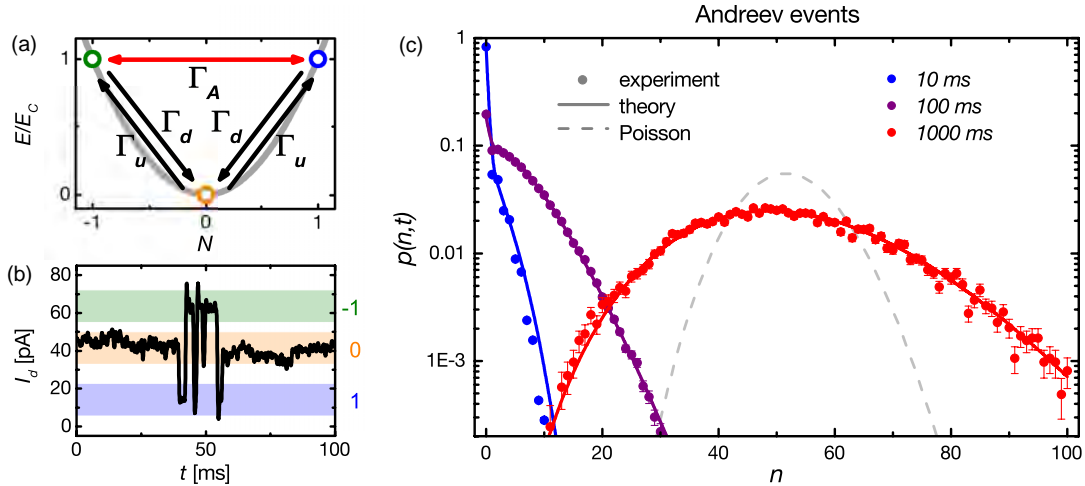


FIG. 3 (color online). FCS of Andreev events. (a) Charging diagram showing Eq. (1) with  $N_g = 0$ . In the ground state, the island is occupied by  $N = 0$  excess charges. A single-electron event may bring the island to a state with  $N = \pm 1$  excess charges. The excitations  $0 \rightarrow \pm 1$  occur with the rate  $\Gamma_u = 12$  Hz. Relaxation to the ground state  $\pm 1 \rightarrow 0$  happens with the rate  $\Gamma_d = 252$  Hz. The transitions  $-1 \rightleftharpoons 1$  correspond to Andreev events with the rate  $\Gamma_A = 615$  Hz. (b) Time trace of the SET-detector current  $I_d$ , which switches between three levels corresponding to  $N = -1$ ,  $N = 0$ , and  $N = 1$ , respectively. (c) Measured FCS of Andreev events for different observation times  $t = 10$ , 100, and 1000 ms. Full lines are calculations based on Eqs. (3) and (4). For comparison a Poisson distribution corresponding to 1000 ms is shown with a dashed line.

single-electron event may bring the system to one of the excited states with  $N = \pm 1$  excess charges. The excited states are energetically degenerate and the island can make transitions between  $N = -1$  and  $N = 1$  through Andreev processes, where two electrons at a time are converted into a Cooper pair in one of the superconductors or vice versa. The Andreev events occur with an average rate  $\Gamma_A$  until the system relaxes back to the ground state through a single-electron event. The current  $I_d$  in the SET detector now switches between three different values corresponding to  $N = -1$ , 0, or 1, see Fig. 3(b). (A fast sequence of single-electron events,  $-1 \rightarrow 0 \rightarrow 1$ , may be mistaken for an Andreev process,  $-1 \rightarrow 1$ , although it is unlikely.) We count the number of Andreev tunneling events to and from the island. Figure 3(c) shows the measured FCS of Andreev events obtained from around 640 000 Andreev processes. Again, the mean value of Andreev events grows with time; however, compared to the FCS of single-electron events, the width of the distributions is surprisingly large and the FCS is strongly super-Poissonian.

To understand quantitatively the FCS of Andreev events, we consider the probabilities  $p_0(n, t)$  and  $p_A(n, t)$  of the island being in the ground state or in one of the excited states, where Andreev events are possible. Both probabilities are resolved with respect to the number  $n$  of Andreev events that have occurred during the time span  $[0, t]$ . The FCS of Andreev events is  $p(n, t) = p_0(n, t) + p_A(n, t)$ , which can be conveniently expressed as the inner product  $p(n, t) = \langle \tilde{0} | p(n, t) \rangle$  of the vectors  $\langle \tilde{0} | = [1, 1]$  and  $|p(n, t)\rangle = [p_A(n, t), p_0(n, t)]^T$  [37,38]. We also introduce the moment generating function  $\mathcal{M}(\chi, t) = \sum_{n=0}^{\infty} p(n, t) e^{i n \chi} = \langle \tilde{0} | p(\chi, t) \rangle$

with  $|p(\chi, t)\rangle = \sum_{n=0}^{\infty} e^{i n \chi} |p(n, t)\rangle$ . The master equation for  $|p(\chi, t)\rangle$  reads

$$\frac{d}{dt} |p(\chi, t)\rangle = \mathbb{M}(\chi) |p(\chi, t)\rangle \quad (3)$$

with the rate matrix (see also Ref. [39])

$$\mathbb{M}(\chi) = \begin{bmatrix} \mathcal{H}_A(\chi) - \Gamma_d & 2\Gamma_u \\ \Gamma_d & -2\Gamma_u \end{bmatrix}. \quad (4)$$

Here  $\mathcal{H}_A(\chi) = \Gamma_A (e^{i\chi} - 1)$  is the generator of uncorrelated Andreev events occurring in the excited states with rate  $\Gamma_A$ . The rate for exciting the system is  $2\Gamma_u$  and  $\Gamma_d$  is the relaxation rate back to the ground state, see Fig. 3(a). The tunneling rates are extracted from the time traces of the SET-detector current [12,13,15,17,19,21,34,35]. Solving Eq. (3), we find  $|p(\chi, t)\rangle = e^{\mathbb{M}(\chi)t} |0\rangle$ , where  $|0\rangle = [2\Gamma_u, \Gamma_d]^T / (2\Gamma_u + \Gamma_d)$  is the stationary probability vector defined by  $\mathbb{M}(0)|0\rangle = 0$  and  $\langle \tilde{0} | 0 \rangle = 1$ . The moment generating function is then  $\mathcal{M}(\chi, t) = \langle \tilde{0} | e^{\mathbb{M}(\chi)t} |0\rangle$ . Finally, by inverting the moment generating function for  $p(n, t)$  we can evaluate the FCS of Andreev events for different observation times  $t$ .

The theoretical predictions agree well with the measurements in Fig. 3(c) using no fitting parameters. Moreover, a physical interpretation of the nontrivial FCS follows from an expansion of the cumulant generating function  $\mathcal{S}(\chi, t) = \log\{\mathcal{M}(\chi, t)\}$  in the smallest tunneling rate  $\Gamma_u \ll \Gamma_d, \Gamma_A$ . At long times, the cumulant generating function is determined by the eigenvalue of  $\mathbb{M}(\chi)$  with the largest real part [40,41]. Importantly, the cumulant generating function for independent processes is the sum of the cumulant

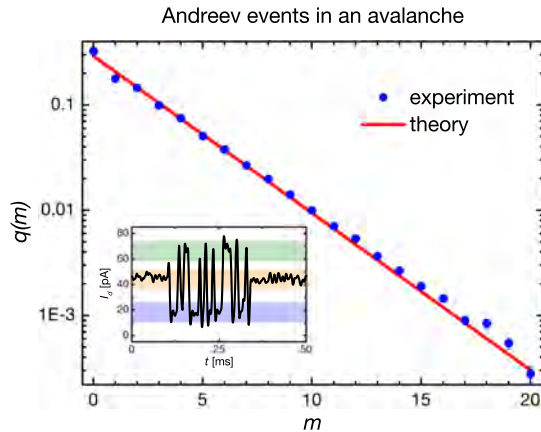


FIG. 4 (color online). Number of Andreev events per avalanche. The full line indicates the theoretical prediction given by Eq. (6) using  $\Gamma_d = 252$  Hz and  $\Gamma_A = 615$  Hz. The inset shows a time trace of the SET-detector current  $I_d$  during an avalanche with  $m = 16$  Andreev events.

generating functions for the individual processes. To lowest order in  $\Gamma_u$ , we find at long times

$$\mathcal{S}(\chi, t) = 2\Gamma_u t \sum_{m=1}^{\infty} q(m)(e^{im\chi} - 1) + \mathcal{O}(\Gamma_u^2) \quad (5)$$

with

$$q(m) = \frac{\Gamma_d}{\Gamma_A + \Gamma_d} \left( \frac{\Gamma_A}{\Gamma_A + \Gamma_d} \right)^m. \quad (6)$$

This shows that the FCS can be approximated as a sum of independent Poisson processes that with rate  $2\Gamma_u$  generate avalanches of  $m$  Andreev events. Each Poisson process is weighted by the probability  $q(m)$  of observing an avalanche with  $m$  Andreev events. In this approximation, correlations between subsequent avalanches are neglected together with the duration of the individual avalanches. These correlations would enter in Eq. (5) as higher-order terms in  $\Gamma_u$ , but would not affect the probabilities in Eq. (6). We note that similar single-electron avalanches have been predicted in molecular quantum transport [42].

To corroborate this physical picture, we turn to the number of Andreev events per avalanche. Figure 4 shows experimental results for the statistics of Andreev events within a single avalanche. The figure illustrates that avalanches with more than ten consecutive Andreev events are possible. This is also evident from the inset showing a time trace of the detector current  $I_d$ , which switches 16 times between the two levels corresponding to  $N = -1$  and  $N = 1$  excess charges, respectively. The agreement between the experimental results and the probabilities  $q(m)$  in Eq. (6) supports the interpretation that avalanches of Andreev events, triggered by the tunneling of single electrons, give rise to the strongly super-Poissonian FCS.

In summary, we have measured the FCS of Andreev events in an SINIS structure which exhibits super-Poissonian distributions due to avalanches triggered by individual single-electron tunneling events. Our experiment opens a number of directions for future research on charge fluctuations in superconductors. These include experimental investigations of the statistics of entangled electron pairs produced in crossed Andreev reflections as well as controllable Cooper pair production and detection for quantum metrological purposes [43].

We thank O. P. Saira who collaborated at an early stage of the work as well as C. Bergenfeldt and M. Büttiker for instructive discussions. We acknowledge the provision of facilities and technical support by Micronova Nanofabrication Centre and Cryohall at Aalto University. The work was supported by the Academy of Finland through its LTQ (project no. 250280) COE grant (V. F. M. and J. P. P.), the National Doctoral Programme in Nanoscience, NGS-NANO (V. F. M), and the Swiss NSF (D. K. and C. F.).

- 
- [1] M. Tinkham, *Introduction to Superconductivity* (Dover, New York, 2004).
  - [2] A. F. Andreev, *Sov. Phys. JETP* **19**, 1228 (1964).
  - [3] L. Hofstetter, S. Csonka, J. Nygård, and C. Schönberger, *Nature (London)* **461**, 960 (2009).
  - [4] L. G. Herrmann, F. Portier, P. Roche, A. L. Yeyati, T. Kontos, and C. Strunk, *Phys. Rev. Lett.* **104**, 026801 (2010).
  - [5] A. Das, Y. Ronen, M. Heiblum, D. Mahalu, A. V. Kretinin, and H. Shtrikman, *Nat. Commun.* **3**, 1165 (2012).
  - [6] X. Jehl, M. Sanquer, R. Calemczuk, and D. Mailly, *Nature (London)* **405**, 50 (2000).
  - [7] L. S. Levitov and G. B. Lesovik, *JETP Lett.* **58**, 230 (1993).
  - [8] Ya. M. Blanter and M. Büttiker, *Phys. Rep.* **336**, 1 (2000).
  - [9] *Quantum Noise in Mesoscopic Physics*, edited by Yu. V. Nazarov (Kluwer, Dordrecht, 2003).
  - [10] B. Reulet, J. Senzier, and D. E. Prober, *Phys. Rev. Lett.* **91**, 196601 (2003).
  - [11] Yu. Bomze, G. Gershon, D. Shovkun, L. S. Levitov, and M. Reznikov, *Phys. Rev. Lett.* **95**, 176601 (2005).
  - [12] S. Gustavsson, R. Leturcq, B. Simovic, R. Schleser, T. Ihn, P. Studerus, K. Ensslin, D. C. Driscoll, and A. C. Gossard, *Phys. Rev. Lett.* **96**, 076605 (2006).
  - [13] T. Fujisawa, T. Hayashi, R. Tomita, and Y. Hirayama, *Science* **312**, 1634 (2006).
  - [14] A. V. Timofeev, M. Meschke, J. T. Peltonen, T. T. Heikkilä, and J. P. Pekola, *Phys. Rev. Lett.* **98**, 207001 (2007).
  - [15] E. V. Sukhorukov, A. N. Jordan, S. Gustavsson, R. Leturcq, T. Ihn, and K. Ensslin, *Nat. Phys.* **3**, 243 (2007).
  - [16] G. Gershon, Yu. Bomze, E. V. Sukhorukov, and M. Reznikov, *Phys. Rev. Lett.* **101**, 016803 (2008).
  - [17] C. Flindt, C. Fricke, F. Hohls, T. Novotný, K. Netočný, T. Brandes, and R. J. Haug, *Proc. Natl. Acad. Sci. U.S.A.* **106**, 10 116 (2009).
  - [18] J. Gabelli and B. Reulet, *Phys. Rev. B* **80**, 161203(R) (2009).

- [19] S. Gustavsson, R. Leturcq, M. Studer, I. Shorubalko, T. Ihn, K. Ensslin, D. C. Driscoll, and A. C. Gossard, *Surf. Sci. Rep.* **64**, 191 (2009).
- [20] Q. Le Masne, H. Pothier, N. O. Birge, C. Urbina, and D. Esteve, *Phys. Rev. Lett.* **102**, 067002 (2009).
- [21] N. Ubbelohde, C. Fricke, C. Flindt, F. Hohls, and R. J. Haug, *Nat. Commun.* **3**, 612 (2012).
- [22] W. Belzig and Yu. V. Nazarov, *Phys. Rev. Lett.* **87**, 197006 (2001).
- [23] W. Belzig and Yu. V. Nazarov, *Phys. Rev. Lett.* **87**, 067006 (2001).
- [24] J. Börlin, W. Belzig, and C. Bruder, *Phys. Rev. Lett.* **88**, 197001 (2002).
- [25] G. Johansson, P. Samuelsson, and A. Ingeman, *Phys. Rev. Lett.* **91**, 187002 (2003).
- [26] J. C. Cuevas and W. Belzig, *Phys. Rev. Lett.* **91**, 187001 (2003).
- [27] W. Belzig and P. Samuelsson, *Europhys. Lett.* **64**, 253 (2003).
- [28] S. Pilgram and P. Samuelsson, *Phys. Rev. Lett.* **94**, 086806 (2005).
- [29] J. P. Morten, D. Huertas-Hernando, W. Belzig, and A. Brataas, *Phys. Rev. B* **78**, 224515 (2008).
- [30] G. C. Duarte-Filho and A. M. S. Macêdo, *Phys. Rev. B* **80**, 035311 (2009).
- [31] A. Braggio, M. Governale, M. G. Pala, and J. König, *Solid State Commun.* **151**, 155 (2011).
- [32] M. Prunnila, M. Meschke, D. Gunnarsson, S. Enouz-Vedrenne, J. M. Kivioja, and J. P. Pekola, *J. Vac. Sci. Technol. B* **28**, 1026 (2010).
- [33] Yu. V. Nazarov and Ya. M. Blanter, *Quantum Transport—Introduction to Nanoscience* (Cambridge University Press, Cambridge, England, 2009).
- [34] V. F. Maisi, O.-P. Saira, Yu. A. Pashkin, J. S. Tsai, D. V. Averin, and J. P. Pekola, *Phys. Rev. Lett.* **106**, 217003 (2011).
- [35] M. G. House, M. Xiao, G. P. Guo, H. O. Li, G. Cao, M. M. Rosenthal, and H. W. Jiang, *Phys. Rev. Lett.* **111**, 126803 (2013).
- [36] O.-P. Saira, A. Kemppinen, V. F. Maisi, and J. P. Pekola, *Phys. Rev. B* **85**, 012504 (2012).
- [37] C. Flindt, T. Novotný, and A.-P. Jauho, *Phys. Rev. B* **70**, 205334 (2004).
- [38] A.-P. Jauho, C. Flindt, T. Novotný, and A. Donarini, *Phys. Fluids* **17**, 100613 (2005).
- [39] A. N. Jordan and E. V. Sukhorukov, *Phys. Rev. Lett.* **93**, 260604 (2004).
- [40] D. A. Bagrets and Yu. V. Nazarov, *Phys. Rev. B* **67**, 085316 (2003).
- [41] C. Flindt, T. Novotný, A. Braggio, M. Sassetti, and A.-P. Jauho, *Phys. Rev. Lett.* **100**, 150601 (2008).
- [42] W. Belzig, *Phys. Rev. B* **71**, 161301 (2005).
- [43] J. P. Pekola, O.-P. Saira, V. F. Maisi, A. Kemppinen, M. Möttönen, Yu. A. Pashkin, and D. V. Averin, *Rev. Mod. Phys.* **85**, 1421 (2013).